Springer Series in
Surface Sciences

5

Editor: Robert Gomer

Springer Series in **Surface Sciences**

Editors: Gerhard Ertl and Robert Gomer

Volume 1: **Physisorption Kinetics**
By H. J. Kreuzer, Z. W. Gortel

Volume 2: **The Structure of Surfaces**
Editors: M. A. Van Hove, S. Y. Tong

Volume 3: **Dynamical Phenomena at Surfaces, Interfaces and Superlattices**
Editors: F. Nizzoli, K.-H. Rieder, R. F. Willis

Volume 4: **Desorption Induced by Electronic Transitions, DIET II**
Editors: W. Brenig, D. Menzel

Volume 5: **Chemistry and Physics of Solid Surfaces VI**
Editors: R. Vanselow, R. Howe

Volume 6: **Low Energy Electron Diffraction**
Experiment, Theory and Surface Structure Determination
By M. A. Van Hove, W. H. Weinberg, Chi-Ming Chan

Chemistry and Physics of Solid Surfaces VI

Editors: R. Vanselow and R. Howe

With 341 Figures

Springer-Verlag Berlin Heidelberg New York
London Paris Tokyo

Professor Ralf Vanselow

Department of Chemistry and Laboratory for Surface Studies,
The University of Wisconsin-Milwaukee,
Milwaukee, WI 53201, USA

Dr. Russell Howe

Department of Chemistry, University of Auckland,
Private Bag, Auckland, New Zealand

Series Editors

Professor Dr. Gerhard Ertl

Institut für Physikalische Chemie, Universität München, Sophienstraße 11
D-8000 München, Fed. Rep. of Germany

Professor Robert Gomer

The James Franck Institute, The University of Chicago, 5640 Ellis Avenue,
Chicago, IL 60637, USA

ISBN-13: 978-3-642-82729-7 e-ISBN-13: 978-3-642-82727-3
DOI: 10.1007/978-3-642-82727-3

Library of Congress Cataloging-in-Publication Data. (Revised for vol. 6). Chemistry and physics of solid surfaces. (v. 1–5: Springer series in chemical physics ; v. 20,) (v. 6: Springer series in surface sciences ; v. 5). At head of title, v. 1: CRC. Vol. 3 edited by: Ralf Vanselow, Walter England; v. 5–6 edited by R. Vanselow and R. Howe. Vol. 3 published in: Boca Raton, Fla. Vol. 4– published: Berlin ; NewYork : Springer-Verlag. Includes bibliographical references and indexes. 1. Surface chemistry. 2. Solid state chemistry. I. Vanselow, Ralf. II. Tong, S.Y. III. Chemical Rubber Company. IV. Series: Springer series in chemical physics ; v. 20, etc. V. Series: Springer series in surface sciences ; 5. QD508.C48 541.3'453 77-25890

Softcover reprint of the hardcover first edition 1986

2153/3150-543210

This volume is dedicated
to two former co-authors,
both pioneers in the field
of modern catalysis

Paul H. Emmett
(1900–1985)

Georg-Maria Schwab
(1899–1984)

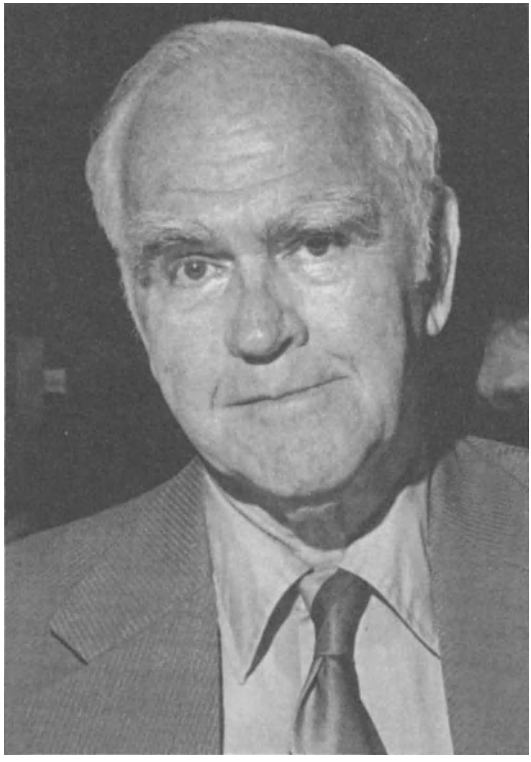

Paul H. Emmett

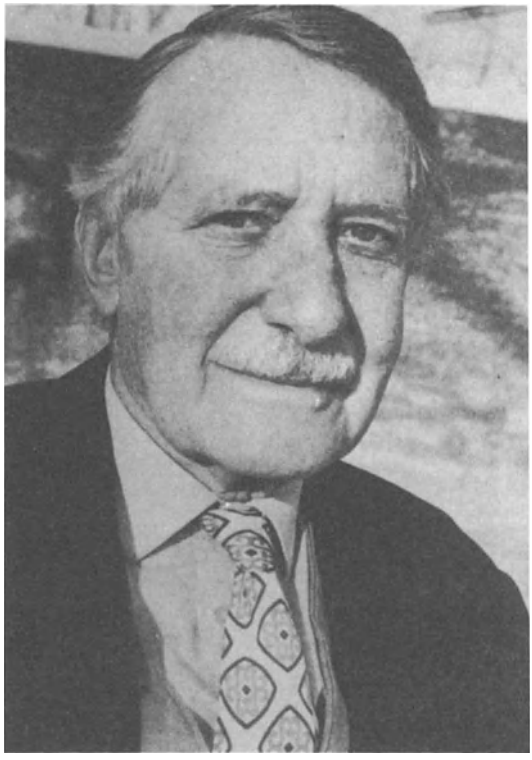

Georg-Maria Schwab

Preface

This volume contains review articles which were written by the invited speakers of the seventh International Summer Institute in Surface Science (ISISS), held at the University of Wisconsin - Milwaukee in July 1985. The form of ISISS is a set of tutorial review lectures presented over a one-week period by internationally recognized experts on various aspects of surface science. Each speaker is asked, in addition, to write a review article on his lecture topic. No single volume in the series Chemistry and Physics of Solid Surfaces can possibly cover the entire field of modern surface science. However, the series as a whole is intended to provide experts and students alike with a comprehensive set of reviews and literature references, particularly emphasizing the gas-solid interface. The collected articles from previous Summer Institutes have been published under the following titles:

Surface Science: Recent Progress and Perspectives, Crit. Rev. Solid State Sci. 4, 125-559 (1974)

Chemistry and Physics of Solid Surfaces, Vols. I, II, and III (CRC Press, Boca Raton, FL 1976, 1979 and 1982), Vols. IV and V, Springer Ser. Chem. Phys., Vols. 20 and 35, (Springer, Berlin, Heidelberg 1982 and 1984).

The field of catalysis, which has provided the major impetus for the development of modern surface science, lost two of its pioneers during 1984 and 1985: Professors G.-M. Schwab (1899-1984) and P.H. Emmett (1900-1985). Both of these distinguished scientists have been associated with ISISS; Professor Emmett presented the opening lecture at the first Summer Institute in 1973 [P.H. Emmett: "Fifty Years of Progress in Surface Science", Crit. Rev. Solid State Sci. 4, 127, 1974] and Professor Schwab's opening lecture at the fourth Summer Institute appeared as a review article in Volume III of this series [G.-M. Schwab: "Development of Kinetic Aspects in Catalysis Research," Chemistry and Physics of Solid Surfaces III (CRC Press, Boca Raton, FL 1982) p.1], although Professor Schwab was at the last minute prevented by ill health from attending the meeting. Chemistry and Physics of Solid Surfaces VI is dedicated to the memory of Professors Schwab and Emmett, and tributes to them are presented in Chaps. 1 and 2 by their former students Professors *J.H. Block* and *W.K. Hall*.

The links between classical catalysis and modern surface science pioneered by Schwab and Emmett are developed further in this volume by *Sinfelt*, who reviews the subject of catalysis by metals with particular emphasis on supported bimetallic clusters. *Hall* uses the molybdena-alumina system to illustrate progress in the understanding of supported transition metal oxide catalysts, while recent advances in the structure determination of zeolite catalysts are reviewed by *Thomas*. The use of model single-crystal surfaces to investigate the effects of promoters and poisons on catalytic reactions is discussed by *Goodman*. Models of a different kind are described by *Gates*, who reviews the use of organometallic complexes to prepare metal cluster cat-

alysts supported on high-surface-area metal oxides. *Madix* describes the use of synchrotron radiation to characterize adsorbed species, and the thermodynamics and kinetics of weakly chemisorbed phases are discussed by *Grunze*. The kinetics of surface reactions is covered by *Yates*. *Campion* describes how recent advances in instrumentation now permit Raman spectra to be obtained from adsorbed molecules on single-crystal surfaces without surface enhancement.

Advances continue to be made in the various forms of microscopy for examining surface structures. *Smith* describes the use of high-resolution electron microscopy to observe surface features, and the new technique of scanning tunneling microscopy for measuring surface topography is reviewed by *Behm*. *Tsong* describes the study of gas-surface interactions with the time-of-flight atom-probe field ion microscope, and *Melmed* gives an account of the current status of field emission microscopy.

Electron scattering from surfaces is considered from a theoretical viewpoint by *Tong*, while *Bauer* describes the use of low-energy alkali ion scattering to determine surface structures. *Kirschner* outlines the use of spin-polarized electrons in various surface analytical techniques. The relatively novel technique of inverse photoemission spectroscopy is reviewed by *Dose*. *Himpsel* discusses surface electronic states, and the subject of wetting of solid surfaces by adsorbed layers is covered in the the final chapters by *Passell* and *Ebner*.

As in previous volumes, an extensive subject index is provided.

We would like to thank the sponsors of ISISS: the Air Force Office of Scientific Research and the Office of Naval Research (Grant No. N00014-85-G0140) as well as the College of Letters and Science, the Laboratory for Surface Studies and the Graduate School of the University of Wisconsin-Milwaukee for making both the conference and publication of this volume possible. The cooperation of the authors and the publisher in achieving rapid publication is also acknowledged.

Milwaukee, Auckland
October 1985

R. Vanselow
R.F. Howe

Contents

1. Georg-Maria Schwab: Early Endeavours in the Science of Catalysis

J.H. Block

Fritz-Haber-Institut der Max-Planck-Gesellschaft, Faradayweg 4-6, D-1000 Berlin 33

Georg Maria Schwab, one of the few Grand Seigneurs in the field of catalysis, died on 23 December 1984, at the age of 85. The sad news of his sudden death came as a surprise since he had been mentally sharp and in excellent health up to the last days of his life. Indeed, he was studying the weather forecast a few days before he died, planning to spend part of Christmas vacation skiing in the Alps. Schwab was active in science till the end of his life. At the VIII International Congress on Catalysis, of which he was the Honorary President, in 1984 in Berlin, Georg-Maria Schwab impressed a large international audience with his excellent scientific lecture. And a few years ago, long after his retirement, Schwab contributed with the "Development of Kinetic Aspects in Catalysis Research" to the 4th International Summer Institute in Surface Science.

The early development of science in catalysis is closely connected with the name Georg-Maria Schwab. He was, like Paul Emmett, one of the great old masters of catalysis, who introduced a scientific foundation to a field which was till then only poorly empirical. As a former student and junior colleague of Schwab in the 50s, the honor falls upon me to present here a sketch of his life and to describe the great influence his thinking and work had upon science.

There was much in Schwab's life that was unusual. The direct personal confrontation with contradictions early on in life may partially explain Schwab's independence. Although born in Berlin, in 1899, he had Bavarian citizenship, which in the Prussia of that time was equivalent to being a foreigner. The reason for this pecularity was his parents' origin in Bavaria; his father had been displaced to Berlin where he was managing editor of an important newspaper. Schwab's role as an outsider lead to a certain restraint regarding the military orientation of Prussia and the obedient respect for authority, which was so much a part of a Prussian upbringing. Consequently, when he was called to serve in World War I as a 18-year-old, he pledged his allegiance not to the Prussian flag, but to the Bavarian.

In 1918 he returned safe and sound from the battlefield of Flanders and began to study chemistry in Berlin. After his examinations he joined the laboratory of Walter Nernst, where he received his doctor's degree in 1923 with a

work on the properties of ozone, which was performed under the guidance of Professor Riesenfeld. Today it is hard to remember that back in the 20s the question was still open as to whether ozone, as a high-atomic-weight modification of oxygen, also included oxozone, O_4. Schwab's task was to determine the amount of active oxygen species (that is, oxygen species higher than O_2) in the form of O_3 and possibly O_4 from vapor density measurements and iodine titration. The presentation of this early problem was argumentatious; typical for Schwab. He set forth a certain doubt or contradiction as his premise and then used the result of his experiments to solve the problem: Both methods, titration and vapor density, only give the right amount of O_3 and O_4 in the composition when used in combination with fractional distillation. In Schwab's own words: "Applied alone or together, they only lead to the correct molecular weight when this weight is assumed from the beginning. This logical error is inherent in most of the work done on ozone in the last century". And so, with his dissertation, G.-M. Schwab had refuted the theory of oxozone.

A similar situation, by the way, arose a few years later with hydrogen. Triatomic hydrogen, H_3, also called ozone hydrogen, was haunting the literature. Sir J.J. Thomson had found H_3^+ ions during his first studies with the mass–spectrometer and surmised that it was formed by the ionization of neutral H_3. Since the differences in characteristics and stability between neutral molecules and ions were not yet very clear, there were quite a few people who were searching for neutral H_3. Among them were Wendt and Landauer from Chicago, and also Paneth and co-workers from Berlin, who published methods for producing and identifying H_3. At that time Schwab and Seuferling were occupying themselves with the chemical processes of silent discharges (coronas), including those of hydrogen, and so they also investigated this question. They were particularly suspicious of the reaction of H_3 with elemental sulfur, which was supposed to yield easily traceable H_2S, so they developed a detection procedure using arsenic. The formulation of their results was logically consistent, but cautious: "We consider it proven that in silent discharges at 50 mm pressure some kind of active hydrogen is formed. For the time being we cannot and do not want to say anything about its nature. It could quite well be identical to atomic hydrogen" [quote from Z. Elektrochem. **34** (1928)].

Today we know that the identification methods used then were not very specific, and that, for example, vibrationally excited molecular hydrogen reacts differently from molecular H_2 in its ground state. And in fact, as early as in 1927 Paneth discredited the theory of "ozone hydrogen", so Schwab's cautious conclusion was indeed justified.

After receiving his doctorate, Schwab worked for more than two years with Max Bodenstein, Nernst's successor. His work at this time was mainly concerned with the kinetics of gases under the influence of electron excitation. The first catalytic investigations came about by chance when it was noticed that on glow cathodes during electron impact on methane, the electron excitation led to different products than did thermal activation on the cathode surface. This was the first time that the Polanyi theory of catalysis was mentioned and the occurrence of an active state with intermediate atomic states was assumed.

These few examples give an idea of Schwab's first scientific papers which at the outset had mostly to do with the characteristic and reactions of gases. Schwab's scientific productivity spans 62 years. His first paper "The Additivity of the Critical Volume as a Quantum Function" [1.1] appeared in 1922. It dealt with a comparison of the mole volumes of different gases. His last paper "On the Apparent Compensation Effect" [1.2] appeared in 1984. In the time between these two publications a diverse assortment of nearly 300 scientific publications appeared with a very unusual breadth of scope, in contrast to the usual narrowness of a researcher's specialty nowadays. He published important papers on everything from reactions in solids to inorganic chromatography, from photochlorination to ferment models, from homogeneous gas kinetics to the photographic process, from the Kjeldahl reaction to parahydrogen conversion, but his most important work was on heterogeneous catalysis, and it is this field which we now examine more closely.

In 1931 Schwab published a book, "Catalysis From the Standpoint of Chemical Kinetics", to great acclaim. Fundamental laws of heterogeneous kinetics were developed. It became a classical issue, was translated into many languages and gained Schwab international recognition.

Forty-five years ago a book appeared which became a milestone on the path of catalytic research. The book was the "Handbuch der Katalyse" and it was written by G.-M. Schwab. In the introduction to this Handbook series Professor Schwab wrote: "Today we still ask with the same unsatisfied curiosity why a certain substance catalyses a particular reaction or does not. Even today this is still an unsolved riddle of catalysis."

We should ask ourselves whether, and if so, to what extent, the question G.-M. Schwab posed 45 years ago can be answered today. In the time since then a large number of effective analytical procedures to characterize the surfaces of catalysts have been thought of and tested. We know a wealth of details about crystallographic structures and their chemical composition, about the properties of adsorption layers and the dynamics of interactions at interfaces. But although over four tumultuous decades of development in interface research lie

behind us, the question G.-M. Schwab asked, why a particular substance will or will not catalyse a particular reaction, is close to being answered only in a few special cases.

If we trace the development of catalysis by using Schwab's work as a basis, we come across many old fundamental questions which today have been approached with new methods. Many of Schwab's earlier papers have been consigned to oblivion and many phenomena already described in Schwab's work have, sometimes reinvented, now become major research fields.

The theory of "adlineation", which he developed with *Pietsch*, was a counterpart to H.S. Taylor's concept of "active centers". In his paper on the topochemistry of contact-catalysis *Schwab* wrote: "We can by now describe the active centres as homogeneous lines, an interpretation within which kinetics laws retain their original validity, also if the existence of active areas is proven" [1.3]. Aspects of this theory of adlineation can be found in more recent papers dealing with the influence of line defects of edges and steps on surface reactions, such as the work done by G. Somorjai.

Schwab's first productive period in Munich was ended by the Nazi regime. The Nürnberg Laws forced him to emigrate. As his place of exile, he chose Greece, where he married Elly Agallidis. They had met in Munich when he was her doctoral advisor. He became a researcher in the Inorganic, Physical and Catalytic Chemistry Department of the Institute Nicolaos Canellopulos in Piraeus, Greece. In this industrial factory he could do basic research only on the side with a few unpaid colleagues. His situation deteriorated steadily after the occupation of Greece by German soldiers. In 1942 his passport was revoked and he was forbidden to publish scientific papers in German-language journals. But, under these almost hopeless circumstances, Schwab continued to do research, granted by very modest resources. In fact, it was during this period, in which he was under deep personal stress, that his most important ideas originated, those having to do with the connection between heterogeneous catalysis and solid state theory. G.-M. Schwab's perception that heterogeneous catalysis is fundamentally connected with solid state physics must count among his most important scientific achievements. This brilliant work was done towards the end of the war when his situation was most dangerous and material privation the greatest. This was the first time that the thesis that metal electrons probably influence catalysis was proposed.

As can be seen from Fig.1.1 (reproduced from the original work), the paper "Metal Electrons and Catalysis" was accepted by Norrish for publication in the "Transactions of the Faraday Society" in January 1946. These diagrams illustrate the relationship between the activation energy of the catalytic dehydrogenation

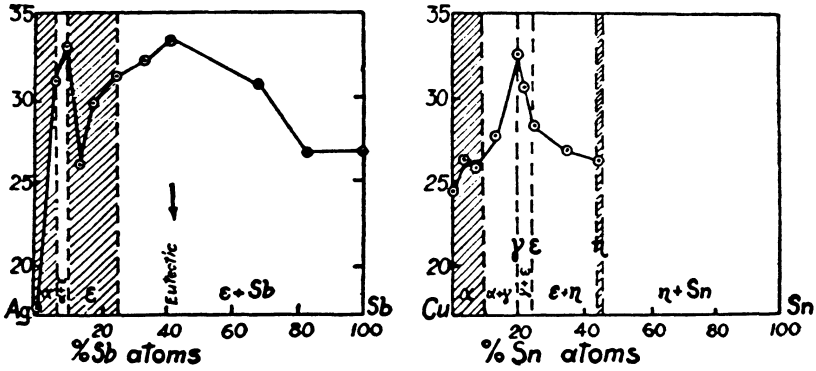

Fig.1.1. The first correlation between electronic properties and catalysis [1.4]

of formic acid and the electron density in alloy phases, which in Ag/Sb and Cu/Sn vary with the doping. These diagrams caused a lot of excitement in scientific circles because the idea of a connection between electron density and catalytic activity was completely new and unexpected.

I would like to quote from the paper's summary:

"It is found that within the domain of the γ-phases of Hume-Rothery alloys, the activation energy increases linearly or less with the solute concentration, but with the square of the excess electron number of the solute",

and

"All the described results may be expressed in terms of the wave-mechanical theory of the Hume-Rothery phases by a dependence of the activation energy on the degree of electron saturation of the first Brillouin zone of the metal. This leads to the concept that catalytic activation consists in a transition of electrons from the substrate to the metallic catalyst".

The conditions under which Schwab had to work are evident from the acknowledgements:

"I desire to express my gratitude to my faithful collaborators, Mrs. E. Schwab-Agallidis, Mr. G. Holz, and Mr. A. Karatzas, and, especially, to Professor G. Matthaeopoulos and Dr. K. Makris who most hospitably received our air-damaged laboratory during the year 1944 in the rooms of their Chemical and Microbiological Institute and so enabled us to finish the present investigations".

A thank-you for financial support was not necessary. He did not receive any.

This was the hour of birth for the theory of "electronic factors" in catalysis. This theory awakened researchers in many nations and provided the basis for lively discussion for decades. At the beginning, consistent rules were

found for the systems investigated, and a certain optimism took hold. Hume-Rothery phases seemed to be a simple case of an electronic factor in catalysis but the more scientists became occupied with related problems, the more they found that a seemingly very simple result can entail some very complicated original facts. All the problems of electron transfer for chemical bond formation and bond excitation are involved and the electronic factor in catalysis is, in general, still an unsolved problem.

Among the many other problems, I would like to select one where an old idea of Schwab's recently gained great attention; it is the connection between phase transitions and catalysis:

In a Swedish journal, *Schwab* published – together with *Elly Schwab-Agallidis* – a paper entitled: "Is There Coupled Gas-Solid Catalysis?" [1.5]. Falling back on work done by Hedvall and co-workers, he studied the influence of the catalytic cracking of formic acid and ethanol on the phase-transition temperatures in solids with the intention to discover whether the reaction is influenced by the phase transition and vice versa. Schwab was not able to reach any generally valid conclusions, however. The question of the reaction kinetic parameters during phase transitions on and in solids is avidly being discussed today, especially in the light of the appearance of the 'chaos phenomenon'. A particularly good present-day example which brilliantly answers the question posed by G.-M. Schwab in 1946, came from *G. Ertl* in 1985 in a publication entitled "Catalysis and Surface Phase Transformation" [1.6]:

"Two different structures are formed in the chemisorption of CO on Pt{100}, a hexagon in the case of little coverage and a 1×1 structure with 1/2 monolayers. The oxidation of the CO with oxygen in the gas phase occurs with a transition from the 1×1 to the hexagonal structure, which reverts once again to 1×1 after the adsorption of CO. The phase transition has a direct effect on the speed of the reaction, which is accompanied by oscillations" and "The observation of kinetic oscillations in the platinum catalyzed oxydation of CO represents a fascinating example for intimate connections between structural phase transitions and catalytic activity of a surface".

This is a precise answer to the question posed by Schwab in 1946.

In 1949 Schwab became Professor for Physical Chemistry at the Technical College in Athens. This position he kept for many years, also after he came back to Germany. From 1950 Schwab was Professor for Physical Chemistry at the Ludwig-Maximillians University at Munich. Here he attracted young scientists from all over the world to perform research work in many disciplines of physical chemistry; problems in catalysis, solid-state reactivity, and chromotography were major fields of interest. More than 300 scientific papers have

been published, many summarizing articles and monographs. Schwab had a talent for languages, he wrote his manuscripts and gave talks in 6 different languages: German, English, French, Greek, Italian, and Spanish. He was an enthusiastic and inspiring teacher. His poetical style has been particularly admired: a master of Spoonerism and a brilliant speaker at banquets. Schwab was a devoted alpinist. As a young man he even climbed up the north front of the three storey Institute building in Munich.

A large number of students and guest scientists, of whom many are now in leading academic and industrial positions, made Schwab's Institute for Physical Chemistry in Munich a world-famous center for catalysis studies. Even after his retirement in 1971 G.-M. Schwab continued to be scientifically active. He devoted a part of his energies to his second homeland. He set about working on methods to save antique art treasures in Greece which had been damaged by environmental pollution.

During his many years of scientific activity Prof. Schwab received many outstanding honors: He was given membership of the Bavarian Academy of Sciences, of the "Leopoldina" in Halle, and of the academies in Vienna and Heidelberg. Numerous honorary doctorates were bestowed upon him, from the universities of West Berlin, Paris, Liêge, and Hamburg. The University of Caracas in Venezuela awarded him an honorary professorship. Among his many other honors were the Liebig Medal of the Association of German Chemists, the St. George Order of Greece, an officership in the order of the Belgian Crown, and many, many honorary association memeberships and chairmanships.

There are certainly very few scientists in this century who have contributed as much to the field of catalysis as Georg-Maria Schwab. His personality was notable for its benevolence and serenity, sparked by an enigmatic and subtle sense of humor. Regarding himself and his achievement he was modest and unpretentious, and his friendly and almost fatherly relationship with his many students was a bond until his death. We will remember G.-M. Schwab as an exceptional human being, ingenious and humorous, who radiated an inner warmth which cannot be forgotten.

Acknowledgement. Mrs. N. Kublin-Brendecke and Mrs. I. Reiffel have been most helpful in preparing the English text.

References

1.1 G.-M. Schwab: Z. Phys. **11**, 188 (1922)
1.2 G.-M. Schwab: J. Catal. **84**, 1 (1984)
1.3 G.-M. Schwab, E. Pietsch: Z. Phys. Chem., Abt.B **1**, 385 (1928)
1.4 G.-M. Schwab: Trans. Faraday Soc. **42**, 689 (1946)
1.5 G.-M. Schwab, E. Schwab-Agallidis: Särtryck ur Svensk Kemisk Tidskrift **58**, 161 (1946)
1.6 G. Ertl: Surf. Sci. **152**, 328 (1985)

2. The Life and Times of Paul H. Emmett

W.K. Hall

Department of Chemistry, University of Wisconsin-Milwaukee, P.O. Box 413, Milwaukee, WI 53201, USA

Another of the great pioneers in the areas of surface science and catalysis has departed. Professor Paul H. Emmett died on April 22, 1985 just a few months before his 85th birthday. It is my privilege to present here a personal account of his career.

Professor Emmett had a special role in the development of the University of Wisconsin-Milwaukee (UWM) and the International Summer Institute in Surface Science. He acted as a consultant to the Department of Chemistry in setting up its new PhD program in 1968, and helped to establish the Laboratory for Surface Studies. He presented the opening lecture at the first International Summer Institute in Surface Science in 1973, lecturing on "Fifty Years of Progress in Surface Science". For his service to UWM, he was awarded an honorary degree of Doctor of Science in 1973. He attended the first Gordon Conference on Catalysis held in 1940, and was its third chairman in 1945. It was a matter of pride with him that he missed only one such conference up to and including 1984.

We who knew him well recognized him as a staunch friend and sound counsellor. He had a prodigious memory, a critical attitude towards research, and time and again guided us in new and promising directions. We all thought of him as someone special. He was so friendly, helpful, and unassuming that few of us ever wondered why. I would like to describe here some of the circumstances which led him to this place of distinction in our hearts and minds.

Professor Emmett once said that in any accounting of the career of a scientist, the circumstances, the events, and the people who influenced his work need to be considered along with his research accomplishments. The following is a summary of his contributions in the perspective of the times during which they were made. Some of the events affecting his life and career are idenified by numbers in Fig.2.1 which correspond to those in parentheses in the text.

Professor Emmett was born (5) on September 22, 1900 in Portland, Oregon. These were truly horse and buggy days. The electric light bulb had been invented only 21 years earlier (1) and in 1900 the first trial of metropolitan lighting was made part of Manhattan (5). The internal combustion engine had

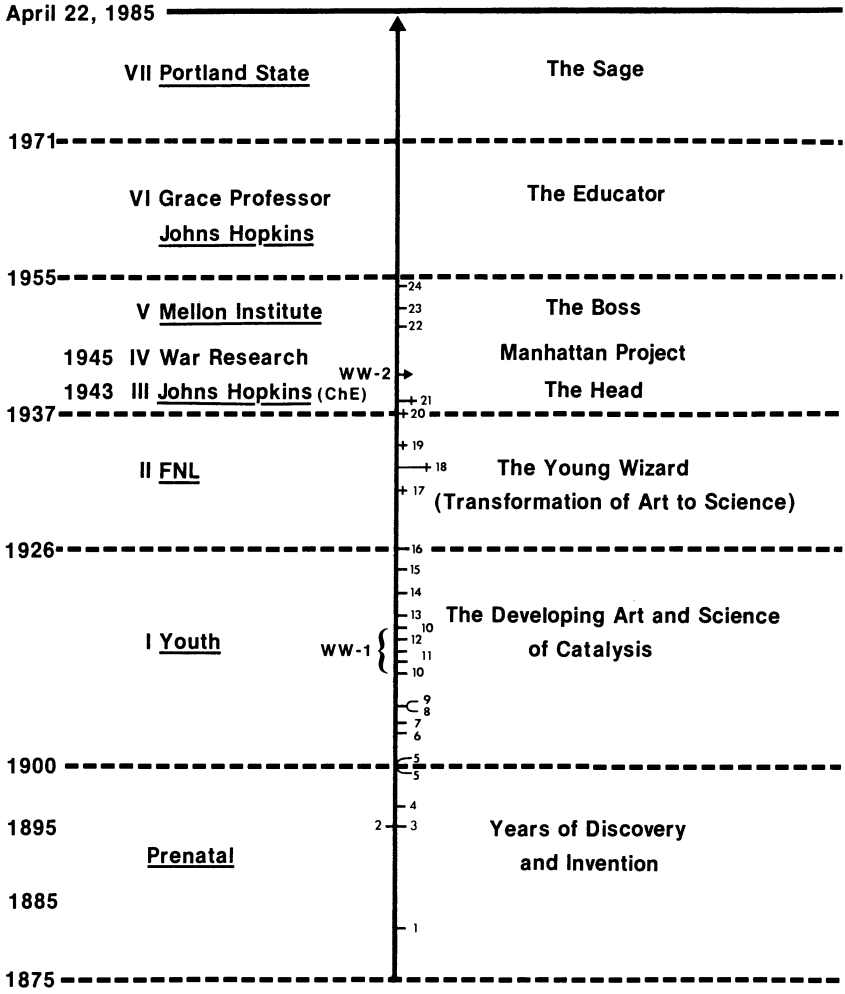

Fig.2.1. The life and times of Paul H. Emmett

been invented (2) only 6 years earlier (1894), and in 1904, the Ford Motor Company was founded (6): the following year, when Emmett was 5, the Wright brothers flew the first plane at Kitty Hawk (7). This was truly a period of great invention and discovery.

Catalysis was in a similar rudimentary condition. Stohman (3) stated in 1894, "Catalysis is a process involving the motion of atoms in molecules of labile compounds which results from the presence of a *force* emitted by another compound, and which leads to the formation of more stable compounds and the liberation of energy." (Note that the postulate of a mysterious force is a

modernization of the old concept of the philosophers stone!) Catalysis received an important stimulus in 1897 when Sabatier (4) observed that he could hydrogenate olefins over nickel. Although his peers recognized this accomplishment as the solution of a long standing problem in chemical synthesis, they considered the catalysis as a mysterious black art which nonetheless deserved a Nobel Prize (1912). Today we know that Sabatier discovered that catalysis can circumvent a "symmetry-forbidden reaction".

Emmett was 9 years old when Fritz Haber (8) solved another long-standing problem; the direct synthesis of NH_3 from the elements. During the last quarter of the 19th century, the laws of mass action and chemical equilibrium had become understood (Nernst and Ostwald). Haber recognized that the equilibrium became less favorable as the temperature was raised (exothermic reaction), but that high temperatures were evidently necessary to break the strong $N \equiv N$ bond. He recalled a hint from Berzelius (1836) that sometimes one can "add a catalyst instead of heat". Thus, having defined the problem he set out to establish feasible reaction conditions; he anticipated that small equilibrium concentrations of NH_3 might be formed and so invented the catalytic recycle reactor and discovered that osmium would function as a catalyst. This change from static systems to dynamic flow systems was a new concept which became one of the foundations of modern chemical engineering. Haber received the Nobel Prize for this work in 1918. The important role of the Haber process in the First World War (WW-1) was not lost on Emmett in his late teens.

Wilhelm Ostwald (9) was the recipient of the Nobel Prize in 1909, partly for his discovery (1904) that HNO_3 could be produced via the catalytic oxidation of NH_3 over Pt. In his laureate address he stated, "The employment of the concept of catalysis has served hitherto as an indication of scientific backwardness." (Ostwald evidently thought that recent developments, his own included, had made catalysis more respectable!)

Haber reached an agreement with BASF in 1909 and the commercial development of the ammonia synthesis was turned over to Carl Bosch and catalyst development to Alwin Mittasch. The approach taken was a brute-force investigation of the periodic table including mixtures of elements and compounds. By the end of 1911 approximately 6500 two-week tests had been carried out over 2500 compositions; by 1919 the number of tests exceeded 10000 over more than 4000 compositions. Several significant points should be made here: a) in 1919 a very successful NH_3 synthesis process had been developed, b) the effectiveness of promoters had been recognized, but not understood, and c) catalyst development was clearly an *art*, not a *science*.

The onset of the First World War (10) had many important consequences. Among these it vastly accelerated the growth of the Haber process in Germany, which reached a capacity of 60000 tons/day in 1917, thus frustrating the British navy's attempt to deprive Germany of a source of (Chilean) nitrates. Indirectly, this led to the establishment of the Fixed Nitrogen Laboratories (FNL) in the United States. Finally, in 1916 a young assistant professor from Princeton, H.S. Taylor, a British citizen, returned to England to initiate with Eric Rideal, the Anglo-American School of Catalysis (12). A result of this collaboration was the book entitled "Catalysis in Theory and Practice", which was published in 1919. It was one of Professor Taylor's students, Dr. Arthur Benton, who became Emmett's research advisor at Caltech (14), and it was from Benton that he learned the state-of-the-art techniques for studies of adsorption and catalysis. Emmett's thesis work, "Investigation of Auto-catalysis in the Reduction of Metal Oxides with Hydrogen, could have been translated as "Factors in Catalyst Preparation". Emmett held Taylor in great esteem; he tended to evaluate papers from his own laboratories in terms of what he thought Taylor would think of them. In later years this respect became mutual.

Two significant events related to the development of surface science occurred about this time. The famous Langmuir papers appeared (11) which identified chemisorption with surface compound formation, defined the chemisorption isotherm quantitatively, and introduced the concept of surface reaction between atoms or molecules chemisorbed on adjacent sites. Langmuir received a Nobel Prize for his work in 1932. Then, as Emmett was completing his thesis work, H.S. Taylor's concepts of activated adsorption and desorption appeared (15). The stage was thus set for Emmett's career to be devoted to the conversion of the art of catalysis into a science.

When the allied armies of occupation entered Germany in 1919, they "liberated" (13) a barrel of the up-to-then secret iron synthetic ammonia catalyst. The barrel was shipped back to the United States to the FNL, where it was shortly found to operate as expected. It was thought that it would be a simple matter to analyze it and duplicate it, but this turned out not to be so. It was not until 1925 that it was discovered that a small amount (about 0.5%) of K_2O made a big difference. This had been understandably missed in the earlier analyses, and then thought to be simply an impurity. Other problems had been encountered, e.g., catalyst preparations of identical composition could not be reproduced, aging and poisoning effects were unpredictable, and the function of promoters was not understood. This was the state of affairs in 1926 when Emmett joined the FNL (16). Nothing was known about the reaction kinetics

or mechanism, uncertainties remained in the thermodynamics, and yet in spite of these unpredictables, large-scale plants producing up to 10^5 tons of NH_3 per day were feasible and proven by the German work.

Emmett was put in charge of a group of FNL and asked to apply the techniques of physical chemistry to solve some of these problems. The accomplishments of this group greatly exceeded any reasonable expectation. The thermodynamics of the important ancillary water gas shift reaction were established (17), and similarly those of the Fe_xN phases were established and found not to function as intermediates in the synthesis. It was noted, however, based on work of Almquist and Black (1926), that the thermodynamics of surface layers could be very different from those of the bulk.

The first reliable kinetic data for NH_3 synthesis and decomposition were obtained (18). Emmett used to tell a story about his technician, Katherine Love, who made these measurements. Miss Love was extremely nearsighted so by removing her glasses and moving her eyes very close to the manometer she could estimate an additional significant figure that no one else could read. Thus, Emmett obtained superior data.

While these studies were going on, Emmett, working with Stephen Brunauer, started looking into the variability of various catalyst preparations. It was soon recognized that a means was needed to measure the surface areas of their catalysts and two approaches were taken: physical adsorption and (following Langmuir) chemisorption. A brilliant and extensive set of experiments revealed that physical adsorption was nonselective and that *Point B* (20) taken from appropriate isotherms could be used to estimate the total surface area of powders to within about 10%. This perspective soon led to the multilayer concept for physical adsorption and the familiar Brunauer-Emmett-Teller (BET) equation (21). However, much more was accomplished. It had been recognized for many years that the upper (higher-pressure) portions of physical adsorption isotherms should be dominated by capillary condensation (Kelvin equation) and a consideration of multilayer adsorption with superimposed capillary condensation led to present-day methods of measuring pore size distributions. Much could be said about this aspect—how the concepts evolved from qualitative to quantitative—but it will suffice to say that it was Emmett a decade later a Mellon Institute who guided the work of Barrett, Joiner, and Hallenda in the development of the sophisticated theory presently used to provide pore volume and area distribution data on a routine basis, and who matched their results with those obtained from mercury porosimeter data. Thus, the work of Emmett and co-workers formed the foundations on which present-day methods of determination of catalyst (adsorbent) morphology, structure, and surface area rest.

Given V_m, the monolayer capacity, the chemisorption approach became equally rewarding. Methods of selective chemisorption were worked out to measure the extent of exposed iron surface on supported catalysts. The differentiation between structural promoters and chemical promoters was made. Using the selective chemisorption of CO_2 to measure the fraction of the surface covered by K_2O, Emmett was able to explain why 0.5% of this promoter could have such a profound effect on the catalytic behavior. His result (27% of the surface covered by K_2O) is in excellent agreement with similar recent estimates based on ESCA (electron spectroscopy for chemical analysis) data.

The chemisorption work revealed as early as 1934 that the rate of NH_3 synthesis was approximately equal to the rate of the chemisorption of N_2. When it was assumed that the rate determining step in the synthesis was the *dissociative* chemisorption of N_2, it was found that the kinetic data were in excellent agreement with the theoretical treatment of Tempkin and Pyzhev (1940). This picture was challenged, then confirmed, and finally beautifully substantiated by the recent works of Ertl, de Boer, and Boudart. Thus, the work at FNL laid a firm foundation for modern surface science. Emmett was elected to the National Academy of Science based on this work (22) in 1949. There are those who feel that he could have been—perhaps should have been—a Nobel laureate.

In 1937, Emmett left FNL to head a newly formed Department of Chemical Engineering at Johns Hopkins University and had it accredited within 3 years. In this period, and while he was on leave to the Manhattan Project between 1943 and 1945, his research at Johns Hopkins continued and was directed toward finding independent ways to measure surface areas with model systems for comparison with the BET results. Some of this continued during his early years at Mellon Institute and was finally nicely corroborated by the absolute method of Harkins and Jura, as well as by the sum of the areas of the pore walls obtained by the Barrett, Joiner, and Hallenda method. Hence, when in 1950 the validity of the BET equation was seriously questioned by George Halsey (23), Emmett simply smiled and noted that, right or wrong, the theory worked. Halsey clained that if the assumption made by BET were valid, the isotherms should have steps. These have since been found for homogeneous surfaces.

Paul Emmett arrived at Mellon Institute in 1945 to head the catalysis research sponsored by the Gulf Research and Development Company. At that time there was great concern about United States petroleum reserves. The German army had used synthetic liquid fuels during the Second World War (WW-2); the United States had plenty of coal, so why shouldn't we follow suit? Interestingly, the first attempts at synthesis of hydrocarbons had been made at

BASF in 1912 with modest (patentable) success. It was an obvious variation to substitute CO for N_2 in the existing pressure flow ammonia synthesis reactors. An interesting story exists leading up to the commercial development in 1938, based on the work of Franz Fischer and Hans Tropsch, but it will suffice to say here that the situation in 1945 was analogous to that concerning the NH_3 synthesis in 1926 (except for the much more complicated product distribution, which was not known in any detail).

Emmett approached this new challenge in much the same way that had been so successful for the NH_3 synthesis. He examined the thermodynamics of the carbide phases which form concomitantly with synthesis and showed that they could not be intermediates. Then, with the evolution of ideas of chain growth, he saw the opportunity to add radioactive compounds into the synthesis. If any of these transformed into the same intermediates being formed from CO and H_2, all products of higher carbon number would have the same radioactivity per mole. This was confirmed and mechanistic ideas were developed which helped establish our knowledge of chain building. He maintained his interest in adsorption problems of all kinds. The Second World War had created new demands for catalysis; catalytic cracking and isomerization to generate aviation gasoline, butadiene for synthetic rubber, etc. Emmett became interested in properties of acid catalysts and in particular how hydrocarbons adsorb, form carbonium ions, and how these transform. He (with MacIver) showed how very small chemisorptions could be detected and measured using a radioactive adsorbate.

I first met Paul Emmett in 1946 and came to work with him in 1951 where I was joined several months later by Richard J. Kokes who became my laboratory partner for the four years. It was here that we learned about some of Emmett's personal attributes. He was an eternal optimist. He foresaw no reason why a complicated rack of glassware built to the specifications of Joe Kummer (6'7") should cause any difficulties for W.K. Hall (5'7"). He would read a paper and rush into someone's laboratory with an idea for a "simple experiment" which should take no more than a day or two. The only problem was, these simple experiments came faster than they could be done. We kept lists and finally learned to select the most interesting and promising ones to work on. I remember one such idea. Why didn't we make gaseous radioactive formaldehyde and introduce it into the Fischer-Tropsch synthesis? We *did*, but it took two months including one 48-hour shift. Emmett was delighted with the results and promptly suggested that we now try radioactive ketene. The exhausted students agreed to put this one on the back-burner, but Paul never forgot and would occasionally ask about the status of this project. We would give him one excuse or another —usually reminding him of some of his more recent ideas. We were finally saved

when Emmett decided to return to Johns Hopkins, where now George Blyholder got the job and managed to get the desired results in something less than two years. Dogged determination was another Emmett characteristic.

Another form of his optimism was exhibited in his approach to people. He always gave the other fellow, even the most lax members of his own group, the benefit of the doubt. In the nearly 40 years that I knew him, I cannot remember a single instance when he made a derogatory remark; as a referee, he never outright rejected a paper; instead he would sometimes prepare two to three pages summarizing changes needed and additional experiments that were required. He served as referee for the Journal of Catalysis up until late last fall when he finally wrote to me that he no longer felt physically able to do a good job.

Another personal characteristic was what was called at Mellon, "the boss has a bee in his bonnet". These were usually farsighted research opportunities and included, as noted above, the use of radioactive tracers to solve mechanistic problems. Paul evidently got this idea while working with Harold Urey on the Manhattan Project. He obtained the first scaling unit east of the Mississippi and with Joe Kummer devised unique methods of synthesizing the needed radioactive compounds as required, gas handling, and counting. Another was the great opportunities afforded by gas phase chromatography to facilitate mechanistic studies in a variety of ways, including the so-called microcatalytic pulse technique devised by Kokes, Tobin and Emmett in 1954. Finally, one that involved me directly was Paul's curiosity about the new ideas concerning electronic factors versus geometric factors in catalysis. These stemmed from the earlier work of Schwab (1946) as amplified in papers by Dowden, Volkenstein, and particularly Otto Beeck, who published results from a remarkable series of experiments in 1950-52 which introduced the concept of percentage d-character as a correlating parameter for a series of transition metals. Emmett was anxious to pursue these ideas. I remember him coming into my office one day and saying "Keith, I can't ask you to abandon your present work if you don't want to, but I do think that if you would examine hydrogenation over Cu/Ni alloys and find out what is really important, electronic factors or geometric factors, it would make a much stronger thesis than one more piece or work on the Fischer-Tropsch synthesis." I took his advice and we were able to show that the rates of ethylene and benzene hydrogenation were controlled by the frequency factors, not the activation energies as postulated by Dowden. The new microcatalytic technique was used in the ethylene work, another first for metal catalysts. For this it was necessary to invent a dosing device made of stopcocks which has now been replaced by the six way valve.

In his final days at Mellon Institute, Emmett completed editing the seven-volume series of books, "Catalysis", which still serves as a reference source for work before 1955. As my thesis advisor, he demanded that I thoroughly review the literature and write up and evaluate the current ideas on electronic versus geometric factors in catalysis. I had the satisfaction of learning later that this became required reading for some of his students at Johns Hopkins where he became Grace Professor of Chemistry in 1955, a position he held until 1971. Here his role became more that of an educator, although his research interests remained essentially unchanged. Some 15 of his former students became university professors and at least as many others rose to positions of considerable prestige, owing much to their educational experience. At Johns Hopkins, Emmett and his students demonstrated the complexity of cracking reaction of paraffins such as cetane. Notable also was the successful chromatographic separation of ortho from para H_2 as well as the hydrogen isotopes. He also demonstrated (with M.J. Phillips) that the Balandin hypothesis failed when benzene was hydrogenated over iron catalysts. Much of this research remains unpublished although it may be found in the Johns Hopkins library in the form of theses.

In 1971 Professor Emmett officially retired from Johns Hopkins, but actually only moved to a new base of operations at Portland State University where he continued research and active participation in professional activities. His last paper, on modified porosity of coals, appeared in 1983. He remained active in meetings, both National and International. As recently as the summer of 1984, he could be found holding discussion groups at the Gordon Conference on Catalysis. He, like Professor Schwab, did not fade away; he died, as the saying is, "with his boots on!". He will be sorely missed by his friends and colleagues.

3. Three Decades of Catalysis by Metals

J.H. Sinfelt

Corporate Research Science Laboratories, Exxon Research and Engineering Company, Annandale, NJ 08801, USA

This chapter reviews some of the developments in the field of metal catalysis during the past three decades, corresponding to the period of time in which the author has been actively working in the field. The paper is not intended to be a comprehensive review of the whole area. Rather, it concentrates on several aspects of metal catalysis which have been of particular interest to the author. The topics covered include bifunctional catalysis, the characterization of dispersed metal catalysts, hydrocarbon reactions on metals, and bimetallic catalysts.

3.1 Bifunctional Catalysis

Shortly after World War II, a new catalytic process was introduced in the petroleum industry. The process, known as catalytic reforming, employed a catalyst containing a small amount of platinum (about 0.5 wt.%) dispersed on alumina [3.1-3]. The surface area of the alumina was high, typically about 200 m^2/g. In the process, a petroleum fraction consisting predominantly of C_6 to C_{10} saturated hydrocarbons was contacted with the catalyst at temperatures in the range of 700-800 K and at pressures of 10-35 atm [3.4,5]. Alkanes and cycloalkanes in the petroleum fraction were converted extensively to aromatic hydrocarbons, which impart excellent "anti-knock" properties to gasolines used as fuels in internal combustion engines. Another reaction which occurred was the isomerization of n-alkanes to branched alkanes. The latter also have improved anti-knock properties.

Platinum on alumina possesses two different types of catalytic functions, and is therefore known as a bifunctional catalyst. One function is associated with platinum sites, which catalyze hydrogenation and dehydrogenation reactions, while the other is associated with acidic sites on the alumina, which readily catalyze reactions involving a rearrangement of the carbon skeleton of hydrocarbon molecules containing carbon-carbon double bonds. The presence of the acidic sites is readily demonstrated by the affinity of the alumina surface

for such basic molecules as ammonia, trimethylamine, n-butylamine, pyridine, and quinoline [3.6,7].

The nature of the acidic sites on alumina has been the subject of much discussion. The surface is characterized by the presence of hydroxyl groups which could conceivably be a source of Brönsted (protonic) acidity. However, it has been concluded that the hydroxyl groups do not contribute significantly as a source of protonic acid sites [3.8], on the basis that infrared spectra obtained after adsorption of ammonia or pyridine on the surface do not exhibit bands due to ammonium or pyridinium ions. However, the surface of alumina in a reforming catalyst normally contains chloride ions which can interact with the hydroxyl groups to enhance their acidity [3.9]. Since the aluminas employed in reforming catalysts are normally heated to high temperatures (775-875 K) in their preparation, there are Lewis acid sites present as a result of dehydroxylation reactions [3.10]. A Lewis acid is defined as a species that can accept a pair of electrons from a base [3.11]. At the surface of dehydroxylated alumina there are incompletely coordinated aluminum atoms (i.e., aluminum atoms coordinated to three oxygen atoms instead of four) which could serve as electron acceptors. The interaction of these aluminum sites with a Lewis base such as ammonia, via bonding involving the lone electron pair on the nitrogen atom, is readily visualized.

For certain types of reactions of importance in catalytic reforming, both types of sites are involved in the sequence of steps leading from reactant to product. The conversion of methylcyclopentane to benzene, for example, first involves a dehydrogenation step on platinum sites yielding methylcyclopentenes as intermediates [3.12]. The latter then isomerize to cyclohexene on acidic sites. Cyclohexene subsequently returns to platinum sites, where it can either be hydrogenated to cyclohexane or dehydrogenated to benzene, the relative amounts of these products depending on reaction conditions. Isomerization of normal alkanes to branched alkanes involves the same kind of reaction sequence in which olefinic intermediates are transported between platinum and acidic sites on the catalyst. The mode of transport of the intermediates must be considered in this type of reaction scheme. A sequence of steps involving transport between platinum and acidic sites via the gas phase gives a good account of much experimental data [3.13-17].

Kinetic investigations have played an important role in advancing the concept of bifunctional catalysis. The isomerization of n-pentane on a platinum-alumina catalyst provides a good example [3.15], where the rate measurements were made at a temperature of 645 K. The n-pentane was passed over the catalyst

in the presence of hydrogen at total pressures ranging from 7.7 to 27.7 atm and at hydrogen to n-pentane ratios varying from 1.4 to 18. Over this range of conditions the rate was found to be independent of total pressure and to increase with increasing n-pentane to hydrogen ratio.

The kinetic data were interpreted in terms of a mechanism involving n-pentene intermediates:

$$nC_5 \overset{Pt}{\rightleftharpoons} nC_5^{=} + H_2 \quad , \tag{3.1a}$$

$$nC_5^{=} \xrightarrow[Site]{Acid} iC_5^{=} \quad , \tag{3.1b}$$

$$H_2 + iC_5^{=} \overset{Pt}{\rightleftharpoons} iC_5 \quad . \tag{3.1c}$$

According to this mechanism the n-pentane dehydrogenates to n-pentenes on platinum sites. The n-pentenes are then adsorbed on acid sites, where they are isomerized to isopentenes. The latter are then hydrogenated to isopentane on platinum sites, thus completing the reaction. The isomerization step on the acid sites has commonly been assumed to involve carbonium ion type intermediates.

At the conditions used, equilibrium is readily established in the dehydrogenation and hydrogenation steps represented by (3.1a,c). The equilibrium concentration (or partial pressure) of n-pentenes in the gas phase is proportional to the molar ratio of n-pentane to hydrogen. The rate-limiting step is the isomerization of the n-pentenes to isopentenes in (3.1b). Consequently, the overall rate of isomerization of n-pentane is determined by the equilibrium partial pressure of n-pentenes in the gas phase, as demonstrated in Fig.3.1 by the circles. Also shown in the figure is a data point (the square) for the

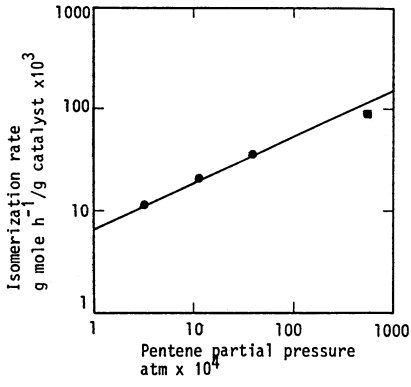

Fig.3.1. Isomerization rate as a function of pentene partial pressure at a temperature of 645 K. The circles are data for the rate of isomerization of n-pentane on a platinum-on-alumina catalyst. For these points the pentene partial pressure represents the equilibrium value, which is determined by the molar ratio of n-pentane to hydrogen in the reactor. The square is a datum point for the isomerization of 1-pentene on the acidic component of the catalyst alone, i.e., on a sample of catalyst which contains no platinum. For this point, the pentene partial pressure is simply the pressure of the 1-pentene reactant [3.15]

rate of isomerization of 1-pentene over a sample of catalyst containing no platinum. For this point the pentene partial pressure is simply the partial pressure of the 1-pentene reactant. The point falls close to the line correlating n-pentane isomerization rate with the equilibrium partial pressure of n-pentenes, as one would expect from the foregoing discussion. Whether one starts with 1-pentene or 2-pentene in this type of experiment should make little difference, since double-bond migration is fast compared to skeletal isomerization of olefins.

3.2 Characterization of Dispersed Metals

In metal catalysts of industrial importance, the metal is generally dispersed on a carrier, as in the case of the platinum-on-alumina catalysts used in reforming. The metal exists in the form of small metal clusters or crystallites, frequently in the size range of 10 - 100 Å. The characterization of the metal component of such catalysts has provided a challenge to the catalytic scientist. Much progress in this area has been made as a result of the development of reliable methods for the determination of chemisorption isotherms. More recently, physical probes such as X-ray absorption spectroscopy and nuclear magnetic resonance have greatly extended our capabilities for the investigation of these catalysts.

3.2.1 Chemisorption Isotherms

Chemisorption measurements have shown that freshly prepared platinum-on-alumina reforming catalysts are characterized by extremely high dispersion of platinum on the surface of the alumina carrier [3.18,19]. In hydrogen chemisorption studies on such catalysts, the amount of hydrogen taken up is frequently close to one hydrogen atom per atom of platinum. It is a generally accepted view that the hydrogen molecule dissociates into atoms during chemisorption on Group VIII metals. Typical data on the chemisorption of hydrogen at room temperature on a platinum-on-alumina catalyst [3.20] are shown in Fig.3.2. The isotherm labeled A is the original isotherm determined on the "bare" catalyst surface. The "bare" surface was prepared by evacuation of the adsorption cell at a high temperature (725 K) subsequent to the reduction of the catalyst in flowing hydrogen at 775 K. After the catalyst was cooled to room temperature in vacuum, it was contacted with hydrogen in the measurement of the isotherm. After isotherm A was completed, the adsorption cell was evacuated at room temperature for ten minutes (to approximately 10^{-6} Torr), and a second isotherm labeled B was measured. Isotherm A represents the total chemi-

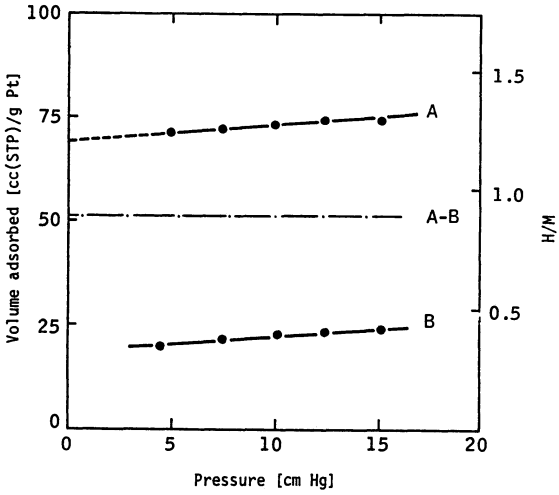

Fig.3.2. Typical hydrogen chemisorption data at room temperature on a platinum-on-alumina catalyst containing 1 wt.% platinum. A: original isotherm. B: second isotherm determined after evacuation of the adsorption cell for 10 mins (to pressure ~ 10^{-6} Torr) after completion of A. The difference isotherm A-B represents the strongly chemisorbed fraction [3.20]

sorption. Isotherm B represents the weakly chemisorbed fraction, since it is removed by simple evacuation at room temperature. This isotherm includes adsorption on the alumina carrier. The difference isotherm, labeled A-B, is obtained by subtracting isotherm B from isotherm A and is independent of pressure over the range of pressures used in obtaining the isotherm. It represents the strongly chemisorbed fraction, i.e., the amount which cannot be removed by evacuation at room temperature. The quantity H/M in the right-hand ordinate of Figure 3.2 represents the ratio of the number H of hydrogen atoms adsorbed to the number M of platinum atoms in the catalyst. If we assume a stoichiometry of one hydrogen atom per surface platinum atom in the case of the strongly chemisorbed fraction, the value of H/M determined from the difference isotherm A-B corresponds to the ratio of surface platinum atoms to total platinum atoms in the catalyst. This ratio is commonly called the metal dispersion, which is about 0.9 for the catalyst in Fig.3.2.

High-resolution electron microscopy studies provide independent evidence of the highly dispersed nature of platinum in platinum-alumina reforming catalysts [3.21]. Such studies have shown that the platinum exists as very small crystallites or clusters of the order of 10 Å in size. Platinum clusters of this size necessarily have a very large fraction of their atoms present in the surface. The fraction would be very close to the value of 0.9 derived from the chemisorption data in Fig.3.2.

The successful application of chemisorption methods in the characterization of platinum-on-alumina reforming catalysts led to their use with other supported metals, including most of the metals of Group VIII [3.22-24]. This represented a major advance in the characterization of supported-metal catalysts. With this capability, the activity of such a catalyst can be referred to the amount of metal in the surface rather than to the metal content of the catalyst as a whole. Data on the activities of different metal catalysts for a given reaction can therefore be compared in a more fundamental manner.

3.2.2 Application of Extended X-Ray Absorption Fine Structure

Extended X-ray absorption fine structure (EXAFS) refers to fluctuations in absorption coefficient which are commonly observed on the high-energy side of an X-ray absorption edge. The fluctuations of interest in EXAFS begin at an energy of approximately 30 eV beyond an absorption edge and extend over an additional range of 1000-1500 eV. The fine structure is observed in the absorption of X-rays by all forms of matter other than monatomic gases, and was first considered theoretically by *Kronig* [3.25-27]. The possibilities of EXAFS as a tool for investigating the structures of noncrystalline materials, however, have been realized only recently, and have emerged as a result of advances in methods of data analysis [3.28,29] and experimental techniques, the latter being due primarily to the application of high-intensity synchrotron radiation as an X-ray source.

In EXAFS we are concerned with the ejection of an inner core electron from an atom as a result of X-ray absorption. The ejected electron (photoelectron) is characterized by a wave vector K, given by

$$K = (2mE)^{1/2} / \hbar \quad , \tag{3.2}$$

where m is the mass of the electron, $\hbar$ is Planck's constant / 2π, and E is the kinetic energy of the photoelectron. The energy E is the difference between the X-ray energy and a threshold energy associated with the ejection of the electron. At the threshold energy, an X-ray absorption spectrum exhibits an abrupt change in absorption coefficient, i.e., the absorption edge. A typical spectrum [3.30] for bulk platinum at 100 K is shown in Fig.3.3. The data cover a wide enough range of energy to include all three of the characteristic L absorption edges, L_{III}, L_{II}, and L_I, corresponding, respectively, to ejection of photoelectrons from $2p_{3/2}$, $2p_{1/2}$, and 2s states. At energies higher than the threshold value corresponding to a particular absorption edge, we note the fluctuations in absorption coefficient which constitute the extended fine structure.

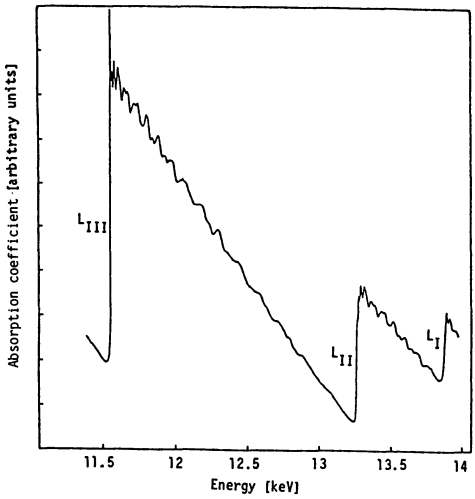

Fig.3.3. X-ray absorption spectrum of bulk platinum at 100 K in the region of the L absorption edges [3.20,30]

In the treatment of EXAFS data, the absorption coefficient in the region of the EXAFS is divided into two parts. One part is identical to the absorption coefficient for the free atom. The other part, which depends on the environment about the absorber atom, is the oscillating part constituting EXAFS. Division of the latter part by the former normalizes the EXAFS oscillations, which are then represented by the EXAFS function $\chi(K)$. Details concerning the determination of $\chi(K)$ from experimental EXAFS data are given elsewhere [3.20, 29].

Plots of the function $K^3 \cdot \chi(K)$ versus K are shown in the left-hand sections of Fig.3.4 for bulk platinum and for two platinum catalysts containing 1 wt.% platinum [3.20]. In one catalyst the platinum was dispersed on silica, while in the other it was dispersed on alumina. Chemisorption measurements on the catalysts indicated platinum dispersions in the range of 0.7 to 0.9. The data in Fig.3.4, which were obtained at a temperature of 100 K, are for EXAFS associated with the L_{III} absorption edge. Fourier transforms of $K^3 \cdot \chi(K)$ are shown in the right-hand sections of the figure. The Fourier transform yields a function $\phi(R)$, where R is the distance from the absorber atom [3.31,32]. Peaks corresponding to neighboring atoms are displaced from true interatomic distances because of phase shifts. The feature in the transforms for the catalysts near R = 0 is an artifact introduced by asymmetry in the EXAFS function, which in turn is due to a limitation in ability to extract the background absorption from the total absorption. Improvements in the characterization of background absorption have largely eliminated this artifact in more recent work.

The EXAFS fluctuations for the dispersed platinum catalysts are substantially smaller than those for bulk platinum. Correspondingly, the magnitudes of the peaks in the Fourier transforms are also smaller (note that the scales in

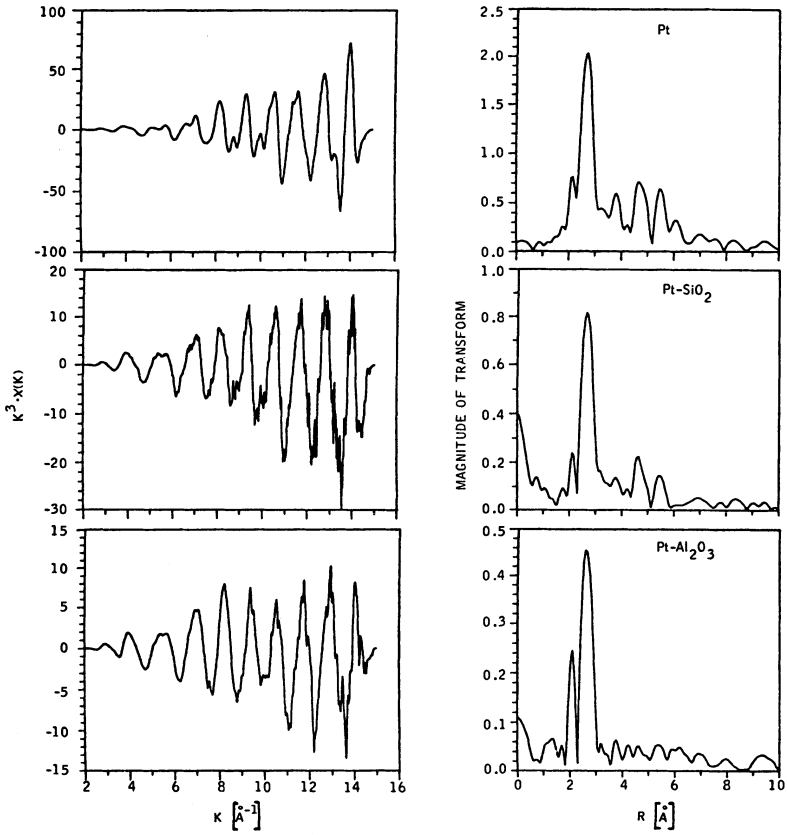

Fig.3.4. Normalized EXAFS data at 100 K and associated Fourier transforms for bulk platinum and for dispersed platinum catalysts containing 1 wt.% platinum [3.20]

the figures are not the same for the dispersed platinum catalysts and bulk platinum). These features are a consequence of a lower average coordination number and/or a higher degree of disorder of the platinum atoms in the dispersed catalysts. The degree of disorder is characterized by a parameter σ, which is the root-mean-square deviation of the interatomic distance about the equilibrium value.

From the EXAFS data in Fig.3.4, values of average coordination number, interatomic distance, and disorder parameter σ were obtained for the platinum clusters in the catalysts. Details of the procedure employed in the analysis of the EXAFS data are described in our original paper [3.20]. The average number of nearest neighbor atoms about a platinum atom in a cluster is 7 for the Pt/Al_2O_3 catalyst and 8 for the Pt/SiO_2 catalyst. The values are significantly lower than the value of 12 for bulk platinum. This result is expected, since most of the platinum atoms in the clusters are surface atoms with

lower coordination numbers than the atoms in the interior of a crystal. Also, atoms at corners and edges have lower coordination numbers than the interior atoms in surface planes of crystals and become increasingly important as the size of a metal crystal decreases. Nearest-neighbor interatomic distances in the platinum clusters differ from the value for bulk platinum by less than 0.02 Å, which is within the estimated uncertainty in the determination of distances. Although differences in distances are small, the values of the disorder parameter σ for the platinum clusters are greater than the value for bulk platinum by a factor of 1.4 - 1.7.

3.2.3 Application of Nuclear Magnetic Resonance

In recent years the author has been collaborating with Professor Charles Slichter and his students at the University of Illinois in the application of nuclear magnetic resonance (NMR) to the characterization of platinum catalysts and molecules chemisorbed on the catalysts. A brief discussion is given here of some experimental results on ^{195}Pt NMR line shapes for a series of air-exposed platinum-on-alumina catalysts of widely different platinum dispersions [3.33]. The results were obtained using the technique of "spin echoes" [3.34].

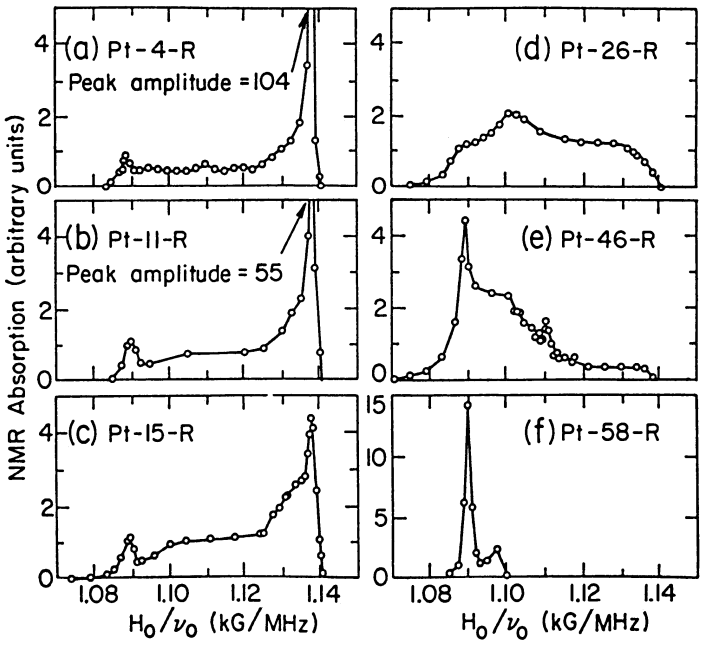

Fig.3.5. Shapes of NMR absorption lines at 77 K and at a frequency (ν_0) of 74 MHz for platinum-on-alumina catalysts of varying platinum dispersion [3.33]

Data are shown in Fig.3.5 for catalysts in which the percentage of surface atoms in the platinum clusters or crystallites (i.e., the platinum dispersion) varied by an order of magnitude from 4 to 58. In Fig.3.5, each catalyst has a designation Pt-X-R, in which X is the platinum dispersion (the letter R signifies "as received", i.e., air-exposed). The values of platinum dispersion were determined from hydrogen chemisorption isotherms. In Fig.3.5 the ordinate is the NMR absorption and the abscissa is the ratio of the static field to the characteristic NMR frequency [3.33]. The NMR lines are very broad, in marked contrast to the very narrow NMR lines observed with liquids.

For the catalysts with low platinum dispersion (4 to 11 %), there is a pronounced peak at $H_0 / \nu_0 = 1.138$ kG / MHz. The resonance for bulk platinum is observed at the same value of H_0 / ν_0, which is 3.4% higher than the value at which the resonance is observed for H_2PtI_6, the standard reference typical of diamagnetic platinum compounds. The large displacement of the resonance for the bulk metal from the resonance for the diamagnetic platinum compounds is due to polarization of the spins of the conduction electrons in the metal. It is known as the Knight shift [3.34]. The peak characteristic of bulk platinum is due to atoms in the deep interior of the platinum crystallites. The small peak at H_0/ν_0 = 1.089 kG/MHz is identified with surface platinum atoms covered by chemisorbed species, which are present because the catalysts were exposed to the air. The position of the peak is in the region characteristic of diamagnetic platinum compounds, indicating that the conduction electrons of the surface platinum atoms are tied up in chemical bonds. The surface platinum atoms are therefore not metallic, and do not exhibit a Knight shift. The broad structureless region of the NMR line between the bulk and surface peaks is attributed to platinum nuclei near the surface, the environments of which are sufficiently different to produce a range of Knight shifts. As the platinum dispersion increases, the surface peak at 1.089 kG/MHz becomes progressively larger, while the bulk peak at 1.138 kG/MHz becomes smaller.

No peak at 1.138 kG/MHz is evident for the catalysts with platinum dispersions of 26 to 58%. The catalysts with platinum dispersions of 46 and 58% exhibit pronounced surface peaks at 1.089 kG/MHz. The ratio of the area of the surface peak to the total area of the NMR line should be equal to the ratio of surface atoms to total atoms in the platinum clusters. In general, there was fair agreement between the value of this ratio obtained from the NMR data and the value obtained from hydrogen chemisorption data. In the determination of the area of the surface peak in cases where only the low-field side of the peak was well resolved from the line, the high-field side was drawn by assuming the peak was symmetric about 1.089 kG/MHz.

When the adsorbed species are removed from the catalysts by a cleaning procedure involving alternate treatments with flowing hydrogen and oxygen at 573 K, followed by evacuation, the surface peak disappears from the NMR spectrum. The surface platinum atoms are then metallic, since their conduction electrons are no longer tied up in chemisorption bonds. The observation of the resonance for surface platinum atoms is therefore dependent on the presence of adsorbed species with which they form chemical bonds.

3.3 Hydrocarbon Reactions on Metals

Metals are catalysts for a variety of reactions of hydrocarbons, including hydrogenolysis, hydrogenation, dehydrogenation, and isomerization. During the past three decades, our knowledge of these reactions has increased substantially. Much has been learned about the specificity of metal catalysts for these reactions. Significant progress has also been made in determining the sensitivity of the reactions to surface structure, and in elucidating general mechanistic and kinetic features of the reactions.

3.3.1 Hydrogenolysis

Hydrogenolysis reactions of hydrocarbons involve the rupture of carbon-carbon bonds and the formation of carbon-hydrogen bonds. The simplest hydrogenolysis reaction of a hydrocarbon is the conversion of ethane to methane

$$C_2H_6 + H_2 \rightarrow 2\ CH_4 \quad .$$

This reaction has been studied in detail over a number of metals [3.22-24, 35-39]. The reaction may be dissected into two separate steps [3.40-42]

$$C_2H_6 \rightleftharpoons C_2H_x(ads) + aH_2 \quad , \qquad C_2H_x(ads) \rightarrow \text{adsorbed } C_1 \text{ fragments} \quad ,$$

where the symbol (ads) signifies an adsorbed species. The quantity a is equal to $(6 - x) / 2$. Ethane is first chemisorbed with dissociation of carbon-hydrogen bonds, ultimately yielding a hydrogen deficient surface species C_2H_x. The latter then undergoes carbon-carbon scission to yield adsorbed C_1 fragments (e.g., adsorbed CH or CH_2) which are subsequently hydrogenated to methane.

A comparison of the catalytic activities for ethane hydrogenolysis of all of the metals of Group VIII and of rhenium in Group VIIA is given in Fig.3.6, which has three separate fields representing the metals of the first, second, and third transition series [3.41,42]. The Group IB metals (copper, silver,

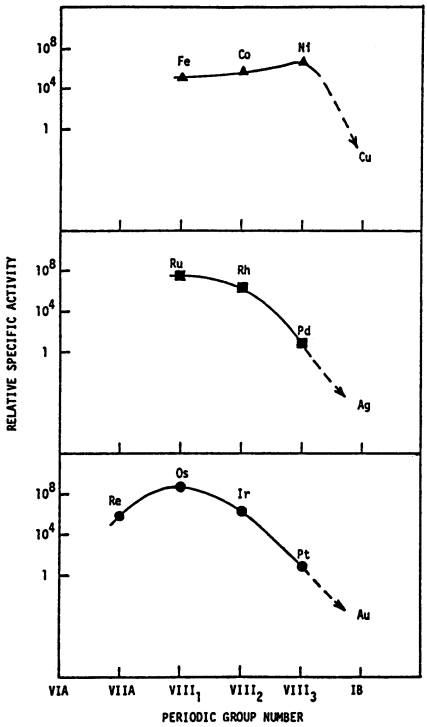

Fig.3.6. Catalytic activities of metals for the hydrogenolysis of ethane to methane [3.41,42]. The activities were determined at a temperature of 478 K and at ethane and hydrogen partial pressures of 0.030 and 0.20 atm., respectively

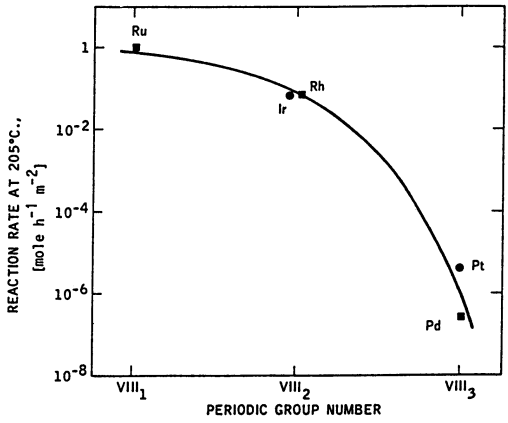

Fig.3.7. Catalytic activities of Group VIII metals for hydrogenolysis of n-heptane [3.41,44,45]. (Conditions: 478 K, 1 atm, H_2/nC_7 mole ratio = 5/1)

gold), for which precise data are not available, are much less active than the least-active Group VIII metals. The most complete data are available for the metals of the third transition series, in which the hydrogenolysis activity attains a maximum value at osmium. From osmium to platinum, the activity decreases by eight orders of magnitude. A similar variation is observed from ruthenium to palladium in the second transition series. In the first transition series, the pattern of variation of hydrogenolysis activity is different, the maximum activity being found in the third rather than the first subgroup within Group VIII. This difference in detail is somewhat analogous to known chemical differences between elements of the first transition series on the one hand, and the corresponding elements of the second and third transition series on the other [3.43].

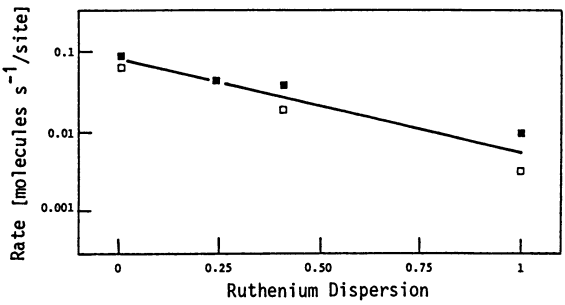

Fig.3.8. The effect of the degree of dispersion of ruthenium on its catalytic activity for hydrogenolysis of cyclohexane to lower carbon number alkanes [3.46]. Filled squares represent rates obtained after 10-20 mins of exposure of the catalyst to reactants; open squares represent data obtained after 2h of exposure

The pattern of variation of catalytic activity of the metals of the second and third transition series for the hydrogenolysis of ethane is also observed in n-heptane hydrogenolysis [3.41,44,45], as shown in Fig.3.7. The products of the hydrogenolysis reaction of n-heptane are C_1-C_6 alkanes, the relative amounts of which depend on the metal. Absolute rates of hydrogenolysis are approximately two to three orders of magnitude higher for n-heptane than for ethane [3.44].

The specific activity of a metal catalyst for the hydrogenolysis of an alkane or cycloalkane depends in general on the state of dispersion of the metal, i.e., the catalytic activity per surface metal atom is different for a large metal crystal from that for a very small metal crystallite or cluster. Data illustrating this point are shown in Fig.3.8 for the hydrogenolysis of cyclohexane over a series of ruthenium catalysts varying in dispersion by two orders of magnitude [3.46]. As indicated earlier, dispersion is defined as the ratio of surface atoms to total atoms in the metal crystallites, and is determined from chemisorption measurements. The products of the cyclohexane hydrogenolysis reaction are alkanes with fewer carbon atoms, predominantly methane. The rate of hydrogenolysis decreases with increasing dispersion, declining by about one order of magnitude as the dispersion increases by two orders of magnitude.

In the interpretation of data on the hydrogenolysis activities of metals, it has commonly been hypothesized that the chemisorbed hydrocarbon intermediate forms a number of bonds with the metal surface and that a surface site consisting of a single active metal atom is not adequate [3.47,48]. Finding a suitable array of surface atoms to accommodate such a chemisorbed intermediate presents no difficulty on a large metal crystal where most of the sur-

face atoms are present in the faces of the crystal. On very small crystallites, however, a large fraction of the surface atoms exists at edges and corners. If the required array comprises a large number of metal atoms, the probability of finding such an array in the surface may be substantially lower than on large crystals. If such an array of active metal atoms is required for hydrogenolysis, one might expect the specific hydrogenolysis activity of highly dispersed metal clusters to be lower than that of large crystals, as observed for ruthenium. One would also expect that atoms of an inactive second element dispersed on top of the surface, or within the surface layer, would greatly decrease the availability of the required arrays and hence decrease hydrogenolysis activity strikingly. As will be seen, this expectation is indeed borne out in hydrogenolysis studies on bimetallic catalysts.

3.3.2 Hydrogenation and Dehydrogenation

In comparison with alkane hydrogenolysis reactions, hydrogenation and dehydrogenation reactions of hydrocarbons on metals exhibit a much smaller range of variation in rate (per unit surface area or per surface atom) from one metal to another. They also exhibit much smaller effects of the degree of metal dispersion on the rate per surface atom. Thus, while rates of ethane hydrogenolysis vary by about eight orders of magnitude among the Group VIII metals [3.41,42], rates of hydrogenation of benzene to cyclohexane and of ethylene to ethane vary by about two and three orders of magnitude, respectively [3.49]. For cyclohexane dehydrogenation to benzene, the available data indicate a similar lower range of variation of rates among the metals [3.47,50-53]. Moreover, rates of benzene hydrogenation and cyclohexane dehydrogenation per surface metal atom are essentially unchanged when metal dispersion is varied by an order of magnitude [3.53-56]. As a consequence of the small effect of metal dispersion on rates for these reactions, they have been characterized as structure-insensitive, the terminology having been introduced by *Boudart* [3.57].

In the case of reactions which have been identified as structure-insensitive, the view is commonly held that the surface site need not consist of a large array of active metal atoms. Perhaps a single metal atom is adequate [3.58]. If this view is correct, incorporating atoms of an inactive second component within or on the surface of the active metal should have a substantially smaller effect in decreasing the number of sites capable of catalyzing the reactions than in the case of reactions in which the required sites consist of large arrays of active metal atoms. Thus, the effects for hydrogenation and dehydrogenation reactions should be very different from those for hydrogenolysis.

3.3.3 Isomerization

As discussed earlier, isomerization reactions of alkanes and cycloalkanes occur very readily on bifunctional catalysts containing both metal and acidic components. However, the reactions can also occur on certain metals, notably platinum, in the absence of a separate acidic component in the catalyst [3.44, 59,60]. While it has been shown that a purely metal-catalyzed isomerization process can occur, the findings do not challenge the commonly accepted mode of action of bifunctional reforming catalysts in which separate metal and acidic sites participate in the reaction. The data available for conditions commonly used with commercial reforming catalysts indicate that a purely metal catalyzed process does not contribute appreciably to the overall isomerization reaction on a bifunctional catalyst. Nevertheless, the metal-catalyzed isomerization reaction is of interest from the point of view of understanding the nature of hydrocarbon transformations on metal surfaces [3.5].

In studies of the conversion of n-hexane on platinum metal films of variable thickness, including ultra-thin films consisting of microcrystallites with sizes of 20 Å or less, it has been reported that the conversion to isomerization products (2-methylpentane and 3-methylpentane) relative to hydrogenolysis products (C_1 - C_5 alkanes) is very much higher on the ultra-thin films than on thick films [3.61]. On the basis of these results, it was concluded that the isomerization reaction could occur on sites consisting of single metal atoms, such as the corner atoms of a crystal. The fraction of metal atoms present at corners is much higher in the microcrystallites constituting the ultra-thin films than in the thick films not characterized by this type of microstructure. The improved selectivity to isomerization in the case of the ultra-thin films then results because hydrogenolysis requires a site consisting of a large array of active metal atoms of the type present in the face of a crystal. As a consequence of this conclusion, one might expect, as in hydrogenation and dehydrogenation reactions, that selectivity to isomerization on an active Group VIII metal surface would be enhanced by the random incorporation of atoms of an inactive second component at the surface (either within, or on top of, the surface layer).

3.4 Bimetallic Catalysts

Bimetallic catalysts have played an important role in the field of heterogeneous catalysis. They have been utilized extensively for fundamental investigations and have had a major technological impact, especially in the petroleum industry [3.62].

3.4.1 Metal Alloys as Catalysts

One of the early interests in metal alloys as catalysts was using them to study the "electronic factor" in catalysis by metals [3.63-65]. The original ideas were based on the electronic structure of a metal crystal as a whole rather than on the localized electronic structures of individual surface atoms. As experimental data on chemisorption and catalysis on alloys have accumulated, however, it has become increasingly clear that localized properties of surface atoms are very important. In the case of a Ni-Cu alloy, for example, the atoms of the two metals retain their inherent chemical differences, although bonding properties of the atoms are probably altered to some degree. The electronic factor in catalysis by alloys is currently being pursued from this point of view.

A complicating feature in catalytic studies on metal alloys is the possibility of a difference between surface and bulk compositions. Evidence for such a difference in the case of Ni-Cu alloys is based on the observation that strong H_2 chemisorption does not occur on copper. The addition of only a few percent of copper to nickel decreases the amount of strongly chemisorbed H_2 severalfold (Fig.3.9), an indication that the concentration of copper in the surface is much greater than in the bulk [3.47]. Similar results have been obtained by several different groups of investigators [3.66,67], and the

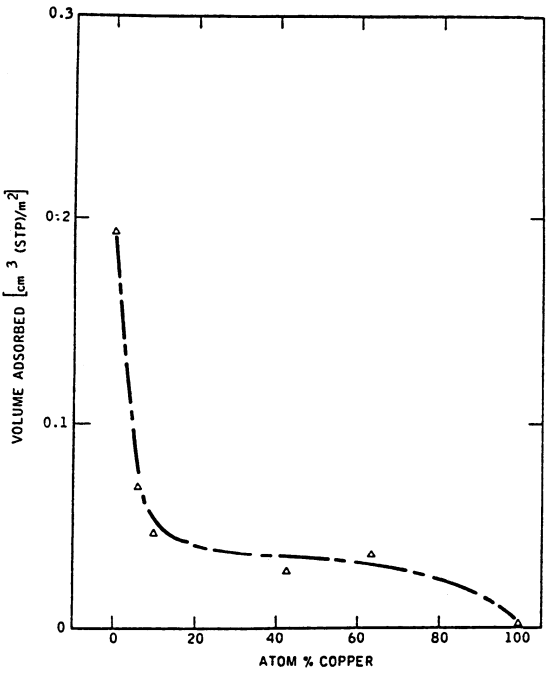

Fig.3.9. Hydrogen chemisorption on Ni-Cu alloys at room temperature [3.42,47]. The data are for strongly chemisorbed hydrogen, i.e., that which cannot be desorbed at room temperature by evacuation for 10 mins to a pressure of $\sim 10^{-6}$ Torr

findings are consistent with the results of studies of surface composition by Auger spectroscopy [3.68]. An important factor in determining surface composition is the nature of the gas in contact with the surface of an alloy. Thus, for Ni-Au alloys, gold concentrates in the surface in an inert atmosphere, whereas nickel is the predominant surface component in the presence of O_2 [3.69]. If the interaction of a gas with one of the components is sufficiently strong and selective, the surface tends to be enriched in that particular component.

The emphasis in early studies on alloy catalysts was on the activity for a particular reaction, often a simple hydrogenation reaction of an unsaturated hydrocarbon. The possibility that the effect of alloying depends on the type of reaction was considered later [3.47,50,70]. A striking example of specificity with regard to the type of reaction is provided by work on Ni-Cu alloy catalysts in which two different reactions were investigated, the hydrogenolysis of ethane to methane and the dehydrogenation of cyclohexane to benzene.

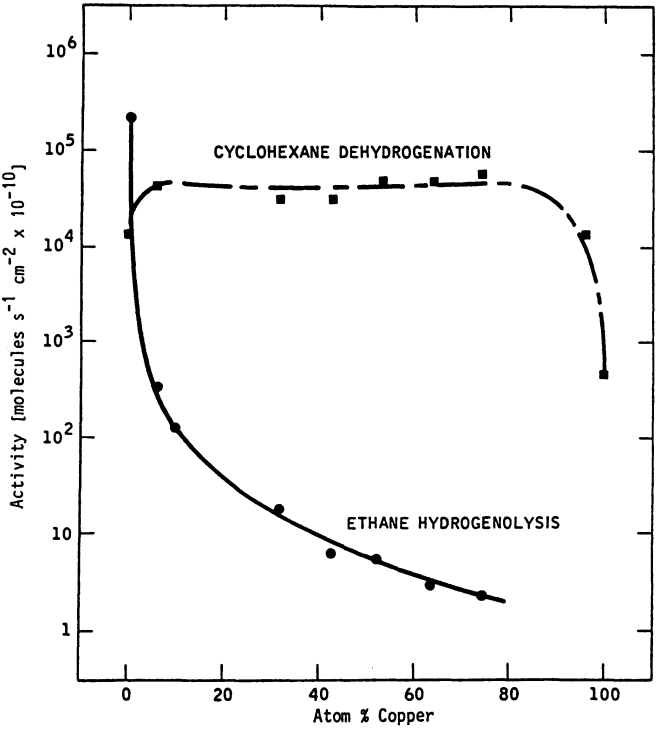

Fig.3.10. Activities of Ni-Cu alloys for the hydrogenolysis of ethane to methane and the dehydrogenation of cyclohexane to benzene [3.47]. The activities are reaction rates at 589 K

The latter type of reaction is important in the production of gasoline components in the petroleum industry [3.4,5]. The effect of copper on the catalytic activity of nickel for cyclohexane dehydrogenation is very different from that found for ethane hydrogenolysis [3.47], as shown by the data on a series of Ni-Cu alloys in Fig.3.10. In the case of ethane hydrogenolysis, adding only 5 atom % Cu to Ni decreases the catalytic activity by three orders of magnitude. With further addition of copper, the activity continues to decrease. However, the activity of nickel for the dehydrogenation of cyclohexane is affected very little over a wide range of Ni-Cu alloy composition and actually increases on the addition of the first increments of copper to nickel. Only as the catalyst composition approaches pure copper is a marked decline in activity for this reaction observed.

In interpreting the ethane hydrogenolysis data, we recall the hypothesis that the reaction proceeds via a hydrogen-deficient surface intermediate, C_2H_x, which is bonded to more than one metal atom in the surface. Such an intermediate would require sites comprising arrays or "multiplets" of adjacent active metal atoms. (The term multiplet is taken from the work of *Balandin* [3.71]). If the active metal atoms are diluted with inactive metal atoms in the surface, the concentration of active multiplets will decline sharply. For the Ni-Cu alloy system, in which the inactive Cu atoms concentrate strongly in the surface, the addition of only a few percent of copper to nickel will result in a markedly lower concentration of multiplet Ni atom sites. Although such a geometric argument can account for a large inhibiting effect of copper on the hydrogenolysis activity of nickel, it is difficult to dismiss the possibility that electronic interaction between copper and nickel may also affect the catalysis. In view of the low ability of copper relative to nickel to chemisorb a variety of hydrocarbons, one might reasonably expect that the addition of copper to nickel in an alloy would decrease the strength of adsorption of hydrocarbon species on the surface. In ethane hydrogenolysis, the strength of bonding between the two carbon atoms in the chemisorbed intermediate might be expected to vary in an inverse manner with the strength of bonding of the carbon atoms to the metal. One would then conclude that rupture of the C-C bond would be inhibited by a decrease in the strength of adsorption accompanying the addition of copper to nickel. If C-C rupture is rate limiting, the rate of hydrogenolysis should then decrease.

The cyclohexane dehydrogenation reaction may not require a site consisting of a multiplet of active Ni atoms. Although this lack of a multiplet site requirement would account for the absence of a steep decline in activity as Cu is added to Ni, it does not explain why copper-rich alloys have dehydrogenation

activities as high or higher than that of pure Ni. However, if the activity is controlled by a step whose rate is inversely related to the strength of adsorption (for example, desorption of the benzene product), the addition of Cu to Ni could increase the activity of a catalytic site and compensate for a decrease in the number of such sites. Over the range of composition from pure Ni to pure Cu, however, it is likely that the rate-determining step changes. For pure Cu, the chemisorption of the cyclohexane itself may be limiting.

3.4.2 Bimetallic Aggregates of Immiscible Components

The Ni-Cu alloys just discussed were prepared under conditions of complete miscibility of the two components. At this point it is pertinent to consider a system such as Ru-Cu, the components of which are essentially completely immiscible in the bulk. The crystal structures of the two metals are different, ruthenium having a hexagonal close-packed structure and copper a face-centered cubic structure. Although the Ru-Cu system can hardly be considered as an alloy-forming system, bimetallic Ru-Cu aggregates can be prepared which are similar to alloys such as Ni-Cu in their catalytic behavior. In such aggregates, the copper tends to cover the surface of ruthenium [3.52,58]. Evidence for this structure comes from studies of hydrogen chemisorption capacity and ethane hydrogenolysis activity, both of which are markedly suppressed when even small amounts of copper are present with the ruthenium. The interaction between the two components may be considered analogous to that which would exist in the chemisorption of copper on ruthenium. The behavior of the Ru-Cu system for ethane hydrogenolysis is similar to that observed for Ni-Cu. In cyclohexane dehydrogenation to benzene, the two systems also behave similarly, in that copper has only a small effect on dehydrogenation activity. However, pure ruthenium exhibits extensive hydrogenolysis of cyclohexane to alkanes of lower carbon number (mostly methane) in addition to dehydrogenation to benzene. Addition of copper to ruthenium suppresses hydrogenolysis strongly relative to dehydrogenation, so that a marked increase in the selectivity to benzene is observed. The chemisorbed intermediates are probably different in the dehydrogenation and hydrogenolysis reactions. As in the case of ethane hydrogenolysis, the intermediate in cyclohexane hydrogenolysis is probably a hydrogen-deficient surface residue which forms bonds with more than one surface metal atom.

In general, the addition of a Group IB metal to a Group VIII metal decreases hydrogenolysis activity markedly but has a much smaller effect on other reactions such as dehydrogenation, hydrogenation, and isomerization of hydrocarbons [3.47,50-52,70,72]. Selectivity is therefore an important aspect of hydrocarbon conversion on bimetallic catalysts of this type.

3.4.3 Bimetallic Clusters

For industrial application of bimetallic catalysts, large metal surface areas are desirable. A good way to obtain a large area is to disperse the metal on a carrier such as silica or alumina [3.51,58,62]. One can prepare highly dispersed bimetallic clusters by impregnating a carrier with an aqueous solution of salts of the two metals of interest. The material is dried and then brought in contact with a stream of H_2 at an elevated temperature to reduce the metal salts. This procedure results in the formation of bimetallic clusters even for cases in which the individual metal components exhibit very low miscibility in the bulk [3.51,58,62]. Examples of such metal clusters which have been investigated are Ru-Cu and Os-Cu supported on silica, in which the metal clusters cover about 1% of the surface of the silica. The metal dispersion, expressed as the percentage of metal atoms present in the surface, is in the range of 50 - 100% in these systems.

As copper is incorporated with ruthenium or osmium in bimetallic clusters, the selectivity for conversion of cyclohexane to benzene is improved greatly (Fig.3.11); hydrogenolysis to alkanes is inhibited markedly, whereas dehydrogenation to benzene is relatively unaffected [3.51,73]. The behavior is similar to that described for unsupported Ru-Cu aggregates and therefore provides clear evidence for the interaction between copper and the Group VIII metal on the carrier.

From the studies on Ru-Cu and Os-Cu catalysts employing chemical probes, we conclude that the copper is present on the surface of the ruthenium or os-

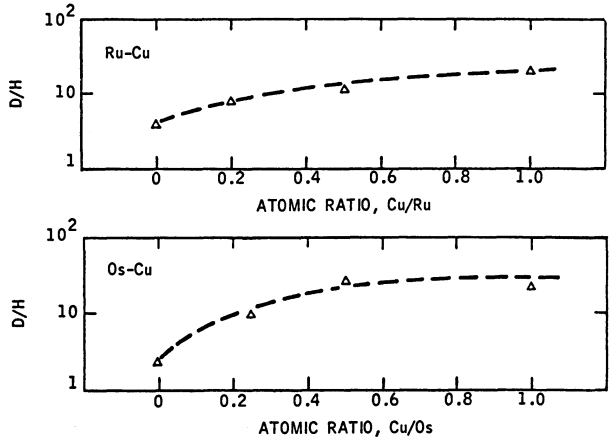

Fig.3.11. Selectivity of conversion of cyclohexane over silica-supported bimetallic clusters of Ru-Cu and Os-Cu at 589 K, as represented by the ratio D/H [3.51,73]. (D is the rate of dehydrogenation of cyclohexane to benzene, and H is the rate of hydrogenolysis to alkanes)

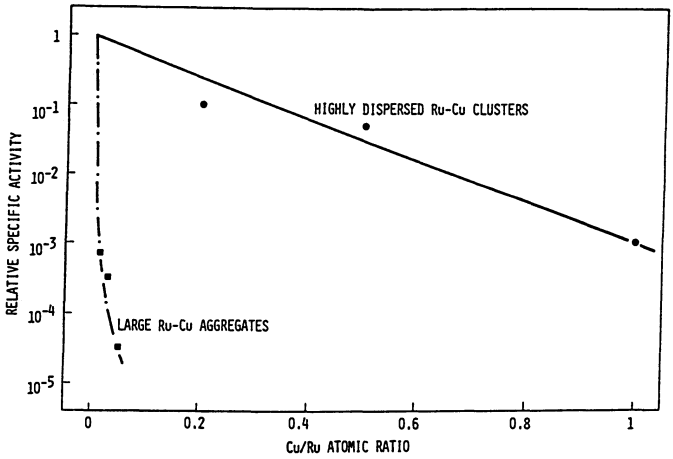

Fig.3.12. Influence of the state of dispersion of Ru-Cu catalysts on the relationship between ethane hydrogenolysis activity and catalyst composition [3.52,58]

mium. If we consider Ru-Cu aggregates in which copper covers a specified fraction of the ruthenium surface, we note that the atomic ratio of copper to ruthenium required for this degree of coverage will increase with decreasing aggregate size. According to this view of the Ru-Cu system, the atomic ratio of copper to ruthenium required to achieve a given extent of inhibition of hydrogenolysis activity will be much higher for highly dispersed Ru-Cu clusters than for large aggregates. This is indeed found to be the case [3.52], as shown in Fig.3.12. The ratio of surface metal atoms to total metal atoms in the bimetallic entities is of the order of 0.01 for the large Ru-Cu aggregates and of the order of 0.5 for the highly dispersed clusters. For the clusters a thousand fold decrease in hydrogenolysis activity is obtained for a copper to ruthenium atomic ratio equal to one. With the large aggregates, however, the same inhibiting effect is observed for a fifty fold lower ratio of copper to ruthenium. Similar effects are observed in hydrogen chemisorption studies, in which a given degree of inhibition of hydrogen chemisorption requires a much higher atomic ratio of copper to ruthenium in the highly dispersed clusters than in the large aggregates [3.52]. These studies employing ethane hydrogenolysis and hydrogen chemisorption as chemical probes provide excellent support for the view that the copper is present on the surface of the ruthenium.

When the initial research on bimetallic clusters such as Ru-Cu and Os-Cu was conducted, the characterization of the clusters was limited to methods involving chemical probes because of the difficulty of obtaining information with physical probes. However, the situation changed decidedly when it became

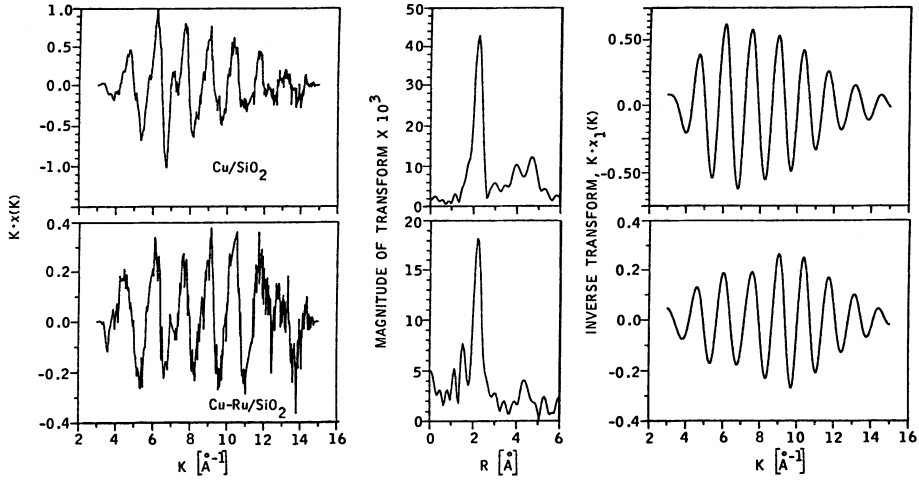

Fig.3.13. Normalized EXAFS data at 100 K (Cu K absorption edge), with associated Fourier transforms and inverse transforms, for silica-supported Cu and Ru-Cu catalysts [3.74]

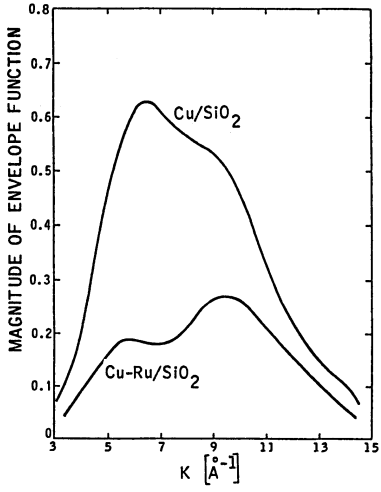

Fig.3.14. Interaction between Ru and Cu dispersed on silica, as illustrated by the marked difference in the EXAFS envelope functions derived from EXAFS data associated with the K-absorption edge of Cu for silica-supported Cu and Ru-Cu catalysts [3.74]

evident that X-ray absorption spectroscopy provided an effective probe for investigating the structures of catalysts. Results of EXAFS studies on Ru-Cu and Os-Cu bimetallic clusters have provided strong evidence in support of the conclusions about structure derived from the studies with chemical probes.

Plots of normalized EXAFS data at 100 K, with associated Fourier transforms and inverse transforms, are given in Fig.3.13 for silica-supported Cu and Ru-Cu catalysts, the former containing 0.63 wt.% Cu and the latter 1.0 wt.% Ru, 0.63 wt.% Cu [3.74]. The EXAFS data are for the extended fine structure beyond the K absorption edge of copper. The inverse transforms were taken over a range of distances chosen to isolate the contribution to EXAFS arising from nearest-neighbor metal atoms, as signified by the subscript 1 in $\chi_1(K)$. An

envelope function obtained from the maxima in $K \cdot \chi_1(K)$ provides a good illustration of the interaction between ruthenium and copper in the Ru-Cu catalyst [3.74], as shown in Fig.3.14. The EXAFS envelope function for the Ru-Cu catalyst is compared with that for the copper reference catalyst. The marked difference in the envelope function shows the effect of the ruthenium on the EXAFS observed in the X-ray absorption spectrum of the copper as a consequence of the copper atoms having nearest-neighbor atoms consisting of both ruthenium and copper instead of copper alone. The data of Fig.3.14 provide clear evidence for the existence of bimetallic clusters of ruthenium and copper in the Ru-Cu catalyst. A quantitative analysis of the data on the Ru-Cu clusters, which have an average diameter of about 30 Å [3.75], indicates that the copper atoms in the clusters have nearest neighbors which are about equally distributed among copper and ruthenium atoms. By contrast, Ru EXAFS data on the catalyst indicate that the ruthenium atoms are coordinated largely to other ruthenium atoms. These results are in excellent agreement with a model of a Ru-Cu cluster consisting of a central core of ruthenium atoms with copper on the surface. Results of EXAFS studies on Os-Cu clusters [3.76] provide a similar conclusion to that derived for Ru-Cu clusters.

The quantitative analysis of EXAFS data on bimetallic cluster catalysts has been described in detail in our original papers [3.74,76]. In the studies which have been made, our analysis has been limited to consideration of contributions of nearest-neighbor atoms to EXAFS. In Fig.3.15, the EXAFS fluctuations represented by the solid line in all three fields of the figure are due to contributions from nearest-neighbor backscattering atoms for a silica-supported Os-Cu catalyst [3.76]. The solid line was derived from experiment by inverting a Fourier transform of EXAFS data associated with the L_{III} absorption edge of osmium over a range of distances chosen to include only backscattering contributions from nearest-neighbor atoms. The points in the upper field (labeled A) of the figure represent values of an EXAFS function calculated using parameters for the Os-Cu clusters obtained from the data by an iterative least-squares fitting procedure. The quality of fit of the points to the line in A is seen to be excellent, except at very low K values. The fits can be improved at the very low K values by modification of the details of the phase shift functions, but there is very little effect of such a modification on the values of the structural parameters obtained. In B and C of Fig.3.15 the points represent the separate contributions of nearest-neighbor copper and osmium backscattering atoms, respectively, to the osmium EXAFS for the Os-Cu catalyst.

In addition to the information which can be obtained from the EXAFS associated with an X-ray absorption edge, valuable information can be obtained

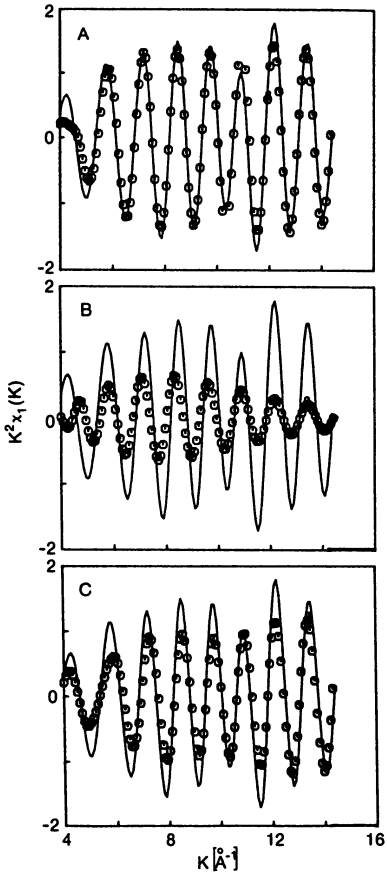

Fig.3.15. Contributions of nearest-neighbor Cu and Os backscattering atoms (points in B and C, respectively) to the EXAFS associated with the Os L_{III} absorption edge of a silica-supported Os-Cu catalyst containing 2 wt.% Os and 0.66 wt.% Cu [3.76]. (The points in A show how the individual contributions combine to describe the experimental EXAFS represented by the solid line)

from an analysis of the structure of the edge itself. From a study of L_{III} or L_{II} absorption threshold resonances, one can obtain information on electronic transitions from a core level, $2p_{3/2}$ or $2p_{1/2}$, respectively, to vacant d states of the absorbing atom [3.77,78]. The electronic transitions are sensitive to the chemical environment of the absorbing atom [3.79]. In the case of silica-supported Os-Cu catalysts, we find that the magnitude of the absorption threshold resonance associated with the osmium atom is decreased by the presence of the copper. This effect is illustrated in Fig.3.16 for the L_{III} absorption edge of osmium. The absorption coefficient μ_N is a normalized absorption coefficient determined by a procedure described in our paper on X-ray absorption threshold resonances [3.79]. In the upper half of Fig.3.16, the left-hand section compares the resonance for a silica-supported osmium catalyst containing 1 wt.% Os with that for pure metallic osmium. The magnitude of the resonance is higher for the osmium dispersed on the support, the

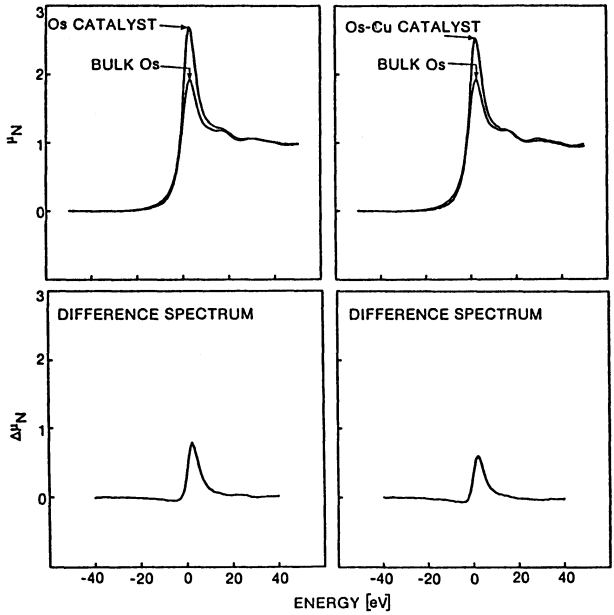

Fig.3.16. The effect of Cu on the threshold X-ray absorption resonance associated with the L_{III} absorption edge of the Os in a silica-supported catalyst [3.76]

extent of increase being indicated by the difference spectrum in the lower left-hand section of the figure. This effect is similar to the results we have reported for iridium and platinum dispersed on an alumina support [3.79]. In the upper right-hand section of Fig.3.16, the magnitude of the resonance for a silica-supported Os-Cu catalyst containing 1 wt.% Os and 0.33 wt.% Cu (1:1 atomic ratio of copper to osmium) is compared with that for pure metallic osmium. The magnitude of the resonance for the osmium in the supported Os-Cu clusters is again higher than that for the pure metallic osmium, the extent of increase being indicated again by the difference spectrum in the lower right-hand section of the figure. However, the increase in this case is about 30% lower than is observed when the supported osmium alone is compared with pure metallic osmium, i.e., the area under the difference spectral line in the lower right-hand section is about 30% smaller than the area under the corresponding spectral line in the lower left-hand section of the figure.

In the case of the catalyst containing osmium alone on silica, the osmium clusters behave as if they are more electron deficient than pure metallic osmium; i.e., there appear to be more unfilled d states to accommodate the electron transitions from the $2p_{3/2}$ core level of the absorbing atom. In the silica-supported Os-Cu clusters, however, the osmium atoms appear to be less electron

deficient than they are in the pure osmium clusters dispersed on silica. The presence of the copper thus appears to have the effect of decreasing the number of unfilled d states associated with the osmium atoms.

Up to this point the discussion of bimetallic clusters has been concerned with combinations of a Group VIII metal and a Group IB metal. Another type of bimetallic cluster of interest is a combination of atoms of two Group VIII metals, e.g., Pt-Ir [3.80-82]. Dispersed Pt-Ir clusters can be prepared by contacting a carrier such as silica or alumina with an aqueous solution of chloroplatinic and chloroiridic acids. After the impregnated carrier is dried and possibly heated to 525-575 K, it is exposed to flowing hydrogen at a temperature of 575-775 K. The resulting material contains Pt-Ir clusters dispersed on the carrier.

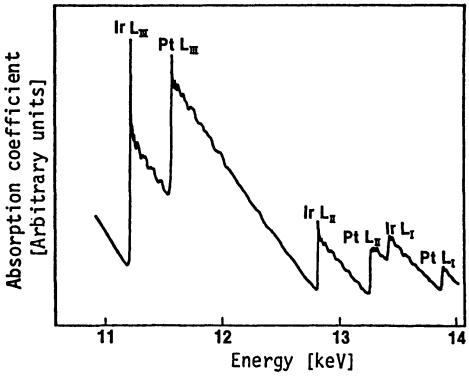

Fig.3.17. An X-ray absorption spectrum at 100 K in the region of the L absorption edges of iridium and platinum for a catalyst containing Pt-Ir clusters [3.83]

An X-ray absorption spectrum at 100 K showing the L absorption edges of iridium and platinum [3.83] is given in Fig.3.17 for a catalyst containing bimetallic clusters of platinum and iridium. The data were obtained over a wide enough range of energies of the X-ray photons to include all of the L absorption edges of iridium and platinum. Since the extended fine structure associated with the L_{III} edge of iridium is observable to energies of 1200-1300 eV beyond the edge, there is overlap of the EXAFS associated with the L_{III} edges of iridium and platinum in the case of a catalyst containing both of these elements. Separating the iridium EXAFS from the platinum EXAFS in the region of overlap is therefore necessary in the analysis of the data. Details of the analysis are presented in [3.83]. We will be concerned only with the results of the analysis here. Briefly, the results on interatomic distances indicate that the average composition of the first coordination shell of atoms (nearest neighbors) surrounding a platinum atom is different from that surrounding an iridium atom. The catalyst appears to exhibit platinum-rich and iridium-rich regions.

One might visualize a distribution of metal clusters with different compositions, some of which are platinum-rich and others of which are iridium-rich. Both the platinum-rich and iridium-rich clusters would contain substantial amounts of the minor component on the basis of the distances derived from the EXAFS data. Alternatively, one can visualize platinum-rich and iridium-rich regions within a given metal cluster. This possibility seems reasonable on the basis of surface energy considerations. According to this view, the platinum rich region would be present at the surface since platinum would be expected to have a lower surface energy than iridium. In support of this expectation, recent work on Pt-Ir films indicates that platinum concentrates in the surface [3.84].

When the ratio of surface atoms to total atoms is equal to 0.5 for clusters containing 50% each of platinum and iridium, one can visualize a situation in which essentially all of the platinum is present in the surface and all the iridium in the interior. There would then be a close resemblance to the Ru-Cu clusters we considered earlier. When the ratio of surface atoms to total atoms approaches unity, the notion of complete or nearly complete segregation of the platinum in a surface layer and of iridium in a central core cannot be accommodated if the clusters are spherically symmetrical. The notion can, however, be accommodated without difficulty if the clusters have a two-dimensional, "raft-like" shape rather than a spherical shape. One can then visualize a central iridium-rich raft with platinum atoms around the perimeter. In very highly dispersed catalysts of the type visualized here, the effect of the platinum on the catalytic properties of the iridium, and vice versa, would presumably be a consequence of the interaction between the two components at the boundary.

Catalysts containing Pt-Ir clusters dispersed on alumina are of interest in the reforming of petroleum fractions for production of high octane number gasoline components. They are more active and exhibit much better activity maintenance than the platinum-alumina catalysts originally used in reforming [3.5,62, 80,85,86]. In parallel with the development of Pt-Ir catalysts in the Exxon laboratories, another reforming catalyst containing platinum and rhenium (a Group VIIA metal) was under development in the laboratories of the Chevron Corporation. During the 1970s, Pt-Ir and Pt-Re catalysts were introduced widely in catalytic reformers. The use of these catalysts was a key factor in making unleaded gasoline feasible.

3.5 Summary

During the past three decades, significant advances of a fundamental nature have been made in the area of metal catalysis, both in the characterization

of catalysts and in the elucidation of important features of the reactions which occur on metals. The fundamental advances have been accompanied by major technological advances, as in the widespread application of bimetallic catalysts in petroleum reforming. On a long-term basis, the outlook for the future is excellent. There are many exciting challenges for workers in this area, and in the field of catalysis in general.

References

3.1 V. Haensel: U.S. Patent 2, 479, 109 (1949)
3.2 V. Haensel: U.S. Patent 2, 479, 110 (1949)
3.3 V. Haensel, G.R. Donaldson: Ind. Eng. Chem. **43**, 2102 (1951)
3.4 J.H. Sinfelt: Adv. Chem. Eng. **5**, 37 (1964)
3.5 J.H. Sinfelt: "Catalytic Reforming of Hydrocarbons", in *Catalysis: Science and Technology*, ed. by J.R. Anderson, M. Boudart, Vol.1 (Springer, Berlin, Heidelberg 1981) pp.257-300
3.6 A.G. Oblad, T.H. Milliken, G.A. Mills: Adv. Catal. **3**, 199 (1951)
3.7 M.W. Tamele: Discuss. Faraday Soc. **8**, 270 (1950)
3.8 E.P. Parry: J. Catal. **2**, 371 (1963)
3.9 B.C. Gates, J.R. Katzer, G.C.A. Schuit: *Chemistry of Catalytic Processes* (McGraw-Hill, New York 1979) pp.259-260
3.10 H. Pines, W.O. Haag: J. Am. Chem. Soc. **82**, 2471 (1960)
3.11 G.N. Lewis: *Valence and the Structure of Atoms and Molecules* (Chemical Catalog Co., New York 1923) p.141
3.12 G.A. Mills, H. Heinemann, T.H. Milliken, A.G. Oblad: Ind. Eng. Chem. **45**, 134 (1953)
3.13 P.B. Weisz, E.W. Swegler: Science **126**, 31 (1957)
3.14 S.G. Hindin, S.W. Weller, G.A. Mills: J. Phys. Chem. **62**, 244 (1958)
3.15 J.H. Sinfelt, H. Hurwitz, J.C. Rohrer: J. Phys. Chem. **64**, 892 (1960)
3.16 J.H. Sinfelt, J.C. Rohrer: J. Phys. Chem. **65**, 978 (1961)
3.17 J.H. Sinfelt, H. Hurwitz, J.C. Rohrer: J. Catal. **1**, 481 (1962)
3.18 L. Spenadel, M. Boudart: J. Phys. Chem. **64**, 204 (1960)
3.19 J.J. Keavney, S.F. Adler: J. Phys. Chem. **64**, 208 (1960)
3.20 G.H. Via, J.H. Sinfelt, F.W. Lytle: J. Chem. Phys. **71**, 690 (1979)
3.21 G.R. Wilson, W.K. Hall: J. Catal. **17**, 190 (1970)
3.22 J.H. Sinfelt, W.F. Taylor, D.J.C. Yates: J. Phys. Chem. **69**, 95 (1965)
3.23 J.H. Sinfelt, D.J.C. Yates: J. Catal. **8**, 82 (1967)
3.24 J.H. Sinfelt, D.J.C. Yates: J. Catal. **10**, 362 (1968)
3.25 R. de L. Kronig: Z. Phys. **70**, 317 (1931)
3.26 R. de L. Kronig: Z. Phys. **75**, 191 (1932)
3.27 R. de L. Kronig: Z. Phys. **75**, 468 (1932)
3.28 D.E. Sayers, F.W. Lytle, E.A. Stern: Phys. Rev. Lett. **27**, 1204 (1971)
3.29 F.W. Lytle, D. Sayers, E. Stern: Phys. Rev. B **11**, 4825 (1975)
3.30 J.H. Sinfelt, G.H. Via, F.W. Lytle: J. Chem. Phys. **68**, 2009 (1978)
3.31 D.E. Sayers, F.W. Lytle, E.A. Stern: Adv. X-Ray Anal. **13**, 248 (1970)
3.32 D.E. Sayers: Ph.D. Dissertation, University of Washington (1971)
3.33 H.E. Rhodes, P.-K. Wang, H.T. Stokes, C.P. Slichter, J.H. Sinfelt: Phys. Rev. B **26**, 3559 (1982)
3.34 C.P. Slichter: *Principles of Magnetic Resonance*, 2nd ed. (Springer, Berlin, Heidelberg 1980)
3.35 K. Morikawa, W.S. Benedict, H.S. Taylor: J. Am. Chem. Soc. **58**, 1795 (1936)
3.36 E.H. Taylor, H.S. Taylor: J. Am. Chem. Soc. **61**, 503 (1939)
3.37 A. Cimino, M. Boudart, H.S. Taylor: J. Phys. Chem. **58**, 796 (1954)
3.38 J.H. Sinfelt: J. Phys. Chem. **68**, 344 (1964)

3.39 D.J.C. Yates, J.H. Sinfelt: J. Catal. **14**, 182 (1969)
3.40 J.H. Sinfelt: J. Catal. **27**, 468 (1972)
3.41 J.H. Sinfelt: Adv. Catal. **23**, 91 (1973)
3.42 J.H. Sinfelt: Catal. Rev. Sci. Eng. **9** (1), 147 (1974)
3.43 F.A. Cotton, G. Wilkinson: *Advanced Inorganic Chemistry*, 1st ed. (Interscience, New York 1962) pp.661, 760
3.44 J.L. Carter, J.A. Cusumano, J.H. Sinfelt: J. Catal. **20**, 223 (1971)
3.45 J.H. Sinfelt: Prog. Solid State Chem. **10** (2), 55 (1975)
3.46 Y.L. Lam, J.H. Sinfelt: J. Catal. **42**, 319 (1976)
3.47 J.H. Sinfelt, J.L. Carter, D.J.C. Yates: J. Catal. **24**, 283 (1972)
3.48 V. Ponec, W.M.H. Sachtler: J. Catal. **24**, 250 (1972)
3.49 G.C.A. Schuit, L.L. van Reijen: Adv. Catal. **10**, 242 (1958)
3.50 J.H. Sinfelt, A.E. Barnett, J.L. Carter: U.S. Patent 3, 617, 518 (1971)
3.51 J.H. Sinfelt: J. Catal. **29**, 308 (1973)
3.52 J.H. Sinfelt, Y.L. Lam, J.A. Cusumano, A.E. Barnett: J. Catal. **42**, 227 (1976)
3.53 J.A. Cusumano, G.W. Dembinski, J.H. Sinfelt: J. Catal. **5**, 471 (1966)
3.54 W.F. Taylor, H.K. Staffin: Trans. Faraday Soc. **63**, 2309 (1967)
3.55 G.M. Dixon, K. Singh: Trans. Faraday Soc. **65**, 1128 (1969)
3.56 P.C. Aben, H. van der Eijk, J.M. Oelderik: Proc. 5th Int. Congress Catal., ed. by J.W. Hightower, Vol. 1 (North-Holland, Amsterdam 1973) pp.717-726
3.57 M. Boudart: Adv. Catal. **20**, 153 (1969)
3.58 J.H. Sinfelt: Acc. Chem. Res. **10**, 15 (1977)
3.59 J.R. Anderson, B.G. Baker: Proc. R. Soc. London, Ser. A **271**, 402 (1963)
3.60 M. Boudart, L.D. Ptak: J. Catal. **16**, 90 (1970)
3.61 J.R. Anderson, R.J. MacDonald, Y. Shimoyama: J. Catal. **20**, 147 (1971)
3.62 J.H. Sinfelt: *Bimetallic Catalysts: Discoveries, Concepts, and Applications* (Wiley, New York 1963)
3.63 G.M. Schwab: Discuss. Faraday Soc. **8**, 166 (1950)
3.64 D.A. Dowden, P. Reynolds: Discuss. Faraday Soc. **8**, 184 (1950)
3.65 A. Couper, D.D. Eley: Discuss. Faraday Soc. **8**, 172 (1950)
3.66 P. van der Planck, W.M.H. Sachtler: J. Catal. **7**, 300 (1967)
3.67 D.A. Cadenhead, N.J. Wagner: J. Phys. Chem. **72**, 2775 (1968)
3.68 C.R. Helms: J. Catal. **36**, 114 (1975)
3.69 F.L. Williams, M. Boudart: J. Catal. **30**, 438 (1973)
3.70 J.H. Sinfelt, A.E. Barnett, G.W. Dembinski: U.S. Patent 3, 442, 973 (1969)
3.71 A.A. Balandin: Adv. Catal. **10**, 96 (1958)
3.72 A. Roberti, V. Ponec, W.M.H. Sachtler: J. Catal. **28**, 381 (1973)
3.73 J.H. Sinfelt: Rev. Mod. Phys. **51**, 569 (1979)
3.74 J.H. Sinfelt, G.H. Via, F.W. Lytle: J. Chem. Phys. **72**, 4832 (1980)
3.75 E.B. Prestridge, G.H. Via, J.H. Sinfelt: J. Catal. **50**, 115 (1977)
3.76 J.H. Sinfelt, G.H. Via, F.W. Lytle, R.B. Greegor: J. Chem. Phys. **75**, 5527 (1981)
3.77 N.F. Mott: Proc. Phys. Soc., London, **62**, 416 (1949)
3.78 Y. Cauchois, N.F. Mott: Philos. Mag. **40**, 1260 (1949)
3.79 F.W. Lytle, P.S.P. Wei, R.B. Greegor, G.H. Via, J.H. Sinfelt: J. Chem. Phys. **70**, 4849 (1979)
3.80 J.H. Sinfelt: U.S. Patent 3, 953, 368 (1976)
3.81 J.H. Sinfelt, G.H. Via: J. Catal. **56**, 1 (1979)
3.82 R.L. Garten, J.H. Sinfelt: J. Catal. **62**, 127 (1980)
3.83 J.H. Sinfelt, G.H. Via, F.W. Lytle: J. Chem. Phys. **76**, 2779 (1982)
3.84 F.J. Kuijers, V. Ponec: Appl. Surf. Sci. **2**, 43 (1978)
3.85 J.H. Sinfelt: U.S. Patent 3, 791, 961 (1974)
3.86 J.L. Carter, G.B. McVicker, W. Weissman, W.S. Kmak, J.H. Sinfelt: Appl. Catal. **3**, 327 (1982)

4. Molecular Organometallic Chemistry and Catalysis on Metal-Oxide Surfaces

B.C. Gates

Center for Catalytic Science and Technology, Department of Chemical Engineering, University of Delaware, Newark, DE 19716, USA

The supported metals used widely in catalysis are aggregates or crystallites of various sizes, shapes, and compositions dispersed on stable large-surface-area metal oxides such as γ-Al_2O_3. Much has been learned about the structures of the metals in these materials from characterization techniques such as high-resolution electron microscopy (Chap.15) and extended X-ray absorption fine structure (EXAFS) [4.1], and a strong foundation of quantitative catalytic reaction kinetics has been laid down [4.2], but there is still a gaping void in our understanding of how catalyst structure at the atomic and molecular level is related to performance. Progress has been made in filling this void from the foundation of molecular surface science of single metal crystals with simple adsorbates; these have yielded to structural determination by high-vacuum techniques such as low-energy electron diffraction (LEED), ultraviolet photoelectron spectroscopy (UPS), and high-resolution electron energy-loss spectroscopy (HREELS), and have been investigated as catalysts at high pressures in the same apparatus [4.3].

The work summarized in this chapter represents a new approach to the elucidation of the structure and reactivity of supported metal catalysts. The supported-metal species described here are molecular in nature, many having structures analogous to those of well-known molecular species such as metal carbonyl clusters. A great advantage of working with these molecular organometallics is associated with their susceptibility to precise characterization by spectroscopic techniques such as EXAFS, infrared, and Raman spectroscopies —the spectra are interpreted by comparison with those of authentic molecular analogues. It is important to recognize, however, that these organometallic surface structures require a stabilizing ligand environment for their very existence, and they are usually not good models of the bare metal aggregates that may be precursors of typical supported-metal catalysts. Further, many of the known surface-bound organometallic structures are not very stable, and there are only a few examples of catalysis involving these materials at high temperatures.

Progress in understanding the structure and reactivity of molecular oxide-supported organometallics has been rapid, occurring chiefly in the last few

years. The objective of this chapter is to summarize the state of this field, with emphasis on polynuclear organometallic species (metal clusters) supported on large-surface-area metal oxides. Much of the recently developed knowledge is derived from the pioneering efforts of the research groups of Basset, Iwasawa, Knözinger, and Ugo and Psaro, among others. The subject of metal clusters in catalysis is treated in depth in a recent monograph [4.4], which includes the subject matter of this chapter.

4.1 Synthesis

The synthetic routes to well-defined ("molecular") oxide-bound organometallics have been inferred from the solution organometallic chemistry of the precursors (typically, neutral metal carbonyl clusters) and the surface chemistry of the supports. Some of the synthetic routes are analogous to those developed for a wide range of mononuclear metal complexes on metal oxides [4.5], involving the reaction of an -OH group of the oxide surface with a metal cluster having a labile ligand. For example, triosmium clusters have been anchored to γ-Al_2O_3 by the reaction [4.6]

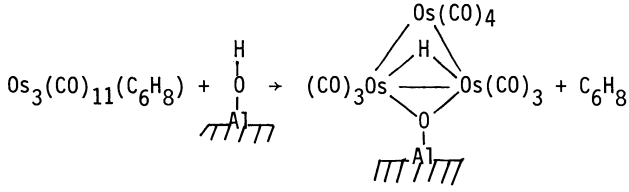

Other labile ligands in addition to cyclohexadiene can be expected to be useful in such preparations, but there are still only a few examples of such preparations involving metal clusters on surfaces [4.6,7].

The most commonly used synthetic route involves deprotonation of acidic hydrido metal clusters by basic surfaces; this method has been used with strongly basic supports (e.g., MgO and CaO) and also with γ-Al_2O_3 [4.8]. Examples involve metal cluster precursors of the family $H_4M_4(CO)_{12}$, namely, $H_4Os_4(CO)_{12}$ [4.9], $H_4Ru_4(CO)_{12}$ [4.10], and $H_4RuOs_3(CO)_{12}$ [4.11]. Evidently, deprotonation of the cluster by basic surface groups generates surface -OH groups and surface ion pairs, including the anion clusters $H_3M_4(CO)_{12}^-$.

Another preparative route is described formally as an oxidative addition reaction involving a surface -OH group, illustrated here for the reaction of $Os_3(CO)_{12}$ with the surface of η-Al_2O_3 [4.7].

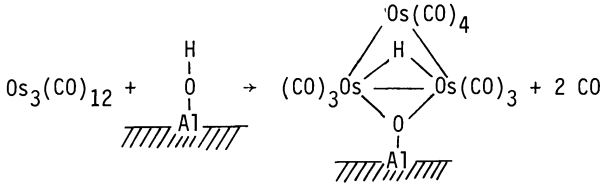

The stoichiometry of this reaction has been confirmed by measurement of the CO evolution [4.7]. Similar reactions evidently occur with γ-Al_2O_3 [4.12,13], SiO_2 [4.7,13], and probably TiO_2 and ZnO [4.7,13].

The surface reactions mentioned above occur simply and cleanly, usually at temperatures near 100°C with the organometallic precursor in a paraffinic solution in contact with the support. Alternatively, the volatile organometallic precursor may be transported to the surface through the gas phase.

Although the above-mentioned reactions occur cleanly, the usual situation is different when organometallic compounds are brought in contact with metal-oxide surfaces: the resulting surface structures are usually complicated mixtures, perhaps including complexes of various nuclearities and metal aggregates. Most attempts to form organometallics with unique moleculear structures on supports have led to such mixtures.

4.2 Structure Determination by Physical Methods

The characterization techniques of greatest value in the determination of structures of surface-bound organometallics are closely comparable to those used commonly in conventional organometallic chemistry; Table 4.1 is a list

Table 4.1. Spectroscopic methods used to characterize supported metal clusters

Spectroscopic method	Comparable method used in conventional organometallic chemistry
Infrared spectroscopy	Infrared spectroscopy
^1H and ^{13}C NMR spectroscopy	^1H and ^{13}C NMR spectroscopy
EXAFS	X-ray diffraction crystallography
Raman spectroscopy	Raman spectroscopy
UV-visible spectroscopy	UV-visible spectroscopy
Inelastic electron tunneling spectroscopy	———

of these techniques. In the following sections, results of the most important characterization methods are illustrated and the techniques are briefly evaluated.

4.2.1 Infrared Spectroscopy

Infrared spectroscopy is the method most easily and widely applied to characterize surface-bound organometallics. For example, spectra in the carbonyl stretching region (Fig.4.1) provide a basis for identification of the anion $H_3Os_4(CO)_{12}^-$ on γ-Al_2O_3. The spectrum of the surface species formed by deprotonation of the neutral metal carbonyl precursor $H_4Os_4(CO)_{12}$ is in good agreement with the spectrum of the anion in solution and with the salt incorporating this anion deposited directly on the surface [4.9]. Infrared spectra providing fingerprints in the carbonyl stretching region have been widely used; this sensitive and easily applied technique is capable of providing characterization of ligands other than carbonyls, but there are few reported examples.

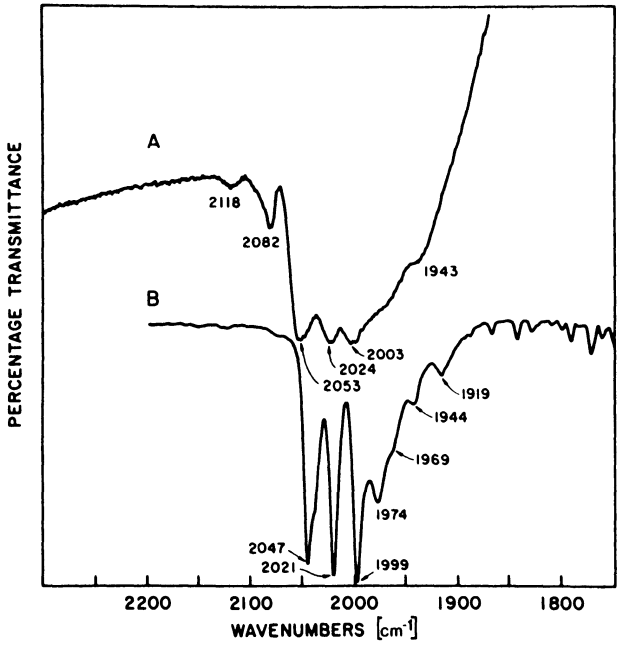

Fig.4.1. Infrared spectra of samples (*A*) (prepared from $H_4O_4(CO)_{12}$ and γ-Al_2O_3, in air, at room temperature, and (*B*) $[(Ph_2P)_2N]^+[H_3Os_4(CO)_{12}]^-$ in CH_2Cl_2 at room temperature [4.9]. Reproduced from *Journal of Catalysis* with permission of Academic Press

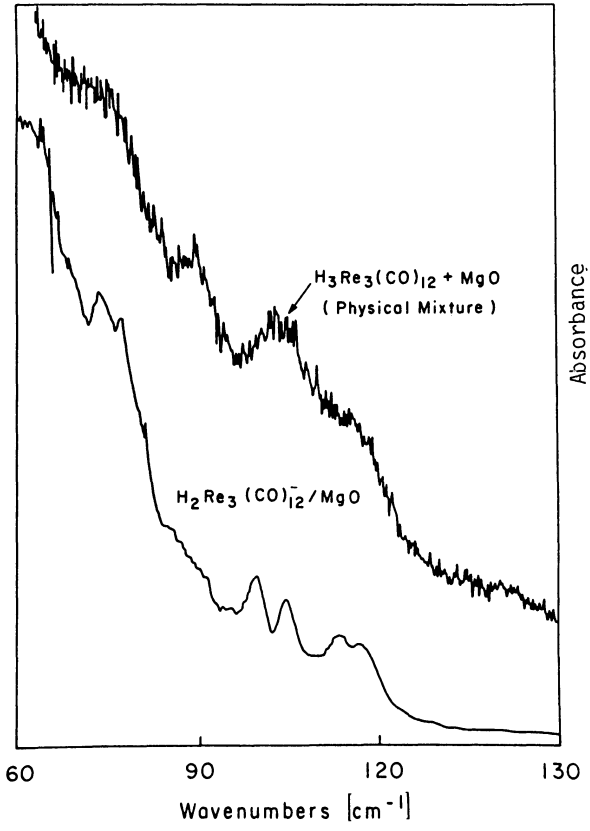

Fig.4.2. Laser Raman spectra in the metal-metal stretching and metal-carbon bending region of $H_3Re_3(CO)_{12}$ + MgO (physical mixture) and $H_2Re_3(CO)_{12}^-$ adsorbed on MgO

4.2.2 Laser Raman Spectroscopy

Laser Raman Spectroscopy provides complementary data, but this vibrational spectroscopy is much more difficult to apply successfully because of the lack of sensitivity of the technique and the difficulty of obtaining spectra of many samples because of fluorescence of the surface and destruction of the sample by the incident laser radiation. Raman spectroscopy provides evidence of ligands such as CO and of metal-metal and even metal-oxygen bonds. For example, the spectra of Fig.4.2 for $H_2Re_3(CO)_{12}^-$ on MgO provide just this kind of information [4.14]. There are, however, only a few examples of Raman spectra characterizing surface-bound organometallics; progress will be facilitated by the availability of more sensitive instruments and cells for proper handling of the often air-sensitive samples in appropriate atmospheres.

4.2.3 Inelastic Electron Tunneling Spectroscopy

The third in the set of vibrational spectroscopies that have been used to characterize surface-bound organometallics is inelastic electron tunneling spectroscopy. The technique requires the surface of the sample to be coated with a conducting layer of a metal such as lead, and the spectra are typically determined at liquid helium temperature so that the tunneling process is rapid; the resolution is less than that of infrared and Raman spectroscopies. The principal advantage of the method is its high sensitivity; the peaks in the spectrum are especially intense for vibrations perpendicular to the surface (and parallel to the direction of electron transport); therefore, the spectra provide evidence of the orientation of the surface species.

Results are illustrated for the anion $Ru_6C(CO)_{17}^{2-}$ on Al_2O_3 (Fig.4.3). The CO stretching bands are consistent with those determined by infrared and Raman spectroscopy [4.15].

4.2.4 Extended X-Ray Absorption Fine Structure Spectroscopy

The most powerful method in prospect for determining the structures of surface-bound organometallics is EXAFS. Spectra of well-characterized standards are essential for the proper interpretation of EXAFS data; the most appropriate

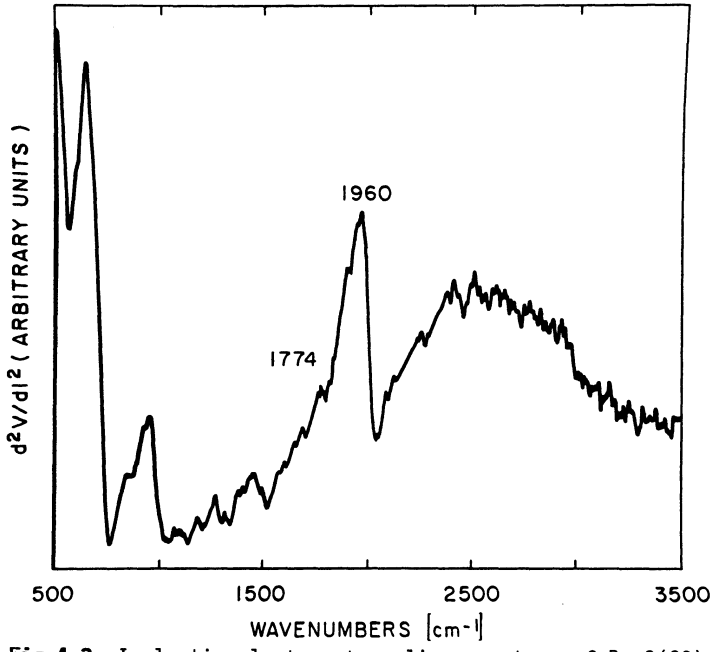

Fig.4.3. Inelastic electron tunneling spectrum of $Ru_6C(CO)_{17}^{2-}$ adsorbed on Al_2O_3 at liquid helium temperature [4.15]

standards are the molecular analogues of the surface species themselves, and it is best to use structural parameters determined from X-ray crystallography as a basis for evaluation of the EXAFS data.

The method has been applied to the γ-Al_2O_3-supported triosmium cluster

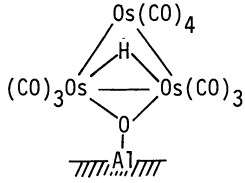

.

Structural parameters characterizing the surface species are summarized in Table 4.2 [4.16]; the results constitute a strong confirmation of the structure of the surface species, which is closely analogous to those of the compounds

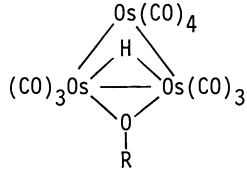

,

Table 4.2. Characterization of γ-Al_2O_3-supported osmium carbonyls by EXAFS [7.15]

Sample	$Os_3(CO)_{12}$[a]	$HOs_3(CO)_{10}O\{Al\}$	$Os(CO)_x\{OAl\}_3$ (x = 2 or 3)
Os-Os distance [Å]	2.88[b]	2.88[c]	——
Os-Os coordination number	2[b]	2[c]	——
C : Os atomic ratio	4	3.35[c]	2.5
Os-$O_{support}$ distance [Å]	—	2.12	2.19
Os-$O_{support}$ coordination number	—	0.65	3

[a] Reference compound, characterized in the crystalline state

[b] Value determined by X-ray crystallography

[c] Value assumed on the basis of data characterizing the reference compound and the surface species (see text)

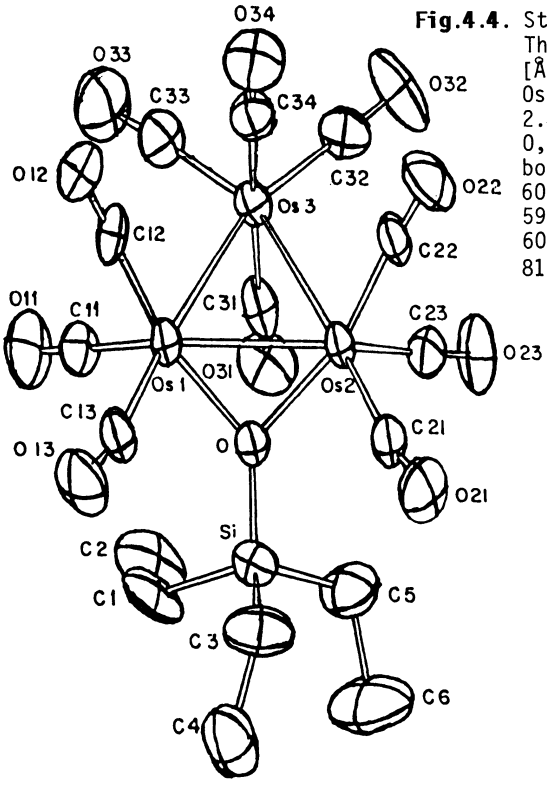

Fig.4.4. Structure of μ-$HOs_3(CO)_{10}(\mu$-$OSiEt_3)$. The bond lengths are [Å] Os(1)-Os(2), 2.777(1); Os(2)-Os(3), 2.816(1); Os(1)-Os(3), 2.820(1); Os(1)-O, 2.110(6); Os(2)-O, 2.126(6); O-Si; 1.658(6). The bond angles are < Os(1)-Os(2)-Os(3), 60.54(1)°; < Os(2) -Os(3)-Os(1), 59.05(1)°; < Os(3)-Os(1)-Os(2), 60.41(1)°; < Os(1)-O-Os(2), 81.9(2)° [4.16]

where R is H, alkyl, or $SiEt_3$ [4.17] (Fig.4.4). The EXAFS data confirm the surface structure that had been inferred from the infrared spectra [4.7,13], Raman spectra [4.18], inelastic electron tunneling spectra [4.19], and the stoichiometry of the surface synthesis [4.7]. This is regarded as one of the best-defined oxide-bound organometallic structures.

4.2.5 Ultraviolet-Visible Reflectance Spectroscopy

The method of UV-visible reflectance spectroscopy offers the advantage of ease of application, but it has been of minor value in the characterization of surface-bound organometallics. It provides evidence of metal-metal bonds [4.20], but since it does not provide highly specific structural information, it is best used to complement the other methods referred to here. In a few instances, the UV-visible spectrum provides a good fingerprint for identification of a surface-bound organometallic; an example (Fig.4.5) is $Os_{10}C(CO)_{24}^{2-}$ on MgO. Excellent agreement is observed between the spectrum of the $[Et_4N]^+$ salt deposited on MgO and that of the surface-bound dianion formed on MgO during CO hydrogenation [4.21].

4.2.6 Nuclear Magnetic Resonance (NMR)

Nuclear magnetic resonance (NMR) spectroscopy has found only little application to surface-bound organometallics [4.22-24], but modern high-field instruments portend greatly increased attention to this method. Supported mononuclear complexes, e.g., rhodium allyl on SiO_2 [4.22], have been characterized by ^1H NMR (without magic angle spinning). Changes in the spectrum (Fig.4.6) provide evidence of conversion of the allyl ligands into propylene and propane as the rhodium (initially in the +3 oxidation state) is reduced at room temperature in H_2 to the zero-valent state, accompanied by formation of rhodium aggregates on the SiO_2 surface.

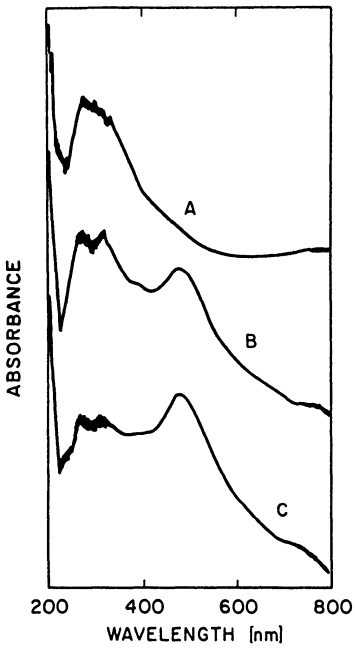

Fig.4.5. Electronic spectra of (*A*) sample prepared from $[H_2Os(CO)_4]$ and magnesia, (*B*) used catalyst, and (*C*) $[Et_4N]_2[Os_{10}C(CO)_{24}]$ adsorbed on magnesia [4.21]. Reprinted from *Journal of the American Chemical Society* with permission of the American Chemical Society

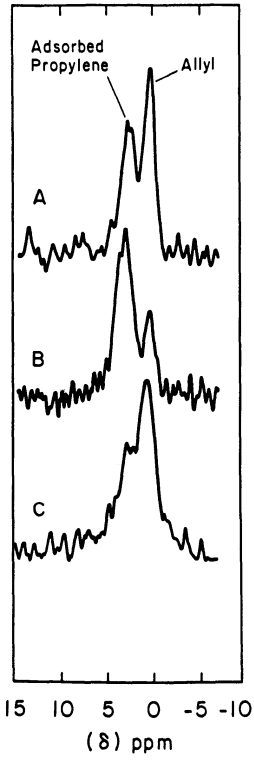

Fig.4.6. Three ^1H NMR spectra of {Si}-O-Rh(allyl)$_2$ (0.75 wt.% Rh) during reaction with D_2: (*A*) after reaction with flowing D_2 for 30 min (760 Torr, 25°C; 500 coadditions); (*B*) after reaction with D_2 for 48 h (760 Torr, 25°C; 500 coadditions); (*C*) subsequent evacuation of sample (1×10^{-3} Torr, 25°C; 2500 coadditions, intensity multiplied by 2.25 vs. spectra *A* and *B*) [4.22]. Reprinted from *Journal of the American Chemical Society* with permission of the American Chemical Society

The use of ^{13}C NMR spectroscopy with magic angle spinning and cross polarization to characterize organometallics on oxide surfaces has just begun; mononuclear molybdenum carbonyl complexes on γ-Al_2O_3 were found to have spectra consistent with $Mo(CO)_x$ subcarbonyls [4.23], and a mononuclear osmium complex on MgO was found to have a spectrum consistent with the structure of the anion $HOs(CO)_4^-$ [4.24]; the latter has been characterized by several other techniques, and the surface chemistry is described in Sect.4.3.

Metal NMR has not yet been reported for supported organometallics, but the prospects are excellent.

4.2.7 Temperature-Programmed Decomposition

Temperature-programmed decomposition of supported organometallics provides quantitative information about the ligands bonded to the surface species. In this experiment, the temperature of a sample in an inert carrier gas stream is ramped at a known (and usually constant) rate, and the gaseous effluent is analyzed to provide a quantitative profile of what has desorbed or formed by chemical reaction; often the chemical reactions involve -OH groups of the surface, which may oxidize the metal [4.25]. A variation of this technique involves use of a reactive gas stream such as H_2 in place of the inert carrier gas, and complementary data are obtained.

Some authors [4.7] have used static methods for decomposition of surface-bound organometallics; whatever the details of the technique, the results provide essential quantitative data determining the ligand environment of surface-bound organometallics; such data are a necessary component of any full characterization.

4.2.8 High-Resolution Transmission Electron Microscopy

Some of the most striking results characterizing metal clusters on supports [4.26-28] have been produced by high-resolution transmission electron microscopy. High resolution is illustrated by the micrograph of hexarhodium carbonyl clusters on Al_2O_3 (Fig.4.7) [4.28]. Very high resolution may be attained when films of the metal oxide support are specially prepared by oxidation of thin films of the metal.

4.2.9 Other Methods and General Points

Other surface characterization methods of potential value for supported metal clusters include electron spin resonance spectroscopy and magnetic susceptibility measurements; Mössbauer spectroscopy, which can be expected to be of greatest value for iron-containing samples; and ultraviolet photoelectron

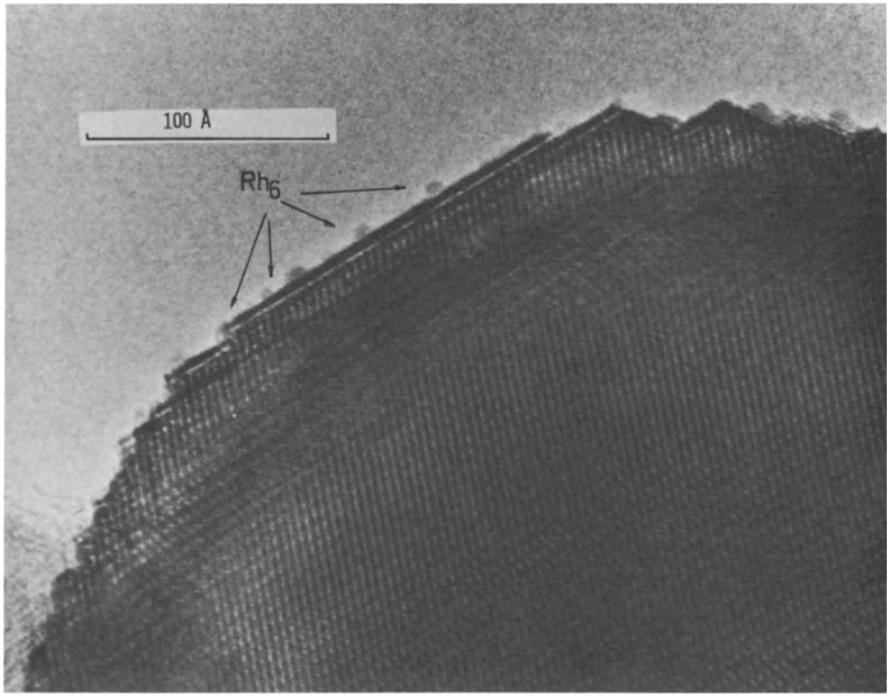

Fig.4.7. Electron micrograph of hexarhodium clusters on Al_2O_3. Provided by courtesy of *M. Ichikawa*. Also see [4.28]

spectroscopy and electron energy loss spectroscopy, which ultimately are expected to offer interesting prospects as the techniques are developed for the supported species. The well-defined supported organometallics offer good prospects for extending the range of these latter methods.

In summary, supported metal clusters are among the best-characterized supported metals and some of the best-characterized molecular species on oxide surfaces. These samples have provided opportunities for demonstrating the power of a range of surface characterization techniques, including EXAFS, laser Raman spectroscopy, inelastic electron tunneling spectroscopy, and high-resolution transmission electron microscopy. The supported clusters are unique in having discrete, molecular structures. Many of the surface characterization techniques appear to be almost optimally suited to these materials, whereas they are difficult to apply incisively to the more traditional supported metals. There is a gap to be bridged: as the simple surface structures are perturbed, they may be transformed into structures more representative of the conventional, widely used, supported metal catalysts; as the changes in structure are fol-

lowed with the techniques mentioned above, opportunities will be recognized for application of the techniques to the broad class of supported metal catalysts.

It is emphasized that the surface-science methods of greatest value in characterizing the supported molecular organometallics are not the ultra-high-vacuum techniques that have proved to be so valuable in characterizing surfaces of single crystals. The "high-pressure" techniques that are appropriate for characterization of the surface-bound organometallics can be used to characterize not only structures but also reactivities. Infrared spectroscopy is the method that has been used most successfully with samples in the presence of reactive atmospheres (even at several hundred degrees Celsius and pressures of tens of atmospheres, as discussed in Sect.4.4). Raman spectroscopy and EXAFS can also be used under such conditions. The potential exists for NMR as well, but this may be much more difficult when magic angle spining of the sample is required.

4.3 Reactivity

Reactivities of surface-bound organometallics are not well understood at the molecular level. The available data indicate the occurrence of the following classes of reactions: (1) breakup of supported metal clusters to give mononuclear surface complexes; (2) the opposite of cluster breakup, namely, condensation reactions leading to the formation of surface-bound metal clusters and aggregates (or crystallites); and (3) oxidation and reduction processes that often accompany these, the reduction processes often leading to the formation of metal aggregates on the oxide surface.

Some of the most thorough reactivity studies have been carried out with the SiO_2- and γ-Al_2O_3-supported triosmium carbonyl clusters mentioned above [4.29]. The results of these investigations (Fig.4.8) demonstrate the breakup of surface-bound clusters as a result of oxidation by surface -OH- groups. At temperatures greater than about 100°C, the triosmium clusters break apart, giving mononuclear Os^{2+} carbonyl complexes; several groups have confirmed these conlusions [4.7,12,13,16,18,26,27]. The stoichiometry of the surface reaction has been determined from measurement of CO and H_2 evolution [4.7]. The resulting supported mononuclear complex on γ-Al_2O_3, having 2 or 3 carbonyl ligands, has been characterized by infrared spectroscopy [4.7,12,13,16,26] and EXAFS (Table 4.2) [4.16]. The Al_2O_3-supported sample with the broken-up cluster no longer gave Raman evidence of Os-Os bonds, as expected [4.18]. The resulting mononuclear complexes on γ-Al_2O_3 are quite resistant to reduc-

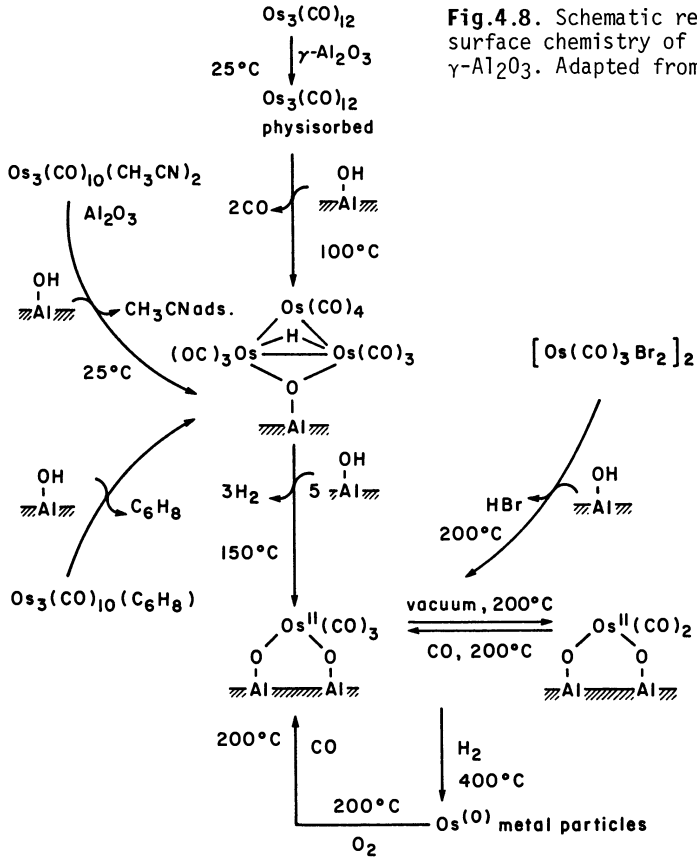

Fig.4.8. Schematic representation of the surface chemistry of osmium carbonyls on γ-Al_2O_3. Adapted from [4.29]

tion in H_2—temperatures of 300-400°C are required for formation of Os metal, present in the form of aggregates [4.7,12,13]. The reactivity of $H_3Os_4(CO)_{12}^-$ on γ-Al_2O_3 is very similar to that of the triosmium cluster; at approximately the same temperature, the surface-bound clusters in helium break up to give the mononuclear carbonyl complexes, as indicated by infrared spectra [4.9].

All the known supported-metal clusters are subject to degradation processes at elevated temperatures. The products are variable and depend on the support. For example, breakup of the triosmium carbonyl clusters on SiO_2 rather easily gives aggregates of Os metal, in contrast to the behavior of the γ-Al_2O_3-supported clusters [4.7].

Small γ-Al_2O_3-supported aggregates of Os of various sizes have been prepared by the treatment in $CO + H_2$ of osmium carbonyls of nuclearities ranging from one to six [4.30]; these aggregates are larger than the precursor clusters and are nonuniform in size, as indicated by electron microscopy, but there may be some correlation of the initial cluster nuclearity with the final average aggregate size [the tetraosmium cluster appears to be exceptional, however,

perhaps because of the relatively high stability of the $H_3Os_4(CO)_{12}^-$ anion initially formed on the γ-Al_2O_3].

Small iron aggregates on MgO have been prepared from $Fe_3(CO)_{12}$ [4.31], and small ruthenium aggregates on γ-Al_2O_3 and MgO have also been prepared from carbonyl clusters; these aggregates often exist in mixtures with mononuclear ruthenium complexes and molecular ruthenium clusters [4.10,32].

Bimetallic clusters have also been used to prepare supported catalysts; relatively stable molecular clusters have been formed on γ-Al_2O_3 [$HRuOs_3(CO)_{13}^-$ and $H_3RuOs_3(CO)_{12}^-$] [4.11], but for the most part, the resulting structures have been metal aggregates. In some instances, the aggregates are probably alloylike [4.33], and in other instances the metals originally present in the cluster segregate, with the formation of aggregates of one metal and separate mononuclear complexes of the other. For example, $FeOs_3$ clusters on SiO_2 evidently give Fe aggregates and Os(II) complexes [4.34]; $RuOs_3$ clusters on γ-Al_2O_3 give Ru aggregates and mononuclear Ru and Os complexes [4.35], and $RhOs_3$ clusters on γ-Al_2O_3 give Rh aggregates and Os(II) complexes [4.36]. Other examples have been reviewed recently [4.37]. Selectivity data for catalytic hydrogenation of CO suggest that there were intriguing variations in the structures formed from $Ru_xOs_{3-x}(CO)_{12}$ on γ-Al_2O_3 [4.38]; these results remain to be explained.

The reactions described in the preceding paragraphs involving reduction of metal and formation of metal-metal bonds are roughly the reverse of the reactions described above as cluster breakup. Occasionally these reduction/aggregation processes have been observed to lead to formation of supported molecular metal clusters rather than structurally indistinct aggregates.

For example, the $Os(II)(CO)_2$ or $Os(II)(CO)_3$ complexes formed by destruction of the above-mentioned surface-bound triosmium carbonyl clusters have been partially reconverted into the original supported clusters, as indicated by infrared spectra [4.7,39]. More thorough evidence of molecular osmium carbonyl cluster formation has been reported for MgO-supported samples initially incorporating the anion $HOs(CO)_4^-$, inferred to be present on the surface in an ion pair with the structure [4.21].

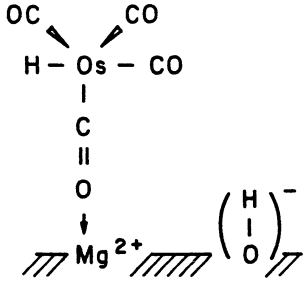

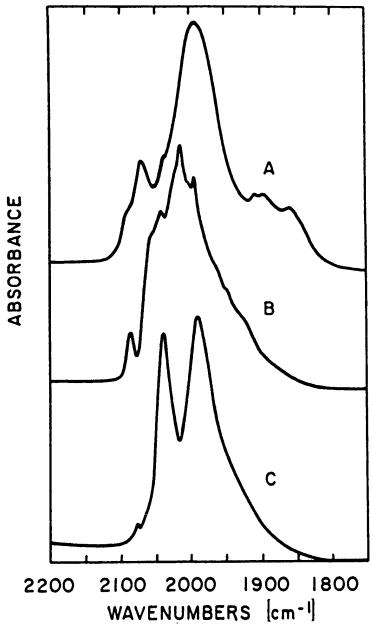

Fig.4.9. Infrared spectra (*A*) unused catalyst incorporating $HOs(CO)_4^-$ prepared from $H_2Os(CO)_4$ and MgO, (*B*) sample after use as a CO hydrogenation catalyst, and (*C*) solid after extraction, incorporating $Os_{10}C(CO)_{24}^{2-}$ [4.21]. Reprinted from *Journal of the American Chemical Society* with permission of the American Chemical Society

This was formed by deprotonation of $H_2Os(CO)_4$ on the basic MgO surface.

When the sample was heated with a 3 : 1 (molar) H_2 : CO mixture at 275°C and 10 atm for about 20 h (the catalytic CO hydrogenation reaction took place, as described in Sect.4.4), a condensation reaction occurred, giving $H_3Os_4(CO)_{12}^-$ [which was extracted from the surface with $(CH_3)_4NCl$ in isopropanol]. The remaining solid had an infrared spectrum characteristic of $Os_{10}C(CO)_{24}^{2-}$ (Fig. 4.9); following the extraction, the solid was red; the UV-visible spectrum of the used catalyst (Fig.4.5) confirms the structural inference. The surface chemistry of the osmium carbonyls on the basic MgO closely parallels the solution chemistry of the osmium carbonyls: in the presence of CO and H_2, the tetranuclear cluster is relatively stable in solution [4.40], and the synthesis of $Os_{10}C(CO)_{24}^{2-}$ takes place in high yield in the presence of Na (a reducing agent) at about 260°C [4.41]. It is inferred that the cluster anions observed on the MgO surface are the thermodynamically favored structures in the presence of $CO + H_2$. There was no evidence of Os aggregates on this surface; it is clear that the combination of ligands (provided by the basic support and the reactive gas atmosphere) was crucial to the stabilization of the molecular clusters at high temperature. Evidently the osmium carbonyls are sufficiently mobile on the surface for the cluster formation reaction to occur.

In summary, there have been only a few systematic investigations of the reactivity of surface-bound clusters. Often the reactions are complex; even when

a structurally well-defined cluster can be prepared on a surface, it often reacts to give complicated mixtures. The known solution chemistry provides the best guide to surface reactivity, but it is imprecise. Understanding of surface reactivity is expected to develop most rapidly for clusters with stable metal frameworks (such as the osmium carbonyls). Characterization by the concerted application of a variety of spectroscopic techniques (plus determination of stoichiometries of reactions involving gain or loss of ligands) will lead to the most rapid progress.

4.4 Catalytic Activity

There are only a few examples of reactions known to be catalyzed by metal clusters in solution [4.42,43], and not surprisingly there are even fewer well-documented examples of catalysis by surface-bound clusters. These examples, cited below, involve reactions of olefins as well as carbon monoxide and hydrogen.

Triosmium clusters bonded to SiO_2 [4.39] and γ-Al_2O_3 [4.44] appear to be catalytically active for olefin isomerization at temperatures less than about 90°C. Infrared spectra of the SiO_2-supported sample measured during catalysis in a flow reactor at atmospheric pressure indicated that the only detectable form of the organometallic species was the coordinatively saturated cluster $HOs_3(CO)_{10}$-O-{Si}. As flow of but-1-ene was initiated over the sample at 85°C, the catalytic activity slowly increased to a maximum and then remained unchanged. Simultaneously, there were small changes in the infrared spectrum in the carbonyl region: two new bands indicated the formation of a small amount of a cluster of different symmetry, inferred to have been formed by coordination of reactants (but-1-ene and/or hydrogen) [4.39]. When CO was introduced into the feed stream, the changes in the spectrum were reversed and catalysis stopped. The results are consistent with the suggestion that the catalytically active species were a small fraction of the surface-bound triosmium clusters, but the nature of the coordinatively unsaturated species that presumably formed (e.g., by dissociation of CO) remains to be determined.

Similar results were observed with the γ-Al_2O_3-supported cluster $HOs_3(CO)_{10}$-O-{Al} [4.44]. Catalytic reaction rate data for isomerization of hex-1-ene in the presence of H_2 are shown in the middle curve of Fig.4.10. The reaction was zero order in olefin and in H_2 partial pressures. These data also are consistent with catalysis by a small fraction of the supported clusters themselves. When the temperature was increased to 120°C, the catalytic activity declined,

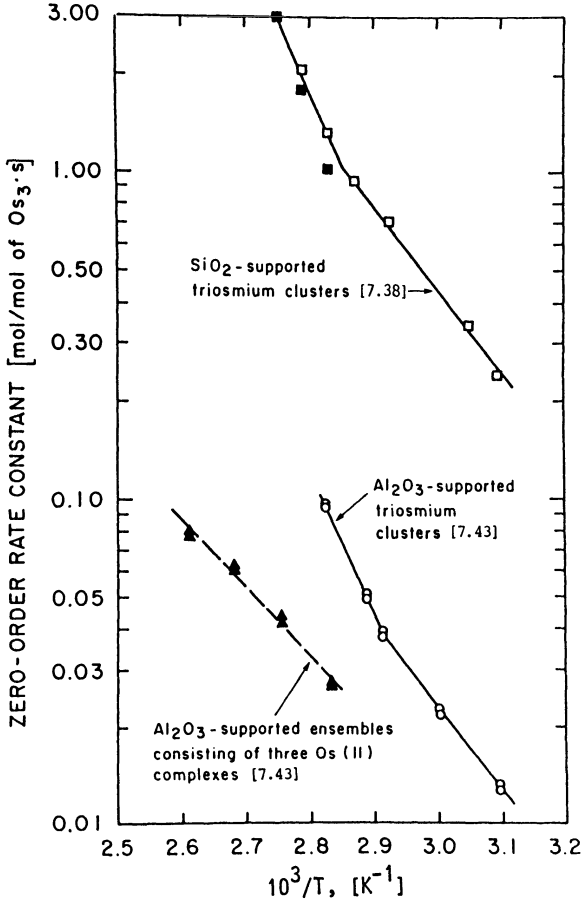

Fig.4.10. Olefin isomerization activities of catalysts incorporating triosmium clusters and ensembles formed by breakup of triosmium clusters on metal oxides

reaching a new steady state in about two hours; during this period, the cluster broke up into the mononuclear Os^{2+} complexes described above, as shown by the infrared spectrum [4.44,45]. Catalytic activity data for the mononuclear complexes are shown in Fig.4.10 (again, the isomerization reaction was zero order in the reactant and in H_2). The complexes are less active than the clusters. This comparison is important in showing that the clusters themselves were catalytically active; the possibility that small amounts of cluster degradation products were actually responsible for the activity attributed to the clusters can be discounted, since the degradation products are significantly less active than the clusters themselves.

Similar catalytic activity for isomerization of but-1-ene has been observed for γ-Al_2O_3-supported $H_3Os_4(CO)_{12}^-$ [4.9] and $H_3RuOs_3(CO)_{12}^-$ [4.11]. In each

case, infrared spectra of the working catalyst indicated that the coordinatively saturated cluster anion was the only detectable organometallic species. Extraction of most of the anions from the surface of each catalyst led to a marked reduction in the catalytic activity. Treatment of the catalyst at higher temperatures (>100°C) led to cluster breakup accompanied by reduction in the catalytic activity. Catalysts prepared by deposition of a salt of the anion on γ-Al_2O_3 had approximately the same activities as the sample prepared by deprotonation of the neutral cluster, as described above.

The SiO_2-supported triosmium clusters have been reported to be catalysts for ethylene hydrogenation in a batch reactor at 70-100°C [4.46]. Infrared spectra and chemisorption data indicated that ethylene and hydrogen coordinated to the cluster, and structures have been hypothesized for the organometallic surface intermediates [4.46]. The reaction orders in ethylene and hydrogen were found to be 0 and 1, respectively, which are the values expected for metal catalysis. One might consider the possibility that small amounts of small Os metal aggregates were formed and were responsible for the catalytic activity.

There are reports of CO hydrogenation in the presence of oxide-supported metal clusters [4.7]. When $HOs_3(CO)_{10}$-O-{Al} was used for CO hydrogenation, catalytic conversion to methane and other hydrocarbons was observed at low pressures (~1 atm) [4.26]; infrared spectra of a used catalyst [4.26] indicated that the clusters had broken up and that Os(II) carbonyl complexes were the predominant species. It has been suggested, however, that undetectably small amounts of Os metal aggregates were the more likely catalytic species [4.31].

When a triosmium carbonyl cluster of undetermined structure supported on MgO was introduced into a flow reactor for CO hydrogenation, methane and other hydrocarbon products were observed at 300°C and 32 atm [4.47]. Infrared spectra of the used catalyst indicated the presence of osmium carbonyl clusters, but their structures were undetermined. This result is tantalizing in suggesting the possibility of involvement of metal clusters in a catalytic reaction at high temperatures.

In a more thorough investigation of catalysis by MgO-supported osmium carbonyls, the initial form of the catalyst incorporated the complex anion $HOs(CO)_4^-$, prepared by surface deprotonation of $H_2Os(CO)_4$ [4.21]. The catalyst was brought up to the operating temperature (275°C) and pressure (10 atm) in a flow reactor; the feed was a 3 : 1 (molar) H_2 : CO mixture. The catalyst was active for the Fischer-Tropsch reaction, giving methane and low-molecular-weight hydrocarbons (the conversion was so low that higher hydrocarbons were not detected) (Fig.4.11). The catalyst lost activity during operation (Fig.

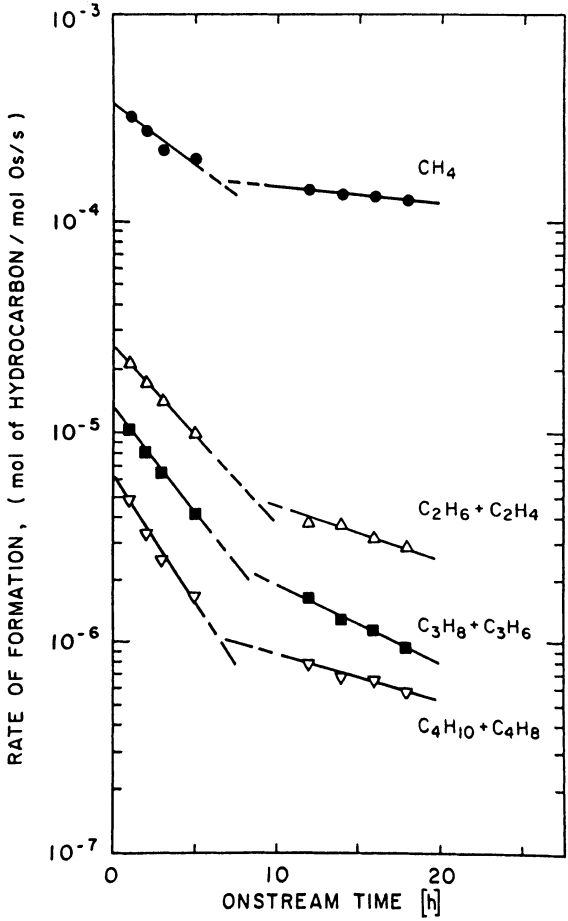

Fig.4.11. Rates of catalytic hydrogenation of CO in a flow reactor at 275°C and 10 atm. The catalyst was initially $HOs(CO)_4^-$ supported on MgO; the feed was a 3:1 (molar) H_2:CO mixture [4.21]. Reprinted from *Journal of the American Chemical Society* with permission of the American Chemical Society

4.11), and analysis of the used catalyst showed that about one-third of the initial Os had been lost, possibly as the volatile $H_2Os(CO)_4$.

The used catalyst was characterized by UV-visible and infrared spectroscopy and by extraction with $(CH_3)_4NCl$, as mentioned above, the results indicating that the only observable surface organometallic species were the stable anions $H_3Os_4(CO)_{12}^-$ and $Os_{10}C(CO)_{24}^{2-}$. Since there was no evidence of Os metal on the surface, it was suggested that the deactivation of the catalyst was associated in part with formation of the decanuclear cluster anion, which might be catalytically inactive.

More work is needed to clarify these results, but they are believed to be important in providing the first evidence of surface-bound molecular clusters stabilized at high temperatures and implicated in a catalytic reaction.

The keys to the stabilization of these clusters are the following:

(1) The stable metal frameworks provided by strong Os-Os bonds.

(2) A favorable metal/support combination, the basic MgO stabilizing the osmium cluster anions.

(3) High CO and H_2 partial pressures to stabilize the clusters.

The best prospects for application of supported molecular clusters as catalysts would seem to be those involving clusters with strong metal-metal bonds (e.g., Os, Ru, Ir) and basic supports such as MgO and CaO and reactants such as CO providing stabilizing ligands.

4.5 Supported Metals with Simple Structures Derived from Supported Organometallics

Reactions leading to changes in the metal framework structure of a supported cluster usually give complex mixtures of surface structures. There appears to be an intriguing exception, however, involving the γ-Al_2O_3-supported cluster $HOs_3(CO)_{10}$-O-{Al}. When heated to about 100-200°C, this cluster breaks up into mononuclear $Os(CO)_2\{OAl\}_3$ and $Os(CO)_3\{OAl\}_3$ complexes, as described in Sect.4.3. It has been suggested [4.26] that the mononuclear complexes were present in the form of ensembles, each consisting of three Os ions; characterization by electron microscopy showed uniform scattering centers on the γ-Al_2O_3 support, all the same size (about 7 Å) (Fig.4.12). The infrared evidence of partial reconstruction of triosmium clusters on SiO_2 and γ-Al_2O_3 (mentioned in Sect.4.3 suggests that the ensembles were formed on each support.

The ensembles appear to be unique among supported metals with respect to their uniformity of structure; the ensembles on γ-Al_2O_3 have been observed to be stable in the high-energy electron beam of the electron microscope [4.27], consistent with the strong ionic bonding of the osmium to the oxide surface indicated by the EXAFS data (Table 4.2). When the sample was treated in hydrogen at 400°C, reduced osmium ensembles of the same size were observed. These constitute perhaps the first example of a zero-valent metal supported on a metal oxide and having a single size of metal aggregate. These aggregates have not been characterized fully, and their stability has not been evaluated.

These results suggest that uniquely simple supported metals might be prepared from metal cluster precursors; variation of the metal cluster nuclear-

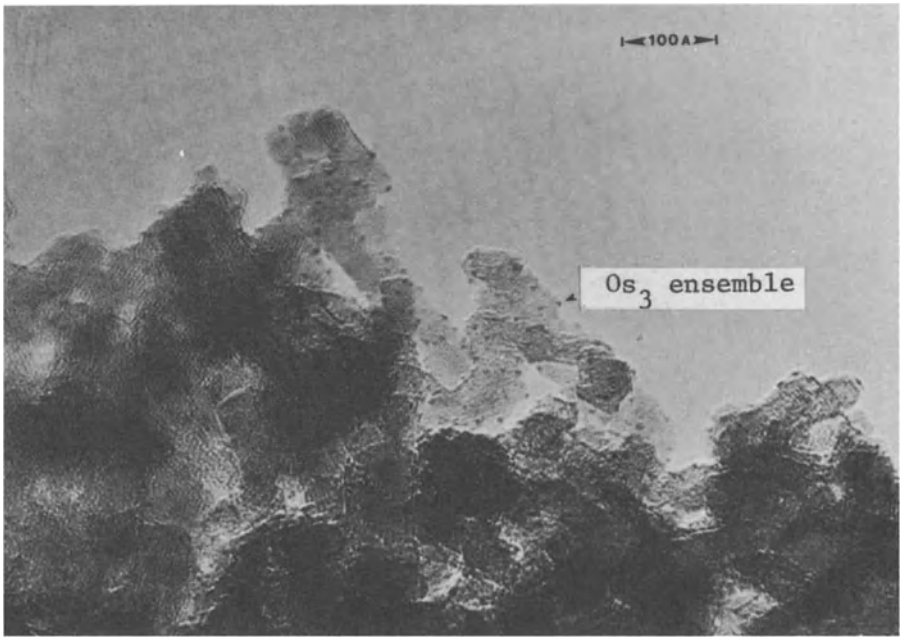

Fig.4.12. Electron micrograph of ensembles consisting of three osmium ions on γ-Al_2O_3, obtained by treating the supported triosmium cluster in argon at 200°C [4.27]. Reprinted from *Journal of Catalysis* with permission of Academic Press

ty could allow systematic variation of ensemble (and aggregate) size, and variation of the metal cluster framework composition could allow systematic variation of ensemble (and aggregate) composition. The lack of stability implies that these goals may not be achieved easily.

4.6 Summary

Supported molecular metal clusters are still a new class of materials, but there have been rapid advances in our understanding of their structures, reactivities, and catalytic activities. The rapid development is a consequence of the simplicity of structure of the materials, which allows incisive characterization with a powerful arsenal of techniques, including EXAFS, infrared, Raman, NMR, and other spectroscopies that can be interpreted on the basis of data obtained from true molecular analogues. A primary limitation of the surface-bound organometallics is their relative lack of stability. There is a need for discovery of more stable surface organometallic structures, not only to allow characterization of more materials over wider ranges of condi-

tions, but to provide good candidate catalysts. New supports and new metal-support combinations are worthy of investigation. The prospects of wholly new surface structures and new catalytic properties are valid, but much work remains to develop stable species that are structurally and catalytically novel.

Acknowledgement. This work was supported by National Science Foundation grant No.CPE-8218311.

References

4.1 J.H. Sinfelt, G.H. Via, F.W. Lytle: Catal. Rev.-Sci. Eng. **26**, 81 (1984)
4.2 M. Boudart: J. Mol. Catal. **30**, 27 (1985)
4.3 G.A. Somorjai: *Chemistry in Two Dimensions: Surfaces* (Cornell University Press, Ithaca, NY 1981)
4.4 B.C. Gates, L. Guczi, H. Knözinger (eds.): *Metal Clusters in Catalysis* (Elsevier, Amsterdam, in press)
4.5 Y.I. Yermakov, B.N. Kuznetsov, V.A. Zakharov: *Catalysis by Supported Complexes* (Elsevier, Amsterdam, 1981)
4.6 P.L. Watson, G.L. Schrader: J. Mol. Catal. **9**, 129 (1980)
4.7 R. Psaro, R. Ugo, G.M. Zanderighi, B. Besson, A.K. Smith, J.M. Basset: J. Organomet. Chem. **213**, 215 (1981)
4.8 H.H. Lamb, P.S. Kirlin, T.R. Krause, B.C. Gates: to be published
4.9 T.R. Krause, M.E. Davies, J. Lieto, B.C. Gates: J. Catal. **94**, 195 (1985)
4.10 R. Pierantozzi, E.G. Valagene, A. Nordquist, P. Dyer: J. Mol. Catal. **21**, 189 (1983)
4.11 J.P. Scott, J.R. Budge, A.L. Rheingold, B.C. Gates: to be published
4.12 H. Knözinger, Y. Zhao: J. Catal. **71**, 337 (1981)
4.13 M. Deeba, B.C. Gates: J. Catal. **67**, 303 (1981)
4.14 P.S. Kirlin, W. Bailey, H.S. Gold, B.C. Gates, et al.: to be published
4.15 F. DeThomas, T.R. Krause, H.S. Gold, B.C. Gates: to be published
4.16 F.B.M. Duivenvoorden, D.C. Koningsberger, Y.S. Uh, B.C. Gates: J. Am. Chem. Soc., in press
4.17 L. D'Ornelas, A. Choplin, J.M. Basset, L.-Y. Hsu, S. Shore: Nouv. J. Chim. **9**, 155 (1985)
4.18 M. Deeba, B.J. Streusand, G.L. Schrader, B.C. Gates: J. Catal. **69**, 218 (1981)
4.19 L.J. Hilliard, H.S. Gold: Appl. Spectrosc. **39**, 124 (1985)
4.20 G. Collier, D.J. Hunt, S.D. Jackson, R.B. Moyes, I.A. Pickering, P.B. Wells: J. Catal. **80**, 154 (1983)
4.21 H.H. Lamb, B.C. Gates: Paper presented at Catalysis Society of North America, Houston, Texas, 1985; J. Am. Chem. Soc. **108**, 81 (1986)
4.22 H.C. Foley, S.J. DeCanio, K.D. Tau, K.J. Chao, J.H. Onuferko, C. Dybowski, B.C. Gates: J. Am. Chem. Soc. **105**, 3074 (1983)
4.23 B.E. Hanson, G.W. Wagner, R.J. Davis, E. Motell: Inorg. Chem. **23**, 1635 (1984)
4.24 H.H. Lamb, R. Farlee, C. Dybowski, B.C. Gates: to be published
4.25 A. Brenner: In *Metal Clusters*, ed. by M. Moskovits (Wiley, NY, in press)
4.26 H. Knözinger, Y. Zhao, B. Tesche, R. Barth, R. Epstein, B.C. Gates, J.P. Scott: Faraday Discuss. Chem. Soc. **72**, 54 (1981)
4.27 J. Schwank, L.F. Allard, M. Deeba, B.C. Gates: J. Catal. **84**, 27 (1983)
4.28 S. Iijima, M. Ichikawa: J. Catal. **94**, 313 (1985)
4.29 R. Psaro, R. Ugo: Ref.4.4, Chap.9.2

4.30 E.O. Odebunmi, B.A. Matrana, A.K. Datye, L.F. Allard, Jr., J. Schwank, W.H. Manogue, A. Hayman, J.H. Onuferko, H. Knözinger, B.C. Gates: J. Catal. **95**, 370 (1985)
4.31 J.M. Basset, B. Besson, A. Choplin, F. Hugues, M. Leconte, D. Rojas, A.K. Smith, A. Theolier, Y. Chauvin, D. Commereuc, R. Psaro, R. Ugo, G.M. Zanderighi: In *Fundamental Research in Homogeneous Catalysis*, Vol. 4, ed. by M. Giongo, M. Graziani (Plenum, New York 1984) p.19
4.32 V.L. Kuznetsov, A.T. Bell, Y.I. Yermakov: J. Catal. **65**, 374 (1980)
4.33 J.R. Anderson, P.S. Elmes, R.F. Howe, D.E. Mainwaring: J. Catal. **50**, 508 (1977)
4.34 A. Choplin, M. Leconte, J.M. Basset, S.G. Shore, W.-L. Hsu: J. Mol. Catal. **21**, 389 (1983)
4.35 J.R. Budge, B.F. Lücke, J.P. Scott, B.C. Gates: Proc. 8th Int. Congr. Catal., Vol. 5 (Verlag Chemie, Weinheim 1984) p.89
4.36 J.R. Budge, B.F. Lücke, B.C. Gates, J. Toran: J. Catal. **91**, 272 (1985)
4.37 L. Guczi: Ref.4.4, Chap.10
4.38 Y. Iwasawa, M. Yamada: J. Chem. Soc. Chem. Commun. 675 (1985)
4.39 R. Barth, B.C. Gates, Y. Zhao, H. Knözinger, J. Hulse: J. Catal. **82**, 147 (1983)
4.40 J.N. Nicholls, D.H. Farrar, P.F. Jackson, B.F.G. Johnson, J. Lewis: J. Chem. Soc. Dalton Trans. 1395 (1982)
4.41 T.C. Hayward, J.R. Shapley: Inorg. Chem. **21**, 3816 (1982)
4.42 E.L. Muetterties, M.J. Krause: Angew. Chem. **95**, 135 (1983)
4.43 L. Markô, A. Vizi-Orosz: Ref.4.4, Chap.5
4.44 X.-J. Li, J.H. Onuferko, B.C. Gates: J. Catal. **85**, 176 (1984)
4.45 X.-J. Li, B.C. Gates: J. Catal. **84**, 55 (1983)
4.46 J.M. Basset, B. Besson, A. Choplin, A. Theolier: Philos. Trans. R. Soc. London, Ser. A **308**, 115 (1982)
4.47 M. Deeba, J.P. Scott, R. Barth, B.C. Gates: J. Catal. **71**, 373 (1981)

5. Catalysis by Molybdena-Alumina and Related Oxide Systems

W. Keith Hall

Laboratory for Surface Studies and Department of Chemistry,
University of Wisconsin, Milwaukee, WI 53201, USA

During the past 30 years, modern surface science and a variety of new spectroscopies have evolved, together with the ability to achieve, easily and routinely ultra-high-vacuum conditions. At first, tungsten surfaces were studied almost exclusively because of the ease with which they could be cleaned, used, and regenerated reproducibly. Today, experiments are carried out on single-crystal planes of many metals of catalytic interest. Similar studies of oxide and sulfide surfaces are just now beginning and they provide the investigator with some new and challenging problems. No longer will the surface be composed of atoms of a single element in various geometric arrangements all having similar chemistry. Instead the surface will contain a variety of configurations of both anions and cations, each having its own chemistry and at times acting cooperatively with each other to activate molecules.

The surfaces of most oxides are terminated by a layer of hydroxyl groups which substitute for an extension of the lattice. Usually these are thermally unstable; they condense with their neighbors to form H_2O and produce surface defects which may be the catalytically active sites [5.1]. Other times they function as Brönsted acids. The point to be remembered is that perfect single-crystal surfaces of oxides will be rare and usually catalytically uninteresting. On the other hand, chemically distinct isolated sites for chemisorption and catalysis may sometimes be characterized.

Much surface science is directed towards understanding the problem of catalysis. Under favorable circumstances, such approaches have proved rewarding. For example, *Ertl* [5.2] has demonstrated that the ammonia synthesis can be described as a series of microscopic steps, each of which can be isolated from the others. Close scrutiny reveals, however, that this success has resulted from a unique feature of this system. As in the work of *Kokes* and *Dent* [5.3] on ethylene hydrogenation over ZnO, the rate-determining step is the reductive cleavage of a strongly held (most abundant) surface intermediate. Only under such circumstances can intermediates be detected, and generally this is not the case.

It is convenient to divide the problem of catalysis into five consecutive steps: the diffusion of molecules to the surface, the chemisorption of molecules on active sites, the chemical transformations, the desorption of the product molecules, and the diffusion of products from the surface. By proper choice of the experimental conditions the diffusion steps can usually be made non-rate-limiting. Thus, the principal problems of interest to the catalytic chemist become the surface chemistry, the number and nature of the catalytic sites and the intermediates which form thereon, as well as the chemical transformations leading to products. In general, much of this information is difficult to obtain and catalytic chemists tend to pick away at the problem from both ends. The gross kinetics are easy to determine, but difficult to interpret. Tracers are employed to establish reaction schemes. Studies of the catalytic reaction are made using model compounds to isolate specific selectivity factors. Selective poisons are employed to estimate the concentration of the catalytic centers on the surface. Analogies to chemistry in homogeneous systems are sought. Then, from the other end, studies of the surface chemistry are made using probe molecules to establish functionality of surface sites. Spectroscopic studies are made both of the surface and of molecules chemisorbed thereon. Properties of these molecules are established by temperature programed desorption, etc. Finally, by synthesizing all of these data from many laboratories, an understanding of the catalytic process may be evolved. In this chapter, this synthesis process is illustrated for the molybdena-alumina system. For convenience, most of the results presented were taken from the work carried out in the writer's laboratory. This is not an exhaustive review; a large volume of related work is referenced in papers cited herein.

5.1 Nature of the Catalyst

Molybdena-alumina catalysts are usually prepared by the impregnation of γ-alumina with aqueous solutions of $(NH_4)_6Mo_7O_{24}$. The paramolybdate ions are chemisorbed on the positively charged alumina surface at low pH [5.4]. On drying and heating, deamnination occurs, together with condensation of the resulting paramolybdic acid with the basic hydroxyl groups of the alumina surface, leading to formation of bound clusters containing seven or so Mo^{+6} ions per cluster [5.5]. A cobalt or nickel promoter may be added to enhance the activity of the final sulfided catalyst. The replacement of the surface hydroxyl groups by bonding to molybdate was demonstrated by the spectra [5.6] shown in Fig.5.1, as well as by direct measurement of the decrease in the hydrogen content of the preparations[5.7]. The alumina O - H stretching bands decreased in

Fig.5.1

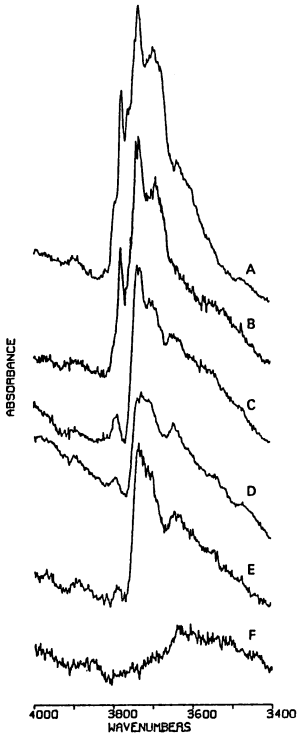

Fig.5.2

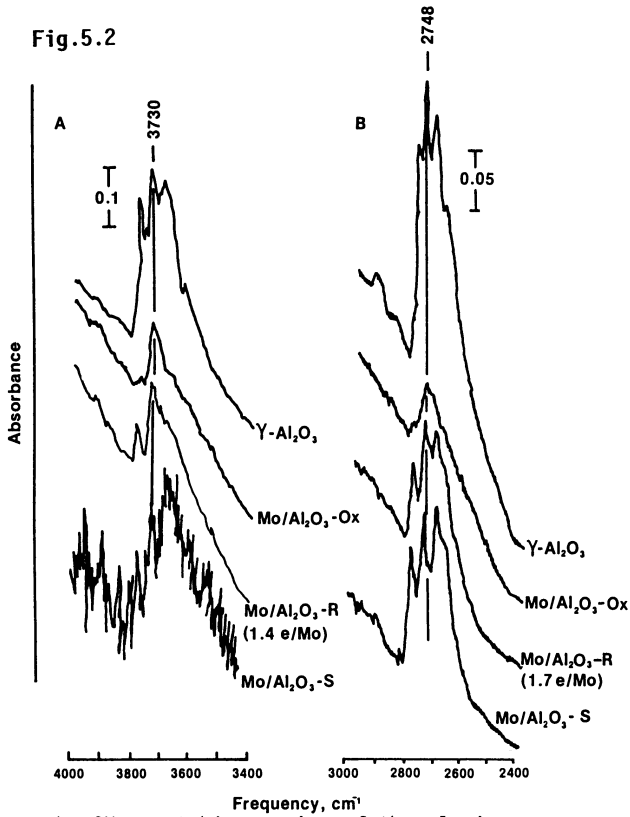

Fig.5.1. Infrared spectra from the OH stretching region of the alumina support (*A*) and from the support loaded with 1.1 (*B*), 2.8 (*C*), 4.6 (*D*), 5.0 (*E*), and $7.3^{(F)} \times 10^{20}$ Mo/g, respectively [5.6]

Fig.5.2. Infrared spectra from (*A*) the OH and (*B*) the OD regions of normal and exhaustively deuterated preparations, respectively. The catalyst, containing $\sim 5 \times 10^{20}$ Mo/g, in its oxidized, reduced, and sulfided state may be compared with the alumina support. All spectra were scaled to the same thickness and loading [5.8]

intensity as the catalyst was loaded with increasing amounts of molybdena and were virtually eliminated when the monolayer capacity was reached at $\sim 7 \times 10^{20}$ Mo / g. This bonding to the alumina surface was partially reversed by reduction or sulfiding. This is evident in the spectra [5.8] shown in Fig.5.2A for the hydroxyl, and in Fig.5.2B for the deuteroxyl regions, respectively. Clearly, the band intensities stemming from the alumina surface hydroxyl groups were greatly reduced when the platelets were loaded with molybdena. It is equally evident that these bands were partially restored when the catalyst was reduced or sulfided. (The extreme noise in the spectrum of the sulfided preparation in the O - H regions was due to its very low transmission of $\leqslant 2\%$ in this re-

Table 5.1. Observations of surface hydroxyl groups by NMR [5.9]

Experiment	Hydrogen content [$H \times 10^{-14}/cm^2$]		
	By isotope dilution (D_2)	By NMR	Percent observed
(A) On alumina support			
Evacuated at 500°C	3.6	2.3	64
After adsorption of D_2O	3.6	3.5	97
(B) On reduced (e/Mo = 1.3) molybdena-alumina			
Evacuated at 500°C	2.4	0.5	21
After adsorption of D_2O	2.4	1.8	75

gion.) As discussed later in this section, it is probable that recrystallization occurred in these steps.

Further evidence of surface segregation of the molybdena phase into islands or clusters on reduction was obtained from measurements [5.9] of the ^{1}H-NMR of the hydroxyl groups (Table 5.1) coupled with observations of the electron paramagnetic resonance (EPR) intensities from Mo^{+5} formed on reduction. The surface hydroxyl concentration following evacuation of the alumina support at 500°C (measured by NMR) was roughly two-thirds as large as the total hydrogen known to be present (measured by the isotope dilution method upon exchange with D_2). The missing protons could be recovered by adding D_2O to the sample, i.e., by rehydrating (healing) the surface. Moreover, the more extensively the alumina was dehydroxylated, the larger was the fraction of the missing protons. It was suggested [5.9] that the large electric field gradients developed upon dehydroxylation greatly increased the relaxation frequency of the ^{27}Al nucleus, and that this in turn broadened the signal from protons on adjacent hydroxyl groups into the noise level.

When these data were compared with those from reduced molybdena-alumina catalysts (Table 5.1) a similar phenomenon was observed, but now only about two-thirds of the missing protons could be recovered by the addition of D_2O. The surprising feature, however, was that a proton resonance signal could be detected at all. On reduction, unpaired electrons are produced and some of these can be seen in the EPR signal from Mo^{+5}. An isolated Mo^{+5} should eliminate the signal from all protons within roughly 10 Å, i.e., from an area of about 315 $Å^2$. A simple calculation showed that, were both the hydroxyl groups and the unpaired electrons uniformly spread over the surface, no signal should be detected from 158 m^2/g of the 184 m^2/g total area. The much higher fraction

observed demonstrated that areas of free alumina surface exist in between the clusters of molybdena. This was confirmed by second-moment calculations from these data, which suggested that the protons being observed on the reduced molybdena-alumina preparations were identical with those attached to free alumina surface.

As described previously [5.4,5], the final calcined catalysts exhibited the same principal Raman bands found on the freshly prepared wet samples (made by the equilibrium adsorption method) as well as those corresponding to $(NH_4)_6Mo_7O_{24}$. Several additional bands were also present, however, which suggested that some monomeric tetrahedral surface species may have been formed. The latter were found [5.5] to be very difficult to reduce with H_2 and could be identified with the observed Mo^{+5} signal.

Recent extended X-ray absorption fine structure (EXAFS) data obtained by several groups [5.10,11] strongly suggested the presence of microcrystalline MoO_2 and MoS_2 in the reduced and sulfided catalysts, respectively. In Fig.5.3 the EXAFS pattern from a sulfided catalyst is compared with those from amorphous and bulk MoS_2. Significantly, the pattern from the sulfided catalyst is almost indistinguishable from that of the amorphous material (surface area ~50 m^2/g) prepared by the method of *Chianelli* et al. [5.12]. With the wafer-like chalcogenide structure of MoS_2, growth would be expected along the edges

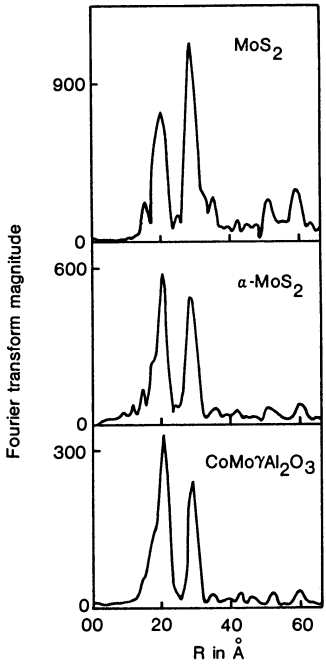

Fig.5.3. The magnitude of the Fourier transforms of EXAFS spectra after background subtraction and multiplication by K^3. All spectra were recorded at 77 K. Polycrystalline and amorphous MoS_2 are compared with a sulfided molybdena-alumina catalyst [5.11]

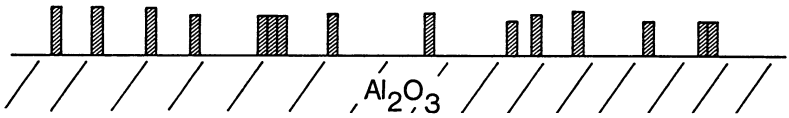

Fig.5.4. Model of a sulfided molybdena-alumina catalyst. Small wafers of MoS_2 are bound to the alumina surface at the growth edges of the chalcogenide structure

of the planes. Thus, perhaps the best model (Fig.5.4) of the molybdena-alumina catalyst in its working condition is that of tiny defective wafers still attached to the alumina surface at the growth edges, the remaining periphery providing the defect centers necessary for catalysis. Evidently, recrystallization has been necessary to transform the bound paramolybdate clusters into the tiny edge-bound wafers. Alumina surface is freed in this process as evidenced by the regeneration of a portion of the hydroxyl groups lost during preparation. In summary, the evidence suggests the presence of at least two forms of molybdena bound to alumina in the unreduced catalysts: a monomeric tetrahedral form in relatively small amounts, and a polymeric bound microcrystalline phase. These are recrystallized on reduction, freeing alumina surface.

Selective chemisorption is a useful tool in the study of supported catalysts. A common application is to distinguish the surface area of supported metal particles from the total surface area of the support plus metal. It has been found [5.8,13] that NO and CO_2 can be used in this way to separate the molybdena component from the alumina support. This is illustrated by the spectra in Fig.5.5. Spectra A and F were obtained on adsorption of NO on the freshly prepared reduced and sulfided catalysts, respectively. Similarly B and G were obtained with CO_2 and C and H resulted when NO was adsorbed on top of the CO_2. Spectra D and I were derived by the subtraction of spectra B and G from C and H using the internal computer of the Nicolet Fourier transform spectrometer. The resulting spectra are virtually identical with A and F, demonstrating that the two molecules adsorbed independently on different portions of the catalyst surface. Spectra E and J were obtained when CO_2 was added to the alumina support after the identical pre-treatment procedures used with the reduced and sulfided catalysts, respectively. Clearly, CO_2 adsorbs selectively on the uncovered alumina portion of the catalyst surface and NO on the molybdena portion. Interestingly, additional strong bands appeared when the alumina was sulfided which were not present without this treatment. This suggested that some sulfur was incorporated into the alumina surface during the reductive treatment with 10% H_2S/H_2.

As shown in Fig.5.6, the free alumina portion of the surface can be varied by increasing the extent of reduction or by sulfiding. The parameter e/Mo is

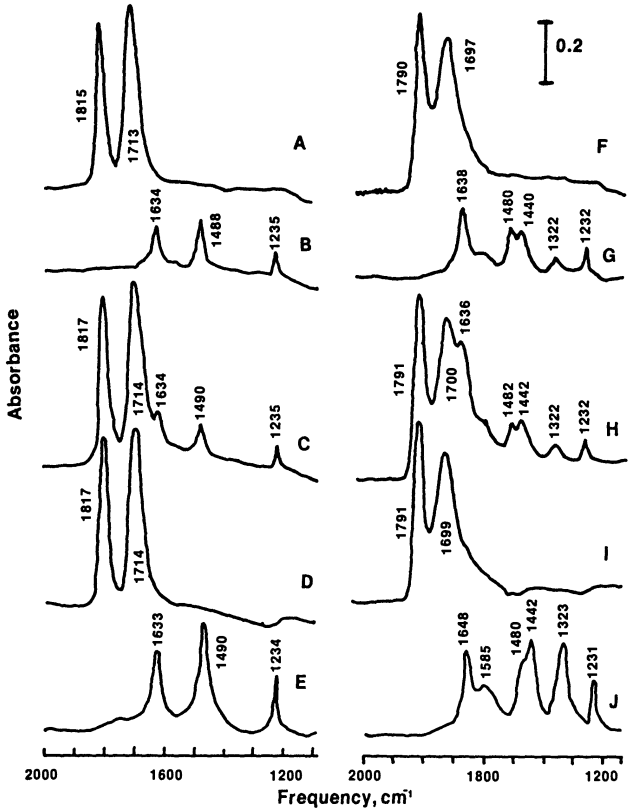

Fig.5.5. Spectra from chemisorbed NO and CO_2 demonstrating that they occur in separate surface sites, i.e., the NO on the catalytically active sites on the molybdena portion of the surface and the CO_2 on the alumina. The left- and right-hand spectra are for adsorption on freshly prepared reduced and sulfided catalysts, respectively. (*A*,*F*): adsorption of NO; (*B*,*G*): adsorption of CO_2; (*C*,*H*): NO adsorbed on top of CO_2; (*D*,*I*): subtraction of spectra (*B*) and (*G*) from (*C*) and (*H*), respectively; (*E*,*J*): CO_2 added to the alumina support (without the molybdena component) [5.8,13]

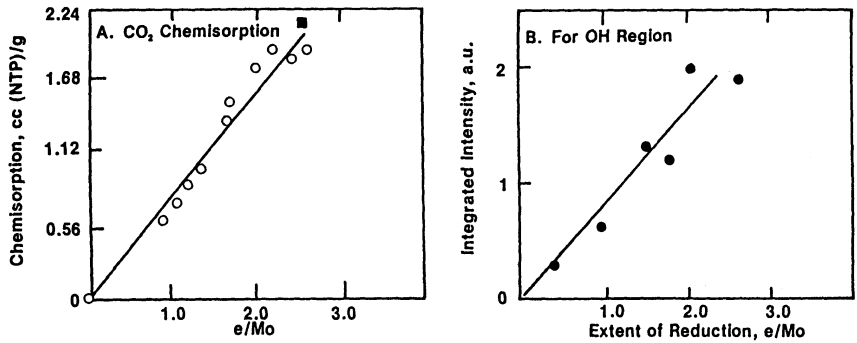

Fig.5.6. Dependence of the free alumina portion of the surface on the extent of reduction as determined by (*A*) CO_2 chemisorption and by (*B*) the integrated intensities of the OH region of the IR spectra. The solid square distinguishes a sulfided preparation from reduced ones plotted as open circles [5.8]

a convenient measure of the average extent of reduction of the molybdena to valence states below Mo^{+6}. It can most conveniently be measured by reoxidation of the preparations [5.14]; e/Mo = 2 corresponds to an average valence state of Mo^{+4}, etc. It must be appreciated that this parameter does not mean that all of the Mo ions have a single valence state; they may be distributed among higher and lower states. Note particularly that when e/Mo > 2.0, the presence of some molybdenum ions in valence states lower than Mo^{+4} is demonstrated. The two plots in Fig.5.6 show that the integrated intensity of the hydroxyl region and the CO_2 chemisorption both increased linearly with the extent of reduction; both measured the extent of the free alumina surface. Carefully controlled measurements with the parent alumina provided a means of estimating the fraction of free alumina surface following these treatments. Data obtained in this way are shown in Fig.5.7. The data for the sulfided form of the catalyst (solid squares) fell on the same plots with the reduced catalysts in Figs.5.6A and 7. Moreover, it can be seen that the average valence state for the sulfided form lies midway between Mo^{+4} and Mo^{+3}, and that approximately 75% of the alumina surface area which was covered with molybdena during preparation has been recovered on sulfiding. Clearly this evidence of a recrystallization process conforms to the picture derived from the EXAFS data.

Weller and co-workers [5.15] have attempted to approach the problem of molybdena dispersion in a manner analogous to the use of chemisorption techniques with supported metals. They noted that O_2 does not chemisorb to an appreciable extent on alumina or on the oxidized form of the molybdena-alumina catalyst. After reduction or sulfiding, however, it chemisorbs irreversibly and conveniently at about -78°C. A calibration was made by determining the total BET

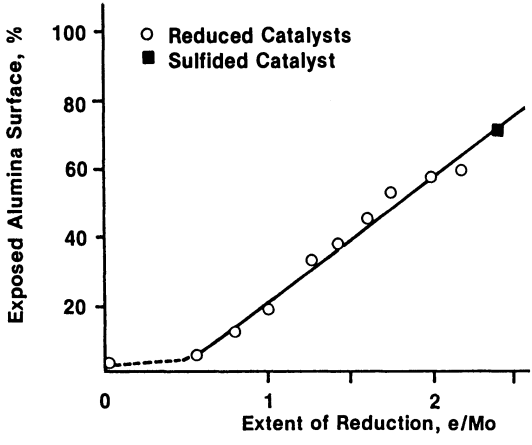

Fig.5.7. Fraction of free alumina surface estimated from data of Fig.5.6 and comparable data for the alumina support [5.8]

(Brunnauer-Emmett-Teller) surface areas of unsupported MoO_2 after the same reductive treatments used with the supported catalysts; the oxygen chemisorption values were then obtained and the value per unit area was used to deduce equivalent molybdena area (EMA) on supported preparations. Implicit was the assumption that the supported molybdena phase was composed of crystalline MoO_2 in a manner analogous to supported metals. This interesting concept has been used as a correlating parameter for catalytic data. Unfortunately, it is an oversimplification of the real system, and we think not the best interpretation of the data [5.16,17].

5.2 Nature of the Catalytic Centers

Molybdena-alumina catalysts exhibit distinct catalytic functions. They are active hydrogenation catalysts for olefins and di-olefins; they function successfully as hydrodesulfurization catalysts; they catalyze olefin metathesis and the isomerization of cyclopropanes. Not infrequently they are said to have a Brönsted acid function, and under severe conditions they can effect hydrogenolysis of cyclopropanes and paraffins.

Simple olefins such as ethene can be hydrogenated rapidly at sub-zero temperatures. The rates are strongly dependent on the extent of reduction and can be too fast to measure under certain circumstances. Some data for propene [5.18,19] are shown in Fig.5.8, where the rates of hydrogenation and meta-

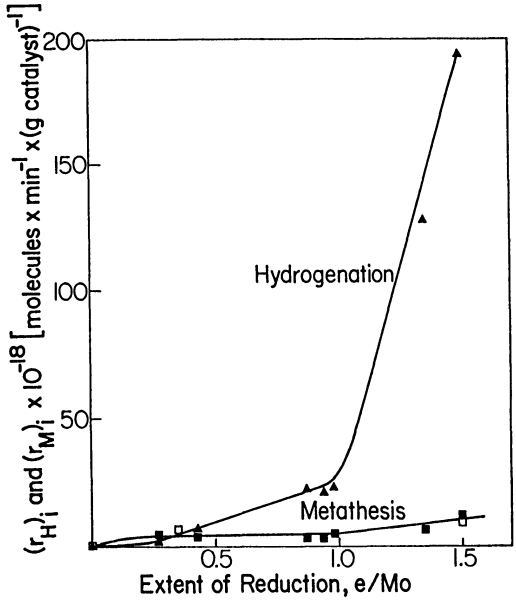

Fig.5.8. Dependence of rate of hydrogenation (or metathesis) of C_3H_6 on the extent of reduction [5.18,19]

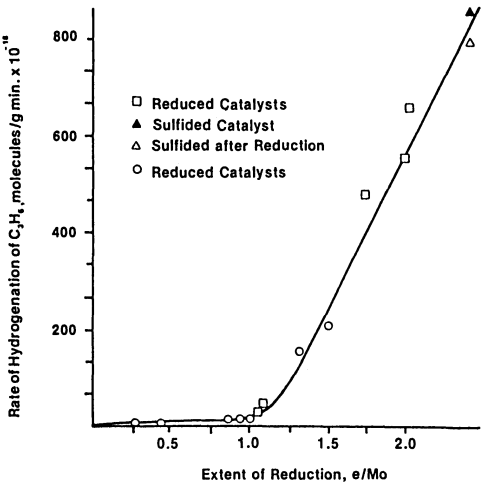

Fig.5.9. Collected data for rates of hydrogenation of C_3H_6 as a function of extent of reduction for reduced and sulfided catalysts [5.8]

thesis at 20°C are plotted as a function of e/Mo. The rates of hydrogenation were relatively slow until e/Mo approached unity; they then increased rapidly. Metathesis on the other hand was turned on at a low extent of reduction, but then was relatively independent of e/Mo. Moreover, the metathesis rate was not much affected by the presence or absence of $H_2(D_2)$ in the gas phase.

These data have now been extended to still higher extents of reduction and to sulfided preparations [5.8]; the data from the several sets of experiments are all collected in Fig.5.9. The hydrogenation rates for the sulfided preparations fit nicely onto the curve defined by the remaining data. This strongly suggests that the catalytic hydrogenation sites for the sulfided and reduced molybdena-alumina catalysts are similar in nature, have the same function, and that the same rate-determining step is involved. Metathesis was eliminated by sulfiding. The shapes of Figs.5.8 and 9 suggest that coordinative unsaturation is being developed as H_2O is removed by reduction. Evidently below e/Mo = 1.0 the degree of coordinative unsaturation is low and hydrogenation slow. Above this point, multiple coordinative unsaturation is developed and the rates of hydrogenation increase rapidly.

A selective poison was sought [5.18,19] to enable the estimation of the fraction of the molybdenum ions which are effective for hydrogenation. Nitric oxide was chosen because it is a strong ligand in bonding to transition metal ions. Reproducible rates could be obtained repeatedly over the unpoisoned catalysts. The freshly reduced catalyst was titrated with varying measured amounts of NO which were quantitatively chemisorbed. Experiments were also attempted where excess NO was added and then partially removed by evacuation at higher and higher temperatures. In this way the data of Fig.5.10 were obtained. The

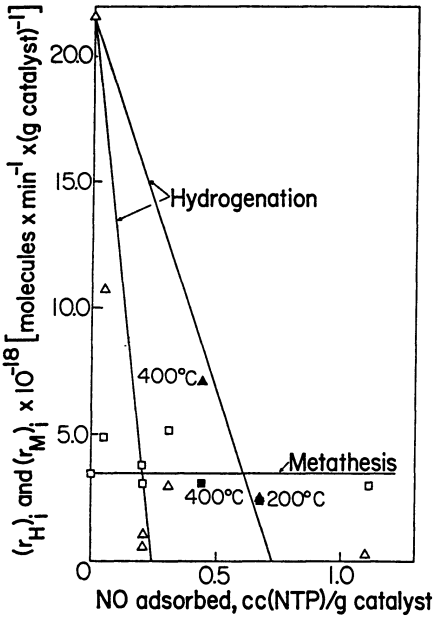

Fig.5.10. Poisoning plot for a reduced molybdena-alumina catalyst. The lethal dose may be determined from the intercept on the abscissa (see text). Note that olefin hydrogenation, but not metathesis, is poisoned [5.18,19]

lethal dose was defined as the smallest amount of NO required to completely poison the catalytic activity under the existing experimental conditions. Non-selective adsorption or complication arising during desorption at higher temperatures can lead to higher values of the intercept on the abscissa, but these are not meaningful. From the data shown on Fig.5.10 the intercept of about 0.25 cc(NTP)/g suggested that only about 1% of the molybdenum ions were effective in this experiment. These data were collected for a catalyst reduced to e/Mo = 0.9, i.e., just at the knee of Fig.5.8. When the experiment was repeated with the same catalyst reduced to e/Mo = 1.3, the lethal dose was found to be about 4 times larger. It may be estimated, therefore, that on the sulfided catalyst it might be something like 20 times larger. In this case the lethal dose would correspond to about one NO molecule for every five molybdenum ions. This would imply that something like 10 to 15% of these ions were active sites, see later in this section.

Catalytic intermediates are usually metastable species having a very short lifetime. Therefore, in the steady state they may be present in very small supply, covering at most a few percent of the surface, and consequently undetectable by ordinary spectroscopic means. Furthermore, spectra are integrals from all (adsorbed or surface) species present. They emphasise the most strongly held species and these are usually not the catalytic intermediates. It is easy for strongly adsorbed byproducts of the reaction to collect on the

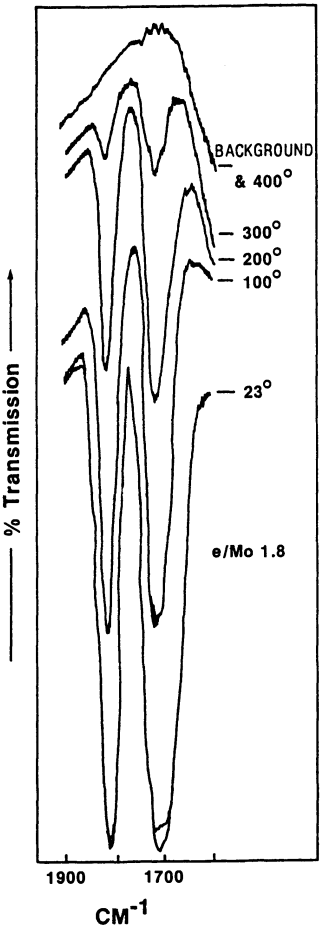

Fig.5.11. Infrared spectra from NO chemisorbed on a reduced molybdena-alumina catalyst showing dinitrosyl bands [5.20]

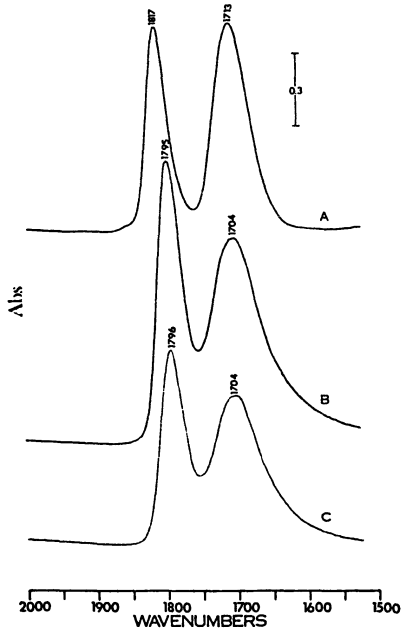

Fig.5.12. Infrared spectra from chemisorbed NO on reduced and sulfided molybdena-alumina catalysts showing similarity of the sites. (*A*): reduced catalyst; (*B*): reduced then sulfided; (*C*): sulfided only [5.21]

catalyst surface; thus, sorting out the intermediate is like looking for the needle in the proverbial haystack. The use of selectively chemisorbed poison molecules having favorable spectroscopic properties affords a way to circumvent this difficulty. Because of its strong dipole moment and characteristic IR bands, NO can be readily detected even when present in small amounts. Thus, catalysts containing the lethal dose or less chemisorbed NO were examined [5.20] and the results are shown in Fig.5.11. Infrared bands were obtained characteristic of dinitrosyl species found in inorganic chemistry. Isotopic substitution of ^{15}NO for ^{14}NO confirmed that these spectra stemmed from two NO molecules bound to a single molybdenum center. Thus, it was established that the sites required for catalytic hydrogenation have a high degree of coordinative unsaturation and are present in relatively small amounts. Moreover, it may be suspected that these centers have lower than the bulk valence

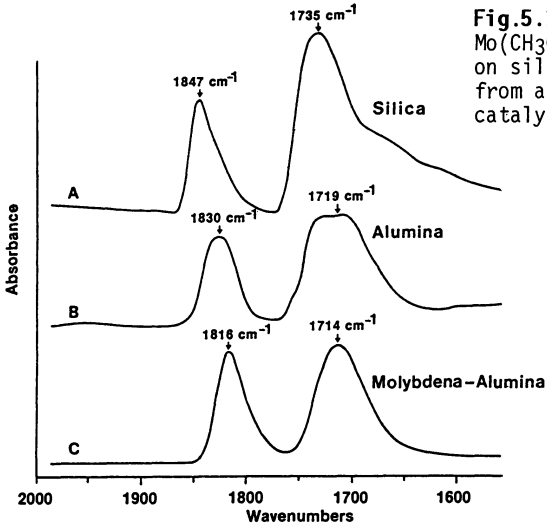

Fig.5.13. Infrared spectra from $Mo(CH_3CN)_4(NO)_2[(BF_4)_2]$ supported on silica gel and on alumina and from a reduced molybdena-alumina catalyst [5.22]

state for MoO_2 or MoS_2. The dinitrosyl spectra from reduced and sulfided catalysts are closely similar. As shown in Fig.5.12, the spectra differed only by a shift of from 10 to 20 cm^{-1} to lower frequencies on sulfiding and by a slight broadening of the bands [5.21]. These spectra closely resemble (Fig. 5.13) those obtained when $Mo(CH_3CN)_4(NO)_2$ $[(BF_4)_2]$ was supported on silica or alumina [5.22].

Oxygen chemisorption determined by the method of *Weller* and co-workers [5.15] may be used as a correlating parameter for catalytic activity, as shown in Fig.5.14. The rate data were taken from Fig.5.7, and the oxygen chemisorption data were determined on duplicate preparations. The data suggest that both oxygen and NO adsorbed on the same sites, i.e., those which effect catalytic hydrogenation. The relationship, however, was not simple.

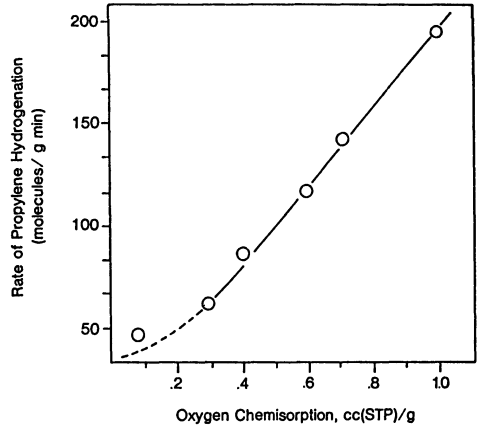

Fig.5.14. Correlation of rates of hydrogenation of C_3H_6 with O_2 chemisorption [5.19]

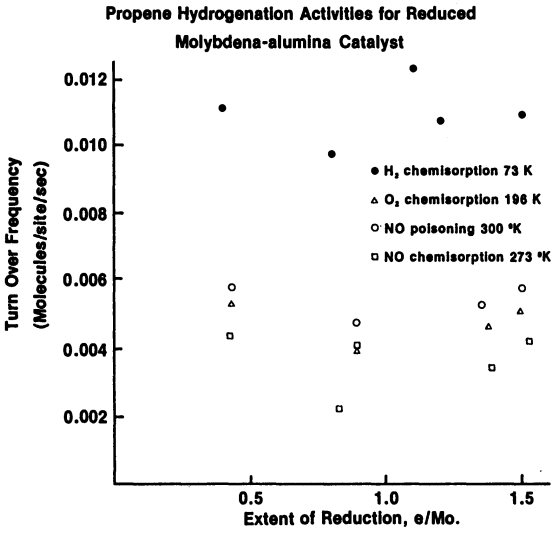

Fig.5.15. Turnover frequencies for catalytic hydrogenation of C_3H_6 based on numbers of sites determined by chemisorption measurements

As shown in Fig.5.15, reasonably constant turnover frequencies for propene hydrogenation could be calculated from O_2 chemisorption, NO chemisorption, and the lethal doses for NO poisoning when a 4 : 1 relationship between NO and O_2 was assumed, i.e., when each site was counted by two NO molecules or by one oxygen atom. This 4 : 1 relationship was confirmed by direct chemisorption measurements [5.21].

Very little O_2 could be adsorbed on a surface where the sites had been previously saturated by the NO, but the reverse was not true. Although no oxygen desorbed when NO was exposed to an oxygen-covered surface, approximately two NO molecules were adsorbed for each oxygen atom already present. These features can be seen in the spectra of Fig.5.16. The results are consistent with

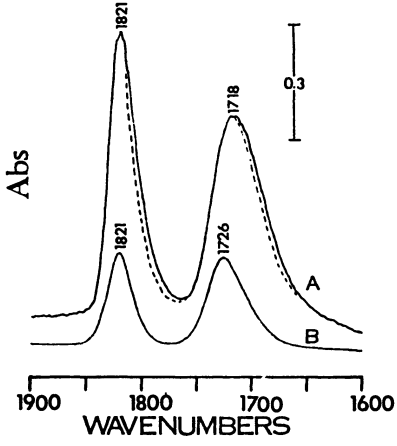

Fig.5.16. Infrared spectra from (*A*) NO adsorbed on reduced molybdena-alumina before and after exposure to O_2 and (*B*) NO adsorbed on the same catalyst after chemisorption of oxygen [5.21]

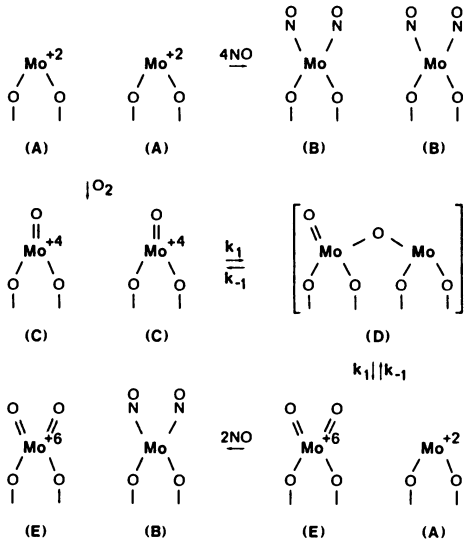

Fig.5.17. Rationale of obserservations on the successive chemisorption of oxygen and NO [5.21]

the grossly oversimplified chemistry written in Fig.5.17. According to this diagnosis, the coordinatively unsaturated centers may be pictured as residing at the edges of anion-deficient surface-bound MoO_2 or MoS_2. These anion deficiencies produce effectively Mo^{2+} centers. Each of these will coordinate two NO molecules just as in the complexes described pictorially in Fig.5.17. The same Mo^{2+} centers may be oxidized by two electrons to hold one oxygen

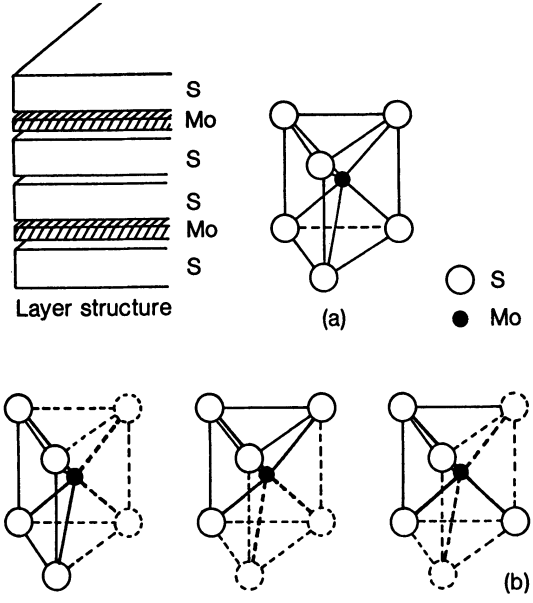

Fig.5.18a,b. Layer model of MoS_2 crystal. (**a**) Perfect unit cell and (**b**) a surface unit cell having two degrees of coordinative unsaturation [5.23]

atom each. When NO is exposed to the oxygen-covered surface, a further rearrangement may be visualized in which half of the oxygen chemisorption sites are freed so that they may now form new dinitrosyl species. A more realistic description of the anion vacancy site is borrowed from *Tanaka* and *Okuhara* [5.23] and shown in Fig.5.18.

5.3 The Chemisorption of Hydrogen on the Catalytic Centers

If catalysis occurs, it is axiomatic that at least one of the reacting molecules must be chemisorbed. Thus, the chemisorption of H_2 was studied [5.24, 25] because it is common to hydrodesulfurization as well as hydrogenation reactions. At 78 K, substantial amounts of H_2 or D_2 were adsorbed. The isotherms (Fig.5.19) were nearly reversible, but contained a very small irreversibly held component. This could be measured directly in pulse experiments, some results of which are shown in Table 5.2. The total adsorption (Fig.5.19) at 500 Torr fell between 0.5 and 1 mmol/g with the D_2 isotherm being approximately 80% higher than that for H_2. The chemisorbed portion shown in Table 5.2 was two orders of magnitude smaller, the amount varying with the extent of reduction, see later in this section. The isotopic separation factors could be deduced as shown in Fig.5.20 from the slopes of the linear plots of the hydrogen pressure versus the deuterium pressure required to maintain the same surface coverage. The rationale for this treatment is as follows: if the adsorption equilibrium constants for H_2 and D_2, K_{H_2} and K_{D_2}, can be written as factorable functions of coverage and pressure, i.e.,

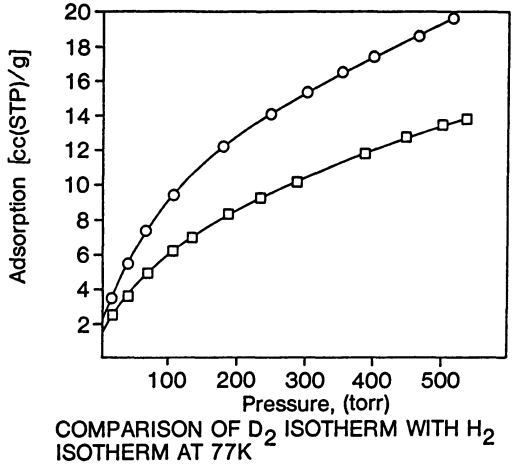

Fig.5.19. Adsorption isotherms for D_2 (o) and for H_2 (□) at 77 K for a catalyst reduced to e/Mo = 1.0 [5.24,25]

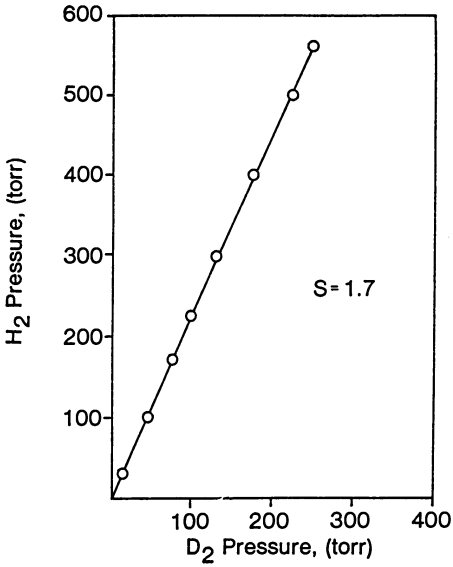

Fig.5.20. Determination of separation factors by application of (5.2) [5.24]

$$K_{H_2} = F(\theta)f(P_{D_2}) \quad , \qquad K_{D_2} = F(\theta)f(P_{H_2}) \quad ; \tag{5.1}$$

then the thermodynamically defined separation factor S may be written as

$$S = K_{D_2} / K_{H_2} = \left[f(P_{H_2}) / (f)P_{D_2}\right]_\theta \approx (P_{H_2} / P_{D_2})_\theta \quad , \tag{5.2}$$

leading to the result of Fig.5.20.

The data of Table 5.2 show that at low temperatures and low extents of reduction, H_2 was chemisorbed as molecules. These could be eluted with D_2 with-

Table 5.2. Hydrogen chemisorption on reduced molybdena alumina catalyst at 78 K[a] [5.25]

e/Mo	H_2 chemisorption [cc(NTP)/g]	Elution by D_2 pulses [0.312 cc(NTP)]			
		Pulse no.	H_2[%]	HD[%]	D_2[%]
0.75	0.090	1	85	0	15
		2	25	0	75
		3	10	0	90
		4	tr	0	∿100
1.3	0.235	1	85	8	7
		2	5	20	75
		3	2	12	86
		4	0	4	96
		5	0	0	100

[a]Chemisorption was carried out by passing repeated pulses containing 0.278 cc(NTP) to saturate over a molybdena-catalyst (5×10^{20} Mo/g or 8% Mo) reduced to various extents. The chemisorbed H_2 was then eluted with D_2.

out isotopic exchange. At higher extents of reduction, the behavior was similar, but isotopic exchange occurred both during the passage of the pulse of D_2 and between pulses. In both cases the chemisorbed hydrogen could be essentially completely removed during the passage of four pulses. These data suggest that the primary process on the strong chemisorption sites is a heterolytic, dissociative adsorption when the thermal energy is sufficient to rupture the H-H bond. This occurs to an increasing extent as the strength of the sites is increased by further reduction. The substantial barrier to rotation associated with the large separation factors for alumina and the unreduced catalysts may be taken as evidence of a strong polarization of the molecules in a high electric field of the type that would lead to a heterolytic dissociative adsorption given favorable energetics [5.26].

The isotherms of the type shown in Fig.5.19 were similar for the parent alumina and for the oxidized and reduced catalysts. The coverages at fixed pressure were highest for the parent alumina, passed through a minimum with catalysts at low extents of reduction, but partially recovered when the catalyst was further reduced. Moreover, the high separation factors obtained by this technique on all these catalysts suggested that most of the reversibly held H_2 was associated with the alumina portion of the surface. This behavior should be contrasted with that of the strong chemisorption shown in Fig.5.21

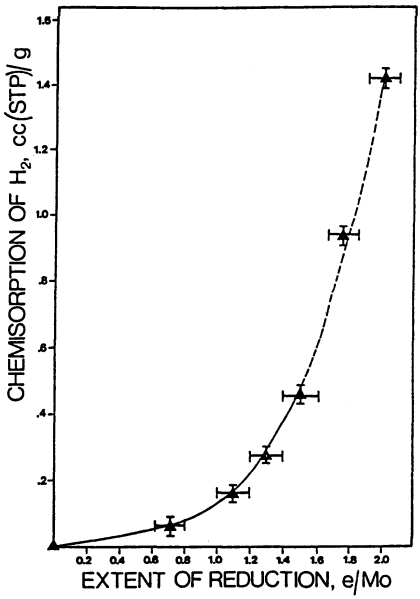

Fig.5.21. Dependence of the irreversible hydrogen chemisorption on the extent of reduction, e/Mo [5.25]

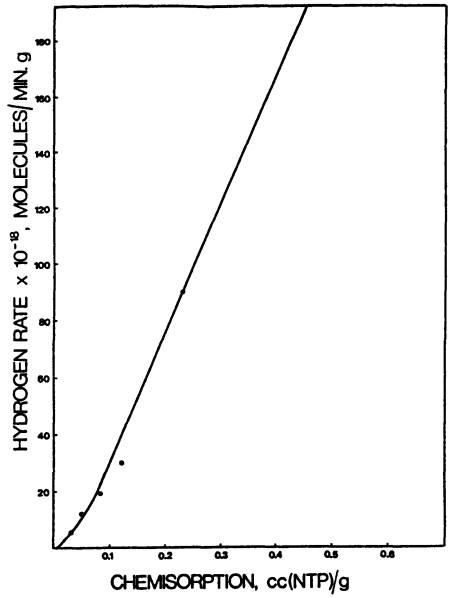

Fig.5.22. Correlation between hydrogen chemisorption and rate of hydrogenation of propene [5.25]

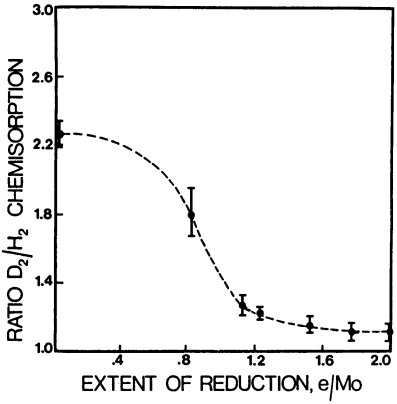

Fig.5.23. Variation of the ratio of strong chemisorption of deuterium to that of hydrogen (V_{H2}/V_{D2}) as a function of the extent of reduction [5.25]

which closely mimics the rates of hydrogenation shown in Figs.5.8 and 9. These data strongly suggest that sites for H_2 chemisorption are created on the molybdena portion of the surface as the catalyst is reduced. Interestingly, a good correlation between the rates of hydrogenation and the H_2 chemisorption is also shown in Fig.5.22 as well as in Fig.5.15. (The higher turnover frequencies than those calculated from the O_2 and NO chemisorption reflect the fact that the H_2 chemisorptions are only about one-half as large, other things being equal. These turnover frequencies could be brought in line with the others by the questionable assumption that the sites should be counted as H-atoms rather than H_2 molecules, as was done for the O_2 chemisorptions.)

When the strong chemisorption of H_2 [5.25] shown in Fig.5.21 was compared with that for D_2, the ratio plotted in Fig.5.23 was obtained. Interestingly, at low extents of reduction where the chemisorption appeared to be molecular, the ratios were similar to the high separation factors obtained from the total adsorptions (Fig.5.20). The ratios fell close to unity, however, as the depth of the reduction was increased into the range where isotopic exchange became rapid. Thus, the values approaching unity can be taken as evidence that the strong chemisorptions had become dissociative.

When the oxygen chemisorption corresponding to the lethal dose for hydrogenation was added to a catalyst reduced to e/Mo$\approx$1.2, the total adsorption of H_2 was reduced to about half its normal value (Fig.5.24). Only the strong chemisorption on the molybdena portion of the surface was eliminated, leaving that on the alumina portion unaffected. Moreover, the ratio of strong D_2 to H_2 chemisorption was reconverted from about 1.0 to $\sim$2.2 by an amount of chemisorbed oxygen which was an order of magnitude less than that required to reoxidize the catalyst from its reduced state (e / Mo = 1.2) back to its completely oxidized from. Thus, the catalyst had been selectively reoxidized at the catalytic centers.

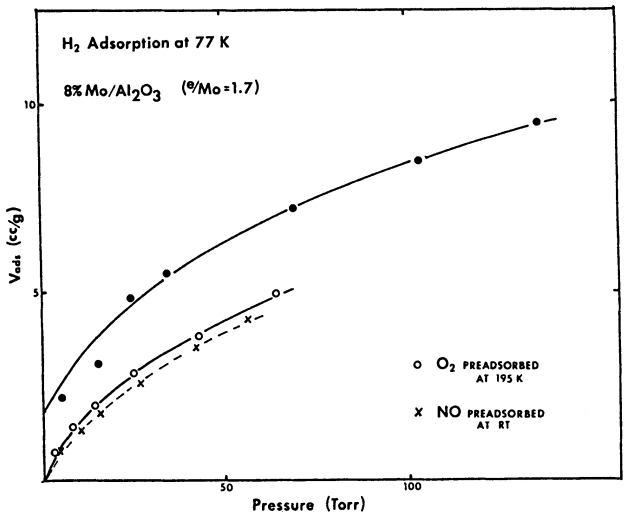

Fig.5.24. Effect of irreversibly chemisorbed oxygen on the total adsorption of H_2 at 77 K on a catalyst reduced to e/Mo≈1.2 with O_2 poisoning (o); with NO poisoning (X) [5.27]

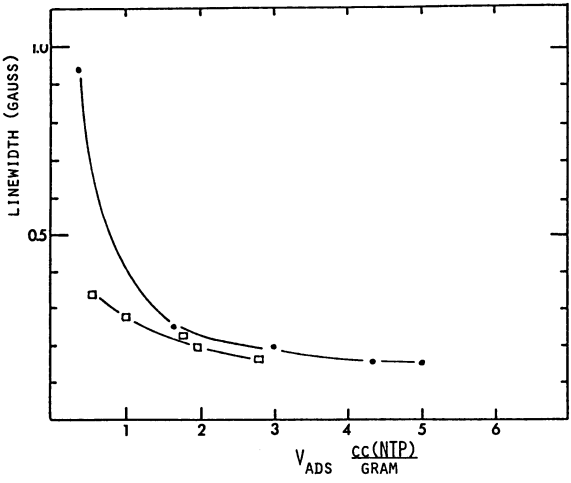

Fig.5.25. Line widths for the ^{1}H-NMR signal (35 MHz, 77 K) as a function of coverage from ortho-H_2 adsorbed on the oxidized form of a molybdena-alumina catalyst (□), and on the parent alumina (•) [5.27]

Another aspect of this interesting phenomenon can be observed in the ^{1}H-NMR spectra from adsorbed ortho-H_2 [5.27]. Spectra were taken under conditions corresponding to the isotherms of Fig.5.19. Figure 5.25 is a plot of the line width versus the amount adsorbed on the parent alumina and on the oxidized catalyst. The two curves converged at high coverage and both increased as the coverage was lowered. These data conform nicely to the Kibby-Kazanski equations [5.28]

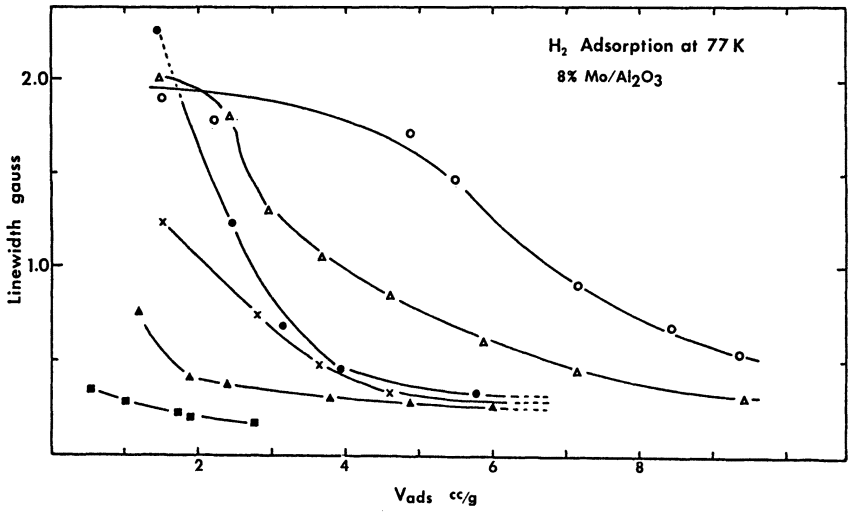

Fig.5.26. Line widths for the ^{1}H-NMR signal (35 MHz, 77 K) from ortho-H_2 as a function of coverage for molybdena-alumina catalysts reduced to various extents, i.e., e/Mo = 0.0 (□), 0.25 (Δ), 0.8 (x), 1.1(•), 1.4(Δ), and 1.7 (o). [5.27]

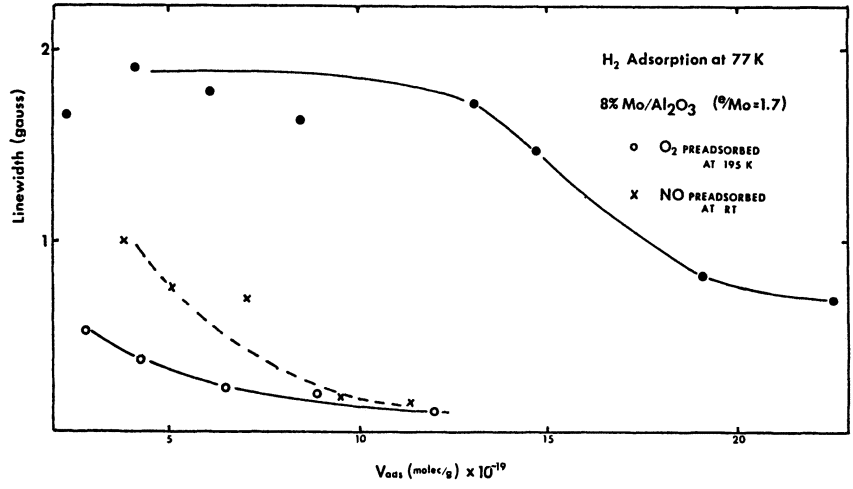

Fig.5.27. Effect of prepoisoning by selective chemisorption of O_2 (o) or NO (x) on the line width of the ^{1}H-NMR signal (at 35 MHz, 77 K) from absorbed ortho-H_2. Unpoisoned catalyst curve (•) taken from Fig.5.26 (e/Mo=1.7) [5.27]

which are based on the assumption that the observed line width results from fast exchange between a strongly chemisorbed species and a loosely bound (physically adsorbed) form of the adsorbate. As shown in Fig.5.26, the behavior changed markedly as the catalyst was reduced into the critical range where H_2 is dissociated (Fig.5.23). In addition to the fast exchange phenomena, a maximum line width was observed which cannot be accounted for by simple theory.

The effects on the line width of prepoisoning by chemisorption of the lethal dose of NO or O_2 are shown in Fig.5.27. THese relatively small chemisorptions had the effect of changing the behavior from that of the deeply reduced catalyst to that of the oxidized form. As with the ratio of the strong chemisorptions of the D_2 to H_2 (Fig.5.23), the effect was to eliminate evidence for dissociative hydrogen chemisorption.

The leveling of the line width for the reduced catalysts (Fig.5.23) suggests that chemisorption on the molybdena portion of the surface is also heterolytic. This maximum line width is about that expected for an isolated surface hydroxyl group. However, the dissociative oxidative addition of H_2 to CUS molybdena centers cannot be completely ruled out. This kind of reaction is well known in organometallic chemistry and leads to hydrogenation by what has become known as Wilkinson's catalysis. This chemistry is, however, associated with metallic ions in low valence states. It might be possible for Mo^{2+} to function in this way, but hardly Mo^{4+}. Nevertheless, the chemistry as written by *Tanaka* and *Okuhara* [5.23], and by *Siegal* [5.29] cannot be unambiguously ruled out.

5.4 Relationships with Catalysis

Molybdena-alumina catalysts were originally designed for hydrodesulfurization reactions. They are good hydrogenation catalysts which produce H_2S in reactions with sulfur-bearing molecules. They also hydrogenate olefins and (much less readily) aromatic systems. They catalyze olefin isomerization and metathesis as well as the isomerization of cyclopropanes. Studies of these reactions have proved helpful in understanding the catalytic chemistry and the nature of the intermediates. Olefin hydrogenation will be considered first.

The dissociative chemisorption of H_2 over ZnO is represented in (5.3). This is the only oxide system for which the mode of chemisorption has been unambiguously determined [5.3,30].

$$(Zn - O)_s + H_2 \leftrightarrow \begin{matrix} H & H \\ | & | \\ Zn_s & O_s \end{matrix} \quad . \tag{5.3}$$

Moreover, *Kokes* and *Dent* [5.3] demonstrated spectroscopically all of the steps in the hydrogenation reaction, i.e.,

$$\begin{matrix} H & H \\ | & | \\ Zn_s & O_s \end{matrix} + C_2H_4(\pi) \xrightarrow{\text{fast}} \begin{matrix} CH_3\text{-}CH_2 & H \\ | & | \\ Zn_s & O_s \end{matrix} \xrightarrow{\text{slow}} C_2H_6(g) + (Zn - O)_s \quad . \tag{5.4}$$

Alkyl reversal to the π-bonded olefin was not observed in tracer experiments. Thus, olefin hydrogenation over ZnO and Cr_2O_3 differed dramatically from that over metals. Deuterated ethenes were not observed when D_2 was substituted for H_2; dideuterioethane was the sole product. Data obtained for reduced and sulfided molybdena-alumina catalysts conformed to this picture much better than to that for metal catalysts where multiple exchange in both olefins and product paraffins is the general rule. However, some alkyl reversal did occur. Typical data [5.8] are given in Table 5.3. Alkyl reversal increased with the extent of reduction and with conversion. In the static circulation reactor used, the effects of secondary reaction were evident. Nevertheless, dideuteroethane remained the principal product followed by the monodeuterated species. This latter observation suggested that the hydrogen removed by exchange with ethene is very efficiently used to form another alkyl without leaving the surface. The smaller amounts of ethane-d_3 resulted from the reaction of D_2 with the exchanged ethene-d_1.

Table 5.3. Deuterium distribution from the reaction of ethene with deuterium over molybdena-alumina catalysts [5.8,19]

Catalyst	Conversion	Ethene					Ethane						
Preparation	%	d_0	d_1	d_2	d_3	d_4	d_0	d_1	d_2	d_3	d_4	d_5	d_6
Reduced	9	95	4	1	-	-	-	11	89	-	-	-	-
	28	91	7	2	-	-	-	16	79	5	-	-	-
	35	86	11	3	-	-	-	18	76	6	-	-	-
Sulfided	25	87	12	2	-	-	-	30	61	8	1	-	-
	45	81	16	2	-	-	-	36	53	10	1	-	-
	66	67	29	5	-	-	-	38	50	11	1	-	-

In agreement with the data of *Tanaka* and *Okuhara* [5.23], exchange over the sulfided catalysts was more important than with the reduced ones, and this was reflected in a further spreading of the distribution in the ethanes. Ethane-d_2 remained the most important product, but the fraction of d_1 and d_3 paraffins increased substantially. Thus, a continuous gradation of behavior exists, from ZnO and chromia catalysts [5.3] at the one extreme, yielding only ethane-d_2 and ethene-d_0 (no alkyl reversal), to the sulfided molybdena-alumina and MoS_2 preparations, where substantial exchange occurred with the reactant olefin. The reduced preparations were intermediate. Significantly, deuterated ethanes higher than ethane-d_3 were usually not observed, even at high conversions. The deuteration appeared to be limited to ethane-d_4. It was for this reason that we previously suggested [5.18,19] that exchange might occur via the reversible

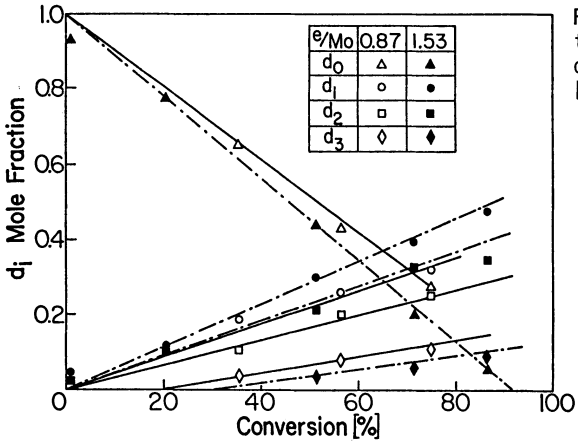

Fig.5.28. Deuterium distribution in propenes as a function of the extent of deuteration. [5.18]

interconversion of alkyl into the ethylidene carbene. In this way, up to four deuterium atoms per molecule could be introduced into the paraffin with essentially no exchange into the olefin.

In spite of sluggish exchange between D_2 and olefin, H_2 exchanged rapidly with D_2 in the presence of ethene to produce HD, and ethane-d_1 was the largest single product [5.18,19]. The exchange rate was slowed considerably in the presence of olefin, but was not virtually eliminated as with some metal catalysts. The exchange patterns may be contrasted with the well-documented ones for metal catalysts [5.31].

With propene, the exchange between D_2 and olefin was considerably faster than with ethene [5.18,19]. The propene-d_0 concentration fell roughly linearly with percent conversion (Fig.5.28) yielding propene-d_1 and -d_2 as the apparent initial products. Propene-d_3 was also formed, but the data suggested that this was a secondary product [5.18,19]. The propanes formed as a result of deutera-

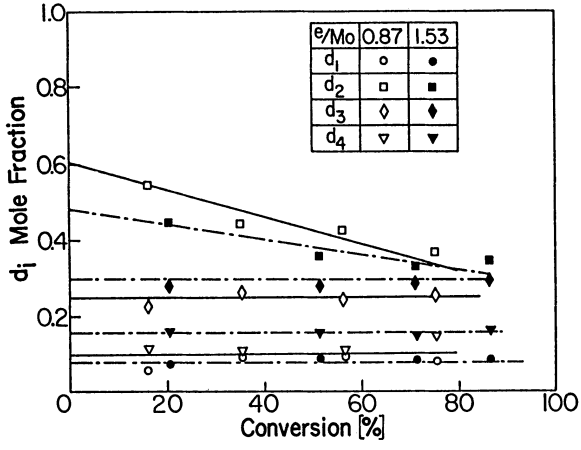

Fig.5.29. Deuterium distribution in the propanes formed in the reaction of propene-d_0 with D_2 as a function of the extent of reaction [5.18]

tion are described in Fig.5.29; they included propane-d_2 as the largest single product, as well as substantial amounts of propane-d_3 and smaller amounts of propane-d_1 and -d_4. All of these were apparently primary products of the reaction. The products produced by the reaction of 1-butene with D_2 were distributed similarly [5.8].

The hydrogenation rate for propene was slower, other things being equal, than for ethene. This may be attributed to additional chemistry which becomes possible with propene due to its allylic hydrogen. Thus, sites which chemisorb the hydrogen (with which the olefins must react to form metalloalkyls) may also be occupied by an allylic species or metallocyclobutanes. With ZnO this competitive process was observed spectroscopically [5.3]. The rates of hydrogenation of propene presented in Fig.5.9 were the original data from [5.18,19] supplemented with additional data [5.8] for reduced and sulfided catalysts (open and filled triangles). The rapid linear increase in rate above e / Mo = 1 was similar to the data for the strong H_2 chemisorption shown in Fig.5.21. In fact, these rate data are nicely correlated with the H_2 chemisorption data in Fig.5.22. Thus, the available evidence suggests that the rate of propene hydrogenation is limited by the availability of chemisorbed hydrogen on the catalyst surface.

Some further insight was gained from studies of the reaction of butadiene with D_2 [5.8]. The initial hydrogenation rate was approximately linear in hydrogen pressure and the reaction was strongly inhibited by increasing the butadiene pressure. Interestingly, an isotope effect, $k_{H_2} / k_{D_2} = 1.43$, was observed for the reaction rate. Since this ratio is approximately equal to the ratio of the collision frequencies of H_2 and D_2 with the surface, it may be taken as further evidence that the rate of arrival of hydrogen or deuterium on the surface is rate limiting. In addition to these kinetic data, the isotopic distributions analogous to those shown in Table 5.3 for ethene were derived from mass spectrometry data. By this time, however, it had become possible to determine the distribution of deuterium at various positions in the molecule by ^{2}H-NMR. THese distributions are shown in Table 5.4 for reduced and sulfided catalysts. These data elucidate clearly the processes taking place. Butadiene slowly undergoes exchange with D_2, mainly at the terminal vinyl positions. Deuteration is superimposed upon this process. The 1-butene formed thus contains approximately one deuterium atom in each of the 3 and 4 positions as well as an appreciable amount at the terminal vinyl group and a small but significant amount at the internal vinyl position. The much higher extent of exchange at the terminal positions suggests that the secondary alkylidene is favored over the primary species (which would lead to exchange at the internal position).

Table 5.4. Isotopic distributions of H and D in products of deuteration of 1.4-butadiene

Product	Isotopic distribution	
	Reduced catalyst (16.6% conversion)	Sulfided catalyst (21.1% conversion)
Butadiene	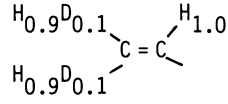	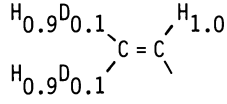
1-Butene	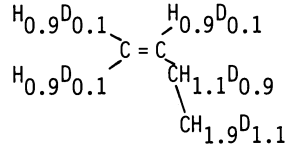	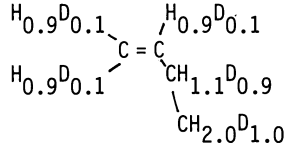
cis-2-Butene	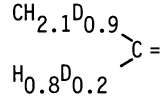	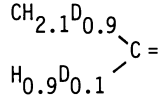
trans-2-Butene	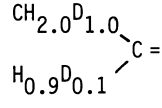	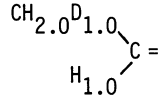

However, as shown by the reaction network depicted in Fig.5.30, this need not be so, because the extent of exchange at the two positions in butadiene depends not only on the relative amounts of the two alkylidenes (I and II) formed, but upon the relative magnitude of the rate vectors k_2 / k_{-1} versus k_4 / k_{-3} as well as upon the relative rates of formation k_1 / k_3. What is clear is that more butadiene is returned to the gas phase after having been species II than from species I.

The reaction network (Fig.5.30) indicates four pathways to form 1-butene and only one to form each 2-butene. Moreover, the isotopic distributions shown in Table 5.4 demonstrated that each of the two butenes was formed by 1-4 addition of D_2 to butadiene. Presumably the 2-alkylidene (species II) may rearrange into the *syn* or *anti*-π-allyl (species III or IV, respectively) from which the *trans*- and *cis*-2-butenes are formed. It would be tempting to speculate that the ratio of these products reflects the ratio of the two π-allyl species, but again this is not necessarily true as their steady-state concentrations will be controlled by the relative magnitudes of the various rate

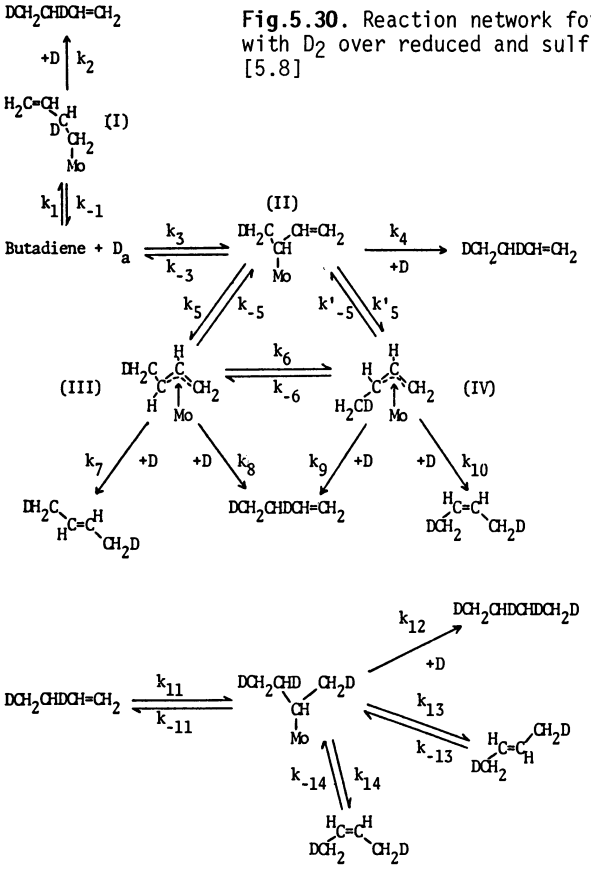

Fig.5.30. Reaction network for reactions of butadiene with D_2 over reduced and sulfided molybdena-alumina. [5.8]

vectors. Interestingly, the initial product contained approximately 70 to 85% 1-butene, 10 to 20% *trans*-2-butene with *cis*-2-butene making up the remainder. As time went on, however, hydrogenation continued to the final product, *n*-butane.

In summary, all of these results point to a reaction system in which molybdenum ions having multiple coordinative unsaturation, and presumably a lower than normal valence state, act as catalytic centers for the dissociative chemisorption of hydrogen or alternatively for the formation of allylic species from olefins. The chemisorbed H can then react with an olefin to form an alkyl or alkylidene; the addition of a second H leads to hydrogenation. The allylic species, on the other hand, serves as an intermediate for isomerization or for formation of metallocyclobutanes and carbenes, see below. The same allylic intermediates may be generated from butadiene by the addition of a hydrogen atom. Finally, the number of active centers may be counted by selective poisoning experiments using NO or O_2. This feature will be lost when reactions re-

quire higher temperatures and hydrogen pressures or when strongly adsorbed substrates displace or remove the poison.

Cyclopropane was chosen as a test reagent with the idea that several catalytic functions might be characterized simultaneously. Originally, it was supposed that the primary isomerization reaction to form propene was acid catalyzed as much of the known chemistry of cyclopropanes involves acid catalysis [5.18,19,32]. Further research convinced us, however, that this could not be the case. First, it was found that the isomerization was reversibly poisoned by small amounts of H_2O [5.33], whereas the acid catalyzed reaction (silica-alumina) was accelerated [5.32]. Second, whereas the oxidized form of molybdena-alumina showed Brønsted acidity [5.6] when contacted with pyridine (and this acidity was enhanced by addition of H_2O), the ability to generate pyridinum ions was lost when the catalyst was reduced. These features are shown in Fig.5.31. The bands at 1540 and 1638 cm^{-1}, which appear in A and B, demonstrated the presence of the pyridinium ion. Note the enhancement in these bands on addition of H_2O. These same bands were absent in Spectra C and D which were obtained from the reduced catalyst. These observations are in accord with chemical intuition, which would lead one to suppose that the acidity of an oxide should decrease on reduction and increase on oxidation. Interestingly, the

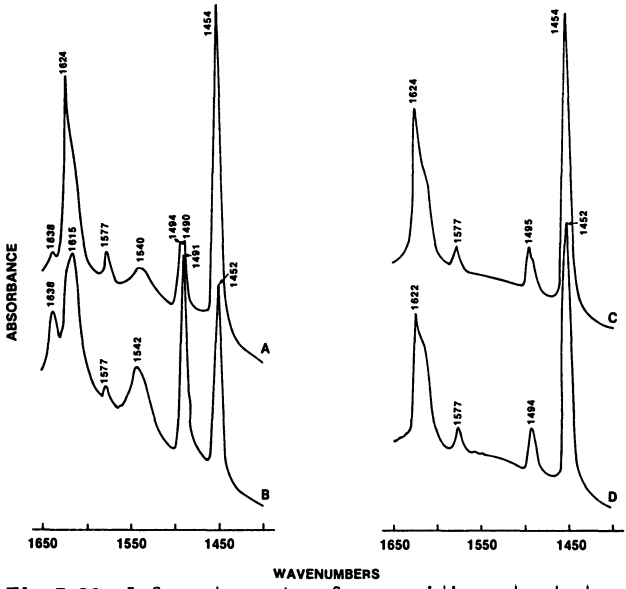

Fig.5.31. Infrared spectra from pyridine adsorbed on the oxidized (*A*,*B*) and reduced (*C*,*D*) forms of a molybdena-alumina catalyst. Spectra (*B*,*D*) were obtained after adding a small dose of water vapor to preparations from which spectra (*A*,*C*), respectively, had been recorded [5.6]

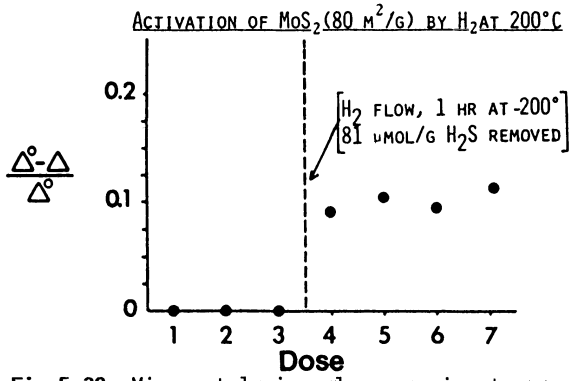

Fig.5.32. Microcatalyric pulse experiments over a microcrystalline MoS_2 catalyst showing activation for cyclopropane isomerization by reductive removal of H_2S [5.34]

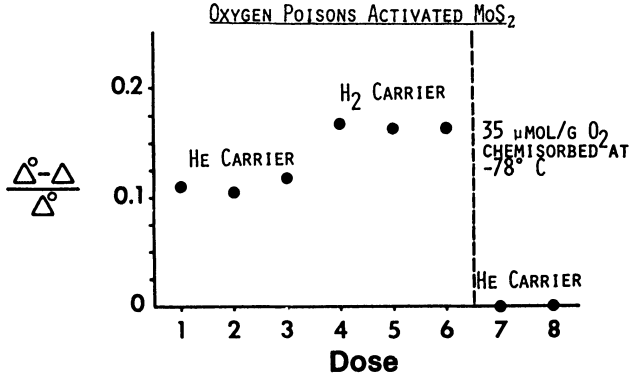

Fig.5.33. Microcatalytic pulse experiments over activated microcrystalline MoS_2 showing complete poisoning by chemisorption of oxygen [5.34]

rate of isomerization increased rapidly with reduction (from essentially zero conversion to nearly complete decomposition). Thus, the catalyst in its acidic form was not very active for cyclopropane isomerization, but it became active as the Brønsted acidity was eliminated. That some other mechanism must be operative was further demonstrated by activation and poisoning experiments made with unsupported MoS_2 [5.34]. As shown in Fig.5.32, no conversion of cyclopropane could be observed when pulses of cyclopropane were passed over freshly sulfided MoS_2 at 100°C. The catalysts could be activated for the reaction, however, by a hydrogen treatment at 200°C, in which a small amount of H_2S (81 µmol H_2S from 350 mg MoS_2) was removed. The ability to isomerize cyclopropane was thus "turned on" by the formation of coordinatively unsaturated centers by removal of sulfur from the periphery of the chalcogenide wafers. This picture was confirmed by selectively poisoning these centers by oxygen chemisorption, as shown in Fig.5.33. Interestingly, the number of oxygen atoms

chemisorbed (70 μmol) was approximately equal to the sulfur atoms removed during the activation in hydrogen.

Early in our work [5.33], it was noted that when pulses of cyclopropane carried in He were passed over the reduced catalyst, ethene, not propene, was the initial product. It was soon recognized that this resulted from the reaction described by *Gassman* and *Johnson* [5.35], which involves the formation of metallocyclobutane by the insertion of a molybdenum ion into the cyclopropane ring (5.5); this species then cleaves to form C_2H_4 plus a surface bound carbene, i.e.,

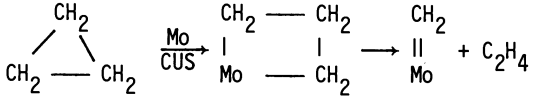

(5.5)

The latter can then function in the metathesis reaction. This chemistry affords an explanation of the non-acid catalyzed isomerization. As shown in (5.6), it is possible for the metallocyclobutane to convert into the allylic hydride which can then revert to the olefin.

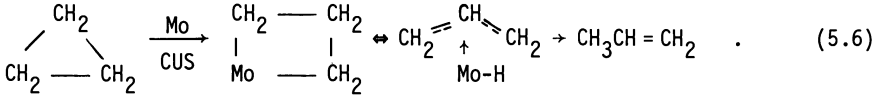

(5.6)

The reverse of this reaction has been suggested as the mechanism for the formation of the surface carbenes which are necessary for olefin metathesis [5.36-39]. Presently, this seems to be the most likely explanation for our observations [5.34]. It is not understood why under certain circumstances ethene is the principal product from the first pulse of cyclopropane and in other cases only propene is observed.

Olefin metathesis is facile over reduced molybdena-alumina catalysts [5.39-42], but not over sulfided ones [5.34]. The accepted mechanism is exemplified by the following chemistry:

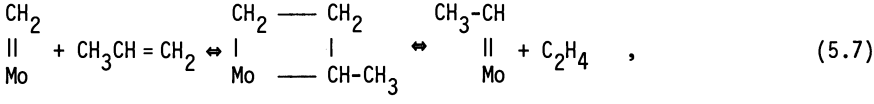

(5.7)

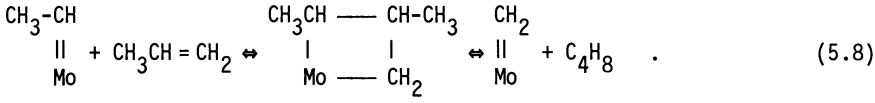

(5.8)

Methathesis is repressed in the presence of H_2 because the olefin is rapidly converted to paraffin.

Hydrogenolysis of propene or propane to form methane and ethane has been reported [5.43,44] for molybdena-alumina preparation made by the decomposition of $Mo(CO)_6$ on alumina. It has not been observed below 450°C with the usual reduced or sulfided preparations which we have studied.

An interesting and as yet not understood feature of the molybdena-alumina system is the very facile exchange reactions between cyclopropane-d_0 and Cyclopropane-d_6. This reaction [5.18,19] frequently achieves equilibrium in one pass over the catalyst, making it impossible to obtain mechanistic information from such experiments. The nature of the bonding and transformations which lead to complete scrambling of the isotopes between two cyclopropane rings without ring opening thus remains a challenging problem for future research, and its solution might go a long way towards unraveling the remaining mysteries of this catalytic chemistry.

The selective poisoning experiments shown in Fig.5.10 indicate that olefin metathesis and olefin hydrogenation occur on different catalytic centers, but further experiments [5.18,19] have revealed that cyclopropane isomerization and olefin metathesis are closely related. This is in general agreement with the chemistry written in (5.5-8).

In summary, the surface chemistry of reduced and sulfided molybdena-alumina catalysts has been described and the nature of the catalytic centers elucidated. Tracer studies of the hydrogenation of olefins and diolefins have revealed that alkyl and alkylidene intermediates function in hydrogenation and that alkyl reversal is slow compared with the final hydrogenation step. Studies of butadiene revealed also that the interconversion of the alkylidene to allylic species permit the formation of the 2-butenes by 1-4 addition. The same allylic species may function as an intermediate in the isomerization of cyclopropanes. Olefin metathesis requires carbene intermediates which are thought to be generated through the decomposition of metallocyclobutane intermediates. It is suggested that the latter are also interconvertable to the allylic intermediate. Still, something is missing. Evidence was presented that olefin metathesis and the dissociative adsorption of hydrogen occur on different catalytic centers. Perhaps on molybdena-alumina, as on ZnO [5.45], H_2 and olefins compete for sites; when H_2 is adsorbed first, alkyl (or alkylidene) species form; when the olefin wins, allylic species result. Yet the collective evidence shows that hydrogenation can be poisoned without much effect on metathesis or cyclopropane isomerization. Perhaps, as suggested by *Siegel* [5.29], hydrogenation requires one more degree of coordinative unsaturation (type C or CH sites) than does isomerization of metathesis (type B).

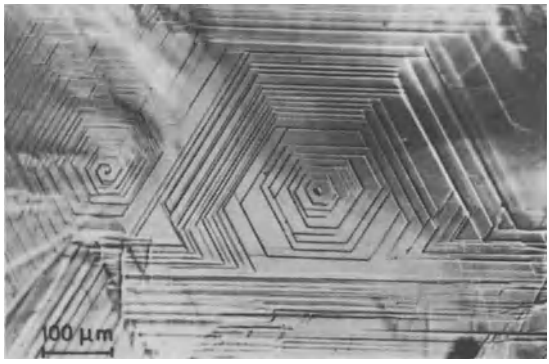

Fig.5.34. Photomicrograph of the surface of a macroscopic crystal of MoS_2 showing edge surface exposed at screw dislocations [5.46]

The chemistry described herein will serve to illustrate some of the additional problem to be faced by the surface scientist in studies of oxides and sulfides. The importance of the edges of the chalcogenide wafers of MoS_2 in the formation of catalytic sites was emphasized. Seemingly, this would make it difficult or impossible to work with single crystals of this material, but this is not necessarily so. As shown in Fig.5.34, laboratory-made crystals of MoS_2 [5.46] contain considerable edge surface as a result of the screw dislocations around which the growth occurs. This affords interesting new possibilities for the surface scientist.

Acknowledgements. The author wishes to thank his students as noted in the references, for their interest and contributions to this work. He also wishes to thank the National Science Foundation for the continuous support over several years, most recently under grant number CHE-85-12520. Finally, thanks are due to Prof. Aaron Wold of Brown University for furnishing the single crystal, and to Dr. R.R. Chianelli of Exxon Research for his continued interest and for helpful discussions.

References

5.1 W.K. Hall: Acc. Chem. Res. **8**, 257 (1975)
5.2 G. Ertl: In *Chemistry and Physics of Solid Surfaces*, Vol. III, ed. by R. Vanselow, W. England (CRC, Boca Raton, FL 1982)
5.3 R.J. Kokes, A.L. Dent: Adv. Catal. **22**, 1 (1972); J. Phys. Chem. **73**, 3772, 3781 (1969)
5.4 L. Wang, W.K. Hall: J. Catal. **66**, 251 (1980); ibid. **77**, 232 (1982)
5.5 W.K. Hall: In Proc. 4th Int. Conf. Chemistry and Uses, of Molybdenum, ed. by H.F. Barry, P.C.H. Mitchell (Golden Colorado, 1982) p.343
5.6 K.I. Segawa, W.K. Hall: J. Catal. **76**, 133 (1982)

5.7 W.S. Millman, M. Crespin, A.C. Cirillo, S. Abdo, W.K. Hall: J. Catal. **60**, 404 (1979)
5.8 W.S. Millman, D.C. Smrz, K.I. Segawa, W.K. Hall: Polyhedron **5**, 169 (1986)
5.9 A.C. Cirillo, F.R. Dollish, W.K. Hall: J. Catal. **62**, 379 (1980)
5.10 B.S. Clausen, H. Topsoe, R. Candia, J. Villandsen, B. Lenzler, J. Als-Nielsen, F. Christensen: J. Phys. Chem. **85**, 3868 (1981)
5.11 D.R. Huntley, T.J. Parham, R.P. Merrill, M.J. Sienko: Inorg. Chem. **22**, 4144 (1983)
5.12 R.R. Chianelli, M.B. Dines: Inorg. Chem. **17**, 2758 (1978)
K.S. Liang, J.P. de Neufville, A.J. Jacobson, R.R. Chianelli, F. Betts: J. Non-Cryst. Solids **35**, 1249 (1980)
K.S. Liang, S.P. Cramer, D.C. Johnson, C.H. Chang, A.J. Jacobson, J.P. de Neufville, R.R. Chianelli: J. Non-Cryst. Solids **42**, 345 (1980)
5.13 K.I. Segawa, W.K. Hall: J. Catal. **77**, 221 (1982)
5.14 J. Valyon, W.K. Hall: J. Catal. 92, 155 (1985)
5.15 B.S. Parekh, S.W. Weller: J. Catal. **47**, 100 (1977); ibid. **55**, 58 (1978)
H.C. Liu, L. Yuan, S.W. Weller: J. Catal. **61**, 282 (1980); ibid. **66**, 65 (1980)
5.16 W.S. Millman, W.K. Hall: J. Catal. **59**, 311 (1979)
5.17 N.K. Nag: J. Catal. **92**, 432 (1985)
5.18 E.A. Lombardo, M. LoJacono, W.K. Hall: J. Catal. **64**, 150 (1980)
5.19 E.A. Lombardo, M. Houlla, W.K. Hall: J. Catal. **51**, 256 (1978)
5.20 W.S. Millman, W.K. Hall: J. Phys. Chem. **83**, 427 (1979)
5.21 J. Valyon, W.K. Hall: J. Catal. **84**, 216 (1983)
5.22 R.P. Rosen, K.I. Segawa, W.S. Millman, W.K. Hall: J. Catal. **90**, 368 (1984)
5.23 K.I. Tanaka, T. Okuhara: J. Catal. **48**, 229 (1977); ibid. **78**, 155 (1982); Catal. Rev.-Sci. Eng. **15**, 249 (1977) and the references cited therein
5.24 W.S. Millman, F.H. van Cauwelaert, W.K. Hall: J. Phys. Chem. **83**, 2764 (1979)
5.25 Proc. 7th Int. Congr. Catal. (Tokyo) (Elsevier, Amsterdam 1980) p.B-1304
5.26 F.H. van Cauwelaert, W.K. Hall: J. Colloid Interface Sci. **38**, 138 (1982)
5.27 A.C. Cirillo, J.M. Dereppe, W.K. Hall: J. Catal. **61**, 170 (1980)
5.28 C.L. Kibby, V.Yu. Borovkov, V.B. Kazinski, W.K. Hall: J. Catal. **46**, 275 (1977) and earlier references cited therein
5.29 S. Siegel: J. Catal. **30**, 139 (1973)
5.30 R.P. Eischens, W.A. Pliskin, M.J.D. Low: J. Catal. 1, 180 (1962)
5.31 G.C. Bond: In *Catalysis by Metals* (Academic New York 1962)pp.183-335
5.32 J.G. Larson, H.R. Gerberich, W.K. Hall: J. Am. Chem. Soc. **87**, 1880 (1965)
5.33 M. LoJacono, W.K. Hall: J. Colloid Interface Sci. **58**, 76 (1977)
5.34 W.K. Hall, R.L. Schneider, J. Goldwasser: In Proc. 8th Int. Congr. Catalysis, Vol. IV (Berlin 1984) p.273
5.35 P.L. Gassman, T.H. Johnson: J. Am. Chem. Soc. **98**, 6055, 6058 (1976)
5.36 M. Ephritikene, M.L.H. Green, R. Mackenzie: J. Chem. Soc. Chem. Commun. **619**, 926 (1976)
5.37 R.H. Grubbs, S.J. Switnick: J. Mol. Catal. 8, 25 (1980)
5.38 M.F. Farona, R.L. Tucker: J. Mol. Catal. **8**, 85 (1980)
5.39 J. Engelhardt, J. Goldwasser, W.K. Hall: J. Catal. **76**, 48 (1982)
5.40 J. Goldwasser, J. Engelhardt, W.K. Hall: J. Catal. **70**, 275 (1981)
5.41 J. Engelhardt: J. Catal. **72**, 179 (1981)
5.42 J. Engelhardt, J. Goldwasser, W.K. Hall: J. Mol. Catal. **15**, 173 (1982)
5.43 R.G. Bowman, R.L. Burwell: J. Catal. **88**, 388 (1984); ibid. **86**, 301 (1984)
5.44 R. Nakamura, D. Pioch, R.G. Bowman, R.L. Burwell: J. Catal. **93**, 388, 399 (1985)
5.45 J. Goldwasser, W.K. Hall: J. Catal. **71**, 53 (1981)
5.46 Thanks are due to Prof. Aaron Wold, Department of Chemistry, Brown University for furnishing this crystal

6. Structure and Catalytic Performance of Zeolites

J.M. Thomas

Department of Physical Chemistry, University of Cambridge, Lensfield Rd, Cambridge CB2 1EP, England

This chapter is concerned with the chemistry and physics of channels, cages, and cavities, the diameters of which are large enough to permit ingress of small organic molecules, but sufficiently small to prevent the entry of larger ones. Aperture diameters of $\sim 3-8$ Å are, therefore, central to our discussion. Cages and cavities of this dimension are common in many branches of chemistry and indeed in numerous biological contexts. The notion that a lock-and-key principle dominates many catalytic phenomena or holds sway in the formation of certain guest:host complexes, has been around since the days of Emil Fischer in the early years of this century. It is also well known that the mode of action of certain enzymes is crucially governed by the shape-selectivity of the recess at which the active sites are centered. In lysozyme, for example, reactant molecules are neatly accommodated and are subsequently cut at the cleft, the active site in the enzyme surface.

Pharmacologists and physiologists who concern themselves with the preferential docking or coordination and transport of inorganic ions and small organic molecules along or through membranes have, in their quest for appropriate hosts, either taken advantage of what biological nature provides – in the form of the cyclodextrins, for example – or have ingeniously designed and prepared new hosts or receptors capable of bonding, in regio-selective, stereo-selective, or chirally discriminating fashion, a variety of guest organic molecules. Hosts such as the crown ethers, cryptophanes, and calixarenes spring to mind. But impressive as these quests are (Fig.6.1) – and many of them are replete with architectonic elegance – they are unlikely to be of major importance in the realm of inorganic, industrial catalysis, where thermal and mechanical stabilities are essential attributes. Fortunately, a class of minerals and their synthetic analogues called zeolites (and identified by that name for over two centuries) possess the structural and physicochemical desiderata that we seek.

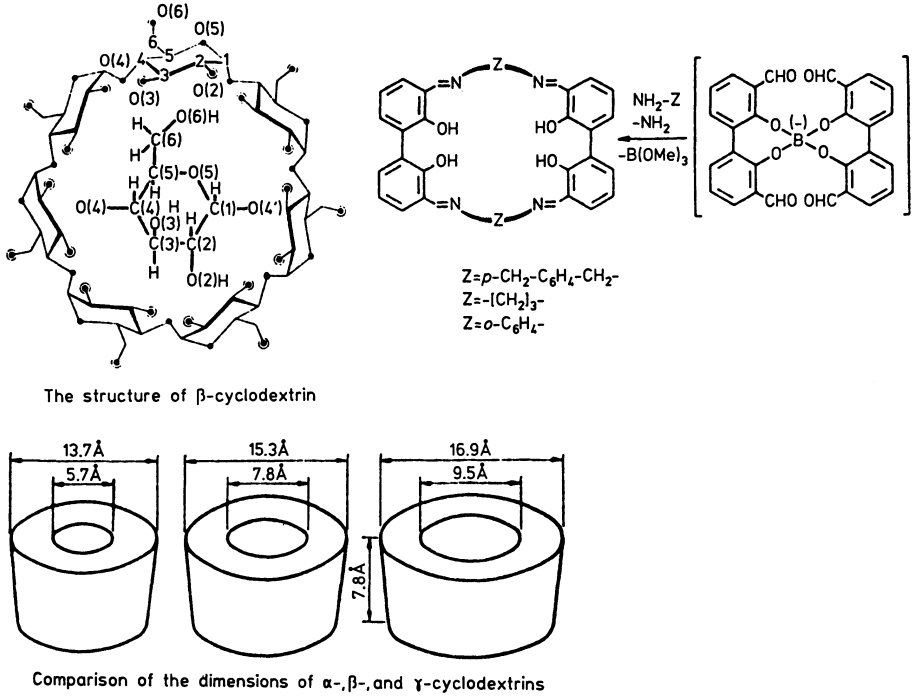

Fig.6.1. Two typical organic host species capable of accommodating guests according to their shape. The cyclodextrins (*left*) are derived from naturally occurring carbohydrates by enzymatic breakdown [6.1]. Receptor molecules such as those on the right are generated by synthesis [6.2]. (The repeat carbohydrate unit is shown inside the β-cyclodextrin, which, in the β-form, has seven carbohydrate units constituting the periphery of the cavity. In the α- and γ-cyclodextrins, the cavities are circumscribed by six and eight carbohydrate units, respectively)

6.1 Introduction to Zeolites

By virtue of their structure, crystallinity, and variable stoichiometry (Sect.6.2) zeolitic catalysts have:

(a) sharply defined pore size distributions;

(b) high and adjustable acidity;

(c) very high surface areas (typically 600 m^2g^{-1}), the majority of which (~95%) is, depending upon crystallite size, internal, and accessible through apertures of defined dimensions;

(d) good thermal stability (e.g., they are capable of surviving heat treatments in air up to 1000°C, depending upon the composition of the zeolite framework).

Moreover, since the framework composition [6.3,4] of zeolites can be changed from the extremes of low-silica to high-silica contents (Sect. 6.2), the inner walls of the channels and cages can be more or less smoothly converted from the hydrophilic to hydrophobic extremes. Other attributes, apart from their relative ease of synthesis, that contribute to the attractive features of zeolitic catalysts are that:

(a) the nature and siting of exchangeable cations can be adjusted and engineered;
(b) the siting and energetics of potentially reactive organic species housed within the catalyst pores can also be engineered to some degree;
(c) the catalytically active sites are uniformly distributed throughout the solid, being accessible at the inner walls of the cavities.

Finally, in view of the fact that the active sites are situated predominantly inside the zeolite, and that all these sites, which are of very high concentration (far in excess of active sites on, for example, supported metal catalysts [6.5]) are at the same time also in the bulk of the solid, zeolitic catalysts can be very well characterized by the powerful new tools that have recently become available for probing local environments within bulk solids. This is particularly true of high-resolution (solid-state) multinuclear NMR, of neutron and X-ray powder profile (Rietveld) methods, of high-resolution electron microscopy and of computer graphics techniques which my colleagues and I at Cambridge, and collaborators elsewhere, have, along with others, been engaged in developing in recent years [6.3,5-21]. Ease of preparation of a zeolite catalyst, mundane as it may seem as one of the attributes of this class of solid, is as important a factor as any in determining the widespread use of zeolites in industrial catalysis. Faujasite, for example, is a very rare mineral: it occurs in only a few locations, and in minute amounts, on earth, but its synthetic analogues, zeolites X and Y (Sect. 6.2), are very easily prepared from solutions of silicates and aluminates. Doubtless, when reliable laboratory syntheses are evolved and subsequently scaled-up in an economically attractive manner, other zeolites too will figure eminently in industrial catalysis.

A typical aperture opening in a zeolite, representing the magnitude of the effective cross section of the channel mouth as a receptacle for the guest molecule, is shown in Fig.6.2, where we use two distinct ways of representing the view down the ⟨001⟩ axis in zeolite-L. Note that, as in the cyclodextrins, oxygen atoms are the principal protruding constituents of the channel lining.

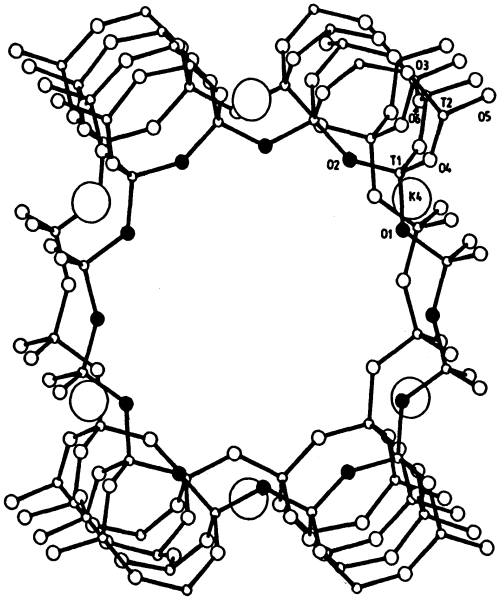

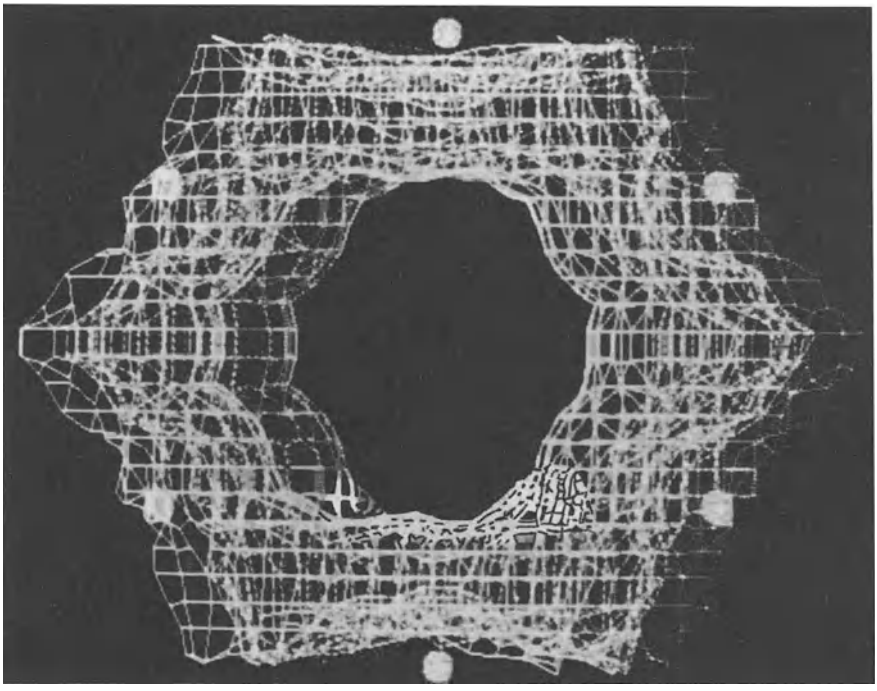

Fig.6.2a,b. Two views down the <001> axis of a portion of the zeolite-L structure. In (**a**) only six of the exchangeable cations are shown, all crystallographically equivalent. The 12 oxygens that line the mouth of the channel have been enlarged (compared with analogously situated oxygens deeper in the channel) and are shown as filled circles. In (**b**) the "network" added to the structural drawing shows the Van de Waals surface of the framework atoms. Adapted from [6.22]

However, whereas the O–C bond figures in the cyclodextrins, in the zeolites it is the O–Si (or O–Al) bond that predominates. This is the root cause of the far greater thermal stability of the zeolites compared with the cyclodextrins or crown ethers. Noted also that the greater the proportion of Si–O bonds in a given structure, the greater is its hydrophobicity, whereas the greater the content of Al–O bonds, the greater the hydrophilicity.

6.2 Some Structural Considerations

Zeolites can be described by the general formula $M_{x/n}[(AlO_2)_x(SiO_2)_y]\cdot m\ H_2O$, where the cations M of valence n neutralize the charges on the aluminosilicate framework, which, in turn, is composed of corner-sharing SiO_4 and AlO_4 tetrahedra. It is the linkages between these units that generate the channels and cages with cross sections comparable to molecular dimensions. The neutralizing, and on the whole exchangeable, cations are located at well-defined sites in the various cavities that exist within the structure, and the water molecules fill up the remaining voids. The water can be expelled upon heating and evacuation and may be replaced by a number of small organic or inorganic guests.

By adjusting the valency or the size of the exchangeable cation, the molecular sieving and hence the shape-selecting property of a zeolite may be fine-tuned. Consider the Na^+ form of zeolite-A, for example (Fig. 6.3). Replacement of Na^+ by Ca^{2+} ions results in the enlargement of the effective void space within the zeolite. Zeolite-A has four-membered, six-membered, and eight-membered apertures within the structure. In each unit of Na_{12}-A all eight of the six-membered, three of the four eight-membered and one of the twelve four-membered rings are "blocked" by Na^+ ions. But in Na_4Ca_4-A, the openings of half of the six-membered rings and all the eight and four-membered rings are vacant. It is no surprise, therefore, that ethane readily percolates through the Na_4Ca_4-A, and even more readily through Ca_6-A compared with its passage through Na_{12}-A.

The microporosity of a zeolite can, in general, be further enhanced by increasing the Si/Al ratio of the macroanionic framework.This is known as dealumination

$$\underset{\text{(Hydrophilic)}}{M_{x/n}[(AlO_2)_x(SiO_2)_y]\cdot m\ H_2O} \xrightarrow[+Si]{-Al,-M,-H_2O} \underset{\text{(Hydrophobic)}}{SiO_2}\ .$$

Indeed when the NH_4^+-exchanged form of the zeolite-Y (Sect.6.2) is heated under hydrothermal conditions the process of dealumination is effected. The result-

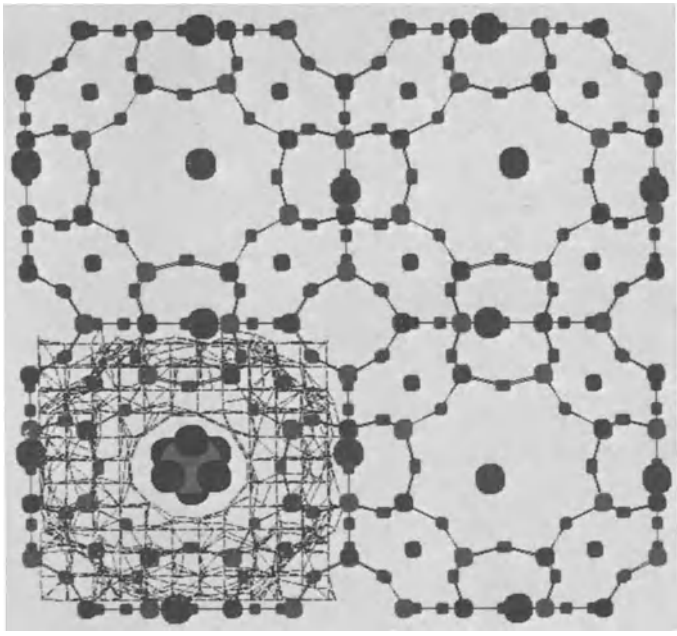

Fig.6.3. Projection down <001> of a portion of the zeolite-A structure. The large filled circles (•) denote positions, in projection, of K^+ ions. To facilitate adsorption, K^+ ions are replaced by divalent cations (e.g., Ca^{2+}). At lower left, the Van der Waals network (see Fig.6.2b) associated with the framework is shown. As indicated, a molecule of ethane may be readily sorbed by Ca^{2+}-A

ing structure is said to be ultrastabilized, in view of the fact that it withstands high-temperature treatment as ~1000°C without loss of structural integrity. During the course of stabilization the Si/Al ratio of the framework changes from an initial value of around 2.4 (depending upon the preparation of the original zeolite) to a final one of beyond 10 or 100. Of late, it has been found to be possible [6.23-25] readily to dealuminate certain zeolites [e.g., those based on faujasite (zeolite-Y)] simply by exposure to the vapour of $SiCl_4$ at an elevated temperature and to achieve Si/Al ratios of greater than 1000. Hydrothermal methods work well for the dealumination of zeolites such as mordenite and offretite and ZSM-5 (to silicalite), and even acid leaching suffices to dealuminate clinoptilolite [6.26,27].

Zeolites X and Y are structurally analogous to the mineral faujasite. The building units are truncated octahedra, also known as sodalite cages, β-cages or tetrakaidecahedra – all three terms are synonymous. These cages, seen in the centre of Fig.6.3 and further represented in Fig.6.4, are linked (in zeolites X and Y) to adjacent ones via hexagonal biprisms, thereby yielding

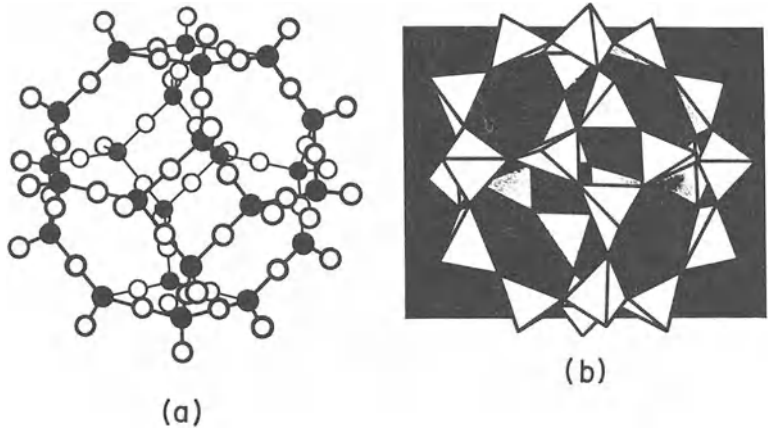

Fig.6.4. Three schematic representations of how a β-cage (sodalite cage) is built up by a process of corner-sharing of twenty four TO_4 tetrahedra (T:Si or Al). The β-cage is a truncated octahedron

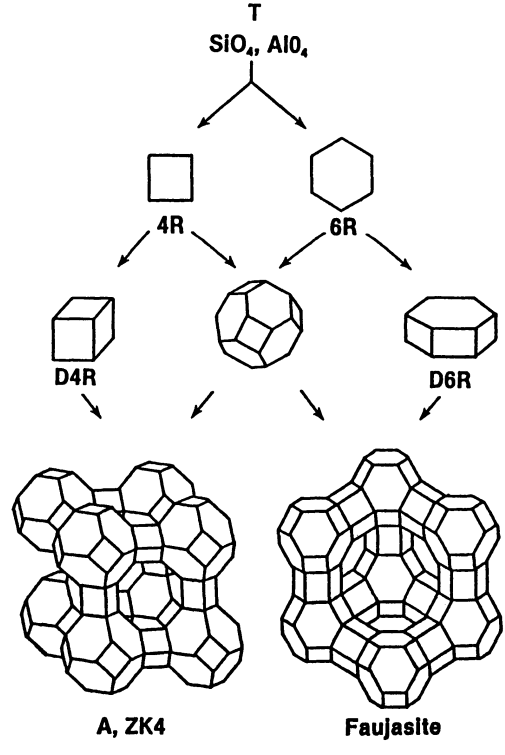

Fig.6.5. Illustration of how zeolites X and Y and zeolites A and ZK4 may be pictured as being assembled from primary (i.e., TO_4) and secondary building units [cubes or double-four (D4) rings; hexagonal prisms or double-six (D6) rings, etc.]

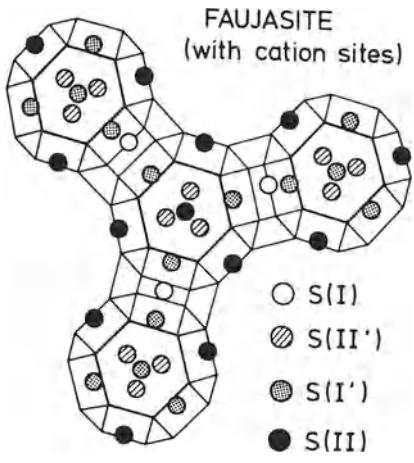

Fig.6.6. The principal (idealized) cation sites in faujasite (zeolites X and Y). Site S(I) is at the centre of the hexagonal biprisms (D6R) which connect the β-cages (forming a diamond lattice of β-cages). The S(II) sites are in the supercages, but sites S(I') ans S(II') are within the β-cages. For a specific cation-exchanged faujasitic zeolite, the precise cation positions differ somewhat from the idealised positions shown here

larger supercages. In zeolite-A and zeolite-ZK4 the β-cages are linked via cubes or so-called double-four (D4) rings (Fig.6.5).

In zeolites X and Y the principal sites for the extra-framework cations are designated S(I), S(I'), S(II), and S(II') sites. The Si–O–Al framework and the locations of the principal cation sites are shown in Fig.6.6, from which we can expect variations in the occupancy factors of the respective exchangeable cation sites. With the aid of Fig.6.6, we can see that cations preferring higher coordination numbers usually occupy the S(I) sites; that adjacent S(I) and S(I') sites are not simultaneously occupied by cations, and that almost all the S(II) sites, situated as they are on the wall of the supercage, tend to be occupied.

More than fifty distinct structures have been identified in the zeolite kingdom for some time. The reader is referred to other sources for further details [6.3, 26-30]. Suffice it to say that there are many well-recognized secondary building units, as shown in Fig.6.7, that are utilized in the various architectural patterns adopted by zeolites. Zeolite-rho, for example, consists of the α-cages (that are present in zeolite-A) joined together in a cubic structure via octagonal prisms (i.e., D8 units).

Zeolites ZSM-5 and ZSM-11 are closely related to one another [6.29]. The former consists of sheets, themselves made up of connected chains of five-membered rings, joined through centres of inversion (designated i). The latter has the same sheets joined at mirror planes (designated σ) – see Fig. 6.8. The Si/Al ratios of ZSM-5 and ZSM-11 can vary from about 10 to 100. At the very high silica extreme (Si/Al ratio beyond a 1000 or so – the precise ratio is arbitrarily defined), these structures are termed silicalite

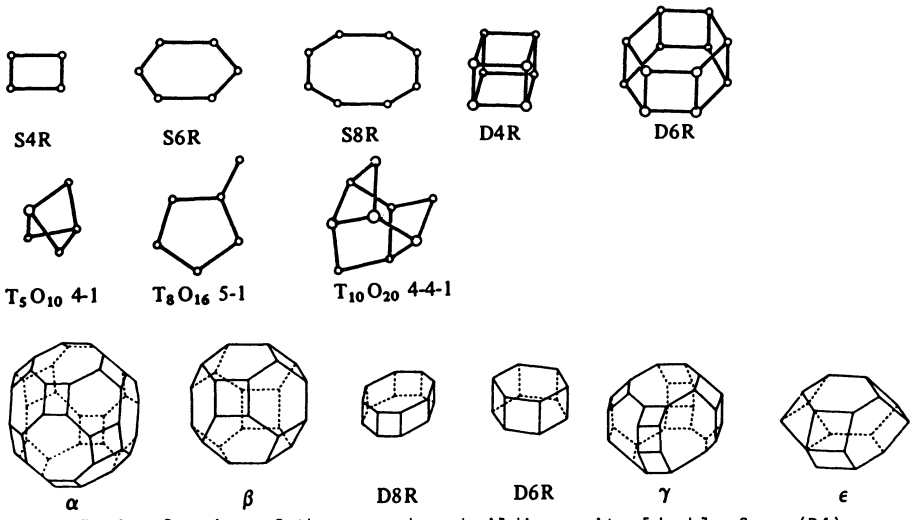

Fig.6.7. A selection of the secondary building units [double-four (D4), double-six (D6) rings; double-eight (D8), sodalite, cancrinite, gmelinite cages, etc.] from which the structures of zeolites are derived. *Bottom left*: gmelinite cage. *Bottom right*: cancrinite cage

I and silicalite II, respectively. The zeolite ferrierite has certain kinships with ZSM-5. Offretite and erionite which tend to coexist and intergrow (a property they share with ZSM-5 and ZSM-11) are members of a large family known as ABC-6 zeolites, details of the structure of which have been described elsewhere [6.3,31]. Individual members of this family differ from one another according to the stacking sequences adopted by puckered sheets, at every vertex of which there is a TO_4 group (T = Si,Al) corner-sharing via oxygen with four other TO_4 units.

Table 6.1. Elements known to occupy tetrahedral[a] sites in crystalline microporous (open-framework) structures containing cages or channels of 3-8 Å diameter

Stoichiometries	TO_2	$M_x^+(T_x'T''_{(1-x)}O_2)^{b,c}$
T,T',T''	Si, Al, B, Ga, Fe, Cr, Ge, Ti, P, V, Zn, Be	

[a]Open-framework structures containing octahedrally coordinated transition metal ions have been prepared and characterized (e.g., [6.32]). Typical stoichiometries are $Fe_5P_4O_{20}H_{10}$ and $Na\ Fe_3P_3O_{12}$, the synthetic analogues of the minerals hureaulite and alluandite, respectively.

[b]When M is H, these are acid catalysts.

[c]These materials are low density analogues of quartz, gallium arsenide, diamond, and silicon. A recently reported [6.33] example is $Zn_{0.06}Al_{0.94}PO_4$.

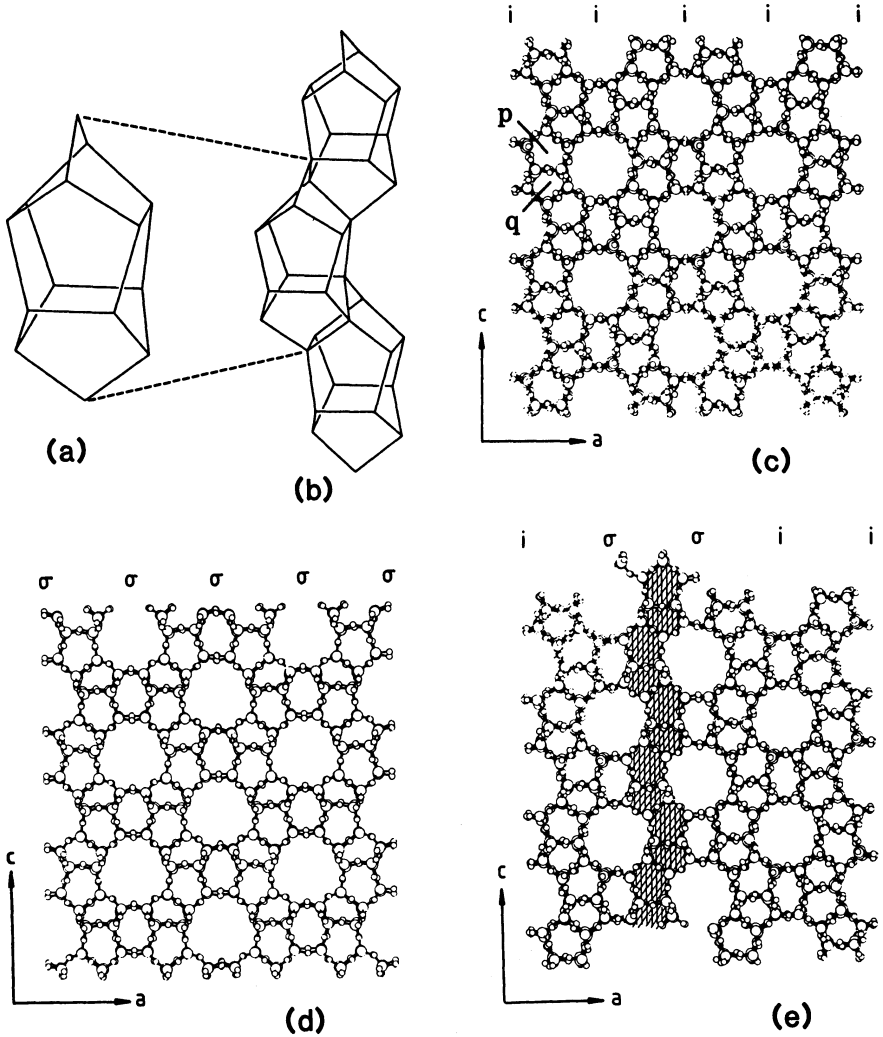

Fig.6.8. (**a**) Segment of the structure of ZSM-5 and ZSM-11 showing connected 5-membered rings composed of linked tetrahedra (SiO_4 and AlO_4). Each connecting line represents an oxygen bridge. (**b**) The chains from which the ZSM-5 and ZSM-11 structures are built are themselves made up by linking the units shown in (**a**). (**c**) In ZSM-5, chains are linked such that {100} slabs are related by inversion (i). Here (p and q) refer to the larger and smaller 5-membered rings, respectively. (The rings are in reality of equal size, but do not appear so in projection.) (**d**) In ZSM-11, chains are linked such that {100} slabs are mirror images (σ) of one another. (**e**) Representation of intergrowth of ZSM-5 and ZSM-11

Whilst it has been traditional until very recently to regard all zeolites as having been derived from aluminosilicates, the definition must now be extended to encompass many other tetrahedrally (T) bonded atoms besides Si and Al. Table 6.1 summarizes the situation as it presently exists. Evidently there are numerous open-framework structures, of stoichiometry TO_2, all made up of corner-sharing tetrahedra, which can in practice be formed. As well as preparing many pure, crystalline silica variants of aluminosilicate zeolites (e.g., faujasitic silica, see Fig.6.9), it is nowadays established that materials such as $GaPO_4$, $AlPO_4$, and $FePO_4$, as well as structures consisting of three or more different elemental tenants of the tetrahedral site, can be prepared [6.34,35].

It is important to emphasize that although X-ray crystallography has yielded the structure of several zeolites (synthetic and natural), there are very many new zeolites recently isolated that have so far not been structurally determined. This is due to a combination of factors, the principal one being the inability to grow zeolite crystals of adequate size for con-

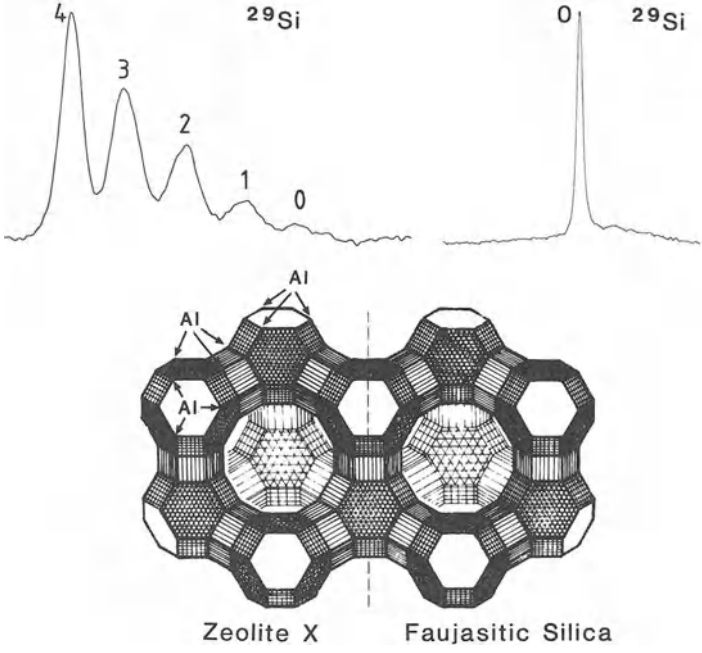

Fig.6.9. Proof of the feasibility of preparing faujasitic silica. The ^{29}Si MASNMR spectra [6.6] show how the original zeolite which has five chemically distinct environments (Si - nAl with n=0, 1...4) is converted upon dealumination essentially to SiO_2 where all silicons are in one type of chemical environment, thereby yielding only one ^{29}Si signal

ventional X-ray analysis. A further obstacle is the tendency for one zeolite to form an intergrowth with another. And even though elegant use has been made [6.36] of synchrotron radiation as an X-ray source (so that single crystals of smaller dimensions can be tolerated for four-circle diffractometry), many unconventional methods of structural analysis have had to be invoked [6.9,17,37,38]. Good progress has been achieved in correlating the performance of zeolite catalysts with the structural characteristics that have been retrieved by the combined use of solid-state NMR, neutron and X-ray (powder) methods, computer modeling, and high-resolution electron microscopy.

6.3 Fundamentals of Catalysis by Zeolites: A Resumé

Although there are several reactions catalyzed by zeolites in which acidity plays only a minor role [6.39], in the main, zeolite catalysts exert their influence because of their high acidity, this being usually of the Brønsted kind. In essence, we may interpret the behavior of zeolitic (acid) catalysts in terms of reactions involving carbonium ions [6.5,9], just as we may interpret the behavior of clay catalysts in similar terms [6.40-44]. Leaving aside for the moment precisely where the "free" proton is situated and its provenance within the zeolite (see later in this section), we utilize the broad mechanistic principles outlined by *Whitmore* [6.45] and others [6.46]. First, carbonium (alkylcarbenium) ions are formed from alkenes by reversible protonation,

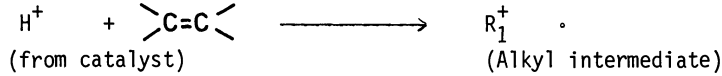

Subsequently we have

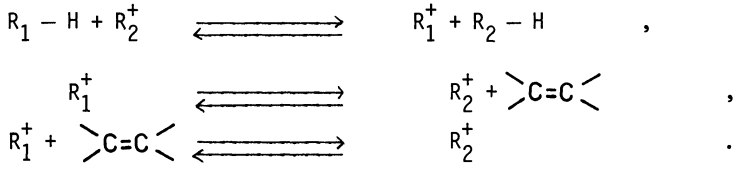

Within this broad set of principles we can also account for the alkylation of benzene by ethylene to yield ethyl benzene over a ZSM-5 catalyst. On dehydrogenation, styrene is produced

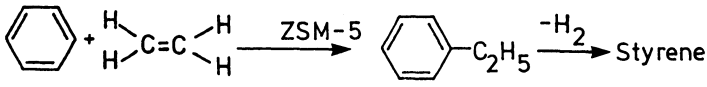

Here, as with several other comparable reactions [6.47] including isomerisation and hydrogenation, the shape-selectivity of the ZSM-5 comes into play,

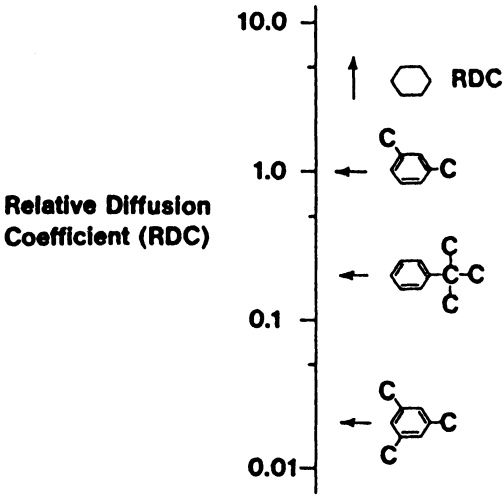

Fig.6.10. Relative diffusion coefficients (RDC) of simple aromatics in ZSM-5

and very little diethyl (or other polyalkylated) benzene is formed. The reality of the shape-selective quality of zeolite catalysts is highlighted when we compare the relative diffusion coefficients of simple and substituted aromatics covering a range of molecular cross selections (Fig.6.10). These data are readily interpretable when we recall that the diameters of the pores in ZSM-5 are ~5.5 Å. It is not surprising, therefore, that the diffusivity of benzene far surpasses that of its trisubstituted analogue. We may also readily interpret catalytic data such as those shown [6.48] in Table 6.2, where the results of competitive isomerizations of hexene-1 on the one hand are set alongside the isomerization of its progressively more highly branched isomers.

The results of recent investigations leave little doubt as to the precise origin of the acidity (i.e., the locus of the detachable proton required for the initial act of Brønsted catalysis). There are two distinct ways in which detachable protons can be generated in a zeolitic catalyst:

Table 6.2. Competitive isomerization of alkenes

Alkene		Selectivity[α]	
1.	2.	k_2/k_1	Temp. [°C]
6-methyl-1-heptene	Hexene-1	1.8	150
3-ethyl-1-pentene	Hexene-1	35	175
[ε]4,4-dimethyl-1-hexene	Hexene-1	120	175

[α]The selectivity is defined as the ratio of the percentage conversions of 2 and 1 in a given time of contact (After Dessau).

(a) by hydrolysis of a strongly polarizing cation; and

(b) by the generation of neutralizing entities to compensate for Al^{3+} ions housed within the framework.

The first of these is represented typically by

$$[La(H_2O)]^{3+} \longrightarrow [La(OH)]^{2+} + H^{+} \quad ,$$

and the second by

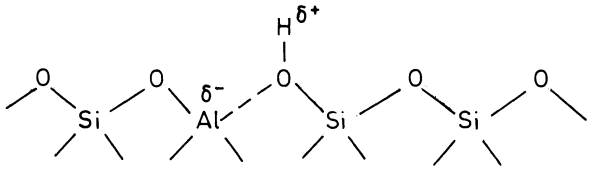

It is hydrogen bound to the O adjacent to the tetrahedrally incorporated Al that has a propensity to free itself as a proton – the active catalytic agent – thereby leaving a macroanionic framework. Infrared evidence substantiates this picture, and quantitative support for it comes [6.49] from solid-state ^{27}Al NMR, which monitors [6.9] the concentration of incorporated, four-coordinated Al. As we see from Fig.6.11, there is a linear dependence of catalytic activity upon Al-content in ZSM-5. We would also expect such correlations with B and Ga tetrahedrally coordinated.

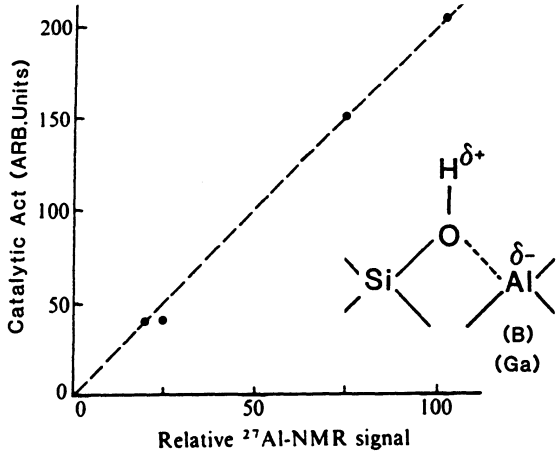

Fig.6.11. The catalytic activity of ZSM-5 shows a linear dependence on the concentration of tetrahedrally coordinated Al since this is the root cause of the acidity. A similar situation exists when either B or Ga replaces the Al. After [6.49]

6.4 Converting a Zeolite to Its Catalytically Active Form

For a given zeolite with a well-defined Si/Al ratio, greater catalytic activity will ensue if polyvalent rather than monovalent ions occupy the sites of the exchangeable cations. Other things being equal, therefore, for the reasons given in the preceding section, a La^{3+} - or Ca^{2+} - exchanged zeolite exhibits greater (Brønsted) catalytic activity than the Na^{+} - exchanged analogue. The logical extension of this argument is that the best activity is activated when H^{+} cations constitute the exchangeable ions, and indeed this is so. One way in which the H^{+} form of a zeolite can be prepared is simply by washing with mineral acid. In general, however, this procedure is not satisfactory because the zeolite framework is broken down in the process. To circumvent this difficulty, the NH_4^{+} - exchanged form is first prepared and this is then heated under hydrothermal conditions to yield the H^{+} zeolite after liberation of NH_3. During the conversion there is much structural reorganisation, but prolonged annealing generally succeeds in healing many, but not all, of the local defects. In zeolite-L, for example, coincidence boundaries are formed [6.3,50] as a result of rotation about an axis parallel to ⟨ 001 ⟩ of one part of the crystal with respect to the other. The $\sqrt{13}$ $\sqrt{13}$ R 32.2° coincidence lattice formed in zeolite-L results in a marked diminution of the diffusion of reactant and product molecules along the channels which run parallel to ⟨ 001 ⟩ in zeolite-L.

It is important to appreciate that both the thermal stability and the catalytic activity of a zeolite are, in general, improved by dealumination. Until recently it was very difficult to monitor the precise degree of dealumination. In zeolites X and Y, for example, the unit cell dimension of the cubic structure was used as a criterion. The inherent cause of the small diminution of unit cell parameter upon dealumination is the replacement of an Al-O bond (~1.76 Å) by Si–O (~1.60 Å). X-ray methods are used [6.51] for this purpose. Other procedures are based on chemical analysis of Si and Al contents either by wet methods or by X-ray fluorescence or atomic emission spectroscopy. These methods are, however, fraught with difficulties as they record *total* Si and Al content. They are intrinsically incapable of discriminating between framework and non-framework locations. However, ^{29}Si magic-angle-spinning NMR (MASNMR) is readily capable of determining the framework Si/Al ratio in a nondestructive fashion, where I(Si–nAl) is the intensity of the peak arising from Si surrounded by n AlO_4 tetrahedra. A striking example of the way in which ^{29}Si MASNMR surpasses X-ray emission for the purposes of determining framework composition is illustrated in Fig.6.12, taken from the work of *Wright* [6.52] on zeolite-rho.

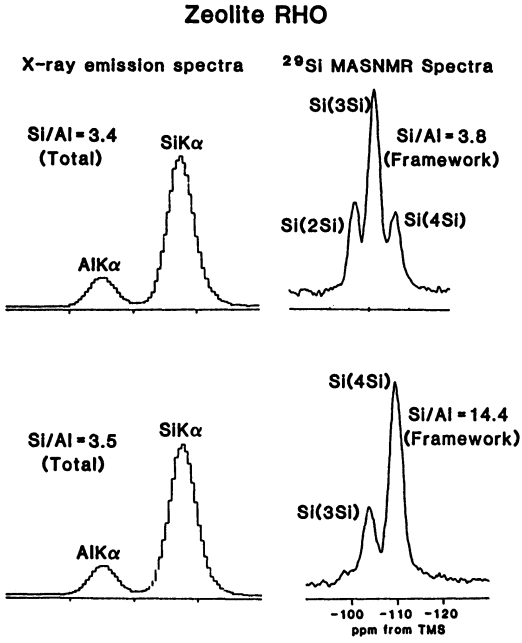

Fig.6.12. When zeolite-rho is dealuminated by hydrothermal treatment of its NH_4^+-exchanged form, the X-ray emission spectrum (*left*) remains essentially unchanged as this method of chamical analysis does not discriminate between framework and and nonframework elements. On the other hand, ^{29}Si MASNMR (*right*) is sensitive [6.14] to changes in framework composition. After [6.52]

Other techniques besides MASNMR are of value in characterizing a zeolite converted into its catalytically active state: infrared spectroscopy, neutron diffraction, thermogravimetric analysis, and acidity gages such as the use of Hammet indicators. In the final analysis, actual catalytic test reactions, such as the decomposition of cumene or the isomerization of xylenes or the cracking of a straight-chain hydrocarbon, are used as realistic yardsticks.

6.5 Influence of Intergrowths on Catalytic Performance

Reference has been made earlier (Sect.6.4) to the fact that the diffusivity of organic molecules in samples of zeolite-L can be adversely affected if there are certain kinds of boundary contained within the crystals of the zeolite. In effect, at the boundary a new (local) structure exists. We also made earlier reference (Sect.6.2) to the tendency for ZSM-5 and ZSM-11 to intergrow, see Fig.6.8. We shall now illustrate, with specific reference to ZSM-5 and ZSM-11, what the catalytic repercussions of such intergrowths amount to.

First, it is relevant to recall that when methanol is converted to gasoline a distribution of aromatic products, typified by that shown in Fig. 6.13, is observed. In practice, however, product distribution curves of this kind are found to vary quite significantly from one preparation of ZSM-5 to

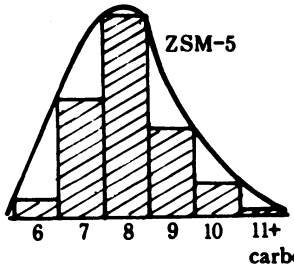

Aromatics distribution from methanol.

Fig.6.13. A typical distribution of aromatic products obtained in the conversion of methanol to gasoline over a ZSM-5 catalyst

another. Moreover, with ZSM-11 the carbon number for the peak as well as the distribution curve itself shifts to higher values, compared with the results for ZSM-5. It is not difficult to appreciate why this is so. There are in ZSM-11 two kinds of cavities created by the intersecting channels. One cavity has a volume about 1.6 times that of the other, the volume and shape of which is exactly the same as the single type of cavity found [6.52] in ZSM-5 see Fig.6.14. The shape and size of these cavities crucially govern [6.29] the maximum dimension attainable in the transition state when the alkylcarbenium ions, formed from methanol, are established inside the zeolite catalyst [6.53]. The shift of the distribution curve (Fig.6.13) to higher values is therefore explicable in terms of the subtleties of the mode of operation of shape-selective catalysts. And the reason why prepa-

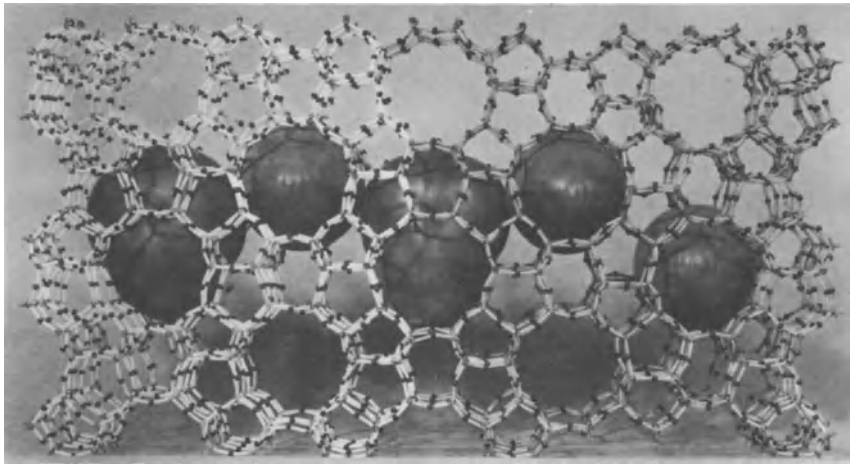

Fig.6.14. Photograph of a scale model showing an intergrowth of ZSM-5 (*left*) and ZSM-11 (*right*). Inflated balloons have been placed at the channel intersections to show that in the ZSM-11 structure, one of the two types of intersections has a larger volume (about 60% more) than the intersections in the ZSM-5 structure. (See also Fig.6.15)

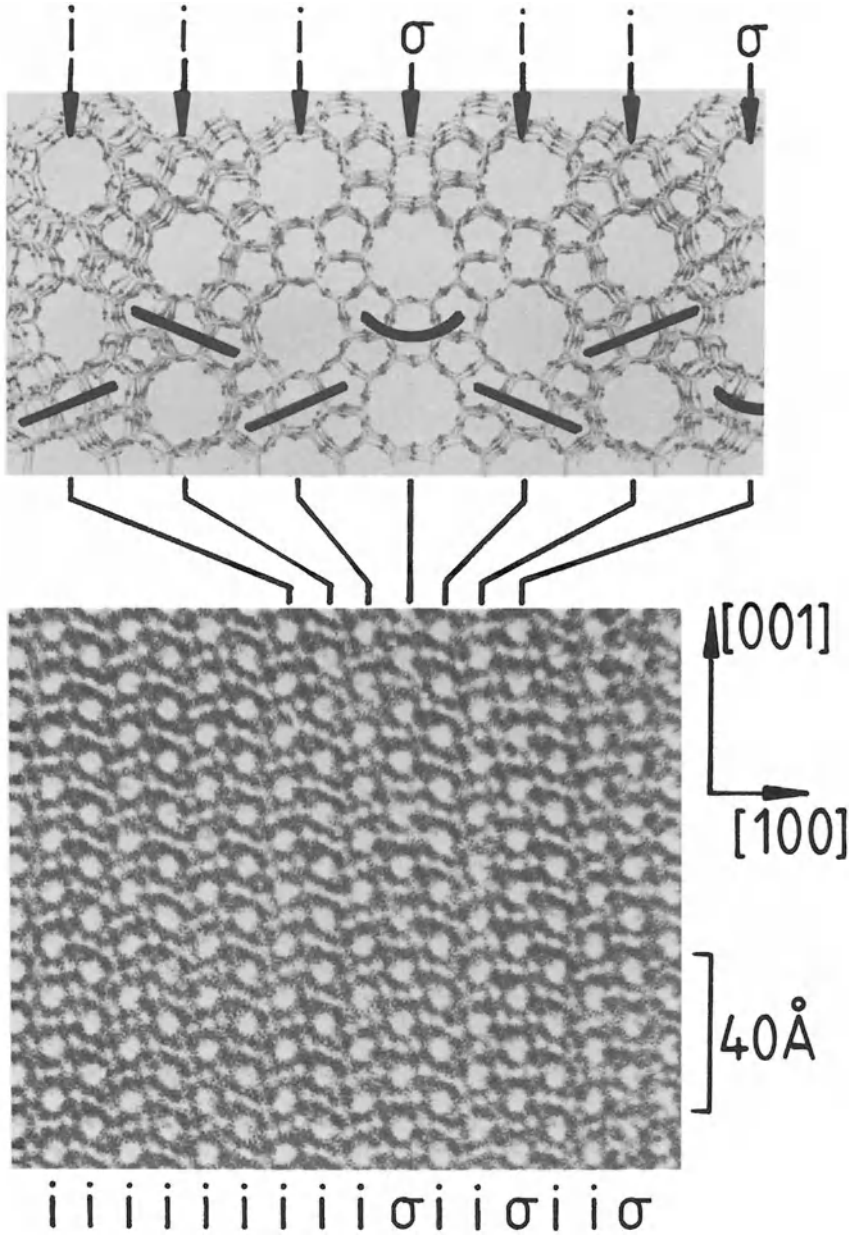

Fig.6.15. High-resolution micrograph of a typical ZSM-5 ZSM-11 catalyst which contains some intergrowths as structural defects. In perfectly ordered ZSM-5, one sheet is related to its predecessor by inversion (i), whereas in ZSM-11 successive sheets are in mirror (σ) relation. See Fig.6.8

rations of ZSM-5 exhibit variability in catalytic performance vis-à-vis product distribution is attributable to the fact that intergrowths of ZSM-11 (present to a variable degree) occur within the ZSM-5. Proof of the occurrence of intergrowths has been presented previously [6.29] and is seen in the high-resolution micrograph that constitutes Fig.6.15.

Intergrowths in which one particular zeolitic structure exists locally within another have been found by high-resolution electron microscopy HREM to be quite common [6.3,9,11,54]. In erionite, a catalyst that is widely used [6.47,48] shape-selectively in the so-called selectoforming process, we have found direct evidence for the coexistence of offretite and of sodalite within the structure. On the basis of prior arguments and structural analogues [6.55], the occurrence of offretite is not surprising, but that of sodalite is.

6.6 Siting and Energetics of Guest Species Inside Zeolite Catalysts

To determine the siting of a guest, one may nowadays use neutron powder *Rietveld* methods [6.18,22], these procedures being at present superior to all other experimental methods, since they can, in principle, be used under conditions that are very close to those used in catalytic practice. X-ray powder methods are also promising [6.56,57] in this regard. There are, however, theoretical approaches which can also be employed. Using atom–atom pairwise evaluation procedures such as those that have proved eminent successful in organic solid-state chemistry [6.58,59], very considerable progress can be made in pinpointing the siting of the guest within the zeolite cavity and channel [6.3]. Early on, *Kiselev* and co-workers [6.60,61] demonstrated that computational procedures yielded values for the enthalpy of adsorption of organic and inorganic molecules inside zeolites that were very close to those determined experimentally from adsorption isotherms.

In a recent study by *Wright* et al. [6.22], encouraging results have been obtained in a joint experimental (neutron Rietveld) and computational determination of the siting of a pyridine molecule inside the channels of zeolite-L. Zeolite-L is a potentially important catalyst for a wide range of cracking, hydrocracking, and other reactions, and although pyridine is not the typical reactant concerned in heterogeneous catalysis involving zeolites, it is the archetypal "acid poisoner". Knowledge of its siting within zeolite-L is, therefore, required.

Figure 6.16 shows the result of the experimental determination of the position of pyridine in the zeolite channel. (Only one of the six crystallo-

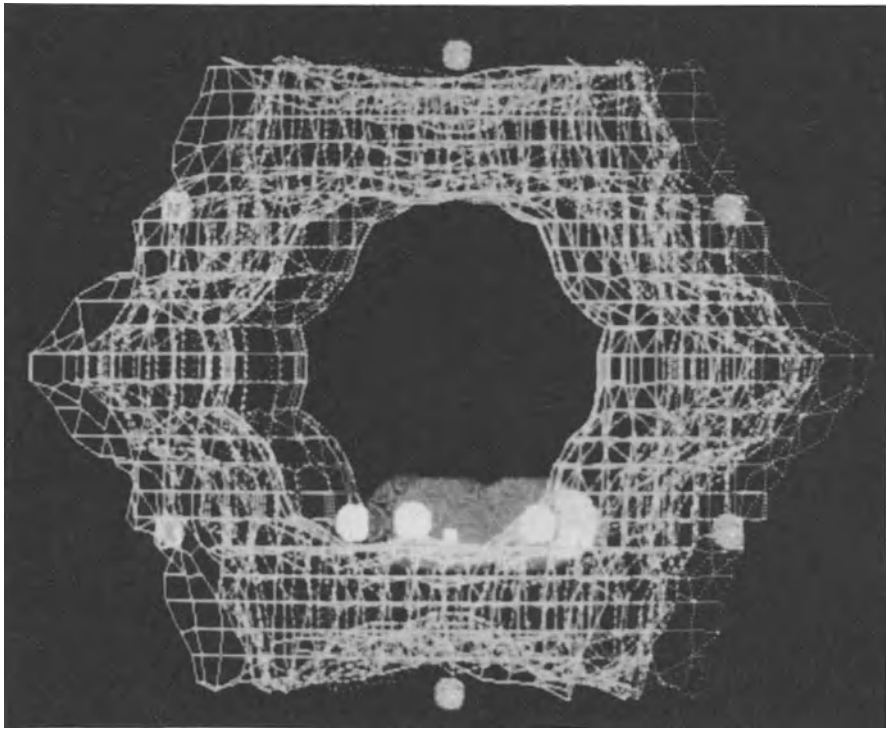

Fig.6.16. Result of neutron Rietveld powder analysis of the siting of a pyridine molecule inside a zeolite-L channel [6.22]. Along the unit cell distance parallel to the channel axis there are six crystallographically equivalent sites where the pyridines are sited. Compare Fig.6.2

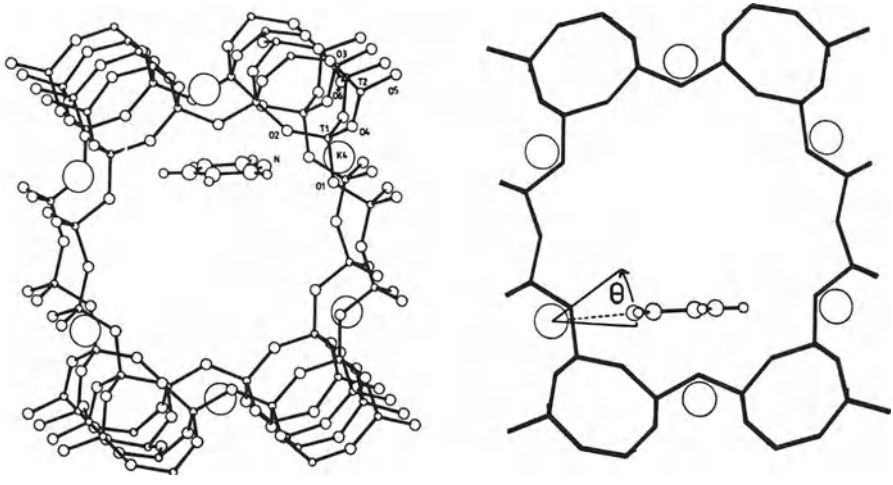

Fig.6.17. Schematic illustration of the "starting" models for the computation of the preferred siting of pyridine inside the channel of K^+-exchanged zeolite-L [6.22]. Empty circles denote K^+ ions (see also Figs.6.2 and 18)

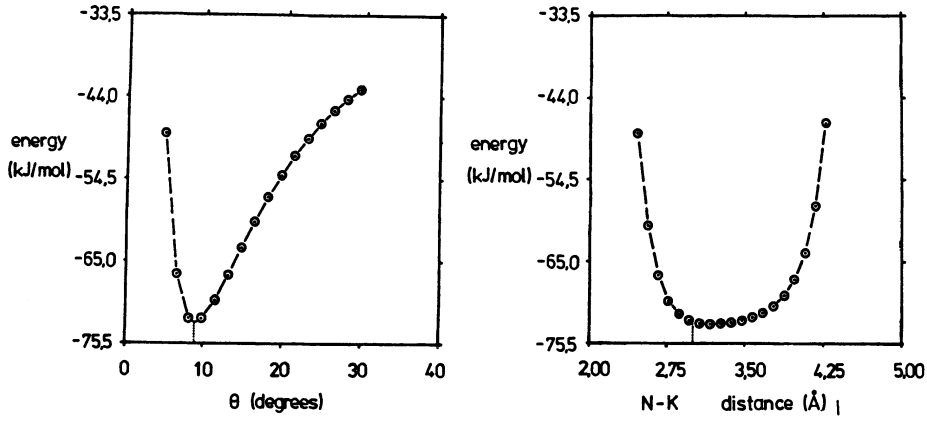

Fig.6.18. Results of computation of preferred siting of pyridine inside zeolite-L. From the right-hand curve, it can be seen that the pyridine can reside in a range of positions with respect to the separation of the N atom on the pyridine and the K^+ ion ($\sim$2.7 - 3.7 Å). The preferred angle of inclination θ, defined in Fig.6.17, turns out to be $\sim$8.5° both experimentally and computationally [6.22]

graphically equivalent pyridine molecules is shown in this projection down the channel axis.) Figure 6.17 difines the positions inside the channels used in the computations, the results of which are shown in Fig. 6.18. It can be seen that agreement between observed and calculated positions is excellent, and augurs well for the solution of similar problems in guest : host interactions.

Plots of interaction energies similar to those shown in Fig.6.18, have been published for the "motion" of a benzene molecule as it proceeds along the channel axis in ZSM-5 [6.3]. The molecule traverses ten energetic maxima and minima in the 20 Å distance corresponding to the unit cell repeat.

6.7 Evaluating Currently Unsolved Zeolitic Structures

We noted earlier that there are many zeolitic materials now extant for which no structural models are available. X-ray structural analysis is not a feasible proposition for these microcrystalline materials, even recognizing that synchrotron radiation (as an X-ray source) enables much smaller crystals than hitherto to be examined. At present new strategies are being evolved to determine the required structures. A combination of high-resolution electron microscopy, electron diffraction, solid-state NMR, catalytic testing [6.62], neutron and X-ray powder diffractometry, infrared spectroscopy, gas adsorption studies, together with model building of one kind or another, is now the "method" of proceeding. Items of information garnered from all these

disparate, individual methods of attack are then synthesized into the final model, but progress so far has not been dramatic. Nevertheless, there have been real successes as recently determined structures of ZSM-23 [6.9] and Theta-1 [6.37] testify. The point to note about such a multipronged structural analysis is that vital clues emerge from several different sources. Thus electron diffraction may yield the spacegroup and the unit cell dimensions; IR may reveal whether or not there are five membered rings (as in ZSM-5, ZSM-11, and ferrierite); ^{29}Si MASNMR on the dealuminated zeolite and the space group tell us [6.16] the maximum number of distinct crystallographic sites there are in the material; the catalytic testing reveals the size of the channel or cavity apertures, and so on. If a plausible model can then be constructed, its reliability can be tested in two distinct ways. First, idealized coordinates are assigned to the atoms (working on the assumption that Si–O bond lengths are close to 1.6 Å and Al–O to 1.76 Å) and an X-ray powder refinement procedure is undertaken. This can be improved using the distance-least-squares (DLS) approach pioneered by Meier and Baerlocher. Second, on the basis of the model, HREM images are calculated [6.8,9] as a function of specimen thickness and defect of focus. A good correspondence between computed and observed images signifies the trustworthiness of the structural model. (Le Roy Eyring and A. Rae Smith have evolved quantitative procedures for assessing the degree of correspondence of computed and observed images).

Figure 6.19 taken from our recent work [6.63] summarizes information garnered in the manner described in the preceding paragraph. We see that ZSM-23 is effectively a twinned version of Theta-1 [6.19], as is exemplified in Fig.6.20. Also included in Fig.6.19, is a proposed model (in projection)

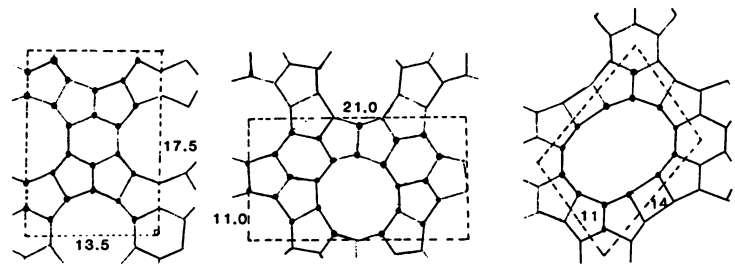

Zeolite	THETA-1	ZSM-23	ZSM-12
Tetrahedra	24	24	14
No. distinct sites	4	7	7
Ratio of sites	2:2:1:1	2:2:2:2:2:1:1	1:1:1:1:1:1:1

Fig.6.19. Models of the projected structures of Theta-1, ZSM-23, and ZSM-12. (Dimensions of unit meshes indicated in Angstroms.)

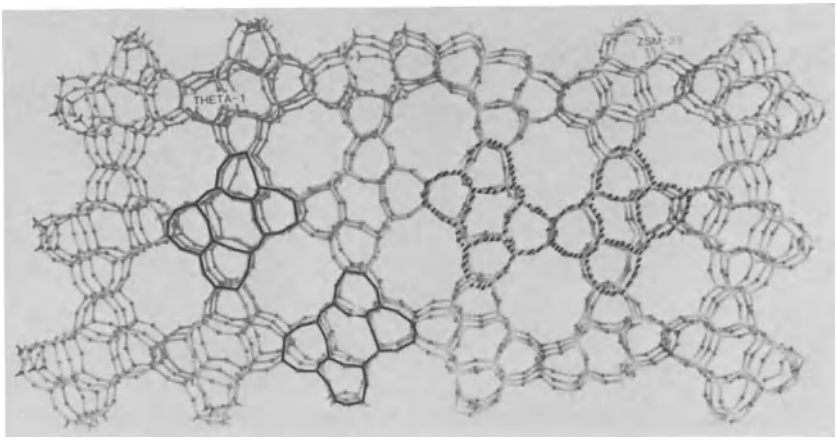

Fig.6.20. Schematic illustration of how the structure of ZSM-23, hitherto unsolved, may be regarded [6.19] as having been derived from Theta-1 by recurrent twinning. The left half is Theta-1, and the strip of structure immediately to the right of the halfway boundary is the twinned (mirror related) version of the strip to the immediate right. In the ZSM-23 structure each strip is a twinned version of its predecessor. The translationally related units in Theta-1, and the mirror-related ones in ZSM-23, have been delineated for clarity

for the structure of ZSM-12. Doubtless many zeolites will yield their structures according to the stratagems outlined here and in other kinds of approach.

6.8 Analogy Between Zeolitic and Selective Oxidation Catalysts

During the course of exerting their influence, zeolite (and indeed clay-based [6.41] catalysts entail removal, transfer, and reincorporation of H^+ ions already present in the solid catalyst and distributed more or less uniformly throughout the bulk. There is another call of catalyst, of growing importance, that functions in a similar fashion but with the important difference that oxygen ions, rather than protons, are now the entities that are removed, transferred and reincorporated. This class embraces several mixed-oxide systems which are widely used for the selective catalytic oxidation of hydrocarbons. For example, Bi_2MoO_6 and other so-called bismuth molybdates $Bi_2Mo_2O_9$ and $Bi_2Mo_3O_{12}$, with or without substitutional additives, are employed [6.64] in the conversion of propylene to acrolein. Also, substoichiometric $CaMnO_{3-x}$ ($0 < x > 0.5$) can be used to convert [6.65] propylene to benzene and isobutene to paraxylene (Fig.6.21). As with the zeolites, this

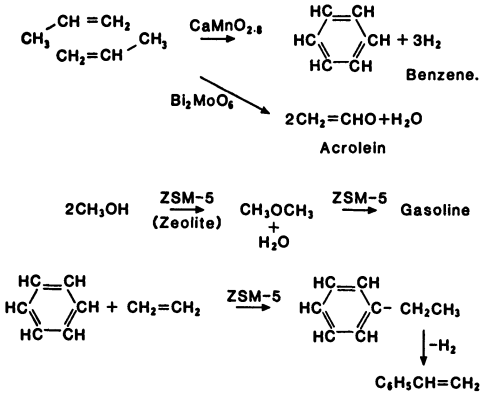

Fig.6.21. Both in catalysts such as Bi_2MoO_6 (or $CaMnO_{3-x}$) and in the acidic zeolites, the active sites from which ions are ditched (O^{2-} and H^+ respectively) are distributed uniformly throughout the solids. Ions are removed, incorporated into the reactants which are converted to products, and are subsequently reincorporated into the solid catalyst. The detailed steps in the conversion of propylene to acrolein are schematized here

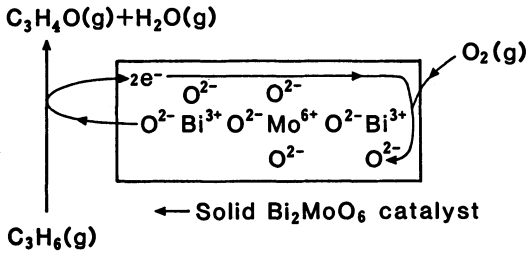

class of catalyst has its active sites (or potential active sites) distributed uniformly throughout the bulk solid. These solid catalysts (in marked contrast to, say, Pt or Ag as selective oxidation catalysts) can release oxygen from their bulk, a loss which is then made good by incorporation of gaseous O_2 into the depleted structure (Fig.6.21). Experiments using $^{18}O_2$ and secondary ion mass spectrometry [6.66] leave little doubt that the solid oxide releases its structural oxygen in the crucial act of catalysis, and that incorporation of O_2 is facilitated by the electrons freed in the step $O^{2-} \rightarrow [O] + 2\,e$.

References

6.1 I. Tabushi, Y. Kobuke, J. Imuta: J. Am. Chem. Soc. **103**, 6152 (1981)
D.J. Cram: Science **219**, 1177 (1983)
G.D. Gutsche: Acc. Chem. Res. **16**, 161 (1983)
J.M. Lehn: Theochem **10**, 153 (1983)

6.2 W. Moreta, P. Baret, J-L. Pierre: J. Chem. Soc., Chem. Commun. 899 (1985)

6.3 S. Ramdas, J.M. Thomas, A.K. Cheetham, P.W. Bettridge, E.K. Davies: Angew. Chem. Int. Ed. Engl. **23**, 671 (1984)

6.4 L. Xinsheng, J.M. Thomas: J. Chem. Soc., Chem. Commun. 1544 (1985)

6.5 J.M. Thomas, D.A. Jefferson, G.R. Millward: JEOL News **23E**, 7 (1985)

6.6 J.M. Thomas, J. Klinowski, C.A. Fyfe, G.C. Gobbi, S. Ramdas, M.W. Anderson, ACS Symp. Ser. **218**, 159 (1983)

6.7 J.M. Thomas, G.R. Millward, L.A. Bursill: Philos. Trans. R. Soc. London, Ser. A **300**, 43, (1981)
6.8 J.M. Thomas: Ultramicroscopy **8**, 13 (1982)
6.9 J.M. Thomas: In Proc. 8th Int. Congr. Catalysis, Berlin 1984, Vol. 1, ed. by G. Ertl, H. Knötzinger (Verlag Chemie, Weinheim 1984) p.31
6.10 O. Terasaki, G.R. Millward, J.M. Thomas: Proc. R. Soc. London, Ser.A **395**, 1435 (1985)
6.11 G.R. Millward, S. Ramdas, J.M. Thomas: Proc. R. Soc. London, Ser. A **399**, 57 (1985)
6.12 S. Ramdas, J.M. Thomas, J. Klinowski, C.A. Fyfe, J.S. Hartman: Nature (London) **292**, 228 (1981)
6.13 J. Klinowski, J.M. Thomas, C.A. Fyfe, G.C. Gobbi: Nature (London) **296**, 533 (1982)
6.14 J. Klinowski, S. Ramdas, J.M. Thomas, C.A. Fyfe, J.S. Hartman: J. Chem. Soc., Faraday Trans. 2, **78**, 1025 (1982)
6.15 C.A. Fyfe, J.M. Thomas, J. Klinowski, G.C. Gobbi: Angew. Chem. Int. Ed. Engl. **22**, 259 (1983)
6.16 J.M. Thomas, J. Klinowski, S. Ramdas, B.K.T. Hunter, D.T.B. Tennakoon: Chem. Phys. Lett. **102**, 158 (1983)
6.17 A.K. Cheetham, J.M. Thomas, M.M. Eddy, D.A. Jefferson: Nature (London) **299**, 24 (1982)
6.18 P.A. Wright, J.M. Thomas, S. Ramdas, A.K. Cheetham: J. Chem. Soc., Chem. Commun. 1338 (1984)
6.19 P.A. Wright, J.M. Thomas, G.R. Millward, S. Ramdas, S.A.I. Barri: J. Chem. Soc., Chem. Commun. 1117 (1985)
6.20 C.R.A. Catlow, J.M. Thomas, S.C. Parker, D.A. Jefferson: Nature (London) **295**, 658 (1982)
6.21 S. Ramdas, J.M. Thomas: Chem. Br. **21**, 49 (1985)
6.22 P.A. Wright, J.M. Thomas, A.K. Cheetham, A. Nowak: Nature (London) **318**, 611 (1985)
6.23 J. Klinowski, J.M. Thomas, M. Audier, C.A. Fyfe, L.A. Bursill, S. Vasudevan: J. Chem. Soc., Chem. Commun. 570 (1981)
6.24 J.M. Thomas: J. Mol. Catal. **27**, 59 (1984)
6.25 M.W. Anderson: Ph.D. Thesis, University of Cambridge (1984)
6.26 R.M. Barrer: *Zeolites* (Academic, New York 1978)
6.27 D.W. Breck: *Zeolites Molecular Sieves* Wiley, New York 1974)
6.28 D.H. Olson, W.M. Meier: *Atlas of Zeolite Structures* (Structure Commision of Int. Zeolite Assoc., Zurich 1978)
6.29 J.M. Thomas, G.R. Millward: J. Chem. Soc., Chem. Commun. 1380 (1982)
6.30 J. Klinowski: Prog. Nucl. Magn. Reson. Spectrosc. **16**, 237 (1984)
6.31 R. Rinaldi, H.R. Werk: Acta Crystallogr., Sec. A **35**, 825 (1979)
6.32 D.R. Corbin, M.M. Eddy, J.F. Whitney, W.C. Fultz, A.K. Cheetham, G.D. Stucky: Inorg. Chem., in press
6.33 G.C. Bond, M.R. Gelsthorpe, K.S.W. Sing, C.R. Theorcharis: J. Chem. Soc., Chem. Commun. 1056 (1985)
6.34 S.T. Wilson, B.M. Lok, C.A. Messina, T.R. Cannan, E.M. Flanigen: A.C.S. Symp. Ser. **218**, 79 (1983)
6.35 J.B. Parise: J. Chem. Soc., Chem. Commun. 1449 (1984); ibid. 606 (1985)
6.36 P. Eisenberger, M. Leonowiz, D.E.W. Vaughan, J.A. Newsom: Nature (London) (1984)
6.37 S.A.I. Barri, G.W. Smith, D. White, D. Young: Nature (London) **312**, 533 (1984)
6.38 J.M. Thomas, J. Klinowski: Adv. Catal. **33**, 199 (1985)
6.39 G.K. Boreskov, M. Minachev (eds.): *Applications of Zeolites in Catalysis* (Akadêmia i Kiadô, Budapest 1979)
6.40 D.T.B. Tennakoon, W. Jones, J.M. Thomas, L.J. Williamson, J.A. Ballantine, J.H. Purcell: Proc. Indian Acad. Sci. Sect. A **92**, 27 (1983)
6.41 J.M. Thomas: In *Intercalation Chemistry*, ed. by M.S. Whittingham, A.J. Jacobson (Academic, New York 1982) p.56

6.42 J.A. Ballantine, J.H. Purnell, J.M. Thomas: Clay Miner. **18**, 347 (1983)
6.43 J.A. Ballantine, J.H. Purnell, J.M. Thomas: J. Mol. Catal. **27**, 157 (1984)
6.44 J.M. Thomas: Philos. Trans. R. Soc. London, Ser.A **311**, 271 (1984)
6.45 F.C. Whitmore: J. Am. Chem. Soc. **54**, 3274 (1932)
6.46 D.M. Brouwer: In *Chemistry and Chemical Engineering of Catalytic Processes*, ed. by R. Prins, G.C.A. Schmit NATO Adv. Study Inst. Ser. **39**, 137 (1980)
6.47 P.B. Weisz: Pure Appl. Chem. **52**, 2091 (1980)
6.48 S.M. Csiszery: Zeolites **4**, 202 (1984)
6.49 W.O. Haag, R.M. Lago, P.B. Weisz: Nature (London) **309**, 589 (1984)
6.50 O. Terasaki, S.Ramdas, J.M. Thomas: J. Chem. Soc., Chem. Commun. 216 (1984)
6.51 R.H. Jarman: Zeolites **5**, 213 (1985)
6.52 P.A. Wright: Ph.D. Thesis, University of Chambridge (1985)
6.53 N.Y. Cheng, W.W. Kaeding, F.G. Dwyer: J. Am. Chem. Soc. **101**, 6783 (1979)
E.G. Derouane: J. Catal. **72**, 177 (1981)
J.R. Anderson, K.Foger, T. Mole, R.A. Rajadhyaksha, J.V. Sanders: J. Catal. 58, 114 (1979)
6.54 G.R. Millward, J.M. Thomas, O. Terasaki, D. Watanabe: Zeolites, in press
6.55 G.T. Kokotailo: In Proc. 6th Int. Zeolite Conf., Reno, ed. by D. Olson, A. Bisio (Butterworths, London 1984) p.760
J.V. Smith: ibid. p.56
R.M. Barrer: ibid. p.17
6.56 I. Gameson, P.A. Wright, T. Rayment, J.M. Thomas: Chem. Phys. Lett. **123**, 145 (1986)
6.57 I. Gameson, T. Rayment: Chem. Phys. Lett., in press
6.58 A.I. Kitaigorodskii: Chem. Soc. Rev. **7**, 133 (1978)
6.59 S. Ramdas, J.M. Thomas: In *Chemical Physics of Solids and their Surfaces*, Vol. 7 (The Chemical Society, London 1978) p.31
6.60 A.V. Kiselev, P.Q. Du: J. Chem. Soc., Faraday Trans. 2, **77**, 17 (1981)
6.61 A.V. Kiselev, V.I. Lygin, R.V. Stardubceva: J. Chem. Soc., Faraday Trans. 2, **68**, 1793 (1979)
6.62 P.A. Jacobs, P. Martens: In Proc. 8th Int. Congr. Catalysis, Berlin 1984, Vol. 4, ed. by G. Ertl, H. Knötzinger (Verlag Chemie, Weinheim (1984) p.357
6.63 P.A. Wright, J.M. Thomas: Unpublished
6.64 R.K. Grasselli, J.D. Burrington: Adv. Catal. **30**, 133 (1981)
A.W. Sleight: In *Advanced Materials in Catalysis*, ed. by J.J. Burton, R.L. Garten (Academic, New York 1977) p.181
6.65 A. Reller, J.M. Thomas. D.A. Jefferson, M.K. Uppal: Proc. R. Soc. London, Ser. A **394**, 223 (1984)
6.66 C.R. Adams, T.J. Jennings: J. Catal. **2**, 63 (1963)

7. Structural Characterization of Molecules and Reaction Intermediates on Surfaces Using Synchrotron Radiation

D.A. Outka and R.J. Madix

Departments of Chemical Engineering and Chemistry, Stanford University, Stanford. CA 94305, USA

One of the principal reasons for studying surfaces is to gain insight into industrially important chemical processes such as catalysis. Advancement in this area in surface chemistry has been aided by several developments in spectroscopic techniques over the past decade which have allowed increasingly detailed characterization of polyatomic adsorbates on single-crystal surfaces. For example, with vibrational spectroscopy [7.1] one can now routinely determine the character of the bonds within polyatomic adsorbates containing a dozen or more atoms and limited information on orientation can be obtained. Further structural information such as bond distances and binding sites have remained elusive, however, except for the simplest of cases. In this chapter we examine two related techniques employing synchrotron radiation which hold promise of providing such structural information: surface extended X-ray absorption fine structure (SEXAFS) and near edge X-ray absorption fine structure (NEXAFS). These techniques are particularly useful in studying surface chemistry in that they provide structural information not only about the surface-adsorbate bond but also about bonds within the adsorbate itself.

The first technique, SEXAFS, is an adaptation of the bulk structural technique EXAFS (extended X-ray absorption fine structure). From this technique the chemisorption site and bond length can be determined. While other techniques such as low-energy electron diffraction (LEED) [7.2] and photoelectron diffraction [7.3] provide similar information, SEXAFS has the advantages of not requiring long-range order and of using a simple, one-electron scattering model. Previous reviews have considered the application of this technique to *atomic* adsorbates [7.4,5]. We will concentrate on recent applications to *polyatomic* adsorbates including the variation in chemisorption geometry observed for formate groups (HCO_2) on copper surfaces as a function of surface crystallography.

The second technique, NEXAFS, has been systematically studied on surfaces only recently [7.6]. It probes the orientation and bond lengths between low-atomic-number atoms within an adsorbate. This information is of particular interest since most techniques are rather insensitive to low-atomic-number atoms.

This technique is rather easier to perform than SEXAFS so several studies have been conducted and can be discussed, including oxidation intermediates of Cu {100}, and hydrocarbons and sulfur-containing hydrocarbons on Pt{111}.

7.1 Principles of X-Ray Absorption

7.1.1 General Features

The absorption of X-rays is accompanied by the excitation of an inner-shell electron. The simplest case is that of an isolated atom such as the noble gas krypton, whose absorption spectrum is shown in Fig.7.1 [7.5]. The spectrum is characterized by an abrupt increase in the absorption coefficient as a function of increasing X-ray frequency. This threshold corresponds to the energy required to excite a K shell electron to an unoccupied level and is known as the absorption edge. The X-ray absorption spectrum of an isolated atom is rather featureless but when there are neighboring atoms such as in a molecule, two additional types of spectral features are observed. For example, the X-ray absorption spectrum of gaseous Br_2 (Fig.7.1) shows a sharp peak just below the ionization energy and an oscillatory absorption coefficient on the high-energy side of the edge. These structures are the NEXAFS and EXAFS, respectively.

Both of these phenomena are due to scattering of the excited electron by neighboring atoms, but differ in the nature of the final state of the electron.

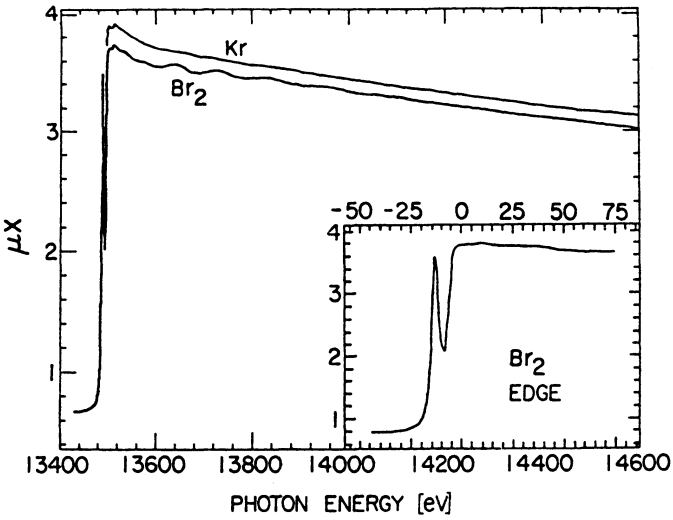

Fig.7.1. The energy-dependent X-ray absorption spectrum of krypton gas showing no EXAFS nor NEXAFS structure, and the spectrum for bromine which has these [7.5]

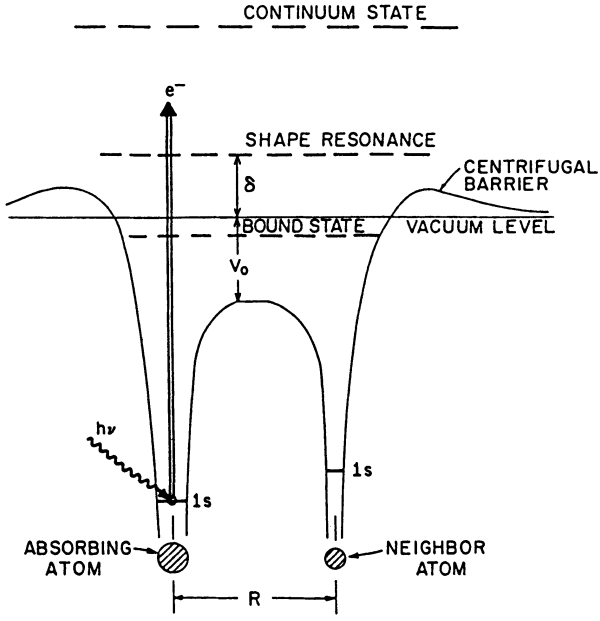

Fig.7.2. Potential energy diagram for a diatomic molecule showing the X-ray absorption process. For NEXAFS, electron transitions to a bound state or to a shape resonance are possible. For SEXAFS, the electron is excited to a continuum state [7.7]

Figure 7.2 shows a schematic potential energy diagram for the X-ray absorption process [7.7]. Depending on the energy of the exciting radiation, the electron can be promoted to various final states. In the case of NEXAFS, the excitation energies are of the order of 10 eV, giving rise to resonances near the absorption edge, and the final state contains an unoccupied orbital in the vicinity of the absorbing atom. The excitation can either be to a state below the ionization threshold of the molecule which is called a "bound state" or to a state just above the ionization threshold which is called a "shape resonance". In the case of EXAFS, the excitation energies are $\gtrapprox 30$ eV above the ionization limit where a continuum of free-electron-like final states exist. In both cases the final states are affected by neighboring atoms.

7.1.2 Surface Extended X-Ray Absorption Fine Structure

Distances to adjacent high-atomic-number atoms can be determined from the high-energy EXAFS spectral region [7.8]. The EXAFS region is straightforward to analyze quantitatively since the final state is free-electron-like, and the high kinetic energy of the photoelectron allows single-electron scattering theory to be applied. The EXAFS oscillations result from backscattering of

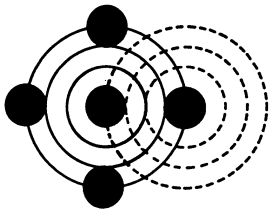

Fig.7.3. Schematic diagram of EXAFS backscattering. The photoelectron emitted from the central atom is backscattered from neighboring atoms, which results in interference

this photoelectron by neighboring atoms (Fig.7.3). This backscattered electron can interfere constructively or destructively with the outgoing photoelectron depending on its wavelength. This gives rise to the oscillatory behavior whose dependence on the electron wave vector k is given by [7.4,8]

$$\chi(k) = \sum_i N_i^* A_i(k) \sin[2kR_i + \phi_i(k)] \quad , \tag{7.1}$$

where the sum extends over shells of i identical neighboring atoms at a distance R_i, $A_i(k)$ is an amplitude function which is largely determined by the atomic number of the backscattering atom, and the term N_i^* accounts for the angle between the incoming X-rays and the vector to the backscattering atom. Distances are derived from Fourier transformation of the EXAFS signal which isolates the periodic portion of this function yielding a peak for each distance R_i. Actual distances are extracted from the peaks of the Fourier transform by applying a phase shift correction $\phi_i(k)$ which is characteristic of the central and backscattering atom. This phase shift can be obtained from theory or reference compounds. In the best cases, distances can be determined to within ±0.02 Å.

In studies with single-crystal surfaces, the EXAFS technique is principally used to probe the chemisorption bond, since the EXAFS is dominated by backscattering only from neighboring atoms with a high atomic number, such as in a metal surface. There are two reasons for this. First, the energetic photoelectrons produced in the X-ray absorption are appreciably affected only by the core electrons of medium- to high-atomic-number atoms. For example, Fig. 7.4 compares the theoretical scattering amplitude of two elements, copper and carbon, as a function of electron wave vector [7.9,10]. The single-electron scattering approximation used in EXAFS is valid $\gtrapprox 4$ Å, in which range the backscattering is dominated by copper. In contrast, the EXAFS amplitude from low atomic-number atoms such as carbon would be weak or unobservable. Second, the bond lengths associated with low-atomic-number atoms are usually small, which implies a long wavelength for the EXAFS oscillations. These long wavelengths are difficult to measure because the amplitude drops quickly with k (Fig.7.4) and only a limited energy range is usually available for observation.

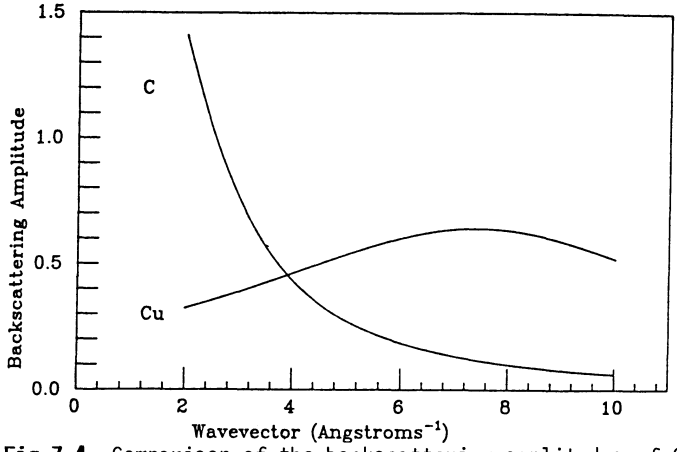

Fig.7.4. Comparison of the backscattering amplitudes of C and Cu atoms as a function of electron wave vector, from [7.9]. The backscattering amplitude maximum for Cu occurs above 5 Å^{-1} which is in the SEXAFS region. That of carbon maximizes at a low wave vector ≈ 1 Å^{-1}, which is in the NEXAFS region [7.10]

Chemisorption sites can be determined from the angular dependence of the SEXAFS amplitude when using single-crystal surfaces and polarized X-rays. This angular dependence is contained in the N_i^* term of (7.1) which for K edges is given by

$$N_i^* = 3 \cos^2(\alpha_i) \quad , \tag{7.2}$$

where α_i is the angle between the electric field vector **E** and the internuclear vector. Note that the EXAFS amplitude is greatest when the **E** vector of the X-rays lies along the internuclear bond. For example, Fig.7.5 shows a simulated absorption spectrum for a methoxy group (CH_3O) on a surface with fourfold symmetry with the oxygen located in the plane of the surface [7.10]. The oxygen K edge SEXAFS is most intense when **E** lies parallel to O - Cu bonds (i.e., in the surface plane) as shown in Fig.7.5c,d. When **E** lies perpendicular to the O - Cu bonds (i.e., perpendicular to the surface), the SEXAFS oscillations are absent and only the weak and broad O - C SEXAFS oscillations are seen (Figs. 7.5a,b). Special cases of (7.2) have been derived for sites of fourfold, threefold, and twofold symmetry [7.4]. The EXAFS amplitude also contains the term $A_i(k)$ of (7.1) which includes Debye-Waller factors, electron-loss terms, and an amplitude function which depends on the backscattering atom. These factors depend little on X-ray incidence angle, however, and thus approximately cancel in the ratio of amplitudes at different incidence angles. Chemisorption sites can therefore be determined from the amplitude ratios measured at various angles

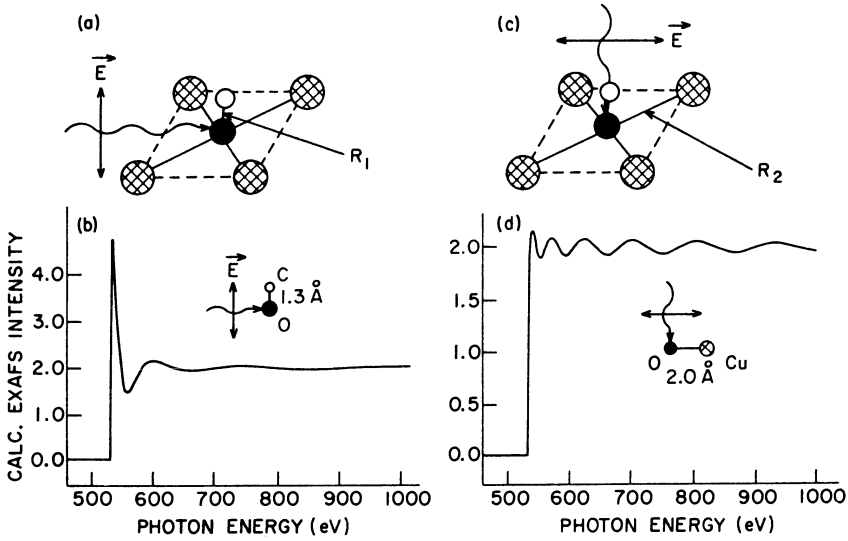

Fig.7.5a-d. Angular dependence of SEXAFS and NEXAFS [7.10]. (**a**) Hypothetical diatomic molecule (*black and white atoms*) in a fourfold hollow site of metal atoms (*dashed atoms*). The molecular axis is normal to the plane containing the black and dashed atoms. The X-rays are incident at a glancing angle with E along the molecular axis. (**b**) SEXAFS spectrum calculated using a single-scattering formalism (7.1) for geometry (**a**) showing intense O-C structure just above the edge (550 - 600 eV) but no O-Cu SEXAFS. (**c**) Same model as (**a**) except the X-rays are at normal incidence with E parallel to the surface. (**d**) Calculated SEXAFS spectrum for geometry (**c**) showing O-Cu SEXAFS but no O-C related NEXAFS or SEXAFS

of incidence by comparison to those calculated from (7.2). These should agree within 20% for the correct geometry.

7.1.3 Near Edge X-Ray Absorption Fine Structure

The NEXAFS spectral region lies near the absorption edge (within $\approx$ 30 eV) and provides information about the orientation and length of bonds between low-atomic-number atoms. These features are more difficult to analyze quantitatively because the excited electron now has little kinetic energy and is therefore multiply scattered by core and valence electron charge distributions. The complexity of this region is seen in the gas-phase spectra of the several dozen small molecules which have been studied using X-ray absorption or electron impact excitation [7.11]. For example, Fig.7.6 shows the electron impact spectrum for gaseous N_2 which shows at least seven peaks [7.12]. Calculations indicated that many of these features are multiple-scattering events [7.13]. There were two dominant features, however, which are attributable to simple electric-dipole transitions. The first and most intense peak in the spectrum

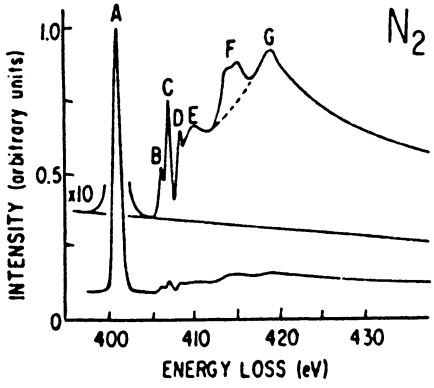

Fig.7.6. Electron impact K shell excitation spectrum of nitrogen [7.12]. The most intense and electric-dipole dominated transitions are due to final states of π symmetry (peak A) and σ symmetry (peak G)

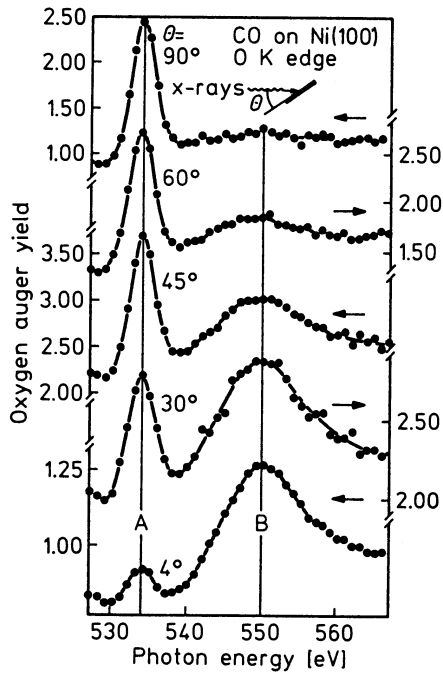

Fig.7.7. Oxygen K edge NEXAFS spectra for CO on Ni{100} as a function of X-ray incidence angle at 180 K [7.6]. The two principal peaks are due to a π^* state (peak A) and a σ^* state (peak B)

of N_2 (Fig.7.6) is due to a transition to a π^* final state. Such a π^* feature is observed in the spectra of unsaturated molecules and is usually sharp, intense, and the lowest-energy peak. The other dominant feature of the N_2 spectrum is the broad peak labeled G which is due to a final state of σ symmetry. This peak is present in the spectra of all molecules and is broad. The other features are weak and not usually resolved in the spectra of condensed-phase species.

The electric-dipole character of these two dominant features can be used to determine the orientation of polyatomic adsorbates on single-crystal surfaces when using the polarized X-rays from a synchrotron source. By varying the incidence angle of the X-rays, the π^* and σ^* transitions can be tuned in or out. This is seen in the spectrum of carbon monoxide on a Ni{100} surface (Fig.7.7) [7.6]. Carbon monoxide is attached to the surface via carbon with the C - O bond normal to the surface. This spectrum shows dominant transitions to a π^* final state (labeled A) and a σ^* final state (labeled B). The transition to the σ^* final state is maximized when **E** lies parallel to the σ orbital of CO (i.e., along the internuclear axis). This occurred at glancing X-ray incidence where **E** was normal to the surface. (The vector **E** is perpendicular to the direction of propogation of the X-rays.) The transition to the π^* final

state has the opposite requirement and is maximized when **E** is paralle] to the lobes of the π orbital of the molecule. This occurred at normal X-ray incidence. The angular behavior of these two peaks is thus consistent with a normal orientation for the C - O bond with respect to the surface.

The angular dependence of these peaks can be quantified to obtain the orientation of an adsorbate on a surface. Because the features are electric dipole dominated, there is a $\cos^2(\alpha)$ dependence in the intensity of these peaks where α is the angle between **E** and the respective π^* or σ^* orbital [7.6]. For example, using this relation, the axis of the molecules CO, NO, and N_2 have been determined to be normal to the Ni{100} surface to within $\pm 10^{\circ}$ [7.6]. This result is in agreement with the orientations for these molecules as determined from angle-resolved ultraviolet photoelectron spectroscopy (ARUPS), low-energy electron diffraction (LEED), and electron energy loss spectroscopy (EELS). The determination of orientation is most straightforward from the π^* resonance since it is generally narrower, and it precedes the absorption edge and does not reside on the edge background. One small complication is that synchrotron radiation is not perfectly polarized so the peaks never vanish completely. The extent of polarization is approximately 80% [7.6], depending on the source, and must be accounted for in calculating orientations.

The positions of the σ^* peak in the NEXAFS can also be used to estimate the length of the σ bond, providing a basis for measuring bond lengths between low-atomic-number atoms within a polyatomic adsorbate. The dependence of the NEXAFS peaks on bond length was suggested from several experimental studies of gases and metal complexes [7.14-16] and calculations [7.17]. These showed that the difference between the π^* and σ^* features increased with decreasing bond length. Actually it is the position of the σ^* peak which is the most sensitive to the bond length, and since this feature exists in all molecules, its position relative to the ionization limit can be used to establish a correlation. Originally, an EXAFS-like R^{-2} correlation between bond distance and position of the σ^* peak was suggested [7.16]. However, further experiments with gas-phase molecules indicated that a simple linear correlation was adequate and gave similar results [7.7]. In either case, the correlating function can be considered to be merely an interpolating function or part of a series expansion of the exact, but unknown, relationship. The validity of this approximation is demonstrated in Fig.7.8 for a series of gas-phase molecules [7.7]. Along each line relating the σ^* resonance position to bond length are molecules with a constant sum for the atomic numbers of the two atoms involved in the σ bond. Thus all the hydrocarbons are included in the top line. Diatomics like N_2 and CO are included together since the sum of their atomic numbers is

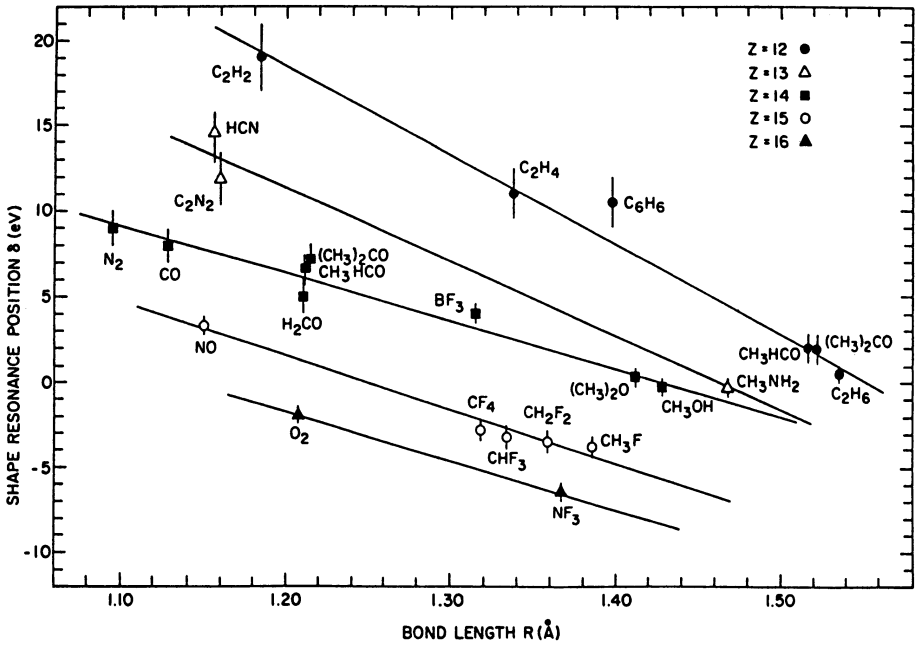

Fig.7.8. Plot of the energy position of the σ^* resonance relative to the ionization potential versus the bond distance for gas-phase molecules [7.7]. Each line is for a constant sum of the atomic numbers of the two atoms involved in the σ bond

14. While there are a few cases like benzene (C_6H_6) which do not fall precisely on a line, the errors associated with assuming a linear relationship even for these cases is $\leq$ 0.04 Å. Usually the error is much less. Thus a linear interpolation provides a simple method of estimating the bond lengths between low-atomic-number atoms of polyatomics on surfaces.

7.1.4 Apparatus

Both SEXAFS and NEXAFS require an intense source of X-rays to compensate for the small number of atoms in a monolayer on a single-crystal surface ($< 10^{15}$) and, especially in the case of SEXAFS, the weak signal. Furthermore, to determine orientations from NEXAFS or binding sites from SEXAFS, the radiation must be polarized. Currently, only a synchrotron radiation source meets these criteria.

The data collection apparatus is the same for both techniques but differs in some respects from the usual practice of bulk EXAFS [7.4]. First in order to prepare and maintain clean surfaces, the experiments must be performed under ultra-high-vacuum conditions ($< 10^{-9}$ Torr). Secondly, the measurement of

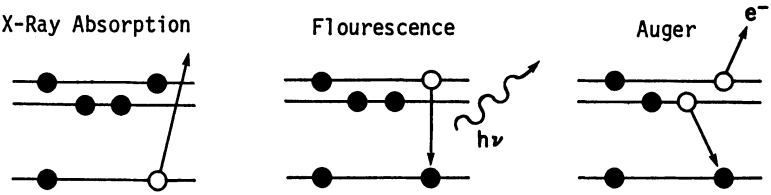

Fig.7.9. Schematic diagram of the X-ray absorption process and decay of the core hole. Two decay pathways are possible: fluorescent decay which yields a photon and Auger decay which leads to ejection of an electron

the X-ray absorption coefficient is less straightforward. For example, in EXAFS studies of bulk compounds, the intensities of the X-rays entering the sample and exiting the sample can be measured directly to obtain the absorption coefficient. This method is not sensitive enough for the small number of absorbers in a monolayer on a single-crystal surface, however. Instead, events associated with the decay of the inner-shell vacancy created by X-ray absorption must be followed. Figure 7.9 shows the X-ray absorption process to create a vacancy in the K electron shell and two relaxation pathways. For elements in the third row of the periodic table or below, it is possible to monitor the decay by fluorescence relaxation. Because of the long path length for X-rays in solids, this detection method also allows meaurements of thin films with thicknesses in the range of micrometers. For second-row elements, however, Auger relaxation is dominate so fluorescence detection is much more difficult. Since the experiments are performed under ultra-high-vacuum conditions, the Auger electron can be collected with a typical electron energy analyzer or an electron multiplier provided with retarding grids [7.4]. Care must be taken to select the incident X-ray energies and electron energy collection ranges for this detection method to avoid spurious peaks from photoemission or other Auger processes. Furthermore, since electrons have only a small escape depth from solids, this method can be applied only to atoms on top of the surface or within the first few atomic layers. In the case of molecules directly on the surface, the decay of the inner-shell vacancy can also lead to stimulated desorption of ions. The probability of this event depends on the orbital overlap between the absorbing atom and that of the desorbing ion. This provides the weakest signals for SEXAFS.

7.2 SEXAFS Studies of Polyatomic Adsorbates

7.2.1 Structure of Formate on the Cu{100} Surface

The formate group (HCO_2) is an intermediate in the copper-catalyzed oxidation of formic acid (HCOOH) and has been well-characterized by a variety of surface

spectroscopies. The mechanism for this oxidation was established on the Cu{100} surface using temperature programmed reaction spectroscopy (TPRS) and isotope labeling. The following mechanism applies [7.18,19]

$$2DCOOH_{(g)} + O_{(a)} \rightarrow 2DCOO_{(a)} + H_2O_{(g)} \quad , \tag{7.3}$$

$$DCOO_{(a)} \rightarrow CO_{2\,(g)} + 1/2\ D_{2\,(g)} \cdot T \geqslant 400\ K \quad . \tag{7.4}$$

While formic acid partially dissociates on a clean copper surface, this dissociation is assisted by oxygen adatoms which abstract the acidic hydrogen atom to form unlabeled water and deuterium-labeled formate groups (7.3). The water desorbs by room temperature, isolating the formate groups. These are stable to about 400 K, whereupon CO_2 and D_2 are liberated in a reaction-limited decomposition of the formate group (7.4). Thus the formate can be isolated on copper surfaces.

The orientation of the formate is reasonably well known from vibrational spectroscopy. The EELS of formate on Cu{100} agreed well with the infrared spectrum of sodium formate salt [7.20]. The frequencies and intensities were in general agreement with a few notable exceptions. In particular, the intense asymmetric C - O stretch and the C - H bending mode were weak or absent in the surface spectrum. The absence of these two features is attributed to a selection rule for the surface vibrational spectroscopy which allows only modes with a dipole-moment component normal to the surface to be observed. Using this selection rule it could be deduced that the formate group belonged to the C_{2v} point group which implied that the plane of the formate group is normal to the surface and that the oxygen atoms are equivalent. The similarity of the vibrational frequencies to formate complexes indicate that the formate is attached to the surface via the two oxygen atoms.

The formate group on copper surfaces has also been studied by other surface spectroscopic techniques, including photoelectron spectroscopy [7.19] and infrared spectroscopy [7.21]. Despite the number of surface analysis techniques with which formate had been studied, bond lengths and the chemisorption site were unknown before SEXAFS analysis.

From the SEXAFS study the *average* Cu - O chemisorption bond length for the formate group on the Cu{100}surface was determined to be 2.38 ± 0.04 Å [7.10, 22]. The raw oxygen K edge X-ray absorption spectrum for an X-ray incidence angle of 15° is shown as the top curve of Fig.7.10. The SEXAFS spectra were analyzed by the same methods used in normal bulk EXAFS analysis. First the background was approximated by two spline polynomials of order three and two, as shown by the dotted line through the raw spectrum. This background was sub-

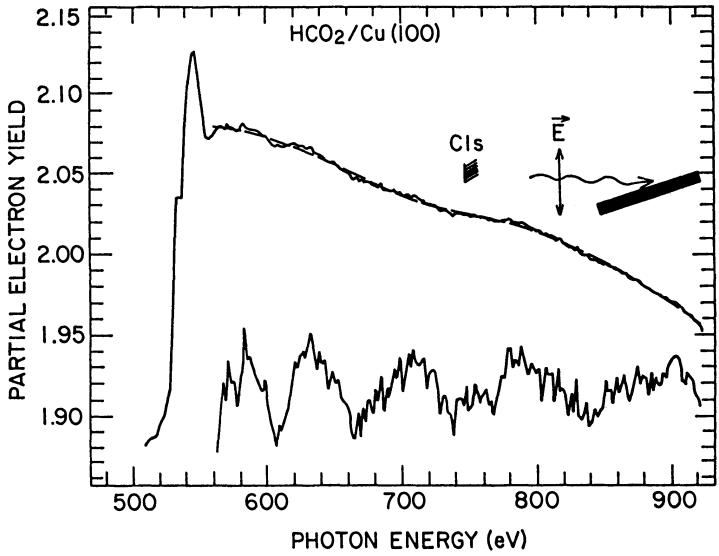

Fig.7.10. The upper curve is the oxygen K edge SEXAFS spectrum for formate on Cu{100} at 300 K and at grazing (15°) X-ray incidence [7.10]. The photon energy where the C(1s) elastic photoemission peak has sufficient kinetic energy to overcome the retarding (-450 V) potential of the partial yield detector and to contribute to the measured signal is marked "C1s". The dashed line through the spectrum is the function used for background subtraction. The lower curve is the enlarged SEXAFS oscillations after background subtraction

stracted out to yield the SEXAFS oscillations shown as the bottom curve of Fig.7.10. A single dominant frequency occurred in this spectrum, as shown by the lone peak in the Fourier transform (FT) of Fig.7.11a. This peak can only be due to backscattering of the photoelectron from copper surface atoms because they are the only atoms with a sufficient number of core electrons to yield an observable EXAFS effect. The Cu - O distance was obtained by applying a phaseshift $\phi_s = 6.17 - (0.46\ \text{Å})k$, derived from a bulk Cu_2O standard, to yield an average Cu - O distance of 2.38 ± 0.04 Å.

The oxygen atoms of the formate group are located approximately in the four-hold hollow site of the Cu{100} surface according to the angular dependence of the amplitude of the SEXAFS. Fourier transformation of the SEXAFS signal at normal X-ray incidence showed the same dominant frequency and the same single peak as at glancing incidence (Fig.7.11c). Averaging the $15^\circ / 90^\circ$ amplitude ratios over the entire k range yielded a value of 1.7 ± 0.1. This experimental value can be compared to that calculated using (7.2) for five possible adsorption geometries (Fig.7.12). In the calculated ratios it was assumed that the nearest neighbor Cu - Cu distances for the surface atoms were unperturbed from the bulk and that there was no azimuthal preference in the orientation for the

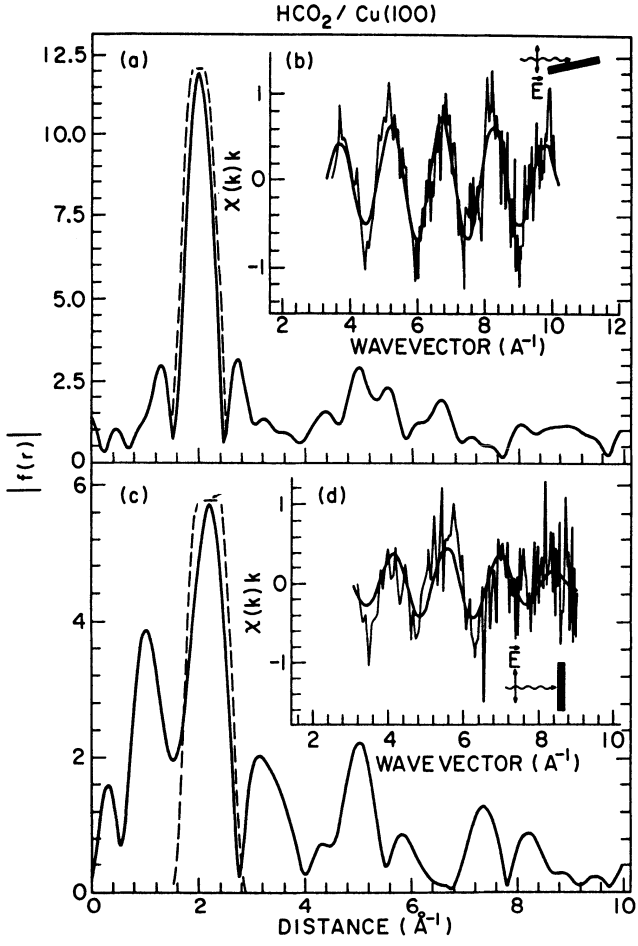

Fig.7.11. (a) Absolute Fourier transform of the SEXAFS signal obtained at grazing (15°) X-ray incidence for formate on Cu{100} [7.10]. The peak near 2.0 Å corresponds to the Cu-O distance before phase shift correction. The dotted line is the window function used for filtering. (b) SEXAFS signal multiplied by electron wave vector k with superimposed sinusoidal function obtained by back-transformation of the peak in the window function in (a). (c) As in (a) except at normal X-ray incidence. The peak near 1 Å is partly due to the C-O formate bond. (d) As in (b) except for spectrum (c)

formate on the surface. In addition, an O - O intramolecular distance of 2.24 Å was used in the calculation, which is typical for a formate group [7.23] and was derived from the NEXAFS studies (Sect.7.3.1). Table 7.1 compares the experimental $15°/90°$ ratio with that of these five possible geometries. Only the 1.86 value derived for the geometry of Fig.7.12a was near the observed 1.7 value. Thus both of the formate oxygens were located near fourfold hollow sites.

Table 7.1. Amplitude ratios for the possible formate adsorption sites on the Cu{100} surface shown in Fig.7.12 using an O - Cu distance of R = 2.38 Å and an unreconstructed surface [7.10]

Geometry	Part of Fig.7.12	$15^{\circ}/90^{\circ}$ amplitude ratio
Observed		1.7 ± 0.1
Hollow	a	1.86
Bridge	b	4.57
On-top	c	422
Chelating	d	6.63
Diagonal bridge	e	20.6

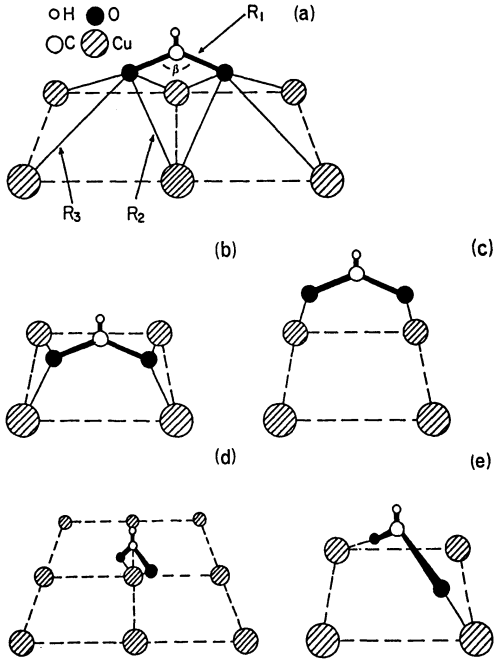

Fig.7.12a-e. Possible chemisorption geometries considered for formate on the Cu{100} surface [7.10]. (**a**) hollow site; (**b**) bridge site; (**c**) on-top site; (**d**) chelating site; (**e**) diagonal bridge site

The formate oxygens were not located precisely in the centers of the fourfold hollow sites, however. The O - O separation typical for a formate group is 2.24 Å while the fourfold hollow sites are separated by 2.56 Å. Only extreme distortion of the formate could allow the oxygens to fit exactly into the fourfold hollow sites, which is not consistent with the similarity of the vibrational spectrum to undistorted formate groups [7.20] nor the NEXAFS ana-

lysis (Sect.7.3.1). On the other hand, the SEXAFS experiment would resolve two Cu-O distances differing by more than 0.15 Å. These two opposing requirements can be met by placing an undistorted formate with the oxygens displaced slightly from the centers of the fourfold hollows. The two resultant Cu-O distances, R_2 and R_3, differ by the allowed 0.15 Å (Fig.7.12a). The actual Cu-O distances were thus in the range 2.31 - 2.45 Å.

The chemisorption geometry of formate on Cu{100} is quite unusual in that the nearest-neighbor (NN) Cu-O distances are at least 0.3 Å larger than typical NN Cu-O distances found in metal complexes or other oxygen-bonded adsorbates on copper surfaces. A typical NN Cu-O distance is approximately 1.8 to 2.0 Å. For example, the Cu-O distances in Cu_2O and CuO are 1.85 and 1.95 Å, respectively. Likewise, the 1.84 Å Cu - O distance for oxygen adatoms on Cu{100} is within this range [7.24]. The minimum 2.31 Å distance for the oxygens of the formate group on Cu{100} is anomalously large.

This long distance is ascribed to a steric interaction for the formate on Cu{100}. In the geometry of Fig.7.12a, the carbon atom is located in a bridge position between two copper atoms. The carbon is not bonded to these atoms, however, according to the vibrational spectrum analysis [7.20] and electronic structure calculations [7.25]. In order to maintain a nonbonding Cu - C distance and maintain a normal configuration for the formate group, a minimum Cu - O distance of 2.30 Å can be estimated from atomic radii [7.10]. This value is quite close to the lower limit for R_2 of 2.31 Å determined by the SEXAFS analysis.

This chemisorption geometry is interesting in that it is apparently a compromise between several opposing forces. On the one hand, the oxygen atoms prefer the high-coordination fourfold hollow site, which is also the site of oxygen adatoms on this surface [7.24]. This site is opposed, however, by the Cu - C steric repulsion and the forces opposing distortion of the formate group itself. Despite these opposing forces, oxygen still chooses to locate near the fourfold hollow rather than relocate to a lower-coordination site. This SEXAFS analysis has thus provided insight into the forces which determine adsorption sites and the complexities which can exist for polyatomic adsorbates which do not exist for simple atomic adsorbates.

7.2.2 Structure of Formate on the Cu{110} Surface

The structure of formate groups on the Cu{110} surface has also been determined by SEXAFS and has significant differences from the structure on the Cu{100} surface [7.26]. The Cu{110} surface is corrugated with rows of close-packed atoms so that the highest symmetry site now available has twofold symmetry.

The formate group has also been well-characterized on this surface [7.18,19, 21] and is formed by the same reactions as on the Cu{100}surface (7.3,4). Likewise, infrared vibrational spectroscopy shows that the formate has C_{2v} symmetry as on the Cu{100} surface [7.21]. The principal difference between the Cu{110} and Cu{100} surfaces is that formate on the Cu{110} surface is azimuthally aligned so that the plane of the formates are parallel to the ridges (<1$\bar{1}$0> direction) of the surface. Otherwise, the frequencies and intensities of the formate vibrational spectra were in general agreement.

From SEXAFS studies of formate on the Cu{110} surface an *average* Cu-O bond length of 1.98 ± 0.07 Å was obtained [7.26]. The raw oxygen K edge X-ray absorption spectra are shown in Fig.7.13 at various angles of X-ray incidence. The SEXAFS oscillations are clearly seen in the two lower spectra of Fig.7.13 as two broad peaks at approximately 575 and 625 eV. Weaker SEXAFS peaks are also apparent in the top spectrum of Fig.7.13a. Using the same methods as previously discussed, a Cu - O distance of 1.98 ± 0.07 Å was obtained.

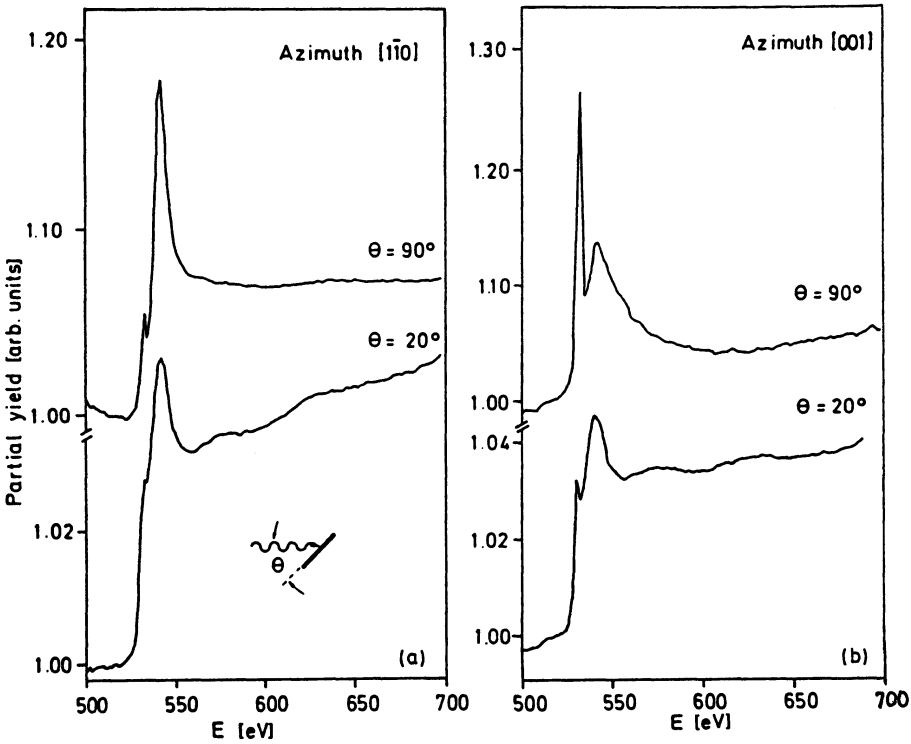

Fig.7.13a,b. Oxygen K edge SEXAFS spectra for formate on Cu{100} [7.26]. The polarization direction of the X-rays for each case was along the <1$\bar{1}$0> direction for those in (a) and along the <001> direction for (b)

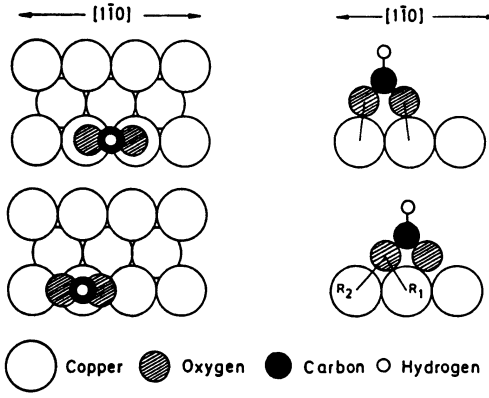

Fig.7.14. The formate geometries considered in the SEXAFS analysis on Cu{110} [7.26]

From the polar and azimuthal angular dependence of the SEXAFS amplitude, the chemisorption site shown in Fig.7.14b was derived for formate on the Cu{110} surface. First it was deduced that the formate resided on top of the atomic "ridges" of this surface rather than in the troughs from the weakness of the SEXAFS signal under normal X-ray incidence (Fig.7.13). Under normal X-ray incidence, **E** is parallel to the surface, and a strong signal would be obtained only for Cu - O bonds with a large horizontal component, such as if the formate oxygens were located in the troughs. Instead the normal incidence SEXAFS was weak or absent, so a site on top of the "ridges" was indicated. Second, two different ridge geometries were considered (Figs.7.14a,b), and they were distinguished by comparing the measured intensities at various incidence angles with that calculated using (7.2). Table 7.2 shows this comparison and that only the model of Fig.7.14b would have a nonvanishing SEXAFS signal at 90° incidence along the <1$\bar{1}$0> direction as observed. Thus the oxygens reside approximately in short twofold bridge sites.

Table 7.2. Amplitude ratios for possible formate adsorption sites on the Cu{1$\bar{1}$0} surface. Values are normalized to unity for $\theta = 20°$, <1$\bar{1}$0> azimuth [7.26]

Azimuth	θ[°]	Theory		Experiment
		Model a	Model b	
<1$\bar{1}$0>	20	1.0	1.0	1.0
<1$\bar{1}$0>	90	0	0.7	0.6 ± 0.2
<001>	20	1.0	1.0	1.0 ± 0.2
<001>	90	0	0	0

The oxygens cannot occupy the centers of the short twofold bridge sites exactly, but are positioned asymmetrically. The distance between the twofold bridge sites is 2.56 Å which is the same separation as for the fourfold hollow sites on the Cu{100} surface (Sect.7.2.1). Since the vibrational spectra [7.21] and NEXAFS (Sect.7.3.1) did not indicate extreme distortion of the formate group, the oxygens cannot occupy the centers of the twofold bridge sites. Instead, the actual Cu - O distances, R_1 and R_2 of Fig.7.14b differ by less than 0.10 Å from the average 1.98 Å distance. As before, SEXAFS could not resolve two distances this close together.

The chemisorption geometry of formate on Cu{110} differs significantly from the formate geometry on Cu{100} in the length of the Cu - O bond and the binding site. On Cu{110} the 1.98 ± 0.07 Å Cu - O distance is typical of NN Cu - O distances found in metal complexes and for atomic oxygen on copper. The absence of a long Cu - O distance for formate on this surface is simply attributable to the absence of a Cu - C steric interaction. That is, for the geometry of Fig.7.14b, there is no crowding of the carbon atom. The difference in binding sites is slightly harder to rationalize since the local geometry of formate on the Cu{110} surface is also available on the Cu{100} surface. There are two possible explanations for this difference. 1) The site for formate near the fourfold hollow on Cu{100} may be energetically favored over the twofold bridge site which formate occupies on the Cu{110} surface. Thus on the Cu{100} surface where both sites exist, the energetically favored site is chosen. On the Cu{110} surface, however, only the energetically inferior site is available so it is occupied. This explanation is plausible in that it ascribes a higher energy to higher coordination site. 2) The site chosen for formate may depend upon electronic details of the surface which are not reflected in the local geometric structure. This is, while the same *local* geometry of surface atoms as shown in the right-hand side of Fig.7.14b exists on both surfaces, the *long-range* geometry is different and thus the electronic states of the surface may also be different on the two surfaces. Further electronic structure calculations will be required to fully understand the differences in chemisorption geometries which have been revealed by SEXAFS.

7.2.3 Structure of Methoxy on the Cu{100} Surface

Methoxy (CH_3O) is a stable intermediate in the copper-catalyzed oxidation of methanol (CH_3OH) [7.27-32]. Methoxy formation is assisted by oxygen adatoms in a reaction analogous to (7.3)

$$2CD_3OH_{(g)} + O_{(a)} \rightarrow 2CD_3O_{(a)} + H_2O_{(g)} \quad . \tag{7.5}$$

The methoxy is stable to approximately 300 K whereupon it undergoes the decomposition reaction

$$CD_3O_{(a)} \rightarrow D_2CO_{(g)} + 1/2\ D_{2(g)} \quad . \tag{7.6}$$

Studies of methoxy by various surface spectroscopic techniques indicate that the methoxy is tilted on the surface but otherwise similar to the group in the parent methanol. The EELS vibrational spectrum compares well with the infrared spectrum of methanol except for the expected absence of the O - H stretch [7.30]. This indicates that methoxy is attached to the surface via the oxygen. Infrared spectroscopy studies indicate that the C - O bond of the methoxy is tilted by approximately 30° from the surface normal [7.31,33]. This was deduced from the nondegeneracy of the two asymmetric C - H stretching modes. The tilted orientation is also supported by NEXAFS studies (Sect.7.3.1), although ARUPS [7.34] and EELS [7.30] have indicated a normal orientation for the C - O bond.

An examination by vibrational spectroscopy of the phonon modes induced by methoxy formation also rules out an a-top adsorption site for the methoxy [7.32]. If the methoxy were chemisorbed with the oxygen in the a-top site then a certain phonon mode becomes dipole allowed and would be observed, as occurs for CO on the Cu{100} surface. Such a mode was not observed for methoxy so the a-top site is ruled out. Otherwise, no structural details of methoxy on Cu{100} were known.

From a SEXAFS study, a Cu - O chemisorption bond length of 1.97 ± 0.05 Å was determined [7.10]. The FT of the oxygen K edge SEXAFS region is shown in Fig.7.15, and a single NN Cu - O peak was obtained. Applying the phase shift from bulk Cu_2O yields the 1.97 Cu - O bond length. This distance is within the 1.8 to 2.0 Å range for normal NN Cu - O bonds (Sect.7.2.1). Thus no steric interactions occur for methoxy on Cu{100} as seen for formate on this surface.

The chemisorption site of methoxy was not completely determined from SEXAFS, but the a-top site was ruled out [7.10]. No Cu - O SEXAFS oscillations were observed at an X-ray incidence angle of 15° (**E** near the surface normal) which implies that the Cu - O bond cannot be near the surface normal. Thus the a-top site was ruled out. However, Cu - O SEXAFS oscillations were observed at X-ray incidence angles of 90° and 45° with an amplitude ratio of 0.92 ± 0.2. If the oxygen of the methoxy group were located in the fourfold hollow site or the twofold bridge site, then 90° / 45° amplitude ratios of 1.46 and 0.53, respectively, are expected from (7.2). The measured value fell between these so does not clearly indicate either site. There are several possible explanations for this intermediate value. 1) The signal-to-noise ratio for the methoxy

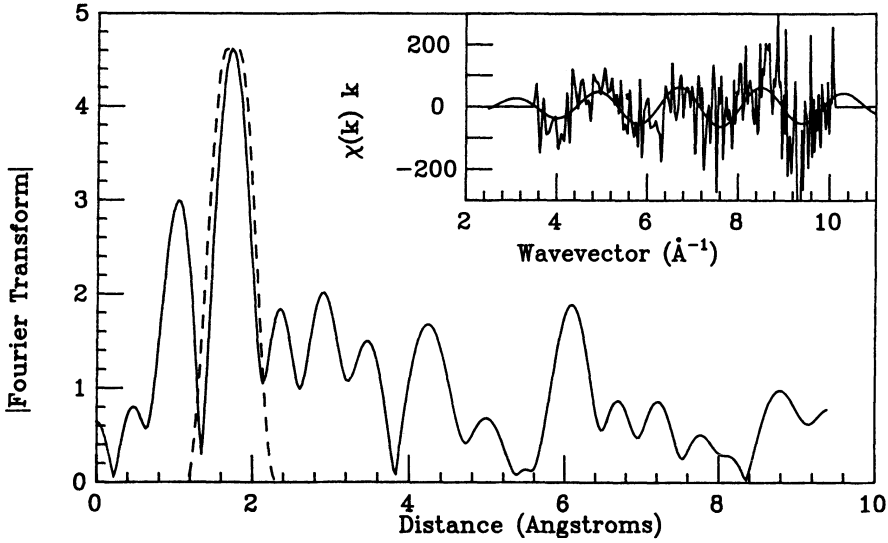

Fig.7.15. (a) Absolute Fourier transform of the oxygen K edge SEXAFS signal for methoxy on Cu{100} at 200 K [7.26]. The peak near 1.7 Å corresponds to the Cu-O distance before phase shift correction. The dotted line is the window function used for filtering. (b) Background-substracted SEXAFS signal multiplied by electron wave vector k, with a superimposed sinusoidal function obtained using the window function of (a)

SEXAFS was worse than for the formate studies due to lower attainable coverages. Thus simply better measurements may be required to clearly discriminate between these two sites. 2) The methoxy may reside in an asymmetric site or occupy both sites. Both of these possibilities would give an intermediate amplitude ratio. These possibilities are plausible since oxygen adatoms also form poorly ordered overlayers at higher coverages. Further study will be required to definitively establish the site of the methoxy group on Cu{100}.

7.3 NEXAFS Studies of Polyatomic Adsorbates

7.3.1 Oxidation Intermediates on Cu{100} and Cu{110}

The series of adsorbates CO, formate (HCO_2), and methoxy (CH_3O) provide a good basis for understanding how changes in the intramoleular bonding of a polyatomic adsorbate are reflected in their NEXAFS spectra. The reason is that all of these molecules contain a C - O abond, yet the bond order varies from 1 to 3. Furthermore, these adsorbates have been well characterized by a variety of other surface spectroscopic techniques.

The NEXAFS spectra of CO on a Cu{100} surface resemble those of CO on Ni{100} and indicate that the C - O axis is normal to the surface [7.22]. Figure 7.16 shows the CO NEXAFS region at X-ray incidence angles of 15° and

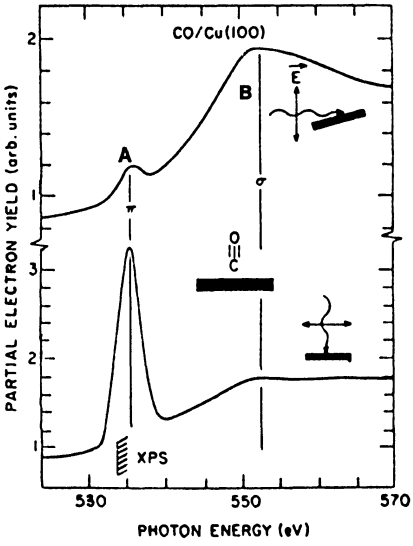

Fig.7.16. Oxygen K edge NEXAFS spectra for CO on Cu{100} [7.22]. The two features were assigned to a π^* resonance (peak A) and a σ^* resonance (peak B)

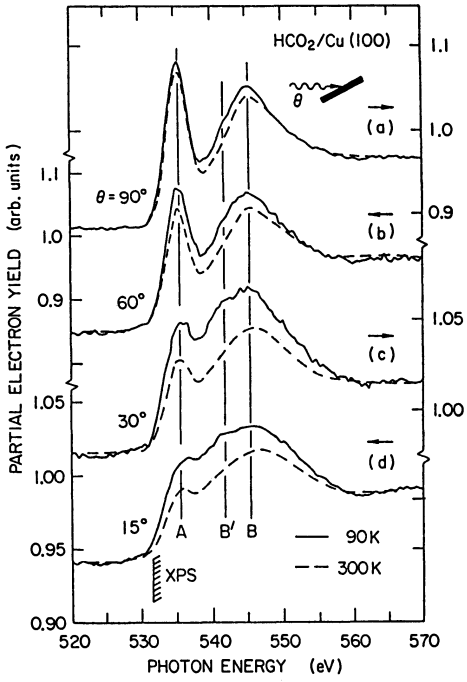

Fig.7.17. Oxygen K edge NEXAFS spectra for formate chemisorbed on Cu{100} at 90 and 300 K as a function of X-ray incidence angle [7.10]. Peak A is the π^* resonance, peak B is the σ^* resonance, and peak B' is ascribed to a σ^* resonance associated with a single bond in an asymmetric formate

90°. Two primary features were observed which were assigned to π^* and σ^* transitions by analogy to CO and Ni{100} (Fig.7.7). Quantitatively analyzing the areas of these peaks as a function of X-ray incidence angle and applying a $\cos^2\alpha$ electric-dipole relation indicates that the C - O bond is within $\pm 10^\circ$ of the surface normal. This conclusion is in agreement with vibrational [7.32] and photoemission studies [7.35].

The formate NEXAFS spectra also have the π^* and σ^* transitions from which a normal orientation for the plane of the formate can be deduced [7.22]. The NEXAFS spectra of formate on Cu{100} are shown in Fig.7.17 as a function of X-ray incidence angle. Two principle transitions were observed which were assigned to the π^* (labeled A) and σ^* (labeled B) resonances. The π^* transitions was maximized at normal X-ray incidence and nearly vanished at glancing incidence. This implies that the lobes of the p orbitals contributing to the π bond are parallel to the surface since the π^* feature was most intense when

E was also parallel to the surface (i.e., normal X-ray incidence). This conclusion is consistent with the results of vibrational studies [7.20].

In principle the angle of the C - O bond with respect to the surface could be derived from the angular dependence of the π^* peak but there are several complications [7.10]. First, the σ^* peak does not completely vanish at any X-ray incidence angle because there is always a nonzero projection onto one of the inclined C - O bonds. Second, the background for the σ^* peak is more difficult to establish because the peak is broader than the π^* resonance. Finally, there is evidence for a minority species, possibly a monodentate formate, which interferes with the measurements of the σ^* peak area. The small σ^* shoulder labeled B' has been tentatively ascribed to this minority species, and it cannot be reliably deconvoluted from the main σ^* peak labeled B. This minority peak is most apparent at low temperatures and 90°, which agrees with the conclusions of an EELS study of formate on Cu{100} [7.20].

From the methoxy NEXAFS spectra, the single-bond character of the methoxy C - O bond and a tilting of the C - O bond from the surface normal are apparent [7.10]. Figure 7.18 shows the methoxy NEXAFS spectra as a function of X-ray incidence angle. No sharp π^* resonance was observed. Instead only a broad σ^* resonance (labeled B) was observed. This is expected by analogy to the single-bond character of the C - O bond of methanol. The σ^* peak area under normal X-ray incidence was larger than expected from the residual cross-polarization component of the synchrotron X-rays. Although establishing a baseline for σ^* peaks is somewhat difficult, the approximate tilt of the C - O bond from the

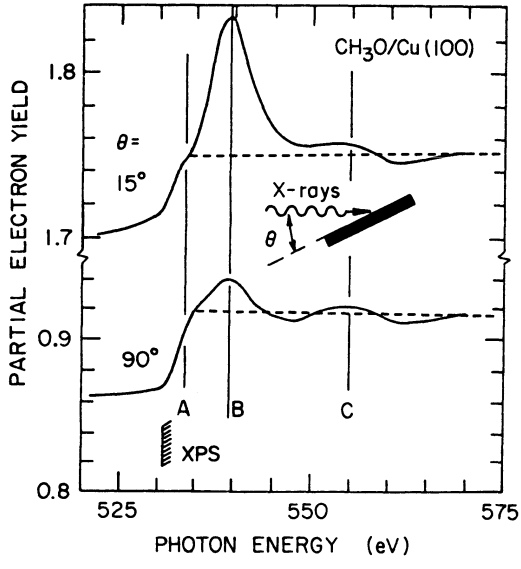

Fig.7.18. Oxygen K edge NEXAFS spectra for methoxy on Cu{100} at 200 K at X-ray incidence angles of 15° and 90° [7.10]. Peak A is an atomiclike step, peak B is the σ^* resonance, and peak C is the first SEXAFS oscillation due to copper backscattering

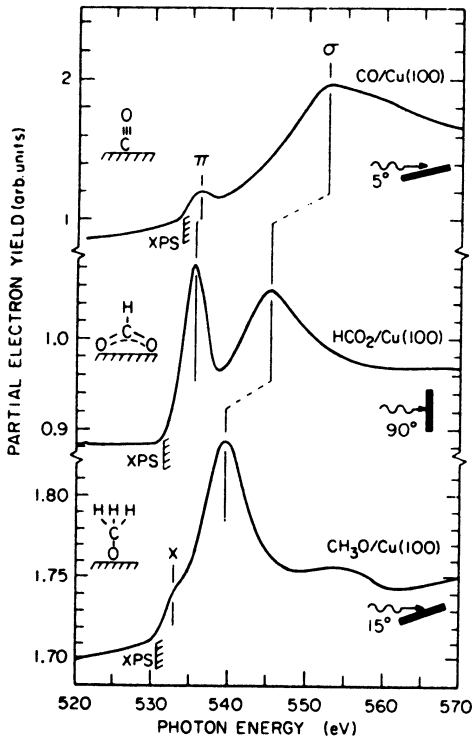

Fig.7.19. Variation in the position of the σ* resonance for the NEXAFS spectra of CO, formate, and methoxy [7.22]. A higher energy position for the σ* resonance is observed for a short C-O bond

surface normal was estimated from the relative areas of the σ* peaks to be 32°. Allowing a generous error in the measured ratio of the σ* peak areas of a factor of two results in an error of only ± 10° in the tilt of the C - O bond. This tilt is in general agreement with an infrared vibrational study of methoxy on Cu{100} [7.31,33].

Because of the wide variation in the C - O bond order among these three molecules, they can form the basis for establishing a correlation between the C - O bond length and the position of the σ* resonance [7.10,22]. Figure 7.19 shows this variation in the position of the σ* peak as a function of C - O bond order for these three molecules. One problem in establishing such a correlation, however, is the absence of independently known C - O bond lengths for adsorbates. In this case the bond lengths of the C - O bonds in carbon monoxide and methoxy on Cu{100} were assumed to be the same as in gaseous carbon monoxide and methanol, respectively. This is supported by the small frequency shifts for the C - O stretches compared to the gas-phase molecules [7.36]. Furthermore, the variation in the C - O bond length for methoxy ligands in complexes is less than 0.02 Å [7.37,38]. These two points established a correlation between C - O bond length and the position of the σ* resonance (Fig.7.20). Note that

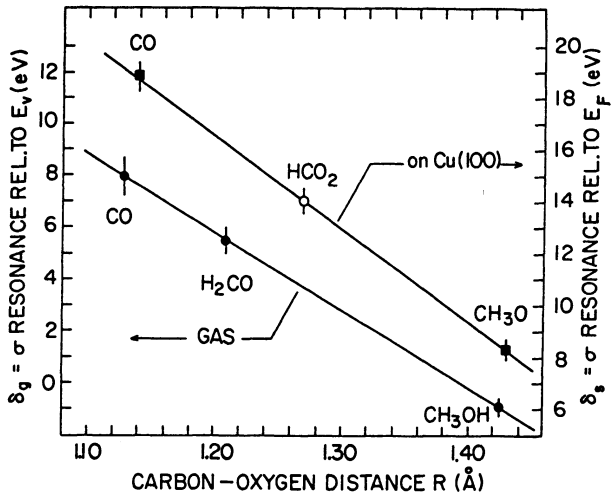

Fig.7.20. Correlation between position of σ* resonance and length of the C-O bond [7.10]. Lower line is for gaseous molecules with σ* peak position measured relative to the vacuum level (1s ionization potential) [7.7]. Upper line is for molecules and reactive intermediates chemisorbed on Cu{100} with the σ* resonance measured relative to the Fermi level

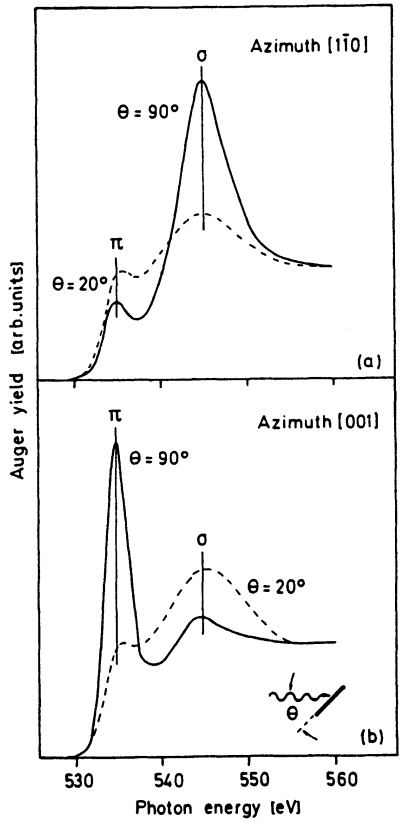

Fig.7.21. Oxygen K edge NEXAFS spectra for formate on Cu{110} [7.26]. The polarization direction of the incident X-rays are along the <1$\bar{1}$0> direction for (**a**) and along the <001> direction for (**b**)

the line for the adsorbates is nearly parallel to the gas-phase correlation but is offset due to differences in references points for measuring the peaks and in relaxation energies. Using this relation, the length of the formate C - O bonds were estimated to be 1.27 ± 0.04 Å. Such a value is quite reasonable by comparison to formate salts where C - O bond lengths of 1.21 to 1.30 Å are reported [7.23].

The formate species on Cu{110} has also been studied by NEXAFS to yield a similar orientation as on Cu{100} and a C - O bond length of 1.25 ± 0.05 Å [7.26]. The formate NEXAFS spectra on Cu{110} are shown in Fig.7.21 as a function of X-ray incidence angle. As on Cu{100}, the π^* feature was maximized at 90° (**E** parallel to the surface) and nearly vanished at glancing incidence (**E** nearly normal to the surface, Fig.7.21b). Thus the plane of the formate is normal to the surface. Furthermore, the π^* peak was only observed with **E** along the <001> azimuth, whereas it was nearly absent along the <1$\bar{1}$0> azimuth. This indicates that the plane of the formate is parallel to the <1$\bar{1}$0> direction. Both of these conclusions are in agreement with SEXAFS (Sect.7.2.2) and infrared spectroscopy studies of this system [7.34]. Using the linear correlation established in Fig.7.19 the formate C - O bonds were estimated to be 1.25 ± 0.05 Å and the O - C - O angle to be $130 \pm 10°$.

7.3.2 Hydrocarbons on Pt{111}

The chemisorption of hydrocarbons on platinum surfaces is of considerable interest with respect to understanding catalytic reforming reactions used in the petroleum refining industry. Molecules such as acetylene (C_2H_2), ethylene (C_2H_4), and benzene (C_6H_6) have been of particular interest as prototype molecules for understanding hydrocarbon adsorption on platinum. These systems have been studied by a variety of other techniques [7.39].

A simple method for determining the orientation of hydrocarbons on platinum and of estimating the length of the C - C bonds is provided by NEXAFS. These are difficult to study by other techniques since hydrocarbon adsorbates often lack the longrange order required for diffraction techniques, and most other structural tools are insensitive to low-atomic-number atoms. For example, NEXAFS has been particularly useful in the study of hydrocarbons on platinum in simply determining their orientation on the surface. While such information has usually been obtained from EELS or ARUPS, these methods do not always yield unambiguous results. For example, many of the most useful vibrational modes of an aromatic molecule are unobservable if the ring of the molecule lies parallel to the surface, making an assignment of orientation or even identify difficult. This problem is compounded by the strong perturbation many hydrocarbons

experience on platinum which causes considerable changes in their vibrational modes and molecular orbitals. Here NEXAFS aids in the understanding of these molecules by providing a simple test for the orientation of σ and π bonds.

In addition, NEXAFS provides an estimate for C - C bond lengths [7.40,41]. One contrast to the NEXAFS studies on copper is that hydrocarbons chemisorbed on platinum are usually strongly perturbed from their gas-phase counterparts. It has therefore been difficult to find reference adsorbates of known C - C bond length with which to establish a bond length versus σ^* position correlation. A different approach has therefore been taken. In this case a simple offset of 7.0 eV was proposed from the gas-phase correlation [7.40]. This offset was determined from a consideration of differences in relaxation and photoemission binding energies between the gas and adsorbed states. Partial justification for this approach is provided in Fig.7.20 where the surface C - O bond correlation on copper is observed to be nearly parallel to the gas phase correlation. The correlation proposed for C - C bonds on platinum is shown in Fig.7.22.

The simple hydrocarbons acetylene and ethylene are strongly perturbed when chemisorbed on platinum [7.40,41]. Their NEXAFS spectra are shown in Fig.7.23. Both molecules exhibited π^* resonances (labeled A or A_X) and σ^* resonances (labeled B). The C - C bond of ethylene is clearly parallel to the surface since the π^* resonance was maximized under glancing X-ray incidence where

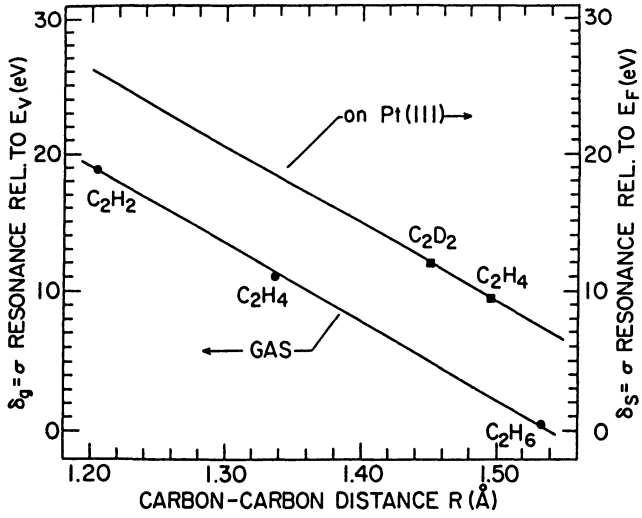

Fig.7.22. The lower curve plots the position of the σ shape resonance relative to the vacuum level versus C-C bond length for gas-phase molecules [7.40]. The lower curve plots the position of the σ shape resonance relative to the Fermi level for chemisorbed hydrocarbons on Pt{111}

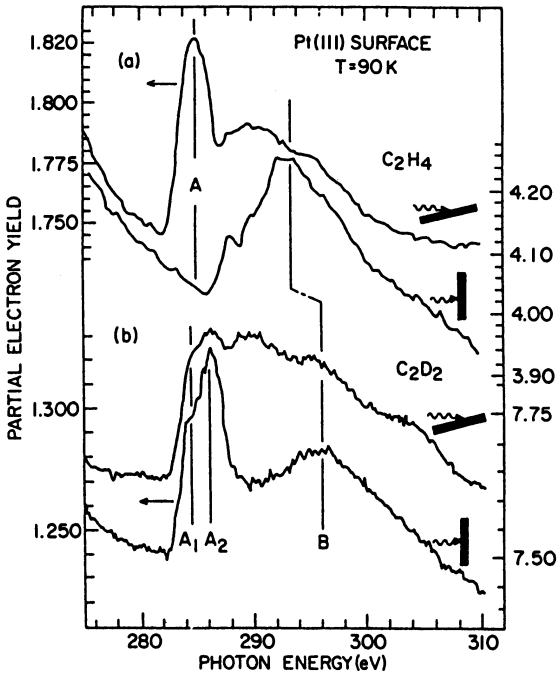

Fig.7.23. Carbon K edge NEXAFS spectra for (*a*) ethylene and (*b*) acetylene on Pt{111} at 90 K for a monolayer coverage [7.40]. Peaks A and A_X are due to π resonances and peak B is due to a σ resonance

both the lobes of the π orbital and **E** were normal to the surface. This orientation is also indicated by the σ^* resonance which was maximized under normal X-ray incidence (i.e., **E** and C - C bond parallel to the surface). The acetylene also lies down on the surface since the angular dependence of the σ^* peak was the same as ethylene. The π^* resonance of acetylene exhibited a different angular behavior because one π^* orbital (A_2) is now parallel to the surface, so maximized with normal X-ray incidence (i.e., **E** parallel to the surface). The other π^* orbital (A_1) is severely rehybridized through interaction with metal orbitals.

The C - C bonds of both molecules are lengthened with respect to the gas phase [7.40,41]. Using the σ^* correlation of Fig.7.22, the C - C bond of chemisorbed ethylene was estimated to be 1.50 ± 0.03 Å which is 0.16 Å longer than gaseous ethylene. The C - C bond of acetylene was estimated to be 1.45 ± 0.03 Å compared to 1.20 Å for gaseous acetylene. Thus both molecules are lengthened to almost the single-bond distance of ethane (C_2H_6 with C - C = 1.53 Å). The presence of the π^* features in the NEXAFS is puzzling, however, in that it suggests that there is residual multiple-bond character in both C - C bonds.

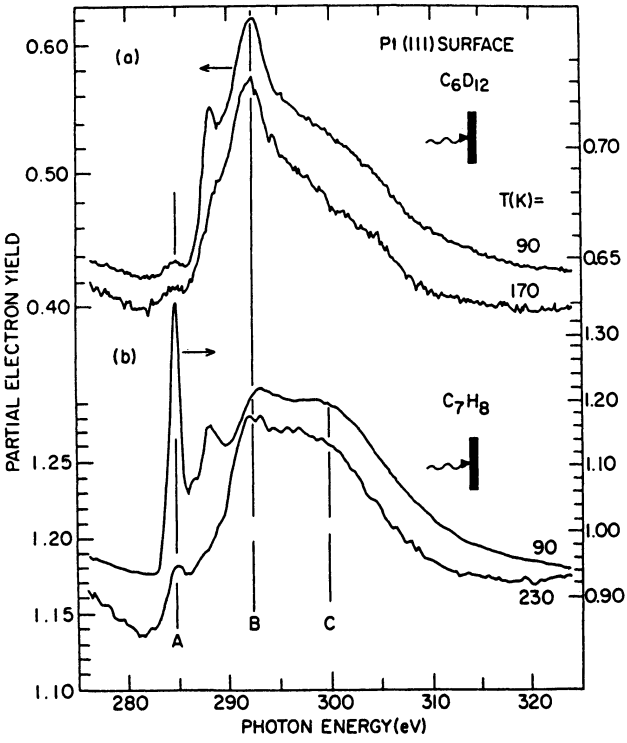

Fig.7.24. Carbon K edge NEXAFS spectra for (*a*) cyclohexane and (*b*) cycloheptatriene on Pt{111} [7.40]. Peak A is assigned to a π resonance, peak B and C to σ resonances

This conclusion differs from that of a vibrational study of ethylene where a di-σ bonding configuration was indicated. Electronic structure calculations reconcile these two views by indicating that the empty π^* orbital belongs largely to the metal and not the C - C bond. Thus care has to be taken in the interpretation of the π^* feature of NEXAFS when the π orbital is involved in bonding to the substrate. Both NEXAFS and vibrational studies agree than substantial stretching of the C - C bond of ethylene occurs upon chemisorption.

Not all hydrocarbons undergo such strong perturbations upon adsorption on platinum. For example, cyclohexane (C_6D_{12}) and cycloheptatriene (C_7H_8) have C - C bond lengths similar to the gas phase [7.40]. Figure 7.24 shows the normal X-ray incidence NEXAFS for multilayers (90 K) and monolayers (170 and 230 K) of these molecules. The spectra of the saturated hydrocarbon, C_6D_{12}, showed only a σ^* resonance (labeled B). This peak nearly vanished under grazing incidence of the monolayer spectrum (not shown) which implies that the C - C bonds were principally parallel to the surface, to the excellent allowed for this

nonplanar molecule. The C_6D_{12} ring itself is thus flat on the surface. The spectrum of C_7H_8 showed both a π^* resonance (labeled A) and two σ^* resonances (labeled B and C) The angular dependence of the NEXAFS spectra of this molecule also indicated that the ring was parallel to the surface. In this case, there were two σ^* peaks due to the single (peak B) and double (peak C) C - C bonds. The lengths of these were estimated to be 1.50 ± 0.03 and 1.37 ± 0.04 Å which are similar to the gas-phase values of 1.356, 1.446, and 1.505 Å. The σ^* peak for the intermediate length C - C bond was not resolved in the surface spectra. In the case of C_6D_{12}, a surface C - C bond length of 1.51 ± 0.03 Å was estimated versus 1.535 Å in the gas phase.

The technique of NEXAFS has also been applied to determining the orientation of other hydrocarbons on Pt{111} including ethylidyne (C_2H_3) [7.41], benzene (C_6H_6) [7.42,43], toluene (C_7H_8) [7.42,43], and pyridine (C_5H_5N) [7.42,43].

7.3.3 Sulfur-Containing Hydrocarbons on Pt{111}

The adsorption of sulfur-containing hydrocarbons on platinum has been studied on single-crystal surfaces as a model system for the industrially important hydrodesulfurization reaction for removing sulfur from fossil fuels. A combination of TPRS, EELS, and NEXAFS techniques have been applied to the understanding of these systems [7.43,44].

The orientation of molecular thiophene (C_4H_4S) varies as a function of coverage [7.43]. The NEXAFS carbon K edge spectra are shown in Fig.7.25 at two temperatures, 150 and 180 K. Four features are apparent in these spectra, which were assigned to a π^* resonance (peak A), and σ^* resonances corresponding to the C - S (peak B), C - C (peak C), and C = C (peak D) bonds. These assignments were deduced from considerations of intensity and energies of the orbitals involved. The angular dependence of the low-temperature spectra indicates that the ring of the thiophene was tilted from the surface normal. Upon annealing to 180 K, however, the π^* feature (peak A) nearly vanished under normal X-ray incidence indicating that the ring was now flat. This change in orientation was accompanied by a reduction in coverage.

Dissociation of the thiophene occurs near 290 K to produce atomic sulfur and a metallocycle where platinum is possibly inserted into the ring of the hydrocarbon residue. The removal of the sulfur atom from the thiophene ring was deduced from Fig.7.26a which shows the sulfur $L_{2,3}$ edge. These spectra showed two principal features due to overlapped π^* and σ^* resonances associated with sulfur in the intact thiophene molecule (peak X) and a peak associated with atomic sulfur (peak Y). As the temperature was raised the thiophene

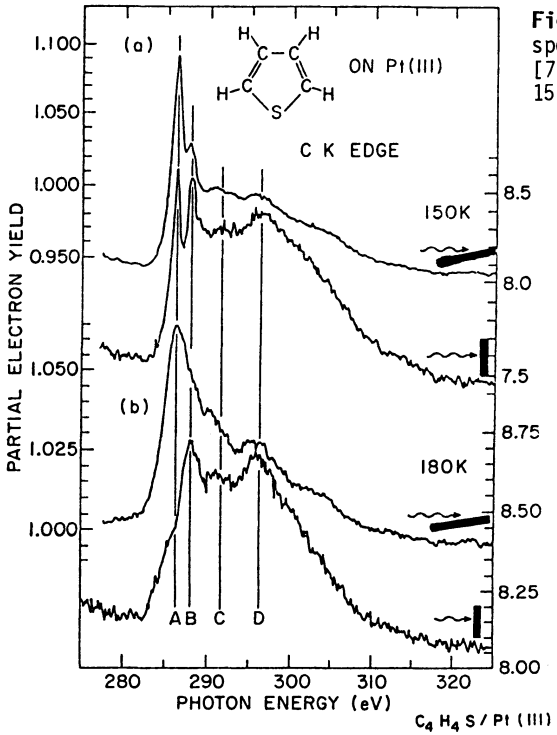

Fig.7.25. Carbon K edge NEXAFS spectra for thiophene on Pt{111} [7.43]. The temperatures are (*a*) 150 K and (*b*) 180 K

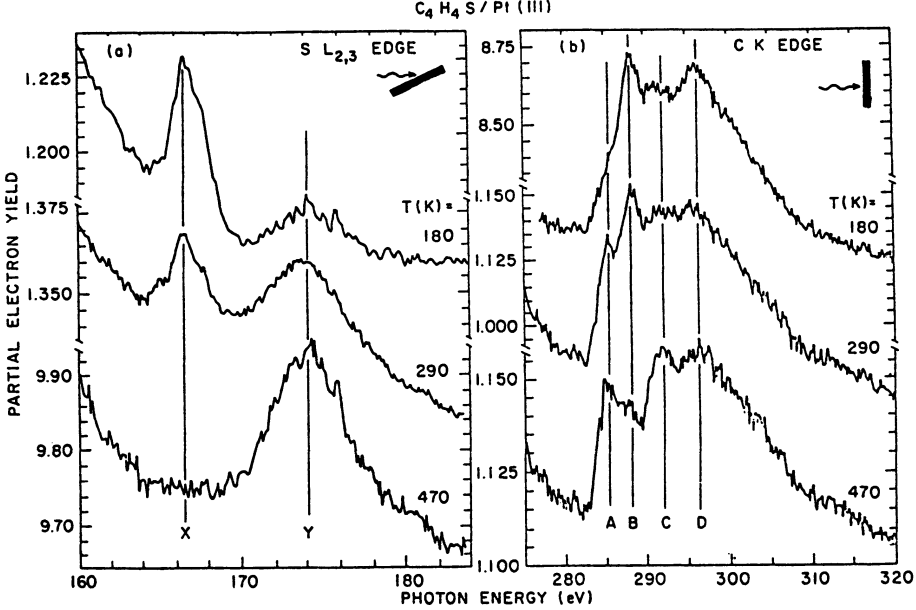

Fig.7.26a,b. NEXAFS spectra for thiophene on Pt{111} as a function of annealing temperature [7.43]. The spectra in (**a**) correspond to the S $L_{2,3}$ edge showing the transition from sulfur in thiophene to atomic sulfur. The spectra in (**b**) show the C K edge showing the transition from thiophene to a ring-like carbon structure without sulfur

dissociated to form molecular sulfur beginning near 290 K and completing by 490 K. Investigations by XPS and EELS supported this mechanism. The carbon residue was also examined by NEXAFS (Fig.7.26b) and numerous peaks were observed despite the dissociation of the thiophene. This indicated that many of the carbon-carbon bonds remained intact. The breaking of the C - S bond was apparent in the carbon edge by the attenuation of the σ^* resonance (peak B). The $\sigma_{C=C}$ resonance (peak D) was also attenuated due to a change in the orientation of the ring. At the same time a new π^* features appeared (peak A) upon heating. This was interpretted as due to formation of a metallocycle ring with the plane slightly inclined from the surface normal. Vibrational spectroscopy also supported the presence of a ringlike structure [7.43].

The adsorption of methanethiol (CH_3SH) has also been studied on Pt{111} [7.44], and several similarities observed between the decomposition of this molecule and the behavior of its oxygen analogue, methanol.

Methanethiol first dissociates to form a thiomethoxy species in a reaction which is similar to the dissociation of methanol to form a methoxy

$$CH_3SD_{(g)} \rightarrow CH_3S_{(a)} + D_{(a)} \quad . \tag{7.7}$$

The NEXAFS carbon K edge spectra of the CH_3S intermediate is shown in Fig. 7.27a. A single σ^* resonance was observed (labeled B). From the angular dependence of this peak a tilt of $45 \pm 10^{\circ}$ from the surface normal was estimated. Upon annealing to 380 K further dehydrogenation occurred to form a stable CH_2S intermediate

$$CH_3S_{(a)} \rightarrow CH_2S_{(a)} + H_{(a)} \quad . \tag{7.8}$$

At the same time, a new peak appeared in the NEXAFS spectra (labeled A) which was ascribed to the π^* resonance of the newly formed C = S bond. The angular dependence of this peak indicates a slight tilt of 20° from the horizontal of the C - S bond. The identity and orientation of these intermediates was also examined with TPRS and EELS which supported these assignments [7.44].

The behavior of methanethiol resembles the decomposition of methanol on copper (7.5,6) in that the sulfur analogues of methoxy and formaldehyde were formed. One difference between these systems was that the thioformaldehyde was stable on platinum, whereas the formaldehyde immediately desorbed from copper as it was formed.

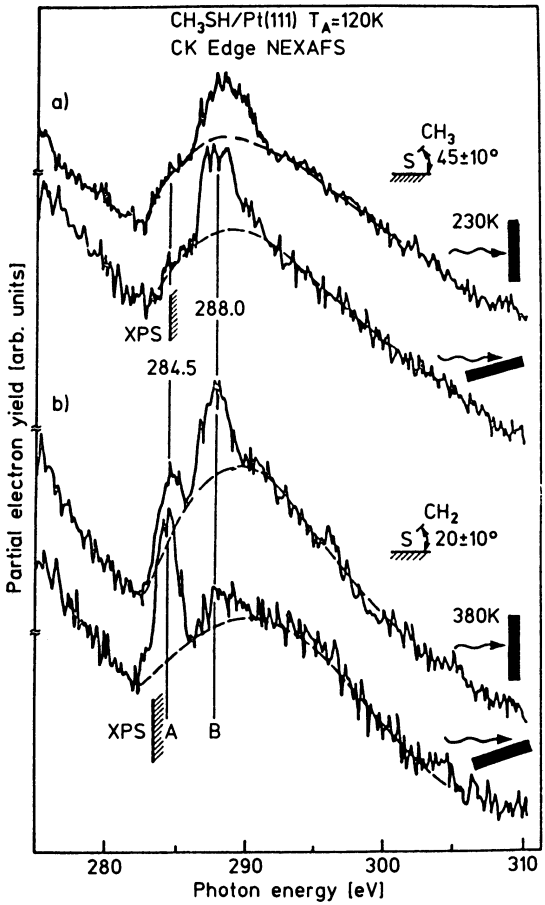

Fig.7.27. Carbon K edge NEXAFS spectra for methanethiol adsorbed on Pt{111} [7.44]. The spectra in (*a*) are of the thiomethoxy intermediate showing only a σ^* resonance (peak A). The spectra in (*b*) are of the thioformaldehyde intermediate with π^* (peak A) and σ^* (peak B) resonances

7.4 Conclusions and Outlook

The technique of X-ray absorption spectroscopy has provided insight into the structure and forces acting upon molecular adsorbates and surface reaction intermediates. In the case of SEXAFS, the ability to determine chemisorption bond lengths and binding sites has revealed that the choice of binding sites for polyatomic adsorbates can depend greatly upon the surface crystallography. Continued examination of systems such as formate on copper will enable a more complete understanding of the electronic, steric and geometric factors which determine chemisorption geometries. In the case of NEXAFS, this is a simple

technique for determining the orientation, order, and length of bonds between low-atomic-number atoms within an adsorbate. Thus, NEXAFS provides a simple independent test of the conclusions regarding orientation and bond order which are usually derived from vibrational studies. In its capacity to quantify the orientation of an adsorbate and the length of bonds between low-atomic-number atoms, NEXAFS exceeds vibrational studies.

Several improvements in these techniques are anticipated which will enhance their usefulness. In the case of SEXAFS, a current limitation is the low intensity of the signal which restricts the studies to fairly high-coverage species, approximately half of a monolayer. As the photon yields of synchrotron radiation sources are increased by the addition of wigglers and undulators, extension to lower coverage regimes is expected. Furthermore, an even more complete geometric description will then be available from measurements of second- and third-nearest-neighbor distances. In the case of NEXAFS, an improved theoretical foundation will provide a clearer understanding of the NEXAFS phenomena. For example, usually the NEXAFS features are not influenced greatly by the substrate bonding. In the case of ethylene on Pt{111} [7.41], however, a π^* resonance was observed whose presence seems to contradict the C - C single-bond length and vibrational frequency. For this system, the substrate bonding appears to be the source of this π^* peak. Further understanding is needed in order to know in which cases such features will be observed. A better theoretical understanding may also lead to better accuracy in bond length determination. Finally, both techniques will be advanced by the anticipated addition of new synchrotron facilities which will alleviate somewhat the current limited availability of this resource.

Acknowledgements. We would like to thank J. Stöhr for fruitful collaborations. We gratefully acknowledge the support of the National Science Foundation (CHE 8319165) for this work. Parts of the work reported here were done at the Stanford Synchrotron Radiation Laboratory which is supported by the Office of Basic Energy Sciences of DOE and the Division of Materials Research of NSF.

References

7.1 H. Ibach, D.L. Mills: *Electron Energy Loss Spectroscopy and Surface Vibrations* (Academic, New York 1982)
7.2 M.A. van Hove, S.Y. Tong: *Surface Crystallography by LEED*, Springer Ser. Chem. Phys., Vol.2 (Springer, Berlin, Heidelberg 1979)
7.3 D.A. Shirley: in *Chemistry and Physics of Solid Surfaces*, Vol.3, ed. by R. Vanselow, W. England (CRC Press, Boca Raton, FL 1982) p.43; S.Y. Tong, C.H. Li: ibid. p.287

7.4 J. Stöhr: in *X-Ray Absorption: Principles, Applications, and Techniques of EXAFS, SEXAFS and XANES*, ed. by D. Koningsberger, R. Prins (Wiley, New York, 1985)
7.5 P. Eisenberger, P. Citrin, R. Hewitt, B. Kincaid: in *Chemistry and Physics of Solid Surfaces*, Vol.3, ed. by R. Vanselow, W. England (CRC Press, Boca Raton, FL 1982) p.269
7.6 J. Stöhr, R. Jaeger: Phys. Rev. B**26**, 4111 (1982)
7.7 F. Sette, J. Stöhr, A.P. Hitchcock: Chem. Phys. Lett. **110**, 519 (1984); J. Chem. Phys. **81**, 4906 (1984)
7.8 For a review of EXAFS see
P.A. Lee, P.H. Citrin, P. Eisenberger, B.M. Kincaid: Rev. Mod. Phys. **53**, 769 (1981); B.K. Teo, D.C. Joy (eds.): *EXAFS Spectroscopy, Techniques and Applications* (Plenum, New York 1981)
7.9 B.K. Teo, P.A. Lee, A.L. Simons, P. Eisenberger, B.M. Kincaid: J. Am. Chem. Soc. **101**, 2815 (1979)
7.10 D.A. Outka, R.J. Madix, J. Stöhr: Surf. Sci. **164**, 235 (1985)
7.11 A.P. Hitchcock: J. Electron Spectrosc. Relat. Phenom. **25**, 245 (1982)
7.12 G.R. Wight, C.E. Brion, M.J. Van Der Wiel: J. Electron Spectrosc. Relat. Phenom. **1**, 457 (1973)
7.13 J.L. Dehmer, D. Dill: J. Chem. Phys. **65**, 5327 (1976)
7.14 A. Bianconi, M. Dell'Ariccia, P.J. Durham, J.B. Pendry: Phys. Rev. B **26**, 6502 (1982)
7.15 A.E. Orel, T.N. Rescigno, B.V. McKoy, P.W. Langjoff: J. Chem. Phys. **72**, 1265 (1980)
7.16 T. Gustafsson, J.J. Levinson: Chem. Phys. Lett. **78**, 28 (1981)
7.17 C.R. Natoli: in *EXAFS and Near Edge Structure*, ed. by A. Bianconi, L. Inoccia, S. Stipcich, Springer Ser. Chem. Phys., Vol.27 (Springer, Berlin, Heidelberg 1983) p.43
7.18 D.H.S. Ying, R.J. Madix: J. Catal. **61**, 48 (1980)
7.19 M. Bowker, R.J. Madix: Surf. Sci. **102**, 542 (1981)
7.20 B.A. Sexton: Surf. Sci. **88**, 319 (1979)
7.21 B.E. Hayden, K. Prince, D.P. Woodruff, A.M. Bradshaw: Surf. Sci. **133**, 589 (1983)
7.22 J. Stöhr, J.L. Gland, W.E. Eberhardt, D. Outka, R.J. Madix, F. Sette, R.J. Koestner, U. Döbler: Phys. Rev. Lett. **51**, 2414 (1983)
7.23 R.W.G. Wyckoff: *Crystal Structures*, Vol.5 (Interscience, New York 1966)
7.24 U. Döbler, K. Baberschke, J. Stöhr, D. Outka: Phys. Rev. B **31**, 2532 (1985)
7.25 T.H. Upton: J. Chem. Phys. **83**, 5084 (1985)
7.26 A. Puschman, J. Haase, M.D. Crapper, C.E. Riley, D.P. Woodruff: Phys. Rev. Lett. **54**, 2250 (1985)
7.27 I.E. Wachs, R.J. Madix: J. Catal. **53**, 208 (1978)
7.28 M. Bowker, R.J. Madix: Surf. Sci. 95, 190 (1980)
7.29 T.A. Carlson, P.A. Agron, T.M. Thomas, F.A. Grimm: J. Electron. Spectrosc. Relat. Phenom. **23**, 13 (1981)
7.30 B.A. Sexton: Surf. Sci. **88**, 299 (1979)
7.31 R. Ryberg: Phys. Rev. B **31**, 2545 (1985)
7.32 M. Persson, S. Andersson: Surf. Sci. **117**, 352 (1982)
7.33 R. Ryberg: Chem. Phys. Lett. **83**, 423 (1981)
7.34 P. Hofmann, C. Mariani, K. Horn, A.M. Bradshaw: Vide, Couches Minces **201** (Suppl., Proc. Int. Conf. Solid Surf., 4th, V1) 541 (1980)
7.35 C.L. Allyn, T. Gustafsson, E.W. Plummer: Solid State Commun. **24**, 531 (1977)
7.36 B.A. Sexton: Appl. Phys. A **26**, 1 (1981)
7.37 For example
T.J. McNeese, M.B. Cohen, B.M. Foxman: *Organometallics* 3, 552 (1984); R.O. Gould, I.A. Stephenson, D.A. Tocher: J. Organomet. Chem. **263**, 375 (1984); S.W. Kirtley, J.P. Chanton, R.A. Love, D.L. Tipton, T.N. Sorrell, R. Bau: J. Am. Chem. Soc. **102**, 3451 (1980)

7.38 L.E. Sutter (ed.): *Tables of Interatomic Distances and Configuration in Molecules and Ions*, Special Publication 18 (The Chemical Society, London 1965)
7.39 R.J. Koestner, M.A. van Hove, G.A. Somorjai: J. Phys. Chem. **87**, 203 (1983)
7.40 J. Stöhr, F. Sette, A.L. Johnson: Phys. Rev. Lett. **53**, 1684 (1984)
7.41 R.J. Koestner, J. Stöhr, J.L. Gland, J.A. Horsley: Chem. Phys. Lett. 105, 332 (1984)
7.42 A.L. Johnson, E.L. Muetterties, J. Stöhr: J. Am. Chem. Soc. **105**, 7183 (1983)
7.43 J. Stöhr, J.L. Gland, E.B. Kollin, R.J. Koestner, A.L. Johnson, E.L. Muetterties, F. Sette: Phys. Rev. Lett. **53**, 2161 (1984)
7.44 R.J. Koestner, J. Stöhr, J.L. Gland, E.B. Kollin, F. Sette: to be published

8. Effects of Surface Impurities in Chemisorption and Catalysis

D.W. Goodman

Surface Science Division, Sandia National Laboratories, Albuquerque, NM 87185, USA

It has long been recognized that the addition of impurities to metal catalysts can produce large effects on the activity, selectivity, and resistance to poisoning of the pure metal [8.1]. For example, the catalytic properties of metals can be altered greatly by the addition of a second transition or Group 1B metal or by the addition of impurities such as potassium or sulfur. On the other hand, catalytic processing is often plagued by loss of activity and/or selectivity due to the inadvertent contamination of catalysts by undesirable impurities. In either case, the catalytic properties are dramatically altered by the modification of the chemistry by the impurity. Although these effects are well recognized in the catalytic industry, the mechanisms responsible for surface chemical changes induced by surface additives are poorly understood. However, the current interest and activity in this area of research promises a better understanding of the fundamentals by which impurities alter surface chemistry. A pivotal question concerns the underlying relative importance of *ensemble* (steric or local) versus *electronic* (nonlocal or extended) effects. A general answer to this question will critically influence the degree to which we will ultimately be able to tailor-make exceptionally efficient catalysts by fine-tuning the electronic structure. If, indeed, low concentrations of surface impurities can profoundly alter the surface electronic structure and thus catalytic activity, then the possibilities for the systematic manipulation of these properties via the selection of the appropriate additive would appear limitless. On the other hand if steric effects dominate the mode by which surface additives alter the catalytic chemistry, then a different set of considerations for catalyst alteration come into play, a set which will most certainly be more constraining than the former. In the final analysis, a complete understanding will include components of both electronic and ensemble effects, the relative importance of each to be assessed for a given reaction and conditions. A major emphasis of our research has been in the area of addressing and partitioning the importance of these two effects in the influence of surface additives in catalysis.

Catalyst deactivation and promotion are extremely difficult questions to address experimentally [8.1]. For example, the interpretation of related data on dispersed catalysts is severely limited by the uncertainty concerning the structural characterization of the active surface. Specific surface areas cannot always be determined with adequate precision. In addition, the knowledge of the crystallographic orientation, the concentration and the distribution of impurity atoms, as well as their electronic states is generally poor. The degree of contamination may vary considerably along the catalytic bed and the impurity may alter the support as well as the metal. Moreover, the active surface may be altered in an uncontrolled manner as a result of sintering or faceting during the reaction itself.

The use of metal single crystals in catalytic reaction studies essentially eliminates the difficulties mentioned above and allows, to a large extent, the utilization of a homogeneous surface amenable to study using modern surface analytical techniques. These techniques allow detailed surface characterization regarding surface structure and composition. Carefully prepared, single-crystal catalytic surfaces are particularly suited to the study of impurity effects on catalytic behavior because of the ease with which impurity atoms can be uniformly introduced to the surface. To date, relatively few studies [8.2-6] have incorporated both surface-science techniques with kinetics at elevated pressures (~1 atm). Kinetics, however, are an essential link between these kind of model catalytic studies and the more relevant practical catalytic systems, establishing the crucial connection between the reaction rate parameters. Although the studies to date are few, the results appear quite promising in addressing the fundamental aspects of catalytic poisoning and promotion.

8.1 Experimental Details

The studies to be discussed were carried out utilizing the specialized apparatus shown in Fig.8.1 and discussed in detail in [8.2,7]. This device consists of two distinct regions, a surface analysis chamber and a microcatalytic reactor. The surface analysis system, with a base pressure of $< 2 \times 10^{-10}$ Torr, is equipped with two collimated molecular beam dosers which face the front surface of the single crystal disk. The crystal, which can be cooled to 80 K, can be rotated to either doser for adsorption of gases. Temperature programmed desorption (TPD) can be carried out with the crystal in front of a UTI 100C multiplexing quadrupole mass spectrometer

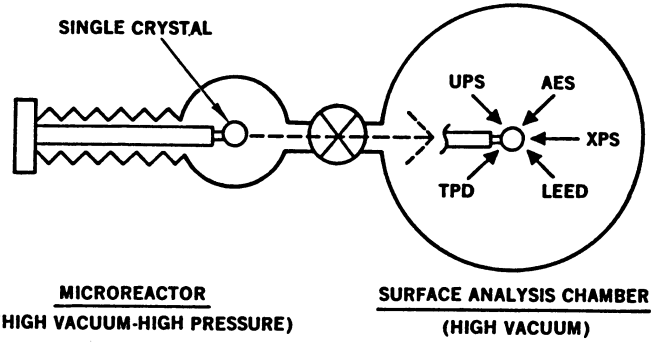

Fig.8.1. An ultra-high-vacuum apparatus for carrying out thermal programmed desorption at ultra-high vacuum and kinetic studies at atmospheric pressures on metal single crystals

(QMS) using a linear ramp of 10 K/s. The mass spectrometer samples 4 mass peaks every 0.7 s with a sampling time of 0.1 s/amu.

The custom-built reactor, contiguous to the surface analysis chamber, employs a retraction bellows that supports the metal crystal and allows translation of the catalyst in vacuo from the reactor to the surface analysis region. Both regions are of ultra-high-vacuum construction, bakeable, and capable of ultimate pressures of less than 10^{-10} Torr. The catalyst samples are typically mounted on tungsten leads and heated resistively. The reactor is operated in a batch mode with sampling subsequent to reaction into an on-line gas chromatograph. Analysis is via a flame ionization detector.

Details of sample cleaning procedures are given in the references accompanying the corresponding data. All reactants were initially of high purity and further purification procedures are generally used to improve the gas quality. These typically include multiple distillations for condensables and/or cryogenic scrubbing using a low-conductance glass-wool-packed trap at 80 K.

The sulfur coverages S(ads) were deposited by dosing H_2S at ~ 600 K until the desired level of S(ads) was obtained [8.8,9]. Coverages of S(ads) were calibrated as described previously [8.8-10]. Coverages of Cl(ads), P(ads), C(ads), and N(ads) were deposited from Cl_2, PH_3, ethylene, and hydrazine, respectively [8.8,9,11,12].

Copper [8.13] and silver [8.14] were evaporated from a resistively heated tungsten wire wrapped with high-purity wire. The metal sources were thoroughly outgassed prior to metal evaporation, and the deposition rates were accurately controlled by monitoring the voltage drop across the tungsten fila-

ment. The metal flux from the evaporator was also checked routinely via a quartz microbalance mounted off-axis to the sample.

8.2 Discussion

8.2.1 Electronegative Impurities

Impurities whose electronegativities are greater than those for transition metals generally poison a variety of catalytic reactions, particularly those involving H_2 and CO. Of these poisons, sulfur is the best known and technologically the most important [8.1]. The first step in the systematic definition of the poisoning mechanism of this category of impurities is the study of the influence of these impurities on the adsorption and desorption of the reactants.

a) Chemisorption

The effect of preadsorbed electronegative atoms Cl, S, and P on the adsorption-desorption of CO and H_2 on Ni{100} has been extensively studied [8.8,9, 11,12,15-18] using TPD, low-energy electron diffraction (LEED), and Auger electron spectroscopy (AES). It has been found that the presence of electronegative atoms causes a reduction of the sticking coefficient, the adsorption bond strength, and the adsorption capacity of the Ni{100} surface for CO and H_2. The poisoning effect becomes more prominent with increasing electronegativity of the preadsorbed atoms [8.9].

Adsorption of Cl, S, and P on nickel causes a reduction in both hydrogen and CO adsorption and a shift of the TPD peak maxima to a lower temperature [8.9]. The effect of preadsorbed Cl, S, and P on the CO TPD behavior is shown in Fig.8.2 and on the H_2 TPD in Fig.8.3. Coverages of impurities are expressed in terms of monolayers (ML) or the ratio of surface impurity atoms to the surface metal atoms. The TPD desorption curves represent the total adsorbate desorption for different impurity coverages after an exposure sufficient to reach the saturation adsorbate coverage. Both CO and H_2 adsorption decrease markedly in the presence of surface imourities. The effects of P, however, are much less pronounced than for Cl or S.

Figure 8.4 shows the observed dependence of the total CO adsorption on impurity coverage. Similarly, Cl, S, and P cause a reduction of hydrogen adsorption and a shift of the TPD peak maxima to a lower temperature [8.9]. At higher impurity levels a lower temperature state for H_2 emerges. The extent of this effect increases in the sequence P, S, Cl. As seen in Fig.8.5, the

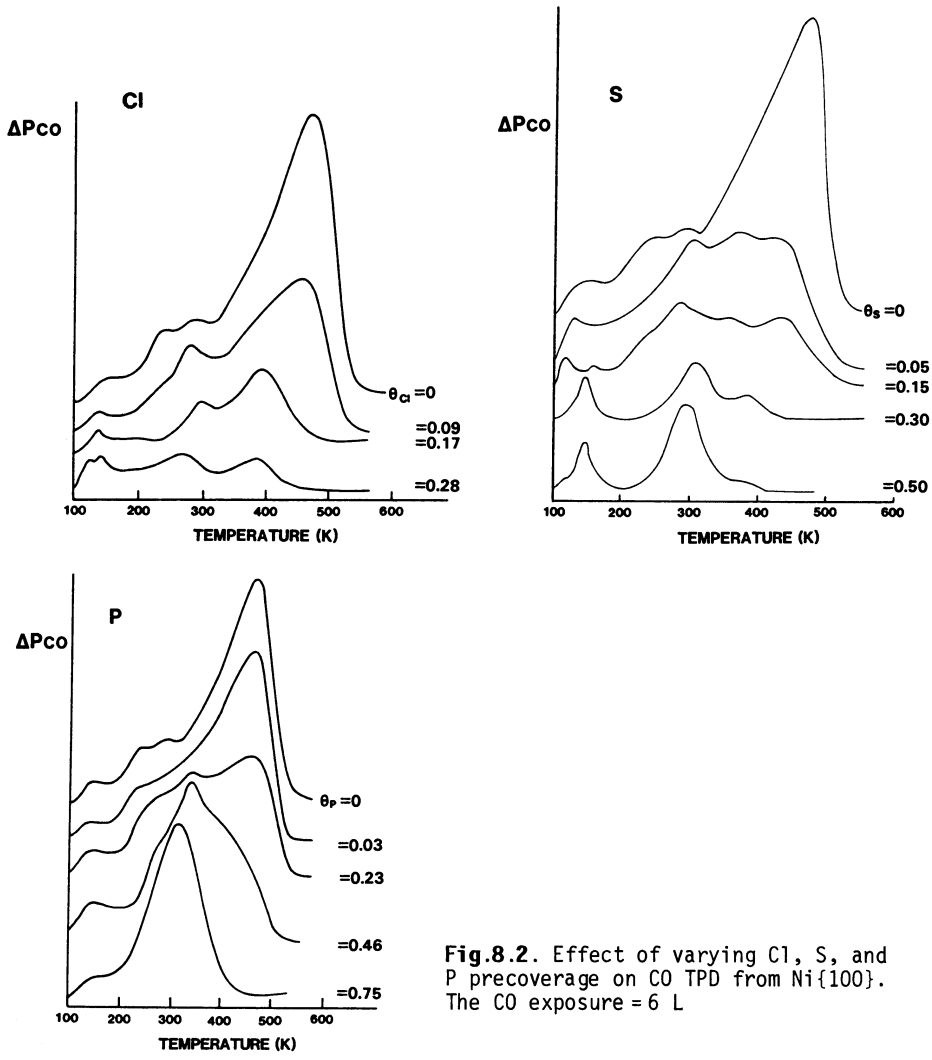

Fig.8.2. Effect of varying Cl, S, and P precoverage on CO TPD from Ni{100}. The CO exposure = 6 L

reduction of H_2 coverage is most apparent in the presence of Cl atoms. The similarity in the atomic radii of Cl, S, and P (0.99, 1.04, and 1.10 Å, respectively [8.19]) suggests a relationship between electronegativity and the poisoning of chemisorptive properties by these surface impurities. Related studies [8.11] have been carried out in the presence of C and N. These impurities have the same electronegativities as S and Cl, 2.5 and 3.0, respectively. The comparison between the results for C and N and those for S and Cl is entirely consistent with the interpretation that electronegativity effects dominate the poisoning of chemisorption by surface impurities with similar atomic size, and which occupy the same adsorption sites. In the case of ad-

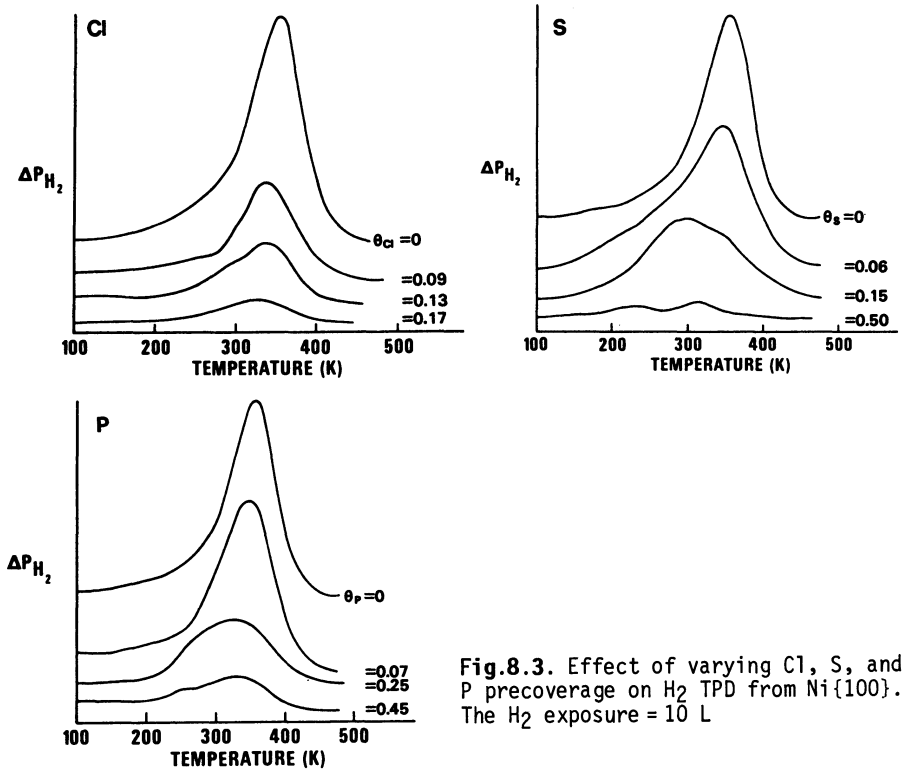

Fig.8.3. Effect of varying Cl, S, and P precoverage on H_2 TPD from Ni{100}. The H_2 exposure = 10 L

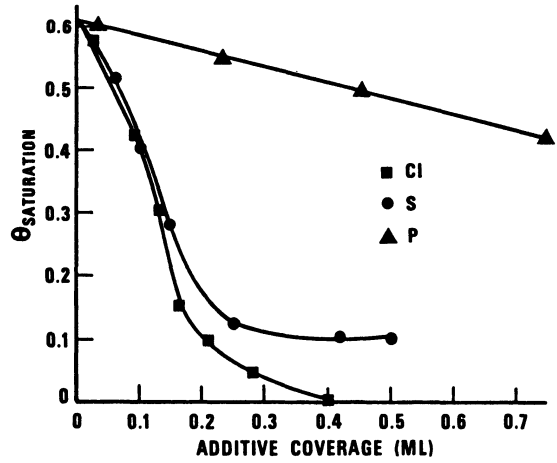

Fig.8.4. Dependence of total CO adsorption on additive precoverage

sorbed impurities with the same electronegativity, but with different atomic radii (S and C, Cl and N), the effect becomes less pronounced with decreasing atomic radius.

Particularly noteworthy in the above studies is the general observation that those impurities strongly electronegative with respect to nickel, Cl,

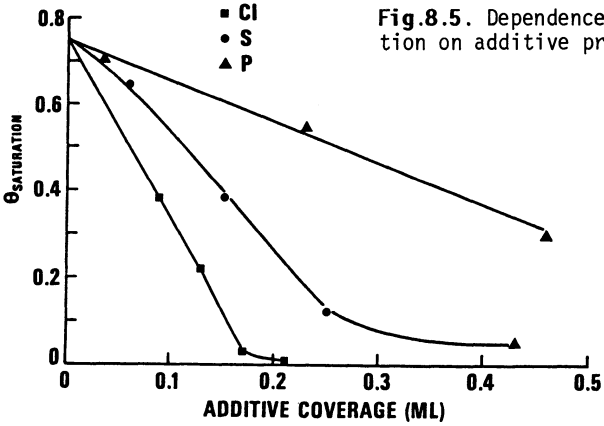

Fig.8.5. Dependence of total H_2 adsorption on additive precoverage

N, and S, modify the chemisorptive behavior far more strongly than would result from a simple site-blocking model. The initial effects of these impurities as shown in Figs.8.4 and 5 suggest that a single impurity atom successfully poisons as many as ten nickel atoms. This result supports an interaction that is primarily electronic in nature.

b) Catalytic Activity

Kinetic studies have been carried out for several reactions as a function of sulfur coverage over single crystals of nickel [8.8,20], rhodium [8.14], and ruthenium [8.21]. For the methanation reaction over Ni{100} [8.8], the sulfided surface (Fig.8.6a) shows behavior remarkably similar to results for the clean surface at a considerably reduced hydrogen partial pressure. For clean Ni{100} [8.2] a departure from Arrhenius linearity is observed at 700 K. Associated with the onset of this nonlinearity or "rollover" is a rise in the surface carbon level. This rise in carbon level continues until the carbon level reaches 0.5 ML, i.e., the saturation level. This behavior of the Arrhenius plot has been interpreted [8.2] as reflecting the departure of atomically adsorbed hydrogen from a saturation or critical coverage. For a sulfur surface coverage of 4%, the reaction rate at identical conditions departs similarly from linearity at 600 K, some 100 K lower in reaction temperature. Here too, an increase in surface carbon level is associated with this deviation from linearity. This behavior indicates that the sulfur, is very effective in reducing the steady-state surface atomic hydrogen coverage which results in an attenuation of the rate of surface carbon hydrogenation. These results are consistent with the chemisorption results [8.9] discussed above for H_2 on sulfur-poisoned Ni{100} surface. Similar results

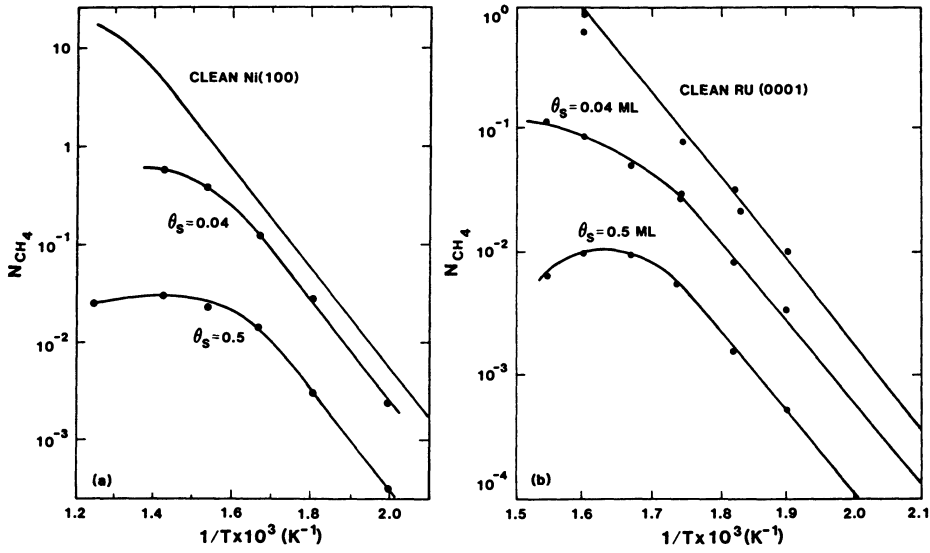

Fig.8.6a,b. An Arrhenius plot of the rate of methanation over sulfided (a) Ni{100} and (b) Ru{0001} catalysts at 120 Torr and a $H/_2CO$ ratio of 4. Coverages (θ_S) are expressed as fractions of a monolayer. N_{CH_4} is the turnover frequency (TF) or the number of methane molecules produced per surface nickel atom per second

(Fig.8.6b) have been seen [8.21] for sulfur poisoning of a Ru{0001} surface toward CO hydrogenation.

Both the kinetics and the TPD studies show that the poisoning effects of sulfur are very nonlinear. Figure 8.7a shows the relationship between the sulfur coverage on a Ni{100} catalyst and the methanation rate catalyzed by this surface at 600 K. A precipitous drop in the catalytic activity is observed for low sulfur coverages. The poisoning effect quickly maximizes with little reduction in the reaction rate at sulfur coverages exceeding 0.2 monolayers. The activity attenuation at the higher sulfur coverages is in excellent agreement with that found for supported Ni/Al_2O_3 by *Rostrup-Nielsen* and *Pedersen* [8.22]. The initial change in the poisoning in Fig.8.7a suggests that more than ten nickel atom sites are deactivated by one sulfur atom.

Similar behavior has been observed for sulfur-poisoned Ru{0001} [8.21] and Rh{111} [8.14] catalysts. Results for these studied are shown in Figs. 8.7b,c. A result common to these studies is that sulfur effectively poisons catalytic activity at coverages less than 10% of the surface metal concentration.

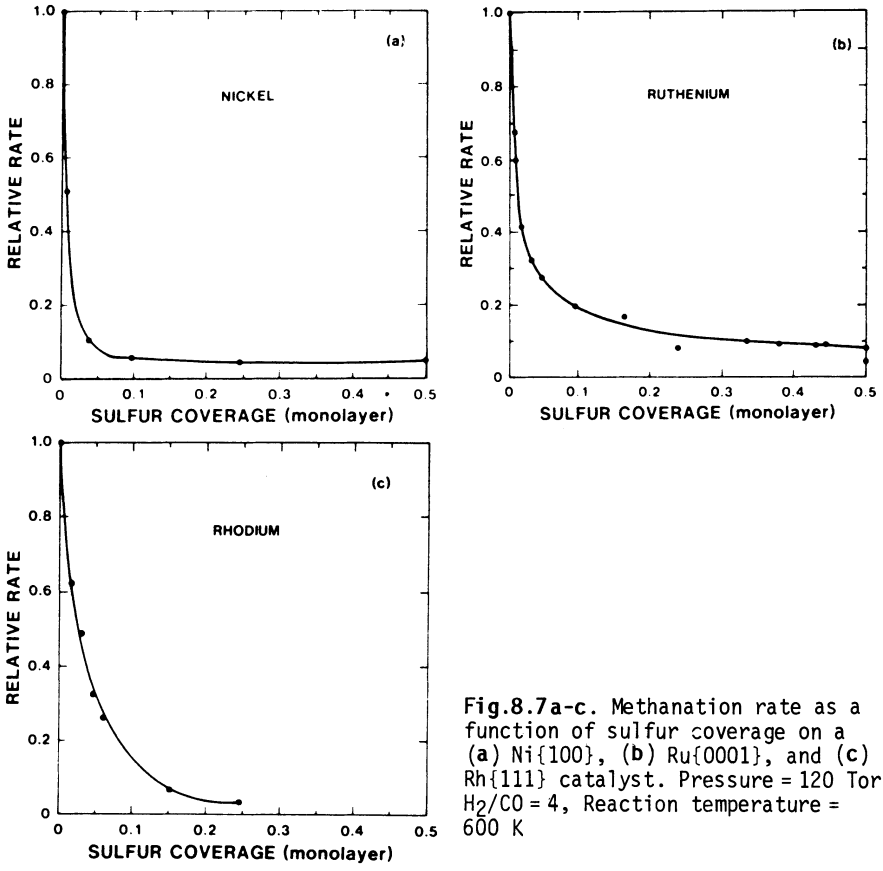

Fig.8.7a-c. Methanation rate as a function of sulfur coverage on a (**a**) Ni{100}, (**b**) Ru{0001}, and (**c**) Rh{111} catalyst. Pressure = 120 Torr, $H_2/CO = 4$, Reaction temperature = 600 K

c) Catalytic Selectivity

For methanation, sulfur is seen to significantly attenuate the surface activity. In those cases where multiple products are possible, dramatic modifications in the distributions of these products have been observed [8.20]. Figure 8.8 shows the effect that progressive sulfiding of a Ni{111} catalyst has on the cyclopropane/hydrogen reaction. A small amount of sulfur (< 0.1 ML) exponentially lowers the rate of methane formation, the dominant product formed on the clean surface. Similarly, the rate of ethane formation falls in concert with the methane suggesting, as is expected, a close correlation between these hydrogenolysis products. In contrast to the methane and ethane products, the production of propane/propylene (C_3) product actually increases with the sulfur addition. Qualitatively, the increase in the C_3 product corresponds to the decrease in the methane rate. These results show rather directly that the initial sulfiding promotes the ring-opening reaction

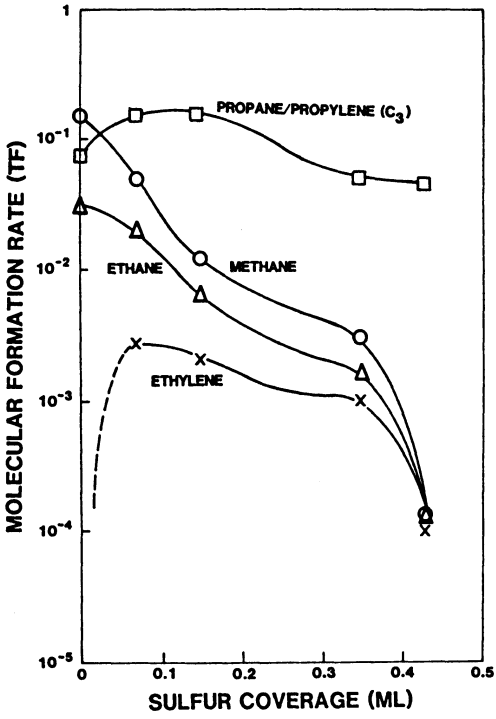

Fig.8.8. Product distribution from the reaction of cyclopropane with hydrogen over a sulfided Ni{111} catalyst. Temperature = 550 K. Total pressure = 100 Torr. H_2/ cyclopropane = 100. TF: turnover frequency

by reducing the tendency of the surface to break more than one carbon-carbon bond.

In contrast to the clean Ni{111} surface where no ethylene was observed as a reaction product, significant amounts of ethylene are found [8.20] for the sulfided surface. In addition to reducing the tendency of the surface to break carbon-carbon bonds, sulfur also lowers the hydrogenation activity. This tendency has been confirmed by measuring directly the attenuation of the hydrogenative character of Ni{111} versus sulfur coverage by monitoring the ethylene/hydrogenative reaction [8.23].

The effect of sulfiding a Ni{111} catalyst for the cyclopropane reaction is threefold: (a) A reduction in the carbon-carbon bond-breaking activity; (b) an increase in the relative propane/propylene product yield; and (c) the appearance of significant amounts of olefin (ethylene) product. The cumulative result of these changes is a dramatic alteration of the measured selectivity of the modified surface compared with the clean surface.

Results which correspond directly to the steady-state kinetics mentioned above have been found in TPD experiments following the adsorption of cyclopropane onto a clean and sulfided Ni{111} surface [8.23]. Figure 8.9, curve a, shows a H_2 TPD following the adsorption of a saturation exposure of cyclo-

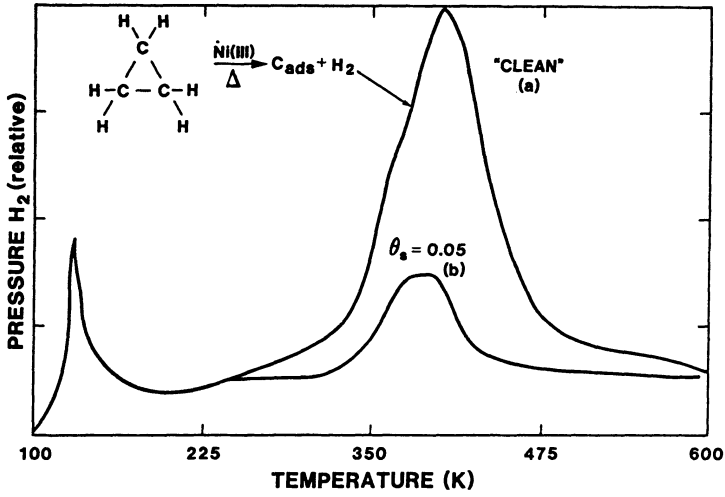

Fig.8.9. Hydrogen TPD following the adsorption of a saturation exposure of cyclopropane onto (*a*) a clean and (*b*) a 0.05 ML sulfided Ni{111} surface

propane onto a clean Ni{111} surface. The small peak at 130 K corresponds to H_2 formed in the QMS during the cracking of the parent cyclopropane, indicating molecular physisorption of cyclopropane. The H_2 desorption at the higher temperatures corresponds to the recombination of atomic hydrogen formed from the decomposition of cyclopropane, or hydrocarbon fragments thereof, to carbon and adsorbed atomic hydrogen. The area under this peak relative to the area measured following a saturation H_2 exposure on the clean Ni{111} surface allows the assessment of the absolute coverage of cyclopropane adsorbed. [8.23]. This coverage corresponds to a closed-packed arrangement of cyclopropane molecules lying flat on the surface. Thus, on the clean surface all the adsorbed cyclopropane undergoes decomposition to carbon (carbidic) and hydrogen (atomic).

The addition of small amounts of sulfur effects significantly the adsorption and dehydrogenation of cyclopropane as measured by TPD. Figure 8.9, curve b, shows a repeat of the experiment on the clean surface, however, with the addition of 5% of a monolayer of sulfur. This small addition of sulfur is seen to reduce the activity of the surface toward breaking carbon-carbon bonds such that only 20% of the subsequently adsorbed cyclopropane decomposes to carbon and hydrogen. The remaining cyclopropane either desorbs molecularly or rearranges to propylene [8.23].

A series of TPD measurements following cyclopropane adsorption with successively larger sulfur coverages [8.23] allows the quantitative assessment

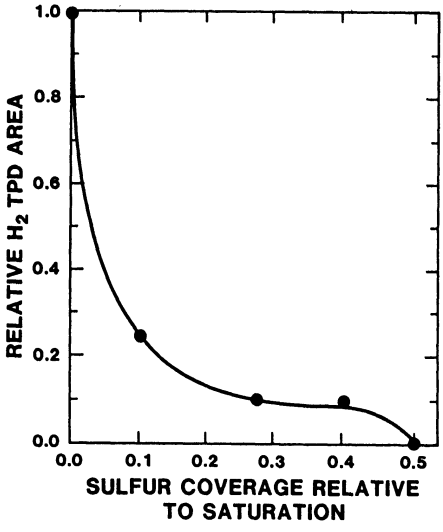

Fig.8.10. Hydrogen TPD areas measured after adsorption of a saturation exposure of cyclopropane on a Ni{111} surface as a function of sulfur coverage

of the change in the ability of the surface to break carbon-carbon and/or carbon/hydrogen bonds with sulfur coverage. This relationship is shown in Fig.8.10. It is noteworthy that the precipitous drop in the carbon-carbon bond breaking ability with sulfur coverage is strikingly similar to the fall in the methane formation rate with sulfur coverage in the steady-state reaction rate measurements of Fig.8.8.

At first glance, one might interpret these results as the simple poisoning of minority or defect sites on the surface and that these sites are crucial to the TPD decomposition and the reactivity at steady-state reaction conditions. However, this is a very unlikely explanation given that numerous studies [8.2,4,10,24-27] have shown a close corresponding between the steady-state rates measured for single-crystal catalysts and those rates found for supported, small-particle catalysts. That the defect densities on these two very different materials would be precisely the same is highly unlikely. It is much more likely that these reactions are not defect controlled and that the surface atoms of the single crystals are uniformly active.

There are two other possible explanations for this result: (1) an electronic or ligand effect as discussed at the beginning of this chapter or (2) an ensemble effect (the requirement that a certain collection of surface atoms are necessary for the reaction to occur). Experimentally, these two possibilities can be distinguished [8.4,12]. If an ensemble of more than ten nickel atoms is required for methanation, then altering the electronic character of the impurity should produce little change in the degree to which the impurity poisons the catalytic activity. That is, the impurity serves

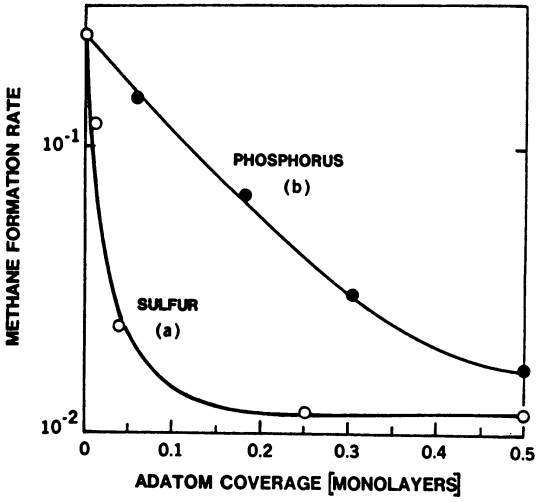

Fig.8.11. Rate of methanation over a sulfided and phosphided Ni{100} catalyst at 120 Torr and a H_2/CO ratio equal to four

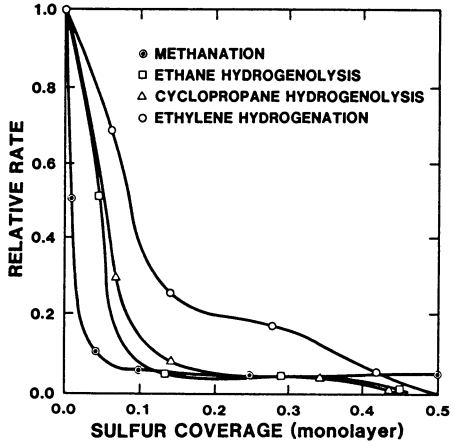

Fig.8.12. Sulfur poisoning of various reactions over nickel. Hydrogen partial pressure = 100 Torr

merely to block a single site in the reaction ensemble, nothing more. On the other hand, if electronic effects play a significant role in the poisoning mechanism, then the reaction rate should respond to a change in the electronic character of the impurity. Substituting phosphorus for sulfur (both atoms are approximately the same size) in a similar set of experiments results in a marked change in the magnitude of poisoning at low coverages as shown in Fig.8.11. Phosphorus, because of its less-electronegative character, effectively poisons only the four nearest-neighbor metal atoms sites.

Effective poisoning of catalytic activity at sulfur coverages of less than 0.1 ML has been observed for other reactions, including ethane and cyclopropane hydrogenolysis [8.20], ethylene hydrogenation [8.23], and CO_2 methanation [8.27]. The results of several studies on nickel are summarized in Fig.8.12.

These studies indicate that the sensitivity of the above reactions to sulfur poisoning are generally less than that for poisoning by sulfur of CO methanation. The rate attenuation is, nevertheless, strongly nonlinear at the lower sulfur levels. A direct consequence of the differing molecular sizes of the reactants (CO, ethylene, ethane, cyclopropane) involved in the reactions investigated is that electronic effects, rather than ensemble requirements, dominate the catalytic poisoning mechanism for these experimental conditions.

Recent studies [8.28] using high-resolution electron energy loss and photoelectron spectroscopy to investigate the effect of sulfur on the CO/Ni{100} system are consistent with an extended effect by the impurity on the adsorption and bonding of CO. Sulfur levels of a few percent of the surface nickel atom concentration were found sufficient to significantly alter the surface electronic structure as well as the CO bond strength.

8.2.2 Electroneutral Impurities

Interest in bimetallic catalysts has risen steadily over the years because of the commercial success of these systems. This success results from an enhanced ability to control the catalytic activity and selctivity by tailoring the catalysts' composition [8.29-40]. A key question in these investigations, as with other impurities, has been the relative roles of ensemble and electronic effects in defining the catalytic behavior [8.41-44]. In gathering information to address this question, it has been advantageous to simplify the problem by utilizing models of a bimetallic catalyst such as the deposition of metals on single-crystal substrates in the clean environment familiar to surface science. Many such model systems have been studied but a particularly appealing combination is that of copper on ruthinium. Copper is immiscible in ruthinium which facilitates coverage determinations by TPD [8.13] and circumvents the complication of determining the three-dimensional composition.

a) Copper Overlayer Structure

The adsorption and growth of copper films on the Ru{0001} surface have been studied [8.13,45-56] by work function measurements, LEED, AES, and TPD. The results from recent studies [8.53-56] indicate that for submonolayer depositions at 100 K the copper grows in a highly dispersed mode, subsequently forming two-dimensional islands pseudomorphic to the Ru{0001} substrate upon annealing to 300 K. Pseudomorphic growth of the copper indicates that the Cu-Cu bond distances are strained approximately 5% beyond the equilibrium bond distances found for bulk copper. This behavior is seen to continue to

the 1 ML level. Additional copper deposition to 2 ML shows a similar two-dimensional island growth but with an epitaxial, or relaxed, Cu{111} structure. Subsequent annealing to 900 K, in both these cases enhances the two-dimensional islanding of the films but does not affect the overall structure. Results from AES and LEED [8.56] show that a 900 K anneal of copper films in excess of 2 ML leads to three-dimensional Cu{111} island formation exposing areas of the surface covered by the original copper bilayer - one pseudomorphic and one epitaxial.

b) Chemisorption

Recent work [8.13,54] has shown that a subtle modification of the preparation techniques of the Cu film on the Ru{0001} substrate can lead to significant changes in the system's chemisorptive properties. For example, in early studies the attenuation of hydrogen chemisorption by copper on Ru{0001} was observed to be quite precipitous by *Shimizu* et al. [8.46] following copper deposition at 1080 K. More recent work [8.13,54] has shown that preparation of the Cu overlayer at 100 K, with or without an anneal to 1080 K, leads to simple site blocking of H_2 chemisorption, that is, poisoning of the hydrogen dissociation on a one-to-one (copper-to-ruthenium) basis. These results together suggest that the degree of the two-dimensional character could differ substantially in the Cu overlayer resulting from these two preparation techniques. In our studies [8.13,54,56] the presence of a distinct "monolayer" and a "multilayer" feature in the copper TPD provides a convenient and definitive method for measuring absolute copper coverage [8.13,54].

A comparison of CO desorption from Ru [8.56], from multilayer Cu (~ 10 ML) on Ru and 1 ML Cu on Ru is shown in Fig.8.13. The TPD features of the 1 ML Cu

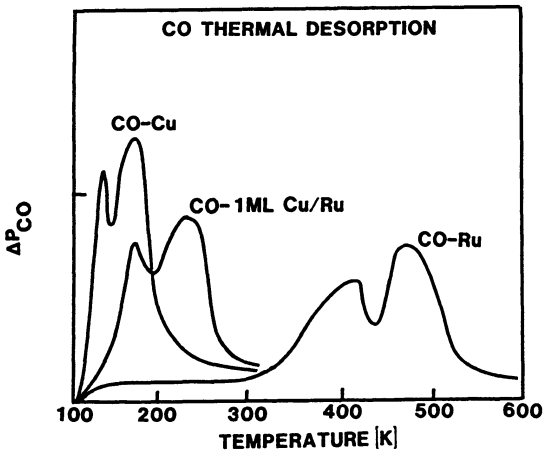

Fig.8.13. Results of TPD for CO adsorbed to saturation levels on the clean Ru{0001}, on multilayer Cu, and on a 1ML Cu covered Ru{0001}

(peaks at 160 and 210 K) on Ru are at temperatures intermediate between Ru and bulk Cu. This suggests that the monolayer Cu is electronically perturbed and that this perturbation manifests itself in the bonding of CO. An increase in the desorption temperature relative to bulk Cu indicates a stabilization of the CO on the monolayer Cu suggesting a coupling of the CO through the Cu to the Ru. The magnitude of the CO stabilization implies that the electronic modification of the Cu by the Ru is significant and should be observable with a band-structure probe. Recent angularly resolved photoemission studies [8.57] indeed show a unique interface state which is probably related to the altered CO bonding on Cu films intimate to Ru.

Figure 8.14 shows the results [8.56] of CO chemisorption on the Cu/Ru{0001} system as a function of the Cu coverage. Copper deposition was at 100 K, followed by an anneal to 900 K. This preparation, as discussed above, is expected to produce significant two-dimensional copper island formation. In each case the exposure (approximately 10 L or 10^{-5} Torr-s) corresponds to a saturation coverage of CO. Most apparent in Fig.8.14 is a monotonic decrease upon addition of Cu of the CO structure identified with Ru (peaks at 400 and 480 K) and an increase of the CO structure corresponding to Cu (peaks at 200 and 275 K). The buildup of a third feature at 300 K (indicated by the dashed line) is assigned to CO desorbing from the edges of copper islands. Integration of the 200, 275, and 300 K peaks provides information regarding island sizes, that is, perimeter to island area ratios, at various copper

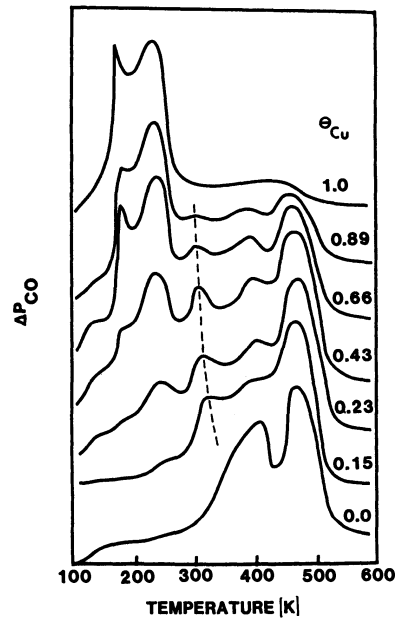

Fig.8.14. Results of TPD corresponding to CO adsorbed to saturation levels on the clean Ru{0001} surface, and from this same surface with various coverages of Cu

coverages. For example, at Θ_{Cu} = 0.66 we estimate the average island diameter to be approximately 50 Å. This island size is consistent with an estimate of the two-dimensional island size corresponding to this coverage of 40-60 Å derived from the width of the LEED beam profiles [8.56].

These results demonstrate that significant structural perturbations of Cu occur at the Cu/Ru interface and that these changes lead to large effects on the chemistry of the altered copper. Such chemical effects are certain to play a role in the enhanced catalytic properties of Cu/Ru bimetallic catalysts.

c) Catalytic Activity

Model studies of the Cu/Ru{0001} catalyst have been carried out [8.21] for methanation and hydrogenolysis reactions and are shown in Fig.8.15. These data suggest that copper merely serves as an inactive diluent, blocking sites on one-to-one basis. A similar result has been found in an analogous study [8.14] introducing silver onto a Rh{111} methanation catalyst.

Sinfelt et al. [8.58] have shown that copper in a Cu/Ru catalyst is confined to the surface of ruthenium. Results from the model catalysts discussed here then should be relevant to those on the corresponding supported, bimetallic catalysts. Several such studies have been carried out investigating the addition of copper or other Group 1B metals on the rates of CO hydrogenation [8.41,59,60] and ethane hydrogenolysis [8.60-62] catalyzed by ruthenium. In general, these studies show a marked falloff in activity with addition of the Group 1B metal suggesting a more profound effect of the Group 1B metal on ruthenium than implied from the model studies. A critical parameter in the supported studies is the measurement of the active ruthenium surface using hydrogen chemisorption techniques. *Haller* and co-workers [8.61,62] have recently suggested that hydrogen spillover during chemisorption may occur from ruthenium to copper complicating the assessment of surface Ru atoms. Recent studies in our laboratory [8.55] have shown directly that spillover from ruthenium to copper can take place and must be considered in the hydrogen chemisorption measurements. Hydrogen spillover would lead to a significant overestimation of the number of active ruthenium metal sites and thus to significant error in calculating ruthenium specific activity. If this is indeed the case, the results obtained on the supported catalysts, corrected for the overestimation of surface ruthenium, could become more comparable with the model data reported here.

Finally, the activation energies observed on supported catalysts in various laboratories are generally unchanged by the addition of a Group 1B metal

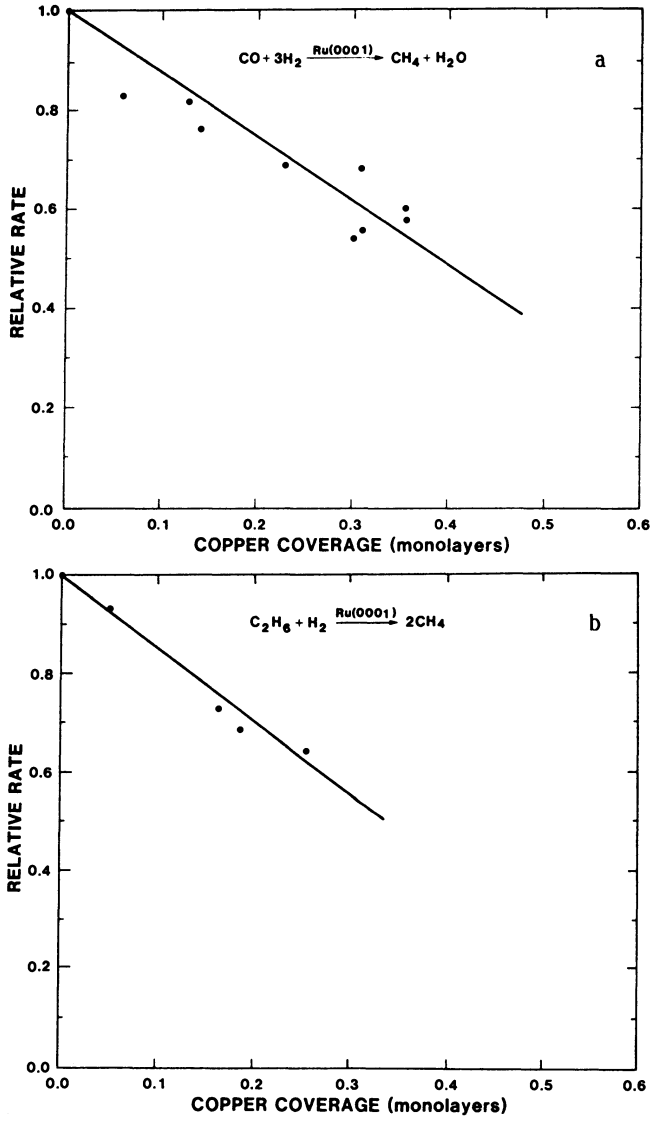

Fig.8.15a,b. Relative rate of (**a**) CO hydrogenation and (**b**) ethane hydrogenolysis as a function of Cu coverage on a Ru{0001} catalyst. Reaction temperature is (**a**) 575 K and (**b**) 550 K

[8.61-63], in agreement with the model studies. A crucial test of the relevance of modeling bimetallic catalysts using single crystals will be the ability of the model systems to alter the selectivity of the catalyst towards dehydrogenation reactions as is generally observed on supported systems [8.64]. These experiments are currently underway in our laboratory.

In general, we find that electroneutral impurities, in contrast to electronegative impurities such as sulfur, tend to act as blocking agents for adsorption and reaction. This is likely a result of minimal perturbing effects on the substrate by the overlayer due to the similarities in electronegativities. Quite clearly, at monolayer and near-monolayer coverages, overlayer metals are perturbed by the substrate and exhibit special chemical properties that are unlike those of the bulk metal. The latter effects are likely to be major contributors to the special properties of multimetallic catalysts.

8.2.3 Electropositive Impurities

A direct consequence of interpreting the poisoning effects of electronegative impurities in terms of electronic surface modification is that additives with electronegativities less than that of the metal should promote a different chemistry reflecting the donor nature of the additive. For example, alkali atoms on a transition metal surface are known to exist in a partially ionic state, donating a large fraction of their valence electron to the metal, resulting in a work function decrease. This additional electron density on the transition metal surface atoms is thought to be a major factor in alkali atoms altering the chemisorptive bonding of molecules such as N_2 [8.65] or CO [8.66], and in promoting the catalytic activity in ammonia synthesis [8.67]. These results are consistent with the general picture that electron receptors tend to inhibit CO hydrogenation reactions whereas electron donors typically produce desirable catalytic effects, including increased activity and selectivity. Recent chemisorption and kinetic studies have examined quantitatively the relationship between the electron donor properties of the impurity and its effect on the catalytic behavior.

a) Chemisorption

The addition of alkali metal atoms to Ni{100} results in the appearance of more tightly bound states in the CO TPD spectra and to an increase in the degree of CO dissociation [8.66]. The dissociation probability increases in the sequence Na, K, Cs, indicating a correspondence between the donor properties of the impurity and its ability to facilitate CO dissociation. On iron [8.68], CO absorbs with a higher binding energy on the potassium-promoted Fe{110} surface than on the corresponding clean surface. The CO coverage increases and the sticking coefficient decreases with increasing potassium coverage. The probability for CO dissociation increases in the presence of potassium [8.68]. Analogously, NO is more strongly adsorbed and dissociated to a greater

extent on sodium-covered Ag{111} than on clean Ag{111} [8.69]. The addition of potassium to iron increases the dissociative adsorption of N_2, isoelectronic with CO, by a factor of 300 over that for the clean surface [8.70]. Recent studies of CO adsorption on potassium-promoted Pt{111} [8.71-73] and Ni{100} [8.74] are consistent with this general picture of donor-enhanced metal-CO bonding. For H_2 chemisorption, *Ertl* et al. [8.75], using TPD techniques, have observed an increase in the adsorption energy of hydrogen on iron. They suggest that the empty state above the Fermi level created by the pronounced electron transfer from potassium to the d-band of iron may possibly be involved via interaction with the H 1s level.

b) Carbon Monoxide Dissociation Kinetics

Adsorbed potassium causes a marked increase in the rate of CO dissociation on a Ni{100} catalyst [8.76]. The increase of the initial formation rate of "active" carbon or carbidic carbon via CO disproportionation [2 CO → C(ads) + CO_2] is illustrated in Fig.8.16. The relative rates of CO dissociation were determined for the clean and potassium-covered surfaces by observing the growth in the carbon Auger signal with time in a CO reaction mixture, starting from a carbon-free surface. The rates shown in Fig.8.16 are the observed rates of carbon formation extrapolated to zero carbon coverage. The carbide buildup kinetics at various temperatures for the clean surface [8.77] and for a potassium coverage of 10% of a monolayer are compared in Fig.8.17 [8.76]. Of particular significance in these studies is the reduction of the activation

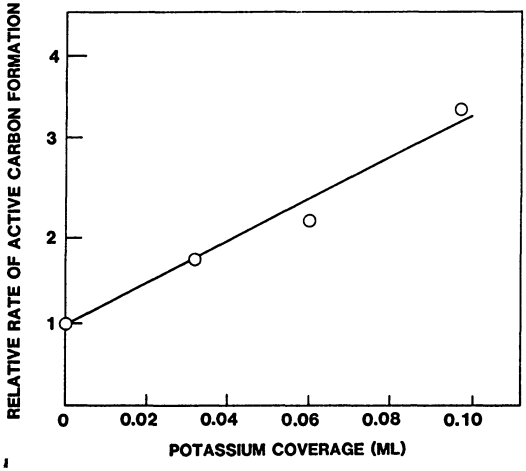

Fig.8.16. The relative initial rate of reactive carbon formation from CO disproportionation as a function of potassium coverage. P_{CO} = 24 Torr, T = 500 K

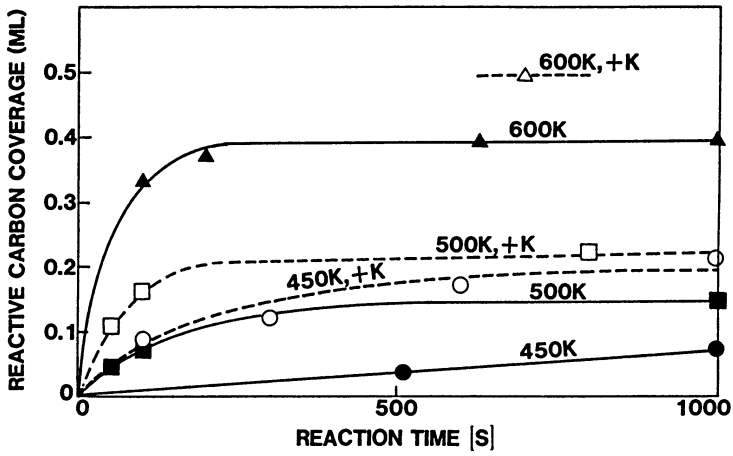

Fig.8.17. Reactive carbon buildup via CO disproportionation at various temperatures for a clean and potassium-doped Ni{100} catalyst. Potassium coverage = 0.10 ML. P_{CO} = 24 Torr

energy of reactive carbon formation from 23 kcal/mole for the clean Ni{100} surface to 10 kcal/mole for a 10% potassium-covered surface [8.76].

c) Methanation Kinetics

Kinetic measurements [8.76] over a Ni{100} catalyst containing well-controlled submonolayer quantities of potassium show a decrease in the steady-state methanation rate under a variety of reaction conditions. These results are summarized in Fig.8.18. The presence of potassium did not alter the apparent activation energy associated with the kinetics of Fig.8.19; however, the po-

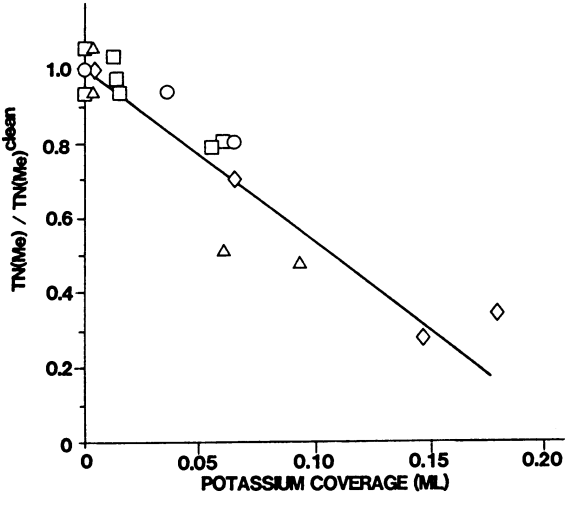

Fig.8.18. Relative rate of methanation reaction as a function of potassium coverage at various reaction conditions

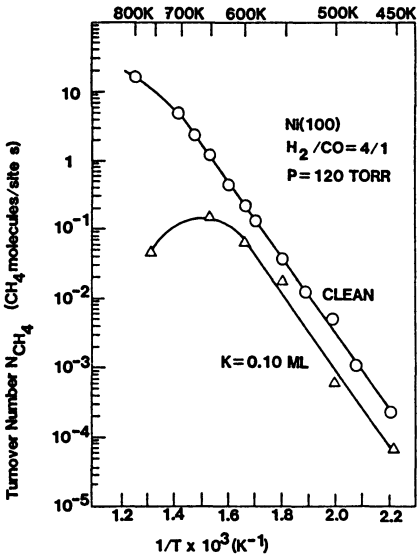

Fig.8.19

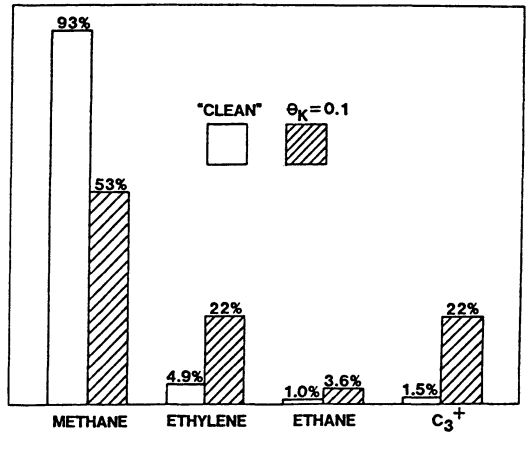

Fig.8.20

Fig.8.19. A comparison of the rate of methane synthesis over a clean single-crystal Ni{100} catalyst to the corresponding rate over a potassium-doped catalyst. Total reactant pressure is 120 Torr, $H_2/CO = 4$

Fig.8.20. A comparison of the product distributions (weight percentage) observed for a clean and a potassium-doped catalyst at T = 500 K, $H_2/CO = 4$, and a total pressure of 120 Torr. Potassium coverage = 0.10 ML

tassium did change the steady-state coverage of active carbon on the catalyst. This carbon level changed from 10% of a monolayer on the clean catalyst to 30% on the potassium-covered catalyst.

d) Promotion of Higher Hydrocarbon Formation

As shown in Fig.8.20, adsorbed potassium causes a marked increase in the steady-state rate and selectivity of nickel for higher hydrocarbon synthesis [8.76]. At all temperatures studied, the overall rate of higher hydrocarbon production was faster on the potassium-dosed surface showing that potassium is a promoter with respect to Fischer-Tropsch synthesis. This increase in higher hydrocarbon production is attributed to the increase in the steady-state active carbon level during the reaction, a factor leading to increased carbon polymerization. Potassium impurities on a nickel catalyst, then, cause a significant increase in the CO dissociation rate and a decrease in the activation energy for CO dissociation at low carbon coverages. These effects can be explained in terms of an electronic effect, whereby the electropositive potassium donates extra electron density to the nickel surface atoms, which in turn donate electron density to the adsorbed CO molecule. This increases

the extent of π-backbonding in the metal-CO complex, resulting in an increased metal-CO bond strength and a decrease in C-O bond strength. This model satisfactorily explains the decrease in the activation energy for carbide buildup brought about by potassium.

Since a local effect by the potassium is sufficient to account for the kinetics , the spatial extent of the effect of potassium in these experiments cannot be assessed. However recent high-resolution electron energy loss spectroscopy (HREELS) of CO on potassium-doped platinum [8.72] and ruthenium [8.78] indicate an alkali influence significantly larger than a simple potassium radius. These results taken together suggest that extended electronic perturbations are effectively altering the surface chemistry via a similar mechanism to that invoked for the poisoning results discussed above.

e) Electronic Compensation Effects

Intrinsic to interpreting catalytic poisoning and promotion in terms of electronic effects is the inference that adsorption of an electron impurity should moderate or compensate for the effects of an electronegative impurity. Recent experiments have shown this to be true in the case of CO_2 methanation [8.27]. As shown in Fig.8.21, the adsorption of sulfur decreases the rate of methane formation significantly. The adsorption of potassium in the presence of sulfur shows that the potassium can neutralize the effects of sulfur.

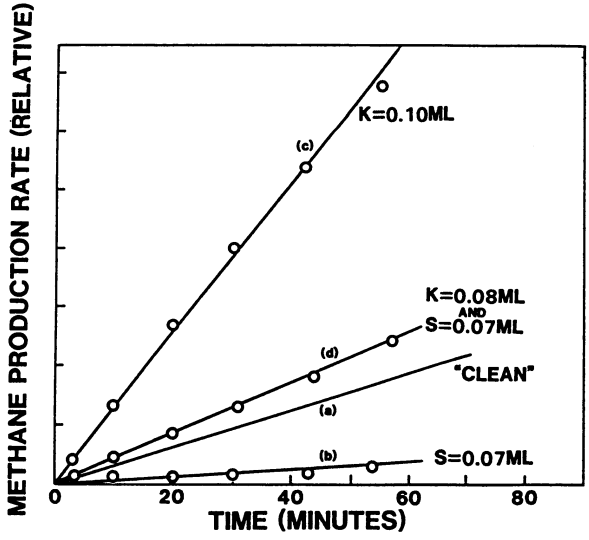

Fig.8.21. Methane production from a CO_2/H_2 reaction mixture over (*a*) a clean, (*b*) a sulfided, (*c*) a potassium-covered, and (*d*) a potassium-and-sulfur-covered Ni{100} catalyst

8.2.4 Related Theory

Theoretical work has been undertaken to address directly the predicted magnitude of the near-surface electronic perturbations caused by impurity atoms. Early work by *Grimley* and co-workers [8.79,80] and *Einstein* and *Schrieffer* [8.81] concentrated on the indirect interactions between adsorbates which occur via the surface conduction electrons. These calculations suggested that atom-atom interactions through several lattice spacings can occur. More recently, *Feibelman* and *Hamann* [8.82] and *Joyner* et al. [8.83] have calculated the change in the surface one-electron density of states due to the adsorption of an electropositive or electronegative atom. Such changes are assumed to affect the interaction of an adsorbing atom or molecule with the surface. The lateral range of these changes is then a measure of the range of the interactions.

The calculations of *Feibelman* and *Hamann* have expressly addressed the surface electronic perturbation by sulfur [8.82] as well as by chlorine and phosphorus [8.84]. The sulfur-induced total charge density vanishes beyond the immediately adjacent substrate atom site. However, the Fermi-level density of states, which is not screened and which governs the ability of the surface to respond to the presence of other species, is substantially reduced by the sulfur even at nonadjacent sites. Finally, the results for several impurities indicate a correlation between the electronegativity of the impurity and its relative perturbation of the Fermi-level density of states, a result which could be very relevant to the poisoning of H_2 and CO chemisorption by S, Cl, and P [8.9], as discussed above.

Theoretical treatments taking into account the direct interaction between adsorbates due to an overlap between their orbitals have also been reported [8.85,86]. Considerations are given to the energy cost of orthogonalization of the orbitals to one another, a factor which dominates at very short adsorbate-adsorbate distances.

In addition, the direct electrostatic interaction between adsorbates has been treated [8.87-89]. At intermediate distances of the order of a surface lattice constant, *Norskov* et el. report [8.88] that this interaction can give rise to substantial ($> \sim 0.1$ eV) interaction energies, when both adsorbates in question induce electron transfer to or from the surface or have a large internal electron transfer.

Both sets of theories, that is, "through bond" or "through space", are consistent with adsorbate perturbations sufficiently large to effect chemically significant changes at next-nearest-neighbor metal sites. This perturbation length is sufficient to explain adequately the observed poisoning of

chemisorptive and catalytic properties by surface impurities reported in the above discussion.

8.3 Conclusions

Model studies using metal single crystals and ultra-high-vacuum surface techniques are profitable in developing an understanding of the mechanisms by which poisons and promoters alter catalytic performance. Kinetic measurements in conjunction with these studies are particularly useful in linking the surface analytical measurements to practical catalysts. Because of the importance of surface chemical modification in catalysis and many related technological areas, much more work should and will be invested in defining in detail the physics and chemistry associated with the changes induced by surface impurities. Of particular interest are the specific bonding sites on and the electronic interaction of the impurity with the substrate. Also, the influence of the impurity on the chemisorptive behavior of the reactants as well as the bond strengths of the reactants are key pieces of information needed. These kinds of data are currently accessible using an array of modern surface techniques. These studies, in parallel with studies on supported catalysts, promise to be most revealing regarding the basic mechanisms of surface chemical modification.

Acknowledgement. We acknowledge with pleasure the partial support of this work by the Department of Energy, Office of Basic Energy Sciences, Division of Chemical Sciences.

References

8.1 B. Imelik, C. Naccache, G. Coudurier, H. Praliaud, P. Meriaudeau, P. Gallezot, G.A. Martin, J.C. Vedrine (eds.): *Metal-Support and Metal-Additive Effects in Catalysts* (Elsevier, Amsterdam 1982)
8.2 D.W. Goodman, R.D. Kelley, T.E. Madey, J.T. Yates,Jr.: J. Catal. **63**, 226 (1980)
8.3 G.A. Somorjai: *Chemistry in Two Dimensions* (Cornell University Press, Ithaca, NY 1981)
8.4 D.W. Goodman: Acc. Chem. Res. **17**, 194 (1984)
8.5a H.J. Krebs, H.P. Bonzel, G. Gafner: Surf. Sci. **88**, 269 (1979)
8.5b H.P. Bonzel: J. Vac. Sci. Technol. A **2**, 866 (1984) and references therein
8.6 C.T. Campbell, M. Paffitt: Surf. Sci. **139**, 396 (1984)
8.7 J.T. Yates, Jr., C.H.F. Peden, J.E. Houston, D.W. Goodman: Surf. Sci. **160**, 37 (1985)
8.8 D.W. Goodman, M. Kiskinova: Surf. Sci. **105**, L265 (1981)
8.9 M. Kiskinova, D.W. Goodman: Surf. Sci. **108**, 64 (1981)
8.10 D.W. Goodman: J. Vac. Sci. Technol. **20**, 522 (1982)
8.11 M. Kiskinova, D.W. Goodman: Surf. Sci. **109**, L555 (1981)

8.12 D.W. Goodman: Appl. Surf. Sci. **19**, 1 (1984)
8.13 J.T. Yates, C.H.F. Peden, D.W. Goodman: J. Catal. **94**, 576 (1985)
8.14 D.W. Goodman: In *Heterogeneous Catalysis*, Proc. IUCCP Conf., Texas A&M University, 1984, ed. by B.L. Shapiro (University of Texas Press, Austin, TX 1984)
8.15 S. Johnson, R.J. Madix: Surf. Sci. **108**, 77 (1981)
8.16 R.J. Madix, M. Thornburg, S.-B. Lee: Surf. Sci. **133**, L447 (1983)
8.17 R.J. Madix, S.-B. Lee, M. Thornburg: J. Vac. Sci. Technol. A **1**, 1254 (1983)
8.18 E.L. Hardegree, P. Ho, J.M. White: Surf. Sci. **165**, 488 (1986)
8.19 C. Kittel: *Introduction to Solid State Physics* (Wiley, New York, 1971)
8.20 D.W. Goodman: J. Vac. Sci. Technol. A **2**, 873 (1984)
8.21a C.H.F. Peden, D.W. Goodman: In Proc. Symp. Surf. Sci. Catal., Philadelphia, 1984, ed. by M.L. Deviney, J.L. Gland, ACS Symposium Series (American Chemical Society, Washington D.C. 1985
8.21b D.W. Goodman, C.H.F. Peden: Ind. Eng. Chem., Fundam. **25**, 58 (1986)
8.22 J.R. Rostrup-Nielsen, K. Pedersen: J. Catal. **59**, 395 (1979)
8.23 D.W. Goodman: to be published
8.24 R.D. Kelley, D.W. Goodman: *The Chemical Physics of Solid Surfaces and Heterogeneous Catalysts*, Vol.4 (Elsevier, Amsterdam 1982)
8.25 R.D. Kelley, D.W. Goodman: Surf. Sci. **123**, L743 (1982)
8.26 S.H. Oh, G.B. Fisher, J.E. Carpenter, D.W. Goodman: J. Catal., in press
8.27 D.E. Peebles, D.W. Goodman, J.M. White: J. Phys. Chem. **87**, 4378 (1983)
8.28 J.E. Houston, J.R. Rogers, D.W. Goodman, N. Belton: J. Vac. Sci. Technol. A **2**, 882 (1984)
8.29 G.M. Schwab: Discuss. Faraday Soc. **8**, 166 (1950)
8.30 D.A. Dowden: J. Chem. Soc. 242 (1950)
8.31 W.K. Hall, P.H. Emmett: J. Phys. Chem. **63**, 1102 (1959)
8.32 W.M.H. Sachtler, G.J.H. Dorgelo: J. Catal. **4**, 654 (1965)
8.33 G. Ertl, J. Kuppers: J. Vac. Sci. Technol. **9**, 829 (1972)
8.34 J. Sinfelt, J.L. Carter, D.J.C. Yates: J. Catal. **24**, 283 (1972)
8.35 F.L. Williams, M. Boudart: J. Catal. **30**, 438 (1973)
8.36 J.J. Stephan, V. Ponec, W.M.H. Sachtler: Surf. Sci. **47**, 403 (1975)
8.37 C.R. Helms, K.Y. Yu, W.E. Spicer: Surf. Sci. **52**, 217 (1975)
8.38 J.J. Burton, C.R. Helms, R.S. Polizzotti: J. Chem. Phys. **65**, 1089 (1976)
8.39 E.M. Silverman, R.J. Madix: J. Catal. **56**, 349 (1979)
8.40 V. Ponec: Surf. Sci. **80**, 352 (1979)
8.41 G.C. Bond, B.D. Turnham: J. Catal. **45**, 128 (1976)
8.42 C. Betizeau, G. Leclercq, R. Maural, C. Bolivar, H. Charcosset, R. Frety, L. Tournayan: J. Catal. **45**, 179 (1976)
8.43 S. Galvagno, G. Parravano: J. Catal. **57**, 272 (1979)
8.44 H.C. de Jongste, V. Ponec, F.G. Gault: J. Catal. **63**, 395 (1980)
8.45 K. Christmann, G. Ertl, H. Shimizu: J. Catal. **61**, 397 (1980)
8.46 H. Shimizu, K. Christmann, G. Ertl: J. Catal. **61**, 412 (1980)
8.47 J.C. Vickerman, K. Christmann, G. Ertl: J. Catal. **71**, 175 (1981)
8.48 S.K. Shi, H.I. Lee, J.M. White: Surf. Sci. **102**, 56 (1981)
8.49 L. Richter, S.D. Bader, M.B. Brodsky: J. Vac. Sci. Technol. **18**, 578 (1981)
8.50 J.C. Vickerman, K. Christmann: Surf. Sci. **120**, 1 (1982)
8.51 J.C. Vickerman, K. Christmann, G. Ertl, P. Heiman, F.J. Himpsel, D.E. Eastman: Surf. Sci. **134**, 367 (1983)
8.52 S.D. Bader, L. Richter: J. Vac. Sci. Technol. A **1**, 1185 (1983)
8.53 C. Park, E. Bauer, H. Poppa: to be published
8.54 D.W. Goodman, Jr., C.H.F. Peden, J.T. Yates: Surf. Sci. **164**, 417 (1985)
8.55 C.H.F. Peden, D.W. Goodman: J. Catal. **95**, 321 (1985)
8.56 J.E. Houston, C.H.F. Peden, D.S. Blair, D.W. Goddman: Surf. Sci. **167**, 427 (1986)
8.57 J.E. Houston, C.H.F. Peden, P.J. Feibelman, D.R. Hamann: Phys. Rev. Lett. **56**, 375 (1986)

8.58 J.H. Sinfelt, G.H. Via, F.W. Lytle: Catal. Rev.-Sci. Eng. **26**, 81 (1984)
8.59 L.J.M. Luyten, M. v. Eck, J. v. Grondelle, J.H.C. v. Hooff: J. Phys. Chem. **82**, 2000 (1978)
8.60 A.K. Datye, J. Schwnk: J. Catal. **93**, 256 (1985)
8.61 A.J. Rouco, G.L. Haller, J.A. Oliver, C. Kemball: J. Catal. **84**, 297 (1983)
8.62 G.L. Haller, D.E. Resasco, J. Wang: J. Catal. **84**, 477 (1983)
8.63 J.H. Sinfelt: J. Catal. **29**, 308 (1973)
8.64 J.H. Sinfelt: Science **195**, 641 (1977)
8.65 S. Anderson, U. Jostell: Surf. Sci. **46**, 625 (1974)
8.66 M. Kiskinova: Surf. Sci. **111**, 584 (1981)
8.67 G. Ertl: Catal. Rev.-Sci. Eng. **21**, 201 (1980)
8.68 G. Broden, G. Gafner, H.P. Bonzel: Surf. Sci. **84**, 295 (1979)
8.69 P.J. Goddard, J. West, R.M. Lambert: Surf. Sci. **71**, 447 (1978)
8.70 G. Ertl, M. Weiss, S.B. Lee: Chem. Phys. Lett. **60**, 391 (1979)
8.71 J.E. Crowell, E.L. Garfunkel, G.A. Somorjai: Surf. Sci. **121**, 303 (1982)
8.72 E.L. Garfunkel, J.E. Crowell, G.A. Somorjai: J. Phys. Chem. **86**, 310 (1982)
8.73 M.P. Kiskinova, G. Pirug, H.P. Bonzel: Surf. Sci. **140**, 1 (1984)
8.74 H.S. Luftman, Y.-M. Sun, J.M. White: Appl. Surf. Sci. **19**, 59 (1984)
8.75 G. Ertl, S.B. Lee, M. Weiss: Surf. Sci. **111**, L711 (1981)
8.76 C.T. Campbell, D.W. Goodman: Surf. Sci. **123**, 413 (1982)
8.77 D.W. Goodman, R.D. Kelley, T.E. Madey, J.T. Yates, Jr.: J. Catal. **64**, 479 (1980)
8.78 F.M. Hoffman: Surf. Sci. Rep. **3**, 107 (1983)
8.79 T.B. Grimley, S.M. Walker: Surf. Sci. **14**, 395 (1969)
8.80 T.B. Grimley, M. Torrini: J. Phys. C **8**, 868 (1973)
8.81 T.E. Einstein, J.R. Schrieffer: Phys. Rev. B **7**, 3629 (1973)
8.82 P. Feibelman, D. Hamann: Phys. Rev. Lett. **52**, 61 (1984)
8.83 R.W. Joyner, J.B. Pendry, D.K. Saldin, S.R. Tennison: Surf. Sci. **138**, 84 (1984)
8.84 P.J. Feibelman, D. Hamann: Surf. Sci. **149**, 48 (1985)
8.85 Y. Muda, T. Hanawa: Jpn. J. Appl. Phys. **17**, 930 (1974)
8.86 J. Benziger, R.J. Madix: Surf. Sci. **94**, 119 (1980)
8.87 K.H. Lau, W. Kohn: Surf. Sci. **65**, 607 (1977)
8.88 J.K. Norskov, S. Holloway, N.D. Lang: Surf. Sci. **137**, 65 (1984)
8.89 H.S. Luftman, J.M. White: Surf. Sci. **139**, 362 (1984)

9. Thermodynamics and Kinetics in Weakly Chemisorbed Phases

M. Grunze

Laboratory for Surface Science and Technology, University of Maine, Orono, ME 04469, USA

In a heterogeneous surface reaction, the reactants, intermediates, and products can be weakly chemisorbed along their respective reaction paths. For example, considering the fragmentation of a molecule into strongly adsorbed atoms, dissociation will occur out of a less strongly bonded molecular entity. But not only the importance for heterogeneous catalytic reactions stimulates the investigation of weakly chemisorbed phases, they also exhibit interesting sequences of phase transitions which are reflected in their thermodynamic functions and in the adsorption and desorption kinetics of the adsorbate. For the present purpose, we define weak chemisorption as a chemical interaction between adsorbate and substrate with a low adsorption energy ($E_B \lesssim 70$ kJ/mol), resulting in a facile balance between the interaction of the individual species with the substrate and lateral forces between the chemisorbed molecules. The distinction between "weak chemisorption" and "chemisorption" is rather arbitrary, but a difference is obvious with respect to pure physisorption involving only Van der Waals forces between adsorbate and substrate.

The facile balance between the interaction of the molecule with the corrugated substrate surface and the lateral forces coming into play at higher adsorbate densities leads to a sequence of interesting phase transitions. A survey of the results presently available for N_2 phases on nickel surfaces and CO phases on copper surfaces suggests that the observation of intermediate fluid (F) phases between the commensurate (C) and incommensurate (I) phases is related to the formation of antiphase domain walls with high local densities. These compression walls seem to be correlated to the experimental observation that N_2 and CO on the {110} and {100} surfaces of nickel and copper, respectively, can only adsorb "on top" of the substrate atom, and not in bridge positions as commonly found in more strongly adsorbed CO-phases on metals.

The order in the adsorbed phase also affects the kinetics of adsorption and desorption, thus providing convenient model systems to correlate thermodynamic and kinetic phenomena. At this time, however, changes in adsorption

and desorption kinetics at phase transitions can only be discussed phenomenologically. As one example of a chemical reaction in weakly chemisorbed phases, the transformation of weakly adsorbed N_2 on a Fe{111} surface into a more-stable bonded precursor state for dissociation will be discussed.

In this chapter, we review the experimental data and only mention theoretical results for the few examples where a correlation between experiment and theory is possible. Experimental techniques are not described; the reader is referred to the original literature or reviews for details. First, the thermodynamic and kinetic formalism describing the properties of the adsorbate phase is summarized.

9.1 Evaluation of the Isosteric Heat and Entropy of Adsorption

The thermodynamics of adsorbed phases have been reviewed recently in some excellent articles, from the points of view of both phenomenological thermodynamics and statistical mechanics [9.1-3]. Thus, here we only briefly recall the basic formalism pertinent to the subject of this chapter, and refer the reader to the cited literature for an in-depth discussion of the complete thermodynamic approaches and the statistical models involved in the description of adsorbed phases.

Under thermodynamic equilibrium conditions the chemical potentials of the gas phase (μ_g) and adsorbate phase (μ_s) are equal, and pressure, temperature, and isosteric heat of adsorption q_{st} at constant adsorbate coverage are related by the Clausius-Clapeyron equation

$$\left(\frac{\partial \ln p}{\partial T}\right)_\theta = \frac{q_{st}}{RT^2} \quad . \tag{9.1}$$

The derivation of the Clausius-Claperyon equation for the isosteric heat of adsorption is analogous to the derivation for calculating liquid/vapor equilibria in three-dimensional systems. In (9.1), p and T refer to the equilibrium pressure and temperature of the system, and the isosteric heat is defined as

$$q_{st} = h_g - \tilde{h}_s \quad , \tag{9.2}$$

$$= (S_g - \tilde{S}_s) \cdot T \quad , \tag{9.3}$$

where h_g and S_g are the enthalpy and entropy of the gas phase, and $\tilde{h}_s$ and $\tilde{S}_s$ are the partial molar enthalpy and entropy of the adsorbed phase:

$$\tilde{h}_s = \left(\frac{\partial h_s}{\partial \theta}\right)_{T,p} \qquad \tilde{S}_s = \left(\frac{\partial S}{\partial \theta}\right)_{T,p} \tag{9.4}$$

Since all heat changes caused by the gas/solid interaction are included in q_{st}, (9.1) holds irrespective of structural or chemical changes of the substrate, as long as these changes are reversible under the experimental conditions.

However, (9.1) is only valid under true thermodynamic equilibrium conditions, i.e., $\mu_g = \mu_s$ and therefore $T_g = T_s$, where T_g and T_s are the temperatures of the gas and adsorbate phases, respectively.

Since the gas temperature is constant ($T_g = 300$ K) and the substrate temperature is varied under common experimental conditions, we first examine the errors involved in using (9.1) to determine the isosteric heat of adsorption. The derivation presented here is similar to the early discussions of *Ehrlich* [9.4] and *Procop* and *Völter* [9.5] on the same problem.

The isobaric experiments are conducted under steady state conditions, where the rate of adsorption r_{ad} is equal to the rate of desorption r_{des}. The rate of adsorption is given by

$$r_{ad} = s^{T_g}(\theta)\frac{p}{(2\pi m k T_g)^{1/2}} \quad , \tag{9.5}$$

where $s^{T_g}(\theta)$ is the sticking coefficient at a gas temperature of T_g and p is the measured pressure in the system. Since equilibrium measurements, and hence desorption at equilibrium, occur at a substrate temperature T_s, we need to calculate r_{ad} for T_s. The same coverage θ produced by a gas of temperature T_g can be established at a gas temperature T_s at a corrected pressure p', with a rate of adsorption

$$r_{ad} = s^{T_s}(\theta)\frac{p'}{(2\pi m k T_s)^{1/2}} \quad . \tag{9.6}$$

This means that we can define a hypothetical equilibrium pressure p' which gives the same adsorption rate as the one with the measured pressure for the gas at $T_g = 300$ K. Since the rate of adsorption at $T_g = 300$ K and $T_g = T_s$ have to be equal, it follows that

$$p' = p \cdot \frac{s^{T_g}(\theta)}{s^{T_s}(\theta)} \cdot \frac{\sqrt{T_s}}{\sqrt{T_g}} \tag{9.7}$$

Inserting the hypothetical equilibrium pressure p' (9.7) into (9.1) and differentiating with respect to T_s (now, for p', $T_s = T_g$), it follows after

rearranging that

$$\left(\frac{\partial \ln p}{\partial T_s}\right)_{(\theta)} = \frac{q_{st}}{RT_s^2} + \frac{1}{2T_s} - \left(\frac{\partial \ln(s^{T_g}/s^{T_s})}{\partial T_s}\right)_{(\theta)} = \frac{q_{st}^{Exp}}{RT_s^2} \tag{9.8}$$

Thus, the isosteric plots (ln p versus $1/T_s$) constructed with the equilibrium pressure at $T_g = 300$ K give an apparent isosteric heat q_{st}^{Exp} which is higher than the true equilibrium isosteric heat (~2% for the system considered here), provided that the sticking coefficient does not depend on gas temperature,

$$q_{st}^{Exp} = q_{st} + \frac{RT_s}{2} \quad . \tag{9.9}$$

For the adsorption systems discussed here, experiments are conducted at $T_s < T_g$ and s is close to unity at $T_g = 300$ K, and it can be safely assumed that s is not different at a lower gas temperature. However, in the case of gas-temperature-dependent sticking coefficients, such as for activated adsorption, the corrections necessary to deduce the true equilibrium isosteric heat can be substantial.

The partial molar entropy of the adsorbate phase can be determined from [9.1-3,5]

$$\begin{aligned} \tilde{S}_s &= S_g + \Delta\tilde{S} \\ &= S_g^o - R \ln\left(\frac{p}{p_o}\right) - \frac{q_{st}}{T} \quad , \end{aligned} \tag{9.10}$$

where $\Delta\tilde{S}_s$ is the differential entropy of adsorption, S_g is the entropy of the gas phase at pressure o, p is the equilibrium pressure and q_{st}/T the isosteric heat divided by the temperature ($T = T_s$), i.e., the entropy loss of the gas upon adsorption. For $T_g \neq T_s$, we have to use p' as the equilibrium pressure and T_s instead of T in (9.10).

Then, substituting (9.7,9) into (9.10), the differential entropy of the adsorbed layer corrected for $T_s \neq T_g$ (and assuming that s does not depend on gas temperature) is given by

$$\tilde{S}_s = S_g^o - R \ln\left(\frac{p}{p_o}\right) - \frac{q_{st}^{Exp}}{T_s} - \frac{R}{2}\left(\ln\frac{T_s}{T_g} + 1\right), \tag{9.11}$$

as derived before by *Procop* and *Völter* [9.5].

Again, the corrections to our experimental values necessary to determine the entropy in the adsorbed layer from our steady-state experiments are

small, and negligible considering the experimental errors inherent in these measurements.

Summarizing the above considerations; it can be shown that the experimental isosteric heats and entropies derived from steady-state experiments will be close to the thermodynamic values obtained under true equilibrium conditions, in the adsorption systems discussed here. We realize, however, that these considerations are not for the real experimental conditions where the adsorption isobars are measured under flow conditions, i.e., when a constant pressure is maintained by dosing the gas into a continuously pumped vacuum chamber.

A correct thermodynamic description has to consider that in a nonisothermal system, matter flow produces an inevitable entropy change, which is related to the heat of transfer Q [9.6]. Prigogine has considered these questions from the viewpoint of kinetic theory and statistical mechanics [9.6], but no reasonable prediction of the magnitude of the effect is possible for the ill-defined matter and heat flow conditions in typical ultra-high-vacuum (UHV) or high-vacuum measurements.

9.2 Correlation Between Thermodynamic and Kinetic Experiments

Desorption experiments have been carried out for several weakly chemisorbed adsorbed phases, and the rate of desorption for molecularity 1 is conveniently described by an Arrhenius-type rate equation

$$r_d = \nu(\theta) N_s \exp\left(-\frac{E_d(\theta)}{RT}\right), \tag{9.12}$$

where $\nu(\theta)$ is the preexponential term in the rate equation, $E_d(\theta)$ the coverage-dependent activation energy of desorption, and N_s the surface density of adsorbate. Several reviews [9.7-10] discuss the applications and limitations of desorption experiments and the refined rate equations for desorption via precursor states. At this point, we only want to summarize how thermodynamic and kinetic parameters are interrelated, following a previous discussion by *Menzel* [9.10].

Under steady-state conditions the rate of adsorption r_{ad} is equal to the rate of desorption. Then, (9.5) and (9.12) can be combined and the preexponential term of desorption is given by

$$\nu(\theta) = s(\theta) \frac{p}{(2\pi m k T_g)^{1/2}} \frac{1}{N_s} \exp\left(\frac{E_d(\theta)}{RT_s}\right) \tag{9.13}$$

$$= s(\theta)\, V_{T_g} \frac{N_g}{N_s} \exp\left(\frac{q_{st}}{RT_s}\right) \quad . \tag{9.14}$$

In (9.14), the thermal velocity $V_T = (kT/2\pi m)^{1/2}$ and the density of the gas phase N_g have been used to express the impingement rate per surface area, and it has been assumed that adsorption is not activated and the activation energy of desorption is equal to the isosteric heat of adsorption. While the assumption of nonactivated adsorption is reasonable for those systems discussed here, the assumed equality of $E_d(\theta)$ and q_{st} neglects the possible influence of precursor kinetics on the desorption energy [9.10] and the correction term (1/2) RT necessary for a comparison of the equilibrium and kinetic expression of the logarithmic derivative of the equilibrium pressure [9.4].

Under equilibrium conditions, i.e., $T_g = T_s$,

$$\frac{N_g}{N_s} = \frac{Q_g}{Q_s} \exp\left(-\frac{q_{st}}{RT}\right), \tag{9.15}$$

where we associate the potential energy in the exponential term with the isosteric heat of adsorption. Here, Q_g and Q_s are the partition function of the three-dimensional gas and the partition function of the adsorbed phase. The partition function of the gas phase is the product of the partition function of the individual degrees of freedom $Q_g = q_{tr}^3\, q_{vib}\, q_r$ (tr = translation, vib = vibrations, r = rotations). For the adsorbate phase, Q_s includes, in addition to the partition function of the degrees of freedom of the adsorbed molecules, the statistics of the adlayer and possible changes in the surface phonon spectrum of the substrate upon adsorption.

It follows then that

$$\nu(\theta) = s(\theta)\, V_T \frac{Q_g}{Q_s} \qquad \text{or} \tag{9.16}$$

$$\nu(\theta) = s(\theta) \frac{kT}{h} \frac{q_{tr}^2\, q_{vib}\, q_r}{Q_s}\,, \tag{9.17}$$

where, depending on the degrees of freedom in the adlayer in the models considered, different values for $\nu(\theta)$ can be obtained [9.10]. From (9.17) it also follows that for a completely mobile molecule with the same vibrational and rotational excitations as in the gas phase, and for $s = 1$, the commonly taken preexponential of $\sim 10^{13}\ s^{-1}$ is derived. *Ibach* et al. [9.11] and *Menzel* [9.10] have shown, however, that such a choice for $\nu(\theta)$ is not realistic for chemisorption systems.

The relation between the entropy in the adsorbate phase and the preexponential is made obvious by considering (9.14) with (9.10) or when the partition functions of the gas phase and the adsorbate phase in (9.17) are expressed by the respective entropies [9.1]. Hence, if the sticking coefficient is known and does not vary strongly in the temperature range of interest, desorption experiments can be used to derive information about the equilibrium entropy of the adlayer and vice versa. However, good agreements between $\nu(\theta)$ derived from desorption experiments and from equilibrium measurements is expected only when desorption is not activated and occurs out of the equilibrium configuration of the adlayer. This has been shown for CO on Ru{0001} by *Pfnür* et al. [9.12,13] and for H_2 on W{100} by *Horlacher Smith* et al. [9.14].

9.3 Structural and Thermodynamic Data on Weakly Chemisorbed Phases

Classical adsorption studies are carried out on large surface area substrates, where a high degree of accuracy in determining the amount of adsorbed gas as a function of temperature and pressure is obtained by volumetric or even gravimetric methods. However, present adsorption studies in surface science are restricted not only by the smaller surface area of the substrate, but also by the pressure range in which experiments can be carried out. Therefore, the surface coverage has to be measured by surface-sensitive probes rather than by observing the pressure decrease or weight gain due to sorption. In the case of weakly chemisorbed phases discussed here, the disturbing effect of the probe on the surface coverage or composition has also to be considered, restricting the time over which experimental observations can be made in LEED or other experiments involving electron probes [9.15,16].

In the following we show the feasibility of several surface-science techniques to determine the isosteric heat of adsorption and the entropy in the adlayer in weakly chemisorbed phases and correlate the thermodynamic quantities with structural information, where available. Since changes in q_{st} or $\tilde{S}_{ad}$ are related to structural changes in the layer, the latter are summarized first. Our discussion focuses on nitrogen adsorption on nickel surfaces and carbon monoxide adsorption on copper substrates as typical model systems.

9.3.1 Phase Diagram for N_2 Adsorbed on Ni{110} and Data for N_2 on Ni{100}

Molecular nitrogen adsorption on Ni{110} surfaces has been studied by low-energy electron diffraction (LEED) [9.15,16], photoelectron spectroscopies

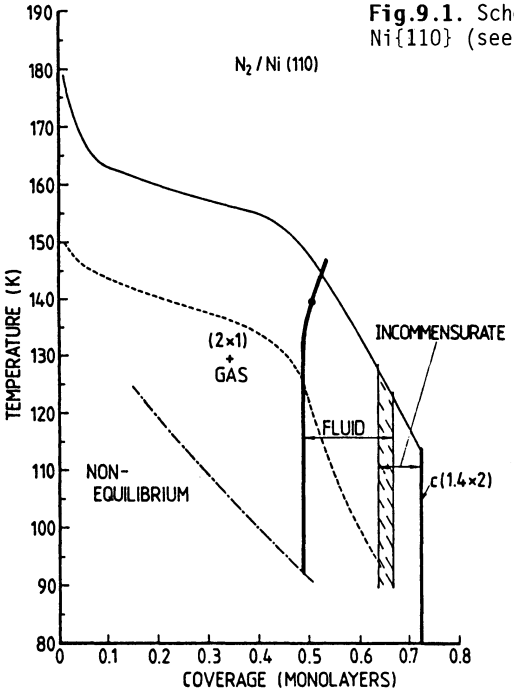

Fig.9.1. Schematic phase diagram for N_2 on Ni{110} (see text for explanation)

[X-ray (XPS) and ultraviolet (UPS)] [9.17-19], low-energy ion scattering spectroscopy (ISS) [9.20], work function measurements ($\Delta\phi$)[9.21], temperature programmed desorption spectroscopy (TPD)[9.22], and vibrational spectroscopy {infrared reflection-absorption spectroscopy (IRAS)[9.21] and high-resolution electron energy loss spectroscopy (HREELS) [9.18,23]}. A convenient starting point for our discussion of structure and thermodynamic quantities is the temperature versus coverage (T,θ) phase diagram for N_2 on Ni{110} [9.15] as shown in Fig.9.1. The full curve in Fig.9.1 is an adsorption isobar for a pressure of 1.3×10^{-6}mbars and represents the upper limit of our equilibrium studies. Below the dashed curve, N_2 is irreversibly adsorbed and an N_2 background pressure is not required to maintain a given coverage. Gas-adsorbate phase equilibrium measurements were made between the full and dashed curves and used to determine thermodynamic quantities. Below the dot-dashed line, long relaxation times precluded equilibrium studies. The LEED patterns observed as a function of coverage and temperature in this phase diagram have been published [9.15] and we only summarize the observations here.

At coverages below one-half monolayer, a disordered gas phase and an ordered (2×1) phase coexist. The (2×1) phase reaches maximum ordering near

one-half monolayer coverage. The θ-axis was calibrated by taking $\theta = 0.5$ to correspond to the maximum intensity of the (1/2,0) beam in the (2×1) structure with the surface in equilibrium with N_2 gas at a pressure of 2×10^{-7}mbar. This point is indicated in Fig.9.1 by the solid dot at $\theta = 0.5$, T = 140K. All other coverages were then determined with respect to this reference point, with $\theta = 1$ corresponding to an N_2 density of 1.15×10^{15}cm^{-2}.

The coverage at which maximum intensity in the (2×1) structure occurred for other experimental conditions is shown in Fig.9.1 by the heavy solid line passing through the calibration point. This line was drawn without curvature in previous publications [9.15]. Clearly the number of N_2 in the best ordered (2×1) structure can be increased at higher temperatures and pressures, meaning that even the best ordered (2×1) phase must contain some imperfections. This, plus the initial appearance of corresponding broad diffuse beams with high diffuse background intensity, indicates that ordered (2×1) islands, with somewhat better ordering along $\langle \bar{1}10 \rangle$ rows, nucleate and grow out of a disordered two-dimensional sea of adsorbed N_2 molecules. As discussed in Sect.9.3.4, evidence for intrinsic higher-energy binding sites which could act as nucleation sites for (2×1) islands is obtained from the low-coverage ISS data.

Since there are two equivalent (2×1) sublattices on a flat {110} surface and four on a surface with steps, only about one-half of the islands will grow together without the formation of antiphase boundaries. As the coverage is increased above that necessary to form the best ordered (2×1) phase, the "banana" phase forms, in which curved diffuse streaks connect the 1/2 order beams. With increasing coverage the LEED beams evolve smoothly from the banana pattern into a disordered incommensurate structure showing streaks at the {2/3, 1/2} positions. This structure, which can be explained by symmetry equivalent domains of a $\begin{pmatrix} 1 & \bar{1} \\ 2 & 1 \end{pmatrix}$ structure, compresses with increasing coverage until a $c(1.4 \times 2)$ pattern is reached at the highest coverage accessible in these experiments ($\theta \sim 0.72$). Nitrogen pressures greater than 10^{-6}mbar and low temperatures are required to develop this structure fully.

The sequence of LEED patterns observed indicates a commensurate-incommensurate phase transition via an intermediate fluid phase, as predicted by theory for uniaxial systems. The theory of commensurate-incommensurate phase transitions for such systems has been reviewed in detail by *Bak* [9.24,25], and we only want to recall some of the major considerations pertinent to the N_2/Ni{110} system. Initially, at low coverages and sufficiently low temperatures, the adsorbed monolayer forms an ordered (2×1) structure which is commensurate with the crystal surface. Increasing the coverage will then lead

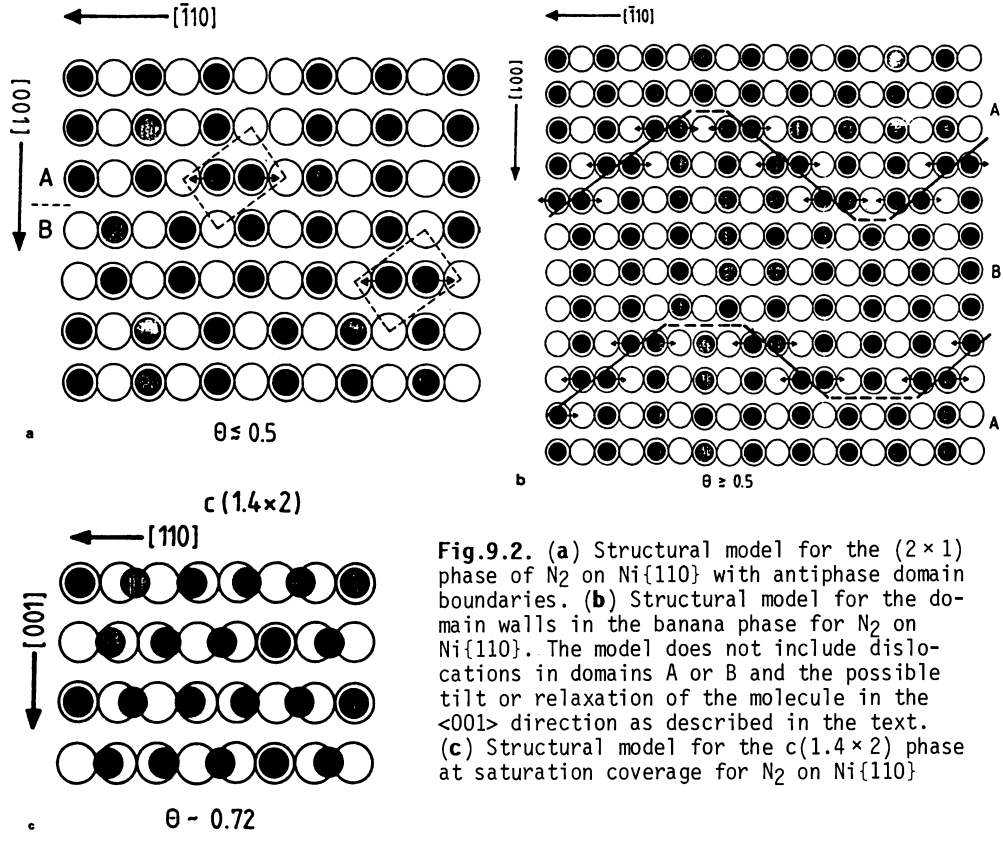

Fig.9.2. (**a**) Structural model for the (2 × 1) phase of N_2 on Ni{110} with antiphase domain boundaries. (**b**) Structural model for the domain walls in the banana phase for N_2 on Ni{110}. The model does not include dislocations in domains A or B and the possible tilt or relaxation of the molecule in the <001> direction as described in the text. (**c**) Structural model for the c(1.4 × 2) phase at saturation coverage for N_2 on Ni{110}

to the situation where the monolayer has to contract and thus becomes incommensurate with the arrangement of the substrate. For a uniaxial symmetry of the substrate and a (p × 1) commensurate phase (in our case, p = 2), it is predicted that the incommensurate phase near the commensurate phase takes the form of a stripped soliton or domain wall structure. For p = 2, this domain wall structure occurring between the C and I phase is unstable with respect to free dislocations at any finite temperature (T > 0) and is thus described as a "soliton liquid" [9.24]. In Fig.9.2 we show possible models for (a) the commensurate (2 × 1) phase at $\theta \lesssim 0.5$, (b) the intermediate liquid, and (c) the final c(1.4 × 2) phase. Fig.9.2a shows antiphase domains and how they could act as nucleation sites for domain walls by inserting an additional molecule leading to a locally higher density. Figure 9.2b then shows schematically how these intrinsic defects in the commensurate phase develop into domain walls separating commensurate areas of the surface structure. It is important to note that these domain walls are highly mobile and cannot be

considered as a frozen-in disorder. Recent kinematic LEED calculations by *Moritz* [9.26], explaining the diffraction pattern from the banana phase, require the direction of the domain walls to switch coherently, as indicated in the model of Fig.9.2b. In Fig.9.2a,b relaxation of the molecules in the wall is indicated by the arrows. This relaxation can involve lateral movement of the molecules from exact "on top" positions and/or a tilt of the molecular axis away from the surface normal to minimize the strong repulsive forces between the N_2 molecules. The Van der Waals radius of a N_2 molecule is ~ 3.5 Å, the next-nearest-neighbor separation in an unrelaxed wall would be 2.56 Å. A slight tilt and relaxation of the molecules by ~ 0.4 Å in the $\langle 1\bar{1}0 \rangle$ direction or an opposite tilt in $\langle 001 \rangle$ maintaining the coordination to a single Ni atom would allow two N_2 molecules to be bonded to two neighboring Ni atoms on top of the $\langle 1\bar{1}0 \rangle$ rows.

The sequence of LEED patterns observed between the banana phase and the final $c(1.4 \times 2)$ structure can be explained by increasing the density of domain walls, leading to the elimination of (2×1) domains and finally, due to the repulsive interactions, to the relaxation of the whole layer into the incommensurate $c(1.4 \times 2)$ phase. A plausible model for this phase is shown in Fig.9.2c.

The observation that the banana pattern transforms into a disordered structure which is streaked in the $\langle 001 \rangle$ direction indicates that the coherence in this direction is lost. It is thus expected that correlated fluctuation of domain walls in the $\langle 001 \rangle$ direction producing a banana-shaped LEED pattern requires large defect-free crystalline areas on the substrate. Recent experiments [9.27] on a stepped Ni{110} 9.46° $\langle 110 \rangle$ surface confirm that a minimum correlation length is required to produce a banana pattern, since only a $p(2 \times 1)$ phase which developed into straight streaks along $\langle 001 \rangle$ and moved smoothly with increasing coverage into the $[\pm(|h| + 2/3), k + 1/2]$ position was observed [9.27].

For N_2 adsorption on Ni{100}, a $c(2 \times 2)$ phase was observed throughout the whole coverage range [9.28]. Diffuse overlayer beams are formed at coverages exceeding $\theta \sim 0.25$ and can be changed to a relatively sharp $c(2 \times 2)$ pattern by annealing the sample in a nitrogen ambient at $T \geq 90$ K or by cooling in a nitrogen ambient. In the annealed $c(2 \times 2)$ pattern, the correlation length ξ is ~ 34 Å, indicating the presence of antiphase domain boundaries preventing the formation of long-range order [9.28]. There was no change in overlayer LEED pattern at the highest coverages obtainable in a nitrogen ambient. Since the size of the $c(2 \times 2)$ unit cell is 12.4 $Å^2$ and approximately equal to the size of the $c(1.4 \times 2)$ unit cell (12.2 $Å^2$) found at saturation cov-

erage on the Ni{100} surface, the c(2 × 2) layer corresponds to a densely packed N_2 layer. However, as described in Sect.9.3.2, the presence of antiphase domain boundaries in the c(2 × 2) phase with locally higher coverages can lead to a fluidlike behavior, as predicted by theory [9.29].

9.3.2 The Isosteric Heat of Adsorption and the Entropy in the Adsorbed Phase for N_2/Ni{110} and N_2/Ni{100}

The phase transitions for N_2 on Ni{110} are reflected in the thermodynamic quantities. Before we summarize these results, we point out, that the nitrogen molecules adsorb throughout the whole coverage range on Ni{110} with their molecular axis on average perpendicular to the surface plane. This follows from the photoemission [9.17,18], infrared reflection absorption [9.21], and HREELS [9.18,23]data. Further, the nitrogen molecule seems to be bonded to a single nickel atom on top of the densely packed $\langle 1\bar{1}0 \rangle$ rows [9.18,20], at least in the coverage range below the c(1.4 × 2) structure. For the saturated monolayer structure, no experimental data are available to infer the coordination of the molecules. A detailed discussion of nitrogen bonding to nickel is given by *Horn* et al. [9.18].

For nitrogen adsorbed on Ni{110}, the effect of photon radiation in valence band photoemission (UPS) studies or in X-ray photoemission (XPS) experiments was found to be negligible during the time, necessary to record adsorption isotherms or isobars [9.17]. In general, XPS is a particularly useful technique to determine relative surface coverages, since the cross section for photoemission is not sensitive to the bonding configuration of the adsorbate. Figure 9.3 shows a sequence of N1s photoelectron spectra as a function of coverage for nitrogen adsorption on a Ni{110} surface [9.17]. The doublet structure in the N1s peak is explained by final-state effects in the photoemission process of nitrogen molecules bonded with their molecular axis, on average, perpendicular to the surface plane [9.30]. The peak at the lower binding energy corresponds to emission from a "screened" final state, the one at the higher binding energy to emission from the "unscreened" final state [9.30]. For substrate temperatures near 110 K, it was established that the peak intensity at 406.7 eV was directly proportional to the integrated area under the total N1s spectrum and thus is a measure of the relative N_2 coverage. This proportionality also indicates that in the coverage regime studied the nitrogen molecule does not change its principal bonding configuration in the adsorbed layer. Thus, the intensity of the N1s emission at 406.7 eV can be monitored continuously to obtain adsorption isotherms or isobars. A set of adsorption isobars recorded by this technique may then be used to determine the isosteric heat of adsorption as shown in Fig.9.4.

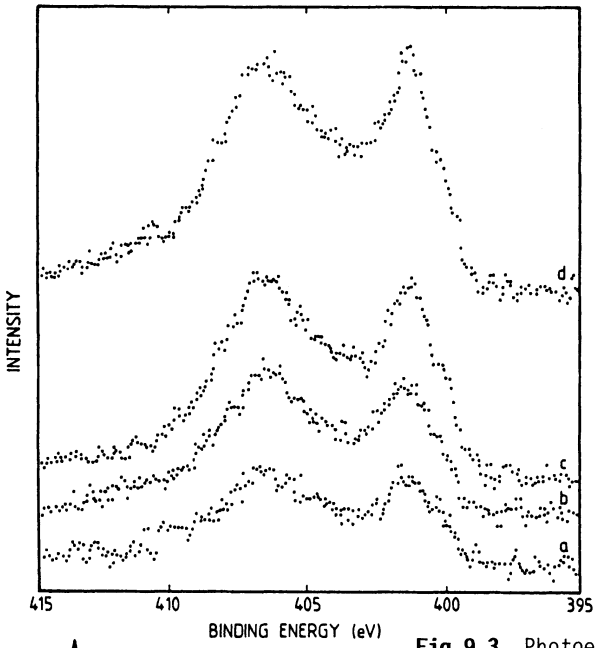

Fig.9.3. Photoelectron (N1s) spectra of N_2 on Ni{110} as a function of exposure and sample temperature: (*a*) T = 130 K, 0.4 L; (*b*) T = 130 K, 1.1 L; (*c*) T = 130 K, 2.3 L; (*d*) T = 105 K, 2.3 L

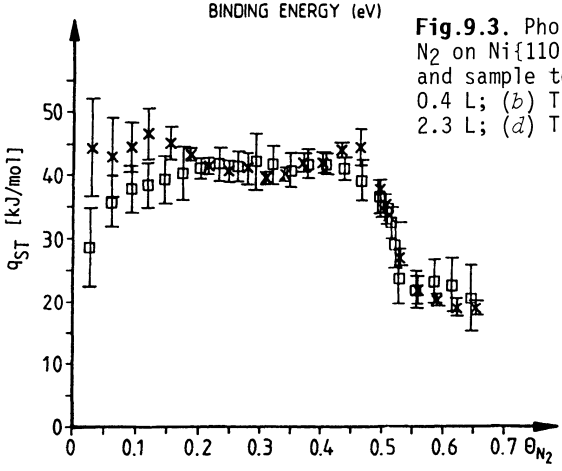

Fig.9.4. The isosteric heat of adsorption of N_2 on Ni{110} deduced from N1s isobars as described in the text

Reproduction of the results is difficult at the low coverages, due to the low signal-to-noise ratio in the data but also because of the presence of defects, as discussed later in Sect. 9.3.4.

Jacobi and *Rotermund* [9.19] showed that the attenuation of the Ni d-band emission on Ni{110} measured by angle-resolved UPS during adsorption of nitrogen is directly proportional to nitrogen coverage and thus can also be used to obtain adsorption isobars. This proportionality was explained by incoherent scattering of d-band photoelectrons in the adsorbate layer. For the

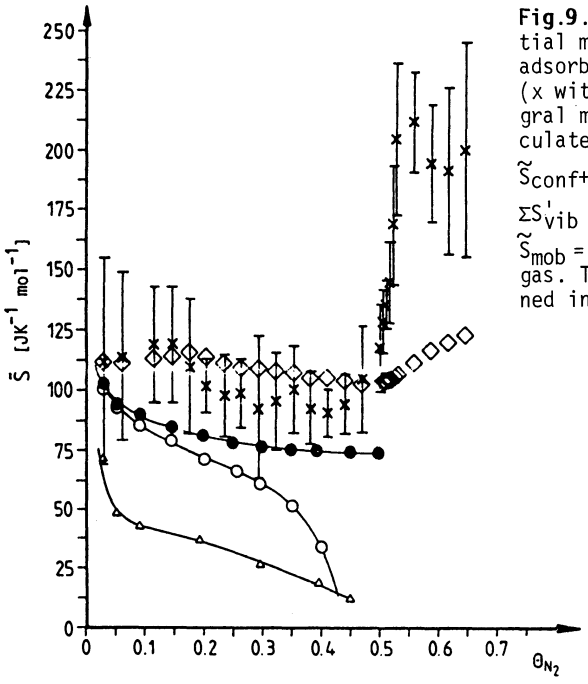

Fig.9.5. Comparison of the partial molar entropy $\tilde{S}_{ad}$ of the adsorbed N_2 layer on Ni{110} (x with error bars) and the integral molar entropy (◇) with calculated entropy values (△): $\tilde{S}_{loc} = \tilde{S}_{conf} + \Sigma\tilde{S}_{vib}$; (•) : $\tilde{S}_{mob} = \tilde{S}^{2D}_{trans} + \Sigma S'_{vib}$ for an ideal 2D gas; (○): $\tilde{S}_{mob} = \tilde{S}^{2D}_{mob} + \Sigma S'_{vib}$ for a Volmer gas. The abbreviations are defined in the text

N_2/Ni{110} system the isosteric heats recorded by UPS isobars proved to be in excellent agreement with the XPS data, except for the high-coverage region where the isosteric heat decreases sharply [9.16]. This discrepancy seems to indicate that the attenuation of the Ni d-band intensity is not a good measure of the N_2 coverage when structural changes in the adsorbed phase occur at the higher coverages.

The isoteric heats for N_2 on Ni{110} can be used to calculate the differential entropy in the adsorbed layer according to (9.11). Figure 9.5 also shows the integral entropy of the adsorbed phase obtained from

$$S_s = \frac{1}{\theta}\int_0^{\theta} \tilde{S}_s d\theta \qquad (9.18)$$

and calculations based on statistical mechanics models discussed below. Considering only the higher initial q_{st} values from Fig.9.4, the differential and integral entropy remains approximately constant up to half-monolayer coverage. The differential entropy rises steeply at the C-F transition to a value of ~200 J K^{-1}mol^{-1}, the integral entropy increases by ~20 J K^{-1}mol^{-1}. Using the low q_{st} values at θ<0.2, the inital entropy $\tilde{S}_s$ is 175 J K^{-1}mol^{-1}.

The statistical mechanics models used to calculate the entropy in the adsorbed phases are described in detail in [9.1,2], and their application

to N_2 adsorption (on Ni{100}) is presented in [9.28]. We therefore only summarize these models here and refer the interested reader to the original literature.

In all the models used, only degrees of freedom of individual molecules and the configurational part of the entropy are included. Modeling of collective exitations, as required to describe the entropy of the fluid like domain boundaries, has not been carried out to our knowledge for weakly chemisorbed phases. We will compare the partial molecular entropy $\tilde{S}_s$ with statistical models; a discussion of the integral molar entropy S_s would allow us to derive the same results [9.28]. For localized adsorption, the differential molar entropy in the adsorbed layer is given by

$$\tilde{S}_{loc} = \tilde{S}_{conf} + \sum \tilde{S}_{vib} ,$$

where $\tilde{S}_{conf}$ is the differential configurational entropy caused by the distribution of the molecules on the adsorption sites and $\sum \tilde{S}_{vib}$ is the differential entropy contribution from the vibrational modes of the adsorbate complex. With the assumptions that the *substrate is not affected by adsorption*, that the adsorbed molecules do not interact with each other, and that one nitrogen blocks two surface sites in the coverage regime $\theta \leqslant 0.5$, the differential molar configuration entropy is given by

$$\tilde{S}_{conf} = R\left(\ln 2 - \ln \frac{\theta^*}{1-\theta^*}\right) ,$$

where $\theta^* = \theta_{max}$ for the particular phase considered (e.g., $\theta^* = 1$ for $\theta = 0.5$). As long as the energies of vibration $h\nu_i$ are independent of the coverage, the vibrational entropy $\sum \tilde{S}_{vib}$ is given by the sum of

$$\tilde{S}_{vib} = R\left(\frac{h\nu_i/kT}{\exp(h\nu_i/kT) - 1} - \ln\left[1 - \exp(h\nu_i/kT)\right]\right)$$

for each vibrational degree of freedom. The two vibrational modes normal to the surface have been determined experimentally for N_2 on Ni{110} at 115 K and were found to be independent of coverage, $\nu(Ni\text{-}N_2)$ = 339 cm^{-1} and $\nu(N \equiv N)$ = 2194 cm^{-1} [9.18,23]. The entropy contribution from the $\nu(Ni\text{-}N_2)$ mode at T = 150 K is only S_{vib} = 1.4 JK^{-1} mol^{-1}, and the contribution from $\nu(N \equiv N)$ mode is even smaller. No experimental data are available for the vibrations parallel to the surface, which are two frustrated rotational and two frustrated translational modes. For a two-dimensional phase they are expected to be low-frequency modes and therefore will each contribute to the vibrational entropy. To estimate this entropy contribution, values calculated by *Richardson* and *Bradshaw* [9.31] for the vibrational modes of linearly bonded CO on Ni{100}

have been used, and give, together with the known N_2 vibrational modes, $\sum \tilde{S}_{vib} = 23\ JK^{-1}mol^{-1}$. The estimated values for $\sum \tilde{S}_{vib}$ are considered as a lower limit, since the frustrated rotations and translations will be softer for N_2 on nickel because of the weaker bond to the substrate. An upper limit for the vibrational entropy is obtained by considering the free rotation of a N_2 molecule in a hemisphere (one nitrogen atom fixed to the substrate). The resulting rotational entropy contribution is $\sim 40\ JK^{-1}mol^{-1}$ at 130 K [9.32]. Allowing free rotation in a solid angle of 20° [which is more realistic considering the packing density of N_2 in (2×1) islands], the rotational entropy contribution is $\sim 10\ JK^{-1}mol^{-1}$ [9.32].

If the adsorbed gas is nonlocalized, the differential molar entropy in the adsorbed layer is $\tilde{S}_{mob} = \tilde{S}^{2D}_{trans} + \sum \tilde{S}'_{vib}$ where the entropy contribution from the vibrational modes $\sum S'_{vib}$ is reduced by the frustrated translations, since this mode is transformed into a two dimensional translation. If we assume that the surface gas is ideal, i.e., the molecules have no eigen-volume, the differential molar entropy of translation is given by [9.2]

$$\tilde{S}_{trans} = R \ln \left(\frac{MTb}{\theta^*}\right) + 267\ JK^{-1}mol^{-1} \quad ,$$

where M is the molecular weight of the molecule, b is the surface area per molecule at saturation coverage of the (2×1) phase and MTb/θ^* is expressed in $K^{-1}cm^2$. If the full area occupied by a molecule is taken into account (Volmer gas), the differential molar entropy of translation is [9.2]

$$\tilde{S}_{trans} = R \ln \left[(1-\theta^*)\left(\frac{MTb}{\theta^*}\right)\right] - \frac{R}{1-\theta^*} + 275\ JK^{-1}mol^{-1} \quad ,$$

with MTb/θ^* once again in $K^{-1}cm^2$.

In Fig.9.5 we included the differential molar entropy of localized ($\tilde{S}_{loc}$) and nonlocalized adsorption ($\tilde{S}_{mob}$) for an ideal gas and a Volmer gas including the respective vibrational entropy contribution.

In the following, we discuss the relation between the experimental entropy values and calculated entropies. We recall that, in the models outlined above, changes in surface structure (reconstruction or relaxation) or changes in the phonon spectrum of the substrate upon adsorption are not considered.

At $\theta < 0.1$, the experimental entropies deduced from the high q_{st} values in Fig.9.4 can be explained by the calculated entropy for a two-dimensional gas plus a vibrational entropy contribution of $10 - 20\ JK^{-1}mol^{-1}$. An initial value of $\tilde{S}_s \sim 175\ JK^{-1}mol^{-1}$, as would follow from the low q_{st} values, requires the postulation of almost free rotation in a hemisphere for the adsorbed molecule. With increasing coverage, the experimental entropies are somewhat higher than

those calculated for the *ideal* two-dimensional gas and become completely inconsistent with the calculated entropy of a two-dimensional Volmer gas. In the coverage regime where large deviations between experimental entropies and those of the Volmer gas model occur, p(2 × 1) island formation is observed and the densities in the adsorbed layer are much too high to be realistically described by an ideal two-dimensional gas. In particular for $\theta \gtrsim 0.5$, it is impossible to explain the high entropy values with the degrees of freedom of individual molecules, and we have to postulate that collective excitations in the adsorbed phase cause the high entropy values. As discussed in detail in [9.28] for N_2/Ni{100}, where abnormally high entropy values at saturation coverage were also found, we suggest that the presence of domain walls which are unstable with respect to free dislocations and, therefore, lead to pronounced density fluctuations in the two-dimensional phase, cause the high entropy values observed for $\theta \gtrsim 0.5$. The configurational entropy increase due to the domain walls in an otherwise ordered surface phase is at maximum $S_{conf} = R \ln 2$, which is much too small to explain the total entropy for N_2 on Ni{110} at $\theta > 0.35$. However, if addition or a softening of vibrational modes is associated with the fluctuations of the domain wall, a substantial entropy increase can result. In general, these low frequency modes need not be vibrational states associated with single species but could be collective longitudinal or transverse modes of the surface layer. Contrary to the individual vibrational modes, these collective modes will show dispersion, and are best described by a frequency spectrum; the difference is analogous to the distinction between the Einstein and Debye theories of lattice vibrations. The density of vibronic states must be known in order to estimate the entropy contribution of the meandering domain walls. Since the frustrated rotations of individual molecules are expected to have frequencies of ~50-100cm^{-1} [9.31], coupled rotational modes will lead to vibronic states at even lower wave numbers. For the incommensurate phase near the C-I transition, *Bak* [9.25] reviewed the theory of low-lying modes corresponding to a modulation of the phase of periodic structure (phasons). These phonon modes in the soliton lattice are very soft because of an exponentially weak interaction between the walls and will thus contribute significantly to the entropy in the adsorbed layer.

The high-coverage entropy for N_2 on Ni{100} also shows a behavior indicative of collective excitations in the adsorbed phase and was rationalized in terms of antiphase domain boundaries formed at saturation of the c(2 × 2) structure [9.28].

Before we discuss results for CO phases on Cu single-crystal surfaces, we would like to point out again that for N_2 on Ni{110} no experimental evidence exists for any adsorption sites other than those for singly coordinated linearly bonded N_2. In [9.28] arguments were given favoring these adsorption sites also on Ni{100}, suggesting that in the high-coverage regime the molecules are locally compressed at antiphase domain boundaries.

9.3.3 Carbon Monoxide on Low-Index Copper Single Surfaces

We continue our discussion on the thermodynamics of weakly chemisorbed phases by reviewing the data for CO adsorption on Cu{110}, Cu{100}, and Cu{111} [9.33-36] to point out common features in adsorption systems having high entropy values at saturation coverage (Cu{100} and Cu{110}). On Cu{100} and Cu{110} a careful search for adsorption sites other than linearly bonded CO on "on-top" positions of copper atoms was not successful [9.37,38]. On Cu{111} only recently, a bridge-bonded CO molecule was detected by *Hayden* et al. at $\theta > 0.33$ [9.36] and the entropy values deduced from the published data behave "normally", i.e., do not require the postulation of low-frequency collective modes in the adsorbate phase. As detailed below, the structural models developed from LEED data for CO on Cu{100} and Cu{110} include continuous antiphase domain walls with high local densities [9.39], whereas the structural model for CO on Cu{111} does not [9.37]. This suggests that, for the adsorbate phases considered here, the high entropy values, which are explained by a fluidlike behavior of fluctuating domain walls, are associated with adsorbate phases in which only one specific adsorption site is populated throughout the whole coverage range.

Thermodynamic data for CO adsorption on copper surfaces have been reported by *Pritchard* and co-workers [9.33,35] and *Tracy* [9.34]. *Pritchard* et al. [9.33,35] used work function measurements with a vibrating capacitor to record adsorption isobars for CO on Cu single crystal surfaces to determine the heat of adsorption. A common feature of the work function changes in the adsorption systems discussed here (including N_2 on Ni{110}[9.21]) is that the work function goes through a minimum with increasing coverage and almost reaches the value for the clean surface at saturation coverage. An example of such behavior is shown in Fig.9.6 from the study of *Hollins* and *Pritchard* [9.35] on the work function change upon CO adsorption on Cu{111}. Figure 9.6a shows the work function change as a function of exposure at 81 K, Fig.9.6b is the desorption isobar recorded in a CO ambient of $p_{CO} = 2.6 \times 10^{-7}$ Torr. As described by Hollins and Pritchard, the adsorption curve from zero to the $\Delta\phi$ minimum could be accurately reproduced at widely different rates of adsorption, whereas beyond the minimum the apparent $\Delta\phi$ dependence on exposure

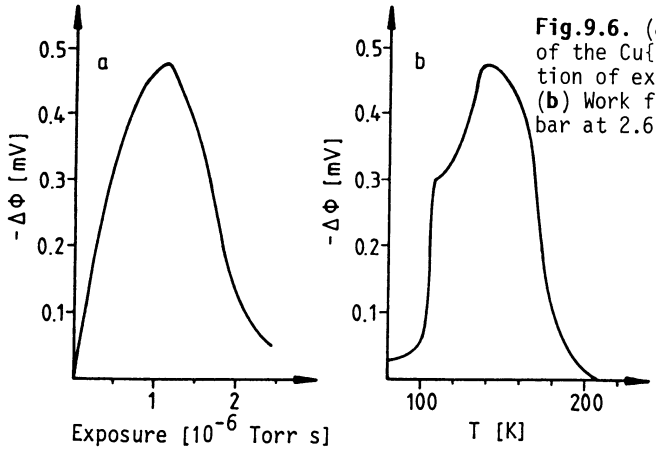

Fig.9.6. (**a**) Work function change of the Cu{111} surface as a function of exposure to CO at 82 K. (**b**) Work function desorption isobar at 2.6×10^{-7} Torr. After [9.35]

varies with the pressure at which the exposure is made. The desorption traces show distinct breaks in the curves, corresponding to the changes in the LEED pattern. At saturation a hexagonal (1.4×1.4) or (1.39×1.39) structure [9.40] was observed, which changes to a $c(4 \times 2)$ or (1.5×1.5) R98° structure [9.40] at the first break (~110 K, Fig.9.5b) and finally to a $(\sqrt{3} \times \sqrt{3}R30°)$ structure at the $\Delta\phi$ minimum. Recent FRAS data by *Hayden* et al. show the appearance of bridge-bonded CO ($\nu_{CO} = 1830$, $1812 cm^{-1}$) at coverage $\theta \geq 1/3$ at T = 77K. At saturation coverage, corresponding to the (1.4×1.4) structure, the integrated band intensities of the bridging bands is almost equal to that of linearly bonded CO supporting an earlier structural model for this phase by *Pritchard* [9.37]. Pritchard showed, that the LEED pattern indicating an apparently incommensurate hexagonal phase is consistent with a structural model where molecules relax their positions to allow occupation of linear and bridge sites yielding a ratio of 13:12. This model is consistent with the quoted IRAS data [9.34] and is shown in Fig.9.7.

Figure 9.8 shows the isosteric heats of adsorption determined from $\Delta\phi$ measurements for CO on Cu{100} [9.34], Cu{110} [9.33], and Cu{111} [9.35] replotted from the original papers. The coverage scale in Fig.9.8 can be con-

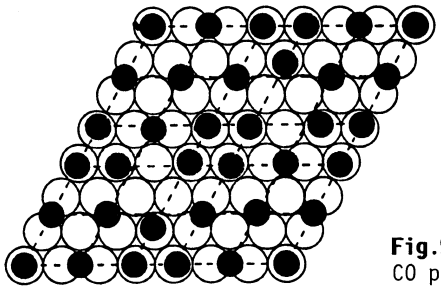

Fig.9.7. Structural model for the saturation CO phase (1.4×1.4) on Cu{111}. After [9.37]

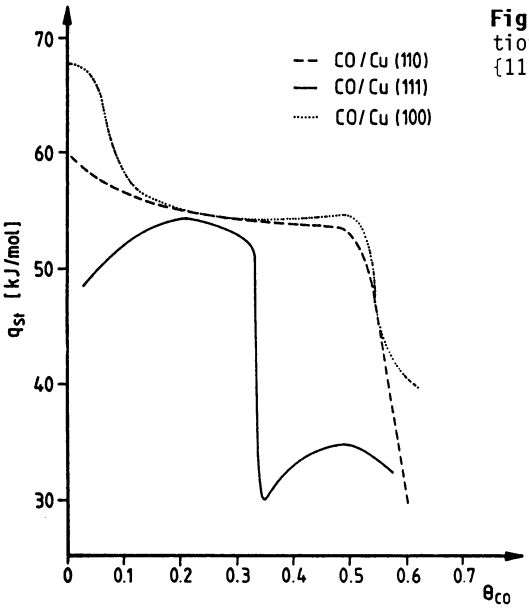

Fig.9.8. Isosteric heat of adsorption for CO on Cu{100}, {110}, and {111} replotted from [9.33-35]

sidered only as a guideline, since it was assumed here that the $\Delta\phi$ changes are linear with coverage and that the $\Delta\phi$ minima correspond to the ideal overlayer structure observed in LEED. For CO on Cu{110} [9.33] and Cu{111} [9.35], only desorption isobars were used for the evaluation of q_{st}, since structural equilibration reflected in the $\Delta\phi$ curves was difficult to establish in adsorption isobars. For CO on Cu{100} [9.34], only measurements at the higher temperatures and pressures, where reversibility was obtained, were considered. On Cu{110}, the isosteric heat remains approximately constant at a value of ~55 kJ/mol up to the work function minimum also observed in this system and then falls sharply. Near the $\Delta\phi$ minimum, a diffuse (2×1) LEED pattern was observed, which sharpens by annealing in a CO ambient at $T \geq 110$ K. Further CO exposure leading to higher coverages and the drop in q_{st} caused the diffuse (2×1) pattern to develop streaks moving into the [h(±2/3)][9.33] or [h(±4/5)] position [9.41]. Only by annealing, this pattern sharpened to a diffuse $c(5/4 \times 2)$ pattern [9.41]. This sequence of LEED patterns for CO on Cu{110} resembles the sequence found for N_2 on Ni{110}, except for the absence of curved banana features at coverages just exceeding $\theta = 0.5$. Although the poor ordering in the adsorbate phase leading only to diffuse superstructures in LEED does not allow deduction of structural models, the similarity to the N_2/Ni{100} LEED data suggests a similar sequence of overlayer structures. The absence of a banana feature in the CO/Cu{100} system could then be a consequence of the lack of a *correlated* switching in the ⟨001⟩ direction of domain walls formed

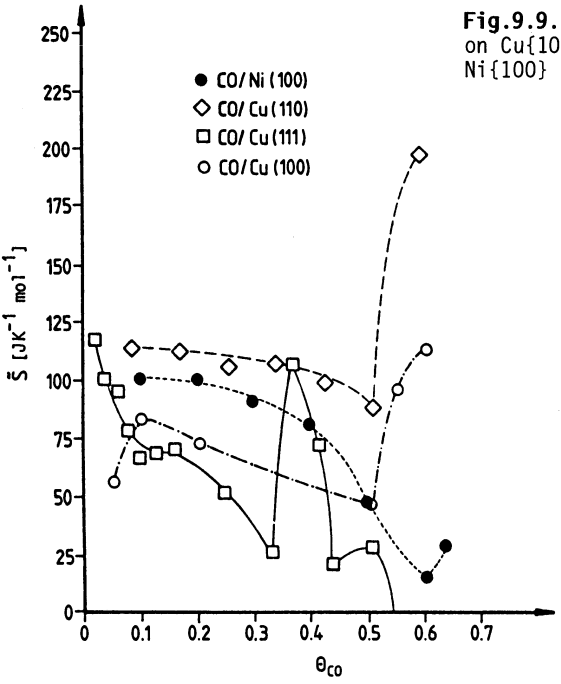

Fig.9.9. Partial molar entropy for CO on Cu{100}, Cu{110}, Cu{111}, and Ni{100}

at antiphase (2 × 1) domains. That collective excitations in the absorbate phase possible related to domain walls are present at $\theta > 0.5$, is evident from the differential entropy $\tilde{S}_{ad}$ calculated from the q_{st} values and corresponding isobars [9.42], plotted in Fig.9.9. The values for $\tilde{S}_{loc}$, $\tilde{S}_{mob}$ for CO on Cu{110} obtained from statistical mechanical models are nearly identical to those for N_2 on nickel surfaces, thus leading to the same conclusions as for the N_2 phases on Ni{110} discussed above.

On Cu{100} [9.34], the isosteric heat of adsorption drops from an initial value of 68 kJ/mol to a value of ~55 kJ/mol at $\theta \sim 0.5$. A further increase in the coverage then causes a further decrease to a value of ~40 kJ/mol. Observations by LEED have been made by several authors [9.34,37,38,43-46]. A c(2 × 2) overlayer structure was observed at $\theta > 0.45$ which splits into a c(7√2 × √2) R45° structure at $\theta > 0.5$. As pointed out by *Tracy* [9.34] the transition from the c(2 × 2) unit mesh to the c(7√2 × √2) R45° structure is accomplished by compression in the ⟨01$\bar{1}$⟩ direction while maintaining the original spacing in the ⟨001⟩ direction. This apparently strong tendency for alignment in the ⟨001⟩ direction is also present in the formation of a (2 × 1) structure for CO on Cu{110} or N_2 on Ni{110}. Tracy interpreted the c(7√2 × √2) R45° structure as a pseudohexagonal structure, whereas Pritchard proposed a model with CO being adsorbed in top and bridge sites [9.37]. However, for CO

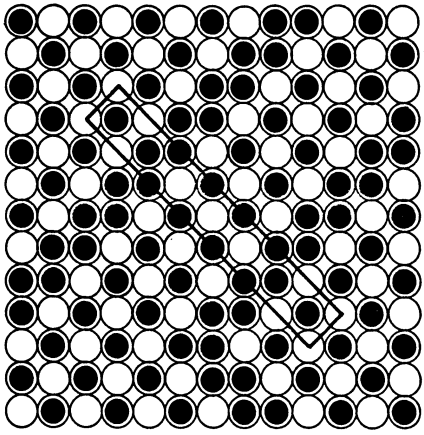

Fig.9.10. Real space model for the $c(7\sqrt{2} \times \sqrt{2})R45°$ structure for CO on Cu{100}. After [9.39]

on Cu{110}, there is no evidence in IRAS and also none in HREELS [9.38] for the existence of bridged CO molecules in this structure. Based on this discrepancy with the models proposed by Tracy and Pritchard, *Biberian* and *Van Hove* [9.39] developed a model where all CO molecules occupy on-top sites and form ordered antiphase domains of $c(2 \times 2)$ strips as shown in Fig.9.10.

In their laser simulations of the diffraction pattern they also considered the relaxation of the CO molecules in the domain walls by (i) a shift of some of the molecules keeping the C-O direction perpendicular to the surface, (ii) a tilt of the molecule still in a linearly bonded situation, or (iii) a translation of the molecules along the mirror planes of the unit cell. Although the close spacing of CO molecules of 2.65 Å in the walls argues for some relaxation, the best fit of the laser simulation with the LEED pattern was obtained for the model with top-site adsorption without relaxation, as shown in Fig.9.10. The model of *Biberian* and *Van Hove* [9.39] proposing antiphase domain walls, which can exhibit a fluidlike behavior as discussed by *Rys* [9.29], can explain the strong increase in $\tilde{S}_{ad}$ for CO on Cu{100} at $\theta > 0.5$ as deduced from Tracy's data and plotted in Fig.9.9. We also note the strong similarity of $\tilde{S}_{ad}$ for CO on Cu{100} with $\tilde{S}_{ad}$ for N_2 on Ni{100} where the presence of antiphase domain walls was postulated only on the basis of thermodynamic data [9.28].

The high-coverage thermodynamic behavior of the CO and N_2 phases. where experimental results suggest occupation of only on-top sites, is different from the CO/Cu{111} phases where occupation of bridge sites was observed at $\theta \geq 0.33$ [9.36] as demonstrated by the $\tilde{S}_{ad}$ values in Fig.9.9.

The entropy decreases up to $\theta = 0.33$, shows a sharp increase at coverages where the $c(4 \times 2)$ phase forms and first bridge sites are occupied, and de-

creases even to negative $\tilde{S}_{ad}$ values when the final (1.4×1.4) structure is observed. The negative $\tilde{S}_{ad}$ values indicate that the addition of CO molecules leads to an effective decrease in the partition function of the adsorbate layer, possible due to the stiffening of vibrational modes and restriction of translational degrees of freedom. An inspection of the structural model for CO saturation phase on Cu{111} (Fig.9.7) shows that distributing the CO molecules equally in the two sites within the (1.4×1.4) unit cell does produce locally higher densities, but not a continuous domain wall as postulated for the adsorption phases of N_2 and CO on the {100} and {110} surfaces of Ni and Cu, respectively.

According to the IRAS data of Hayden et al., the observation of two bridging bands for CO on Cu{111} at 77 K is attributed to a facile interconversion of CO between two- and threefold bridging sites. With respect to the structural model, however, collective oscillation with long wavelengths, as in continuous antiphase domain walls [9.25], and thus a high entropy contribution, cannot develop in the CO/Cu{111} phase.

Also included in Fig.9.9 is the differential entropy for CO on Ni{100} deduced from *Tracy*'s original publication [9.47]. A $c(2 \times 2)$ structure with CO being adsorbed into in top sites changes at $\theta > 0.5$ into a $c(5\sqrt{2} \times \sqrt{2})$ R45° structure in which also bridge sites are populated. Tracy also reports the existence of a compressed structure at $\theta = 0.68$, whose notation would be $p(3\sqrt{2} \times \sqrt{2})$ R45°[9.39]. The real space structures developed by *Biberian* [9.39] do not include dense domain walls since the molecules can relax into bridge sites at antiphase domain boundaries. Following our previous argument this relaxation eliminates long-wavelength collective excitations and thus leads to a decrease in entropy with increasing coverage, which is expected if the entropy is mainly determined by the individual degrees of freedom of the molecules (Fig.9.9).

The above considerations correlating structure and thermodynamic observations at high coverages are based on the *negative* experimental results, that no bridge bonded species are detected by vibrational spectroscopies. However, as discussed by *Pritchard* [9.37] before the data from *Hayden* et al. [9.36] became available, there are reasons why it may be difficult to detect bridge-bonded CO on copper surfaces.

We stress again that our interpretation of the high entropy values for the nitrogen phases on nickel and carbon monoxide phases on copper assumes that the substrate remains unaffected upon adsorption. If the substrate surface phonon spectrum changes upon adsorption, because of either reconstruction or relaxation of the surface, significant changes in the entropy of the adsorbate phase are also expected to occur.

9.3.4 Thermodynamic Measurements at Very Small Coverages

We now briefly consider the situation where the density in the adsorbate phase is low and the temperature sufficiently high to exclude interactions between adsorbed species.

The work function is extremely sensitive to the adsorption of gases and coverages $\theta \sim 10^{-2}$ can be measured. Another technique with a very high sensitivity to adsorbate coverage is low-energy ion scattering (ISS) which was used by *Möller* et al. to measure the thermodynamics of nitrogen adsorption on a Ni{110} surface in the very low coverage regime [9.20]. Figure 9.11 shows a comparison of an UPS isobar with an isobar constructed from the attenuation of the nickel intensity in an ion scattering experiment [9.16]. Particularly apparent is the decrease in Ni signal at N_2 coverages where the d-band intensity in the UPS data is not affected, indicating the high sensitivity of ISS for low adsorbate coverages. It was estimated that the lowest Ni coverage measured by ISS is between 10^{-3} and 10^{-2} monolayers. [9.26]. The inital decrease of Ni intensity is observed at the same temperature at which ion scattering from adsorbed nitrogen or the first changes in $\Delta\phi$ are detected. As discussed by *Möller* et al. [9.20], at low coverages nitrogen has a high shadowing factor α_{ex} of 3.5 ± 0.2 which smoothly de-

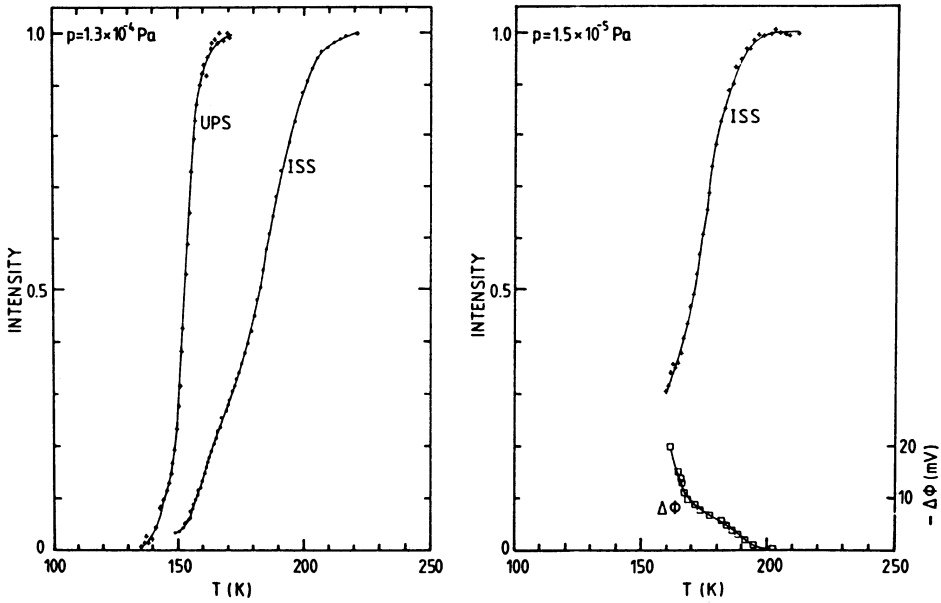

Fig.9.11. Comparison of N_2 adsorption isobars on Ni{110} obtained from the attenuation of the Ni intensity in ISS experiments with isobars obtained by the attenuation of the Ni d-band in UPS experiments and the work function change

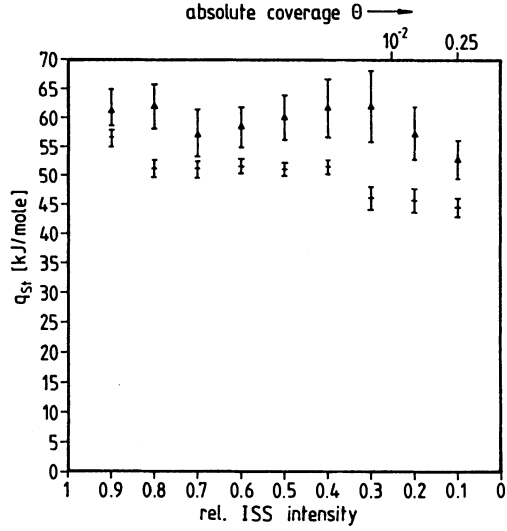

Fig.9.12. Isosteric heat for N_2 adsorption on Ni{110} deduced for two sets of ISS isobars (see text)

creases to 0.8 ± 0.1 at saturation. From incidence angle variations it follows that such a large shadowing factor can only be understood if nitrogen is adsorbed *on top* of the ridges on the Ni{110} surface and *not* in the furrows. If adsorption isobars recorded by ISS are used to evaluate the heat of adsorption, the possible effect of the ion beam on the adsorbate layer has to be considered because of sputtering and ion implantation. As detailed elsewhere, the ion-beam-induced effects in the N_2/Ni{110} system are considered unimportant at a low incident ion flux and for measuring times not exceeding ~1000 s [9.20].

The isosteric heat of adsorption for two different sets of ISS isobars is shown in Fig.9.12 [9.16]. The lower coverage scale is given in relative Ni ISS intensity, the adsorbate coverage indicated in the upper scale was derived from parallel UPS and XPS experiments. We note, that the initial isosteric heat of adsorption is higher but decreases at $\theta \sim 0.25$ approximately to the values obtained from the XPS and UPS isobars. Further, the q_{st} results from the different isobar sets vary considerably, indicating a different state of the crystal surface. Since contaminants are ruled out as a source of irreproducibility, the most likely explanation is that initial adsorption of N_2 with a higher heat of adsorption occurs on defect sites on the Ni{110} surface with their relative density varying from experiment to experiment and not evident by a visual inspection of the LEED pattern. Ion-induced defects are not important, since the initial heat of adsorption determined by ISS is in agreement with those obtained from $\Delta\phi$ measurements.

The higher adsorption energy on steps on the surface is also found in thermal desorption experiments on a stepped Ni{110} 9.46° ⟨1$\bar{1}$0⟩ surface [9.27]. In addition to the TPD maxima found on a Ni{110} surface, a distinct new desorption state with a desorption energy of ~46 kJ/mol is found on the stepped surface [9.27]. The entropy in the very low coverage N_2 adsorbate phase also indicates that the molecules are confined to defect sites or translate along defect lines [9.16].

From these experiments it follows that surface defects provide adsorption sites with a higher binding energy for N_2 on Ni{110}. The presence of these defects in different concentrations may thus explain the irreproducibility of q_{st} at low coverages obtained from ISS and also XPS isobars, which makes it difficult to deduce anything about the lateral interactions in the low-coverage phase leading to the formation of (2 × 1) islands. From an analysis of single XPS isobars and TPD data, it follows that weak attractive lateral interactions of W ~1.2 kJ/mol are present in the (2 × 1) phase [9.17,22].

9.4 Kinetics in Weakly Adsorbed Phases

Only limited data have been published for kinetic measurements in weakly chemisorbed phases in contrast to the many studies existing for more strongly chemisorbed gases on metal surfaces. Examples where the relation between the thermodynamics of the adlayer and desorption and adsorption data has been evaluated in more strongly chemisorbed phases include the work by *Behm* et al. [9.48] for CO on Pd{100}, *Pfnür* et al. [9.12,13] for CO in Ru{001}, and *Horlacher Smith* et al.[9.14] for H_2 on W{100}.

In the following we will discuss the few experimental results available for kinetics in weakly chemisorbed phases, e.g., N_2 on W{110} [9.49], Ni{110} [9.50]and Ru{001} [9.51,52], CO on Cu{110} [9.41], and for N_2 on Fe{111} [9.53-56]. Except for this last system, adsorption of the respective gases is always associative and kinetic measurements refer to the adsorption and desorption kinetics of the molecules. However, for N_2 on Fe{111}, a slow chemical transformation of weakly chemisorbed N_2 into a π-bonded precursor for dissociation is observed and will be described here as an example of chemical reactions in weakly chemisorbed phases.

Before we discuss the adsorption/desorption kinetics, we need to recall a common observation in the systems discussed here, i.e., the very slow ordering in the adsorbed phase leading to hysteresis in $\Delta\phi$ adsorption/desorption isobars [9.16,21,33,35]. These slow ordering processes are most pronounced at lower temperatures and lower pressure [9.16]. Measurements

of LEED intensity as a function of time and temperature at fixed coverage for N_2 on Ni{110} reveal that ordering into the (2×1) phase, i.e., elimination of domain boundaries, is associated with an apparent activation energy of 10-20 kJ/mol [9.16]. These slow ordering processes are also obvious in the desorption data of CO from Cu{110} [9.41] when a wide range of heating rates is applied in the TPD experiments, as discussed in Sect.9.4.1. It should be noted that these weakly chemisorbed phases seem to be suitable candidates to test theories on the kinetics of domain growth in two dimensions experimentally.

9.4.1 Adsorption and Desorption Kinetics

A clearly resolved two-peak structure is observed in the desorption traces from a nitrogen-saturated Ni{110} surface [9.16,22]. The high-temperature desorption peak is saturated at $\theta = 0.5$ and the low-temperature peak then grows with increasing coverage. Thus, the two desorption peaks are explained by molecules desorbing out of the (2×1) and the high-coverage phases, respectively. This interpretation is supported by an analysis of the activation energies of desorption determined from desorption isosteres which are, within the error bars, identical to the isosteric heat of adsorption for $\theta \lesssim 0.5$. At $\theta > 0.5$, this method of evaluating the desorption energy gave values with very large error bars, but the same trend as in q_{st} at $\theta > 0.5$ is obvious [9.50]. The preexponential of desorption, evaluated from the isosteres by assuming straight first order desorption or desorption via a precursor state [9.22,50] is around $10^{14} s^{-1}$ until the steep drop in q_{st} and E_D at $\theta \gtrsim 0.5$ (Fig.9.13). Also included in Fig.9.13 are the preexponential factors for desorption evaluated from the equilibrium measurements for $\theta < 0.5$ from (9.13) using the experimental sticking coefficient. In the coverage and temperature regime of the equilibrium measurements, the sticking coefficient is constant and high ($s \sim 1$) [9.57]. The agreement between the values of $\nu(\theta)$ determined by different methods is good, and we conclude that desorption occurs out of the equilibrium configuration of the adsorbate phase as represented by the entropy of the adsorbate phase in Fig.9.5. However, there are several assumptions and limitations inherent in the evaluation of data using detailed balancing arguments as discussed by *Menzel* [9.10] and *Pfnür* et al.[9.12,13] and the reader is referred to these articles and the references therein for a detailed discussion.

Excellent agreement between kinetic measurements and equilibrium measurements is also given for the sticking coefficient. By integration of the desorption traces, a plot of coverage versus exposure can be made, from which

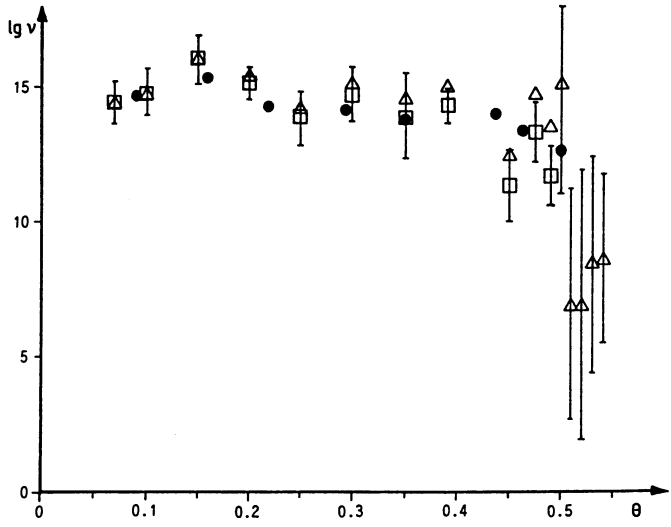

Fig.9.13. Preexponential of desorption for N_2 on Ni{110}. (Δ): data evaluated assuming a mobile precursor state; (□): data evaluated for first order desorption; (●): $\nu(\theta)$ evaluated from equilibrium data (see text)

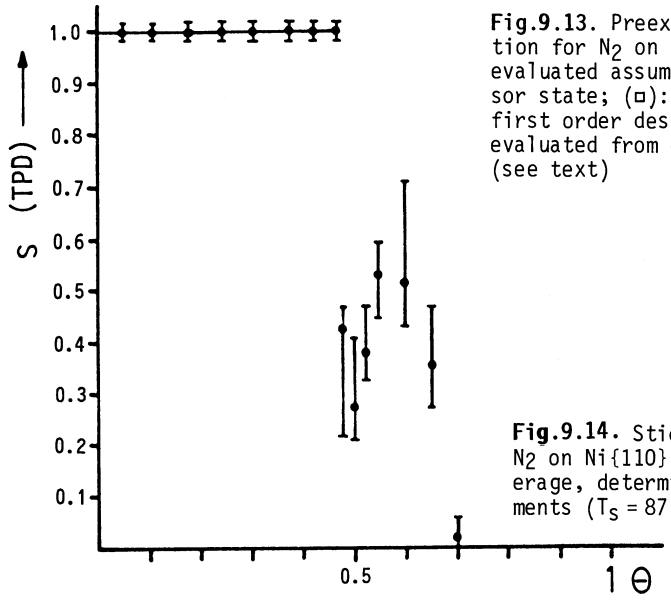

Fig.9.14. Sticking coefficient for N_2 on Ni{110} as a function of coverage, determined from TPD experiments (T_S = 87 K)

the sticking coefficient, $s=f(\theta)$, can be calculated. In Fig.9.14 the sticking coefficient is displayed as a function of coverage θ. The sticking coefficient s is constant up to θ=0.48, then drops to a value of s~0.3, increases again and diminishes at saturation coverage. This behavior is observed not only at low temperatures, but is evident at all temperatures where the commensurate-fluid phase change is observed in the LEED experiments. At the higher temperatures, experiments involving adsorption and subsequent desorption cannot be

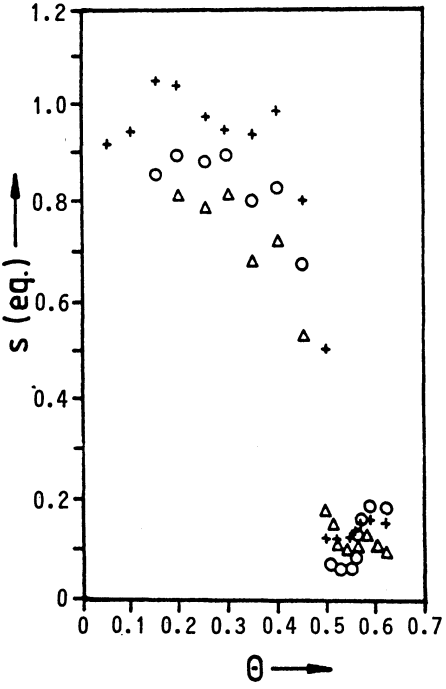

Fig.9.15. Sticking coefficient of N_2 on Ni{110} obtained from equilibrium isobars. (Δ): $P_{N_2} = 5 \times 10^{-6}$ mbar; (+): $P_{N_2} = 1 \times 10^{-6}$ mbar; (○): $P_{N_2} = 1 \times 10^{-7}$ mbar

carried out, since the residence time of the molecules on the surface becomes much too small. Therefore, detailed balance arguments were used to extract the sticking coefficient from equilibrium measurements using (9.13). Figure 9.15 shows the result for $s(\theta)$ [note that $s(\theta)$ is not an isothermal quantity anymore!] obtained from three isobars. The agreement with the $s(\theta)$ data from the desorption experiments is surprisingly good. In particular, we note that at $\theta > 0.5$ also under equilibrium conditions a discontinuity in $s(\theta)$ occurs, which thus is clearly related to the commensurate-fluid phase transition.

The constant sticking coefficient up to saturation coverage can be explained by assuming a mobile "precursor" state, i.e., a molecule impinging onto the surface is not reflected into the gas phase, but moves over the surface for a time sufficient to accommodate its translational and internal energy ($T_{gas} = 300$ K, $T_s < 200$ K) and becomes chemisorbed. A distinction is made between "intrinsic" and "extrinsic" precursor states; the former being trapped over the bare surface, the latter on top of a chemisorbed layer. The kinetic formalism relating these precursor states to the experimental sticking coefficient has been reviewed in several articles [9.8-11]. A spectroscopic characterization of precursor states for molecular adsorption was

was carried out at low temperatures for a few adsorption systems, e.g. N_2 on Ni{110}and Re{001} [9.58], N_2 on Ni{111} [9.59], and CO on Ni{111} [9.60]. These low-temperature data ($T \gtrsim 20$ K) revealing the existence of an extrinsic precursor for N_2 chemisorption can qualitatively explain the behavior of $s(\theta)$ on Ni{110} for $\theta \sim 0.5$ [9.57,58]. The explanation of the behavior of $s(\theta)$ at the phase transition at $\theta \sim 0.5$ follows from the observation that condensation into a second-layer precursor species starts before completion of the chemisorbed monolayer, because molecules lose their translational energy before finding an empty site [9.58]. With increasing temperature ($T \gtrsim 50$ K) [9.58] the residence time of the extrinsic precursor decreases and some of these molecules will desorb before finding a vacant site in the almost saturated commensurate phase, leading to a decrease in the sticking coefficient. Apparently, once a high mobility in the adsorbate phase is present at $\theta > 0.5$, it will be more probable again for the extrinsic precursor molecules to become inserted into the chemisorption layer during their residence time on the surface. This qualitative explanation, however, is speculative and needs to be tested in simulations relating the kinetics of adsorption and desorption to the geometry and energy changes in the adsorbed layer.

Data on the sticking coefficient of N_2 on other metal surfaces also show a complex behavior. In the classic study of *Bowker* and *King* [9.49] of the sticking coefficient of N_2 on W{110} using a technique giving absolute values for $s(\theta)$, they found an increase in $s(\theta)$ from $s_0 = 0.22$ to $s \sim 0.38$ at a coverage of 1.7×10^{14} molecules cm^2 followed by a decrease to saturation coverage (4.5×10^{14} molecules cm^2). The data were explained by a model where the rising sticking coefficient is attributed to improved transfer from a precursor to the chemisorbed γ-state when a nearest-neighbor site is already occupied by chemisorbed γ-nitrogen.

Whereas in the study of Bowker and King a continuous change in the sticking coefficient with coverage was found, an abrupt change in s was observed by *Pfnür* and *Menzel* for N_2 adsorption on Ru{001} [9.51,52]. In the coverage range of $0.2 < \theta < 0.33$ the sticking coefficient of molecular nitrogen shows a sudden jump from $s \sim 0.4$ to about twice this value. Menzel et al. found that a different binding state close to physisorption is populated even before completion of the $(\sqrt{3} \times \sqrt{3})$ R30° structure in which N_2 is bonded upright on top of Ru atoms. Electron-stimulated desorption (ESD), TPD and electron spectroscopy data suggested that the new state adsorbed onto the surface is not caused interactionally, but is a distinct new species which may be lying on the surface filling the area on the surface between the $(\sqrt{3} \times \sqrt{3})$ R30° islands of chemisorbed γ-nitrogen. The increase in s is then explained by the sudden

opening of the adsorption channel for this species when the $(\sqrt{3} \times \sqrt{3})$ R30° structure is near completion, but adsorption into the γ-state still continues. A distinct drop in the isosteric heat of adsorption, the desorption energy, and the preexponential of desorption is observed at $\theta = 0.25$, a somewhat higher coverage than that associated with the increase in the sticking coefficient [9.52]. This behavior of $s(\theta)$ was in contrast to CO adsorption on the same surface, where a compression of the chemisorbed layer sets in after complete filling of the $(\sqrt{3} \times \sqrt{3})$ R30° structure at $\theta = 0.33$ resulting in an adlayer with roughly identical molecules at each coverage [9.12,13]. The population of a N_2 species being physisorbed into the vacancies of a γ-nitrogen layer was also reported by *Umbach* [9.59] in his low-temperature study of N_2-adsorption on a Ni{111} surface. He was able to prove by argon coadsorption experiments that this physisorbed species is confined to the metal surface and is not physisorbed on top of the γ-layer.

A nonequilibrium distribution of adsorbed molecules in the adlayer can have drastic effects on desorption data. *Harendt* et al. [9.41] studied the adsorption of CO on Cu{110} by LEED and TPD. Their LEED observations are qualitatively comparable to those by Horn and Pritchard, but they found a decrease in the activation energy of desorption from their isosteric evaluation of TPD data well below the saturation of the (2×1) LEED pattern (defined by Harendt et al. as $\theta = 0.5$) at $\theta = 0.35$. Obviously, repulsive interactions in the adlayer are refelcted in the desorption traces at coverages well below saturation of the (2×1) phase. In the desorption data, only a broad peak centered around ~205 K was observed at saturation coverage (Fig.9.16) and not a two-peak structure as, for example, for N_2 on Ni{110}, where a similar sequence of LEED patterns was found. Also, the desorption maximum from a saturated CO layer shifted with increasing heating rate in the TPD experiments first to higher temperatures (as expected) but then reversed to lower temperatures, as shown in Fig.9.16. These results suggest that during slow heating in the desorption experiment the adsorbed phase can relax and minimize the repulsive interactions caused by a nonequilibrium distribution of molecules adsorbed at a low temperature, whereas the molecules desorb out of a nonequilibrated layer when higher heating rates (>4K/s) are applied. Simulation of the desorption data using a model with two different adsorption states having different coverage-dependent desorption energies and preexponentials of desorption, and a slow and activated interconversion rate between the two states (comparable to the desorption rate) reproduced their experimental observations reasonably well (Fig.9.16b) [9.61]. It then appears that CO adsorption on Cu{110} is an extreme example of slow equilibration in the adlayer.

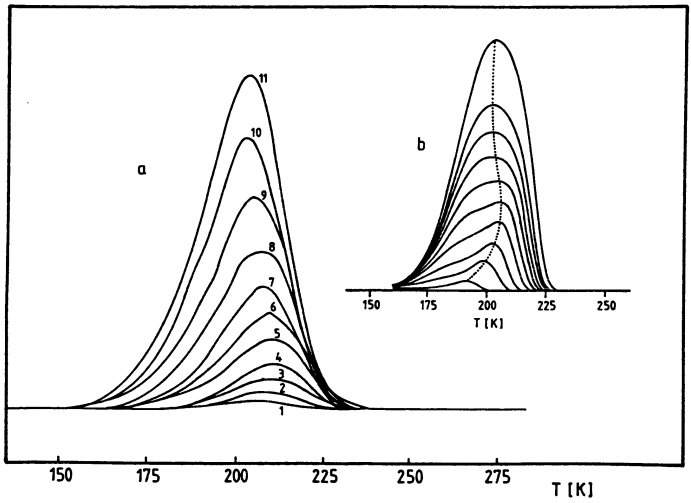

Fig.9.16. (**a**) Experimental desorption traces from a CO-saturated Cu{110} surface using different heating rates (from curve 1: 0.25 K/s to curve 11: 10 K/s). (**b**) Modeling of desorption traces as a function of heating rate assuming an activated transition of CO molecules between two different adsorption states (see text)

9.4.2 Chemical Reactions in Weakly Chemisorbed Phases

Nitrogen adsorption on nickel surfaces is, in the temperature range below the desorption temperature, always associative. Only at higher temperatures and large exposures has dissociation been reported on nickel surfaces [9.21, 62]. Also on a W{110} surface, nitrogen seems to adsorb associatively, and only (100) defect sites are believed to contribute to the dissociative interaction reported on W{110} [9.63]. Recent molecular-beam studies revealed that N_2 dissociation on W{110} is a direct process, since the dissociation probability depends on the translational energy of the impinging gas molecules [9.64]. Dissociation out of a chemisorbed phase occurs for CO on W{110}, as studied in detail by *Umbach* and *Menzel* [9.65].

We will finally review the data for N_2 dissociation on an Fe{111} surface, since it comprises one of the few examples where a combination of experimental and theoretical studies have revealed some important microscopic details of the nature of the dissociation process. The purpose of studying the details of N_2 dissociation on iron surfaces is to gain a detailed understanding of the ammonia synthesis reaction [9.66]. Ammonia synthesis on iron is a structure-sensitive reaction with the Fe{111} surface being the most active low-index single-crystal plane [9.66]. Using various methods, it has been demonstrated for clean iron surfaces that the rate-determining step for the overall reaction involves nitrogen dissociation, since the subsequent hydrogen-

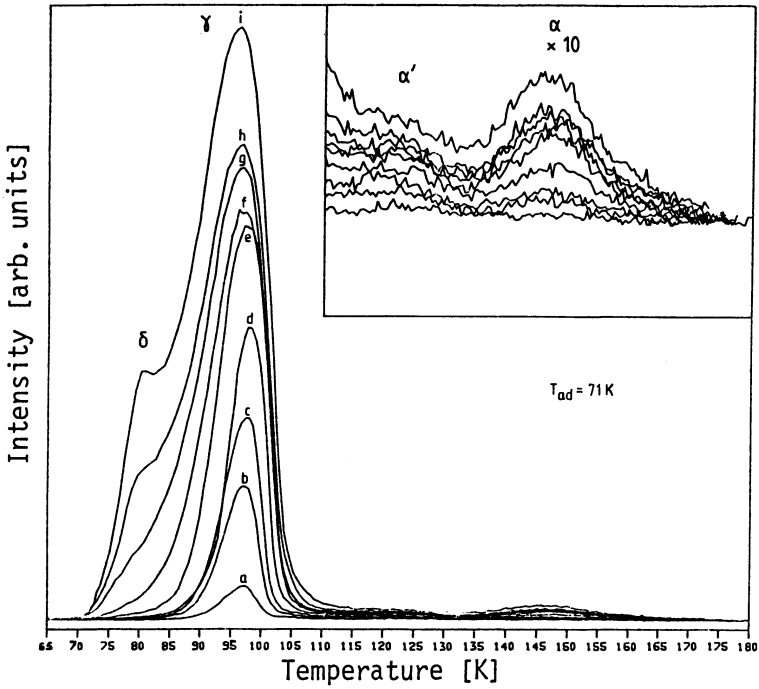

Fig.9.17. Data from TPD for N_2 adsorbed on Fe{111} as a function of apparent exposure. (*a*) 0.5 L; (*b*) 2.0 L; (*c*) 3.0 L; (*d*) 4.0 L; (*e*) 6.0 L; (*f*) 8.0 L; (*g*) 10 L; (*h*) 20 L; (*i*) 100 L

ation of atomic nitrogen to ammonia proceeds at much higher rates. The kinetics of dissociative nitrogen adsorption on Fe{111} have been studied by *Ertl* et al. [9.67] in detail, and it was concluded that this process proceeds through a molecularly adsorbed precursor state (α-state) with a rather low activation barrier. Recently, it was shown [9.53-55] that this α-state is preceded by a more weakly chemisorbed nitrogen state, which desorbs between 70 and 120 K.

Figure 9.17 shows the desorption spectra of $^{15}N_2$ from Fe{111} as a function of exposure at 65 K [9.55]. The data were recorded with a differentially pumped apertured mass spectrometer, eliminating the background in the TPD data. As a function of exposure, three desorption states denoted α, γ, and δ are distinguishable. The insert of Fig.9.17 shows, however, that also between the α and γ states, the signal is above the background, By dosing the crystal at $T \gtrsim 90$ K, the intensity of the α and α' peaks can be increased substantially and both grow simultaneously [9.68]. In previous reports, no distinction between α' and α state was made. Transitions into the α' and α states were found to be activated and to occur from the γ-state with an apparent·activation

energy of ~18 kJ/mol and with a transmission coefficient of $s_0(T) \sim 10^{-2}$-10^{-3} [9.53]. Isotopic exchange experiments show [9.67] that in the α-state the molecular unity is preserved. The sticking coefficient into the γ-state was found to be close to unity [9.53]. The δ-state, which grows in before the γ-state is saturated, did not show a complete isotopic exchange after dosing the crystal subsequently with $^{14}N_2$ and $^{15}N_2$, and it was suggested, that the δ-state is adsorbed onto the γ-layer resembling an extrinsic precursor state [9.55]. Recent experiments, however, question this interpretation and leave the possibility that the different desorption peaks are caused by adsorption into energetically different sites on the open {111} surface. A similar interpretation based on the intrinsic heterogeneity of the Fe{111} surface with a variety of adsorption sites [9.69] can explain the difference between α' and α-states.

In x-ray photoemission experiments [9.53] and work function measurements [9.69], a clear distinction is possible only between γ, α, and the atomic β adsorption states (no XPS data for the δ state are available). In Fig.9.18 we show the characteristic N1s spectra of the three nitrogen states (γ,α,β) distinguishable by XPS on Fe{111}. Spectrum a shows the doublet structure of two bands at 405.9 and 401.2 eV below E_F observed for the weakly bonded γ-state. As for N_2 on Ni surfaces, the observation of a doublet structure for

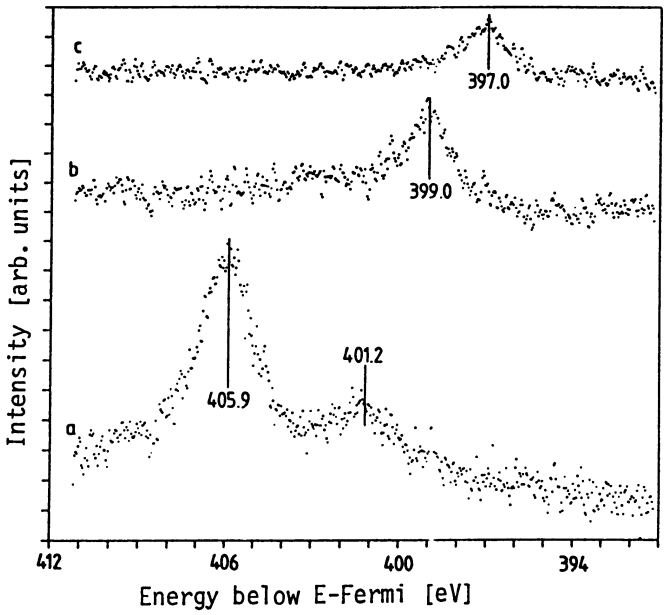

Fig.9.18. N1s core level spectrum for (*a*) the weakly chemisorbed γ-state, (*b*) the π-bonded α-state, and (*c*) the atomic β-state

a single species is due to final-state effects in the photoemission process. A comparison of spectrum a with those of N_2 bonded on Ni{110} [Fig.9.3] shows that intensity is transferred to the "unscreened" final-state peak, indicating a weak interaction with the substrate, which is also evident from the low activation energy of desorption of ~25 kJ/mole. This γ-state then transforms, as a function of time and temperature, into the α-state producing the XPS spectrum shown in Fig.9.18b. The XPS data for the α'- and α-states [9.53, 54] and the HREELS results for the α-state [9.54,69] reveal, however, a strong interaction of the two nitrogen atoms with the surface. A comparison of the ν_{N-N} stretching frequency observed by HREELS with those in π-bonded inorganic dinitrogen complexes, as well as CNDO-CI (complete neglect of differential overlap-configuration interaction) calculations of the N1s spectrum show that (a) the molecule bonds with its molecular axis parallel to the surface, (b) that bonding to the surface involves charge donation from the $1\pi_u$ orbital of the molecule to the substrate and a $1\pi_g^*$ backbonding from the substrate to the molecule, and (c) that the charge transfer into the antibonding (with respect to the dinitrogen bond) $1\pi_g^*$ orbital increases the N-N bond length to ~1.25 Å, compared to the N-N bond distance of 1.1 Å in the free molecule. Thus, the effective activation barrier for dissociation is lowered and dissociation of N_2 is observed at low temperatures ($T \gtrsim 120$ K). The α- (or α'-plus α-) state transforms as a function of time and temperature into the dissociated β-state, as observed in XPS and HREELS experiments [9.53,54,69].

From a study of the N1s spectra as a function of gas pressure, temperature, and time, the kinetics of adsorption, desorption, and interstate conversion between γ- and α- nitrogen were determined [9.53,55] and it was concluded that at high temperatures ($T \sim 700$ K) adsorption into the π-bonded α-states proceeds with a similar rate to the actual dissociation of the N_2 molecule [9.53] and thus becomes important for the consideration of the ammonia synthesis reaction mechanism.

The microscopic mechanism of dissociation of N_2 on Fe{111} was also investigated theoretically by calculating the potential energy surface for this reaction [9.56]. The theoretical treatment involves calculation of the total energy E_{tot} of the system as a function of the height h of the molecule above the surface and the intramolecular distance d. The Fe{111} surface is approximated by a twelve-atom cluster and the molecule is lowered onto the surface with different orientations of its molecular axis with respect to the substrate. The best agreement between theory and experiment is obtained when the molecule becomes adsorbed with its axis parallel to the surface on

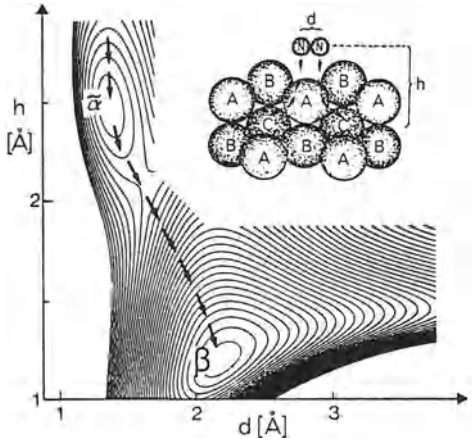

Fig.9.19. Potential energy surface E_{tot} (h,d) for N_2 on Fe{111}. The dissociation path is indicated by the arrows, the equipotential lines have a separation of 0.2 eV. After [9.56]

the edge of an A atom in the precursor state for dissociation (Fig.9.19). The calculations show that in this intermediate α-state, charge is transferred into the antibonding $1\pi_g^*$ orbital of N_2, leading to a calculated increase of the N-N distance of $d \approx 1.4$ Å. By surmounting a potential energy barrier of $E_{diss} \approx 40$ kJ/mole (compared to experimental value $E_{diss} = 28$ kJ/mole), the molecule dissociates and forms the atomic β-state. From this calculation it also follows that the height of the activation barrier, E_{diss}, is critically dependent on the charge transfer into the $1\pi_g^*$ orbital of N_2.

The reaction path for trapping of a γ-state molecule into an α-state was also studied theoretically by *Tomanek* and *Bennemann* [9.56] and resulted in a model consistent with the experimental observations, i.e., an activated transition between two molecular adsorption states.

The simple dissociation reaction in a weakly chemisorbed phase discussed above is an example in which the microscopic mechanism of the heterogeneous fission of an intramolecular bond has been identified both experimentally and theoretically. We emphasize that on the open {111} surface of bcc iron, several molecular adsorption states separated by small activation barriers exist. For the dissociation reaction, it may be concluded that partial occupation of antibonding molecular orbitals by substrate electrons is one of the crucial steps in dissociation. Details of the geometry and electronic overlap in the precursor of dissociation will, however, depend on the particular system under study.

9.5 Summary

This chapter has reviewed some recent experimental studies on the thermodynamic and kinetic behavior of weakly chemisorbed phases and attempted to correlate the observations with structural models based on results obtained from LEED and vibrational spectroscopy experiments. A comparison with theoretical predictions on the sequence of phase transitions is only possible in a qualitative fashion, since no experimental results on the exact nature and order of the observed phase transitions in the adsorbate phases considered is available. It appears, however, that in those adsorbate phases where the high entropy can be rationalized by the presence of meandering domain walls, only on-top adsorption sites are populated by the adsorbate molecules. This statement, based on *negative* experimental results, however, has to be considered with caution, since bridge-bonded CO or N_2 molecules may be difficult to detect, in particular if the adsorption bands are broad and their concentration is low, as pointed out by *Pritchard* [9.37]. The slow and activated ordering processes in these phases complicate thermodynamic euqilibrium studies and are reflected in kinetic measurements, but on the other hand make these phases suitable candidates for the investigation of the kinetics of phase transitions. Until now, such measurements have not been performed systematically enough to allow a comparison with theoretical work [9.70,71]. The study of finite-size effects in weakly chemisorbed phases comprises another area of future work, since it will not only provied a more detailed insight into the nature of the intermediate fluid phase caused by fluctuations of domain walls, but also relates the thermodynamic behavior found on large single crystalline surfaces to the thermodynamic results obtained on small promoted catalyst particles [9.28]. The importance of understanding the properties of weakly chemisorbed phases also follows from their obvious relation to heterogeneous catalytic reactions proceeding at high pressures with an appreciable equilibrium coverage of reactants and products. As shown for the Fe{111} surface, the activated transformation of a weakly chemisorbed N_2 molecule into the precursor for dissociation is the initial step in the ammonia synthesis reaction.

Acknowledgements. The experiments concerning N_2 adsorption on nickel and iron surfaces described were performed at the Fritz-Haber-Institut der Max-Planck-Gesellschaft and at the Free University of Berlin with financial support from the Deutsche Forschungsgemeinschaft, Sonderforschungsbereich 6. I am grateful to my present and past co-workers M. Golze, G. Strasser, P.A. Dowben, and R.K. Driscoll. For stimulating discussions, I thank J. Pritchard, W.N. Unertl, P. Kleban, M. Neumann, and D. Tomanek, and J. Goschnik and W. Moritz for the communication of data prior to publication. Once more, I thank G. Mehnert at the Fritz-Haber-Institut for typing the manuscript.

References

9.1 S. Cerný: In *The Chemical Physics of Solid Surfaces and Heterogeneous Catalysis*, Vol.2, ed. by D.A. King, D.P Woodruff (Elsevier, Amsterdam 1983) p.1
9.2 A. Clark: *The Theory of Adsorption and Catalysis* (Academic, New York 1970)
9.3 M.J. Sparnay: *Thermodynamics with an Emphasis on Surface Problems*, Surf. Sci. Rep., Vol.4, No.3/4 (1984)
9.4 G. Ehrlich: Adv. Catal. **14**, 255 (1963); J. Chem. Phys **36**, 1499 (1962)
9.5 M. Procop, J. Völter: Surf. Sci. **47**, 514 (1975)
9.6 I. Prigogine: Physica **15**, 272 (1949); Phys. Chem **55**, 265 (1951)
9.7 D.A. King: Surf. Sci. **47**, 384 (1975); In *Chemistry and Physics of Solid Surfaces*, Vol.2, ed. by R. Vanselow, CRC, Boca Raton, FL (1979)
9.8 R. Gorte, L.D. Schmidt: Surf. Sci. **76**, 559 (1978)
9.9 A. Cassuto, D.A. King: Sci. **102**, 388 (1981)
9.10 D. Menzel: In *Chemistry and Physics of Solid Surfaces IV*, ed. by R. Vanselow, R. Howe, Springer Ser. Chem. Phys., Vol.20 (Springer, Berlin, Heidelberg 1982) p.389
9.11 H. Ibach, W. Erley, H. Wagner: Surf. Sci. **92**, 29 (1980)
9.12 H. Pfnür, D. Menzel: J. Chem. Phys. **79**, 2400 (1983)
9.13 H. Pfnür, P. Feulner, D. Menzel: J. Chem. Phys. **79**, 4613 (1983)
9.14 A. Horlacher Smith, R.A. Barker, P.J. Estrup: Surf. Sci. **136**, 327 (1984)
9.15 M. Grunze, P.H. Kleban, W.N. Unertl, F.Rys: Phys. Rev. Lett. **51**, 582 (1983)
9.16 M. Grunze, W.N. Unertl, M. Golze, M. Neumann, W. Heiland: to be published
9.17 M. Golze, M. Grunze, R.K. Driscoll, W. Hirsch: Appl. Surf. Sci. **6**, 464, (1980)
9.18 K. Horn, J. DiNardo, W. Eberhard, H.-J. Freund, E.W. Plummer: Surf. Sci. **118**, 465 (1982)
9.19 K. Jacobi, H.H. Rotermund: Surf. Sci. **133**, 401 (1983)
9.20 J. Möller, W. Heiland, W.N. Unertl: Nucl. Instrum. Methods **B2**, 396 (1984)
9.21 M. Grunze, R.K. Driscoll, G.N. Burland, J.C.L. Cornish, J. Pritchard: Surf.Sci. **89**, 381 (1979)
9.22 M. Golze, M. Grunze, W. Hirschwald: Vacuum **31**, 697 (1981)
9.23 B.J. Bandy, N.D.S. Canning, P. Hollins, J. Pritchard: J. Chem. Soc., Chem. Commun. 58 (1982)
9.24 P. Bak: In *Chemistry and Physics of Solid Surfaces V*, ed. by R. Vanselow, R. Howe, Springer Ser. Chem. Phys. Vol.**35** (Springer, Berlin, Heidelberg 1984) p.317; and references therein
9.25 P. Bak: Rep. Prog. Phys. **45**, 587 (1983)
9.26 W. Moritz: private communication
9.27 M. Grunze: unpublished results
9.28 M. Grunze, P.A. Dowben, R.G. Jones: Surf. Sci. **141**, 455 (1984)
9.29 F. Rys: Surf. Sci. **152/153**, 868 (1985)
9.30 J.C. Fuggle, E. Umbach, D. Menzel, K. Wandelt, C.R. Brundle; Solid State Commun. **27**, 65 (1978)
9.31 N.V. Richardson, A.M. Bradshaw: Surf. Sci. **88**, 253 (1979)
9.32 P. Kleban: private communication
9.33 K. Horn, M. Hussain, J. Pritchard: Surf. Sci. **63**, 244 (1977)
9.34 J. Tracy: J. Chem. Phys. **56**, 2748 (1972)
9.35 P. Hollins, J. Pritchard: Surf. Sci. **89**, 483 (1979)
9.36 B.E. Hayden, K. Kretschmar, A.M. Bradshaw: Surf. Sci. **155**, 553 (1985)
9.37 J. Pritchard: Surf. Sci. **79**, 231 (1979)
9.38 S. Anderson: Surf. Sci **89**, 477 (1979)
9.39 J.P. Biberian, M.A. Van Hove: Surf. Sci. **118**, 443 (1982)

9.40 P. Hollins, J. Pritchard: Surf. Sci. **99**, L389 (1980)
9.41 C. Harendt, J. Goschnick, W. Hirschwald: Surf. Sci. **152/153**, 453 (1985)
9.42 K. Horn: Ph.D. Thesis, London University (1976)
9.43 J. Pritchard: J. Vac. Sci. Technol. **9**, 895 (1972)
9.44 R.W. Joyner, C.S. McKee, M.W. Roberts: Surf. Sci. **26**, 303 (1971)
9.45 M.A. Chesters, J. Pritchard: Surf. Sci. **28**, 460 (1971)
9.46 C.R. Brundle: In Proc. 7th Int. Vacuum Congr. 3rd Int. Conf. Solid Surfaces, Vienna 1977, ed. by R. Dobrozemsky, F. Rüdenauer, F.P. Viehböck, A. Breth (Vienna 1977) p.117
9.47 J.C. Tracy: J. Chem. Phys. **56**, 2736 (1972)
9.48 R.J. Behm, K. Christmann, G. Ertl, M.A. Van Hove: J. Chem. Phys. **73**, 2984 (1980)
9.49 M. Bowker, D.A. King: J. Chem. Soc., Faraday Trans. 1, 2100 (1979)
9.50 M. Grunze, M. Golze, W.N. Unertl: In Proc. Symp. Surf. Sci., Obertraun, Austria 1983, ed. by P. Braun (HTU-Druck, Vienna 1983) p.218
9.51 P. Feulner, D. Menzel: Phys. Rev. B **25**, 4295 (1982)
9.52 D. Menzel, H. Pfnür, P. Feulner: Surf. Sci. **126**, 374 (1983)
9.53 M. Grunze, M. Golze, J. Fuhler, M. Neumann, E. Schwarz: In Proc. 8th Int. Congr. Catal., Berlin, 1984, Vol. IV (DECHEMA, Frankfurt am Main 1984) p.133
9.54 M. Grunze, M. Golze, W. Hirschwald, H.-J. Freund, H. Pulm, U. Sep, M.C. Tsai, G. Ertl, J. Küppers: Phys. Rev. Lett. **53**, 850 (1984)
9.55 G. Strasser, M. Grunze, M. Golze: In Proc. 3rd Symp. Surf. Sci., Obertraun, Austria 1985, ed. by G. Betz, H. Störi, W. Husinsky, P. Varga (HTU-Druck, Vienna 1985) p.82
9.56 D. Tomanek, K.H. Bennemann: Phys. Rev. B **31**, 2488 (1985)
9.57 M. Grunze: In Proc. 2nd Israel Mat. Engineering Conf., ed. by A. Grill, S.I. Rokhlin (Ben Gurion University, Beer Sheba, Israel 1984) p.208
9.58 M. Grunze, J. Fuhler, M. Neumann, C.R. Brundle, D.J. Auerbach, J. Behm: Surf. Sci. **139**, 109 (1984)
9.59 E. Umbach: In Proc. 3rd Symp. Surf. Sci., Obertraun, Austria 1985, ed. by G. Betz, H. Störi, W. Husinsky, P. Varga (HTU-Druck, Vienna 1985) p.53
9.60 M. Schayegan, E.D. Williams, R.E. Glover III, R.L. Park: Surf. Sci. **154**, L239 (1985)
9.61 C. Harendt, J. Goschnick: private communication
9.62 G. Wedler, G. Alshorachi: Ber. Bunsenges. Phys. Chem. **84**, 277 (1980)
9.63 S.P. Singh-Boparai, M. Bowker, D.A. King: Surf. Sci. **53**, 55 (1975)
9.64 J. Lee, R.J. Madix, J.E. Schlegel, D.J. Auerbach: Surf. Sci. **143**, 626 (1984)
9.65 E. Umbach, D. Menzel: Surf. Sci. **135**, 26 (1983)
9.66 For reviews see: G. Ertl: Catal. Sci. Rev. **21**, 201 (1980) M. Grunze: In *The Chemical Physics of Solid Surfaces and Heterogeneous Catalysis*, Vol.4, ed. by D.A. King, D.P. Woodruff, (Elsevier, Amsterdam 1982) p.143 G. Ertl: In *Catalysis: Science and Technology*, ed. by J.R. Anderson, M. Boudart, Vol.4, (Springer, Berlin, Heidelberg 1983) p.209; J. Vac. Sci. Technol. **A1**, 1247 (1983)
9.67 G. Ertl, S.B. Lee, M. Weiss: Surf. Sci. **114**, 515 (1982)
9.68 M. Golze, G. Strasser, M. Grunze: to be published
9.69 M.-C. Tsai, U. Seip, I.C. Bassignana, J. Küppers, G. Ertl: Surf. Sci. **155**, 387 (1985)
9.70 A. Sadiq, K. Binder: Phys. Rev. Lett. **51**, 674 (1983)
9.71 J.D. Gunton, K. Kaski: Surf. Sci. **144**, 290 (1984)

10. Kinetic and Spectroscopic Investigations of Surface Chemical Processes

J.T. Yates, Jr., J.N. Russell, Jr., and S.M. Gates

Surface Science Center, Department of Chemistry, University of Pittsburgh, Pittsburgh, PA 15260, USA

The study of the surface-catalyzed decomposition of molecules on single crystal surfaces is one of the major themes in surface chemistry today. This theme, combined with the study of the chemical structure of surface species, forms a driving force for the development of a systematic understanding of surface chemistry. Such a systematic picture of molecules and processes at surfaces will ultimately yield a predictive and a conceptual basis of understanding which may be extended beyond the realm of model systems.

In selecting the experimental methods for the study of surface chemistry, one must often make a choice between the use of a surface spectroscopic method and a surface kinetic method. The dominant factor to be considered is whether the species to be studied by spectroscopic methods are related to the chemical process under investigation, and whether the surface concentration will be sufficiently high to permit their observation. The direct measurement of the presence and the behavior of the critical surface species by spectroscopic means is often difficult or impossible because of the existence of a mixture of surface species, because of the low steady-state concentration of the species, or because of the inapplicability of the spectroscopic method under reaction conditions.

In this chapter, it will be shown that kinetic methods can give deep insight into chemical reaction processes on surfaces. In particular, kinetic techniques will be introduced which quickly and efficiently provide a survey of the multiple reaction pathways which are operative on a surface. It will be shown that a new method, scanning kinetic spectroscopy (SKS), can rapidly dissect a complex sequence of reaction steps which are occurring sequentially as a complex molecule undergoes thermal decomposition on a surface.

All of these types of experiments make use of the deuterium kinetic isotope effect (DKIE) to sharpen their sensitivity to details of the elementary steps at work. Here, deuterated molecules, with labeling in specific positions in the molecules, are used to investigate specific bond-breaking processes.

10.1 Experimental Methods

The experiments to be described here were all carried out in the ultra-high-vacuum (UHV) apparatus shown in top view in Fig.10.1. A single-pass cylindrical mirror analyzer (CMA) (Perkin Elmer) is used for Auger electron spectroscopy (AES) measurements on a single crystal which is mounted on a manipulator with an offset of 6.4 cm from the chamber axis. Argon ion bombardment combined with annealing is used to clean the crystal. The crystal may be cooled to 77 K using liquid nitrogen cooling of the support assembly. The crystal temperature may be controlled by means of an electronic temperature programmer [10.1]. A collimated molecular beam of reactant molecules is directed to a point in front of the quadrupole mass spectrometer (QMS) sampling orifice, and the crystal may be quickly rotated into the beam for an experiment. The

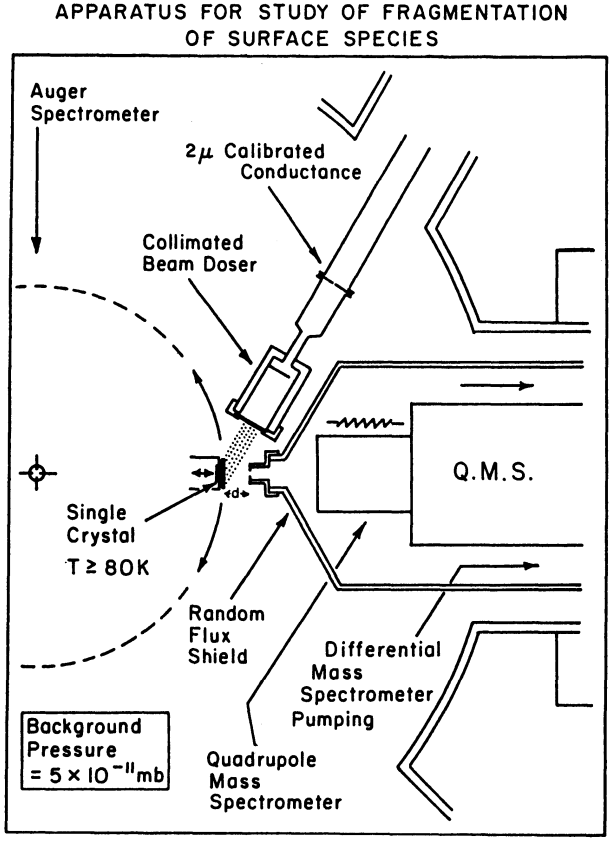

Fig.10.1. Top view of the UHV apparatus constructed for study of surface reaction kinetics on single-crystal surfaces

"in-beam" position shown in Fig.10.1 locates the crystal about 1 cm in front of the 0.3-cm diameter orifice in the front of the mass spectrometer random flux shield. The shielded QMS is differentially pumped with a 60 l/s triode ion pump. The mass spectrometer may be multiplexed between any desired mass peaks, conveniently sampling each mass peak for times of the order of 0.2 s [10.2].

The molecular-beam doser consists of a calibrated conductance aperture (nominally 2-μm diameter), in front of which is placed a scattering shield to randomize the gas flux inside the doser. A glass microcapillary array containing 25-μm channels of 500-μm length is used to collimate the beam over an 0.86-cm^2 area. The angular distribution of molecules emitted by this doser has been calculated by *Campbell* and *Valone* [10.3], and our measurements are in good agreement with their calculation [10.2].

Three different kinds of experiments have been performed with this apparatus, as outlined below.

1) Conventional temperature programmed desorption (TPD) [10.4] may be carried out by raising the crystal temperature linearly with time and using the mass spectrometer as a detector of all desorbing species. The limit of detectability of this method is about 10^{10} molecules/s. The crystal may be close-coupled to the mass spectrometer orifice in order to achieve maximum sensitivity and to select molecules desorbing mainly from the center of the single-crystal surface, avoiding artifacts due to desorption from heating leads, crystal edges, etc.

2) Isothermal adsorption experiments may be carried out with the crystal receiving adsorbate in the calibrated molecular beam. By measuring the scattered flux of unreacted species, compared to the scattered flux under conditions where no reaction occurs, it is possible to measure a reactive sticking coefficient for adsorption plus reaction. This can be done in the limit of zero-coverage of adsorbate. The method will also work for studies of the rate of a surface reaction under steady-state conditions.

3) Scanning kinetic spectroscopy experiments may be carried out in which the mass spectrometer sequentially samples the desorption flux of all products as well as the reactant while the crystal is being temperature programmed. This method scans the opening of reaction channels at characteristic surface temperatures. Quantitative correlations between the onset temperature of evolution of different products and the consumption of reactant are often observed.

10.2 Kinetic Studies of Methanol Decomposition on Ni{111}

10.2.1 Isothermal Decomposition of Methanol on Clean Ni{111}

The interaction of methanol with a Ni{111} surface was studied by rapidly moving a clean Ni{111} crystal into a molecular beam of methanol and recording the evolution of gaseous species from the crystal using the differentially pumped multiplex mass spectrometer [10.5]. Typical results for this experiment are shown in Fig.10.2 for two isotopic methanol molecules, CH_3OD and CD_3OH. As shown in the lower two panels of Fig.10.2, a small signal from the methanol is observed prior to the crystal rotation, which is designated P_1. At zero time, the crystal is rotated into the beam, and the methanol signal rises immediately to P_2. At this point, essentially no methanol has impinged on the surface. As time passes, the scattered methanol signal rises, and after several hundred seconds, reaches a steady state value, P_3. The time between points P_2 and P_3 is the time for the system to reach steady-state conditions. Simultaneously, the D_2 signal was monitored (as shown in the

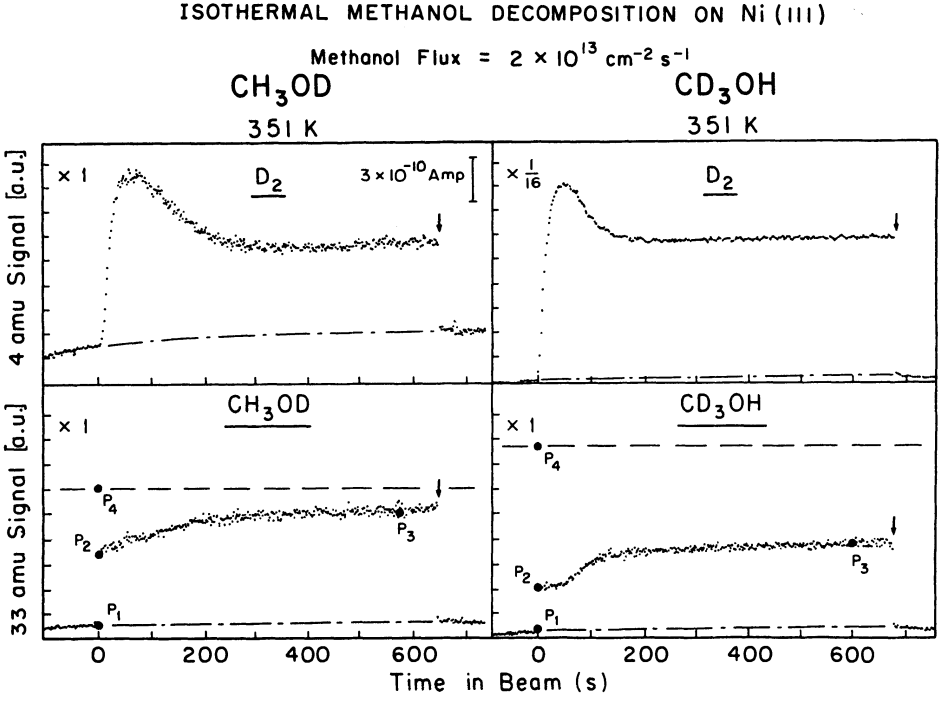

Fig.10.2. Representative data showing isothermal decomposition of CH_3OD (left) and CD_3OH (right) on Ni{111} at 351 K. Zero time and vertical arrows show rotation of the crystal in and out of the methanol beam, respectively. Pressures P_1, P_2, P_3, and P_4 are explained in the text

upper two panels) for both isotopic versions of methanol. Again, it is observed that steady state conditions are achieved. This observation of D_2 product in both cases implies that at 351 K both O-H and C-H bonds are breaking.

Point P_4 is obtained in separate experiments where the crystal is covered with an overlayer of CO, where no reaction of methanol occurs. From the data of Fig.10.2, it is possible to calculate a *zero-coverage* reactive sticking coefficient S_0^R from the relationship

$$S_0^R = \frac{P_4 - P_2}{P_4 - P_1} \quad . \tag{10.1}$$

The use of (10.1) assumes that the scattering angular distribution of methanol species is the same for both experiments. The normal orientation of the orifice to the mass spectrometer is located 60^o away from the specular beam direction to be reasonably certain that scattering from accommodated methanol molecules is primarily measured. An examination of the two lower panels in Fig. 10.2 shows that the reactivity of CH_3OD is lower than that of CD_3OH. This is indicative of a DKIE when comparing O-H and O-D functionalities.

The measurement described above was repeated for three isotopic methanol molecules (Fig.10.3) for a number of isothermal experiments between 300 K

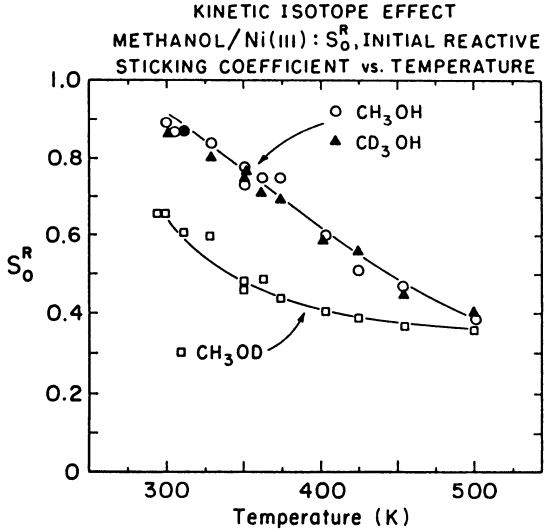

Fig.10.3. Zero-coverage reactive sticking coefficient S_0^R versus temperature for 3 methanol isotopes. Duplicate data points at 350 K indicate reproducibility

Table 10.1. Calculated deuterium kinetic isotope effect for CH_3OH versus CH_3OD

Temp. [K]	$\frac{k_H}{k_D}$ = DKIE[a]	Vibrational modes considered as contributing to DKIE	Footnote
350	1.61±0.08 (observed)		
500	1.10±0.08 (observed)		
350	42.3	All 12 normal modes	b
500	14.7		
350	34.1	3 hydroxyl modes listed below	
500	14.0		
350	7.40	O-D, 2720 cm^{-1} O-H 3687 cm^{-1} Stretch	c
500	4.00		
350	2.74	C-O-D 867 cm^{-1} C-O-H 1346 cm^{-1} Bend in plane	c
500	2.12		
350	1.57	H-C-O-D 475 cm^{-1} H-C-O-H 655 cm^{-1} Torison	d
500	1.47		

[a]From vibrational partition functions, calculated in the harmonic oscillator approximation.
[b]Gas-phase IR frequencies from [10.6].
Liquid-phase Raman modes 7, 11 only [10.7].
[c]Gas-phase IR [10.6].
[d]Liquid-phase IR, mode 12 only [10.6].

and 500 K. It is apparent in the upper curve that CH_3OH and CD_3OH yield the same value of the reactive sticking coefficient, whereas CH_3OD reacts more slowly. This means that C-H motions are not of importance in describing the reaction coordinate which controls the overall methanol consumption reaction, and that the rate-controlling step in the overall consumption of methanol resides in the O-H moiety. Measurements of the DKIE from these data yield a ratio of k_H/k_D = 1.6 (300 K) and k_H/k_D = 1.1 (500 K). These measurements correspond to the rate of reaction on a clean Ni{111} surface on which no reaction products have been allowed to accumulate.

Considerations of the vibrational modes for methanol have led to a model in which a low-frequency mode in the adsorbed methanol molecule becomes the reaction coordinate. Thus, in Table 10.1, we systematically show the values of the DKIE calculated for various combinations of the normal modes or for various single normal modes which are being converted to a translational mode in the activated complex according to reaction rate theory [10.8]. Only

when a low-frequency bending or torsional mode is identified as the reaction coordinate do we calculate values for the DKIE which resemble the measured values over the temperature range of the experiment.

Westheimer [10.9] and *Melander* and *Saunders* [10.10] have proposed models for low k_H/k_D ratios for gas- and liquid-phase reactions. Their models discuss a highly asymmetric linear three-center transition state, A···H-B, with bond strengths A···H and B-H different by about a factor of 10. Such a model appears inappropriate because the O-H bond energy in CH_3OH (102 kcal/mole) and the H-Ni surface bond energy (about 63 kcal/mole) differ by less than a factor of 2.

Eliminating the O-H stretch implies a major contribution to the reaction coordinate from the lower-frequency vibrational modes of the hydroxyl group. These modes yield calculated DKIE values in the range of the observed DKIE when each is considered separately as the model reaction coordinate (Table 10.1). Figure 10.4 depicts a proposed surface transition state involving the in-plane C-O-H bending mode as the reaction coordinate α. Here, as suggested by the experimental data, the methyl group motions are not participating in the rate-controlling step for the reaction.

10.2.2 Steady-State Kinetics of Methanol Decomposition on Ni{111}

The data shown in Fig.10.2 also permit us to measure the steady-state rate of catalytic decomposition of methanol. For this, measurements of the frac-

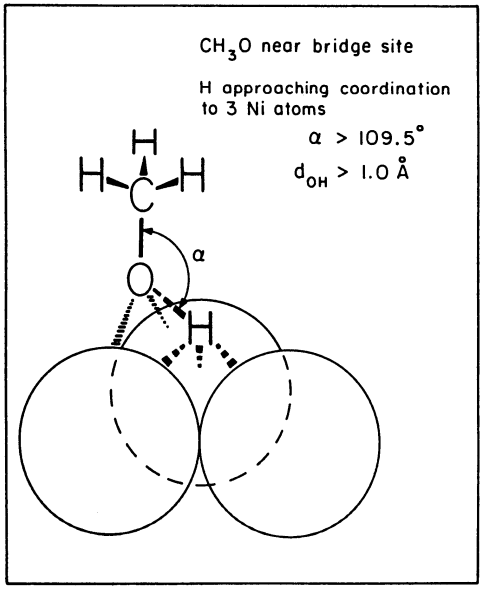

Fig.10.4. Possible transition state controlling CH_3O formation on Ni{111}. The hydroxyl H atom is approaching coordination in a 3-fold site [10.11]. Methoxy (CH_3O) is shown in a bridge site. The O-H bond distance d_{O-H} is greater than 1 Å, and the C-O-H angle α is increasing

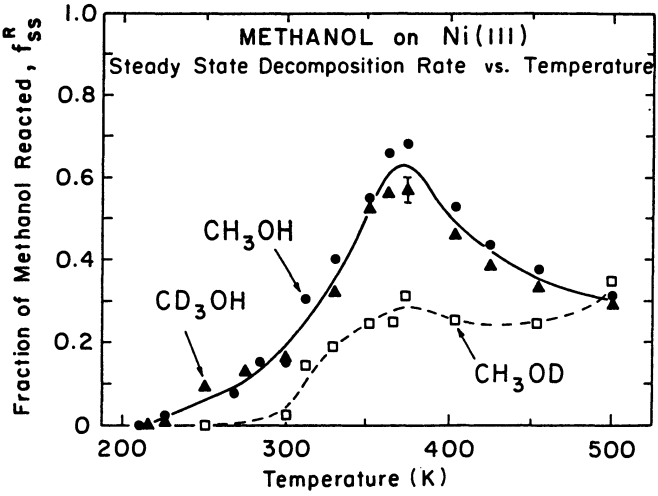

Fig.10.5. Fraction of methanol reacted at steady state f_{SS}^R, versus temperature for three methanol isotopes. The error bar for CD_3OH at 374 K indicates reproducibility. The exposure at which P_3 is measured is selected as described in [10.12]

tion of methanol removed from the beam at *steady state* f_{SS}^R are made according to

$$f_{SS}^R = \frac{P_4 - P_3}{P_4 - P_1} \quad . \tag{10.2}$$

Data for a number of temperatures are shown in Fig.10.5, where once again the three isotopic methanol molecules are compared. By using thermal desorption procedures to monitor the steady state coverage of CO(ads) and H(ads), it was possible to show rigorously that the experiment was in fact operating at steady state, since the surface composition was invarient with time after the initial buildup of coverage of reaction products [10.12]. The rate of the reaction is identical for CH_3OH and CD_3OH over the entire temperature range and is slower for CH_3OH over most of the range. Again we see that the O-H moiety seems to be involved in the rate-controlling step for steady-state decomposition kinetics, just as it was for the decomposition reaction on the clean Ni{111} surface. Also, we see that the steady-state rate of methanol decomposition has a maximum at about 375 K.

In an attempt to explain the peaked shape of the rate curve shown in Fig. 10.5, we measured, by thermal desorption, the steady-state surface coverage of the decomposition products, H(ads) and CO(ads), as a function of temperature under conditions where the surface is experiencing a constant flux

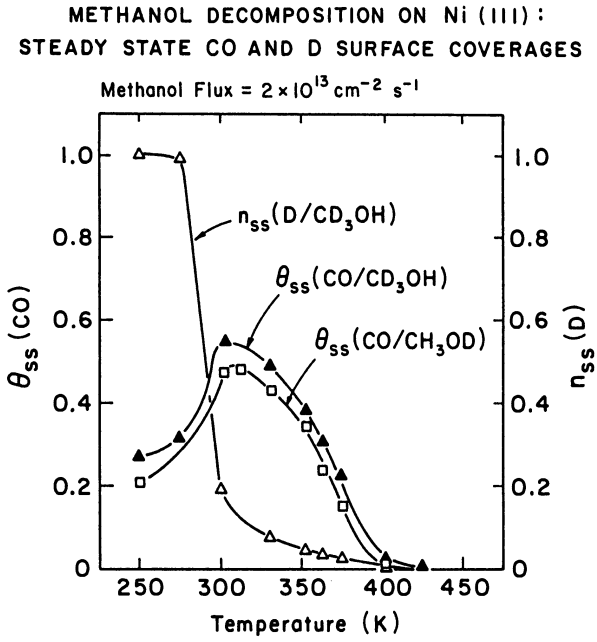

Fig.10.6. Plot of steady-state CO absolute coverages. $\Theta_{ss}(CO)$ versus temperature comparing CD_3OH and CH_3OD. The relative steady state D coverage $n_{ss}(D)$ for CD_3OH is also shown

of methanol reactant of 2×10^{13} molecules cm^{-2} s^{-1}. A plot of these coverages is shown in Fig.10.6. It can be seen that below 300 K the steady D(ads) coverage drops precipitously, while the CO(ads) coverage rises to a maximum and then falls. Above ~ 400 K, neither H(ads) nor CO(ads) remains on the surface. Because the rate of CH_3OD reaction is smaller at all temperatures than the rate of CD_3OH reaction due to the DKIE, the steady-state coverages of CO from the two isotopic molecules differ by a small systematic amount, as seen in Fig.10.6. By calibrating the TPD measurement of CO and H_2 using known full-coverage layers of these adsorbates, it is possible to estimate absolute surface coverages of each species [10.12]. This information is used to construct a basic kinetic model to explain the shape of the steady-state rate-of-reaction curve shown in Fig.10.5.

In Fig.10.7, the kinetic model is schematically deduced from measurements described in this chapter. Panel A of Fig.10.7 is the calculated fractional coverage of the surface species H(ads) and CO(ads) derived from Fig.10.6. These data may be converted to the information shown in panel B (the fractional number of open sites as a function of temperature). Panel C is a plot of the reactive sticking coefficient on an open site, previously measured in

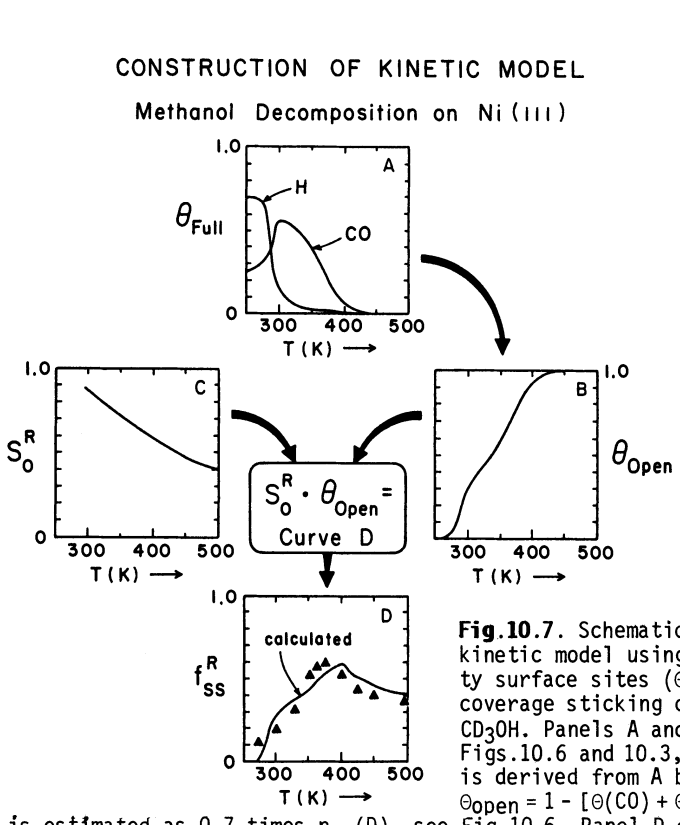

Fig.10.7. Schematic construction of the kinetic model using the fraction of empty surface sites (Θ_{open}) and the zero coverage sticking coefficient (S_0^R) for CD_3OH. Panels A and C are redrawn from Figs.10.6 and 10.3, respectively. Panel B is derived from A by subtraction: $\Theta_{open} = 1 - [\Theta(CO) + \Theta(H)]$, where $\Theta(H)$ is estimated as 0.7 times $n_{SS}(D)$, see Fig.10.6. Panel D compares the product $S_0^R \cdot \Theta_{open}$ with CD_3OH steady rate data of Fig.10.5 (solid triangles)

Fig.10.2. The product of the functions in panels B and C lead to the calculated solid curve shown in panel D, and this is compared with the experimental points for the steady-state decomposition rate for CD_3OH. It is seen that the comparison is very good.

The opening up of empty sites is the dominant factor controlling the decomposition kinetics below 375 K. Above 400 K the decline in the reactive sticking coefficient for methanol on open sites is the dominant factor controlling the falloff in decomposition rate. The absence of a kinetic isotope effect for C-D versus C-H in methanol decomposition must indicate that the decomposition proceeds through a surface methoxy intermediate, and that the rate-determining step is the rate of methoxy formation under both steady-state and clean conditions.

The involvement of the surface methoxy species is consistent with other work. Thus, *Richter* and *Ho* and co-workers have used electron energy-loss spectroscopy (EELS) in a time-resolved mode to study the kinetics of metha-

nol decomposition on Ni{110} [10.13]. Here, surface methoxy is seen and its decomposition kinetics are measured.

The reason for the falloff in the reactive sticking coefficient S_0^R with increasing temperature has not been investigated in this work. It is possible that methanol remains in a mobile precursor state for some period before reaction, and that its lifetime in this state decreases in a manner which reduces its ability to undergo reaction as the surface temperature rises.

10.3 Scanning Kinetic Spectroscopy (SKS) Methods for the Study of the Decomposition of Alcohols on Ni{111}

10.3.1 Rationale for the SKS Method

A polyatomic molecule interacting with a solid surface may, in its catalytic decomposition, encounter multiple competing reaction pathways. As the temperature of the surface is increased, the available reaction pathways would be expected to open up at characteristic temperatures as particular activation energy barriers are surmounted. The open pathways, along with surface concentration effects, will determine the observed surface chemistry at any temperature. Correlation of such incisive thermal information for the various reaction processes constitutes a "temperature-scanned kinetic spectrogram" for the particular molecule-plus-surface system.

Experimetally, by programming upwards the temperature of a single crystal catalyst while it interacts with a beam of reactant molecules, we can observe the opening of reaction pathways as we simultaneously measure reactant consumption and product evolution as a function of temperature. This method forms the basis for a rapid, new probe of surface reaction kinetics, scanning kinetic spectroscopy [10.2]. The SKS method differs from the earlier temperature programmed reaction spectroscopy (TPRS) in one major way. In TPRS, an adsorbed overlayer is programmed upwards and desorption products are monitored [10.14]. In SKS, the same information is obtained, but in addition the temperature dependence of reactant consumption from the molecular beam is measured simultaneously. Thus TPRS represents a limiting condition of SKS, where the flux of arriving molecules is zero. The concept of temperature scanning while making reaction kinetic measurements on a single-crystal catalyst was presented in 1981 by *Goschnick* and *Grunze* [10.15]. The absence of a direct line of sight over a small distance to the QMS detector in their experiment limited the measurement to net reaction rates, excluding information on elementary surface processes.

The main purpose of SKS experiments is to delineate the various reaction channels and to determine their onset temperature. It is a survey technique,

efficiently giving information about the pattern of kinetic events, the products of these kinetic steps, and (using the DKIE) the bond-breaking processes which control the surface chemistry at work in each reaction channel. The SKS technique is a preliminary tool for more detailed studies in which reaction kinetics and reaction dynamics are investigated for the elementary processes resolved by SKS. The SKS method also forms a sound basis for the study of the spectroscopy of surface species which are intermediates in a reaction process, supplying the temperature conditions where these intermediates are stable.

10.3.2 Methanol Decomposition on Ni{111} – SKS Measurements

A kinetic spectrogram for the interaction of CD_3OH with Ni{111} is shown in Fig.10.8. The clean Ni{111} surface was saturated with CD_3OH at 187 K (exposure = 1×10^{16} CD_3OH cm^{-2}) and then rotated into the beam. Following the establishment of a steady condition, the crystal was temperature programmed

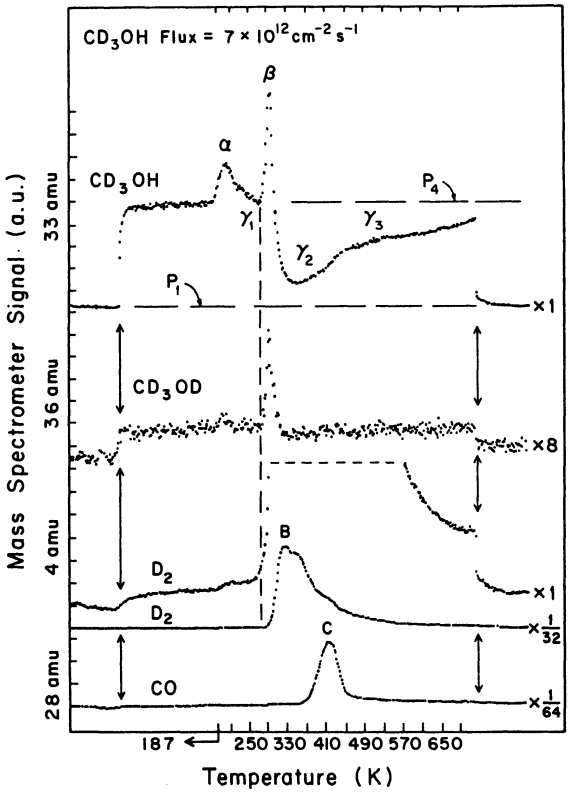

Fig.10.8. Basic scanning kinetic spectrogram for the CD_3OH plus Ni{111} system. Before the experiment, an exposure of 1×10^{16} cm^{-2} CD_3OH was made at 187 K, the initial crystal temperature

while in the beam. Multiplex mass spectrometric measurements were made as shown in Fig.10.8. It is observed that the individual SKS traces are quite rich in detail, and that correlated behavior is observed between the individual SKS traces where certain onset temperatures agree accurately from one SKS trace to another.

Four characteristic temperature regions of reactant CD_3OH evolution and consumption are observed in the data set at the top of Fig.10.8. These regions correspond respectively to CD_3OH desorption from the adsorbed molecular species (α region); CD_3OH consumption (γ_1); CD_3OH and CD_3OD desorption due to recombination of CD_3O with H or D (β); enhanced CD_3OH consumption due to site opening by H_2 (D_2) and CO desorption (γ_2); and finally a decrease in the reactive sticking coefficient for CD_3OH with increasing temperature of the essentially clean surface (γ_3).

The repeatability of the SKS scan in successive measurements (without deliberate surface cleaning between measurements) can be used to monitor surface poisoning by nonvolatile reaction products. Contamination of the Ni{111} by surface C or by surface O is possible of a methanol decomposition pathway involving irreversible C-O bond scission occurs. In the case of methanol, the repeatability of the successive SKS scans and AES analysis following an experiment indicate that contamination does not occur.

The assignment of the β channel to recombination of surface methoxy with surface hydrogen is verified by the SKS study of CD_3OD evolution shown in Fig.10.8. The onset temperature (290 K) and the sharp peak shape of the β features for CD_3OH and CD_3OD are in excellent agreement. The CD_3OD product can only arise as a result of C-D bond scission. We believe that this is indicative of a "hydrogen-flooding" phenomenon on the surface containing methoxy species, and this triggers the recombination process observed. The "hydrogen-flooding" would be expected to result in the production of H···H, H···D, and D···D recombination events also, and the SKS measurement shows that this does indeed occur with an onset temperature near 290 K, as shown in Fig.10.8, where only D_2 desorption is plotted.

The desorption of hydrogen species and the later desorption of CO molecules opens Ni sites for reactive chemistry with the incoming molecular beam of CD_3OH, and the two γ regions reflect the onset of reaction with the beam as the Ni sites open, in agreement with the ideas inherent in the model for methanol decomposition devised in Fig.10.7.

The dependence of the SKS behavior for this system has been thoroughly investigated as a function of the incoming flux of methanol and this information is reported elsewhere [10.2]. In addition, the exchange between ad-

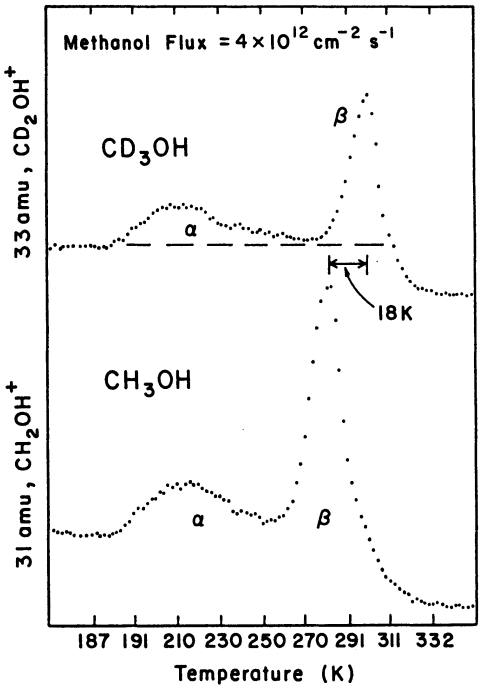

Fig.10.9. Kinetic isotope effect in SKS data with expanded temperature axis for CH_3OH and CD_3OH methanol isotopes. Intact methanol desorption peak α is not affected by isotopic substitution. Recombination of methoxy species, peak β, shows a C-H (C-D) bond breaking isotope effect of 18 to 20 K in both peak and treshold temperatures. Top: $CD_3OH(a)$ plus $CD_3O(a)$ plus $CD_3OH(g)$. Bottom: $CH_3OH(a)$ plus $CH_3O(a)$ plus $CH_3OH(g)$

sorbed methanol and an isotopically labeled methanol in the beam has been characterized [10.2].

A fascinating example of the utility of the DKIE used in conjunction with the SKS method is shown in Fig.10.9. Here, expanded SKS plots are shown for the CD_3OH and CH_3OH molecules. The desorption of undissociated methanol molecules exhibits no discernible DKIE in the α channel, and the desorption peak temperatures are identical for the two isotopic methanol molecules. However, the β channel shows a pronounced DKIE which causes an 18 K upward shift in the β peak temperature when C-D bonds are involved. This kinetic isotope effect is precisely opposite to that observed for the overall decomposition of methanol (Figs.10.3,5) and represents the *extreme power of SKS* in *picking a specific channel for detection of the DKIE* under conditions where an opposite DKIE controls the overall net process. The 18-K shift in the β peak tells us that the elementary step being observed here is controlled by the breaking of C-H(C-D) bonds in adsorbed methoxy, a result consistent with the observation of CD_3OD product as shown in Fig.10.8.

If "hydrogen flooding" of the surface is responsible for the β recombination process, then it should be possible to influence the hydrogen surface concentration artificially and to see effects of this on the β process. We

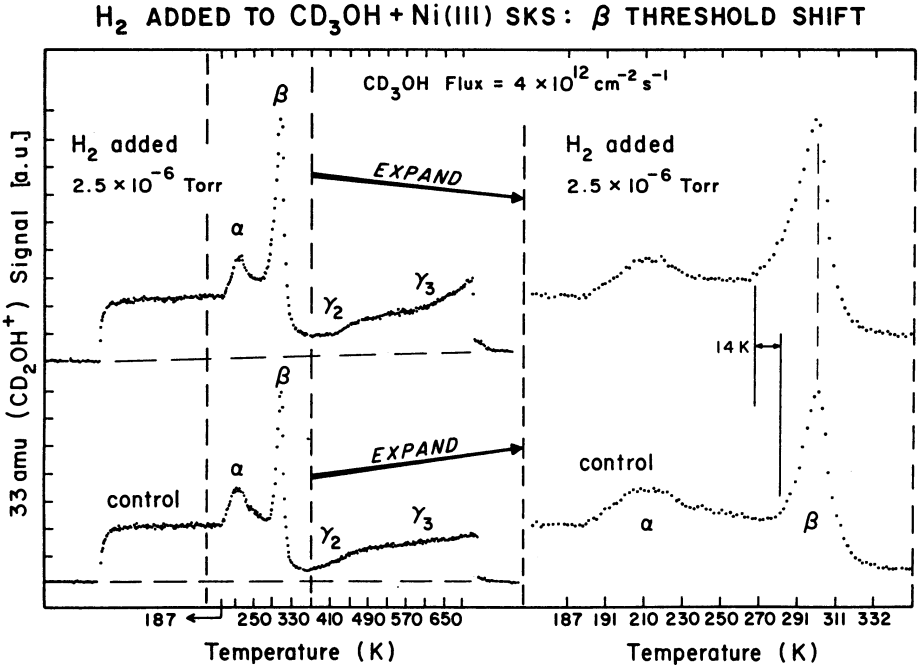

Fig.10.10. SKS data for a standard CD_3OH plus Ni{111} SKS experiment (*lower data*) and for the same experiment in a 2.5 x 10^{-6} Torr H_2 ambient (*upper data*). Left panel: full CD_3OH SKS data. Right panel: expanded temperature scale for the same experiments. Before each experiment, a CD_3OH exposure of 1 x 10^{16} cm^{-2} was made at 187 K

have done this by carrying out the SKS measurement in an ambient background of H_2 gas, as shown in Fig.10.10. It is seen that this additional surface hydrogen produces a downward shift of 14 K in the onset temperature for the β process. The peak temperature of the β feature is not influenced, because at this temperature hydrogen supply is dominated by C-H bond breaking in methoxy species rather than by the presence of surface hydrogen atoms delivered from the gas phase at a pressure of 2.5 × 10^{-6} Torr.

We have also studied the influence of the preadsorption of hydrogen on the SKS behavior of methanol [10.2]. Basically, hydrogen preadsorption decreases the ratio of the β to α processes. Hydrogen acts as a site blocker, rendering methanol(ads) the majority species and methoxy(ads) the minority species. Thus, adsorbed hydrogen blocks the O-H bond scission process needed to produce methoxy from adsorbed methanol.

Using the methanol plus Ni{110} system. and a unique time-resolved electron energy-loss spectrometer (TREELS), *Ho* and co-workers [10.13a] have directly observed CH_3O decomposition on the surface, while temperature pro-

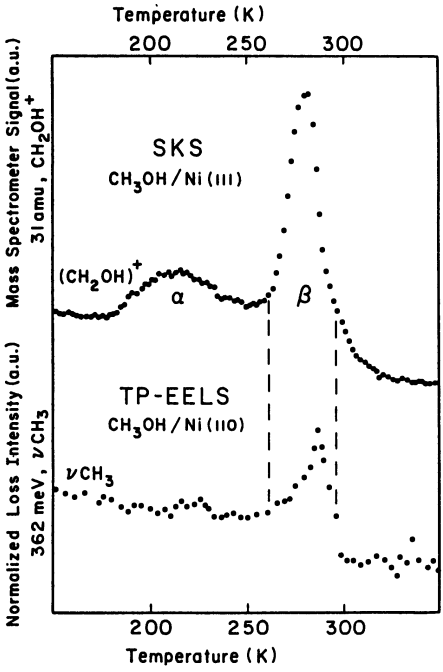

Fig.10.11. Comparison of SKS data (*top*) with TP-EELS data (*bottom*) from [10.13a] for CH_3OH on 2 Ni surfaces. Note the temperature agreement for the SKS β recombination peak and the TP-EELS C-H stretch signal

gramming the crystal. Under high-coverage conditions, this process is observed in the temperature range 270-300 K, in excellent agreement with our observation of the β-process methoxy recombination on Ni{111}. Figure 10.11 compares our CH_3OH SKS data with the temperature dependence of the intensity of the C-H stretching mode for methoxy on Ni{110}. As seen in Fig.10.11, the C-H intensity first increases and then decreases in the temperature range where the β recombination process occurs. We believe that the results suggest that a conformational change in the $-CH_3$ group orientation occurs as recombination of methoxy and adsorbed hydrogen takes place, leading to an increase in dipole scattering intensity in the TREELS measurement. The comparison of the two different methods shown in Fig.10.11 involves two different crystal planes of Ni; the methanol plus Ni system apparently exhibits little structure sensitivity.

10.3.3 Ethanol Decomposition on Ni{111} Using SKS

Ethanol is a molecule containing 9 atoms connected by two-electron, single bonds. These bonds may be organized into five types: O-H, C-O, C-C, C-H (methylene), and C-H(methyl). We will demonstrate here that the DKIE may be used incisively to determine the sequence of bond scission steps for the O-H and C-H bonds in ethanol decomposition. Figure 10.12 illustrates the basic sequence of surface reaction steps which have been discerned, and gives,

Sequence of Bond Scission

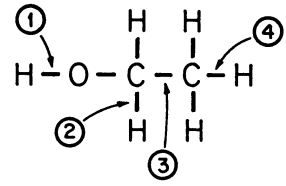

Reaction

$$CH_3{}^*CH_2OH(g) \longrightarrow CH_3-{}^*\overset{O}{\overset{\|}{C}}-H(g) + H_2(g) + {}^*CO(g) + CH_4(g) + C(a)$$

Schematic Mechanism

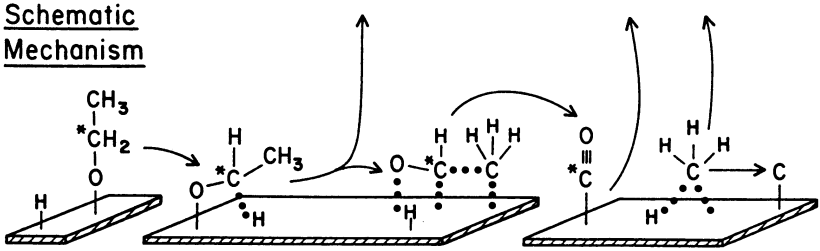

Fig.10.12. Summary of sequence of bond scission, products formed, and schematic mechanism for the decomposition and reaction of ethanol on Ni{111}. The structures of the two intermediates at lower center are inferred, and are discussed in the text

in addition to the desorption products observed, a pictorial representation of the surface intermediates which have been inferred from our data.

In Figure 10.12, CH_3CH_2O(ads), ethoxy, appears at the lower left of the figure. It is a stable surface intermediate below about 260 K. Two intermediates are schematically represented at the center of this mechanism, CH_3CH_2O(ads) and CH_3CHO(ads). These are unstable, reactive intermediates. The right-hand section of this mechanism shows adsorbed CO as a stable surface species when formed below the CO desorption temperature threshold (~380 K). Also shown is surface methyl CH_3(ads), which may either recombine with adsorbed hydrogen to produce CH_4 or decompose to form H(ads) and C(ads).

An adsorption temperature of 240 K was selected in order to study the initial surface intermediate formed by reaction of ethanol with Ni{111}. This temperature is about 15-20 K below the desorption threshold for acetaldehyde and methane (as shown in Fig.10.14), and is 65 K above the desorption maximum at 175 K for weakly chemisorbed molecular ethanol (Fig.10.14).

Figure 10.13 compares the rate of the initial reaction with Ni{111} at 240 K measured using four different isotopic ethanol molecules. The ordinate of the figure is the C to Ni AES peak-to-peak height ratio. The abscissa of the figure is the ethanol exposure, measured accurately using the calibrated molecular-beam doser shown in Fig.10.1. Each data point represents a sepa-

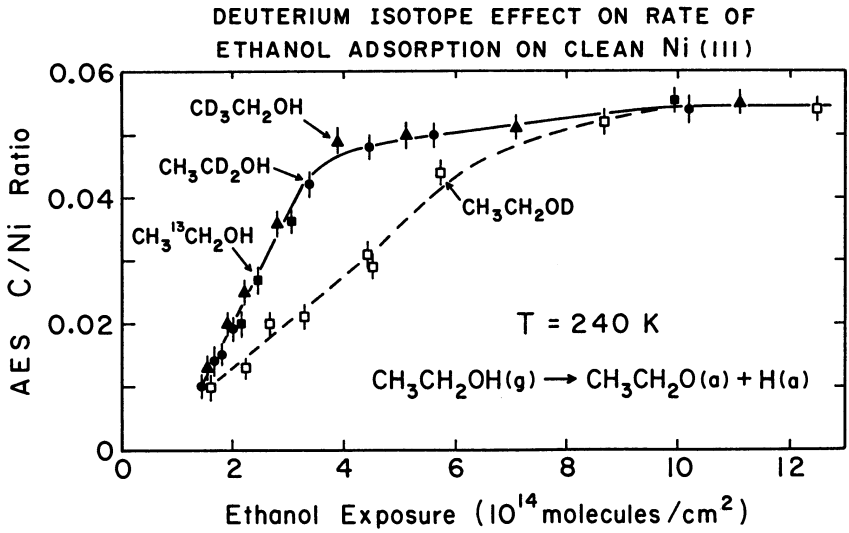

Fig.10.13. Carbon (272 eV) to Nickel (860 eV) peak-to-peak height ratio in AES plotted versus exposure of Ni{111} to four isotopic ethanol molecules at 240 K. Each data point is a separate measurement for ethanol exposed to the *clean* surface, so that electron beam damage is not accumulated. The AES instrument parameters are 0.4 μA beam current, 3 kV energy, 3 V p.p. modulation and 0.5 eV/s sweep rate

rate experiment on the clean surface, so that electron beam damage effects were not accumulated through any series of points. $CH_3{}^{13}CH_2OH$ may be considered as a reference compound in this study when observing the effect of deuterium substitution on the rate of formation of a saturation coverage of adsorbed species, because no deuterium is present in this molecule. The initial slopes of the plots in Fig.10.13 are proportional to the reactive sticking coefficient S^R. It is clearly seen in Fig.10.13 that substitution of deuterium in the alkyl group, either at CH_3 or CH_2 has no effect on S^R. In contrast, deuterium substitution on the hydroxyl hydrogen causes a DKIE, reducing S^R by about a factor of 2 at 240 K. The hydroxyl group is therefore the site for the initial reaction of ethanol with Ni{111}, and the rate-controlling step for this reaction involves the production of adsorbed ethoxy at 240 K. This is consistent with results reported earlier for methanol decomposition on Ni{111}, and even the magnitude of the DKIE is comparable for the two molecules, using two entirely independent methods for measurement.

A complete SKS measurement for CD_3CH_2OH is shown in Fig.10.14. The surface is initially saturated with the ethanol molecule, and then heated at 2 K/s in the beam. A small desorption peak for undecomposed ethanol is observed at ~ 175 K. As the surface temperature is increased, and decomposition pro-

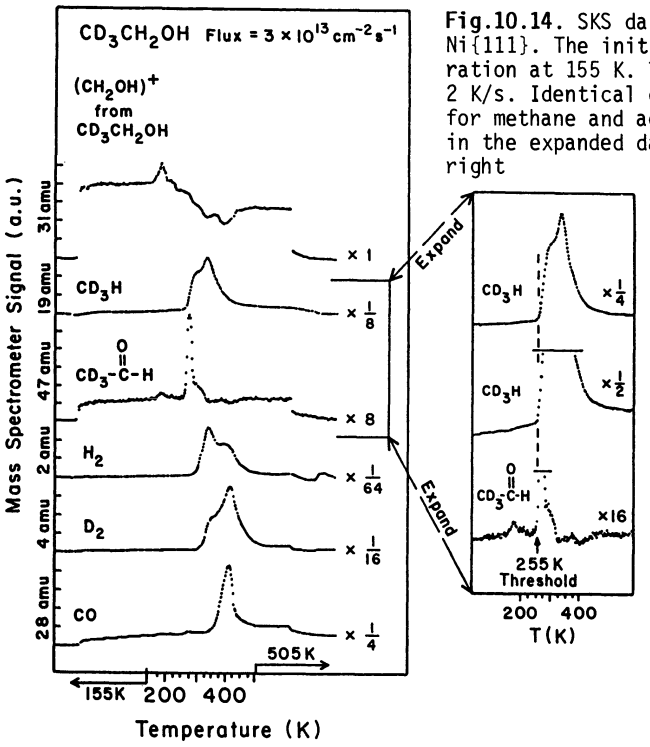

Fig.10.14. SKS data for CD_3CH_2OH plus Ni{111}. The initial coverage is saturation at 155 K. The heating rate is 2 K/s. Identical desorption thresholds for methane and acetaldehyde are shown in the expanded data panel on the right

ducts desorb from the surface, ethanol is removed from the beam by reaction with open sites on the surface, and we observe that the reflected ethanol signal decreases in discrete steps.

The desorption of various reaction products is also shown in Fig.10.14. Both acetaldehyde and methane are observed as reaction products and their desorption temperature thresholds are reproducibly identical (255 K) within experimental error (±4 K). This is shown in more detail in the expanded data panel at the right-hand side of Fig.10.14.

We have explored the details of the bond activation in this reaction in more detail, as shown in Fig.10.15, where TPD experiments for various deuterium-substituted ethanol molecules are compared. Here we are comparing deuterium substitution on the methylene C with deuterium substitution on the methyl carbon. For reference, TPD results using deuterium-free ethanol adsorbate are also shown. The products acetaldehyde and methane are examined in detail here. It is noted first that the threshold temperature for acetaldehyde and methane production is independent of deuterium labeling in the methyl group (bottom two TPD spectra). However, when deuterium is substituted for hydrogen in the methylene position, a prominent DKIE is observed for both acetaldehyde and methane. This is an *incisive observation* about the

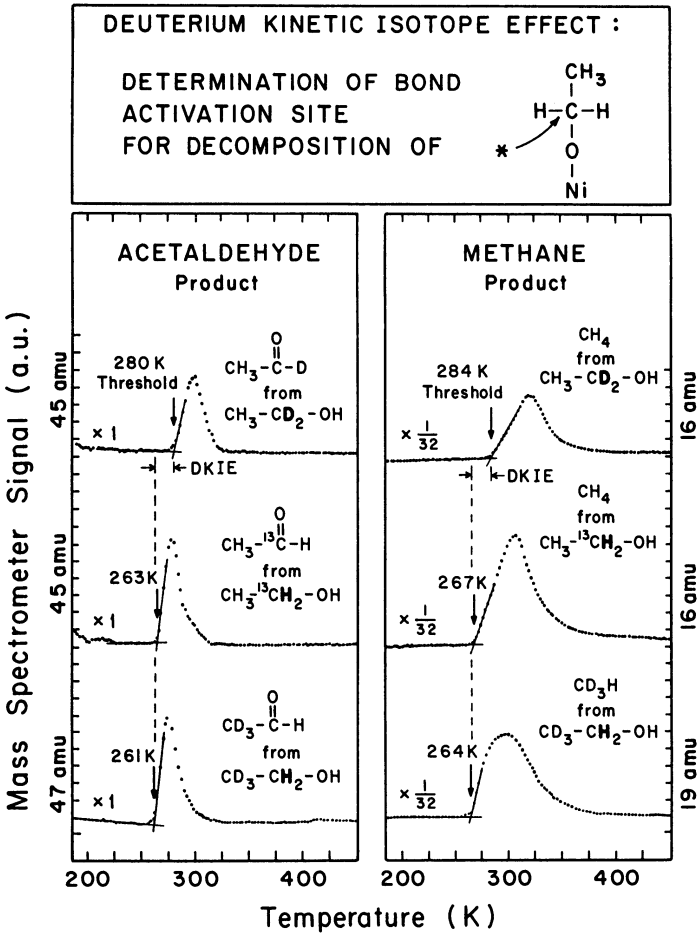

Fig.10.15. TPD data for three isotopic ethanol molecules on Ni{111}. Initial coverage: saturation at 155 K. Heating rate: 2 K/s. From CH_3CD_2OH, acetaldehyde and methane desorb with a threshold temperature $\approx$ 18-20 K higher than for $CH_3{}^{13}CH_2OH$ and CD_3CH_2OH. This is a measure of the DKIE at the $CH_2(CD_2)$ carbon

bond activation site which controls the final fragmentation process of adsorbed ethoxy. The crucial molecular site controlling the chemistry is the C-H bond in the methylenic position in adsorbed ethoxy. Once this C-H bond breaks, the C-C bond can break, yielding CH_3(ads). The CH_3(ads) recombines with H(ads) to produce CH_4 which desorbs with essentially the same threshold temperature as the acetaldehyde product. We estimate that the activation energy for the methylene C-H bond breaking is about 16 kcal/mole, using an assumed preexponential factor of 10^{13} s^{-1} [10.16]. Using TREELS, *Richter* and *Ho* [10.13b] have estimated that the activation energy for C-H bond breaking

in CH_3O(ads) adsorbed on Ni{110} is 17 kcal/mole with a measured preexponential factor of about the same value as we have assumed.

Ethanol decomposition chemistry on clean Ni{111} [10.16] and on clean Ni{100} [10.17] involves the surface ethoxy intermediate on both surfaces. However, acetaldehyde was not detected on the clean Ni{100} surface but was induced to form by addition of 1/4 monolayer of sulphur (Ni{100}-p(2×2)S). We have detected acetaldehyde desorption from ethoxy on Ni{111} at coverages ranging from saturation to about 1/10 saturation. The absence of detectable acetaldehyde formation on clean Ni{100} [10.17] may indicate a structure-sensitive character for this reaction channel.

It is interesting to speculate why C-C bond scission in the unstable CH_3CHO(ads) surface species (lower center, Fig.10.12) is easily triggered by C-H bond scission in the methylene group. One possible mechanism involves sequential bond breaking. This is shown schematically in Fig.10.12. Methylene C-H bond scission leads to coordinatively unsaturated methylene C atoms, which may be stabilized by a bonding interaction with the Ni{111} surface. The Ni-C bond forms after one C-H bond has broken, and this causes a weakening of the C-C bond, leading to CH_3(ads) formation, which will be discussed in more detail next. An alternative explanation involves an initial bonding interaction of the methylene C atom with the surface. A formally pentavalent C atom would characterize a highly unstable intermediate which decomposes by a combination of C-H and C-C bond scission events.

The production of surface methyl(CH_3) has been suggested by the above discussion, as shown in Fig.10.12, as a result of C-C bond scission. We have used the molecule CD_3CH_2OH to investigate this possibility. In Fig.10.16 is shown the mass spectrum observed for methane production from this isotopic ethanol. The black bars are the experimental result, and it is seen that the dominant methane isotope is CD_3H (19 amu). This is compared with a model in which a 1:1 atom pool of H(ads) and D(ads) (originating from the equimolar D and H from the CD_3CH_2OH molecule) is assumed to statistically produce isotopic methanes. The predicted methane mass spectrum is shown by the hatched bars for this random recombination process. It is clear from these data that the random process is not the dominant route to methane. These measurements, along with other measurements for CH_3CD_2OH, show that methyl fragments are produced from ethanol in Ni{111}, but these fragments undergo partial hydrogen exchange processes with surface H(D)(ads). In fact, ethanol provides a convenient route for the introduction of CH_3(ads) to a Ni{111} surface, and this has been exploited in a study of the elementary processes in the catalytic methanation reaction [10.18].

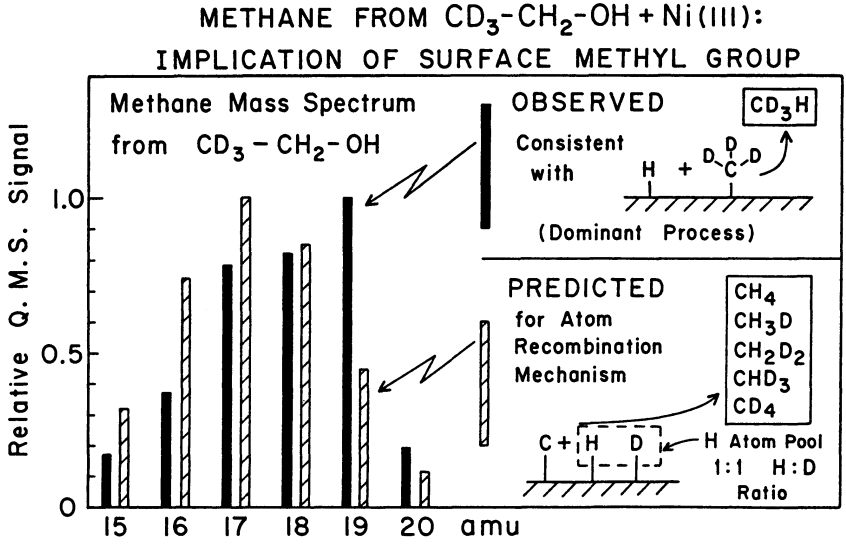

Fig.10.16. Comparison of methane spectrum observed from CD_3CH_2OH by TPD with a predicted methane spectrum. The latter is based on an atom recombination mechanism, and details of the calculation appear in [10.16]

10.4 Summary of Results

These studies of the interaction of alcohol molecules with the Ni{111} surface have illustrated the power of the use of isotopic labeling in order to observe the kinetic details of adsorption and catalytic decomposition. In particular, the use of the deuterium kinetic isotope effect (DKIE) is incisive when combined with scanning kinetic spectroscopy (SKS) to investigate particular reaction channels in a complex sequence of interrelated steps on the surface. The methods of surface kinetics are powerful in giving details which might not be observable in experiments involving surface spectroscopies alone, a fact long recognized in gas-phase chemistry. It is suggested that surface kinetics investigations, combined with well-defined surface spectroscopic studies, form an efficient and powerful procedure for the determination of the nature of elementary processes at surfaces. Such studies, carried out on well-defined single crystal substrates, are providing baseline information of importance to many areas of surface chemistry.

Acknowledgement. We gratefully acknowledge support of this work by the Army Research Office under Contract No. DAAG29-83-K-0141.

References

10.1 R.J. Muha, S.M. Gates, P.Basu, J.T. Yates,Jr.: Rev. Sci. Instrum. **56**, 613 (1985)
10.2 S.M. Gates, J.N. Russell, Jr., J.T. Yates, Jr.: Surf. Sci. **159**, 233 (1985)
10.3 C.T. Campbell, S.M. Valone: J. Vac. Sci. Technol. A **3**, 408 (1985)
10.4 J.T. Yates, Jr.: in *Methods of Experimental Physics*, Vol. 22, ed. by R.L. Park, M. Legally, (Academic, New York 1985) p.425
10.5 S.M. Gates, J.N. Russell, Jr., J.T. Yates, Jr.: Surf. Sci. **146**, 199 (1984)
10.6 M. Falk, E. Whalley: J. Chem. Phys. **34**, 1554 (1961)
10.7 G. Herzberg: *Molecular Spectra and Molecular Structure*, Vol. II, *IR and Raman Spectra of Polyatomic Molecules* (Van Nostrand, New York 1956)
10.8 S. Glasstone, K.J. Laidler, H. Eyring: *The Theory of Rate Processes* (McGraw-Hill, New York 1941)
10.9 F.H. Westheimer: Chem. Rev. **61**, 265 (1961)
10.10 L. Melander, W.H. Saunders: *Reaction Rates of Isotopic Molecules* (Wiley, New York 1980)
L. Melander: *Isotope Effects on Reaction Rates* (Ronald, New York 1960)
10.11 K. Christmann, R.J. Behm, G. Ertl, M.A. van Hove, W.H. Weinberg: J. Chem. Phys. **70**, 4168 (1979)
10.12 S.M. Gates, J.N. Russell, Jr., J.T. Yates, Jr.: J. Catal. **92**, 25 (1985)
10.13 L.J. Richter, B.A. Gurney, J.S. Villarrubia, W. Ho: Chem Phys. Lett. **111**, 185 (1984)
L.J. Richter, W. Ho: J. Vac. Sci. Technol. A **3**, 1549 (1985)
10.14 The Madix group at Stanford University has been preeminent in using TPRS methods to study the reaction of organic molecules with metal single crystals.
10.15 J. Goschnick, M. Grunze: J. Vac. Sci. Technol. **18**, 561 (1981)
10.16 S.M. Gates, J.N. Russell, Jr., J.T. Yates, Jr.: Surf. Sci., accepted
10.17 S.W. Johnson, R.J. Madix: Surf. Sci. **115**, 61 (1982)
10.18 J.T. Yates, Jr., S.M. Gates, J.N. Russell, Jr.: Surf. Sci. **164**, L839 (1985)

11. Raman Spectroscopy of Adsorbed Molecules

A. Campion

Department of Chemistry, University of Texas, Austin, TX 78712, USA

Raman spectroscopy has become a powerful tool for investigating the structures and reactions of molecules adsorbed on surfaces. As recently as a few years ago, it was generally thought that the Raman technique would not offer sufficient sensitivity to examine adsorption at low coverages on low-surface-area materials; two developments have radically altered that view, however. The important discovery of surface-enhanced Raman spectroscopy (SERS) and the application of multichannel optical techniques for unenhanced surface Raman spectroscopy have increased the effective sensitivity of the method so that it is now possible to study adsorbates at coverages on the order of 1 % of a monolayer. In SERS, the scattered intensities can be more than a million times larger than expected from gas-phase Raman scattering cross sections and the density of adsorbed molecules. The origin of this enormous effect has stimulated a great deal of research activity over the past few years, and the general features of the mechanisms involved are reasonably well understood. The increased intensity of SERS makes it possible to study adsorption and surface chemical processes at low coverages and even make time-resolved measurments using conventional Raman instrumentation. In addition, the surface selectivity of the technique ensures that the processes under observation originate on or very close to the surface. Unfortunately however, SERS has not proven to be a very general technique; because of rather strict requirements on the dielectric constant and morphology of the surface under study, SERS experiments have been essentially restricted to silver, copper, and gold surfaces. For these materials, however, SERS has been a tremendously important technique shedding light on a number of important surface and electrochemical problems.

Stimulated by the interest and power of the SERS experiments, we sought to develop a technique for surface Raman spectroscopy that would be more general than SERS; in particular we wanted to be able to study planar surfaces of catalytically important transition metals for which there is no enhancement of the Raman scattering. Simply by understanding the behavior of the electromagnetic field near a conducting surface, in order to optimize exci-

tation and detection, and by using multichannel optical detection to increase the detection efficiency, we have been able to achieve submonolayer sensitivity for essentially any adsorbate on essentially any substrate.

Raman spectroscopy has a number of important advantages as a surface spectroscopic tool. First, because of the high spectral resolution and the well-known ability of vibrational spectroscopies to fingerprint molecules, the method is molecularly specific. This feature is essential for studying subtle changes in molecular orientation and bonding on surfaces, and for following the course of surface chemical reactions. Second, as an optical technique, the method is not restricted to the high-vacuum environment of the popular electron spectroscopies used in surface science. Also, since the specularly scattered beam is not analyzed, smooth surfaces are not required. Thus Raman spectroscopy has the appealing feature that it can be applied to a wide variety of substrates under a wide range of conditions, for example, to study adsorption on single crystal surfaces under ultra-high vacuum or under one atmosphere of an ambient gas phase as well as to study the surfaces of technical catalysts under reaction conditions. Third, the spectral range includes the entire region in which molecular vibrations occur. Since both the incident and scattered beams are visible light, there are no window or detector problems, even for very low vibrational frequencies. Finally, the incident laser can easily be focused to a spot less than a micrometer in diameter, so that mapping the surface chemical composition at very high spatial resolution is possible.

In this chapter, the unenhanced Raman experiment is discussed in some detail, as the physical considerations that underlie the design of the experiment are important and bear upon the SERS problem as well. The experimental requirements, selection rules and a discussion of the angular dependence of the scattering are presented. Several examples which illustrate important features of the method are presented. The second half of the chapter reviews the observations that appear to be universally accepted in SERS research and discusses the currently accepted views of the origins of the effect. The chapter closes with an assessment of future opportunities.

11.1 Unenhanced Raman Spectroscopy of Adsorbed Molecules

To appreciate the sensitivity requirements, consider the Raman intensity expected from a monolayer of molecules adsorbed on a planar surface. The number of scattered photons can be calculated from

$$I_R = nF\left(\frac{\partial\sigma}{\partial\Omega}\right)\Omega \quad ,$$

where n is the number of molecules in the scattering area, F is the laser flux in photons $cm^{-2}s^{-1}$, $\partial\sigma/\partial\Omega$ is the differential scattering cross section, and Ω is the solid collection angle. For a monolayer containing 10^{14} adsorbates cm^{-2}, and a laser focused to an area of $10^{-4}cm^2$, n = 10^{10} molecules. Typical Raman cross sections are of the order of 10^{30} $cm^2molecule^{-1}$ sr^{-1} and collection angles of 1 sr are common. Thus, for an incident laser power of 100 mW, a scattered intensity of 250 counts per second is expected. Since typical monochromator throughputs and photomultiplier quantum efficiencies are each of the order of 0.1, a peak count rate of a few counts per second is expected. Using a conventional scanning double monochromator covering 3000 cm^{-1} at a resolution of 5 cm^{-1} with a signal-to-noise ratio of 10:1 would require more than 5 hours, which is clearly unacceptably long for a surface experiment, even in ultra-high vacuum. The solution to this problem is to use a multichannel detector. With 1000 resolution elements, the same spectrum can be scanned in a few minutes which is similar to the time required for other surface spectroscopic probes.

11.1.1 Surface Electromagnetic Fields

An understanding of the electromagnetic field at a surface is essential for the proper design and execution of any surface spectroscopic experiment. *Greenler* was the first to consider the implications of the behavior of the surface fields on surface infrared and Raman experiments and all subsequent work in these areas rests upon that foundation [11.1,2]. Upon reflection from a surface, both the phase and the amplitude of light are altered. The coherent superposition of the incident and reflected fields is the net standing wave field experienced by the molecule at the surface. Anticipating the Raman case, we call this the primary field. The amplitude and orientation of the primary field are strongly dependent upon the angle of incidence and polarization of the incident light and upon the wavelength-dependent complex dielectric function of the surface. The local fields can be calculated from the Fresnel equations, which are solutions to the Maxwell equations for this planar geometry. The equations are presented elsewhere [11.3], but it is useful to look at the results of the calculations graphically to get a feel for the behavior of the surface fields. Figure 11.1 shows the electric component of the electromagnetic field at a silver surface for 5 μm radiation. The optical constants of silver at that wavelength correspond very nearly to those of a perfect reflec-

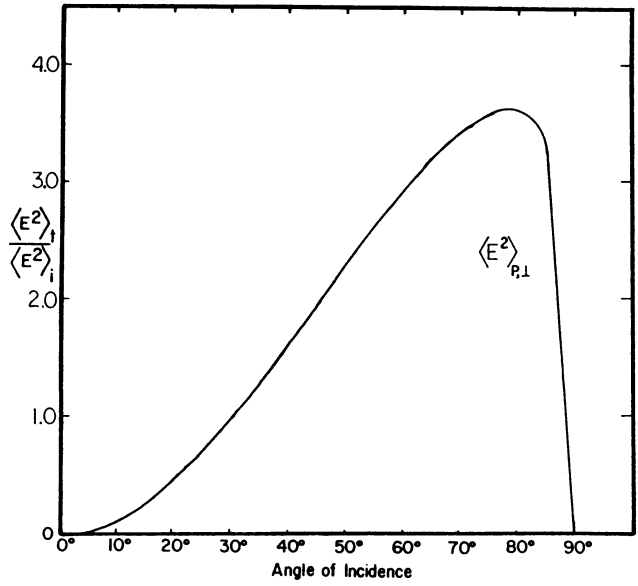

Fig.11.1. Mean square electric field amplitude at a silver surface in vacuum relative to the incident field amplitude. The wavelength $\lambda = 5$ μm, for which the optical constants of silver are $n = 3.50$ and $k = 30.40$. Here P refers to the incident polarization and $\perp$ means the normal component of the field

tor, for which the tangential component of the incident field is completely screened by the conduction electrons while the normal component is reinforced. As can be seen from the figure, the normal component (which results only from light polarized parallel to the plane of incidence, p-polarized light) follows a $\sin^2$ dependence, which is simply the square of the projection of the incident electric vector onto the surface normal. The screening of the tangential fields is so complete at infrared frequencies that they are indistinguishable from zero on this plot; they are about two to three orders of magnitude weaker than the normal fields. It is clear from these results that the maximum primary field occurs near grazing incidence, hence, surface infrared experiments should be conducted using this geometry.

The primary field created with visible light is quite different from that created with infrared radiation because of less-efficient screening of the fields at the higher visible frequencies. As can be seen in Fig.11.2, the magnitude of the normal component of the electromagnetic field is reduced as the excitation wavelength moves to the visible, and the magnitudes of the tangential fields increase. The presence of the tangential component of the primary field is not important for the most common experimental geometry for surface Raman scattering, but it can be used to advantage in alternative geo-

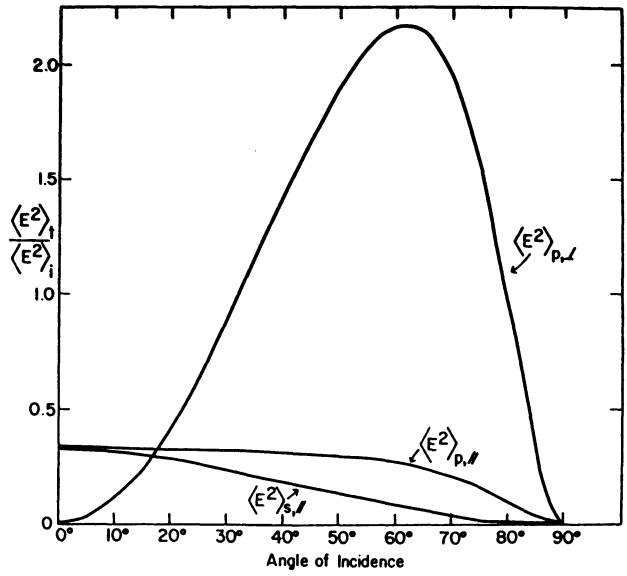

Fig.11.2. Mean square electric field amplitude at a silver surface in vacuum relative to the incident field amplitude. The wavelength $\lambda = 520$ nm, for which the silver optical constants are $n = 0.0427$ and $k = 3.3988$. Here p and s refer to light polarized in and perpendicular to the plane of incidence respectively and $\perp$ and $\parallel$ refer to normal and tangential surface fields

metries to emphasize non-totally symmetric vibrational modes, as will be discussed in Sect. 11.1.2.

The presence of the surface determines the magnitude and orientation not only of the primary field, but also of the secondary field, which is defined as the coherent superposition of the radiation emitted by the induced dipole and that reflected from the surface before reaching the detector. The model of *Greenler* and *Slager* [11.2] is used to understand the angular dependence of the scattered radiation. Figure 11.3 shows the angular distribution of the radiation which has been Raman scattered by a molecule near a metal surface. Three orientations of the dipole radiator are considered as illustrated in Fig.11.3a. Case I refers to a dipole oriented normal to the surface; Case II is a dipole oriented parallel to the surface and in the scattering plane; Case III is a dipole oriented parallel to the surface and perpendicular to the scattering plane. The physics is identical to that leading to the creation of the primary field except that the incident radiation is now provided by the Raman dipole. In the limit that the observer is located infinitely far from the surface, the curves are identical. The curves shown in Fig.11.3b include the effects of collection optics of finite aperture. Again, note how tangential dipoles can be observed, in contrast to the infrared case.

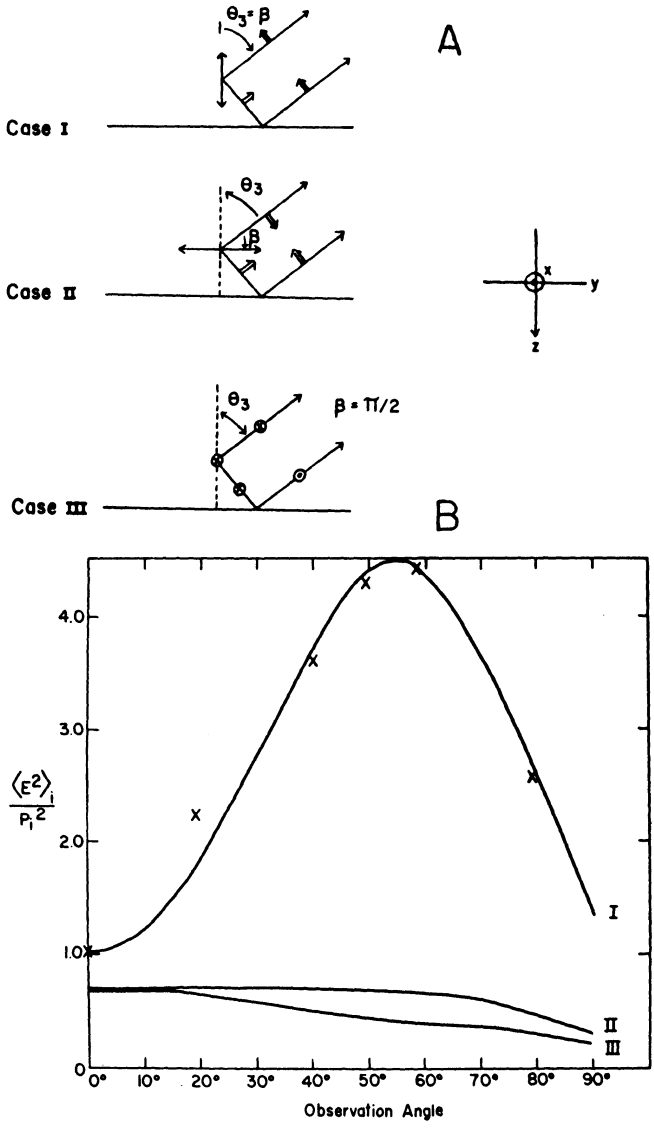

Fig.11.3. (**A**) Three orientations of a dipole oscillator near a surface. (**B**) Angular distribution of light emitted by dipoles oriented as shown in (**A**). The solid curves were calculated for $\lambda = 520$ nm with $n = 0.0427$ and $k = 3.3988$. The finite aperture of the collection optics was explicitly included by integrating over the range of trajectories intercepted by the collection lens. The crosses are the experimental points for Raman scattering by the 992 cm^{-1} ring breathing mode on benzene, adsorbed on Ag{111}

The considerations outlined above immediately suggest the optimum experimental geometry for surface Raman spectroscopy. The most intense electromagnetic field possible at the surface is oriented normal to the surface and is produced by p-polarized light at an angle of incidence near 60°. For totally symmetric modes, which are usually the most intense Raman scatterers, the induced dipole is parallel to the incident electric polarization. Thus we expect to induce a dipole oriented normal to the surface. The radiation from such a dipole is emitted into a cone, oriented at around 60° to the surface normal, thus, the detector should be placed off-normal. This latter conclusion is not intuitively obvious and underscores the importance of the analysis of Greenler and Slager. For reasons of convenience (preventing the specularly scattered beam from entering the spectrometer) we have adopted a geometry in which the incident and observation planes are orthogonal.

To summarize this section briefly then, Raman scattering by adsorbed molecules can be thought of in three parts. The primary field, which drives the Raman oscillator, is the superposition of the incident field and that reflected from the surface. A dipole moment is induced in the molecule through the Raman polarizability tensor. The dipole radiates at the Stokes-shifted Raman frequency and interference between the directly emitted photons and those reflected from the surface prior to reaching the detector results in the secondary field. The tensorial nature of the Raman process and the incomplete screening of visible electromagnetic fields by metal surfaces suggest ways in which the symmetry of the normal modes may be determined.

11.1.2 Angle-Resolved Surface Raman Scattering

In order to determine whether the simple electromagnetic analysis outlined above is adequate to interpret surface Raman experiments, we have measured the angular distribution of the Raman-scattered radiation from benzene adsorbed on a Ag{111} surface. This system was chosen because the benzene is physically adsorbed on the surface, allowing us to look selectively at the purely physical electromagnetic effects of interest. In addition, the orientation of benzene on this surface is known from other measurements [11.4], thus, for a given set of excitation conditions, the orientation of the induced dipole is known. Figure 11.3b shows the expected and measured angular dependence of the Raman-scattered intensity for the 992 cm^{-1} benzene ring-breathing mode, for benzene adsorbed at half-monolayer coverage on Ag{111} at 100 K. The surface was illuminated by p-polarized light at 60° incidence, creating an electric field that is oriented along the surface normal. Since benzene adsorbs flat on this surface, and since the ring-breathing mode is

totally symmetric, the induced dipole also lies along the surface normal. The solid line is calculated from the model of Greenler and Slager for a normal dipole using the known dielectric function of silver at the Raman-shifted frequency. The crosses are the experimental points. Apart from normalization to the intensity at 0° there are no adjustable parameters. The excellent fit suggests strongly that the model is adequate and that we can use the angular dependence to make mode assignments. In this case since we used high angle of incidence p-polarized excitation the primary field was along the surface normal Z (capitalized coordinates are surface fixed). The angular profile bears the signature of a normal dipole, hence the mode must transform as α_{ZZ}.

It is probably not necessary to measure the complete angular profile to determine mode symmetries; comparison can simply be made between different excitation and observation conditions. For example, totally symmetric modes will show greatest intensity under the conditions used in the benzene experiment discussed above. A mode transforming as α_{XZ} or α_{YZ} will be preferentially excited by p-polarized high-angle excitation, but will radiate preferentially along the surface normal. Finally, modes transforming as α_{XY} can be observed by exciting at normal incidence and observing along the surface normal. Thus, different excitation and observation conditions emphasize different normal modes in much the same way as off-specular (impact scattering) high-resolution electron energy-loss spectroscopy (EELS) is used to observe non-dipolar scattering [11.5].

11.1.3 Selection Rules

Moskovits has presented a complete description of the selection rules for Raman scattering by molecules adsorbed on planar surfaces [11.6]. He used the electromagnetic model of Greenler and Slager but folded in the tensorial nature of the Raman scattering processes. Explicit predictions were given for the relative intensities of normal modes of different symmetries, based upon the extent to which the relevant surface fields can be supported at the frequencies of interest. He produced a set of propensity rules to predict relative intensities: modes transforming as ZZ are more intense than modes transforming as XZ or YZ, which are in turn much more intense than those transforming as XY. The origins of this behavior are clear; since the Z field is the strongest at the surface, the intensities scale as the power of Z appearing in the Raman tensor component. *Sass* et al. have suggested that, due to the presence of strong electromagnetic field gradients near the surface (microscopic boundary conditions on the Maxwell equations) dipoles can also be in-

duced through the dipole-quadrupole polarizability as well as the usual dipole-dipole polarizability [11.7]. Considering again the dominance of the Z component of the surface field, Moskovits has made predictions for relative intensities if the quadrupole mechanism dominates.

Hexter and co-workers have presented a group theoretical formulation of the problem, in which they consider the symmetry of the molecule and its image induced in the metal [11.8-10]. This procedure is intuitively appealing to molecular spectroscopists because it is reminiscent of standard operating procedure in making spectral assignments in condensed matter. Reduction in the symmetry of the free molecule in the condensed phase results in the appearance of bands which are forbidden in the gas phase; analysis of the symmetries of the modes that appear can be used to deduce the site symmetry. There are two points of caution regarding the use of the procedure of Hexter's group. First, the image formalism is exact only in the limit of perfect reflectivity. Second, the effect of the secondary field on the scattered intensities was omitted resulting in erroneous predictions. We have recently included the effect of the secondary field following the general group theoretical arguments of the Hexter group, and were able to recover the correct result in the limit of perfect reflectivity, and also produce a simple procedure that incorporates the effects of imperfect screening. The net result is to show the equivalence of the two approaches.

As an experimental test of our conclusions, we have taken Raman spectra of a number of molecules of different symmetries physically adsorbed on Ag{111} and Ag{110} surfaces [11.11]. The idea was to separate the purely physical effects of a nearby conducting surface from any chemical effects resulting from charge transfer, for example, and to provide surfaces having distinctly different adsorption site symmetries in order to assess the sensitivity of the spectra to the site. The Raman spectra of benzene-d_6 provide a clear illustration of the important effects.

As shown in Fig.11.4, the spectra of benzene adsorbed at submonolayer coverages on Ag{111} and Ag{110} are distinctly different from the spectrum of the liquid and from each other. The spectrum obtained on the {111} surface shows only two bands, the totally symmetric ring-breathing mode near 945 cm^{-1} and a Raman forbidden (in the free molecule) C-H out-of-plane bending mode at 515 cm^{-1}. The absence of the e modes in this spectrum is striking and immediately supports the idea that modes transforming as α_{XZ} or α_{YZ} will be suppressed relative to the totally symmetric modes. The absence of these modes is consistent with the flat geometry proposed earlier [11.4]: under our excitation conditions the primary field is a Z field, which induces a tangential

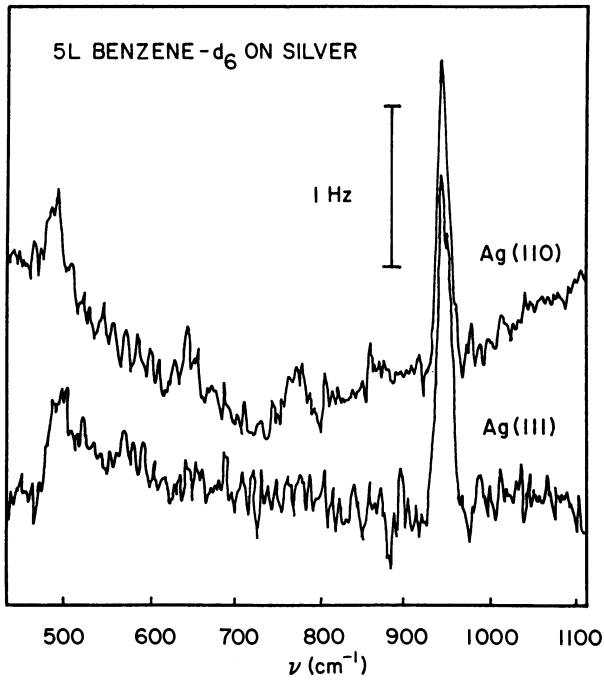

Fig.11.4. Surface Raman spectrum of benzene-d_6 adsorbed at 90 K on Ag{111} and Ag{110}

dipole (through XZ or YZ) which is effectively screened. The presence of the a_{2u} mode immediately suggests a reduction in symmetry at least to C_{6v}. The inversion center must be lost in order for that mode to appear, which is consistent with the general expectation that adsorption destroys inversion symmetry. The spectrum of benzene adsorbed on Ag{110} provides evidence of the sensitivity of the molecule to the adsorption site and argues against the importance of the dipole-quadrupole polarizability. First, note that the intensity of the totally symmetric ring-breathing mode is the same in the two spectra. Since the Raman tensor of benzene is anisotropic, the molecule must be adsorbed in the same configuration on both surfaces. Second, the appearance of several e modes in the spectrum is clear evidence for the reduction of the site symmetry to C_{2v}; the intensity of these modes is surprising but can be rationalized by comparison with spectra of C_{2v} para-disubstituted benzenes in which these particular modes gain in intensity. Finally, comparison of the relative intensities of the a_{2u} modes on the two surfaces shows minimal differences, If the dipole-quadrupole polarizability were the dominant factor in determining intensities, larger differences related to the difference in work function should have been observed,

In summary then, the selection rules for Raman scattering by adsorbed molecules should really be called propensity rules; the incomplete screening of

optical fields leaves residual intensity in bands that would otherwise be "forbidden". Prediction of spectra follows time-honored procedure in molecular spectroscopy. The free molecule symmetry is reduced in the adsorption site and then the intensities scale as predicted by Moskovits: ZZ > XZ, YZ >> XY.

11.1.4 Examples

Since the technique for unenhanced surface Raman spectroscopy is relatively new, the number of examples reported so far is small. With other research groups entering the field, this number should grow rapidly in the near future. The first example of unenhanced Raman scattering from molecules adsorbed on a well-characterized single-crystal metal surface was provided by our research group [11.12]. In this example, the chemistry that occurred was unravelled by the Raman spectrum itself, proving our claim that the method would be very powerful in the study of surface chemistry. Figure 11.5 shows the Raman spectrum of nitrobenzene adsorbed at multilayer (A) and submonolayer (B) cover-

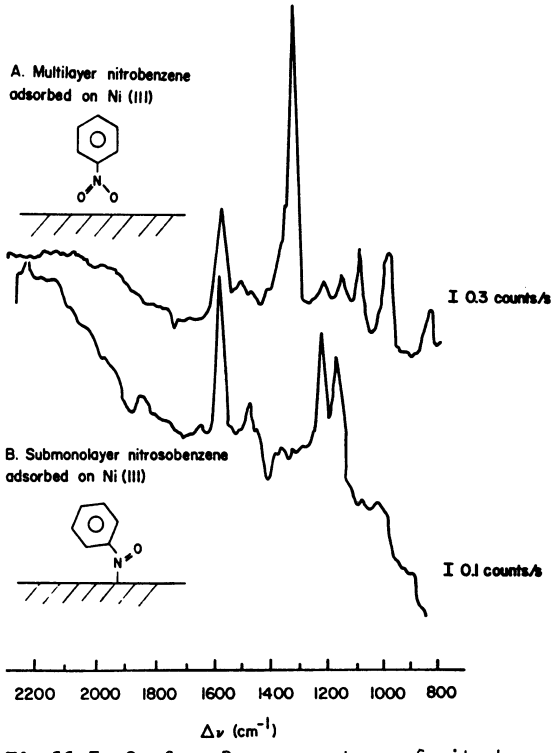

Fig.11.5. Surface Raman spectrum of nitrobenzene adsorbed at multilayer (*A*) and submonolayer (*B*) coverage on Ni{111} at 100 K

ages on a Ni{111} surface. The substrate was chosen to ensure the absence of the SERS effect; electromagnetic resonances cannot be excited on planar surfaces by light due to the failure to conserve momentum and nickel is sufficiently lossy that the quality of any possible resonance would be very poor. Nitrobenzene was chosen as the adsorbate because it has a large and very accurately known Raman cross section. Estimates of sensitivity for other molecules can be made by comparison of their cross sections with that of nitrobenzene. The experiments were conducted in an ultra-high-vacuum environment with the surface being prepared and characterized by standard surface analytical techniques. The Raman spectra were taken using off-normal p-polarized excitation at 514.5 nm and off-normal collection. A single spectrograph with a colored glass filter to reject the elastically scattered light was coupled to a multichannel optical detector. Figure 11.5a shows the spectrum of a nitrobenzene multilayer film estimated to be 5 nm thick. The film was produced by exposing a cooled (100 K) surface to a 100 L (Langmuir, uncorrected) dose of nitrobenzene vapor. The excellent signal-to-noise ratio obtained in less than 10 min of signal averaging shows the power of the method in studying the structures of thin films on surfaces. The spectrum is essentially identical to that of liquid nitrobenzene, as expected for a physically adsorbed system, but there are some differences in intensity that may provide information about the orientation of the molecules in the film.

Figure 11.5b shows the Raman spectrum obtained from a 3-L dose which produced a coverage of about half a monolayer. The radical differences between this spectrum and that of the multilayer immediately suggest dissociative chemisorption. In particular the absence of the NO_2 symmetric stretch implies cleavage at that site, whereas the integrity of the phenyl modes implies that the ring remains intact. The simplest assignment consistent with these observations is that nitrobenzene has been partially reduced on the surface to form nitrosobenzene, with the oxygen being chemisorbed atomically on another nickel atom. This chemisorbed species has been observed in the X-ray photoelectron spectrum of this system [11.13]. The assignment of the spectrum of Fig.11.5b to nitrosobenzene has been confirmed by adsorbing nitrosobenzene from the gas phase onto the nickel substrate; an identical spectrum was observed. This study of the adsorption of nitrobenzene on Ni{111} provided the first example of our ability to obtain unenhanced Raman spectra of molecules on well-characterized metal surfaces.

A second example is the Raman spectrum of ethylene adsorbed at submonolayer coverage on Ag{110}. Silver is used commercially for the catalytic conversion of ethylene to ethylene oxide, yet despite decades of research the

molecular mechanism of this reaction remains elusive. We are attempting to elucidate the mechanism of this reaction by looking for the various postulated intermediates while the reaction is run over a single-crystal silver model catalyst. In particular, it should be possible to distinguish clearly between the possible adsorbed oxygen species which have been implicated in the partial oxidation.

As a first step in this investigation, and in an effort to assess the limits of detection for weak Raman scatterers, we have obtained the Raman spectrum of ethylene adsorbed on a Ag{110} surface which had been precovered with half a monolayer of atomic oxygen. The role of the oxygen is to enhance the adsorption of the ethylene so that coverages of about 0.5 monolayer can be realized. Figure 11.6 shows the Raman spectrum obtained for saturation coverage of ethylene on silver. Both the C=C stretch near 1580 cm^{-1} and the C-H in-plane deformation near 1320 cm^{-1} are clearly observed. These bands are shifted to lower frequencies by approximately 20 cm^{-1} compared to the gas phase, showing a relatively small perturbation which is characteristic of weak chemisorption. The weakness of the chemisorption bond in this system is confirmed by the low (~150 K) desorption temperature. Since the Raman scattering cross section of ethylene is about a factor of ten smaller than that of nitrobenzene and is comparable to molecules like CO, this system provides encouragement that the technique can be applied to essentially any small molecule of chemical interest.

Given the importance of transition metals in heterogeneous catalysis, the motivation for studying adsorption and reactions over metal surfaces using Raman spectroscopy is clear. Metals turn out to be exceptionally good candidates for substrates for two reasons: there are no Raman-active phonons for the cubic metals so that bulk phonon scattering will not overwhelm that of

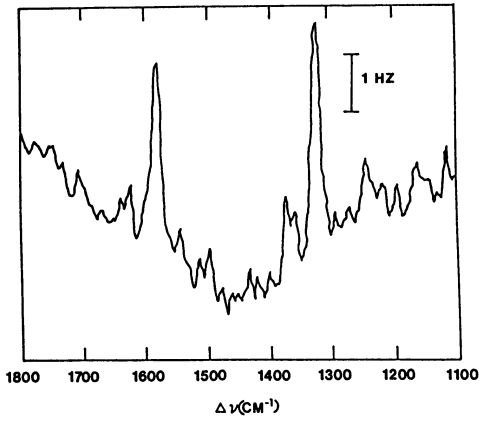

Fig.11.6. Surface Raman spectrum of ethylene adsorbed on a Ag{110} surface that had been preexposed to oxygen to saturate a 2×1 LEED pattern

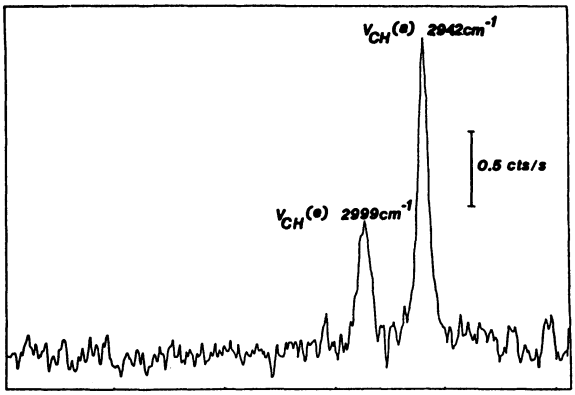

Fig.11.7. Surface Raman spectrum of a thin layer of acetonitrile physisorbed on Si{100} at 100 K

the adsorbate, and the optical penetration depth in most metals is of the order of 10 nm so that the contribution to the background from a continuum of electronic excitations is also minimized. Semiconductors, on the other hand, provide an interesting challenge because of the presence of interfering bulk phonon losses and the possibility of increased continuum scattering. With an interest in applying the Raman technique as an in situ diagnostic of semiconductor processing reactions, we wanted to see how much of a problem the factors mentioned above would be.

As a test system, we chose the adsorption of acetonitrile on the Si{100} 2X1 reconstructed surface. Silicon was chosen for obvious reasons, the reconstructed {100} surface being easy to prepare reproducibly. Acetonitrile has a rather small Raman cross section, typical for a number of small molecules, and showed no tendency to contaminate the surface with graphitic carbon, a very strong Raman scatterer. Figure 11.7 shows the spectrum obtained when a few monolayers of acetonitrile were condensed onto a cold surface; the features observed agree well with the liquid values and the excellent signal-to-noise ratio indicates that submonolayer sensitivity is within reach. Examination of the entire spectral range reveals that only two small regions near the one- and two-phonon losses have enough bulk scattering to preclude the observation of surface adsorbates; with this large spectral window, a wide variety of adsorbates can be examined. Looking to the future, ultraviolet excitation may eliminate even this problem. The penetration length for visible light is a few hundred nanometers in silicon but only ten for ultraviolet light. Excitation in the UV spectral region should result in bulk scattering that is sufficiently reduced to permit accurate background subtraction, even in the neighborhood of the silicon phonon losses.

11.2 Surface-Enhanced Raman Spectroscopy

Surface-enhanced Raman spectroscopy has grown into such an enormous field over the past few years that it is not possible to provide a comprehensive review here. It would probably be most useful therefore, simply to provide an introduction to the field. There is no space here to discuss the many interesting applications of SERS; fortunately several excellent review articles have been published recently, emphasizing certain aspects of the field or presenting specific points of view, so that a relatively complete picture of the field is available [11.14-20].

The discovery of SERS was made ten years ago by *Fleischman* et al. [11.21] who observed intense Raman signals from pyridine adsorbed on a roughened silver electrode. *Jeanmaire* and *Van Duyne* [11.22] and, independently, *Albrecht* and *Creighton* [11.23] repeated the Fleischman experiments and recognized that something very dramatic was occuring. By roughening the electrode much less extensively than in the earlier experiments, these groups produced even higher intensities and, by carefully estimating the adsorbate density and the free-molecule scattering cross sections, concluded that the scattering was enhanced by some six orders of magnitude. Intense activity followed these initial experiments and SERS was observed from a large number of molecules adsorbed on a relatively small number of surfaces. The results of some of the early work differed greatly from laboratory to laboratory, largely because of lack of consistency in preparing and characterizing the surfaces under study. Most of these problems have since been resolved and there is a core of general observations about which most researchers agree.

1) Surface-enhanced Raman spectroscopy has been observed on roughened surfaces of silver, copper, gold, lithium, potassium, and sodium. While submicroscopic (10-100 nm) roughness is effective in generating SERS activity, the role of atomic scale roughness remains to be elucidated.
2) The enhancement may be very long range: enhanced scattering may be observed from molecules separated by as much as tens of nanometers from the surface.
3) The intensities of the Raman bands generally fall off with increasingly large Stokes shifts.
4) Excitation profiles often show broad resonances that do not correspond to any molecular resonances.
5) The spectra are completely depolarized.
6) Molecules adsorbed in the layer immediately adjacent to the surface often show larger enhancement factors, shifted vibrational features, and even new bands compared with molecules adsorbed in subsequent layers.

7) Selection rules appear to be relaxed, resulting in the appearance of bands that are Raman inactive and even infrared inactive in the gas phase.
8) Vibrational frequencies and excitation profiles are both functions of potential in electrochemical experiments.
9) Surfaces that are SERS active invariably produce a weak ineleastic continuum even without an adsorbed species.

The mechanisms that have survived the tests applied to date fall into two classes: electromagnetic and molecular. For surfaces with roughness features of dimension 5-50 nm, the incident laser can excite conduction electron resonances which produce tremendous local electric fields at the surface. In effect the rough surface acts as an amplifier for both the laser and the Raman radiation. This purely electromagnetic mechanism is nonselective among adsorbates but the enhancement depends critically upon the substrate morphology and dielectric constant. The molecular mechanism, on the other hand, is analogous to resonance Raman scattering, in which scattering cross sections increase dramatically as the exciting wavelength approaches a molecular electronic state. For SERS, the electronic states involved are proposed to be charge transfer states between the metal and the adsorbate.

11.2.1 Electromagnetic Enhancement

Surface plasmons, the collective electronic excitations of the conduction electrons, can be excited either on rough surfaces, surfaces with periodic structures, or by injection of radiation with many wave-vector components, as can be achieved in an attenuated total reflection experiment. The latter two cases involve propagating surface plasmons, which cannot be excited by light in planar geometries due to the failure to conserve momentum. The plasmon fields extend some distance outside the surface, and it is the increased amplitude of these fields that is responsible for the electromagnetic contribution to SERS. Since the overwhelming majority of SERS studies have been conducted using the localized surface plasmons of randomly roughened surfaces, the following discussion focuses on these.

Examination of a SERS-active electrode under an electron microscope reveals that the surface is covered with almost spherical bumps that range in size from 20 to 100 nm. These particles were created during the oxidation-reduction cycle necessary to activate the surface, as many monolayers of silver were dissolved and then redeposited. Surface-enhanced Raman spectroscopy has been observed on many different rough surfaces, including island films, ellipsoids prepared microlithographically, and colloids. An isolated sphere provides a good model of a colloid particle, and at least a zero-order picture of the

electrode surface, but more importantly, contains all of the physics necessary to understand the electromagnetic mechanism.

As long as the size of the particle is much smaller than the wavelength of light, the local fields may be calculated by solving Laplace's equation of electrostatics, or by looking up the solution in a textbook, which is even easier [11.23]. The local field at the surface of the sphere is related to the uniform external electromagnetic field of the laser by

$$E_{in} = \left(\frac{\varepsilon_1(\omega)-\varepsilon_2}{\varepsilon_1(\omega)+2\varepsilon_2}\right) E_{out} \quad , \tag{11.1}$$

where $\varepsilon_1(\omega)$ is the complex frequency-dependent dielectric function of the metal and ε_2 is the dielectric function of the ambient medium. Resonance occurs at frequencies where $Re\{\varepsilon_1\} = -2\varepsilon_2$ with the result that extremely large fields can be produced at the surface of the sphere. This result alone explains the extraordinary enhancing properties of the Group IB metals. The resonance condition for these materials happens to be fulfilled in the visible region of the spectrum, and the imaginary part of the dielectric function happens also to be small in the resonance region. The magnitude of the imaginary part of the dielectric functions controls the quality of the resonance.

The spherical particle amplifies not only the incident radiation but also the Stokes-shifted Raman radiation. The trick is to think again in electrostatic terms, calculating the dipole induced in the sphere by the Raman dipole, and then to let the sphere radiate. The magnitude of the dipole thus induced is also given by [11.1], but with the laser frequency replaced by the Stokes frequency. Since the fields involved are dipolar fields, with the dipole located at the center of the sphere, we can immediately fold in the distance dependence of the effect by incorporating the dipole decay law twice. Finally, remembering that the intensities involve the squares of the fields, we arrive at the complete enhancement factor for a sphere in the electrostatic limit:

$$G = \left(\frac{\varepsilon_1(\omega_L)-\varepsilon_2}{\varepsilon_1(\omega_L)+2\varepsilon_2}\right)^2 \left(\frac{\varepsilon_1(\omega_S)-\varepsilon_2}{\varepsilon_1(\omega_S)+2\varepsilon_2}\right)^2 \left(\frac{r}{r+d}\right)^{12} \quad . \tag{11.2}$$

Most of the observations listed above can be explained by this simple model. The resonance condition is satisfied when $Re\{\varepsilon_2\} = -2\varepsilon_1$ at either the laser or the Stokes frequency. The largest enhancement occurs for small Stokes shifts, where both conditions are satisfied simultaneously; the diminution of intensity of high-frequency vibrations is easily explained since one of the fields must be off resonance. The material properties enter through the substrate dielectric constant, and the excitation profiles are those of the conduction

electron resonances. For small Stokes shifts, where both fields are resonant with the sphere, the magnitude of the enhancement is roughly proportional to $(\mathrm{Im}\{\varepsilon_1\})^{-4}$, which shows why highly reflective (low-loss) metals are the best enhancers. That appreciable enhancement occurs at relatively large separations from the surface is contained in the dipole decay law - molecules 5 nm away from a 25 nm particle still show 10% of the enhancement observed in the first layer. It is easy to rationalize the different distance dependences reported by various laboratories in the early work, in which different sample preparations led to roughness features of different sizes. For small particles, SERS is effectively confined to the first layer, whereas for larger particles a larger region of enhanced scattering is observed. Finally, the distribution of molecular orientations and the variation in the orientation of the electric fields over the surface of the sphere result in large depolarization ratios.

For larger spherical particles, the enhancement factor decreases due to radiation damping (the loss of energy from the induced moment by radiation) and dynamic depolarization (the partially destructive interference between radiation emitted at different points of the particle). *Schatz* has presented an excellent discussion of these points [11.24]. Electrodynamic calculations explicitly incorporate these effects; results are now available for isolated spheres and ellipsoids. Unfortunately, however, it has not been possible to prepare such systems in the laboratory. Particles on surfaces have all sorts of complicating interparticle and particle-surface interactions and colloids have a tendency to aggregate. It is very important to be able to test the electromagnetic theory quantitatively and it is hoped that a suitable system can be produced in the laboratory with which to compare the theoretical results.

11.2.2 Chemical Enhancement

Several lines of evidence suggest that the electromagnetic mechanism is not sufficient to explain SERS completely. First, the magnitudes of the enhancement factors calculated are a factor of 10-100 less than those observed in the laboratory. Since the electrostatic calculations for isolated particles represent an upper limit to the enhancement factors, it is clear that another mechanism must contribute some intensity. Second, the enhancement factors for molecules chemisorbed in the first layer are often larger than what would be expected from extrapolation of the multilayer intensities using the known distance dependence of the electromagnetic mechanism. Third, in electrochemical experiments, it has been shown that extremely small quantities (a few percent of a monolayer) of metal atoms added by underpotential deposition

quench SERS, suggesting that there is a small number of SERS-active sites [11.25,26]. Finally, the potential dependence of the SERS intensity is much more complicated than can be explained by changes in the surface concentrations alone. Although all of the observations listed above suggest the existence of another mechanism, the first three could also be rationalized within the framework of the electromagnetic mechanism as follows. Suppose that the surface has two sizes of roughness features, small and large. The small bumps necessarily have a larger proportion of atomic-scale defects which provide sites for strong chemisorption. Furthermore, they also have the largest enhancement factors. Thus the coverage-dependence experiments can be rationalized by asserting that the first-layer effect simply reflects the propensity of the molecules to find the defects which happen to be located on the strongest-enhancing roughness features. Similarly, in the underpotential deposition experiments, the metallic poisons simply displace irreversibly the adsorbates from the defects. Thus it is very important to design experiments that can separate these effects cleanly.

Enhanced Raman scattering cross sections can arise when the exciting laser frequency approaches an electronic adsorption in a molecule. This resonance Raman effect has been known for many years and produces a perhaps six-orders-of-magnitude increase in the scattering cross section in favorable cases. Since most SERS-active molecules are transparent at the commonly used laser wavelengths in the visible region, the question arises: how could such a resonance Raman mechanism contribute intensity in SERS? The answer was provided by an important experiment by *Demuth* and co-workers [11.27,28], who discovered charge transfer transitions for pyridine adsorbed on both single-crystal and evaporated silver surfaces. These charge transfer transitions just happen to be resonant with the blue-green argon ion laser lines and could serve as resonant intermediate states in a resonance Raman mechanism. Interestingly, the transitions are much more intense and somewhat narrower on the evaporated films, suggesting the possible importance of atomic-scale defects.

Persson has presented a simple theory with which to estimate the charge transfer contribution to the enhancement [11.29]. Using a modified Newns-Anderson Hamiltonian with dipolar electron-photon coupling and linear electron-phonon coupling, he was able to calculate the enhancement factor numerically, by assuming a Lorentzian adsorbated density of states and using the position and width of the adsorbate affinity level as well as the laser frequency as parameters. Taking values for these parameters from the experiments of Demuth et al., Persson calculated an enhancement factor of 30, in rough agreement with a number of experimental observations.

It has been difficult to arrive at a quantitative estimate of the contribution the chemical mechanism makes to the total enhancement. This difficulty arises from the fact that most experiments performed to date have relied upon some degree of electromagnetic enhancement for reasons of sensitivity. This has two adverse consequences. First, it convolutes the problem since a submicroscopically rough surface is necessarily rough on an atomic scale. Second, the dynamic range of the experiments is very limited; one is searching for a factor of 10-100 on top of a factor of 10^4 or so.

Faced with this problem, we have devised a novel approach to investigate possible chemical enhancements in the absence of any electrodynamic contribution (apart from the small factor of four because the surface acts as a mirror). Since we have the ability to observe Raman scattering from molecules adsorbed on metal surfaces without enhancement, we can examine the adsorption and Raman scattering of pyridine on a smooth silver single-crystal surface and then create defects that can be characterized using surface crystallographic and spectroscopic techniques. We are in a position to test theory quantitatively by measuring the scattering cross section, the excitation profile, and the electronic absorption spectrum using high-resolution electron energy-loss spectroscopy.

The first measurements yielded somewhat surprising results. No enhancement of the scattering cross section was observed for pyridine adsorbed on the smooth low-index faces of silver [11.30]. The absence of SERS was supported by some qualitative evidence which included highly polarized spectra, relative band intensities and frequencies that were unshifted from the liquid, and a linear dependence of the scattered intensity upon coverage. These results are all in direct contrast to those obtained in SERS experiments. Interestingly, the pyridine did not chemisorb to the silver surface, as indicated by the unshifted vibrational bands and the very low thermal desorption temperature. This was a surprising result since a number of very reasonable theories had predicted SERS by molecules simply located *near* a conducting surface. Evidently that is not a sufficient condition.

We then examined a number of stepped and kinked surfaces in an effort to explore the relationship between chemisorption and SERS, reasoning that a step site of low coordination number might provide a chemisorption site. The lowest coordination site achievable by cutting steps in a fcc lattice is derived from the open {110} surface. As can be seen in Fig.11.8, the step atoms are coordinated to five other atoms. The Raman spectrum of pyridine adsorbed at monolayer coverage on this {540} surface is shown in Fig.11.9, along with a reference spectrum on the {111} surface [11.31]. The pyridine is clearly chemi-

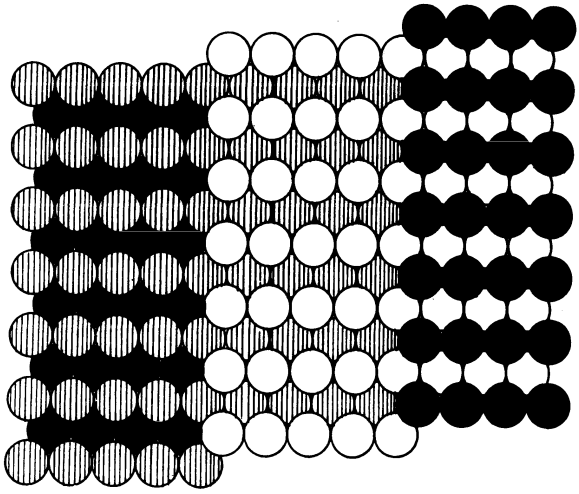

Fig.11.8. The stepped Ag{540} surface

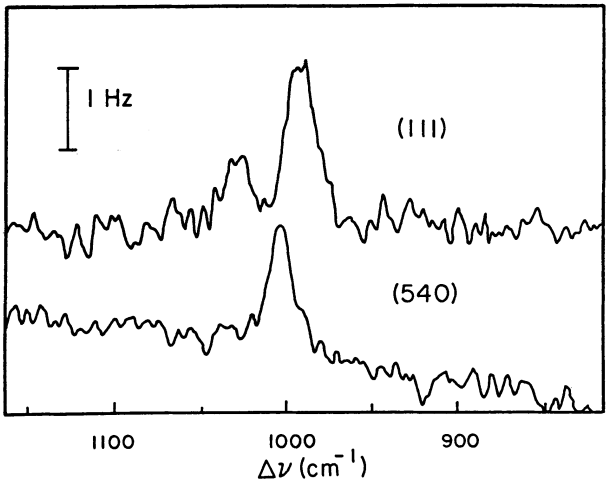

Fig.11.9. Surface Raman spectrum of pyridine adsorbed at submonolayer coverage on Ag{111} and Ag{540} at 100 K

sorbed, as the shifts in the intensity and frequency of the ring-breathing modes reveal. What is most interesting, however, is the lack of any apparent enhancement, as determined by comparing the integrated intensities for spectra on the two surfaces. The conclusion of this experiment is that chemisorption alone is not sufficient to produce SERS. Several directions suggest themselves. Perhaps a site of even lower coordination is required. The width of the charge transfer state is very important in determining the intensity if a resonance Raman mechanism is operative. The closer the defect resembles an isolated adatom, the narrower the (atomic like) state is expected to be. Thus we plan to evaporate submonolayer amounts of silver onto a cold {111} surface to create "isolated" adatoms. A second possibility is that coadsor-

bates may influence the chemical mechanism. As mentioned in Sect. 11.1.4, preadsorption of oxygen greatly enhanced the adsorption of ethylene on silver and similar results are expected for pyridine. Thus we could attempt to model the electrochemical environment by pre- or co-adsorbing electronegative elements like oxygen and chlorine, for example. Our hope is to discover the structural and electronic nature of these SERS-active sites (if they exist).

11.3 Future Work

The future of surface Raman spectroscopy looks very bright indeed. Major improvements in sensitivity are expected over the next year or so, as a result of combining ultraviolet excitation, high aperture ellipsoidal collection and a new generation of charge-coupled device multichannel detectors. Hopefully the absolute magnitudes of the enhancement in SERS will be determined for each of the mechanisms involved so that the method can be made quantitative. The recent discovery of surface-enhanced hyper-Raman scattering [11.32] is very exciting since it yields all of the infrared active modes. Finally, the number of applications is bound to increase. Raman spectroscopy has the unique advantage that it provides high spectral and spatial resolution over the entire range of vibrational frequencies. Furthermore, it can easily be applied to both smooth and rough samples over a very wide range of pressures. Finally, it is uniquely suited to the study of buried interfaces since the penetration depth is of the order of nanometers. There are few, if any, other techniques in surface science with such versatility, which will be invaluable as we attempt to connect the world of model studies under carefully controlled conditions to the real world of technical materials.

Acknowledgement. It is a pleasure to acknowledge the hard work and careful thought of my students Vickie Hallmark, Keenan Brown, Dave Mullins, Camille Howard, and Curtis Shannon, who conducted the experiments I described in this article. I am grateful for financial support to the Robert A. Welch Foundation, the Research Corporation, the National Science Foundation, the University of Texas Research Institute, the Camille and Henry Dreyfus Foundation, and the Alfred P. Sloan Foundation.

References

11.1 R.G. Greenler: J. Chem. Phys. **44**, 310 (1966)
11.2 R.G. Greenler, T.L. Slager: Spectrochim. Acta **29** A, 193 (1973)
11.3 A. Campion: Annu. Rev. Phys. Chem. **36**, 549 (1985)
11.4 Ph. Avouris, J.E. Demuth: J. Chem. Phys. **75**, 4783 (1981)
11.5 H. Ibach, D.L. Mills: *Electron Energy Loss Spectroscopy and Surface Vibrations* (Academic, New York 1982)
11.6 M. Moskovits: J. Chem. Phys. **77**, 4408 (1982)

11.7 J.K. Sass, H. Neff, M. Moskovits, S. Holloway: J. Phys. Chem. **85**, 621 (1981)
11.8 R.M. Hexter, M.G. Albrecht: Spectrochim. Acta **35** A, 233 (1979)
11.9 H. Nichols, R.M. Hexter: J. Chem. Phys. **73**, 965 (1980)
11.10 H. Nichols, R.M. Hexter: J. Chem. Phys. **75**, 3126 (1981)
11.11 V. Hallmark, A. Campion: J. Chem. Phys., in press
11.12 A. Campion, J.K. Brown, V.M. Grizzle: Surf. Sci. **115**, L153 (1982)
11.13 K. Kishi, K. Chinomi, Y. Inoue, S. Ikeda: J. Catal. **60**, 228 (1979)
11.14 T.A. Egerton, A.H. Hardin: Catal. Rev.-Sci. Eng. **11**, 71 (1975)
11.15 W.N. Delgas, G. Haller, R. Kellerman, J.H. Lunsford: *Spectroscopy in Heterogeneous Catalysis* (Academic, New York 1979)
11.16 R.K. Chang, T.E. Furtak (eds.): *Surface Enhanced Raman Scattering* (Plenum, New York 1982)
11.17 A. Otto: "Surface-Enhanced Raman Scattering: 'Classical' and 'Chemical' Origins", in *Light Scattering in Solids IV*, ed. by M. Cardona, G. Güntherodt, Topics in Applied Physics, Vol.54 (Springer, Berlin, Heidelberg 1984)
11.18 H. Metiu: Prog. Surf. Sci., in press
11.19 A. Campion: In *Vibrational Spectroscopy of Molecules on Surfaces*, ed. by J.T. Yates, T.E. Madey, (Plenum Press, New York, in press)
11.20 R.K. Chang, B.L. Laube: CRC Crit. Rev. Solid State Mat. Sci. **12**, 1 (1984)
11.21 M. Fleischman, P.J. Hendra, A.J. McQuillan: Chem. Phys. Lett. **26**, 163 (1974)
11.22 D.J. Jeanmaire, R.P. Van Duyne: J. Electroanal. Chem. **84**, 1 (1977)
11.23 J.A. Stratton: *Electromagnetic Theory* (McGraw-Hill, New York 1941)
11.24 G.C. Schatz: Acc. Chem. Res., in press
11.25 T. Watanabe, N. Yanagihara, K. Honda, B. Pettinger, L. Moerl: Chem. Phys. Lett. **96**, 649 (1983)
11.26 T.E. Furtak: 185th Meeting of the Am. Chem. Soc. (Seattle, 1983) Abstract
11.27 J.E. Demuth, P.N. Sanda: Phys. Rev. Lett. **47**, 57 (1981)
11.28 D. Schmeisser, J.E. Demuth, Ph. Avouris: Chem. Phys. Lett. **87**, 324 (1982)
11.29 B.N.J. Persson: Chem. Phys. Lett. **82**, 561 (1981)
11.30 A. Campion, D.R. Mullins: Chem. Phys. Lett. **54**, 576 (1983)
11.31 A. Campion, D.R. Mullins: Surf. Sci. **158**, 263 (1985)
11.32 R.P. Van Duyne: Private communication

12. The Time-of-Flight Atom-Probe and Its Application to Surface Analysis and Gas-Surface Interactions

T.T. Tsong

Physics Department, The Pennsylvania State University, University Park, PA 16802, USA

The time-of-flight (ToF) atom-probe field-ion microscope (FIM) is a microanalytical tool with sensitivity capable of detecting single atoms [12.1-4]. It is a combination of a field-ion microscope and a time-of-flight mass spectrometer. The tip is mounted on either an external or an internal gimbal system, and a small probe hole covering a few atom image diameters is open at the screen assembly. Behind the probe hole is a ToF tube and an ion detector. To operate the atom-probe, the tip orientation is adjusted until the image of the atoms intended for identification falls on the probe hole. A nanosecond-duration high-voltage pulse is applied to field evaporate these surface atoms as well as others. However, only the field-evaporated ions of these surface atoms can pass through the probe hole, enter the flight tube, and reach the ion detector. From the flight times measured, the chemical identity of these atoms can be determined. This high-voltage pulse atom-probe is very useful for the microanalysis of materials, especially for metals and alloys where field evaporation proceeds from plane edges, atom by atom. Thus, atomic layer by atomic layer compositional analysis can be carried out, as will be discussed in Sect.12.2.2. There are, however, many insurmountable problems in applying this instrument to the study of gas-surface interactions. Adsorbed atoms or molecules often cannot be field desorbed without also field evaporating the substrate atoms. Even if the adsorbed molecules can be field desorbed by the pulsed high electric field, they are almost always field dissociated by the very high electric field needed for the pulsed field desorption. Thus, the desorbed species carry little information about their true states of adsorption. These difficulties have now been largely overcome by the introduction of the pulsed-laser technique to the ToF atom-probe [12.5,6] and especially by the development of a high-resolution pulsed-laser ToF atom-probe [12.4]. In the pulsed-laser field desorption, atoms and molecules are either thermally desorbed first and subsequently field ionized, or they are simply ionized by thermal enhanced field desorption at

a greatly reduced field, where the problem of field dissociation is much less severe [12.7]. In fact, the true desorbed species and those species produced by field dissociation can be distinguished by the ion energy distributions in the pulsed-laser atom-probe. A few meaningful atom-probe studies of H_3 formation and synthesis of NH_3 on metal surfaces have since then been reported [12.8-10]. As the pulsed-laser atom-probe has been available for only a few years, most of these studies are still preliminary.

Here, I will describe the basic principle of the ToF atom-probe, including a detailed discussion of the mass and energy resolution, a new scheme of ion-reaction-time amplification for measuring ion reaction rates, statistics needed for single ion counting, and application of these techniques to the study of gas-surface interactions, including the identification of reaction intermediates in the ammonia synthesis. I will also include a brief discussion of atom-probe studies of the surface segregation of alloy species and impurities since this subject is closely related to the reactivity of surfaces, which is the central theme of this volume.

12.1 The Time-of-Flight Atom-Probe

12.1.1 Basic Principles

In a ToF atom-probe, the sample, in the form of a tip, is mounted on an external or internal gimbal system, and a small probe hole from one to a few millimeters in diameter is open at the screen assembly. Behind the probe hole is the ToF tube leading to an ion detector. To operate the atom-probe, the tip orientation is adjusted until the images of those atoms intended for chemical identification fall on the probe hole (Fig.12.1). Slow pulsed field

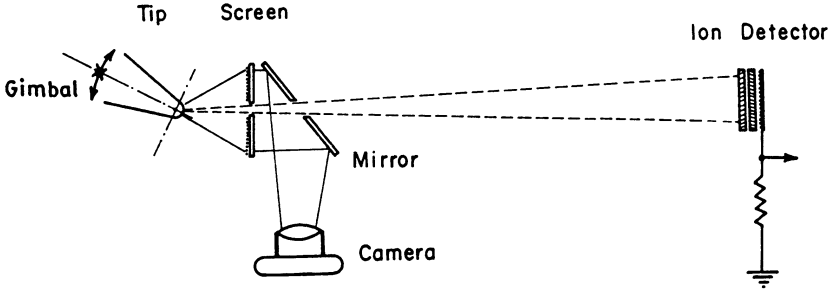

Fig.12.1. Basic principle of the time-of-flight atom-probe

evaporation of the surface is then carried out. Although field evaporation occurs over the entire surface, only ions of the intended surface atoms can pass through the probe hole, enter the flight tube, and reach the ion detector. The basic operational principle of the atom-probe is shown in Fig.12.1.

The mass-to-charge ratio of an ion is given approximately by

$$\frac{M}{n} \cong 2\ eV\ \frac{t^2}{\ell^2} \quad , \tag{12.1}$$

where e is the elementary charge, V is the total tip voltage, t is the flight time, and ℓ is the flight path length. In the nanosecond-width high voltage pulse operated atom-probe, because of the difficulty of terminating the ac transmission line right at the tip, the largest possible kinetic energy of the ion is given not by $ne(V_{dc} + V_p)$, but by $ne(V_{dc} + \alpha V_p)$, where V_{dc} is the applied dc voltage, V_p is the pulse height, and α is a pulse enhancement factor which may range from 1 to 2. As the transmission of electronic signals takes time, the true flight time of the ion is given by $(t + \delta)$ where t now represents the measured flight time and δ is a time delay constant of the system electronics. Thus, for the linear-type, high voltage (HV) pulse ToF atom-probe, the mass-to-charge ratio is given by

$$\frac{M}{n} \cong C(V_{dc} + \alpha V_p)(t + \delta)^2 \quad , \tag{12.2}$$

where $C = 2e/\ell^2$ is a flight path constant.

In the high-resolution pulsed-laser ToF atom-probe shown in Fig.12.2, pulsed field evaporation is induced mainly by a thermal effect [12.7]. The thermal energy, of the order of kT, is negligible. The maximum kinetic energy of the ion is, however, given by $(neV_{dc} - \Delta E_c^{n+})$, where ΔE_c^{n+} is the critical energy deficit of the ion. From a conservation-of-energy argument and experimental measurements, ΔE_c^{n+} has been shown to be given by [12.11]

$$\Delta E_c^{n+} = \Lambda + \sum_{i=1}^{n} I_i - n\phi - Q \approx \Lambda + \sum_{i=1}^{n} I_i - n\phi \quad , \tag{12.3}$$

where Λ is the sublimation energy or the binding energy of the desorbed atom with the substrate, I_i is the i^{th} ionization energy of the atom, ϕ is the average work function of the flight tube, and Q is the activation energy of field evaporation, which is very small compared to other terms unless the temperature of the laser pulse heating becomes excessively high. Thus the mass-to-charge ratio is given by

$$\frac{M}{n} = C\left\{V_{dc} - \frac{\Delta E_c^{n+}}{ne}\right\}(t_0 + \delta)^2 \quad , \tag{12.4}$$

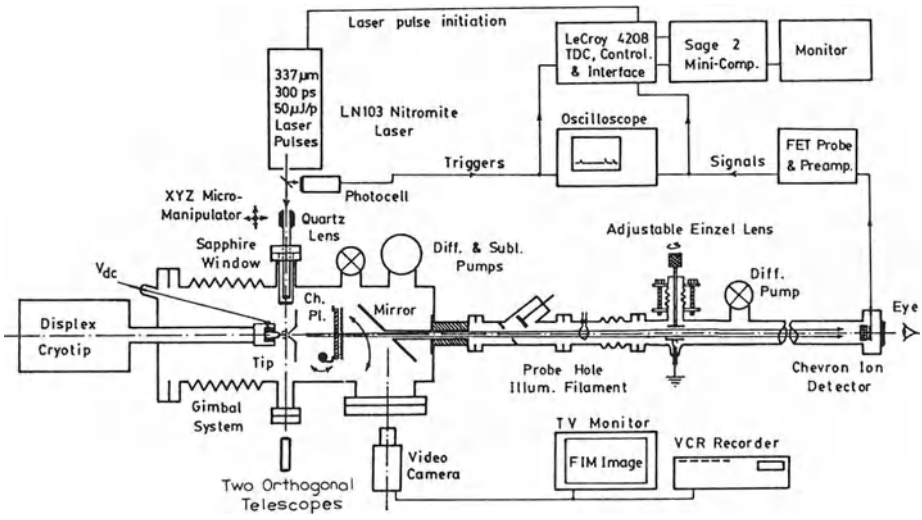

Fig.12.2. The high-resolution pulsed-laser time-of-flight atom-probe, which is not only a high-resolution mass analyzer, but also a high-resolution ion energy analyzer and an ion-reaction-time measuring device of 20-fs time resolution

where t_0 is the onset flight time of the ion species, or the flight time of the most energetic ion of that ion species.

12.1.2 Mass Resolution

Two kinds of mass resolution will be considered. The first kind refers to the ability of the instrument to separate two mass lines of nearly equal masses within a mass spectrum. This resolution is related to the full width at half maximum (FWHM) of the mass lines [12.4]. The second kind refers to the ability to distinguish two ion species of nearly identical masses not necessarily in the same mass spectrum. This resolution is related to the sharpness of reference points in the mass lines, such as the onset flight times t_0 of the ions, and the overall stability of the system [12.4]. In this section we will consider the former kind. The latter will be discussed in connection with the pulsed-laser atom-probe.

Equation (12.1) gives the uncertainty in the mass determination as

$$\frac{\Delta M}{M} \approx \left[\left(\frac{2\Delta \ell}{\ell}\right)^2 + \left(\frac{2\Delta t}{t}\right)^2 + \left(\frac{\Delta V}{V}\right)^2\right]^{\frac{1}{2}} \quad . \tag{12.5}$$

Consider the first term: $2\Delta\ell/\ell$. Here, $\Delta\ell$ is the maximum difference in flight path lengths of two ions taking the shortest and the longest possible flight paths. For the case where there is no ion focusing and the ion detector has a flat detecting surface,

$$\Delta\Omega \approx \frac{d^2}{8\ell} \quad , \tag{12.6}$$

where d is the diameter of the circular detector. In deriving (12.6), we assumed that the center of the detector is on the central axis of the ion beam and the detector face is perpendicular to the axis. Otherwise $\Delta\ell$ will be larger. If an einzel lens is used to focus the ion beam, the minimum $\Delta\ell$, obtained by having the ion trajectories parallel to the axial direction after passing through the einzel lens, is given by

$$\Delta\ell \approx \frac{1}{2} f\alpha^2 \approx \frac{1}{8} f \frac{d_p^2}{r_p^2} \quad , \tag{12.7}$$

where f is the focal length of the einzel lens or the distance from the tip to the einzel lens, α is the half angle subtended by the probe hole at the tip, d_p is the diameter of the probe hole and r_p is the distance from the probe-hole to the tip. Ways to reduce $2\Delta\ell/\ell$ are to increase ℓ and reduce the size of the probe hole. For a typical design (2"-diameter Chevron or 2 mm probe hole at ~15 cm from the tip) $2\Delta\ell/\ell$ is about 4×10^{-5} to 1×10^{-4} for the 200-cm flight path, and about $(1\text{-}3) \times 10^{-5}$ for the 400-cm flight path.

The time uncertainty comes mainly from two sources. They are the time width of the pulsed field evaporation and the time resolution of the detecting device. In a HV pulse operated atom-probe, the pulse width used is usually about 10 ns and the time counting device has a resolution of about 1 ns. Thus $\Delta t \approx \sqrt{10^2 + 1^2}$ ns = 10 ns. In a pulsed-laser atom-probe, the pulse width can be as short as a few picoseconds. Thus, Δt in field evaporation is essentially limited by the cooling time of the tip, and by electronic timer resolution in field desorption of adsorbed species. Usually, Δt is about 1 to 5 ns depending on the specific system and experiment. With a typical ion mass around 50, $2\Delta t/t$ ranges from 1×10^{-3} for a HV pulse atom-probe of 200-cm length to 5×10^{-5} for a pulsed-laser atom-probe of 400-cm length.

The most severe limitation in mass resolution of the linear-type HV pulse atom-probe is due to the $\Delta V/V$ term, which accounts for the energy spread of the field-desorbed ions. Assuming that the HV pulse is a perfectly rectangularly shaped pulse, then the maximum final kinetic energy of an ion desorbed at the very beginning of the pulse is $ne(V_{dc} + \alpha V_p)$, provided

that the pulse width is wide enough for the ion to travel to a nearly field-free region before the HV pulse expires. For an ion desorbed at the very end of the HV pulse, the final kinetic energy will be neV_{dc}. Thus an ion energy difference as large as $ne\alpha V_p$ can result for the two ions. This corresponds to a $\Delta V/V$ of $\alpha V_p/(V_{dc}+\alpha V_p)$. Measurements show that a $\Delta V/V$ as large as 0.03 is common for pulsed HV atom-probes. In the pulsed-laser atom-probe, the ion energy spread is on the order of kT if no photoexcitation occurs. Thus $\Delta V/V \approx 5 \times 10^{-6}$. If photoexcitation occurs, then $\Delta V/V$ is $(2\text{-}5) \times 10^{-4}$. We have to consider also the natural width of the ion energy distribution, which is about 2 neV. One should recognize that this term is intrinsic to the ion formation process, and cannot be improved by better electronics or a longer flight path.

The resolution of the system can either be defined as $M/\Delta M$ or as $nM/\Delta M$ where ΔM refers to FWHM. A slightly more precise definition which accounts for the mass line shape has also been proposed [12.4]. For our discussion here, we will adopt $R = nM/\Delta M$, as has been commonly used in atom-probe field-ion microscopy. It is quite obvious from the above brief discussions that the mass resolution of the linear-type, pulsed HV atom-probe can never be improved beyond ~200, no matter how good the electronics and how long the flight path. This limitation prompted the development of the flight time focused atom-probe, as will be discussed in Sect.12.1.3. For the pulsed-laser atom-probe, the mass resolution can be improved by using better electronics, a longer flight path, and a smaller probe hole. Using a flight path of 4.2 m, an electronic timer of 1-ns resolution and a probe hole of $\alpha \approx 1^{\circ}$, an overall resolution of 2000 to 6000 is routinely achieved by the Penn State Pulsed-Laser Atom-Probe [12.4].

12.1.3 Pulsed High-Voltage Atom-Probes

The first atom-probes developed were the linear-type pulsed high-voltage atom-probes. This type of atom-probe usually uses a flight path of 1 to 2 m, and a Chevron channel plate of 1" or 2" diameter for ion detection. Since this is the simplest type of atom-probe with a reasonable mass resolution of 200 (sufficient for many metallurgical applications), it is still the most commonly used atom-probe. However, it is now gradually being recognized that mass spectroscopy of even the most commonly used alloys requires a better mass resolution since each element usually contains a few isotopes. Isotope overlap is often a problem for accurate data analysis.

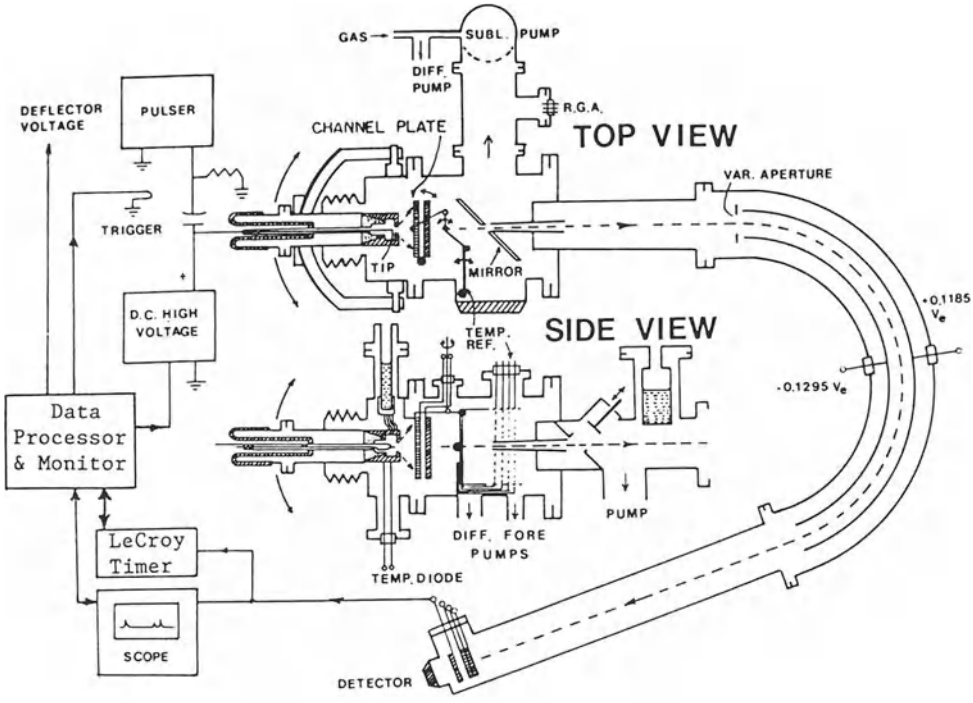

Fig.12.3. The flight time focused atom-probe which uses a 163° Poschenrieder lens to achieve excellent mass resolution. The system is now equipped with electronic timers of 1-ns resolution

A new type of pulsed-voltage ToF atom-probe based on a flight time focusing scheme of *Poschenrieder* [12.12] has since then been developed, which can improve the mass resolution by a factor of 10 [12.3]. Figure 12.3 shows the Penn State Flight Time Focused ToF Atom-Probe, and Fig.12.4a shows a mass spectrum of a Pt-5% Au alloy. This system is equipped with a 163° electrostatic lens and electronic timers of 1 ns resolution. The basic idea of the flight time focusing scheme [12.12] is the following. Ions of the same mass-to-charge ratio can be time focused to arrive at the detector simultaneously even if their energies differ by a few percent. Those ions with excess energy will travel in an orbit of larger radius and those with less energy will travel in an orbit of smaller radius in the spherical lens section, thus, their flight times can be made equal by the specially designed electrostatic lens. This type of atom-probe is especially convenient for metallurgical applications since it is easy to use, compared to the pulsed-laser atom-probe, and the excellent resolution needed for material analysis is always

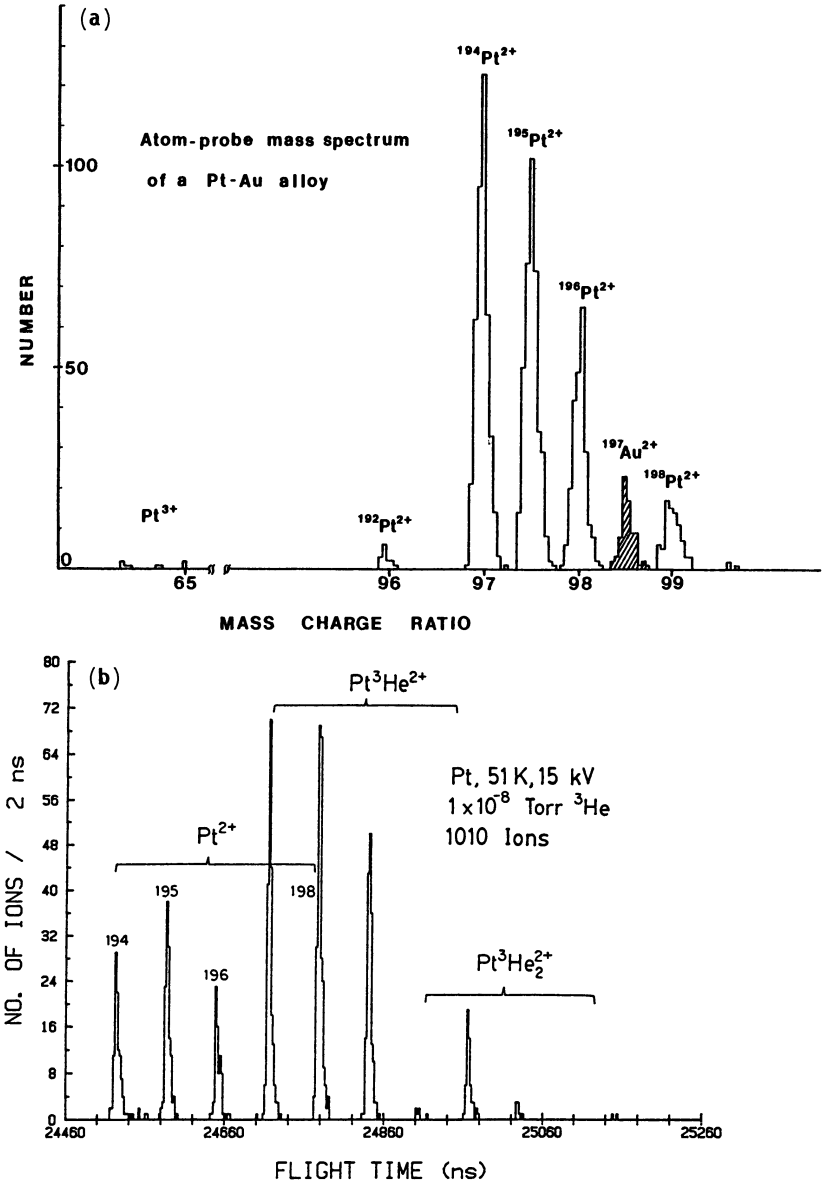

Fig.12.4. (**a**) Atom-probe mass spectrum of Pt-5% Au taken with the flight time focused atom-probe. (**b**) Pulsed-laser atom-probe mass spectrum of Pt taken in 1×10^{-8} Torr of ^3He. Note the formation of $PtHe^{2+}$ and $PtHe_2^{2+}$

achieved without the need of a fine adjustment of the experimental conditions. The disadvantages are those common to the pulsed HV atom-probe and the elaborate mechanical designs needed for the focusing lens and the HV pulse termination.

12.1.4 The Pulsed-Laser Time-of-Flight Atom-Probe

The fast pulsed field evaporation needed for a time-of-flight spectrometry can also be achieved by laser pulses. Several advantages of pulsed-laser atom-probes are [12.5,6]:

(1) Laser pulses induce field evaporation mostly by a heating effect. The energy spread of ions, which should be on the order of kT, or less than 0.1 eV, is negligibly small compared to the HV pulsed field evaporation. Thus, good mass resolution can be achieved without the need of an elaborate flight time focusing scheme. Even if photoexcitation effects occur in pulsed-laser stimulated field desorption, the energy spread will still only be a few electron volts, which is still smaller than that of the high-voltage pulsed field desorption by a factor of about 100.

(2) The mechanical and electrical designs are greatly simplified since there is no need for a proper transmission line termination of the nanosecond HV pulses of more than 1 kV amplitude.

(3) One of the most serious problems in applying the pulsed HV atom-probe to the study of gas-surface interactions is the excessively high field needed to pulse desorb the adsorbed species. The desorbed species are often completely field dissociated, thus bearing no resemblence to the states of the adsorbed species. In fact, some of the adsorbed species, such as field-adsorbed inert gas atoms, cannot be desorbed without also field evaporating the substrate atoms. In pulsed-laser atom-probes, adsorbed species are either desorbed thermally by laser pulses (subnanosecond flash desorption) and are subsequently field ionized, or desorbed by thermal enhanced field desorption. The field needed for desorption using laser pulses can be less than 1/3, or with less than 1/10 of the effect of the applied field, of that needed when HV pulses are used. The field dissociation effect can be greatly reduced and a meaningful study of gas-surface interactions can be done.

(4) It is found that emitters made of low-conductivity materials such as a high-purity Si cannot be field evaporated by HV pulses, since the nanosecond-width HV pulses cannot transmit across the tip. This limitation is overcome when laser pulses are used.

(5) Although the Poschenrieder-type flight time focusing lens can greatly improve the mass resolution of the pulsed HV atom-probe, this artificial focusing lens excludes the use of the atom-probe as an ion energy analyzer and an ion-reaction-time measuring device. The pulsed-laser atom-probe is a mass analyzer [12.4], an ion-energy analyzer [12.11] and an ion-reaction-time measuring device of excellent resolution [12.13]. Thus, the pulsed-laser ToF atom-probe greatly widens the applicability of the atom-probe.

The pulsed-laser atom-probe also has its weaknesses. Focusing of the laser beam on the tip seems to need more experience and also takes more time, although it now usually takes us less than a few minutes to achieve the desired degree of focusing. The mass resolution and energy resolution are very sensitive to the laser power. Experimenters tend to use lasers with too much power, which may either overheat the tip or deteriorate the mass resolution very badly by a combined photoexcitation and thermal effect. When one is aware of these various possible deteriorating effects, a mass resolution of 2000-6000 can be easily achieved with a flight path length of 420 cm, a timer of 1-ns time resolution, and laser pulse width of 1 ns or less. The mass resolution is limited mainly by the natural width of the ion energy distribution which is about 2n eV where n is the charge state of the ions. Our pulsed-laser atom-probe, shown in Fig.12.2, achieved that kind of resolution right from the start of its operation in 1981. A mass spectrum of Pt field evaporated in the presence of He, thus forming $PtHe^{2+}$ and $PtHe_2^{2+}$, is shown in Fig.12.4b.

The pulsed-laser atom-probe, in fact, has a much better resolution in measuring the absolute mass and the kinetic energy of the ions. As pointed out earlier, the resolution of this type of measurement is very different from the kind of resolution we discussed earlier. It is determined by the precision and stability of the various devices used to measure physical parameters such as the flight time and the tip voltage. The system, equipped with an electronic timer of 1-ns resolution and a digital voltmeter of 5 1/2 digit resolution, is capable of achieving an accuracy of ±5 parts in 10^5 in absolute ionic mass and ion energy measurements [12.4,11]. This corresponds to ±1-ns uncertainty out of 20 000 ns flight time. To achieve this accuracy, accurate values of the flight time constant C and the time delay constant δ in (12.4) have to be known. These two constants can be determined to high accuracy by using the fact that ionic masses of elements such as inert gases are known to an accuracy better than 1 part in 10^6. The ionization energies of inert gases are known from spectroscopic data to better than 0.01 eV.

Table 12.1. Experimental ionic masses and the critical energy deficits

Ion species	Ionic mass [u]	Theoretical ΔE_c [eV]	Mass measured [u]	δM [u]	ΔE_c measured [eV]	$\delta(\Delta E_c)$ [eV]
$^{4}He^{+}$	4.002054	20.10	4.001881±0.000445	-0.000173	19.82±0.87	-0.28
$^{20}Ne^{+}$	19.991890	17.00	19.992687±0.000950	0.000797	17.29±0.31	0.32
$^{22}Ne^{+}$	21.990835	17.00	21.991173±0.002552	0.000338	17.18±0.74	0.21
$^{103}Rh^{2+}$	51.452201	21.8	51.448751±0.002324	-0.003450	20.5 ±0.84	-1.3

$C = 0.01073628\ u\ \mu s^{-2} kV^{-1}$, $\delta = 28.3$ ns, $r^2 = 0.999999988$.

Equation (12.4) can be written as

$$t_0 = \frac{1}{\sqrt{C}} \left(\frac{M/n}{(V_{dc} - \Delta E^{n+}/ne)} \right)^{\frac{1}{2}} - \delta \quad . \tag{12.8}$$

Thus, by measuring the onset flight time t_0 of inert gases as a function of V_{dc}, and taking a linear regression of t_0 versus $[M/n(V_{dc} - \Delta E_c^{n+}/ne)]^{\frac{1}{2}}$, values of C and δ can be derived from the slope and intercept of the plot. As shown in Table 12.1, this method is applicable even when an einzel voltage is applied to focus the ion beam, and, although the value of C changes by almost 1%, the same accuracy is achievable in both absolute ion mass and ion energy measurements. The linearity of the plot (12.8) can be seen from the value of the coefficient of determination which differs from 1 by only 2×10^{-8}. The ionic masses measured by our pulsed-laser atom-probe differ from standard table values by only about 0.0005 u to 0.005 u for light to heavy elements. We can also use the fact that ionic masses are already accurately known. Thus by measuring the onset flight times, values of $\Delta E_c^{n+}/ne$ can be derived. These values are listed in Table 12.1. We find that the experimental values agree with (12.3) to within ±0.2n eV to ±0.3n eV, where n is the charge state of the ions, if the laser-stimulated field desorption is carried out at low laser power. If laser power is too high, ions with an excess energy as high as 10 eV can be formed. These high-energy ions can be produced only by a photoexcitation effect. As has been emphasized earlier, the pulsed-laser ToF atom-probe is also an ion energy analyzer and an ion-reaction-time measuring device of excellent energy and time resolution. These properties will be discussed in Sect.12.4.

12.1.5 A Statistical Method of Counting Single Ions

The time-of-flight atom-probe detects single ions by direct counting of the number of signal pulses registered in the detector. For a good mass resolution system, if more than one ion of the same mass-to-charge ratio are field evaporated in one pulsed field evaporation, they will be counted as one ion. Thus unless a proper statistical method [12.14] is used, the compositional analysis done with the atom-probe will give a false result.

We have to recognize here that field evaporation does not occur at a constant rate, because of the atomic step structure of the nearly hemispherical sample surface. However, if the probe hole is sufficiently large and is aimed at a high-index plane, or if the probe-hole is always adjusted to aim at the lattice step of a low-index plane, then the field evaporation rate can be considered to be nearly constant. The average number $\bar{n}$ of ions field evaporated per laser pulse within the area covered by the probe hole can be taken to be constant, but the actual field evaporation events should still be nearly random. Therefore, the probability that n atoms are field evaporated in one pulse covered by the probe hole is given by the Poisson distribution

$$P_n(\bar{n}) = \frac{(\bar{n})^n}{n!} \exp(-\bar{n}) \quad . \tag{12.9}$$

Let us consider a binary system with the true fractional abundances of the two components represented by f_A and f_B. Since field evaporation of a surface layer normally takes place at the plane edge, the two components field evaporate at the same rate, a rate controlled solely by the receding rate of the layer. The probability that exactly n_A of the n atoms field evaporated are A atoms is given by

$$p_{n_A}(n) = \frac{n!}{n_A!(n - n_A)!} f_A^{n_A} f_B^{(n-n_A)} \quad . \tag{12.10}$$

A field-evaporated ion is detected if it reaches the detector and successfully stimulates a detector signal. This probability is given by $e_t e_d$. The probability that all the n_A ions of type A fail to produce an A signal is

$$(1 - e_t e_d)^{n_A} \quad . \tag{12.11}$$

Therefore, the probability that an A signal is successfully recorded by the field evaporation of n_A atoms is given by

$$\left[1 - (1 - e_t e_d)^{n_A}\right] \quad . \tag{12.12}$$

The average number of A signals detected by the atom-probe for each high-voltage pulse is given by

$$\bar{n}_A = \sum_{n=0}^{m} \sum_{n_A=0}^{n} \left[1 - (1 - e_t e_d)^{n_A}\right] p_{n_A}(n) P_n(\bar{n})$$

$$\cong \sum_{n=0}^{\infty} \sum_{n_A=0}^{n} \left[1 - (1 - e_t e_d)^{n_A}\right] p_{n_A}(n) P_n(\bar{n})$$

$$= 1 - \exp(-e_t e_d f_A \bar{n}) \quad , \tag{12.13}$$

when each pulse removes only a small fraction of an atomic layer. The same equation can also be derived from

$$\bar{n}_A \cong \sum_{n_A=0}^{\infty} P_{n_A}(f_A \bar{n}) \left[1 - (1 - e_t e_d)^{n_A}\right] = 1 - \exp(-e_t e_d f_A \bar{n}) \quad .$$

Similarly, for B atoms,

$$\bar{n}_B = 1 - \exp(-e_t e_d f_B \bar{n}) \quad . \tag{12.14}$$

The normalized fractional abundances for A- and B-type atoms, as recorded by the atom-probe signals, are given by

$$F_A = \frac{1 - \exp(-e_t e_d f_A \bar{n})}{2 - \exp(-e_t e_d f_A \bar{n}) - \exp(-e_t e_d f_B \bar{n})} \tag{12.15}$$

$$F_B = \frac{1 - \exp(-e_t e_d f_B \bar{n})}{2 - \exp(-e_t e_d f_A \bar{n}) - \exp(-e_t e_d f_B \bar{n})} \quad . \tag{12.16}$$

The quantities F_A and F_B are the "apparent abundances" of the sample for A- and B-type atoms, respectively. A few asymptotic behaviors can be noted.

(1) When $e_t e_d \bar{n} \to 0$, $F_A \to f_A$ and $F_B \to f_B$. The atom probe gives the true composition of a sample only if the evaporation is done at an extremely low rate.
(2) An atom-probe with a low $e_t e_d$ gives more accurate compositions. However, such a system has a lower sensitivity, and thus more limited capability.
(3) When $e_t e_d \bar{n} \gg 1$, both F_A and F_B approach 0.5 as a limit for all combinations of f_A and f_B.
(4) The true compositions, f_A and f_B, can be derived from F_A and F_B using a numerical method.

The statistical analysis can also be easily extended to multiple-component systems. For an N-component system with fractional abundances $f_1, f_2, \ldots, f_N$,

one has

$$\bar{n}_j = 1 - \exp(-e_t e_d f_j \bar{n}) \quad \text{and} \tag{12.17}$$

$$F_j = \frac{1 - \exp(e_t e_d f_j \bar{n})}{N - \sum_{i=1}^{N} \exp(-e_t e_d f_i \bar{n})} \quad , \quad \text{for } j = 1,2,\ldots,N \ . \tag{12.18}$$

The important thing is to recognize *the statistical nature of atom-probe data even if the detection efficiency of the system is 100%*. In general, the true composition can be obtained simply by very slow field evaporation; at a rate at which only one ion is detected for every 10 to 20 pulses. No statistical correction is then needed. This statistical method, however, can be used to study impurities of very low concentrations with the atom-probe.

12.1.6 Imaging Atom-Probes

An imaging atom-probe is basically an ordinary FIM, but the screen is now replaced by a curved Chevron channel plate assembly which can detect single ions and can also give rise to a greatly intensified desorbed ion image [12.15]. A schematic diagram of this type of atom-probe is given in Fig.12.5. The imaging atom-probe is therefore a time-of-flight mass spectrometer as well as an ion microscope. The pulsed field desorption can either be done

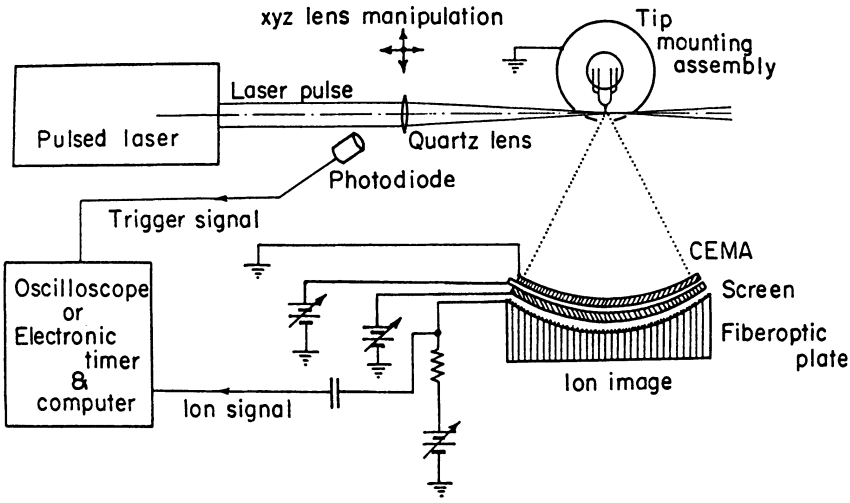

Fig.12.5. Pulsed-laser imaging atom-probe (schematic)

with HV pulses [12.15] or with laser pulses [12.6,9]. In vacuum, pulsed field desorbed ions will form a field desorption image; at the same time, a time-of-flight mass spectrum is obtained. The desorption image will reveal the spatial distribution of these desorbed species on the emitter surface. As the flight path is only about 10-15 cm and the flight time is usually less than 1 μs, the mass resolution is very limited. It is usually no better than 30 to 60 at half peak height.

However, this instrument has unique capability. The system is capable of revealing the spatial distribution of a selected species on the emitter surface by using a flight time gating technique. Specifically, the Chevron channel plate is activated for only 40-60 ns by a high-voltage pulse just at the moment the selected ion species is expected to arrive at the Chevron ion detector. All these operations, in fact, do not have to be done in vacuum. They can be done in the presence of an image gas, provided the gas pressure is low enough to ensure that the random field ionization signal is low. The imaging atom-probe has been actively employed to study metallurgical problems. Only after the pulsed-laser technique had been introduced, could it be meaningfully applied to study gas-surface interactions and simple chemical reactions on solid surface [12.8,9,16].

12.1.7 A Method for Ion-Reaction-Time Amplification

In general, ion reaction rates can be measured with a time-of-flight mass spectrometer with a time resolution comparable to that of the electronics of the system, which is about 10^{-9}-10^{-10}s. The rate measurement can achieve a much better time resolution by using an ion-reaction-time amplification method [12.13]. The basic principle of this method will be discussed in general terms, and an application of this principle to field-ion emission will be discussed in connection with a study of field dissociation of metal-helide (MHe) ions. The amplification scheme is needed to measure an ion reaction time with a time resolution much better than the time resolution of the instrument.

An ion-reaction-time amplification means that those ion-reaction events taking place in a very short time period $\delta\tau$ will have their detection stretched over a much longer time period δt. The amplification factor can be defined as

$$A \equiv \frac{\delta t}{\delta \tau} \quad . \tag{12.19}$$

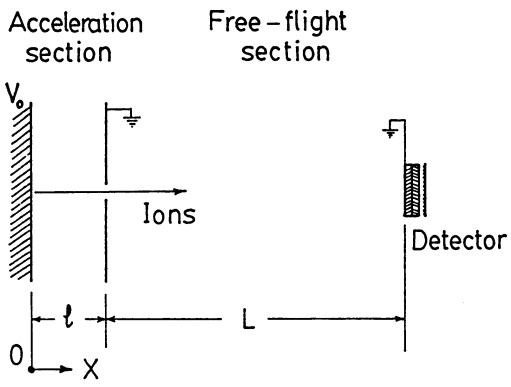

Fig.12.6. Principle of ion-reaction-time amplification for a time-of-flight spectrometer

The basic idea is to build the time-of-flight mass spectrometer in two well-separated sections: The acceleration-reaction section of very small length l, and a field-free-flight section of very large length L, as shown in Fig. 12.6. Thus the total flight time of an ion is determined almost entirely by the kinetic energy of the ion when it leaves the acceleration-reaction section. This energy, however, depends entirely on the location in the acceleration-reaction section where the ion is formed. The location depends, of course, on the rate of the ion reaction, or the ion reaction time. The basic principle can be best illustrated by a simple and idealized example: a photodissociation reaction represented by

$$(M + m)^{n+} \xrightarrow[\text{absorption}]{\text{photon}} M^{n+} + m^{+} + e^{-} \text{ (into metal)} \quad . \tag{12.20}$$

The compound ions $(M+m)^{n+}$ are assumed to be formed right at the surface, e.g., by pulsed ion bombardment of a surface, and they are subsequently dissociated by absorption of photons from a continuous laser source or a pulsed laser source with the pulse width much larger than the dissociation time. The total flight time of the M^{n+} ion formed at x is given by

$$t \approx \frac{L}{v_f(x)} = L\left\{\frac{2neV_0}{M}\left[1 - \left(\frac{m}{m+M}\right)\frac{x}{l}\right]\right\}^{-\frac{1}{2}} , \tag{12.21}$$

where $v_f(x)$ is the final velocity of the M^{n+} ion. A difference in the flight times of δt for two ions will correspond to a difference δx in the locations of their formation, which in turn will correspond to a difference $\delta\tau$ in the times of their formation. They are related by

$$\delta t = \frac{\frac{neV_0}{M}\left(\frac{m}{m+M}\right)\frac{L}{l}\,\delta x}{\left\{\frac{2neV_0}{M}\left[1-\left(\frac{m}{m+M}\right)\frac{x}{l}\right]\right\}^{3/2}} \quad , \quad \text{and} \tag{12.22}$$

$$\delta\tau(x) = \frac{\delta x}{v(x)} \quad , \quad \text{where} \tag{12.23}$$

$$v(x) = \left(\frac{2neV_0}{(M+m)}\,\frac{x}{l}\right)^{\frac{1}{2}} \tag{12.24}$$

is the velocity of the compound ion $(m+M)^{n+}$ just before its dissociation. Combining (12.21-24), one finds

$$A(x) = \frac{\left(\frac{Mx}{ml}\right)^{\frac{1}{2}}}{\left(\frac{m+M}{m}-\frac{x}{l}\right)^{3/2}}\,\frac{L}{2l} \quad . \tag{12.25}$$

Thus the amplification factor is proportional to L/l, and is also dependent on the location where the ion reaction occurs. Maximum amplification occurs if x = l or if the dissociation occurs after the parent ion has already gained the full energy of the acceleration voltage,

$$A(l) = \left(\frac{m}{2M}\right)\frac{L}{l} \quad . \tag{12.26}$$

Equation (12.26) suggests that, whenever possible, one should measure the flight time distribution, or the energy distribution of the ion species with the smaller mass. An amplification factor of 10^3-10^5 can easily be achieved with $l \approx 5$ mm and $L \approx 10$ m. Thus with a system time resolution of 1×10^{-9}s to 1×10^{-10}s, easily achievable with modern electronics and laser units, a time resolution of 10^{-14} to 10^{-15}s can be obtained in ion-reaction-time measurements using this ion-reaction-time amplification scheme. An example will be presented in Sect.12.4 in connection with field dissociation of metal-helide ions. The scheme can be used in any time-of-flight system to study ion reactions such as spontaneous dissociation of atom cluster ions, photofragmentation, Coulomb explosion, field dissociation, etc.

12.2 Structural and Compositional Analysis of Solid Surfaces

12.2.1 Atomic Structures of Emitter Surfaces

The field-ion emitter surface prepared by low-temperature field evaporation of a metal or an alloy tip is nearly hemispherical in shape. It is atomically smooth, i.e., many small atomically perfect crystal facets of circular shape are developed along different crystallographic directions [12.2,17]. For high-atom-density planes, such as {110} of bcc and {111} of fcc structures, the surface structure is too smooth to produce a field ion image in these cases, only plane edge atoms can be seen. These planes thus appear as concentric rings in the image. Each ring represents one atomic step. For low-atom-density planes such as {111} of bcc and {012} of fcc, surface atoms are sufficiently separated so that all the atoms in the top surface layer can be imaged. Field-ion images of a bcc metal, tungsten, and a fcc metal, gold, are shown in Figs.12.7 and 8.

Fig.12.7

Fig.12.8

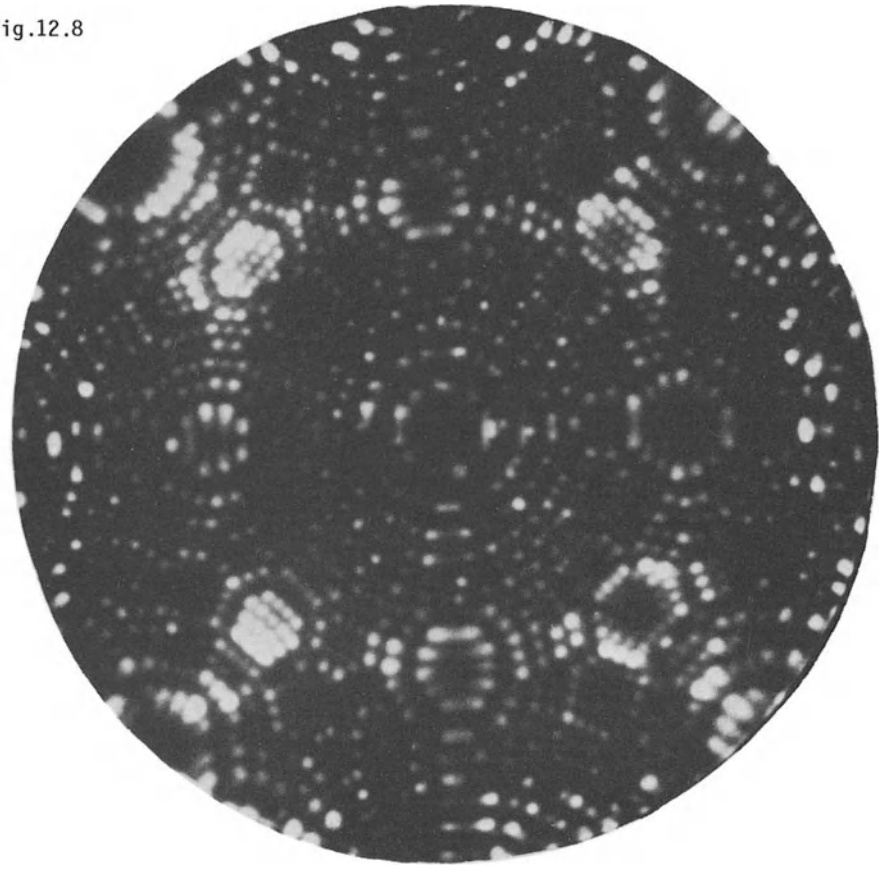

Fig.12.8. Neon field-ion image of a fcc gold surface taken at 55 K

Fig.12.7. Helium field-ion image of a bcc tungsten surface taken at 21 K

It is well known that metal surfaces are often reconstructed, i.e., the atomic structure of a surface is different from what one would expect from truncating a solid. Low-temperature field-evaporated surfaces, however, often do not show these atomic rearrangements, since at low temperatures surface atoms are immobile and thus cannot assume a thermodynamic equilibrium surface structure. They have been observed, however, in a few exceptional cases, e.g., on W{100}, where high-temperature field evaporation produces a superstructure of the surface [12.18]. In the case of an alloy, one alloy species may not be imaged [12.19]. For an ordered alloy or a compound, the field-ion image thus reveals the atomic structure and symmetry of the sublattice of the imaged species. For random alloys, field-ion images are very irregular,

revealing often only random spots with barely recognizable crystallographic symmetry.

12.2.2 Compositional Analysis of Surface Atomic Layers: Alloy Segregations and Impurity Segregation

In thermal equilibrium, the surface composition of an alloy may be different from that in the bulk due to segregation of one of the species to the surface [12.20]. Also impurity atoms may segregate to the surface. Surface segregation has important implications in alloy catalysis, physical metallurgy, and materials' properties. Although the composition of the top and near-surface layers can be derived with surface-sensitive, macroscopic analytical techniques such as Auger-electron spectroscopy (AES), ultraviolet photoelectron spectroscopy (UPS), and low-energy ion scattering (LEIS), accurate in-depth composition profiles with true single atomic layer depth resolution have been obtained only by the time-of-flight atom-probe field-ion microscope [12.21, 22].

The experimental procedure for deriving a composition depth profile is illustrated in Fig.12.9. An alloy tip is first pretreated by low-temperature field evaporation and the surface characterized by the field-ion image. It is then annealed at 600 to 700°C for 3 to 5 minutes in a pressure range of about 10^{-10} Torr to equilibrate the distribution of alloy species in the near-surface layers, and subsequently quenched to liquid nitrogen temperature.

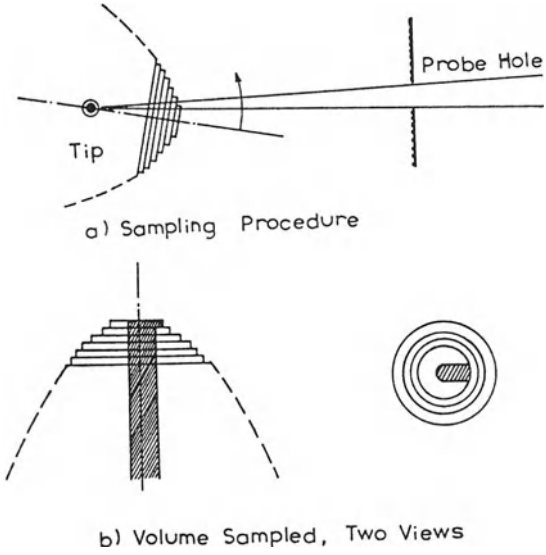

Fig.12.9. Procedure for obtaining a composition depth profile with true single atomic layer depth resolution. The volume of the emitter sampled is also shown

The quenching rate is estimated to be $10^{4\circ}$C/s which effectively freezes the alloy species distribution. The field-ion image of the thermal end form always shows large faceting of high-atom-density planes such as {111} and {001} of fcc and {110} of bcc materials. Very slow pulsed field evaporation is then carried out with a pulsed-voltage fraction of ~20%. The probe hole is always aimed at the edge of the top layer by constantly adjusting the tip orientation using the gimbal system. Thus, there is no intermixing of signals from adjacent atomic layers and the depth profile derived has a true single atomic layer depth resolution. Figure 12.9 also shows the volume of the tip sampled by this procedure, and Fig.12.10 gives an example of the depth profile of a PtRh alloy. It is found that the top layer is enriched with Rh, the second layer is depleted of Rh and enriched with Pt, and from the third layer on, the composition returns to values close to those found in the bulk. The same behavior has been observed for all five of the different PtRh alloys studied (Fig.12.11). The most interesting feature of the PtRh alloys is that

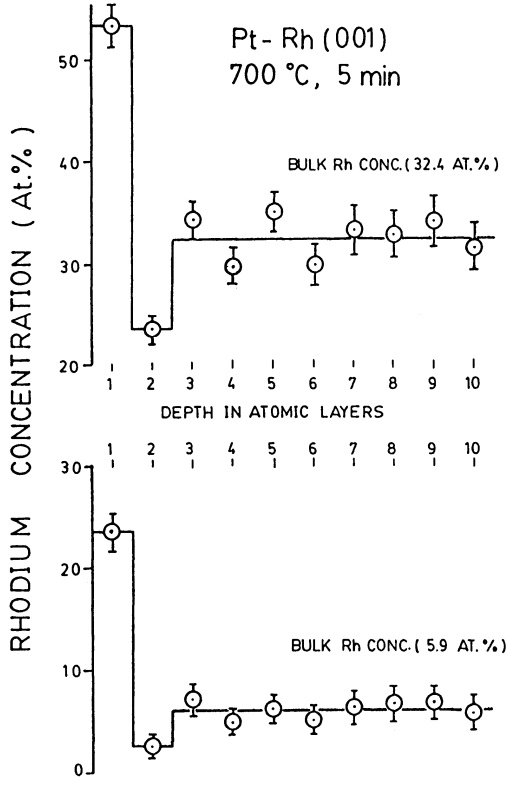

Fig.12.10. Composition depth profiles of two PtRh alloys obtained with the atomprobe. The annealing was done at 700°C in a vacuum better than 2×10^{-10} Torr

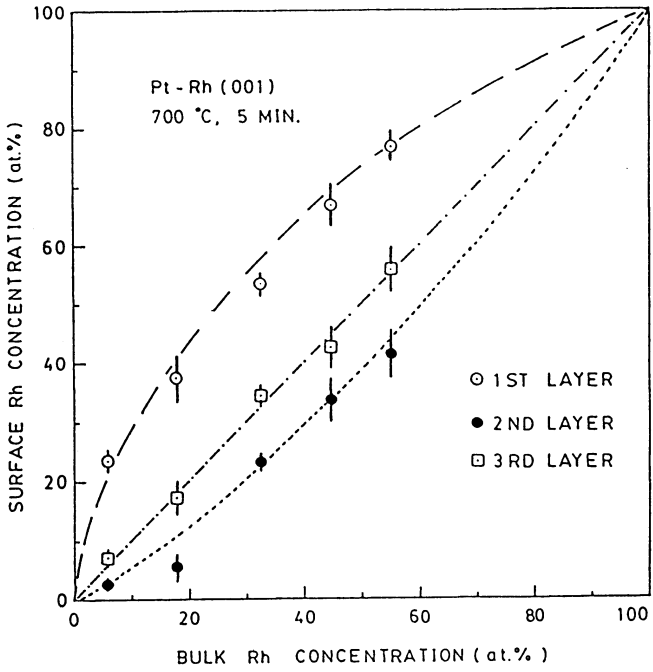

Fig.12.11. Composition of the top three {001} layers of five PtRh alloys equilibrated at 700°C

Table 12.2. Binary-alloy surface segregation behavior observed in atom-probe studies

Alloy system	Segregating element	Extent of segregation [no. of atomic layers]	Nature of convergence to bulk value
Pt-Rh	Rh	1	Oscillatory
Pt-Ir	Pt	2	Monotonic
Pt-Au	Au	4	Monotonic
Ni-Cu	Cu	1	Oscillatory

the concentration of Rh decays nonmonotonically into the bulk, indicating that atomic interactions in alloys may not be monotonic in distance dependence [12.23]. In Table 12.2, results obtained with the atom-probe [12.21,22] are listed. It is quite clear that each individual alloy behaves quite differently from the others.

An example of impurity segregation in metals or alloys is the segregation of sulfur found in PtRh alloys. Although the total impurity content of these alloys is less than 100 ppm, an overlayer of sulfur is found after each annealing. The coverage of sulfur is also found to be linearly proportional to

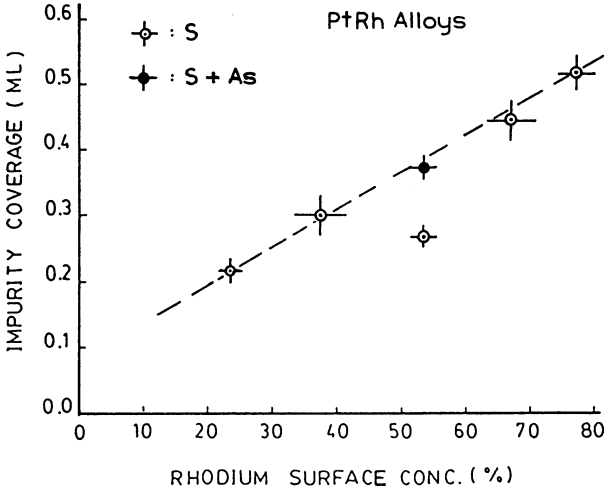

Fig.12.12. The coverage of the sulfur overlayer is found to be linearly proportional to the Rh concentration, thus inversely proportional to Pt concentration, in the top surface layer, indicating an attractive interaction between Rh and S atoms

the concentration of Rh in the top surface layer, as shown in Fig.12.12, suggesting a strong attractive interaction between Rh atoms and S atoms. Sulfur atoms are known to promote certain catalytical reactions, while poisoning some other chemical reactions. Study of cosegregation of S in binary alloy is thus of great interest and importance to catalysis.

12.3 Gas-Surface Interactions

12.3.1 Field Adsorption

In the atom-probe study of gas-surface interactions, one has to differentiate carefully the genuine effect of the surface and the effect of the high applied electric field. The high electric field needed for field ionization and field evaporation can promote adsorption of gases by a field-induced dipole-dipole interaction between gas molecules and surface atoms [12.24]. This interaction is of the order of 0.1-0.3 eV and the adsorption sites should be on top of the surface atoms. This energy is enough to induce close to a monolayer of adsorbates at a temperature below 120 K. However, it is still very small compared to the chemisorption energy of most gases on metal surfaces or the binding energy of atoms in a molecule. Thus, while we have to be careful in interpreting some of the atom-probe data, we expect the conclusions drawn from the atom-probe in surface reactivity studies to represent well the genuine condition of the surface, as will be discussed further. Nevertheless, we will consider field adsorption here.

Field adsorption of inert gases can occur at a temperature as high as 120 K [12.24]. It is produced by a field-induced dipole-dipole interaction between gas atoms, or molecules, and surface atoms. The equilibrium probability of field adsorption p, at a given temperature T, has been shown to be given by

$$p = \left[1 + \frac{\nu_0 KT}{p_g F_0} \exp\left(-\frac{H}{kT}\right)\right]^{-1} \tag{12.27}$$

where K is the gas supply function, ν_0 is the preexponential factor in the thermal desorption equation, p_g is the gas pressure, F_0 is the applied field, and H is the field adsorption energy. This equation can be best expressed as

$$\tau \equiv \ln\left[\left(\frac{1}{p} - 1\right)/T\right] = \ln\left(\frac{\nu_0 K}{p_g F_0}\right) - \frac{H}{kT} \quad . \tag{12.28}$$

Thus, by experimentally measuring p as a function of T and plotting τ versus 1/T, one gets a straight line with slope -H/k and an intercept of $\ln(\nu_0 K/p_g F_0)$. The probability of field adsorption may be measured with the pulsed-laser atom-probe. However, one has to correct for the fact that the probe-hole usually covers more than one adsorption site and the detection efficiency, which includes the ionization efficiency for a thermally desorbed atom and the detector efficiency, is not unity. Also, correction for multi-ion counting, as discussed in Sect.12.1.5 must be made. All these detailed methods of data analysis have been worked out [12.25] and will not be given here. Experimental data [12.26] taken at 4.5 V/Å for field adsorption of helium on the W{112} plane, plotted as τ versus 1/T, is shown in Fig.12.13. It is found that the data points at high temperatures do indeed fit well to a straight line which gives an adsorption energy of 0.17 eV. The low-temperature data deviate considerably from the straight line. This can be accounted for by an additional secondary adsorption state of energy 0.10 eV. Other systems, Ne and Ar on W{112}, show a similar behavior. *Kellogg* [12.16] studied the field dependence of the average field adsorption energy of hydrogen on the entire W emitter surface using a pulsed-laser imaging atom-probe. He concludes that the average field adsorption energy indeed depends on the square of the applied field, as expected from the field-induced dipole-dipole interaction [12.24]. In the imaging atom-probe, signals are collected from the entire emitter surface. The adsorption energy measured represents the average energy for various planes of the emitter surface.

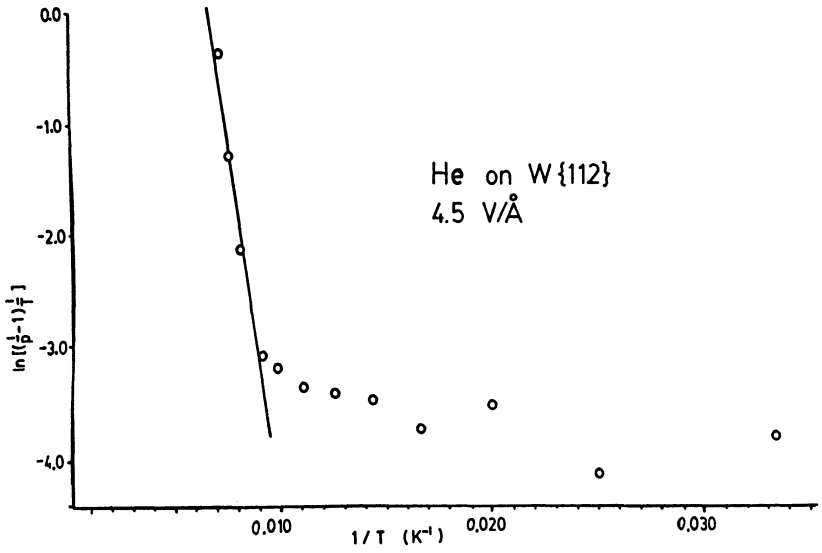

Fig.12.13. Probability of field adsorption as a function of surface temperature, plotted as τ versus 1/T, for He on the W{112} plane

12.3.2 Surface Reactivity in the Formation of H_3

The reactivity of a surface depends on many factors. These include: the adsorption energies of chemical species and their dissociation behavior, their diffusion on the surface, the adatom-adatom interactions, the active sites where a chemical reaction can occur, and the desorption behavior of a new chemical species. The site specificity depends on at least three factors: the atomic geometry, the electronic structures of the surface, and the localized surface field. In the atom-probe, the desorption sites can be revealed by the time gated desorption image, the electronic structure effect can be investigated by the surface material specificity of a chemical reaction, and the surface field can be modified by the applied field. We shall discuss now a study of the reactivity of metal surfaces in H_3 and NH_3 formation using the atom-probe.

On a metal surface, the surface field is produced by an electronic charge smoothing effect and a gradual decaying of the electronic charge density beyond the positive ion core background [12.27]. Since a surface consists of facets of different atomic structures and of lattice steps, the surface field also varies from one location to another. Although a detailed distribution of the surface field is not known for a realistic metal surface, the surface

field strength can be estimated from a jellium model calculation by Lang and Kohn. It is found that for transition metals, a typical surface field varies from ~3 to 1 V/Å at a distance of 0.5 to 2.5 Å from the surface. This field is comparable in strength to the applied field encountered in field-ion experiments, where the field strength is an adjustable parameter. The applied field needed in field-ion experiments, thus, will not be expected to change significantly the reactivity of the metal surface, since an intrinsic surface field of comparable magnitude already exists [12.9]. The applied positive field will, however, extend the short-range surface field to far above the surface so that a desorbed molecule can be field ionized and detected. Also, the intrinsic reactivity, although not expected to be changed by the applied field, can be enhanced by the following effects: (1) The adsorbed atoms are now bound closer to the ion core of the substrate atoms. (2) The flux of atoms or molecules arriving at the emitter surface will increase by a field enhancement factor of $(\alpha F_0^2/2kT)$, where α is the polarizability of the molecules, F_0 is the applied field, and T is the temperature of the gas. This enhanced gas supply arises from a polarization force in the inhomogeneous field near the emitter surface, and the enhancement factor is in general greater than 100. We discuss here a study of H_3 formation on metal surfaces, focusing on three aspects, namely, the effect of the surface atomic geometry, the effect of the applied field, and the effect of the electronic properties of the surface as represented by the material specificity of the reaction.

Molecules of H_3 are not stable in free space, although its optical spectrum has recently been obtained by *Herzberg* in a plasma discharge tube [12.28]. The ion, H_3^+, has been known to be stable since J.J. Thomson's mass spectroscopic studies in 1912. In hydrogen plasma, H_3^+ is the most abundant species. It is also believed to be the most abundant ionic species in interstellar clouds. In field-ion mass spectroscopy of hydrogen from W surfaces, *Clements* and *Müller* [12.29] find a small fraction of H_3^+ in the field range from 2.0 to 2.5 V/Å, coming mostly from protruding surface sites. This atomic site dependence has been shown most vividly by time gated field desorption images of H_3^+ [12.8,9]. *Jason* et al. [12.30] find H_3^+ in the field ionization of condensed hydrogen layers, and measure the appearance energy to be 12.7 eV. This value is 2.9 eV smaller than that of H_2^+. *Ernst* and *Block* [12.31] conclude from a similar experiment that an H_3^+ ion is formed at the moment when a chemisorbed H combines with a field-adsorbed H_2 via

$$H_2(\text{field-ad.}) + H(\text{ch.ad.}) \longrightarrow H_3^+(g) + e^-(\text{metal}) \quad . \tag{12.29}$$

In all these "steady-state" methods, hydrogen molecules are supplied to the emitter surface continuously, and H^+, H_2^+, and H_3^+ ions are steadily emitted. The role of the substrate is not completely transparent.

A new type of experiment using pulsed-laser stimulated field desorption has been reported by *Tsong* et al. [12.6,7]. Hydrogen is first adsorbed on the surface at a gas pressure as low as 1×10^{-8} Torr to 8×10^{-9} Torr. It is desorbed by laser pulse of 300 ps. From a study of the energetics in pulsed-laser field desorption of gases they conclude that the observed ion species with sharp ion energy distributions are produced by field ionization at the field ionization zone of thermally desorbed neutral molecules [12.7]. They, therefore, conclude that neutral H_3 molecules exist on the metal surface in a field adsorption state [12.8]. The H_3^+ ions observed are produced by field ionization beyond the critical distance of field ionization for the thermally desorbed H_3 molecules. This conclusion has now been substantiated by an electron-stimulated field desorption study by *Ernst* and *Block* who interpret their result to agree best with linear H_3 molecules field adsorbed on the emitter surface [12.32].

The H_3^+ ion is most abundant from protruding atomic sites of the emitter surface [12.8]. The field dependence of the relative abundance of H^+, H_2^+, and H_3^+ in pulsed-laser field desorption are shown in Fig.12.14. As can be seen from this figure, H_3^+ is quite abundantly emitted at $F \approx 2.3$ V/Å from the W{110} steps, but not from the smooth {110} surface. The field dependence

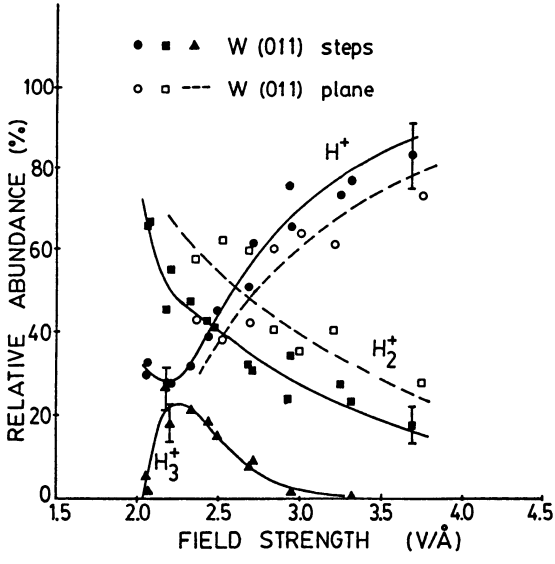

Fig.12.14. Relative abundance of H^+, H_2^+, and H_3^+ in pulsed-laser stimulated field desorption of hydrogen from W{110} steps and from the W{110} plane. Note that no H_3^+ is detected from the flat surface

curves do not, however, indicate that H_3 is not desorbed at high field, since H_3^+ can be field dissociated into H_2^+ and H, or further field ionized into H_2^+ and H^+, at high fields.

An important question is how H_3 molecules are formed on the emitter surface. At least two distinctive mechanisms can be considered. They are dissociative and associative mechanisms as represented, respectively, by

$$\begin{cases} 2^* + H_2\ (\text{gas}) \rightarrow 2H\ (\text{ad}) \\ H\ (\text{ad.}) + H_2\ (\text{gas}) \rightarrow H_3\ (\text{field-ad.}) \end{cases} \tag{12.30}$$

and

$$\begin{cases} ^* + H_2\ (\text{gas}) \rightarrow H_2\ (\text{field-ad.}) \\ 3H_2\ (\text{field-ad.}) \rightarrow 2H_3\ (\text{field-ad.}) \end{cases} . \tag{12.31}$$

An asterisk (*) here represents an adsorption site. There are several observations which provide strong support for the association mechanism represented by (12.31). First, H_3^+ is observed from some metals such as Au which is known not to show dissociative chemisorption of H_2 at low temperatures. Second, for some metals such as Ir, even though adsorption of H_2 is dissociative, few H_3^+ ions can be observed. Third, when a H_2-D_2 mixture is used, atomic mixing always occurs for the triatomic molecular ions regardless of whether the adsorption of hydrogen is dissociative or not [12.8]. However one has to be careful. Even though all the indications are that H_3 is formed by an associative mechanism, the steps involved may be different from those given in (12.31).

The material specificity of H_3 formation on metal surfaces has been investigated by *Ai* and *Tsong* for about 20 transition metals [12.9]. There seems to be no clearly predictable trend except that the maximum values of the relative abundance of H_3^+ can be as high as 40% for some hcp metals like Be, Ti, Hf, and Re. For bcc metals like W, Mo, Ta, and Fe it is about 10 to 20%, while fcc metals have the smallest values, ranging from 0 to 10%, with the exception of Au which is over 20%. Also, H_3^+ is more readily formed for metals on the left-hand side of the periodic table. This material specificity clearly indicates that H_3^+ observed in field ion emission experiments is a true product of surface reactivity and not an artifact of the applied field, although its formation may have been enhanced by the applied field.

12.3.3 Atomic Steps and Reaction Intermediates in Ammonia Synthesis

Identification of reaction intermediates is generally considered to be a key to the detailed understanding of heterogeneous catalytic reactions at the atomic (molecular) level and also of the selectivity of catalysts in catalytic reactions [12.33]. We discuss here an atom-probe study of the reaction intermediates in the synthesis of ammonia [12.10], which is one of the oldest and best-known catalytic reactions. Although industrial processes are conducted at high temperatures and pressures and with complicated catalysts, surface science studies are usually performed in high vacuum, at low temperatures, and on surfaces of pure metals [12.34]. Even under such idealized conditions, the detailed atomic steps involved in forming ammonia are not yet fully understood. Two possible mechanisms which have been discussed are the dissociative and the associative mechanisms [12.33]. It is generally accepted that heterogeneous catalysis involves the active site, which will be represented by an asterisk (*). The detailed steps and the reaction intermediates of the two possible mechanisms are listed in Table 12.3. It is clear that the two mechanisms will give rise to different reaction intermediates. Thus, by finding the reaction intermediates, the atomic steps of the catalytical reaction can be identified.

Table 12.3. Dissociative and associative mechanisms in ammonia synthesis on solid surfaces[a]

Dissociative	Associative
$2^* + N_2 \rightleftarrows 2^*N$	$^* + N_2 \rightleftarrows {}^*N_2$
$2^* + H_2 \rightleftarrows 2^*H$	${}^*N_2 + H_2 \rightleftarrows {}^*N_2H_2$
${}^*N + {}^*H \rightleftarrows {}^*NH + ^*$	${}^*N_2H_2 + H_2 \rightleftarrows {}^*N_2H_4$
${}^*NH + {}^*H \rightleftarrows {}^*NH_2 + ^*$	${}^*N_2H_4 + H_2 \rightleftarrows 2NH_3 + ^*$
${}^*NH_2 + {}^*H \rightleftarrows {}^*NH_3 + ^*$	$N_2 + 3H_2 \rightleftarrows 2NH_3$
${}^*NH_3 \rightleftarrows NH_3 + ^*$	
$N_2 + 3H_2 \rightleftarrows 2NH_3$	
Reaction intermediates	
N, H, NH, NH_2, NH_3	N_2, N_2H_2, N_2H_4

[a]An asterisk (*) represents an active site on the surface, which may well be a site of a displaced surface atom or a kink atom.

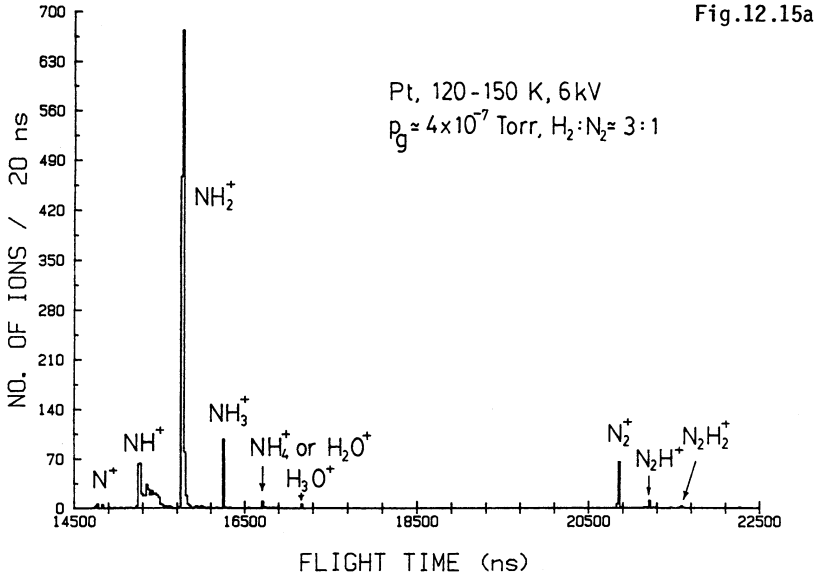

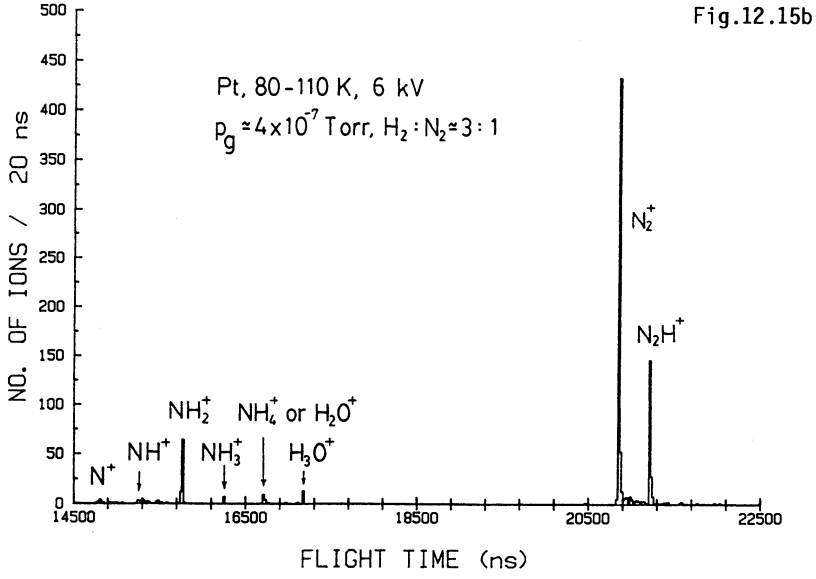

Fig.12.15. (**a**) Pulsed-laser stimulated field desorption mass spectrum obtained with a Pt tip at 120-150 K in 4×10^{-7} Torr of a mixed gas of H_2:N_2=3:1. (**b**) Mass spectrum as in (**a**) except that the tip temperature is now 80-110 K

In the pulsed-laser atom-probe, adsorbed species are thermally field desorbed within a few atomic vibrations, and if the field is high enough, before they have any additional chance of interacting with other molecules or atoms on the surface. Thus, the desorbed species directly represent the reaction intermediates [12.10]. Figure 12.15a shows a pulsed-laser field desorption mass spectrum from a Pt surface, with a tip temperature of ~140 K, and a gas pressure of 4×10^{-7} Torr. The composition of the mixed gas is H_2:N_2=3:1. The probe hole was aimed at a lattice step near the central [001] pole. The ion species detected are N^+, NH^+, NH_2^+, NH_3^+, N_2^+, N_2H^+, and $N_2H_2^+$. The most abundant ion species are NH^+, NH_2^+ and NH_3^+. When the temperature is lowered to ~90 K, these ion species disappear rapidly and the most abundant species are now N_2^+ and N_2H^+. Whenever NH_3^+ is observed, N^+, NH^+, and NH_2^+ are also present. This observation clearly demonstrates that NH_3 is formed by a dissociation mechanism, and the reaction intermediates are N, NH, NH_2, and NH_3. At low temperatures when dissociative chemisorption of nitrogen becomes improbable, the reaction intermediates disappear quickly. As N_2 and N_2H exist in field-adsorbed states at low temperatures, N_2^+ and N_2H^+ become dominant.

There is another piece of information in the mass spectra which is of great significance, i.e., the line shape of these mass lines, or the ion energy distributions. As one can see from Fig.12.15a, the line shape of NH^+ is not as sharp as NH_2^+ and NH_3^+. In fact the NH^+ mass line consists of a sharp peak and a much broader peak. The low-energy, broad peak is produced by field dissociation of NH_2^+ and possibly also of NH_3^+. Ions in the sharp peak, on the other hand, come directly from the surface. Thus, all the expected reaction intermediates from the dissociative mechanism have been observed and they are desorbed directly from the surface.

Ai and *Tsong* [12.9], using a pulsed-laser imaging atom-probe, find that an atomically perfect iron surface, prepared by low-temperature field evaporation, is corroded by chemisorption of nitrogen. Iron atoms are displaced from lattice sites to the adsorption sites. These displaced atoms are stable in their new sites. Gated desorption images show that NH_3 and the intermediates are desorbed from these sites. It is from these sites that NH_3 and the reaction intermediates are desorbed. Thus, the study of the reactivity of an atomically perfect single-crystal surface, using a macroscopic technique, may not represent the real reactivity of the perfect surface. *The reactivity of a surface is determined by the small number of displaced surface atoms*, as our result indicates. This also explains why a small fraction of a monolayer of impurity atoms such as S can poison the entire surface, since the small number of de-

sorption sites, which are possibly also the active sites, may be poisoned by the S atoms. On the other hand, if S atoms act as a promotor, the activity of the surface is greatly increased by a small number of S atoms attached to these displaced surface atoms.

12.4 Ion-Reaction-Time Measurement — Field Dissociation by Atomic Tunneling

Very fast ion reactions with a reaction time in the 10^{-13}s range can be studied in the pulsed-laser time-of-flight atom-probe with a time resolution as good as 20 fs by using the ion-reaction-time amplification scheme described in Sect.12.1.7. We present an example here which not only shows the basic principle of the ion-reaction-time measurement, but also an ion reaction involving direct tunneling of atoms. The reaction is the field dissociation of compound ions [12.35].

It is already well known that metal-helide ions can be formed by field evaporating metals in helium at low temperatures [12.2,8]. Our data show the following general rules for metal-helide ion formation [12.11]: (1) Metal-helide ions can be observed only if the evaporation field is above ~4.2 to 4.5 V/Å. (2) When there are ions of more than one charge state, metal-helide ions are found only for the highest charge state, provided that the ionization energy of the metal atom of this charge state is still less than the first ionization energy of helium. For example, no helide ion is found for nonrefractory metals Au, Cu, Ni, Fe, etc. Also in field evaporation of W in He, ions of 2+, 3+, and 4+ can be present simultaneously in the mass spectrum, but only the 3+ ions contain helide ions. Obviously for W^{4+}, the ground-state energy is below that of He^{+}. Thus, if a 4+ helide ion is formed, it should have the form of W^{3+}-He^{+}, which cannot be a stable ion because of the Coulomb repulsive force. All these experimental observations indicate that a metal-helide ion is really a neutral helium atom bound to a metal ion by a polarization force. The binding energy of this ion-neutral atom interaction is estimated to be 0.1 to 0.3 eV [12.8,36].

If metal-helide ions can be formed in a high electric field, some of them can also be field dissociated before they leave the high-field region. This field dissociation is especially obvious for $RhHe^{2+}$, as shown in Fig.12.16, 17 [12.37]. Figure 12.16 is a mass spectrum and an ion energy distribution of Rh^{2+} formed by pulsed-laser stimulated field evaporation of Rh in vacuum.

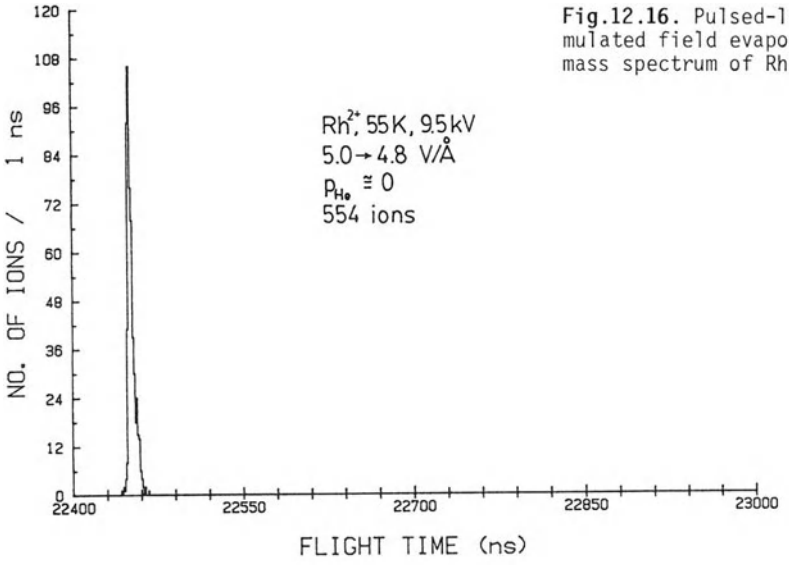

Fig.12.16. Pulsed-laser stimulated field evaporation mass spectrum of Rh in vacuum

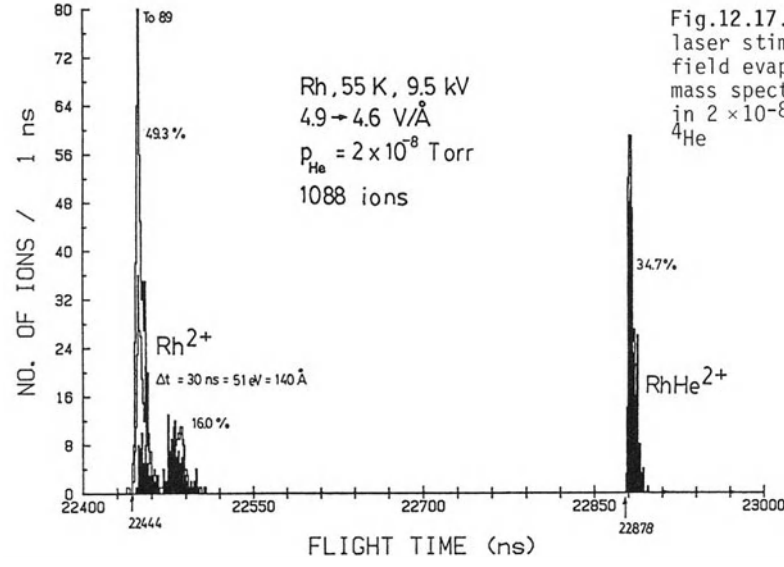

Fig.12.17. Pulsed-laser stimulated field evaporation mass spectrum of Rh in 2×10^{-8} Torr of ^4He

The ion energy distribution shows a FWHM of only 3 to 5 eV, which corresponds to a zone of ion formation of width 0.3 to 0.5 Å. Figure 12.17 is a mass spectrum taken in 1×10^{-8} Torr of He. Besides the regular Rh^{2+} mass line, a mass line of $RhHe^{2+}$ of similar width and a secondary Rh^{2+} peak appear. The critical energy deficit of $RhHe^{2+}$, calculated from the onset flight time, is al-

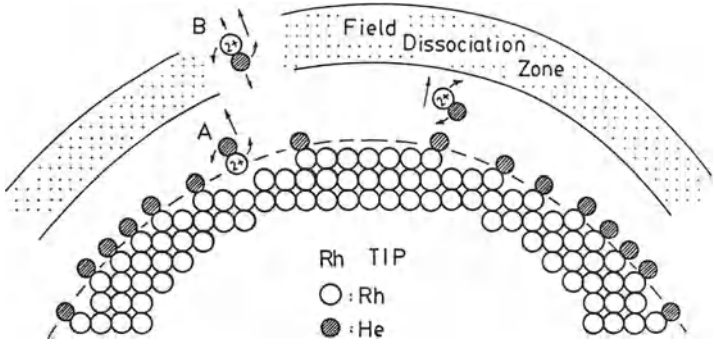

Fig.12.18. Diagram illustrating the mechanisms of field dissociation by atomic tunneling of $RhHe^{2+}$

most identical to Rh^{2+}, indicating that $RhHe^{2+}$ is formed right at the metal surface, and that it is indeed a He atom bound to a Rh^{2+} by a polarization force as illustrated in Fig.12.18.

The secondary peak in Rh^{2+} is due to those Rh ions with much larger energy deficits, i.e., they are formed at a large distance away from the metal surface [12.36]. They can only be formed by field dissociation of $RhHe^{2+}$ ions via

$$RhHe^{2+} \xrightarrow[\text{tunneling}]{\text{atomic}} Rh^{2+} + He \quad . \tag{12.32}$$

The energy difference ΔE between Rh^{2+} ions in the main peak and in the secondary peak can be found from

$$\frac{\Delta E}{E} \approx \frac{\Delta E}{neV_0} = \frac{2\Delta t}{t_0} \quad , \tag{12.33}$$

where $n = 2$ is the charge state, t_0 the onset flight time of the main peak, and Δt is the difference between the flight times of the main peak and the secondary peak. If one goes through the details of the energetics of ion formation, using the parabolic electrode configuration for the electric field distribution near the tip surface, one finds ΔE to be related to the location x where the field dissociation occurs by

$$\Delta E = \frac{neV_0}{2k(1 + M/m)} \ln\left(1 + \frac{2x}{r_0}\right) \quad , \tag{12.34}$$

where r_0 is the tip radius, $k \approx 5$, M is the mass of Rh and m is the mass of He. From (12.33,34) one finds

$$x = \frac{r_0}{2} \exp\left[4k\left(1 + \frac{M}{m}\right)\frac{\Delta t}{t_0}\right] - 1 \quad . \tag{12.35}$$

Using the experimental data shown in Fig.12.17, $\Delta t = 30$ ns, $t_0 = 22444$ ns, $M = 103$ u, $m = 4$ u, $r_0 = 420$ Å, and $k = 5$, one obtains $x = 220$ Å. The flight time of the $RhHe^{2+}$ over this distance can be shown to be given by

$$t(x) = \int_0^x \frac{dx'}{v(x')} = \sqrt{\frac{k(m + M)}{neV_0}} \int_0^x \frac{dx'}{[\ln(1 + 2x'/r_0)]^{\frac{1}{2}}} \quad , \tag{12.36}$$

$$t(220\ \text{Å}) = 7.9 \times 10^{-13}\text{s} \quad .$$

Thus, our experiment shows that a significant fraction of $RhHe^{2+}$ ions are field dissociated in a spatial zone of about 150 Å width which is centered around 220 Å above the surface, as shown in Fig.12.18. The field dissociation occurs in 8×10^{-13}s. Once a $RhHe^{2+}$ passes through this field dissociation zone it becomes stable, as can be understood from the theory of field dissociation of *Hiskes* described below [12.35].

Field dissociation of a compound ion is a quantum mechanical tunneling phenomenon of atoms which has no classical analog. The equation of relative motion of the atom and the ion is given by

$$-\frac{\hbar^2}{2\mu}\nabla^2\psi(\mathbf{r}_n) + \left[U(\mathbf{r}_n) - \frac{2eFz_n}{(1 + M/m)}\right]\psi(\mathbf{r}_n) = E\psi(\mathbf{r}_n) \quad , \tag{12.37}$$

where $\mu = m/(1 + m/M)$ is the reduced mass of the compound ion, $\mathbf{r}_n$ is the vector from the neutral atom to the ion, and z_n is its component along the direction of the electric field. From the sign of the term $2eFz_n/(1 + M/m)$ it is clear that atomic tunneling can occur only if z_n is positive, corresponding to orientation B shown in Fig.12.18. When a $RhHe^{2+}$ is just desorbed, it has the orientation shown in A of Fig.12.18. In this orientation, the $RhHe^{2+}$ cannot field dissociate. As the ion accelerates away, it also rotates due to the torque of the electric force. When it has rotated by 180° into orientation B, it can field dissociate. This corresponds to the peak position in the dissociation zone. If it does not field dissociate, it will take another full rotation of 360° to be in the right orientation again. By this time, it is too far away from the tip and the field is too low for field dissociation to occur. Thus the field dissociation zone is the result of the interplay of rotation, vibration, and atomic tunneling. For comparison, in field ionization, the ionization zone is the result of the electron tunneling rate and the Fermi level of the metal [12.2,17].

The rotational motion of $RhHe^{2+}$ can be estimated to be the following. If we neglect the electric force, the rotational energy is given by

$$E_{rot} = \frac{J(J+1)\hbar^2}{2\mu r_n^2} \quad , \tag{12.38}$$

where $\mu = 6.39 \times 10^{-27}$kg is the reduced mass of the ion, and $r_n \approx 2.6$ Å is the distance between the Rh and He nuclei. One can easily show that the time needed for a rotation of 180° is given by

$$t_\pi = \frac{\pi\mu r_n^2}{[J(J+1)\hbar^2]} \approx \frac{\pi\mu r_n^2}{J\hbar} \tag{12.39}$$

If we use $t_\pi = 8 \times 10^{-13}$s, we find the rotational quantum number of J = 1, which corresponds to an average temperature of ~510 K. This seems to be much higher than the surface temperature. The tip was kept at 55 K and a laser pulse heated the surface to less than 300 K for ~1 ns. However, if we consider the forced rotation by the electric force, using classical mechanics,

$$\mu r_n^2 \frac{d^2\theta}{dt^2} = 2eFr_n\left(\frac{m}{m+M}\right)\sin\theta \quad , \tag{12.40}$$

we find

$$t_\pi = \int_0^\pi \frac{d\theta}{[(4eF/Mr_n)(1-\cos\theta) + \omega_0^2]^{\frac{1}{2}}} \quad . \tag{12.41}$$

Using numerical integration, one can easily show that $t_\pi = 3.35 \times 10^{-13}$s for J = 1. The calculated time is too short by a factor of 3. Of course, the classical mechanical calculation may not be correct, and the changes in J caused by the acceleration due to the applied electric force may take a much longer time. At the moment, no such calculation is available.

Another interesting observation supporting field dissociation of $RhHe^{2+}$ as an atomic tunneling phenomenon is a dramatic change in the dissociation behavior when ^4He is replaced by ^3He, as shown in Fig.12.19. The secondary Rh^{2+} peak is no longer there, although a few scattered low-energy ions can still be found. This observation can be qualitatively understood by considering the tunneling probability. From (12.37) one can see that with ^3He the reduced mass of $RhHe^{2+}$ will be smaller, thus the barrier penetration probability will increase. However, the potential barrier reducing term $-2eF_z/(1+M/m)$ is also mass dependent. With a smaller m, the magnitude of this term is reduced, thus the barrier penetration will decrease. Apparently,

Fig.12.19

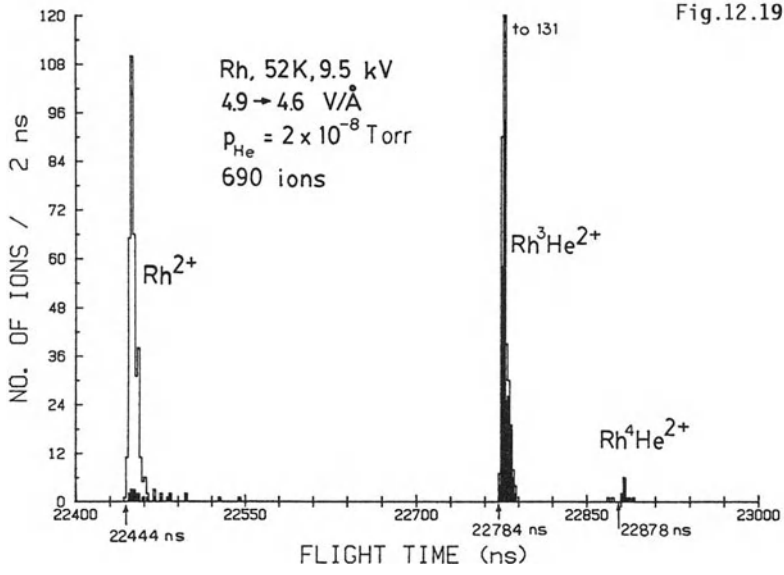

Fig.12.19. Pulsed-laser stimulated field evaporation mass spectrum of Rh in 1×10^{-8} Torr of ^{3}He. Note the disappearance of the secondary Rh^{2+} peak

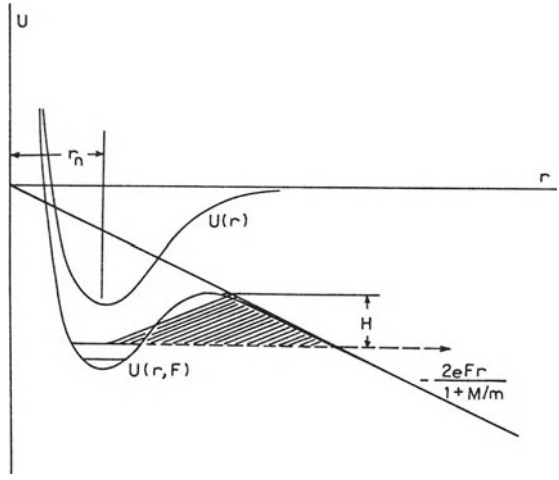

Fig.12.20. Potential barrier used for estimating the atomic tunneling probability in field dissociation

the latter effect is more significant for $RhHe^{2+}$ as can also be seen from a WKB estimation. For this purpose we will approximate the effective potential barrier by an equilateral triangle of height H and width (1 +M/m) H/2eF, as shown in Fig.12.20, where H is the barrier height for a $RhHe^{2+}$ ion. The barrier penetration probability per encounter of the potential barrier is then

$$D(H,V(x)) \approx \exp\left[-\left(\frac{8\mu}{\hbar^2}\right)^{\frac{1}{2}} 2 \int_0^{(1+M/m)H/2eF} \left(\frac{2eFx}{(1+M/m)}\right)^{\frac{1}{2}} dx\right]$$

$$= \exp\left[-\frac{4}{3}\left(\frac{2\mu}{\hbar^2}\right)^{\frac{1}{2}}\left(\frac{1+M/m}{eF}\right) H^{3/2}\right] \quad . \tag{12.42}$$

A reasonable value of the barrier height H is 0.05 eV, similar to the activation energy in field evaporation. At a field of 4.8 V/Å one has

$$D(^4He) = 0.033 \quad ,$$

$$D(^3He) = 0.017 \quad .$$

This is in fair qualitative agreement with the experimental data, which shows that about 10 to 15% of Rh^4He^{2+} are field dissociated (thus indicating 4 to 6 vibrations) and that perhaps less than 2 to 3% of Rh^3He^{2+} are field dissociated. The calculated ratio $D(^4He)/D(^3He) \approx 2$ is smaller than the experimental data by a factor of 3 to 5. A detailed calculation [12.36] can account for the experimental observation, which also gives an estimate of the binding energy of ^4He and Rh^{2+} as $\sim 0.6 \pm 0.3$ eV. However, it is quite clear from the detailed discussion of this example that a high-resolution ToF spectrum contains information on dynamics and energetics of ion formation, and that ion reaction times in the 10^{-13}s range, such as an effect of the rotational motion of ions, can also be measured. Our data, although still too small, seem also to show the effect of vibration. In other types of metal-helide ions we find that Mo^{3+} shows secondary peaks whenever $MoHe^{3+}$ ions are formed, and no secondary peaks are found for Pt^{2+} and Ir^{2+}, even when helide ions are formed. At the moment we have no satisfactory explanations.

The dissociation time measured in this experiment must represent one of the fastest ion reactions ever measured. The ion-reaction-time amplification factor in this experiment can be shown to be

$$A(x) = \frac{\delta t}{\delta \tau} = t_0 \left[\frac{neV_0}{k(m+M)} \ln\left(1 + \frac{2x}{r_0}\right)\right]^{\frac{1}{2}}\left[2k\left(1 + \frac{M}{m}\right)r_0\left(1 + \frac{2x}{r_0}\right)\right]^{-1} \quad . \tag{12.43}$$

Using the experimental data, one finds that $A(220\ Å) = 4.8 \times 10^4$. The time resolution of this measurement is, therefore, as good as 1 ns/4.8×10^4, or 21 fs!

We want to point out here that in field-ionization mass spectroscopy, an exponentially decaying low-energy tail in the mass line of a gas species can be interpreted as being due to field dissociation [12.38] or as being due to autoionization (ionization in free space) [12.39]. In pulsed-laser field desorption no such uncertainty exists, since autoionization will not occur.

The data shown in Figs.12.16 and 17 are, therefore, some of the most direct experimental evidence of field dissociation of ions by atomic tunneling.

12.5 Summary

With the development of the pulsed-laser time-of-flight atom-probe, the capability of the atom-probe has now been extended well beyond the originally proposed mass analysis of metals and alloys. The newly developed high-resolution pulsed-laser atom-probe is capable of allowing accurate ion mass and energy analyses, and also of ion-reaction-time measurements with a time resolution of 10 to 20 fs. It is also capable of being used to study gas-surface interactions and to analyze low electrical conductivity materials. Since the high-resolution pulsed-laser atom-probe was developed only recently, its full potential has yet to be explored. The experimental results available are still limited. The examples presented here are intended to show the various possible applications and the potential of further progress along these directions. Scientists always aim to understand physical phenomena in terms of microscopic theories. In this sense, atom-probe field-ion microscopy is most valuable and should be able to make many more unique contributions in the near future.

Acknowledgements. The author acknowledge the support of NSF and DOE for much of the work reported here, and his co-workers for their contributions.

References

12.1 E.W. Müller, J.A. Panitz, S.B. McLane: Rev. Sci. Instrum. **39**, 83 (1968)
12.2 E.W. Müller, T.T. Tsong: Prog. Surf. Sci. **4**, 1 (1973)
12.3 E.W. Müller, S.V. Krishnaswamy: Rev. Sci. Instrum. **45**, 1053 (1974)
Yee S. Ng, S.B. McLane, T.T. Tsong: J. Vac. Sci. Technol. **17**, 154 (1980)
12.4 T.T. Tsong, S.B. McLane, T.J. Kinkus: Rev. Sci. Instrum. **53**, 1442 (1982)
T.T. Tsong, Y. Liou, S.B. McLane: Rev. Sci. Instrum. **55**, 1246 (1984)
12.5 T.T. Tsong: Surf. Sci. **70**, 211 (1978)
12.6 W. Drachsel, S. Nishigaki, J.H. Block: Int. J. Mass Spectrom. Ion Phys. **32**, 333 (1980)
G.L. Kellogg, T.T. Tsong: J. Appl. Phys. **51**, 1184 (1980)
12.7 T.T. Tsong, T.J. Kinkus, S.B. McLane: J. Chem. Phys. **78**, 7497 (1983)
12.8 T.T. Tsong, T.J. Kinkus, C.F. Ai: J. Chem. Phys. **78**, 4763 (1983)
12.9 C.F. Ai, T.T. Tsong: Surf. Sci. **138**, 339 (1984); J. Chem. Phys. **81**, 2845 (1984)

12.10 W. Liu, T.T. Tsong: Surf. Sci. **165**, L26 (1986)
12.11 T.T. Tsong: Phys. Rev. B30, 4946 (1984)
12.12 W.P. Poschenrieder: Int. J. Mass Spectrom. Ion Phys. **9**, 357 (1972)
12.13 T.T. Tsong: J. Appl. Phys. **58**, 2404 (1985)
12.14 T.T. Tsong, S.V. Krishnaswamy, S.B. McLane, E.W. Müller: Appl. Phys. Lett. **23**, 1 (1973)
12.15 J.A. Panitz: Rev. Sci. Instrum. **44**, 1043 (1973)
12.16 G.L. Kellogg: J. Chem. Phys. **74**, 1479 (1981)
12.17 E.W. Müller, T.T. Tsong: *Field Ion Microscopy, Principles and Applications* (Elsevier, New York 1969)
12.18 A.J. Melmed, J.J. Carrol, W.R. Graham, R.T. Tung, G.D.W. Smith: Phys. Rev. Lett. **43**, 1521 (1979)
A.J. Melmed: Chap.13 in this volume
12.19 T.T. Tsong, E.W. Müller: Appl. Phys. Lett. **9**, 7 (1966); J. Appl. Phys. **38**, 545, 3531 (1967)
12.20 P. van der Plank, W.M.H. Sachtler: J. Catal. **12**, 35 (1968)
J.H. Sinfeld, J.L. Carter, D.J.C. Yates: J. Catal. **24**, 283 (1972)
12.21 T.T. Tsong, Yee S. Ng, S.V. Krishnaswamy: Appl. Phys. Lett. **32**, 778 (1978)
Yee S. Ng, T.T. Tsong, S.B. McLane: Phys. Rev. Lett. **42**, 599 (1979)
T.T. Tsong, Yee S. Ng, S.B. McLane: J. Chem. Phys. **73**, 1464 (1980)
12.22 M. Ahmad, T.T. Tsong: Surf. Sci. **149**, L7 (1985); J. Chem. Phys. **83**, 388 (1985)
12.23 R.N. Barnett, R.G. Barrera, C.L. Cleveland, V. Landman: Phys. Rev. B28, 1667, 6647 (1983)
12.24 T.T. Tsong, E.W. Müller: Phys. Rev. Lett. **25**, 911 (1970); J. Chem. Phys. **55**, 2884 (1971)
12.25 T.T. Tsong: Surf. Sci. **140**, 337 (1984)
12.26 T.J. Kinkus, T.T. Tsong: J. Vac. Sci. Technol. A3, 1521 (1985)
12.27 R. Smoluchowski: Phys. Rev. **60**, 661 (1941)
See also N.D. Lang: Solid State Phys. **28**, 225 (1973) and references therein
12.28 G. Herzberg: J. Chem. Phys. **70**, 4806 (1979)
12.29 T.C. Clements, E.W. Müller: J. Chem. Phys. **37**, 2684 (1962)
12.30 A. Jason, B. Halpern, M.G. Inghram, R. Gomer: J. Chem. Phys. **52**, 2227 (1970)
12.31 N. Ernst, J.H. Block: Surf. Sci. **126**, 397 (1983)
12.32 N. Ernst, J.H. Block: J. Phys. (Paris) **45**, C9-231 (1984)
12.33 M. Boudart: In *Physical Chemistry: An Advanced Treatise*, ed. by H. Eyring, W. Jost, D. Henderson (Academic, New York 1975)
12.34 G. Ertle: J. Vac. Sci. Technol. A1, 1247 (1983); CRC Crit. Rev. Solid State Mater. Sci. **10**, 349 (1982)
12.35 J.R. Hiskes: Phys. Rev. **122**, 1207 (1961)
A.C. Riviera, D.R. Sweetman: Phys. Rev. Lett. **5**, 560 (1960)
12.36 T.T. Tsong, Y. Liou: Phys. Rev. Lett. **55**, 2180 (1985)
T.T. Tsong: Phys. Rev. Lett. **55**, 2826 (1985)
12.37 M. Hotokk, T. Kinsted, P. Pyykko, Bo Roos: Mol. Phys. **52**, 23 (1984)
12.38 H.D. Beckey: *Field Ionization Mass Spectrometry* (Pergamon, Oxford 1971)
12.39 R. Gomer: *Field Emission and Field Ionization* (Harvard University Press, Cambridge, MA 1961)

13. Field Emission Microscopy – Trends and Perspectives

A.J. Melmed

Surface Science Division, National Bureau of Standards, Gaithersburg, MD 20899, USA

Microscopy came early to the science of surfaces, but somehow was neglected in the rush of effort applied to harvesting the many kinds of information made available by the various more popular methods of surface investigation. It is fair to consider that modern surface science originated with the impressive works of Irving Langmuir. The field grew rapidly in the late 1950s with the emerging commercial availability of reliable metal ultra-high-vacuum (UHV) apparatus, coupled with the newly simplified approach to low-energy-electron diffraction (LEED), and the rapid development of various surface spectroscopies, which attracted the majority of surface scientists to nonmicroscopic approaches to the study of surfaces. By that time, of course, optical microscopy was rather mature, electron microscopy was maturing rapidly and the field emission microscopies were experiencing a flurry (albeit of modest proportions) of activity. Optical microscopy generally was relegated to use as a test for surface smoothness by the metallographer in preparing a surface for subsequent surface study, or on a few occasions was used in an actual surface investigation. Electron microscopy was occasionally used in an investigation of surface phenomena. However, in general, neither of these microscopies was integrated into the UHV regime of the surface scientists of the 60s and 70s. Only in the past approximately five years have serious efforts been made to do electron microscopy in the UHV environment with the intention of studying surface phenomena. Field-electron emission and field-ion microscopy (FIM) made very important contributions to the early development of surface science. They have been used less extensively, however, in more recent years, for reasons whose discussion is outside the scope of the present chapter, although they are compatible with and complementary to many of the nonmicroscopic techniques of surface science. Suffice it to mention that the atomic resolution capability of FIM has not been directly applicable to answering most of the surface science questions regarding gaseous atomic and molecular interactions with surfaces.

Moreover, as surely as there are differences in the personalities of people, there are differences in the approach to scientific inquiry among surface scientists. These approaches, for present purposes, can be divided

into the set of those who wish to have a direct look into the "black box" of scientific mystery and those who wish to determine the contents of the black box through measurements of its response to various probes. The course of development of surface science thus far would seem to indicate that most surface scientists are in the latter set. However, with the increasing use of UHV electron microscopy, the spreading interest in scanning tunneling microscopy and the increasing use of atom-probe field-ion microscopy, the balance is shifting. Microscopy in surface science is certainly becoming more popular, and it has become abundantly clear that it is not maximally fruitful to adopt a purely microscopic - or a purely nonmicroscopic - approach to solving problems in surface science. Generally, a multidisciplinary approach, including both kinds of inquiry, is most profitable.

The aim of this chapter is to describe briefly the field emission microscopies, field-electron emission microscopy (FEEM) and field-ion microscopy, to illustrate their contributions to surface science and to offer a personal outlook for the future roles of these microscopies. In general, the interesting high-field surface effects that have been discovered through FEEM and FIM will not be discussed, except as they pertain to explanations of the capabilities of the microscopies.

13.1 Historical Background

Any serious discussion of FEEM and FIM must be punctuated throughout by the name of Erwin W. Müller, originator and developer of both microscopies as we now know them. The point projection microscope, which came to be known as the field-electron emission microscope or simply the field emission microscope, derived from Müller's efforts to understand quantitatively the phenomenon of electron tunneling into vacuum from a metal with an applied electric field. In this effort, he was by no means alone. In the years following the theoretical description by *Fowler* and *Nordheim* [13.1], there was considerable interest in experimental verification of the field-electron tunneling phenomenon. This led to various combinations of field-electron sources and detectors, mostly lacking an analytically correct description of the electron source geometry. E.W. Müller finally devised a pointed W electron emission source which could be thermally smoothed and cleaned in high vacuum to produce an improved point electron source, and he used a phosphor screen to display the spatial distribution of the field-emitted electrons. In addition to providing a tool for quantitative verification of the field-electron emission theory, this was the origin of the field-electron emission microscope [13.2].

In 1951, Müller introduced the positive-ion version of his point projection microscope, the field-ion microscope (FIM, also) [13.2]. Under the prevailing experimental conditions, although isolated single atoms on a W surface clearly were made visible by the FIM, then operated at room temperature, the point-to-point spatial resolution, that is the resolution for adjacent atoms in the surface lattice, was only about 6 Å. In 1956, the low-temperature feature of FIM was introduced [13.4], and this made 3 Å lateral resolution routinely possible.

One further large step was taken in 1967 when Müller introduced the atom-probe field-ion microscope. This took advantage of the unique capability of the field emission microscopes to dissect the specimen atom by atom, using the process of field evaporation. The fundamental effect of field desorption had been discovered in 1941 by *E.W. Müller* [13.5]. Time-of-flight measurements of the effluent ions then provided a mass/charge analysis with single-ion sensitivity.

The larger part of the following discussion will be devoted to field-electron microscopy because it has received relatively little attention in recent years. In view of the natural tendency for researchers to gravitate towards the most rapidly developing areas of their science, most recent works, and consequently the recent reviews, have dealt with field-ion mictroscopy and atom-probe analyses. The achievements of FEEM tend to be given less attention in the general technical literature than this author believes to be justified.

A comment concerning the perturbation of phenomena by the act of observing the phenomena is appropriate here. For some as yet unpublished reason, the observations and measurements made by the field-emission microscopies are very often taken to be subject to uncertainty due to the observational probe, namely the electric field, whereas most surface research by other observational techniques is rarely subjected to the generically equivalent uncertainty. That this situation has persisted, due to the real or pretended ignorance of the facts of some authors, will be emphasized throughout the remainder of this chapter by the redundant explicit statement, where appropriate, that the phenomenon under study occurs in the total absence of an electric field.

13.2 Some Comments Related to Curved and Planar Surfaces

In the older, most general consideration of surfaces and their properties, namely the thermodynamics approach, surface curvature is a property usually to be neglected as innocuously small in its consequences unless the radii of curvature are infinitesimally small [13.6]. It is now well known from the

viewpoint of surface science that well before that curvature regime is reached, important differences prevail between planar and curved surfaces in general. These differences derive from structural differences on an atomic scale and their effects on surface chemistry and physics. The elements of such structural differences, namely surface steps and kinks, play important roles in many surface processes [13.7]. However, it is interesting to note that certain features of the surfaces used in surface science investigations may change as a function of real experimental time. These changes, which largely have been ignored, play a perhaps deceptively important role in diminishing the differences. It is inevitable [13.8-10] that the resultant shapes, after sputtering, chemical reactions, heating, etc. of most crystalline specimens have both curved and planar surfaces. Qualitatively, it is the ratio of steps to planar area that is important, and any complete surface study should include such a characterization during the course of the study. Thus arises one major research need for careful surface microscopy or topography.

13.3 Field-Electron Emission Microscopy

13.3.1 Conceptual

Fundamentally, FEEM is based on the phenomenon of field-electron emission, sometimes referred to as cold cathode emission or electron tunneling from a conducting solid into vacuum [13.11]. The phenomenon has been treated theoretically using a one-dimensional, free-electron quantum mechanical model [13.1], for a metal at zero temperature. A negative electric potential is applied to the specimen; combined with the potential due to the image force on an electron, this creates a finite-width potential barrier near the surface. Electrons supplied by the specimen can tunnel through this barrier into vacuum, with a probability determined by the barrier shape. The electron current density [A/cm^2] is described by the Fowler-Nordheim (F-N) equation [13.1] as

$$I = 6.2 \times 10^{-6} \frac{\mu^{1/2}}{(\phi + \mu)\phi^{1/2}} F^2 \exp(-6.8 \times 10^7 \times \phi^{3/2}/F) \quad , \qquad (13.1)$$

where μ is the chemical potential of an electron and ϕ is the electron work function. Here, F is expressed in V/cm. Later treatments added small modifications to the equation [13.12], but no substantial changes in its form resulted.

The F-N equation is strictly valid only for low temperatures ($T \approx 0$ K) and the theoretical description becomes more complicated at elevated temperatures [13.12] in the temperature range intermediate between cold cathode and therm-

ionic emission. The higher-temperature modification of the F-N equation was approximated by *Young* [13.13] in a derivation based on total electron energy instead of the earlier-used normal energy. This recognized that in an actual experimental measurement of the energy distribution of field emitted electrons, it is the total energy distribution which is measured.

13.3.2 The Microscopy

a) The Microscope

Field-electron emission microscopy is a point-projection microscopy utilizing the approximately straight-line radial projection of electrons field-emitted from the small, rounded apex of an electrically conducting solid specimen (the tip) onto a larger diameter detector, usually a phosphor screen [13.14], and the projection geometry may be described as more-or-less spherical. (A cylindrical form of field-electron microscope was demonstrated [13.15], but it has found very little use.) Conceptually and structurally, it is rather simple when compared to most other microscopes. However, as with other microscopies, some of the related measurements that can be made using secondary apparatus are rather complex.

The essential elements of the field-electron emission microscope (FEEM, also), as conceived by *Müller* [13.2], are a tip, which can be heated by passing current through its support loop, an anode ring, and a phosphor screen to display the spatial distribution of field-emitted electrons. If no other elements are needed for additional purposes, then the anode ring can be deleted and an electrically conductive, optically transparent film on the inside surface of the glass can be used instead. The tip may be attached to the support loop in various ways (simple spot welding, for example), and two more wires may be added to the loop near the tip so that the potential and current through that part of the loop can be measured to determine specimen temperature, with appropriate radiation-loss corrections at higher temperatures. The FEEM elements are usually enclosed in an envelope attached to a vacuum system, and other elements are added to enable elemental or molecular deposition onto the emitter surface and for measurement of other properties of the field-emitted electrons. Specimen cooling to liquid nitrogen or liquid hydrogen temperature is relatively easy [13.16], and the entire microscope can be made small enough to be immersed entirely in liquid nitrogen, liquid hydrogen or liquid helium [13.17]. Additional environmental control can be achieved in conventional ways, and the microscope can be attached to or incorporated in a general surface studies chamber. The usual size of a FEEM is about 10-20 cm in its largest dimension, but microscopes for special purposes have been made

with their largest dimension about 2 m and at least one has been built with its largest dimension less than 25 mm. The microscope chamber can be of mostly metal construction, although mostly glass envelopes seem to be preferred by the users. Aside from differences in the ease of construction and cost, there are subtle differences in the local environment of the specimen due to the different vacuum-related properties of the metals and glasses used.

The FEEM is, of necessity, an UHV microscope for most purposes. The electric field needed for imaging imposes a stress on the emitter tip [13.16], which has not been a practical limitation, but limits or precludes imaging at high ambient gas pressures, due to the possibility of specimen damage from energetic back-accelerated gas ions produced in the field near the specimen. Only brief imaging is tolerable, for example, in 10^{-6} Torr oxygen. The situation is improved by using short-duration pulsed fields for imaging, but is generally still poor. Therefore, unless one wishes to investigate the effects of an intense electric field on some surface phenomenon, the field is generally turned off during interactions at any temperature and pressure, or instead of the customary dc field, a pulsed field with a low duty cycle is used to minimize field effects. Thus, the full range of temperatures, pressures, and adsorbates used in surface science investigations is available for use in FEEM. The field is used only for observations and measurements before and after interactions, and at these times, ultra-high vacuum and relatively low (usually room temperature or lower) temperature of the specimen prevails. The phenomenon under study occurs in the total absence of an electric field.

b) Magnification

The magnification for direct radial projection of the surface of a relatively small sphere of radius r onto the inner surface of a confocal spherical envelope of radius R is

$$M = R/r \quad . \tag{13.2}$$

In the FEEM, the emitting part of the specimen is not exactly spherical and the envelope is not confocal with the specimen shape and the projected image has certain distortions; that is, the magnification is not uniform. Additionally, the nearly hemispherical specimen tip is attached to its shank, which is more nearly conical in shape. This introduces an overall image compression, and the magnification for a small region of the tip is given by

$$M = R/\beta r \quad , \tag{13.3}$$

where R is now the distance of the center of curvature of the region to its

image on the screen, r is the local radius of curvature, and β is a number, usually about 1.5 [13.18]. Magnifications of 10^5-10^6 are common in practice and such magnifications are more than adequate to utilize the available resolution. For example, a typical value for R is 5 cm, and a typical average tip radius of curvature is 2000 Å, giving an average magnification of 1.7×10^5. Since the compression factor β varies significantly with the emitter shape [13.18,19], the magnification is usually not characterized better than ± 15%, unless the tip shape is measured independently, by transmission electron microscopy for example.

c) Contrast

Contrast in the FEEM image depends on several factors, some related to tip features and some to the detector. An extensive analysis is not justified here; instead only the major factors will be discussed. Conforming to the theoretical description above, the major factors are the local work function and the local surface topography, which is implicitly contained in the value of the local electric field strength. Referring to the F-N equation (13.1), it is clear that both of these parameters affect the local field emission current density strongly. Their variation over the emitter surface provides image contrast. For a so-called smooth surface, for example a thermally cleaned field emitter, the image consists of bright and dark areas with smoothly varying intensity between these areas. If the tip is a single crystal, then the pattern of bright and dark areas is usually quite simply related approximately to the orthographic or stereographic projection for the particular structure in the corresponding orientation. Illustrative examples of clean-surface field-electron emission images for bcc, fcc, and hcp metals are given in Fig.13.1 [13.20]. The dark areas are parts of the surface that have the higher work functions and also are less curved. For example, the central (dark) region of the W image, the (011) region, has the closest atomic packing and therefore the largest flat facet and also the highest work function for the clean W surface [13.21].

The strong dependence of emission current density on both local work function and topography is generally a favorable circumstance as it tends to make visible a wide variety of surface features. However, in some instances ambiguity of image interpretation can arise. For example, as the result of chemisorption, the local work function generally changes, but surface rearrangement may also occur, changing the local topography. Such ambiguities can usually be sorted out by experienced microscopists. However, for unambiguous image interpretation in those cases where it is feasible, the specimen may

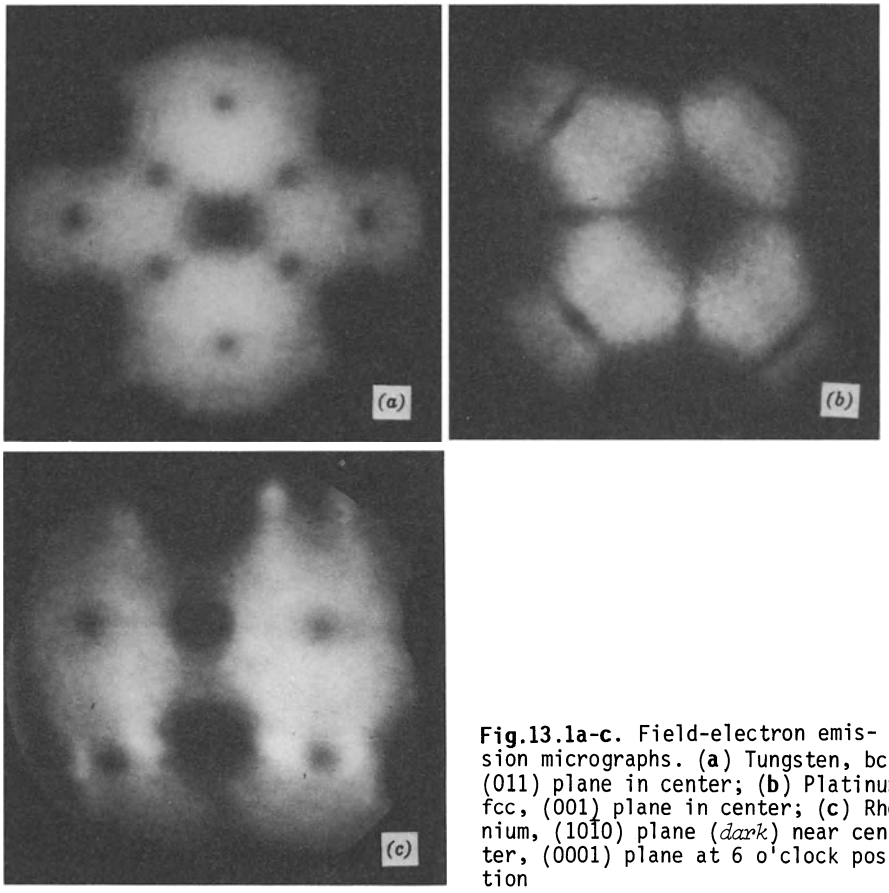

Fig.13.1a-c. Field-electron emission micrographs. (**a**) Tungsten, bcc, (011) plane in center; (**b**) Platinum, fcc, (001) plane in center; (**c**) Rhenium, (10$\bar{1}$0) plane (*dark*) near center, (0001) plane at 6 o'clock position

be examined by field-ion microscopy, which is sensitive primarily to topography, or may be probed by the combination of electron energy distribution analysis and current-voltage (F-N) measurement to determine the work function independent of topography.

d) Resolution

The theoretical lateral resolution of the FEEM for a smooth surface has been derived [13.12] in the form

$$\delta = \{Ar\phi^{-1/2}\,[1 + B(\phi/V)^{1/2}]\}^{1/2} \qquad (13.4)$$

Typically, r = 1000 Å, V = 2500 V, ϕ = 4.5 eV and A and B are constants, giving a resolution of δ = 23 Å. Reducing the radius, that is using a sharper tip, improves the calculated resolution, so that if the radius can be kept at 100 Å, a resolution of < 10 Å is predicted [13.14]. In practice, resolu-

tions significantly less than 15 Å are not usually achieved [13.12]. The resolution is determined also by the spreading of the electrons as they travel from emitter to screen, that is the magnification, the wavelengths of the emitted electrons, and the tangential components of the electron velocities. Interestingly, small bumps on an otherwise smooth emitter surface, acting essentially as emitters of very small radii, do provide improved resolution [13.22]. For example, individual barium atoms have been resolved [13.23] when adsorbed on a higher work function field emitter surface. Images of small oxide molecules [13.24,25] and organic molecules [13.14] have been seen in the FEEM, but unresolved questions remain regarding the imaging mechanism, so that it is not clear whether the theoretical description for a smooth surface given above applies.

e) The Specimen

It has been brought to the reader's attention amply that the field emitter used in FEEM is, perforce, a solid with a curved surface. Such a shape is needed to achieve the high field strengths at reasonable voltages and also to obtain high magnifications in reasonable-size microscopes. For illustration, the field at the surface of a typical field emitter is given by

$$F = V/kr \quad , \tag{13.5}$$

the value if k depending on the emitter geometry [13.14]; typically k = 5. Field strengths of about 0.3-0.5 V/Å are usual, giving currents of 10^{-6}-10^{-5} Å for applied voltages of a few thousand volts.

Most of the surface science studies with the FEEM employ crystalline emitters, the field emitter thus presenting for investigation a wide range of surface geometries, including a variety of single-crystal planes and stepped regions. This unavoidable circumastance endows the FEEM with both benefits and shortcomings. Unfortunately, only the very low-index crystal planes are developed significantly on the thermally cleaned (the usual case) surface. For example, it is not ordinarily possible to develop {111} planes on a thermally cleaned W surface. Fortunately, however, low-temperature field evaporation 13.5, which both cleans and smooths the surface, does develop these important planes. Unfortunately, subsequent experiments on surfaces prepared by low-temperature field evaporation are generally limited to temperatures below the onset of surface self-diffusion, which would severely disarrange the surface. Fortunately, many important experiments can be done below such temperatures (about 600 K for W, for example). Surface phenomena which may involve long-range forces, greater than about 100 Å, can be studied by FEEM only on the

very low-index planes, especially if plane edges (steps) must be avoided. However, for studying the effects of surface steps on surface phenomena, such as nucleation, the FEEM is exceptionally well suited. It should be mentioned in this regard, that the simple FEEM described above may be modified in various ways so that the user can isolate the emission from a selected area of the emitter surface for detailed study. By use of probe-hole techniques [13.26,27], the properties of individual surface planes or stepped areas can be explored.

The FEEM specimen is also well suited to studying phenomena at low temperatures, adsorbed gas/metal surface diffusion, for example. Due to the high magnification and contrast available, small quantities of adsorbate can be followed to measure adsorption and surface diffusion. The small distance scale involved allows measurements to be made in relatively short times and over a variety of surface facets and stepped regions. The short times tend to minimize interference due to contamination from the ambient, and the presence of various types of surface geometry during the same experiment implies similar conditions for the comparison of results for these surfaces.

The total FEEM image provides information about the surface conditions over a large part of the curved specimen. The field emission current mostly comes from step edges and lower work function planes, and information from the high work function areas is derivable only by sensitive curent measurements from those areas. However, simple visual observation of the overall FEEM image or pattern provides a qualitative picture of, for example, the distribution of an adsorbate. Furthermore, various heat treatments can cause characteristic pattern changes due to the physical redistribution of surface atoms - geometric reconstruction - or crystallographically specific adsorption that results in specific local work function variations [13.12]. This allows the FEEM to be used as a sensitive qualitative residual gas analyzer. Thus, various simple gases such as oxygen, carbon monoxide, hydrogen, and nitrogen, when adsorbed on tungsten, can be identified after some specimen heat treatment. The sensitivity derives from integrating the effects of the adsorbate, that is just waiting for some time to accumulate the fraction of a monolayer necessary for an identification.

f) Criteria for a Clean Surface

There are many ways to produce a surface which is said to be clean within the framework of surface science. They include cleaving in UHV, heating in UHV, oxidation followed by annealing in UHV, reduction followed by annealing in UHV, sputtering followed by annealing in UHV, low-temperature field evapora-

tion and vapor deposition of clean material. There are many ways to test a surface for the presence of contamination, perhaps as many as there are techniques for studying surfaces. In real-world experiments, there is no doubt that different methods of surface characterization have different sensitivities for degrees and kind of contamination. Consequently, sometimes earlier work is thrown into questionable status based on new work using a more sensitive technique.

Within the discipline of FEEM, there are definite criteria for a clean surface. However, they are largely subjective and rely strongly on the diligence and patience of the scientist. For a specimen that has been heated in UHV as the last step in an attempted cleaning process, the usual procedure in FEEM is to declare the specimen clean if the following criteria are satisfied [13.12]:(1) The FEEM image is relatively simple, containing facets of low intensity and bright regions, with smooth gradations from dark to light. (2) The FEEM image does not change qualitatively upon further heating to higher or lower temperatures, except for the subtle changes in faceting known to occur as a function of temperature. The first criterion derives from vast experience with W field emitters and an appreciation of the fact that the field emitter surface, due to its curvature, contains a very high density of atomic steps and kink sites, usually representing the likely binding sites for contaminants. Decoration of such binding sites generally leads to abrupt changes of local image intensity. The second criterion guards against the presence of sub-surface contamination since such contamination, in general, diffuses into and out of the bulk at various temperatures. This test is not always done but is mandatory in this author's view, first, because sub-surface contamination can influence surface phenomena [13.28], and second, because sub-surface contamination may diffuse to the surface during later experiments if done at temperatures other than the cleaning temperature.

Two very nice features of smallish curved-surface specimens should be noted here. Such specimens have rather large surface-to-volume ratios (by virtue of small volume) and they can be heated repeatedly to high temperatures while approximately retaining their shape. These features make thermal cleaning an easier process compared to the parallel situation with macroscopic, flat specimens.

Finally, producing a clean surface for FEEM by low-temperature field evaporation in UHV provides, in general, a surface with the same purity as the bulk, but introduces some limitations on the subsequent use of the specimen, as mentioned earlier.

g) Specimen Materials

Specimen material in an FEEM must have sufficient electron conductivity to sustain the necessary high field at its surface and to allow an emission current of, perhaps, some nanoamperes; metals and semiconductors generally meet this requirement. Additionally, the material must have sufficient tensile strength to sustain the stress associated with the electric field; most solid metals and semiconductors meet this requirement. There may be additional requirements, depending on the specific nature of the experiments to be performed. For example, if a clean surface is required, then obviously the material must be cleanable by the techniques available in the FEEM.

Most of the early FEEM work was done using W specimens because problems abounded which could be researched using W, and W was easy to prepare and to clean in UHV. In recent years, many other specimen materials have been used: Ta, Mo, Ir, Pt, Rh, Pd, Ni, V, Au, Os, Nb, Re, Ru, Si, Ge, Hf, and Zr come to mind. Additionally, many metals have been used as field-electron emitters in the form of single or polycrystalline layers epitaxially grown from the vapor phase [13.29,30]. These include Cu, Ag, Fe, Y, Pb, Dy, Gd, Sm, and Eu. Thus, it is clear that FEEM has come a long way from the W days. Further breadth in the variety of specimen materials could have been realized earlier had the need for obtaining a clean surface been taken less as a mandate and more as desiratum.

13.3.3 Selected Field-Electron Emission Microscopy Research

a) Visibility of Atomic and Molecular Objects

There are at least two reasons, related to surface science, for demonstrating the capability of a microscope to visualize adsorbed atomic and molecular objects. The first is to establish an impressive range of applicability of the microscope to see small-scale surface events, and the second is to stimulate further research into those surface phenomena involving atoms and molecules. During the approximately 25 years following the introduction of the FEEM, there was considerable activity centered on the question of its practically achievable resolution. It was clear, both experimentally and theoretically, that the FEEM could not be expected to resolve the lateral spacings of surface lattices, but the resolution of small adsorbed objects might be quite a different matter. In order to test the FEEM for such resolution, various metallic atoms and oxide and organic molecules were adsorbed onto the field emitter surface.

Müller studied the adsorption on W of K, Cs, Ba, Sr, Th, U, Zr, S, Se, BaO, and a large number of different organic molecules [13.14]. Special attention

was given to Ba/W studies from which he concluded that individual Ba ions in an adsorbate aggregate could often be resolved, that is seen as individual atoms. *Ashworth* concurred, and further concluded that individual hydrogen and oxygen molecules could occasionally be seen [13.31]. The issue of whether or not the FEEM could see individual Ba atoms became a matter of some controversy, inspiring some very nice research, but ultimately the issue subsided when the FIM was introduced and was recognized to have far superior resolution, anyway.

The images produced by the adsorption of organic molecular vapors on field emitter surfaces generated even more difference of opinion among the many researchers attracted to the subject. The initial experimental results [13.32] were spectacular for they indicated very clearly that individual dye molecules (pthalocynine) could not only be seen by the FEEM, but also that details of their shape could be resolved. This issue became rather murky, however, when the original workers [13.14], and others [13.33], found that all of the various organic molecules, ranging in size from benzene to pentacene and larger, and including a variety of (theoretical) shapes, appeared the same in the FEEM images. This led to various, nonrigorous ideas about the imaging mechanism and to questions about what was actually being imaged; that is, were the images due to individual molecules, as Müller originally claimed, or something else such as sputtered pieces of substrate material or molecular clusters?

Later work [13.34] showed that the "molecular" images sometimes correspond to adsorbed individual molecules, but also sometimes originate from stacks of 2-6 molecules. When the adsorption is done on a surface maintained at a low temperature (77 K), there are distinguishable differences in the FEEM images of some molecules [13.20]. Although several mechanisms of image formation have been proposed [13.14,33-41], the interpretation of the molecular images has never been rigorously established or widely accepted.

There seems to be no doubt that the FEEM can see individual molecules; the question remains, however, why the images do not always look like the textbook models. Field-ion microscopy images of Cu-pthalocyanine [13.42] show that the ion image of the object giving rise to a molecular image in the FEEM typically is some 10-20 times smaller than the corresponding FEEM image. This and other characteristics of the FEEM molecular images have prompted a number of suggestions that scattering of electrons tunneling (possibly with resonances) from the substrate through the adsorbed molecules gives rise to the characteristic singlet, doublet, and quadruplet molecular images.

Further research based on the ability of the FEEM to see organic (and some other) molecules seems still to be in the potential stage, although some frag-

mentary work was done to test for polymerization in a series of related organics [13.43]. Image interpretation questions have probably been a deterrent.

b) Surface Diffusion

The FEEM has been used to measure parameters of surface diffusion by utilizing the strong dependence of image contrast on work function and on the local radius of curvature. As the attentive reader will note, the FEEM can and has been used to measure surface diffusion both in the presence of an electric field and in the absence of such a field. Moreover, the effects on the measurements due to the negative field strengths used in FEEM are usually small, amounting to about 15 % of the activation energy for metal adsorbates of average atomic polarizability [13.44], and probably much less for inorganic molecular or atomic gases. Only for atoms of very high polarizability [13.45] does the FEEM field cause a significant perturbation to the diffusion process. The perturbation can be reduced by using low-duty-cycle pulsed fields or image amplification and lower field strength.

Investigations by FEEM of surface diffusion have been extensive and very productive, but these have been limited almost entirely to diffusion on metal surfaces or to metal surface self-diffusion. The limitation to metals has been due to two main reasons. First, it is generally harder to clean semiconductor field emitters than metals [13.46,47]. Second, no one seemed to be interested in studying diffusion on dirty semiconductor surfaces, although some experimental estimates have been made for surface self diffusion of Si and Ge [13.48]. There have been interesting problems enough in the regime of diffusion on metals.

i) Gases on Metals

The early pioneering research of *Gomer* on the diffusion of oxygen and hydrogen on tungsten and hydrogen on nickel [13.49,50] vividly demonstrated the capabilities of FEEM in this area and in gas/metal adsorption in general. This work took full advantage of the curved-surface microscopy, as discussed in Sects. 13.3.2e,f to uncover the effects of gas coverage, surface temperature and surface structural heterogeneity on surface diffusion.

The technique devised by Gomer for adsorbate diffusion studies consisted of first depositing the gas onto some fraction, perhaps half, of the field emitter surface from a gas source located to the side of the emitter. The deposition was performed with no applied field and with the entire FEEM immersed in liquid hydrogen or liquid helium. Gas not adsorbed on the emitter structure condensed on the cold walls of the FEEM, and the "shadowed" region of the

emitter remained clean. The gas dose could be controlled and calibrated to result in coverages ranging from submonolayer to multilayer. Subsequent heating of the emitter, with the field on, caused diffusion and spreading of the adsorbed layer(s) into the initially clean region of the emitter surface; the movement could be observed in real time due to the difference in work function between clean and covered parts of the emitter. Measurements of the migration distance x as functions of time t, and temperature T obeyed the Einstein and Arrhenius equations written simply as

$$\frac{x^2}{t} = D_0 \exp\left(\frac{-Q}{kT}\right) \quad , \tag{13.6}$$

where k is Boltzman's constant, from which determinations of the diffusion activation energy Q and a preexponential term D_0 could be made.

Three types of surface diffusion were found [13.17]. For hydrogen on tungsten, uniform spreading with a sharply defined boundary (seen with ~20 Å resolution) occurred at temperatures < 20 K for initial deposits greater than a monolayer. Anisotropic spreading with a sharp boundary occurred at higher temperatures, 180-240 K, and boundary-free spreading occurred for lower coverages. Similar experiments were done for other gases and yielded values of preexponential factors and activation energies not then measurable by other means.

More recently, another technique was developed which enables surface diffusion measurement with the FEEM. The field-electron emission from a selected crystallographic region of the surface can be isolated, or probed, and this electron current can be measured and analyzed. While the current of electrons emitted from a clean metal field emitter exhibits mostly shot noise, adsorption of atoms or molecules causes the electron emission to exhibit a different spectrum of noise, termed flicker noise [13.51]. This fluctuation of field emission current has been related to surface diffusion of the adsorbate and very interesting and informative measurements have been made of metal and gas atomic diffusion on single crystal planes [13.52,53]. The technique has some advantages compared to the other FEEM method, described above, for measuring adsorbate surface diffusion. Measurement of diffusion on high work function planes of the substrate is easier and detecting directional effects on individual planes is possible [13.54,55]. However, the technique is irrevocably locked into the need to use an electric field during the diffusion process being measured.

ii) Metals on Metals

Surface diffusion of an adsorbed metal on another metal substrate was measured for Ba and W in early FEEM experiments [13.56], and more accurately a few

years later [13.44]. The procedures for measuring surface diffusion parameters are usually similar to those used in the deposit-and-spread method described above for gas/metal surface diffusion. The microscope is often equipped with cryogenic fluid cooling for the field emitter to ensure that the as-deposited metal is confined initially to the area of the emitter "seen" by the metal vapor source used to deposit the metal onto the emitter. The metal adsorbate can be seen due to a generally different work function compared to the substrate and also due to its different microgeometry. Thus, it is usually possible to observe and measure diffusion of the second and third monolayers on top of the preceding layers. In all studies to date, the substrate metal has had a higher melting point than the deposited metal, for experimental simplicity. It is generally easier to clean the surface of a higher-melting-point metal, and it is generally easier to construct a clean vapor source for lower-melting-point metals. The general rule observed is a decrease in the diffusion activation energy as the coverage increases. An exception known to this author is the case of gold diffusion on tungsten [13.57].

As for gas/metal surface diffusion, metal/metal diffusion is observed with no boundary at submonolayer coverages and with a sharply defined boundary for multilayer diffusion. Varying degrees of anisotropy in the diffusion rates and the activation energies occur for diffusion over different crystallographic regions and different directions on the substrate, and these also vary significantly with admetal and surface contamination [13.58]. It is a straightforward matter to measure metal/metal surface diffusion for the zero-field case by causing the diffusion to occur during periods when the field is off, and then lowering the specimen temperature quickly and measuring the position of the diffusion front [13.44]. A positive electric field has also been applied during surface diffusion. The effect of a positive field is large, for incompletely explained reasons, but the effect of the negative field, ordinarily used for FEEM imaging, is much smaller [13.44].

iii) Surface Self-Diffusion

This kind of surface diffusion was evident even in the earliest FEEMs whenever the specimen was heated in the presence of the electric field [13.23]. Due primarily to the tapered shape of the field emitter and its shank, the field strength generally increases as the apex is approached from the tip support-loop direction. Thus, there is a force driving atoms, polarized in the field, to migrate towards the apex [13.21]. Given sufficient thermal activation, surface atoms will migrate and reform or "build up" a revised tip shape. This build-up process can be repeated at different temperatures and

field strengths and between experiments the original shape can be restored approximately by annealing the tip without the field. Field-dependent activation energies can be measured and atomic polarizabilities can be determined.

Zero-field surface self-diffusion can be measured by at least two different methods in the FEEM through blunting and smoothing of field emitters. Blunting of a heated field emitter occurs due to thermodynamic driving forces [13.9] which cause material to be transported from the tip apex to the shank regions in the absence of an electric field. This process results in a loss of material from the original apex. The process was FEEM monitored intermittently by *Müller* [13.59] who determined the change of tip geometry with time and temperature from its field emission characteristics. Later workers improved the accuracy of this type of measurement by determining tip-shape changes using transmission electron microscopy [13.21]. The measurement of surface self-diffusion can be done more precisely in the FEEM by using the emitter-smoothing method. This method consists of first causing a reproducible small perturbation to the original smooth emitter shape by field build up while monitoring the process by measuring the field emission current at constant applied voltage. The shape is then smoothed by zero-field heating; the specimen is then tested again for current at the constant voltage. From such sequences repeated at various temperatures, it can be learned whether Arrhenius diffusion behavior is followed and, if so, diffusion parameters can be calculated.

Whereas this type of surface self-diffusion is relatively easy to measure, it is not crystal-face specific, and is not simply the hopping motion of adsorbed atoms, to be discussed in Sect. 13.4.2a. It is more closely related to the scratch-smoothing diffusion experiments made on macroscopic specimens [13.60,61], which involve relatively large amounts of mass transport. In the FEEM measurements, the experimental times are short, typically on the order of 100 s, due to the high magnification, good resolution, and UHV conditions, so that little or no contamination occurs during the diffusion processes.

c) Nucleation and Crystal Growth

The FEEM is exceptionally well suited for the study of a certain few aspects of the nucleation and growth of crystals from the vapor phase. This was recognized early by *Gomer* [13.17,62,63], who used a modified form of FEEM to investigate the growth kinetics and other features such as crystallographic orientation of Hg whiskers grown from Hg vapor. Gomer was able to obtain an estimate of whisker tensile strength, to determine that growth obeyed a positive exponential law until limited by diffusion of Hg atoms along the whisker sides,

to estimate the surface diffusion activation energy at about 1.1 kcal and occasionally to observe elastic twisting, which he ascribed to the presence of axial screw dislocations. Subsequently, *Parker* and *Hardy* [13.64] used the technique to study K whisker growth on W. This technique was later generalized to enable studies of higher-melting-temperature metal and semiconductor whisker growth [13.65] and some effects thereon of gaseous impurities in the vapor [13.58]. Heterogeneous nucleation from the vapor phase, under equilibrium and nonequilibrium conditions, has been the subject of many FEEM studies [13.66]. Since it is necessary to turn off the field during nucleation and growth, the so-called "critical nucleus" [13.67] size cannot be accurately determined but nucleation sites can be located and coverage conditions necessary for heterogeneous nucleation can be ascertained. Epitaxial relationships can be determined as can effects due to contamination. The FEEM capability of measuring surface diffusion enables an understanding of nucleation site selection as a function of substrate temperature [13.68].

The ability to nucleate and grow crystal layers by vapor deposition epitaxy in the FEEM has provided a relatively easy method of preparing field emitters for further studies. In those systems that have been tried [13.29], the growth parameters have been reproduced easily for macroscopic specimens in a LEED apparatus. Thus far, the growth has been always on the lowest-index crystal plane for the macroscopic specimen and epitaxial relationships have always been the same for both the FEEM and the LEED specimens.

Only crystals of lower melting temperature than the substrate have been grown in the FEEM; it would probably be impractical to grow more-refractory crystals on a less-refractory tip for at least two reasons. First, the less-refractory tip might not be cleanable and second, removing the more-refractory crystal (which usually must be done several times until optimum growth conditions are determined) would prove difficult or impossible without destroying the substrate tip by blunting or alloying. It should be possible however, to grow the less-refractory crystal by vapor deposition epitaxy on a very refractory tip, and then to use the less-refractory crystal as the substrate for vapor deposition growth of a more-refractory material. Safe high-temperature erasure should be straight forward for such a system.

d) Cleaning Platinum Field Emitters

Platinum has not proven to be a metal which is easy to clean by the favored method of specimen cleaning in the FEEM, that is by heating in UHV [13.69]. The extent of difficulty in preparing a clean field emitter depends on the initial impurities in the emitter material, possible doping due to the method

of attachment to the support loop, impurities in the support loop, possible specimen doping from the ambient atmosphere during and after bakeout of the microscope, and the length of the tip shank which sets an upper limit to the temperature to which the tip can be heated. Similar impurities can arise in macroscopic Pt specimens, in addition to the possible contamination arising from the act of surface characterization itself. Platinum specimens have been cleaned successfully in the FEEM by prolonged heating to 1500-1600 C in UHV and have met the requirements for a clean surface specified in Sect. 13.3.2f [13.69,70]. Special attention was given to testing for the out-diffusion of impurities due to lower-temperature heating after high-temperature cleaning.

The most persistent contamination of the Pt field emitters has been observed as bright rings around the step edges of the {001} planes. Early FEEM work [13.71] suggested that the contaminant might be oxygen or some oxide. It was shown that heating a clean Pt field emitter to ~1000° C in oxygen did indeed result in the {001} contamination pattern [13.70] and, importantly, heating in hydrogen or carbon monoxide reduced the extent of contamination. More recently, *Mundschau* and *Vanselow* (MV) [13.69,72] used high-resolution Auger electron spectroscopy (AES) to analyze Pt FEEM specimens under various conditions. They found, interestingly, that P, Si, and S impurities in the bulk Pt segregated to the surface in the {001} areas. Heating to temperatures "close to the melting point" resulted in a surface which appeared to be clean, by the image-appearance criterion described in Sect. 13.3.2f, but further heating to lower temperatures caused additional segregation of impurities to the {001} areas. Ultimately, a clean FEEM pattern, independent of temperature, was achieved [13.69].

These results are very important as a demonstration of the rather strong binding sites for several kinds of contamination that are associated with Pt{001}. (Qualitatively similar FEEM observations have been made for Ir{001} and Au{001} [13.73]. The FEEM work has also emphasized the difficulty of removing the last traces of contamination from the Pt surface. These results might cause some questions regarding the possibility that the so-called clean-surface Pt{001} reconstruction, derived from LEED observations [13.74], might be due to contamination. The LEED studies used surface characterization by AES to document surface cleanliness. The MV investigation convincingly demonstrated that both Si and S are particularly difficult to detect on Pt by AES. They found also that large concentrations of surface Si caused the formation of Pt{012} planes in addition to contaminating the Pt{001} areas; {012} factes were reported in some of the LEED work [13.69]. Mundschau and Vanselow conclude that "much LEED {001} reconstruction work" probably dealt with observa-

tions on specimens with overlooked contamination. The totality of evidence thus escalates the earlier level of suspicion from "some question" to very suspect. However, relating curved-surface observations to planar-surface observations is not a simple matter. One must recognize the fact that the last traces of contamination of the FEEM specimens are observed at the step edges around {001} planes; the {001} planes themselves are dark and indistinguishable, on the basis of FEEM images alone, from their appearance when the step-edge contamination is not present. Thus, it is possible and consistent with all of the observations that the macroscopic specimens used in the LEED experiments were contaminated, but the contamination was restricted to the step edges and thus did not affect the LEED reconstruction results. The main message from MV is a justified plea for those who study macroscopic specimens to be more careful in characterizing specimen cleanliness.

e) Electron Energy Distributions

For some years following the (1928) F-N formalism describing low-temperature field electron emission, there was confusion about the interpretation of measurements of field-electron energy distributions. The earliest measurements (1932) by *Henderson* and *Badgley* [13.75], using a cylindrical retarding-grid analyzer, gave very wide distributions but did show clearly that the onset of field-electron emission occurred near the Fermi level in agreement with the F-N theory. In later papers, *Henderson* et al. described experiments with thin-wire field emitters in cylindrical analyzers [13.76-78] and with a point field emitter in a spherical analyzer [13.78,79]; results with the latter were described as total energy distributions. They derived the normal energy distribution [13.78] from the F-N theory, but their measured distributions were too wide. *Müller*, however, using a pointed field emitter in a spherical analyzer [13.26,80] obtained excellent aggreement with the theoretical normal energy distribution. *Young* later recognized that the energy distribution measured in the spherical analyzer is indeed the total energy distribution which he calculated [13.13]. *Young* and *Müller* [13.81] accurately measured this distribution which was about 1/3 the width of the calculated normal energy distribution, or as narrow as 0.14 eV. The older agreement with the incorrectly calculated distribution was then realized to have been fortuitous due to poor instrumental resolution.

Total agreement of experiment and theory did not prevail. Energy distributions measured in the W<110>, <111>, <112>, <116>, and <130> directions agreed with theoretical distributions, but measurements in the W<100> direction gave anomalous results [13.82,83]. An anomalous shoulder, or hump, was found at

about 0.35 eV below the Fermi level. This was due to features of the W electronic structure and could not be predicted by the F-N theory which was based on an ideal free-electron model. Further theoretical development ensued [13.84], and the measurements of field emission energy distributions (FEEDs) have continued to be useful. In particular, they have provided interesting information relating to adsorbed gases and metals. This application of FEEM was enhanced when it was pointed out by *Duke* and *Alferieff* [13.85] that simply describing the effect on electron emission of adsorbed atoms and molecules in terms of work function changes could be a serious error. They impressed upon the field emission researchers the importance of possible resonance tunneling effects. This certainly expanded the theoretical horizon in FEEM, explained some earlier "anomalous" work function results and, of course, led to further experimental work, which has confirmed the theory.

The phenomenon of anomalous energy distribution for the <100> direction of W [13.82] is rather interesting in relation to the clean-surface reconstruction of W (001) which will be addressed in Sect. 13.4.2b. Measurements of FEEDs are excellently suited to the investigation of surface states, responding only to the electronic structure of the surface [13.84]. Consequently, the anomalous hump has come to be accepted as evidence for a surface state, although the detailed description of this state has had a controversial history. Results of FEED measurements have demonstrated also that, whereas a single adsorbed Ca atom does not remove the hump [13.86], a monolayer of adsorbed active or inert gas certainly destroys it [13.87].

As FEED measurements have progressed, they have evolved into a limited, but powerful kind of surface spectroscopy, a near-Fermi-level spectroscopy.

13.4 Field-Ion Microscopy

13.4.1 The Microscopy

a) The Microscope

As originally conceived [13.3], the FIM was simply an FEEM with reversed tip voltage (+) and some added hydrogen or, later, helium as the ambient gas. With field strengths about ten times greater than those used for FEEM, an image was projected by streams of positive ions, instead of electrons, from the tip to the screen. These modifications were made to overcome the limitation of FEEM resolution due to the tangential velocities of the field electrons. The successful development of FIM in its early stages is a tribute to the experimental skill of its inventor, E.W. Müller; in the first approximation, the early images were almost too faint to be seen by the unaided eye - a dim view indeed. Even after the importance of a low temperature for the specimen was recognized

and implemented in 1955 [13.4,80,88], long exposure times, up to 45 min, using high-speed photographic film and optics were necessary to record FIM images. This difficulty was removed about 15 years ago with the availability of microchannel-plate image intensifiers, so that the FIM image can now be made sufficiently intense to be seen clearly in ordinary room light.

The outward appearance of the FIM has never been standardized. One can find in use today various sizes of mostly glass or mostly metal, bakeable, or nonbakeable microscopes with or without a specimen quick-change facility, having various configurations of cryogenics systems, vacuum and gas-handling apparatus, and various kinds of electrical and/or electronic accessories. The essential elements, consisting of a pointed specimen raised to voltages of about 2-25 kV positive relative to an image detector and display, remain the same as when originally introduced. However, most instruments utilize internal microchannel plates or external image intensification to intensify the FIM image by a factor of some 10^2-10^6.

b) The Image

Image formation in the FIM is initiated by ionization of a gas or vapor within a few Ångstroms of the specimen surface under the influence of an electric field [13.16,89,90]. The field-ionized atoms or molecules are then accelerated by the electric field and impinge directly onto a phosphor screen detector or onto an image intensifier. A detailed description of the surface-electronic and gas-field-adsorption and diffusion effects which may enter into the image formation process is outside the intended scope of this brief review; instead, an operational viewpoint will be adopted. The parameters which are commonly available to the microscopist to control the imaging process are specimen temperature, image gas, and field strength or voltage.

Specimen temperature influences image resolution, intensity, and contrast, all of which improve, generally, with lower temperatures. Also, surface stability increases with lower temperatures, due to less energy being available for activation of atomic displacements, whether partial or complete. Most FIMs are equipped to cool the specimen to at least 78 K, and often 20 K or lower, and FIMs which are intended to be used for surface science investigations have the capability to heat the specimen to higher temperatures and to measure specimen temperature.

Although it is not strictly necessary to avoid the use of thermal cleaning methods, almost all FIM studies have used field evaporation instead. By increasing the positive field strength, the potential barrier for evaporation of a surface atom can be sufficiently lowered to allow escape of the atom in the

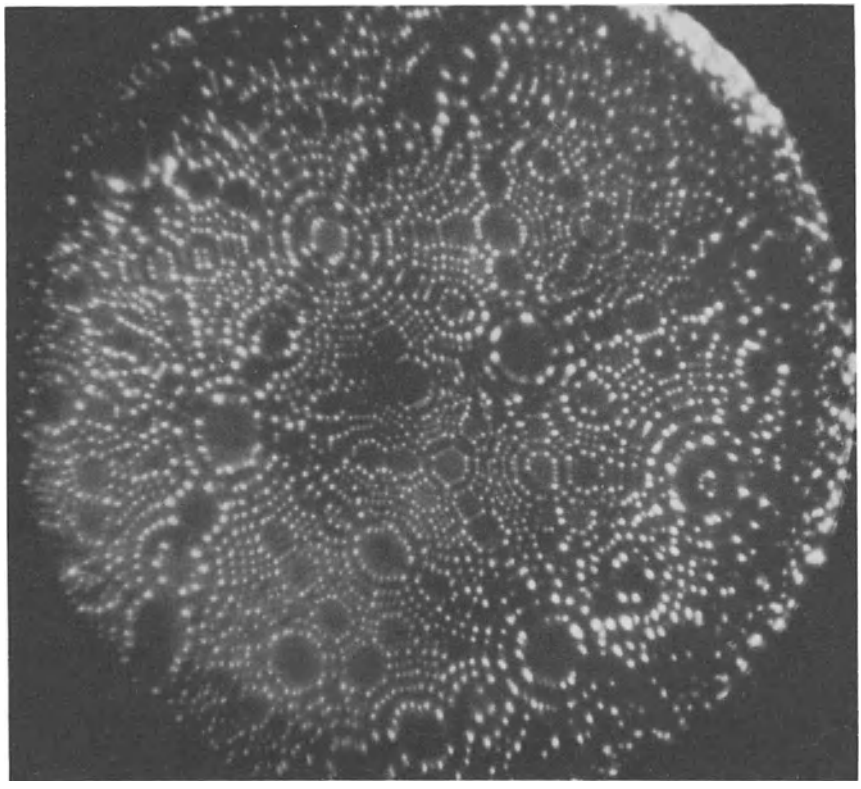

Fig.13.2. Field-ion micrograph of hafnium. Imaging conditions: voltage: 16.8 kV; temperature: about 35 K; Ne imaging gas. Diameter of image corresponds to about 100 nm

form of a positive ion, even at low temperatures [13.16]. The process, which is uniquely controllable in FIM, is termed field desorption, for the removal of foreign atoms, and field evaporation, for surface atoms of the primary specimen. The net result of low-temperature field evaporation is a very smooth and generally clean (as discussed earlier) surface. Figure 13.2 shows a typical FIM image from a low-temperature field-evaporated surface.

Various gases and vapors are usable and have been used for FIM imaging; inert gases, such as helium, neon, and argon as well as hydrogen are most common, with mixtures also finding use [13.91,92]. The first ionization potential of the imaging gas atoms or molecules determines the field strength necessary for imaging; for the gases just mentioned, helium field-ion imaging requires a field strength of about 4.4, neon 3.5, argon 2.2, and hydrogen 2.2 V/Å [13.16]. Thus, the choice of image gas significantly affects the (negative hydrostatic) stress on the specimen. The image contrast is also affected by the imaging gas in complicated ways, and in the case of hydrogen can be in-

fluenced through chemical interactions with various parts of the surface. It should be noted also that the choice of imaging gas determines a low-temperature limit to imaging due to formation of liquid on the specimen surface.

The imaging field strength, which is adjusted by setting the applied voltages (approximately, F = V/5r), is usually variable over a few percent; thus, the voltage for sharpest image, the so-called best image voltage, is well defined [13.16] for metals. The voltage range for semiconductor imaging is usually much broader due to field penetration. A criterion which must be met for stable imaging in the FIM is that the field strength for imaging must be less than the field strength for disrupting the surface. For a given imaging gas, this condition is met more easily as the specimen size increases; that is, the ratio of imaging field/evaporation field decreases with increasing tip size.

The projected image displays a one-to-one correspondence with those surface atoms over which the field-ionization probability and gas supply are sufficient to cause a significant rate of ionization. The projection geometry depends, in detail, on the specimen shape and the detector shape, but usually is approximately orthographic or stereographic. Due to the various local atomic geometries, so abundant and varied on curved surfaces, there is a variety of local magnifications ordinarily present in an FIM image and these are understood, at least for crystalline materials [13.91]. In terms of the local radius of curvature, magnification is as given in Sect. 13.3.2b for the FEEM.

Considering the image of Fig.13.2, it is apparent that the only surface atoms that generally contribute to the image are those at steps and in the lower-index crystal planes (other areas appear dark). There are techniques, i.e., using mixtures of imaging gases or carefully adjusting the field strength, for increasing the percentage of atoms that image on some planes, but for crystalline specimens in general it is never possible to image all of the surface atoms in a single image. Sequences of images taken during a slow field-evaporation sequence can, in favorable cases, depict all of the atoms of some surface region, but this is a difficult procedure.

Surface resolution in FIM is theoretically described in terms of the distribution of transverse velocities of the emitted ions and their spreading due to magnification [13.16]. The transverse velocities may be limited by diffraction, described by Heisenberg uncertainty, or by the kinetic energy of the gas atoms just prior to ionization. Thus, one derivation for temperatures which are not too low [13.93] gives the resolution δ as

$$\delta = [0.6\ r\ (3kT + \alpha F^2)/eF]^{1/2} \quad , \tag{13.7}$$

where α is the gas-atom polarizability and e is the electron charge. To image

a specimen of average radius 50 nm using He imaging gas in an FIM, the field strength required would be about 4.5×10^8 V/cm (11 000 V would accomplish this), and the theoretical lateral resolution would be 0.12 nm for the specimen at 21 K and 0.23 nm at 78 K. For smaller specimen radii, the resolution improves, so that for a specimen with 1-nm average radius, the theoretical resolution for He FIM at 21 K is about 0.04 nm [13.93].

Practically achieved lateral resolution for lattice atoms are larger than predicted, as usual in a real microscope, and are generally between 0.2 and 0.3 nm for the most favorable conditions. It is interesting to note that individual W atoms resting on a W(011) plane can easily be "seen" even though the surface lattice resolution of the He-FIM for large-radii specimens at room temperature was determined to be about 0.5 nm [13.12].

The direct vertical resolution of the FIM has not been quantitatively defined. However, it is abundantly clear that surface steps of height as small as 0.05 nm can be resolved [13.94]. The vertical resolution in practical cases is probably limited by the available contrast.

c) More About Field Evaporation

The high-field effect of field evaporation has been investigated elaborately by FIM and continues to be the second most important feature of the microscopy, after the imaging feature. Several theoretical treatments of the phenomenon have appeared and it is still not fully understood. Nevertheless, field evaporation is used, generally at low specimen temperatures, in most FIM work to prepare a surface for surface science experiments by removing contamination layers and surface roughness, for the controlled removal of surface atoms for chemical analyses in the atom-probe FIM, or to explore internal atomic structures. One formulation [13.16] describing field evaporation of an atom in n^{th} charge state is

$$Q_n = \lambda_0 + I_n - n\phi - (n^3 e^3 F)^{1/2} + P(F) \quad , \tag{13.8}$$

where Q_n is the field-dependent evaporation activation energy, λ_0 is the zero-field binding energy, I_n is the n^{th} ionization potential and P(F) represents all polarizability effects. The rate, R, of field evaporation is then

$$R_n = A \exp(-Q_n/kT) \quad . \tag{13.9}$$

Field evaporation of W at 77 k, for example, begins at $(5.6\text{-}6.7) \times 10^8$ V/cm [13.16].

It is always found experimentally that increasing the field strength causes an increased rate of field evaporation, making it apparent from (13.8) that

the polarization effects are not dominant and field evaporation should be more probable for surface atoms which experience the greater local field strengths. This provides a basis for understanding the ordinarily experienced field-evaporation sequence for surface atoms of a crystalline material. When a crystalline FIM specimen is field evaporated, by application of either a steady or a pulsed field, the surface atoms generally evaporate in an orderly sequence, the outer edge atoms of net planes evaporating before the next row in, etc., resulting in the appearance of collapsing rings of atom images.

Field evaporation can, of course, be carried out over a wide range of temperatures. In recent years, field evaporation by a steady field with heating by a pulsed-laser beam has become a useful technique [13.95], particularly in connection with atom-probe mass analysis. This is an aspect of FIM which is currently being actively investigated in several laboratories, and its full range of applicability is still to be elucidated.

d) The Specimen

In order to be imaged in an FIM, the specimen must have a shape that includes one, and only one, single point with a sufficiently small average radius to produce a field strength high enough for copious field ionization of some imaging gas, given the conductivity of the specimen at an available applied voltage. Additionally, the specimen material must have sufficient tensile strength and atomic binding energy to remain intact under the applied field. In practice, these conditions have been met by a wide range of materials having a wide range of initial morphologies.

In fact, the time is long past when a complete list of specimens imaged by FIM could be set down on paper by this author in a finite time. However, some indication of approximate limits is evident. Tensile strength as little as that of pure Al or Be suffices, and resitivity as high as 5×10^5 Ω cm has not been an impediment. Most of the metallic and several of the semiconducting elements and numerous compounds and alloys have been imaged.

Other factors, however, determine how well or poorly a given specimen material can be imaged, that is the FIM image quality. These factors include ductility, melting temperature, atomic structure, and, in the case of compounds and alloys, the specific combination of elements. In any case, it is clear that the days of tungsten needles as the only practical FIM specimens are past. (This is not meant to imply that W is no longer useful to the field-ion microscopist.) Furthermore, FIM is still a developing discipline, and innovations in specimen preparation are probably yet to come.

13.4.2 Selected Field-Ion Microscopy Research

a) Surface Diffusion

The outstanding application of FIM in surface science research is undoubtedly the observation and measurement of atomic surface diffusion, where the power of the microscope is directly brought to bear on a phenomenon in its ultimate dimensions. *Müller* raised the possibility of using the FIM for surface diffusion studies [13.96], and subsequently *Ehrlich* and *Hudda* reported [13.97] the first successful measurement and analysis of single-atom diffusion on well-characterized crystal planes. This attracted several others to the use of the FIM for such work, and a steady stream of credible information has been forthcoming (e.g. [13.98-100]). From the beginning, the intention was to make observations and measurements which could be compared with theory, and, therefore, rather stringent experimental conditions were considered to be essential. Thus, FIM has been developed into a very useful technique for determining the kinetics and energetics of atoms moving on near-ideal surfaces, and for exploring the nature of interatomic forces at surfaces.

Field evaporation is used to prepare a surface which has facets, one of which is selected for the measurements. Such facets are atomically smooth. In those instances when all of the associated atoms have been images, the atomic structures have been perfectly or nearly perfectly formed. Field evaporation can be easily continued until a perfectly formed, atomically smooth plane is realized. When an atomically close-packed plane such as W(011), for example, is used, the interior atoms of the plane are not imaged and, therefore, could contain defects unknown to the experimenter. However, repeated measurements on several of these planes guard against such hidden problems.

Elaborate care is usually exercised to ensure that the thermal vapor source used for depositing atoms for the diffusion measurements and the FIM tip are outgassed thoroughly, and that no adsorption of ambient gas occurs on the plane of interest during the course of a set of measurements. After one or more atoms are deposited onto the plane with no applied field, their initial positions are recorded, usually by introducing an imaging (inert) gas and photographing the FIM image. The field then is removed again and the specimen temperature, which is kept low (often about 21 K) for imaging purposes, is raised to some temperature T for some time t to allow surface migration to occur. The specimen is then cooled and the field once again applied for low-temperature FIM imaging. This cycle is repeated at various temperatures using the same heating time interval. The set of FIM micrographs is used to determine the positions of each adatom relative to the underlying surface plane, following each heating interval. The net atomic displacements which occured

in each interval are measured from the micrographs from which the mean square displacement $\langle R^2 \rangle$ is calculated. Then the diffusivity D is

$$D = \langle R^2 \rangle / 2dt \quad , \tag{13.10}$$

where d is 1 or 2 for atomic motion in one or two dimensions, respectively. The activation energy and preexponential factor can then be obtained using (13.6,10).

The technique has been used to study the migration of single atoms and dimers [13.101] on a few metals; unfortunately, it has not been applicable to the interesting problems of gas/solid adsorption and surface diffusion, since the high field used during imaging would cause desorptions. Investigations of atomic self-diffusion have been reported for W, Ir, Pt, Rh, and Ni and for Re atomic diffusion on W [13.102].

The results of *Ehrlich* and *Hudda* [13.97] illustrate well the kinds of information obtained. For W on W, they found that measurable atomic migration occurred at surprisingly low temperatures, 288-337 K for random movement on the central (011) plane, and 224-288 K for migration along channels in the {112} plane; diffusion required less energy on the {112} plane than on the {011} plane. Mobility was least on {111} and increased in the order {111} ~ {013} < {011} ~ {112}. Atoms were found frequently to be reflected at the boundaries of {011}, {112}, and {123} planes, and migration took place preferably along the natural atomic rows of the {112} and {113} planes rather than across the rows. Interesting edge effects were indicated by the finding that diffusion was significantly easier along {112} rows than along the similar rows of a {123} plane. Their diffusion data gave for {011}, $D = 3 \times 10^{-2}$ exp (-22/kT), for {123}, 1×10^{-3} exp (-20/kT) and for {112}, 2×10^{-7} exp (-13/kT), and some estimates of the entropies of activation.

This FIM technique has developed into a very fruitful area of study related to the fundamental understanding of the growth of crystalline layers and crystals, as well as to an understanding of interatomic forces at the smooth and stepped parts of clean metal surfaces. In addition to quantitative information on atomic migration, a considerable amount of qualitative information has been obtained [13.103] about the atomic geometry of metal adsorption sites.

b) Clean-Surface bcc {001} Atomic Structure

In the investigation of atomic migration, the surface probe is really the migrating atom or atoms; the microscope is used only for recording images. Field evaporation is another type of probe which can give information about the in-

teratomic forces on surface atoms, and the research discussed in this section illustrates this point.

The atomic structure of a crystal surface plane is not necessarily identical to what is expected on the basis of a simple termination of the bulk atomic structure. Most planes which have been examined thus far, however, have the expected lateral atomic structures. Interestingly, a few crystal planes have been found to be anomalous, that is they have structures which are not simply terminations of the bulk structure; these are said to be reconstructed surfaces. Among the fcc and bcc metal surface planes so far found to be reconstructed, FIM has been applied rigorously only to the bcc metals W [13.104] and Mo [13.105].

With regard to clean metal surface reconstruction, certainly the W{001} plane has been the most extensively investigated plane studied by FIM. Two of the most obvious features commonly observed during low-temperature field evaporation of W are the anomalously irregular appearance of the {001} planes and the frequent appearance of small c(2×2)-oriented clusters of 3-5 atoms during the final stage of evaporation of a {001} plane.

Research by LEED on reportedly clean W{001} surfaces, with only small amounts of reported contamination, has let to different reconstruction models [13.106-109] to account for the diffraction observations. The most widely accepted model, due to *Debe* and *King* [13.108], describes the W{100} surface as a (1×1) structure which undergoes a high-order structural phase transition at about 370 K as the temperature decreases. The model originally included a prohibition of reconstruction for parts of the surface within ±20 Å from any monoatomic step. Atomic displacements of the reconstruction were determined to be 0.32 Å diagonally in alternating <11> directions; more recently, the amplitude of the displacements was reduced to 0.16 Å [13.110]. Small amounts of gaseous contamination of the surface were shown to destroy the reconstruction [13.107,108].

Two FIM investigations came to opposite conclusions. *Tsong* and *Sweeney* [13.111] reported finding no evidence for reconstruction of W{001} in their low-temperature (21 K) FIM images; that is, within the resolution of their microscope, the images were consistent with a (1×1)-symmetric atomic structure. *Melmed* et al. [13.112], however, and *Tung* et al. using results of FIM imaging and careful field evaporation, concluded that W{001} is reconstructed in a subtly complicated way, including vertical components to the atomic displacements, over a wide range of temperature from about 15 K to at least about 580 K, and that this is almost always not evident from the FIM images alone. The field-evaporation results were used to derive indirectly information about

the zero-field atomic structure. Additionally, *Tung* et al. concluded that monoatomic steps do not prevent the occurrence of reconstruction. Later LEED work [13.113] confirmed this, and other LEED work [13.114] also confirmed the existence of reconstructed W{001} at temperatures up to about 700 K. *Tung* et al. also found the structurally related W{013} plane to be similarly reconstructed.

A large amount of activity by several experimental and theoretical techniques has been devoted to the question of the geometric and electronic structure of W{001} and related planes in other bcc metals during the past six years. Focusing on the relatively small role of FIM, it is clear that in the W{001} case it provided new information. Regarding the related Mo{001} plane, FIM results [13.105] again indicated reconstruction, differing in detail from the W case, over a wide range of temperature with no prohibiting effect of monoatomic height steps. Using FIM Nb{001} and Ta{001} were found to have normal, that is not reconstructed, structures [13.114].

Both the Mo and Nb results were predicted by LEED investigations that found Mo{001} to be reconstructed, and Nb{001} to be unreconstructed. The structure of Ta{001} was found to be unreconstructed, first by FIM [13.104] and then by LEED [13.115]. Thus, the question of whether a surface is reconstructed or normal has been answered by FIM and LEED with consistent agreement. The detailed description of atomic displacements by the two techniques is different, however, and this may be due to the different probe characteristics of each technique [13.116,117]. The reconstruction atomic displacements are extremely small, and theoretically are affected by very small driving forces.

The application of FIM techniques to the study of clean-surface reconstruction seems, with the present capabilities and limitations of FIM, to be limited. While it is feasible to produce large crystal planes (that is, perhaps 90-100 nm in diameter) in some cases [13.12], it is also true that the specimen treatment necessary to achieve such large planes (heating with field) may well cause specimen contamination from the bulk or the shank. Additionally, the visibility contrast for atoms in the interior of such large planes is usually nonexistent. In practice, only simple small-scale reconstructions can be identified. Probably the most important role for FIM would be to survey various materials for the occurrence of reconstruction. This can be done quickly and under credibly clean surface conditions. Controversies that might arise over the details could then be accumulated for later, more leisurely argument.

13.5 Summary and Future Outlook

Following the early stages of FEEM, during which the techniques of microscope design, specimen preparation, and measurement procedures were developed and evaluated, the capabilities and limitations of FEEM were known and the microscopy settled into use for various surface studies. The high current density and narrow energy distribution of electrons supplied from a field-electron emitter began receiving attention from workers with practical application in mind; significant and widespread use for the field emitter ultimately became a reality. Within surface science, the major thrust of FEEM research was the study of gas-metal interactions, that is adsorption, surface diffusion and desorption of inorganic gases on clean metal surfaces. Considerable effort was put into the study of metallic deposits on clean metal surfaces. Investigations by FEEM of the electronic structure of metals and the effects of adsorption on the electron energy distribution, that is field-electron spectroscopy, were appearing with increasing frequency. However, at least two causes together resulted in a substantial reduction in the ranks of surface scientists maintaining active interest in FEEM. Macroscopic surface investigations became more attractive, and for those surface scientists who maintained an interest in curved-surface microscopy, FIM burst onto the scene and promised the attainment of the microscopist's goal of atomic resolution.

Field-ion microscopy developed rather slowly due to initial difficulties with the instrumentation. In the effective absence of commercialization of the microscope, individual research laboratories faced considerable time-consuming problems merely to begin successful imaging. Ultimately, after the advent of convenient UHV-compatible image intensification, the microscopy became more popular. Surface science applications have been in the areas of surface atomic structure, field ionization and field-ion appearance spectroscopy, field evaporation, atomic polarizability, surface diffusion, metallic overlayer adsorption and corrosion. However, FIM has always had *more* applicability to metallurgy and materials science than to surface science. This is, *perhaps*, even more so now, with the rapid development of the atom-probes. As with the field-electron emitter, the field-ion emitter has the properties of high brightness and very small spread in beam energy, and this has made it attractive for applications as a point source of positive ions. Liquid ion source developers, in particular, have been exploiting these properties.

Normally, it is not possible to predict, even approximately, the events of the future in the world of science, which is so replete with innovation. At most times, it seems certain that all of the major innovations have been made already and that not much further first-order change is possible. These state-

ments are contradictory, of course. If no further innovations are reasonably to be expected, then the prediction of future events is easy - business as usual, or simply an extrapolation from a knowledge of what has already happend.

Based on past and presently perceived trends in FEEM, it seems reasonable to expect a constant (low) level of activity to continue along traditional lines. There are still many adsorption systems to be explored, for example. Also, in view of the continued widespread interest in heterogeneous catalysis and the expanding interest in various aspects of very thin films on solids, there will be further FEEM activity related to these areas.

The field (of study) will mature to the realization that a wealth of information can be obtained using contaminated field-electron emitters as substrates for careful surface science investigations, and this will enhance the level of activity in both the experimental and theoretical aspects if FEEM.

Ultimately, lower-field FIM should be feasible, allowing the investigation of gaseous adsorption with possibly somewhat less resolution. This and other advances in specimen preparation techniques, will enable very realistic investigation of adsorption on metallic and semiconducting catalyst particles.

References

13.1 R.H. Fowler, L.W. Nordheim: Proc. Roy. Soc. London, Ser.A **119**, 173 (1928)
13.2 E.W. Müller: Z. Phys. **106**, 541 (1937)
13.3 E.W. Müller: Z. Phys. **131**, 136 (1951)
13.4 E.W. Müller: Z. Naturforsch., Teil A **11**, 88 (1956); J. Appl. Phys. **27**, 474 (1956)
13.5 E.W. Müller: Naturwissenschaften **29**, 533 (1941)
13.6 J.W. Gibbs: Trans. Conn. Acad. **3**, 108 (1876); ibid. **3**, 343 (1878)
13.7 W.K. Burton, N. Cabrera, F.C. Frank: Philos. Trans. R. Soc. London **243**, 299 (1950)
13.8 See, for example, F.C. Frank: In *Metal Surfaces: Structure, Energetics and Kinetics* (American Society for Metals, Cleveland, OH 1963)
13.9 C. Herring: Phys. Rev. **82**, 87 (1951); In *Structure and Properties of Solid Surfaces*, ed. by R. Gomer, C.S. Smith (University of Chicago Press, Chicago 1953)
13.10 J.M. Blakely: *Introduction to the Properties of Crystals* (Pergamon, Oxford 1973)
13.11 W. Schottky: Z. Phys. **14**, 63 (1923)
13.12 R.H. Good, Jr., E.W. Müller: In *Electron-Emission. Gas Discharges I*, Handbuch der Physik, Vol. 21 (Springer, Berlin, Göttingen, Heidelberg 1956) pp. 176-231
13.13 R.D. Young: Phys. Rev. **113**, 110 (1959)
13.14 E.W. Müller: Ergeb. Exakten Naturwiss. **27**, 290 (1953)
13.15 R.P. Johnson, W. Shockley: Phys. Rev. **49**, 436 (1936)
13.16 E.W. Müller, T.T. Tsong: *Field Ion Microscopy Principles and Applications* (Elsevier, New York 1969)
13.17 R. Gomer: *Field Emission and Field Ionization* (Harvard University Press, Cambridge, MA 1961)

13.18 R. Haefer: Z. Phys. **116**, 604 (1940)
13.19 W.P. Dyke, J.K. Trolan: Phys. Rev. **89**, 799 (1953)
13.20 A.J. Melmed: In *Experimental Methods of Material Research*, Vol.1, ed. by H. Herman (Interscience, New York 1967)
13.21 W.P. Dyke, W.W. Dolan: *Advances in Electronics and Electron Physics*, Vol.8, ed. by L. Marton (Academic, New York 1956)
13.22 D.J. Rose: J. Appl. Phys. **27**, 215 (1956)
13.23 E.W. Müller: Z. Phys. **108**, 668 (1938)
13.24 J.A. Becker: Adv. Catal. **7**, 136 (1955)
13.25 E.W. Müller: Z. Elektrochem. **59**, 372 (1955)
13.26 E.W. Müller: Z. Phys. **120**, 261 (1943)
13.27 W.P. Dyke, J.K. Trolan, W.W. Dolan, F.J. Grundhauser: J. Appl. Phys. **25**, 106 (1954)
13.28 A.J. Melmed, J.J. Carroll: J. Vac. Sci. Technol. **10**, 164 (1973)
13.29 For an extensive list of references, see A. Ciszewski, A.J. Melmed: J. Cryst. Growth **69**, 253 (1984)
13.30 A.J. Melmed, V. Maurice, O. Frank, J.H. Block: J. Phys. (Paris) **45**, C9-47 (1984)
13.31 A.J. Ashworth: *Advances in Electronics and Electron Physics*, Vol.3, ed. by L. Marton (Academic, New York 1951)
13.32 E.W. Müller: Z. Naturforsch., Teil A **5**, 473 (1950)
13.33 P. Wolf: Z. Angew. Phys. **6**, 529 (1954)
13.34 A.J. Melmed, E.W. Müller: J. Chem. Phys. **29**, 1037 (1958)
13.35 E.W. Müller: Z. Naturforsch., Teil A **5**, 475 (1950)
13.36 R. Haefer: Acta Phys. Austriaca **8**, 105 (1953)
13.37 E. Hörl, F. Stangler: Acta Phys. Austriaca **10**, 1 (1956)
13.38 J.A. Becker, R.G. Brandes: J. Appl. Phys. **27**, 221 (1956)
13.39 R. Gomer, D.A. Speer: J. Chem. Phys. **21**, 73 (1953)
13.40 A.P. Komar, A.A. Komar: Zh. Tekh. Fiz, **31**, 231 (1961)
13.41 I. Giaever: Surf. Sci. **29**, 1 (1972)
13.42 A.J. Melmed: In *Field-Ion Microscopy*, ed. by J.J. Hren, S. Ranganathan (Plenum, New York 1968)
13.43 A.J. Melmed: unpublished
13.44 H. Utsugi, R. Gomer: J. Chem. Phys. **37**, 1706 (1962)
13.45 A. Ciszewski, A.J. Melmed: Surf. Sci. **145**, L509 (1984)
13.46 L.A. D'Asaro: J. Appl. Phys. **29**, 33 (1958)
13.47 W.D. McNeil, W.B. Shepherd: Rev. Sci. Instrum. **43**, 1636 (1972)
13.48 F.G. Allen: Phys. Chem. Solids, **19**, 87 (1961)
13.49 R. Gomer, R. Wortman, R. Lundy: J. Chem. Phys. **26**, 1147 (1957)
13.50 R. Wortman, R. Gomer, R. Lundy: J. Chem. Phys. **27**, 1099 (1957)
13.51 Ch. Kleint: Surf. Sci. **25**, 394 (1971)
13.52 Ch. Kleint: Surf. Sci. **25**, 411 (1971)
13.53 R. Gomer: Surf. Sci. **38**, 373 (1973)
13.54 D.R. Bowman, R. Gomer, K. Muttalib, M. Tringides: Surf. Sci. **138**, 581 (1984)
13.55 M. Tringides, R. Gomer: 45th Ann. Conf. Physical Electronics, Milwaukee, WI (1985)
13.56 M. Drechsler: Z. Elektrochem. **58**, 340 (1954)
13.57 J.P. Jones, N.T. Jones: Thin Solid Films **35**, 83 (1976)
13.58 A.J. Melmed: J. Appl. Phys. **37**, 275 (1966)
13.59 E.W. Müller: Z. Phys. **126**, 642 (1949)
13.60 W.W. Müllins: J. Appl. Phys. **30**, 77 (1959)
13.61 J.M. Blakely, H. Mykura: Acta Metall. **9**(**1**),23 (1961)
13.62 R. Gomer: J. Chem. Phys. **26**, 1333 (1957)
13.63 R. Gomer: J. Chem. Phys. **28**, 457 (1958)
13.64 R.L. Parker, S.C. Hardy: J. Chem. Phys. **37**, 1606 (1962)
13.65 A.J. Melmed, R. Gomer: J. Chem. Phys. **34**, 1802 (1961)
13.66 See, for example, K.L. Moazed, G.M. Pound: Trans. Metall. Soc. AIME **230**, 235 (1964)

13.67 J.P. Hirth, G.M. Pound: *Condensation and Evaporation* (Pergamon, Oxford 1963)
13.68 A.J. Melmed: J. Appl. Phys. **36**, 3585 (1965)
13.69 For an extensive list of references, see M. Mundschau, R. Vanselow: Surf. Sci. **155**, 121 (1985)
13.70 A.J. Melmed: J. Appl. Phys. **36**, 3691 (1965)
13.71 R. Vanselow: Phys. Status Solidi **4**, 697 (1964)
13.72 M. Mundschau, R. Vanselow: Phys. Rev. Lett. **53**, 1084 (1984)
13.73 A.J. Melmed: unpublished results
13.74 S. Hagstrom, H.B. Lyon, G.A. Somorjai: Phys. Rev. Lett. **15**, 491 (1965)
13.75 J.E. Henderon, R.E. Badgley: Phys. Rev. **38**, 590 (1931)
13.76 J.E. Henderson, R.K. Dahlstrom, F. Abbott: Phys. Rev. **41**, 261 (1932)
13.77 J.E. Henderson, R.K. Dahlstrom: Phys. Rev. **45**, 764 (1934)
13.78 J.E. Henderson, R.K. Dahlstrom: Phys. Rev. **55**, 473 (1939)
13.79 R.K. Dahlstrom, K.V. Mackenzie, J.E. Henderson: Phys. Rev. **48**, 484 (1935)
13.80 E.W. Müller, K. Bahadur: Phys. Rev. **102**, 624 (1956)
13.81 R.D. Young, E.W. Müller: Phys. Rev. **113**, 115 (1959)
13.82 L.W. Swanson, L.C. Crouser: Phys. Rev. Lett. **16**, 389 (1966)
13.83 L.W. Swanson, L.C. Crouser: Phys. Rev. **163**, 622 (1967)
13.84 This development is described in J.W. Gadzuk, E.W. Plummer: Rev. Mod. Phys. **45**, 487 (1973)
13.85 C.B. Duke, M.E. Alferieff: J. Chem. Phys. **46**, 923 (1967)
13.86 E.W. Plummer, R.D. Young: Phys. Rev. B **1**, 2088 (1970)
13.87 C. Lea, R. Gomer: J. Chem. Phys. **54**, 3349 (1971)
13.88 E.W. Müller: Ann. Meeting Electron Microscope Soc. America, Pennsylvania State University (1955)
13.89 K.M. Bowkett, D.A. Smith: *Field Ion Microscopy* (North-Holland, Amsterdam 1970)
13.90 R. Wagner: *Field-Ion Microscopy,* Crystals, Vol. 6 (Springer, Berlin, Heidelberg 1982)
13.91 E.W. Müller: Surf. Sci. **8**, 462 (1967)
13.92 L.W. Swanson, D.E. Reed, A.E. Bell: 14th Field Emission Symposium, Washington, D.C. (1967)
13.93 E.W. Müller: *Advances in Electronics and Electron Physics,* Vol. 13, ed. by L. Marton (Academic, New York 1960)
13.94 A.J. Melmed: Surf. Sci. **8**, 191 (1967)
13.95 G.L. Kellog, T.T. Tsong: J. Appl. Phys. **51(2)**, 1184 (1980)
13.96 E.W. Müller: Z. Elektrochem. **61**, 43 (1957)
13.97 G. Ehrlich, F.G. Hudda: J. Chem. Phys. **44**, 1039 (1966)
13.98 T.T. Tsong: Phys. Rev. B **6**, 417 (1972)
13.99 D.W. Bassett, D.R. Tice: In *The Physical Basis for Heterogeneous Catalysis,* ed. by E. Drauglis, R.I. Jaffee (Plenum, New York 1975) p. 231
13.100 R.T. Tung, W.R. Graham: Surf. Sci. **97**, 73 (1980)
13.101 G. Ehrlich: In *The Structure of Surfaces,* ed. by M.A. Van Hove, S.Y. Tong, Springer Series Surf. Sci., Vol.2 (Springer, Berlin, Heidelberg 1985) p. 375
13.102 For a summary of results and further references, see G. Ehrlich: Proc. 9th Int. Congr. and 5th Int. conf. on Solid Surfaces, ed. by J.L. de Segovia, A.S.E.V.A., Madrid (1983), Asociación Española de Vacío y sus Aplicaciones
13.103 T.T. Tsong, M. Ahmad: In *The Structure of Surfaces,* ed. by M.A. Van Hove, S.Y. Tong, Springer Series Surf. Sci., Vol.2 (Springer, Berlin, Heidelberg 1985) p. 389
13.104 R.T. Tung, W.R. Graham, A.J. Melmed: Surf. Sci. **115**, 576 (1982)
13.105 R.T. Tung: Ph.D. Thesis, University of Pennsylvania (1980)
13.106 K. Yonehara, L.D. Schmidt: Surf. Sci. **25**, 238 (1971)

13.107 T.E. Fetter, R.A. Barker, P.J. Estrup: Phys. Rev. Lett. **38**, 1138 (1977)
13.108 M.K. Debe, D.A. King: Surf. Sci. **81**, 193 (1979)
13.109 P. Heilmann, K. Heinz, K. Müller: Surf. Sci. **89**, 84 (1979)
13.110 J.A. Walker, M.K. Debe, D.A. King: Surf. Sci. **104**, 405 (1981)
13.111 T.T. Tsong, J. Sweeney: Solid State Commun. **30**, 767 (1979)
13.112 A.J. Melmed, R.T. Tung, W.R. Graham, G.D.W. Smith: Phys.Rev. Lett. **43**, 1521 (1979)
13.113 T.-M. Lu, G.-C. Wang: Surf. Sci. **107**, 139 (1981)
13.114 A.J. Melmed, W.R. Graham: Appl. Surf. Sci. **11/12**, 470 (1982)
13.115 S.T. Ceyer, A.J. Melmed, J.J. Carroll, W.R. Graham: Surf. Sci. **144**, L444 (1984)
13.116 A. Fasolino, G. Santoro, E. Tosatti: Phys. Rev. Lett. **44**, 1684 (1980)
13.117 A.J. Melmed, W.R. Graham: Surf. Sci. **123**, L706 (1982)

14. Scanning Tunneling Microscopy

R.J. Behm[1] *and W. Hösler*[2]

[1]Institut für Physikalische Chemie, Universität München, Sophienstr. 11, D-8000 München 2, F.R.G.
[2]Institut für Kristallographie, Universität München, Theresienstr. 41, D-8000 München 2, F.R.G.

The scanning tunneling microscope (STM) – developed by Binnig and Rohrer – has recently appeared as a new instrument for surface structure investigations with atomic resolution. This chapter is intended to give a general overview of the current status of the STM and to illustrate its potential and performance with typical examples, supplemented by an updated listing of previous STM work. It is subdivided into the following parts: First we provide a short general introduction to scanning tunneling microscopy, then we list the experimental problems, give an overview of the different instrumental concepts, and discuss some typical problems of STM measurements related to the instrument. The next section is concerned with the current understanding and modeling of the correlation between the tunnel current and the shape and size of the tunnel barrier, which also includes the question of the resolution of the STM. The following section then deals with different applications and examples of surface microscopy. It also contains a brief look at other applications of the STM. In the fifth section we focus on spectroscopic data, i.e., results on the electronic structure of the surface. The conclusions in the last section summarize these features and give a brief perspective of some future uses of the STM.

14.1 Introduction

In 1981 *Binnig* and *Rohrer* reported first results which demonstrated that the STM really performs vacuum tunneling [14.1,2], in 1982 the first image of a surface on an atomic scale was presented [14.3], and further progress is demonstrated by several articles on scanning tunneling microscopy [14.4-11].

The STM probes surface structures and electronic properties by moving a tip in close (a few angstroms) proximity to a surface along the surface. The tunnel current between surface and tip serves as the actual probe, and thus the instrument works nondestructively. It produces real-space images of the surface investigated. Within a few years of development, a resolution of 2-5 Å laterally and better than 0.1 Å vertically has been achieved [14.7,12].

The tunnel effect, a well-known quantum mechanical effect, is the physical basis of the microscope. It describes the finite probability for a particle to penetrate ("tunnel through") an energy barrier which is higher than the energy of the particle. This probability depends sensitively on the height and width of the barrier. In the STM, the probing electrons tunnel through a vacuum gap from the sample to the tip or vice versa. A vacuum gap as used in the STM represents the simplest possible barrier. The first experimental observations explained by a tunneling process—the autoionization of hydrogen [14.13] and the emission of electrons from a cold metal surface [14.4], both induced by a strong electric field—consequently referred to this situation. Tunneling through a vacuum gap between two metal electrodes was also treated theoretically as early as 1930 [14.15], but experimentally verified only in 1976 [14.16]. In 1981 *Poppe* reported on vacuum tunneling in a study of the energy gap in superconductors (Sects.14.5.1,5.3) [14.17]. These experiments were performed in an apparatus very similar in design to the STM except for the scanning capability [14.17]. In 1965 *Young* and coworkers first tried to exploit the tunneling effect for surface structural studies [14.18,19]. Mainly problems associated with the stability of the feedback control prevented them from operating their instrument in the tunneling mode [14.20]; its topographic resolution was not better than 25 Å vertically and several thousand angstroms laterally [14.18]. In contrast, tunneling spectroscopy, using mainly thin oxide layers as insulating tunnel barriers, has with time developed into a powerful spectroscopic probe [14.21-23]. Electron tunneling is also the basis of field emission and field ion microscopy the development of which is connected with the name of E.W. *Müller* [14.24]. Since these techniques are topics of separate chapters in this (Chaps.12,13) and the preceding volume [14.25], they are mostly not mentioned throughout this chapter although they are in many respects closely related to and of direct relevance for STM work. The same holds for high-resolution electron microscopy which is also dealt with in this volume (Chap.15).

Figure 14.1 schematically depicts the setup of an STM. The sample S is faced by a sharp tip at a very close distance of only a few angstroms. The tip is moved in three mutually perpendicular directions by a tripod of piezoelectric ceramics, with the tip motion typically limited to 1 μm in each direction. The sample is transported over large distances (a few millimeters to one micrometer) by a carrier, in this case a small piezoelectric ceramic device, referred to as the "louse" L. Once it is sufficiently close to the tip, alternately the tip and the sample move slowly towards each other until

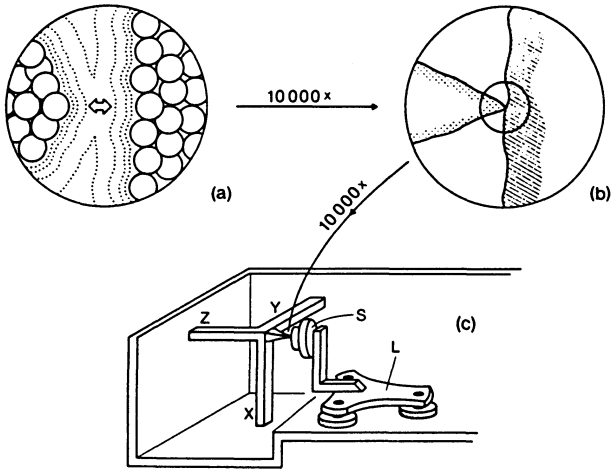

Fig.14.1a-c. The physical principle and technical realization of STM. **a** Apex of the tip (*left*) and surface (*right*) at a magnification of about 10^8. The circles indicate atoms, the dotted lines electron density contours. The path of the tunnel current is given by the arrow. **b** Scaled down by a factor of 10^4, the tip (*left*) appears to touch the surface (*right*). **c** STM with rectangular piezoelectric drives X, Y, Z of the tunnel tip (length of each leg ~5 cm) at left and "louse" L (electrostatic "motor") for rough positioning (μm to cm range) of sample S. (After [14.7])

a tunnel current is measured, in order to avoid accidental mechanical contact. During tunneling the sample remains in its place while the tip is moved.

A "tunnel voltage" of a few millivolts to a few volts is applied between tip and sample. The resulting tunnel current of typically 1-10 nA is recorded either as a function of tunnel voltage or sample distance, or it is used for a feedback loop to control the vertical position of the tip. These modes also indicate the different ways the STM can be operated to detect different surface properties. To record the surface topography, the tunneling current and, to a zero-order approximation, the sample-tip distance are kept constant while the surface is scanned. The motion of the piezoelectric ceramics then provides a real-space image of the surface. In other modes, the relation between tunnel current and distance (~ barrier height) or tunnel voltage (~ density of states) is investigated. These measurements can either be performed at a fixed position or – in a modulated measurement – during a two-dimensional (2D) scan. In this way an image of the local barrier height (local work function) or of the spatial distribution of electronic states [scanning tunneling spectroscopy (STS)] is obtained.

14.2 Experimental Considerations

The operation of the STM depends on the ability to reliably keep tip and sample a distance of five to ten angstroms apart without touching each other. Since good lateral resolution is also desired, the basic requirement for building and operating an STM is to keep the tip mechanically stable with respect to an arbitrary reference point on the sample surface. The respective application of the instrument can lead to additional restrictions in construction details or the choice of materials. Again, we want to emphasize general features while construction details can be obtained from the referenced original literature.

The system of sample and tip can be regarded as an oscillator which can be excited externally (e.g., by external vibrations) or internally (e.g., by the movement of the piezoelectric drives). The transmission of outside vibrations must be greatly reduced by vibrationally decoupling the tunnel unit from its surroundings. A rigid design of this unit reduces internal vibrations and the impact of residual vibrational amplitudes from the environment. Because of these requirements, the motion of sample and tip with respect to each other has to occur indirectly, i.e., without mechanical contact to the outside, at least during the tunnel measurements. For technical reasons, this motion is split up: a well-controlled motion over short distances (in the Angstrom to micrometer range) is achieved by moving the tip via piezoelectric ceramics, while larger distances are covered by an independent (coarse) drive which in most cases moves the sample. These problems will be discussed separately in the following part. Since most STMs currently used or planned are intended for work in an ultra-high-vacuum (UHV) environment, we will also deal with the implications of UHV compatibility.

In their first microscope, *Binnig* et al. achieved vibrational decoupling by magnetic levitation, i.e., a plate with permanent magnets floated on a helium-cooled, superconducting lead bowl [14.2]. In subsequent designs by this and other groups, a three-stage system coupled via two sets of springs yielded good results. Additional eddy-current damping leads to suppression of the vibrational eigenmodes of the system. It is achieved by strong permanent magnets close to massive copper blocks which are mounted on the different stages. Transmission of high frequencies is effectively damped by the use of Viton connectors and spacers. The damping properties of Viton in fact are so good that in their most recent design —the "pocket size STM" —the IBM group has used only Viton damping and still achieved good stability [14.26]. Decoupling in this way rules out any solid connections to the sample, which is particularly desirable for cooling. In order to avoid this drawback,

Willis et al. vibrationally decoupled their entire vacuum vessel, including the cooling connections, from the surroundings [14.9]. In other designs for low-temperature STMs, the tunneling unit hangs in a cooled Dewar [14.27-29] or even in liquid N_2 [14.30].

A wide variety of different methods have been devised to bring sample and tip close enough together to be within reach of the piezoelectric drives (~1 μm). The original design, the "louse", used a combination of piezoelectric elongation/contraction and electrostatic clamping [14.5]. Subsequent groups slightly modified this concept by using frictional [14.31] or magnetic [14.32] clamping instead. Other drive mechanisms have been based on piezoelectric bending elements [14.33,34], or on magnetic [14.35-37] or electrostatic [14.27-29] propulsion.

In a completely different approach, sample and sampleholder are moved by direct mechanical drive [14.8,9,38]. The necessary sensitivity is obtained by simple mechanical transmission, for example, by a differential screw or a reduction lever system. The instrument of *Demuth* et al. was demonstrated to lead to a very stable tip-sample arrangement [14.38]. The design of *Coleman* et al. [14.31,39] comprises elements of an STM and a squeezable tunnel junction, which had previously been successfully used by *Moreland* et al. to measure tunnel characteristics in the form of current-voltage curves [14.39-42].

The precise movement of the tip (against a fixed sample) is always performed via piezoelectric drives, which are arranged in three mutually perpendicular directions. Two of them serve for lateral scanning, while the third provides the motion vertical to the surface. Minor differences within this general concept concern only the type and shape of the piezoelectric material, which determines (via the conversion factor) the drive voltages and the maximal scan range. The conversion factors of different piezoelectric materials were precisely calibrated with a capacitance dilatometer at different temperatures down to 4 K by *Vieira* [14.43].

In the topographic mode, the z-piezo is part of a feedback loop, which is shown in more detail in Fig.14.2. A PID regulator (in fact, an integrator is sufficient) [14.44] maintains a constant tunnel current by controling the z-piezo and thus also the gap width. The response time of the feedback system limits the scan speed and should therefore be as short as possible. To prevent instabilities, however, the gain must be sufficiently low at the frequencies of the eigenmodes of the tunnel unit [14.44]. Typical values for these modes are 1-1.5 kHz, which necessitate cutoffs at time constants above 1 ms [14.45-47].

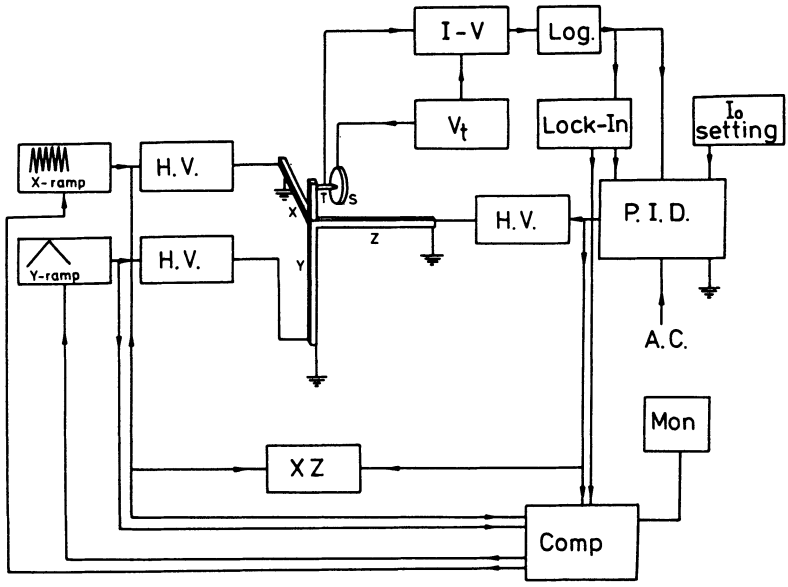

Fig.14.2. Schematic of the tip position control: The output of the high voltage amplifiers (HV) determines the expansion of the piezoelectric drives X, Y, Z and thus the position of the tip T with respect to the sample S. The tunnel current, I_t – resulting from the tunnel voltage V_t – is transformed into a voltage (I-V), its logarithm (Log) is compared in a PID controller with a preset value (I_0). The output controls the z-piezo and is recorded either on an XY recorder (XZ) or in a computer (Comp). Ramp generators or the computer drive the lateral motion of X and Y

The determination of surface distances from the voltages applied to the piezoelectric drives can lead to geometric distortions in the measured pattern. All deviations from a linear voltage-expansion correlation, such as those caused by thermal changes, hysteresis, or creep effects, result in such distortions [14.43]. Hysteresis and creep effects become evident, for example, from the considerable drift that can be observed after large movements of the piezoelectric bars or at the turnaround points of the scans. Thermal drift, however, is by far the most significant contribution, particularly in experiments which do not permit sufficient thermal equilibration. Rather small changes in the temperature of the sample and also the tunnel unit can cause corresponding movements over even wider distances than those the tip drive can compensate for, making measurements on an angstrom scale impossible. *Van de Walle* et al. designed a composite tip drive within which temperature effects cancel out, but there is still sufficient material between sample and tip drive to allow thermal drifts on an appreciable scale [14.46,47].

The earlier tunneling tips were prepared mechanically, e.g., by grinding tungsten wires [14.7]. Though these tips are very rough on a microscopic scale and certainly do not resemble a sharp needle with a small tip radius, lateral resolutions of ~10 Å were easily achieved. The most plausible explanation is that the tunnel current depends so strongly on the gap distance that only the tip region closest to the sample (the "minitip") contributes effectively to the tunnel current. In contrast to field emission, the influence of the tip curvature on the maximum current density can be neglected. Later, it was shown that chemically etched tips provide higher resolution and, especially, are more stable with respect to whisker formation [14.38,48]. The tips are further processed in vacuum, applying standard procedures as used in field ion microscopy, like field desorption/evaporation, sputtering, and annealing of the tip. Direct measurements of the tip size on a scale relevant for tunneling are not yet available. Scanning electron microscopy (SEM) pictures gave an impression of the overall shape of the tip, but they could not resolve the tunneling region itself [14.26,31,49]. Since the interpretation of highly corrugated surfaces depends strongly on the tip size, this motivated two groups to set up a combined field ion microscope (FIM) and STM in order to define the tunneling tip by field ion microscopy [14.50, 51]. First FIM pictures of tunnel tips have already been presented [14.50]. They demonstrate that a tip prepared by chemical etching, sputtering, and annealing from a single crystalline W wire exhibits a spherical tip end and a regular shape over several hundred angstroms [14.52].

The two main advantages of working in UHV are the possibility of preparing clean surfaces and the potential combination with other surface-sensitive techniques. While the STM itself can operate in air—although the stability is reduced by coupling to acoustic vibrations—the operation of most other techniques is limited to low pressures. To fully exploit these advantages, the STM design is required to be UHV compatible *and* to permit easy access to these techniques without complicated sample transfers. The direct comparison of STM measurements with results from other methods, however, suffers from the fact that i) most of the other techniques analyze and, therefore, average over a much wider surface area and ii) they may measure a different area on the surface than the STM. Therefore, it must be verified that the STM measurements are representative of the surface area under investigation. Considerable improvement came from a recent construction of the group at IBM Zürich, which combined a STM and a SEM in such a way that SEM pictures can be taken in situ from the sample region measured by STM as well as from the tip itself [14.26]. The SEM can provide a larger-scale overview

of the area around the scan region. Its variable magnification makes it an ideal supplement to the STM which has a rather limited scan range (~1 μm) and thus only little "zoom" capability.

14.3 Tunnel Current and Tunnel Barrier

14.3.1 Basic Model Calculations and Approximations

Tunneling was first described in 1928 for the ionization of a hydrogen atom in an electric field [14.13] and for field emission from metals [14.14]. While tunneling from hydrogen is a one-electron problem, tunneling of electrons out of a larger atom, out of a solid material or between two solid electrodes represent many-body problems, which are properly described by a many-body Hamiltonian. Earlier approximations, however, used the "independent electron model" in which many-body interactions are neglected. On this basis a variety of different theoretical treatments were developed. All of them describe tunneling either from a free-electron metal plane into vacuum or between two parallel planes with distinct shapes of the barrier potential. The tunneling probability was derived by exact solutions including numerical integration, within the WKB approximation or using further approximations (an overview of different methods is given in [14.23]). The Fowler-Nordheim equation [14.14] represents an "exact" solution for tunneling of independent electrons through a triangular barrier into vacuum. *Simmons* [14.53] in turn introduced an average (square) barrier to describe tunneling (between two planar electrodes) through a trapezoidal barrier, which is a more approximate description than the WKB method [14.23].

Although the problem of solving the Schrödinger equation for the many-body Hamiltonian is still too complex, more rigid treatments have been designed which include the many-body character of the tunneling process. In general, its description is divided into the following parts [14.10]:

(1) Treatment of the effective bulk potential and the resulting band structures and wave functions of the electrodes;

(2) Formulation of the same properties close to the surface region, which are influenced by the fast variation of the electron density; and

(3) Characterization of the tunneling process through the potential Barrier given by (2) and the respective tunnel voltage.

Bardeen introduced the "transfer Hamiltonian" concept which basically allowed him to evaluate the tunneling current from the eigenfunctions of the separate systems and a tunneling operator without the need to calculate the

eigenfunctions of the entire system [14.54]. In this method, the tunnel current is calculated from the overlap of the tails of the wave functions of the two electrodes in the region of the tunnel barrier.

The correlation between tunnel current and distance represents a direct measure of the barrier height (which is related but not identical to the local work function, see [14.55]). We have therefore listed current-voltage relations resulting from some of the above calculations in Table 14.1, adapted to the limiting cases of low bias voltage ("tunneling") and high bias voltage ("field emission"). Obviously, the different models do not cause a difference in the exponential part of this relation for the respective limits.

Table 14.1. Calculated current-voltage relations adapted to the limiting cases of low and high bias voltages

Model	Ref.	Current-voltage relation Low bias (Tunneling)	High bias (Field emission)
Fowler-Nordheim equation	[14.14]	-	$I \propto \exp\left(-0.67\phi^{3/2}\,\frac{s}{V}\right)$
WKB model	[14.22]	$I \propto V \exp(-A\phi^{1/2}s)$	$I \propto \exp\left(-A\phi^{3/2}\,\frac{s}{V}\right)$
"Average barrier"	[14.55]	$I \propto V \exp(-A\phi^{1/2}s)$	$I \propto \exp\left(-A\phi^{3/2}\,\frac{s}{V}\right)$

$$A = \frac{2\sqrt{2m}}{\hbar}$$

14.3.2 Calculations for Nonplanar Tip-Surface Geometries

With one exception [14.56], the earlier theoretical work had been restricted to planar electrodes. The recent success of the STM, however, has stimulated calculations for other geometries, specifically, for other tip-sample surface arrangements. Basically, two completely different approaches have been used to investigate the physical background of STM measurements, i.e., to clarify which properties of a surface are actually measured in an STM scan and to answer questions concerning the resolution and sensitivity of the STM and the shape and size of the tunnel barrier.

Using the concept of the transfer Hamiltonian described above, *Tersoff* and *Hamann* calculated STM traces obtained from scanning a Au{110} surface [14.57,58]. *Feuchtwang* et al. also used this method for a general consider-

ation of tunneling in the STM [14.59]. A second approach was to determine the tunneling conductance by calculating the transmission of incident electrons across the tunnel gap using a coupled channels method with periodic boundary conditions ("transmission model") [14.60]. We will concentrate here on some main aspects of these calculations and give a brief evaluation of their characteristics. More details are presented in the original literature [14.57-62] and in brief reviews of the theory [14.9,10,59,63,64]. Theoretical aspects related to the resolution of the STM are dealt with in Sect.14.3.4.

Tersoff and *Hamann* modeled the tip-sample surface system with a thin slab and a hemispherical tip [14.57,58]. The surface wave functions were calculated using a local density potential, and an s-wave function ($l = 0$) was used for the tip. In these limits, they obtained for the tunneling conductance σ,

$$\sigma \approx 0.1\ R^2\ e^{2kR}\ \rho(r_0,E_F) \quad , \tag{14.1}$$

where r_0 defines the position of the center of the tip and R is its radius (Fig.14.3a), $k = \hbar^{-1}(2m\phi_0)^{\frac{1}{2}}$ is the inverse decay length of the wave functions in vacuum, ϕ_0 is the work function and $\rho(r_0,E_F)$ determines the charge density in states at the Fermi energy E_F and at the position r_0. The charge density is determined by the wave functions of the surface via

$$\rho(r_0,E_F) = \sum_{\nu} |\psi_\nu(r_0)|^2 \delta(E_\nu - E_F) \quad ; \tag{14.2}$$

their decay into vacuum is assumed to follow

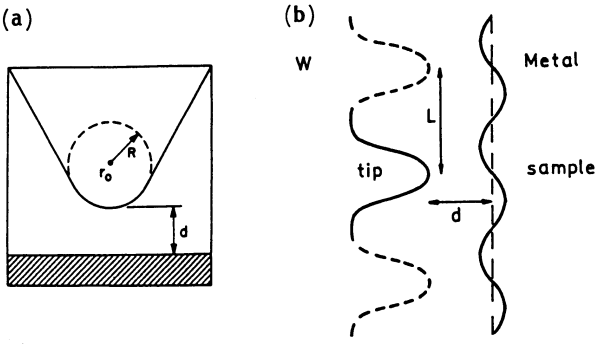

Fig.14.3a,b. Tunneling geometry. (a) Calculation by Tershoff and Hamann: probe tip is assumed locally spherical where it is closest to the surface (*shaded*). R: radius of tip curvature, d: distance of closest approach, r_0: center of curvature of tip (After [14.57]). (b) Transmission calculations: Lateral profile of the tip sample system. The tip is repeated with period L large enough to decouple the tips. r_t: Radius of tip curvature, r_s: radius of surface curvature, d: distance tip-surface plane) (After [14.60])

$$|\psi(r_0)|^2 \propto e^{-2k(R+d)} \quad . \tag{14.3}$$

Therefore (14.1) also predicts

$$\sigma \propto \exp(-A\phi_0^{\frac{1}{2}}d) \quad , \tag{14.4}$$

where d is defined in Fig.14.3a and $A = 2\sqrt{2m}/\hbar \approx 1.028\ \text{Å}^{-1}\text{eV}^{-\frac{1}{2}}$, which is identical to the results presented in Table 14.1. In this model, the tip thus scans the surface following a line of constant density of states at E_F at the center r_0 of the tip sphere[1].

In the transmission calculations introduced by *Garcia* et al. [14.60] and also used by *Stoll* et al. [14.61,62], the sample surface is represented by a corrugated potential with an amplitude h_s; the tip is replaced by an artificial array of tips to achieve periodic boundary conditions (Fig.14.3b). The tips are, however, sufficiently distant from each other to be decoupled. The interface potential is approximated by an abrupt potential step at the jellium edges of the tip and sample surface as shown in Fig.14.4. The transmission and reflection of single electrons approaching the tip surface and

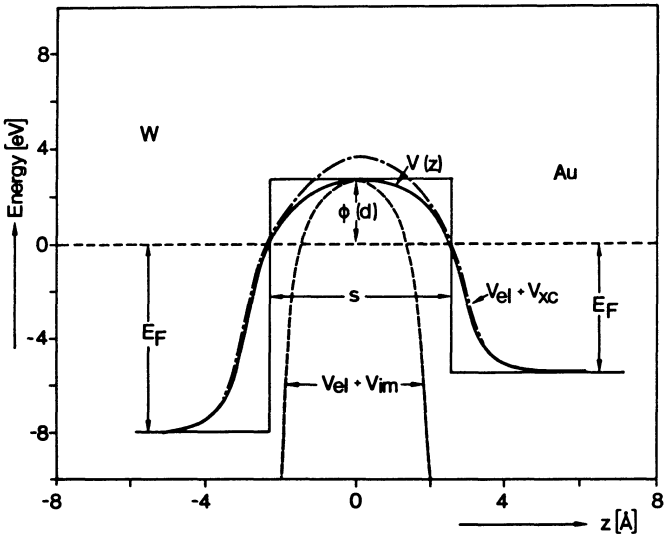

Fig.14.4. Potentials for a W-Au vacuum tunnel junction with s = 6 Å. $V_{el}(z)$: electrostatic potential, $V_{im}(z)$: image potential, $V_{xc}(z)$: local exchange and correlation potential, $V(z)$: tunnel barrier, ϕ_d and s: height and width, respectively, of approximate square tunnel barrier (After [14.55])

1 This does not mean that the charge density at the center of the tip is of any physical relevance, it is merely a result from the integration over the entire tip surface area.

tunneling to the sample were calculated by numerical techniques developed for atom scattering on surfaces, such as the so-called GG and GR methods [14.65,66]. The total intensity and the current density are obtained by integrating over all electrons in a spherical shell representing the Fermi surface of the tip with an energy window of 0.01 eV. The energetic parameters are chosen to simulate tunneling associated with the s-wave functions of both metals, which is assumed to be the dominant contribution [14.67]. Analyzing different types of corrugation, tunnel distance, etc., they found a rather similar expression for the tunnel conductance [14.60]

$$\sigma = \frac{eh}{2m} \cdot N(E_F)G(R_{eff})\exp\{-A[(1+\beta)\phi_0]^{\frac{1}{2}}d\} \quad , \tag{14.5}$$

where G is a function of the effective radius R_{eff},

$$R_{eff}^{-1} = r_t^{-1} + r_s^{-1} \quad , \tag{14.6}$$

with r_t the tip radius and r_s the radius of the surface corrugation (Fig. 14.3b). Over a wide range of different values of R_{eff}, G is proportional to R_{eff}, in which case the tunnel conductivity σ is also proportional to R_{eff}. This differs from the results of Tersoff and Hamann, who found $\sigma \times R^2$. The introduction of β accounts for the fact that the average barrier height is virtually increased because the dominant contribution to the tunnel current comes from electrons tunneling at an angle of 20°-30° from the surface normal, for which $E_{kin,z} < E_F$ [14.60]. In earlier work, the factor $A(1+\beta)$ was replaced by its numerical analogue of $2.14\sqrt{2m}/\hbar$.

In conclusion, both methods yield similar σ-d dependences and roughly identical estimates of the resolution (Sect.14.3.4). The principal difference between the two approaches is that in the first method (using the transfer Hamiltonian) the electronic corrugation of the sample surface as seen by the STM is calculated self-consistently, while in the transmission calculations the surface corrugation (for the states at E_F) and its amplitude h_s represent an *assumed* parameter and the tunnel current is calculated subsequently. For smoothly corrugated metal surfaces, the amplitude can be estimated from results of other techniques (e.g., atom scattering), but for surfaces exhibiting more abrupt changes or local electronic states this is not possible. In these cases, the scattering calculations lose the advantage of fast computation since the surface corrugation at E_F has to be calculated as well. The scattering calculations themselves have the advantage of being rather fast and transparent. They are well suited to gaining information about current densities and their spatial distribution, the resolution of the STM, etc. Some apparently open questions are the effect of the $l = 0$

limitation on the tip wave function and the quality of the calculated surface wave functions at rather large distances from the surface (10-15 Å) in the first scheme, the effects of the potential step approximation and of coupling between the tips and the correct choice of the surface corrugation in the second method. As a consequence of treating tunneling as a perturbation, the transfer Hamiltonian method is limited to low transmissivities, which, however, is no serious restriction.

To reduce the computational efforts and to expand the application to larger unit cells, Tersoff and Hamann proposed to (a) use the contour lines of the total charge density rather than of that at E_F and (b) construct these from a superposition of atomic charge densities [14.57,58]. The latter method of constructing charge density contours has already been used to describe atom scattering, since the repulsive scattering potential for the neutral atoms could be directly related to the local charge density [14.68]. Despite rather reasonable results for Au{110} (Sect.14.3.4), the method proposed by Tersoff and Hamann cannot be expected to be generally valid. The states at E_F can exhibit a spatial distribution quite different from that of the total charge. This method also ignores all electronic effects such as localized states, etc. [14.64]. The interpretation of atom scattering data based on this approximation for the local charge density, which was quite successful, is less affected, since differences between actual local charge densities and those computed from superposition of atomic charge densities become more important at larger distances from the surface. The turnaround point for He scattering, however, is mostly closer to the surface than the center of the tunneling tip. It typically follows charge density contours of $\sim 10^{-5}$ $au^{-3}eV^{-1}$ at ~5 Å from the atomic cores of the surface as compared to 10^{-13}-10^{-17} $au^{-3}eV^{-1}$ and 10-15 Å for the tip center. As a consequence, the corrugation evaluated from the scattering experiments should be larger than that observed with the STM.

14.3.3 The Effect of the Image Potential

A charged particle in front of a metal surface creates an image charge within the metal which produces an attractive image potential $V_{im} = -e^2/4r$ seen by the particle at a distance r from the image plane [14.55]. In the case of tunneling through a narrow vacuum gap, the potential contains contributions from the image charges in both electrodes, which cause considerable deviaitions from a square or trapezoidal barrier shape.

Using an "average" square barrier as an approximation, the effect of the image potential was treated within the quasi-classical WKB theory for tun-

neling between two planar "free electron metal" electrodes [14.23,53,69]. *Feuchtwang* et al. [14.59,70,71] and *Bono* and *Good* [14.72] performed WKB calculations and estimates of the electric fields for tunneling between a planar electrode and a planar electrode plus a spherical protrusion; they emphasized the contributions of multiple images in the two planes.

These examples and also the following one are based on the assumption of a "static" image potential, i.e., that at all times the tunneling electron sees the image charge corresponding to its instantaneous position. This assumption was justified recently by *Büttiker* and *Landauer*, who calculated that the rearrangement of the (image) charge within the metal is much faster than the tunneling process itself [14.73,74]. *Weinberg* and *Hartstein* in contrast claimed the image force to be absent for electron tunneling [14.75].

Binnig et al. investigated the influence of the image potential on STM measurements, applying the transmission method outlined above [14.55]. They described the potential contribution from the image and contour image in the two (jellium) electrodes by

$$V_{im} \approx -\frac{e^2}{d}\left[\ln 2 - 1 + \left(\frac{z}{d}\right)^2 + \frac{1}{1 - 4(z/d)^2}\right] \quad , \tag{14.7}$$

where $d = s - 1.5$ Å is the distance between the image planes, s the distance between the jellium edges as indicated by *Lang* and *Kohn* [14.76] and z is measured from the middle point of the two surfaces. The actual potential V(z) suggested by these authors merges into the exchange-correlation potential V_{xc} plus the electrostatic potential V_{el} inside and very close to the surface (matching point at E_F), while at larger distances it approaches the sum of the image potential V_{im} plus V_{el} (Fig.14.4). The image potential thus rounds off the potential edges and reduces the central height of the barrier for $d < 15$ Å, which represents typical tunneling distances in the STM. At larger distances, the barrier height saturates into the macroscopic work function ϕ_0. The reduction in barrier height by the image potential was suspected to be responsible for anomalously low values of the barrier height ϕ_{exp} found in STM measurements (Sect.14.5.4). Also, it was not clear whether the distance dependence in the barrier height still permits a linear relationship between $\ln(I_t)$ and d. The study of *Binnig* et al. aimed to evaluate the contribution of the image potential and tip-sample surface geometry to the observed correlation of tunnel current with distance [14.55].

In that study, the actual barrier was replaced by a square barrier together with a distance-dependent barrier $\phi_d = \phi_0 - \alpha/d$. In order to account for the tip geometry effects as described in (14.5), an effective barrier

height ϕ_{eff} is used

$$\phi_{eff} = (1 + \beta)\left(\phi_0 - \frac{\alpha}{d}\right) . \tag{14.8}$$

The term α/d, with $\alpha \approx 9.97$ eV Å, describes the barrier lowering due to the image force [14.55]. Using this approximation, the authors computed straight lines for plots of $\ln(I_t)$ versus d over wide ranges of d that closely resemble the experimental findings (dashed lines in Fig.14.5). This result can also be rationalized by forming the logarithmic derivative of $I_t(d)$ from (14.5). One finds[2]

$$\frac{d(\ln I_t)}{d(d)} \approx -A(1 + \beta)^{\frac{1}{2}}\phi^{\frac{1}{2}}\left(1 + \frac{\alpha}{8\phi^2 d^2} + 0\,\frac{1}{d^3}\right) , \tag{14.9}$$

i.e., the first-order term in 1/d, although present in ϕ_d, cancels for the slope of $\ln(I_t)$ versus d. Only at higher conductances do the dashed lines in Fig.14.5 bend upward. Since $dI_t/d(d) = dI/ds$ we will for simplicity use the latter term henceforth.

To demonstrate the effects of (a) the image potential and (b) the square barrier approximation, Fig.14.5 also contains the calculated conductance for a tip-sample surface geometry using a constant square barrier with $\phi_{eff} = \phi_0$ (dash-dotted lines). Finally, in order to distinguish between (a)

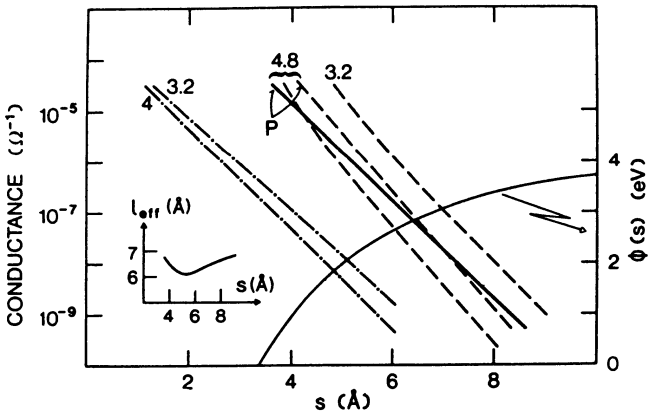

Fig.14.5. Calculated conductances as functions of electrode separation for a barrier height ϕ_d (*solid curve at right*) and a spherical tip of radius R = 5 Å (the two curves denoted by P are for planar junctions of area πR^2). The numbers with the curves give the values of ϕ_0 used. *Dashed curves* are for ϕ_{eff} according to (14.8), *dash-dotted ones* for $\phi_{eff} = \text{const} = \phi_0$, and for the *solid line* the "real" barrier V(z) was used. The inset shows the lateral resolution L_{eff} of the STM for a tip radius of 5 Å (After [14.55])

2 There is an algebraic error in [Ref.14.49, Eq. (8)].

and (b), the conductance of a planar junction was also calculated, once using the square barrier approximation and once a numerical integration of the potential V(z) (indicated by P in Fig.14.5). The distance dependence of the effective tunnel barrier is also displayed in this figure. The most obvious effect resulting from considering the image potential is the overall increase in conductance or the shift of the $\ln(I_t)/d$ curves to larger distances by 2-3 Å. In all cases, these curves are linear over very wide ranges of I_t, thus confirming that the consideration of the image potential in the tunneling process is compatible with the experimental observation of linear $\ln(I_t)/d$ curves [14.55].

Inspection of the slopes of the calculated $\ln(I_t)/d$ curves reveals that the square barrier approximation leads to a considerable increase in the slope, as is evident from the comparison of the two lines labeled P: the dashed line (square barrier approximation) and the solid line [numerical integration of V(z)]. If we evaluate the curves in Fig.14.5 in the same way as experimental data to obtain the experimental barrier height ϕ_{exp} from $d(\ln I_t)/ds \approx -A\phi_{exp}^{\frac{1}{2}}$ - see Table 14.1 - we notice that for curve P the size of ϕ_{exp} is comparable to the macroscopic work function ϕ_0 used for the computation, while the square barrier approximation gives even higher values for ϕ_{exp} as compared to ϕ_0. These results suggest that the image force only slightly lowers the slope of the $\ln(I_t)/d$ curves, although it reduces the barrier height drastically. Therefore, reasonable values for ϕ_{exp} on flat metal surfaces, as determined by this method, are expected to be of the order of 3-5 eV [14.9], see Sect.14.5.4.

In this model, the influence of surface and tip roughness on the image potential was neglected, but it is not expected to contribute substantially [14.55]. Also, this calculation was performed for a constant, low bias potential. Using the WKB approximation for planar electrodes [14.53], Paynes and Inkson computed recently that different effective barrier heights are obtained if the distance-dependent tunnel conductance is determined via current or bias variation [14.9,69]. For standard current densities of $\sim 10^6$ $A \cdot cm^{-2}$, they saw an appreciable reduction of the observed barrier height ϕ_{exp} from 4.5 to 3.2 eV by going from the first to the second mode ($\phi_0 = 4.5$ eV) [14.69].

14.3.4 Resolution of the STM

a) Lateral Resolution. On rather flat surfaces, the tunnel current can be modeled to flow between the (spherical) front region of the tip and the sample surface. In these limits, the resolution of the STM can be described

by the diameter of the area over which tunneling occurs, in accord with the standard definition of the resolution L of scanning electron microscopes ($L = 2\sqrt{d}$, where d is the diameter of the electron beam) [14.70,77].

Garcia et al. defined the area covered by the tunnel beam and its diameter, the effective beam diameter L_{eff}, in terms of the ratio of total tunnel current I_t to the maximum component of the current density in the tunnel current distribution around the tip j_{max}: $\pi(L_{eff}/2)^2 = I_t/j_{max}$ [14.60]. The ratio I_t/j_{max} depends on the tip shape and surface corrugation. It turned out, however, that in the limits of $r_t, r_s > \max(d, k^{-1})$, the resolution can also be described by [14.9,60,63]

$$L_{eff} \approx \sqrt{R_{eff}} \quad . \tag{14.10}$$

Tersoff and *Hamann* gave $[2(r_t + d)]^{\frac{1}{2}}$ as a rough estimate of the resolution [14.57,58]. Applying formulas for tunnel currents between two planar electrodes, *Willis* et al. obtained a comparable relation for the current spread between a hemispherical tip and a planar electrode [14.9].

More physical insight is provided by the calculations of Tersoff and Hamann. In their model, the tip follows the line of constant charge density at E_F at the center of the (spherical) tip [14.57,58]. The sharpest tip possible would consist of a single localized orbital. In this case the tip would basically follow the contour line at the front end of the tip, which can be defined as the highest attainable or intrinsic resolution of the STM [14.57, 58,64]. It is worthwhile noting that even at closer distances this line does not completely reflect the corrugation of the centers of the atomic ion cores. This is documented in Fig.14.6, which gives the charge density at E_F for the (1×2) and the (1×3) reconstructed Au{110} surface (from [14.57,58]). The corrugation in these contour lines, and thus also the observed corrugation, decays exponentially with the distance of the contour line (i.e., tip center) from the surface.

Stoll et al. quantitatively investigated the influence of tip radius and sample-tip separation on the observed corrugation of the same surface using the GR method [14.61,62]. In the limit of very weakly corrugated surfaces (jellium corrugation amplitude $h_s \leq 0.1$ Å due to restrictions in the GR method) the observed normalized corrugation was found to decay exponentially with increasing tip radius or tunneling distance (Fig.14.7) [14.61,62].

The two theoretical treatments described in Sect.14.3.2 thus predict similar trends and differ only with respect to the absolute numbers for the resolution of the STM. For the same experimental result, the corrugation of the (1×2) and the (1×3) reconstructed Au{110} surface, *Garcia* et al. and

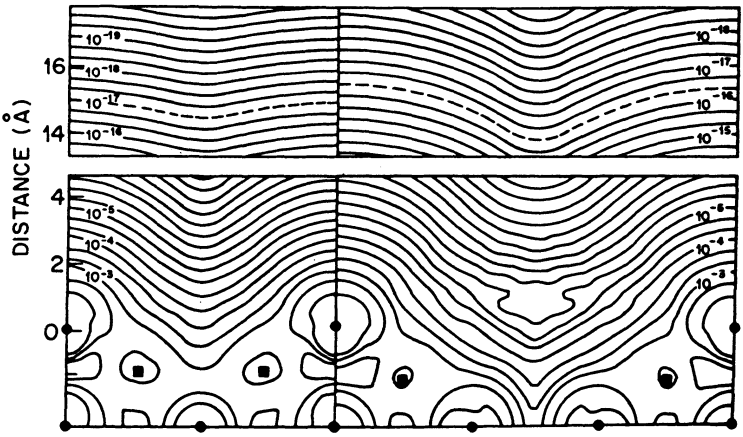

Fig.14.6. Calculated $\rho(r,E_F)$ for Au{110} (2×1) (*left*) and (3×1) (*right*) surfaces. The (1$\bar{1}$0) plane through the outermost atoms is shown. Positions of nuclei are indicated by solid circles (in plane) and squares (out of plane). Contours of constant $\rho(r,E_F)$ are labeled in units of $au^{-3}eV^{-1}$ (note break in distance scale). Peculiar structure around the 10^{-5} contour of (3×1) is due to limitations of the plane-wave part of the basis in describing the exponential decay inside the deep troughs. Center of curvature of probe tip follows dashed line (After [14.57])

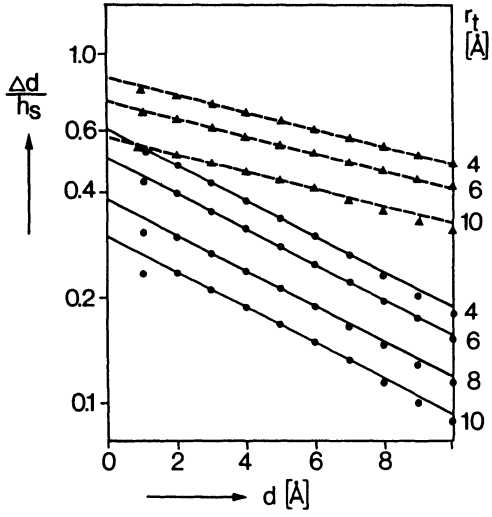

Fig.14.7. Ratio of observed to real corrugation for different tip radii r_t versus minimum tip-sample separation d. The tip consists of a spherical cap of height $h_t = 3$ Å protruding from a plane base. The sample profile has a sinusoidal corrugation with amplitude $h_s = 0.1$ Å and period a = 8.15 Å (*solid lines*) and a = 12.23 Å (*dashed lines*) corresponding to the (2×1) and (3×1) reconstructions on Au{110}, respectively. The Fermi energy, 5.53 eV, and the work function, 5.22 eV, are also representative of Au. The results shown are based on computations with L = 5a and N = 30 (After [14.62])

Stoll et al. calculated a tip radius of $r_t = 3.5$ Å and a surface-tip distance of 4 Å[14.55,60-62]. *Tersoff* and *Hamann*, in contrast, get values of 9 Å and 6 Å, respectively [14.57,58]. This means that the center of the tip moves along the 7.5 Å contour line in the first case and along the 15 Å line in the latter case. Based on these numbers the STM is seemingly ascribed a higher resolving power by *Tersoff* and *Hamann* than by *Garcia* et al., since identical corrugation is seen for (slightly) larger distances and (signifi-

cantly) larger tip radii. Considering the approximations used in both calculations (e.g., the assumption of the actual surface corrugation h_s in the latter model), this is still fairly good agreement. (In the transmission calculations [14.60], the tip-surface distances are quoted with respect to their jellium edges, which are 1/2 lattice spacing outside the position of the ion cores. The above values for the tunnel distance should strictly speaking be corrected by that amount for comparison with data from *Tersoff* and *Hamann* [14.57] who refer to ion core positions). A more detailed account of these differences of resolution in both models is given in [14.64,70].

In the atom superposition approximation, Tersoff and Hamann calculated about 30% less corrugation for either of the two reconstructed Au{110} surfaces than they obtained in their slab calculations for similar distances. Correspondingly, the corrugation of both reconstructions could be fitted with a tip radius of $r_t = 4$ Å at a fixed surface distance of $d = 6$ Å as compared with $r_t = 9$ Å in the slab calculations.

All of these calculations, however, do not include effects of the image potential. As pointed out by *Binnig* et al., the latter tends to additionally smooth the observed corrugation [14.55], such that for metals no measurable degradation of the resolution is expected in a range of 5-10 Å (see the shallow minimum of L_{eff} in Fig.14.5). [14.55]. Significant effects of localized states leading to enhancement of the spatial resolution have not been reported yet for metals, but were found for semiconductor surfaces like Si{111} [14.38,78,79] (see also Sect.5).

b) Vertical Resolution. The vertical resolution of the STM describes its ability to detect a vertical modulation within the first layer. For relatively open surfaces, where deeper lattice planes are also "visible" to the tip, structural information concerning these planes as well might be expected.

For demonstration, two different geometries of the (1×3) Au{110} surface will be used. In one of them, Au atoms only in the first layer are missing, in the other one, second-layer atoms are also removed, which leads to the formation of {111} microfacets [14.80]. The charge density contour lines from atom superposition [14.58] show markedly different profiles close to the surface (He scattering), however, at a distance of 10 Å (STM) the corrugation amplitudes differ by only 15% at a total value of 1.4 Å (Fig.14.8). Thus, STM measurements will effectively not distinguish whether or not the second layer is changed in such a case. The larger corrugation observed experimentally for the (1×3) structure (1.4 Å), as compared to the (1×2) phase (0.45 Å), is entirely due to the greater surface lattice constant which permits clearer resolution of the peaks and troughs [14.58].

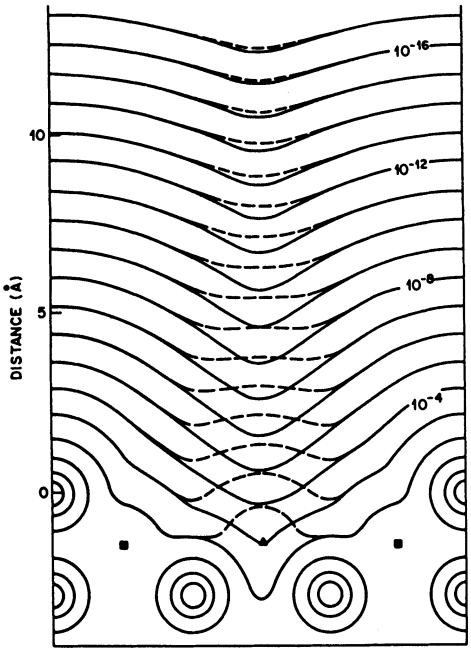

Fig.14.8. Atom superposition charge density (au^{-3}) for two possible geometries of Au{110} (3×1). *Solid lines* are for the same geometry as in Fig.14.6. *Dashed lines* are for the geometry with no atom missing in the second layer. The *triangle* shows the site of an atom (out of plane of figure) present only in the latter case; squares show positions of other out-of-plane atoms (After [14.58])

c) Rough Surfaces. When considering large scale roughnesses, one can no longer use the concept of the spherical tip end anymore. The entire tip surface can potentially serve as a probe for tunneling. For deep trenches or steep protrusions one effectively measures a convolution of the tip shape and the sample surface. Such effects were reported by *Gimzewski* et al. for the topography of silver films deposited at low temperature [14.81,82]. The exact determination of the topography of rough surfaces thus requires an detailed knowledge of the overall tip shape.

14.3.5 Sample Conductivity

The preceding discussion of the tunnel current was based on the assumption that it is limited by the tunnel resistance. In the case of metallic samples and tips this is certainly correct. But semiconductors also exhibit sufficient conductivity to enable STM measurements. Recently, *Miranda* et al. even reported STM patterns on insulators like TiO_2 films (3000 Å thickness) [14.83]. Evidently, the conductivity due to lattice defects in these insulators is sufficiently large to make the tunnel resistance, rather than the substrate conductivity, the current-limiting process.

Although tunneling is possible on semiconductor surfaces as well, the voltages required are often much higher than for metals. Depending on the dopant concentration, threshold potentials of up to a few electron volts are

necessary, compared to milli-electronvolts for metals. This potential drops, however, almost entirely in a space-charge region within the sample and not at the tunnel junction as described recently by *Flores* and *Garcia* [14.84]. The electric field applied by the tip spreads into the semiconductor and leads to band bending and also to an accumulation of charge carriers in a region near the contact. The size of this region ("spreading resistance region") is given by the mean free path of the carriers in the sample.

The charge density at the surface, and therefore also the tunneling current, is strongly affected by the electric field. The loss of surface charge due to tunneling is compensated by diffusion of charge carriers (electrons or holes) from a "diffusion region" into the spreading resistance region. A more quantitative description, which also treats the effect of dopants, is given in [14.84].

A second point concerns the question of energy dissipation in the tunneling area. Tunnel currents of the order of nanoamperes result in rather high current densities ($\sim 10^6$ A/cm^2) in this region. Nevertheless, this converts to a total number of only $\sim 10^{11}$ electrons/s. The intermediate times are long compared to relevant transit times [14.73,85] and to phonon vibration and relaxation times. The electrons may therefore be viewed as tunneling one at a time and effects such as space charge (on metals) and sample heating should be negligible.

14.3.6 Effect of Adsorbates

From geometric arguments, one would expect protrusions in the STM graphs corresponding to the size of the adsorbate, whenever the tip is moved over an adsorbed particle. From the preceding discussion, however, this picture is clearly incorrect. Rather than sensing the topography, the STM will reflect the local variation in the tunnel current induced by the adsorbate. According to the Bardeen approximation, it will show how the adsorbate affects the density of states and the shape of the wave functions at E_F, for tunneling from the sample, or the respective empty states, for tunneling into it.

In the case of tunneling from the sample into the tip, the two extremes are represented by (a) an adsorbate that leads to an effective reduction in the density of states N(E) at E_F and also does not provide orbitals close to E_F and by (b) an adsorbate that increases N(E) at E_F or that has orbitals close to E_F which extend into the vacuum. In the first case, the local tunnel current is reduced, in the second one, it is increased. In the topographic mode, the STM will respond to the adsorbate by an indentation or a pro-

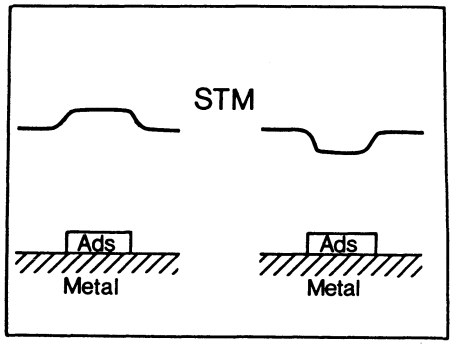

Fig.14.9. Response of STM scans (*upper lines*) to adsorbates leading to an increase (*left*) and to a decrease (*right*) in the local tunnel current

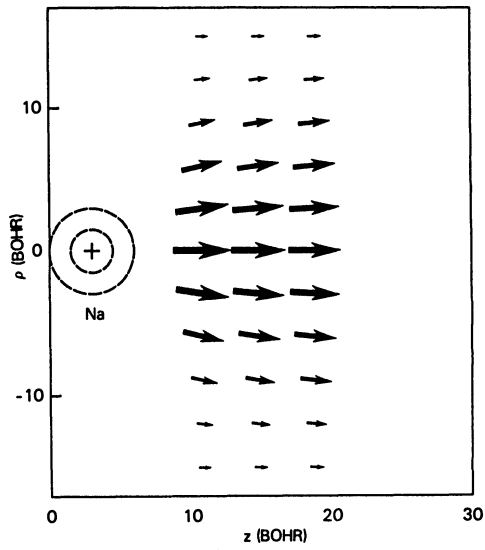

Fig.14.10. Current density for the case in which a Na atom is adsorbed on the left electrode. Length (and thickness) of arrow is proportional to $\ln(e \cdot j/j_0)$ evaluated at the spatial position corresponding to the center of the arrow. x: direction along electrode surface, z: distance normal to the electrode surface (After [14.87])

trusion, respectively (Fig.14.9). Comparable arguments can be made for tunneling into the sample, in which case the variation in the empty states/orbitals above E_F is tested. Consequently, we expect little correlation between the geometric size of an adsorbate and the form of the local STM pattern.

These qualitative arguments are supported by recent calculations by *Lang* [14.86,87]. Using the transfer Hamiltonian formalism, he calculated the tunnel current density between two planar jellium electrodes, one of them carrying an adsorbate atom. For an adsorbed Na atom, this in fact leads to an enhancement of the current density in the vicinity of this atom by up to a factor of 20 (Fig.14.10). An adsorbed S atom, in contrast, results in almost no increase of the local tunnel current, leading to an almost flat STM response [14.87].

First experimental evidence for these effects was seen for CO adsorbed on Pt{100}. The presence of CO_{ad}, which was proven indirectly from the adsorbate-induced phase transformation, did not cause a significant change in the STM traces at a variety of different tunneling voltages [14.88]. This would indicate that the CO_{ad} is essentially invisible to the STM, comparable to the calculated behavior of S_{ad} [14.87].

14.4 Surface Microscopy

The information about the microscopic topography that is extractable from STM measurements depends strongly on the respective roughness of the surface. This can vary on a wide scale between atomically flat, single-crystalline surfaces and macroscopically rough surfaces. Therefore, such surfaces are dealt with separately in this section.

14.4.1 Topography of Flat Surfaces

In the standard picture, which is based on the results of many techniques, single-crystalline, flat surfaces consist of large terraces separated by well-defined steps. In addition, periodic structures can, in some cases, be resolved. Early STM images of such surfaces did not at all resemble this picture but displayed rather round and hilly structures for various metal surfaces (Pd [14.35-37,89], Pt [14.8,32], Au [14.3], Ag [14.46,90]), in strict contradiction to the description given before. However, later STM results were in better agreement, as is evident from an image of the Au{100} surface taken by *Binnig* et al. which displays exactly such flat terraces separated by distinct steps (Fig.14.11) [14.91]. On other areas of the same sample, small flat areas (clean as concluded from the presence of the reconstruction) coexisted with little hills which the authors assigned to

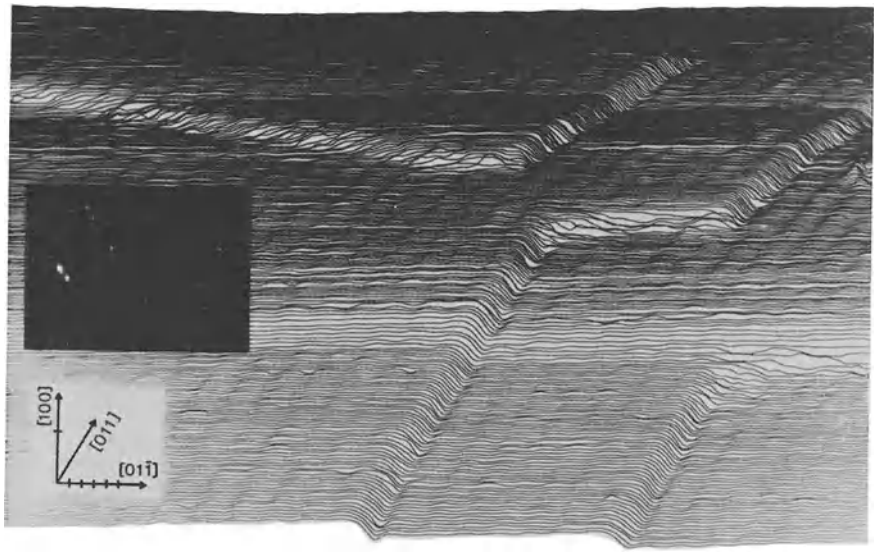

Fig.14.11. STM picture of a clean (1 × 5) reconstructed Au{100} surface. Divisions on the crystal axes are 5 Å with approximately 1.5 Å from scan to scan. The second inset shows the LEED pattern of the predominant (1 × 5) reconstruction taken in situ. (After [14.91])

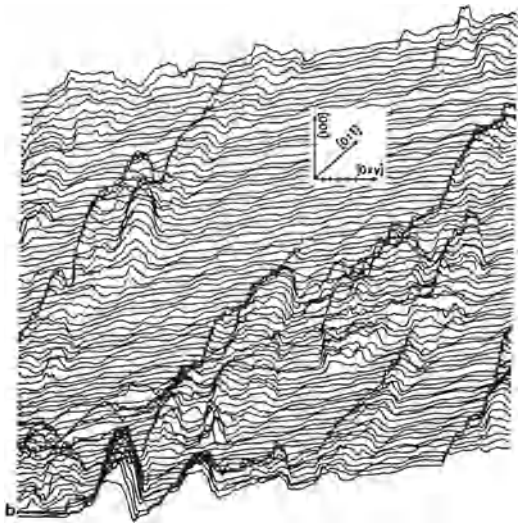

Fig.14.12. Sharply structured carbon islands on the reconstructed Au(100) surface (smooth parts). Division on the crystal axes are 5 Å apart. Owing to strong thermal drifts, the scale along the [011] axis and the direction of the [Oxy] axis (in the picture roughly 60° from the [011] axis) are not well determined. (After [14.91])

carbon (Fig.14.12) [14.91]. For Pt{100} it was found that following extensive cleaning and annealing cycles, the surface forms large flat terraces which extend over several hundred to thousand angstroms, and are separated by mostly mono- and biatomic steps (Fig.14.13) [14.92,93].

These data provide good evidence that well-cleaned and annealed single-crystal close-packed metal surfaces will form flat terraces of at least several hundred angstroms width, in good agreement with common models. For more open metal surfaces (e.g., Au{110} [14.80]) and for semiconductor surfaces, extensive scans exhibiting an equally flat surface area have not been published yet. The correlation between chemical cleanliness and topographical regularity observed on Pt{100} in turn also indicates that metal surfaces that are not free of contamination in the near-surface region will also exhibit round and crested rather than flat surface structures [14.88,92,93].

14.4.2 Periodic Structures of Single-Crystalline Surfaces

The exact determination of atomic positions in periodic structures is a measurement domain of various scattering and diffraction techniques, which, however, yield only indirect information on the large-area averaged structure. In addition to the fascination of a direct view of a surface on an atomic scale, the STM can provide very valuable contributions in the case of structures that, for various reasons, are still too complex to be resolved by the other methods. This includes surface structures that contain either a large number of structural parameters and/or large unit cells or surface

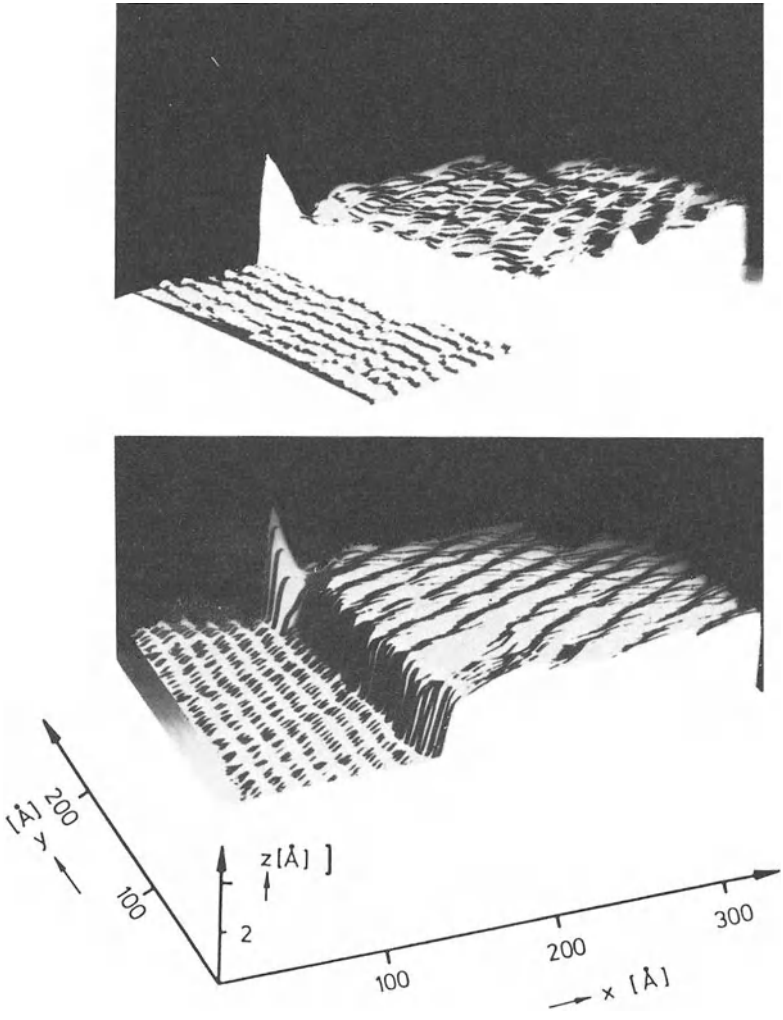

Fig.14.13. Relief of the rotated hexagonal reconstructed Pt{100}surface obtained from a two-dimensional STM scan, which displays two domains with different rotational orientation separated by a monatomic step (scales as indicated). (After [14.93])

structures which exhibit a significant degree of disorder. In all of these cases, the corrugation pattern determined from STM scans can serve to either confirm or rule out existing models, or at least to narrow down the number of possible structures. The other techniques can then concentrate on these possible structures.

The periodic structures investigated by STM so far are listed in Table 14.2. They all involve a reconstruction of the respective metal or semicon-

Table 14.2. Periodic structures investigated by STM so far

Surface	Structure	References
Au{110}	(1×2),(1×3)	[14.80]
Au{100}	(5×1)	[14.91]
Pt{100}	rot. hexagonal	[14.88,92]
O/Ni{110}	(2×1)	[14.94]
Si{111}	(7×7)	[14.38,78,79]
Si{111}	(2×1)	[14.48,95]
Si{100}	(2×1)	[14.96]
GaAs{110}	(1×1)	[14.95,97]
Ge/Si{111}	(7×7), (2×2) c(4×2),c(2×8)	[14.98]
graphite	basal plane	[14.12]

ductor surface, and most of them also form rather large unit cells. How structure information may be gained from STM measurements is briefly discussed below by examining three characteristic examples.

An STM study of the Pt{100} surface, which in its most stable state is known to be reconstructed, gave a clear impression of the reconstruction-induced surface modification, regardless of the large unit cell [14.99]. A model composed of a two-dimensional scan of the surface exhibits a surface corrugation formed by parallel furrows (Fig.14.13). The furrows are rotated by $\sim 5^{\circ}$ with respect to the substrate lattice. The amplitude and wavelength (corrugation length) of this corrugation amounts to 0.4 Å and ~14 Å, respectively. The corrugation length is identical to five lattice constants, which also represents the characteristic periodicity in LEED patterns of this surface. In addition, Fig.14.13 also reveals the existence of a second, much weaker corrugation (amplitude ~0.1 Å, length ~35 Å) normal to the first one. These observations could easily be rationalized [14.88]: For the thermodynamically stable, rotated hexagonal structure, the formation of a hexagonal topmost layer of Pt atoms was predicted [14.100], leading to $\begin{bmatrix} 12 & 1 \\ -1 & 5 \end{bmatrix}$ units which are rotated by 4.8° with respect to the substrate lattice [14.101]. The corrugation results from the mismatch between the hexagonal dense topmost layer and the second layer of Pt atoms with square symmetry. Similar arguments are also possible for the other surfaces exhibiting close-packed topmost layers, for example, Au{100}. In STM scans of Au{100}, additional structure within the corrugation could be resolved, implying a very large unit cell which is approximately $\begin{bmatrix} 26 & 0 \\ -5 & 48 \end{bmatrix}$ [14.91].

The Au{110}-(1×2) reconstruction represents an example of a periodic structure exhibiting much local disorder, which is indicated by streaked extra beams in the diffraction pattern [14.102]. The STM scans of this sur-

face displayed two distinctly different corrugation features of double and threefold lattice spacing, which were assigned to (1 × 2) and (1 × 3) units coexisting on the surface [14.80]. From the amplitude and shape of the corrugation, a missing row structure, rather than the recently proposed sawtooth model [14.103], was favored. The existence of the missing row structure was confirmed by recent grazing-incidence X-ray [14.104] and LEED [14.102] measurements.

This study also illustrates the limits of STM-based structure determinations. Clearly, the lateral and vertical changes in the atom positions in the second and deeper layers as determined by diffraction methods [14.102, 103], cannot be sensed by the STM. As described in Sect.14.3.4b, it was demonstrated that due to its larger corrugation length, the observed amplitude in the (1 × 3) unit should be considerably larger than that of the (1 × 2) structure. The distinction between {111} faceting with second layer atoms missing as well [14.80] and a order-disorder transition with only the top layer modified [14.9,105]), therefore, is hardly possible on the basis of the STM data.

Using diffraction techniques, the structure determination of reconstructed semiconductor surfaces is generally impeded by their large number of variable structural parameters. The "classic" (7 × 7) reconstructed Si{111} surface was the first semiconductor surface to be investigated by STM with atomic resolution. A very pronounced two-dimensional structure was found [14.78,79]. In the model of this surface in Fig.14.14, which is derived from STM scans, a variety of different features are clearly resolved. The (7 × 7) unit cell exhibits deep holes ("missing atoms") at its respective corners. Along each side of the cell perimeter three local maxima stand out, which —using the nomenclature common to current models of the (7 × 7) structure [14.106] —were assigned to adatoms. In a subsequent investigation of the same surface, but using a heavily p-doped instead of an n-doped sample, the Zürich group essentially confirmed its earlier findings [14.79]. *Demuth* et al. also characterized this surface by STM measurements and found a corrugation pattern exhibiting similar features [14.38], see Fig.14.15. Smaller differences in the absolute elevation of some details are related to the different tunnel voltages applied [14.38,79] (Sect.14.5). The rather high tunnel voltages and the observation of threshold voltages reported in these studies are typical for tunneling on semiconductors surfaces. In many cases, however, only a small fraction of that voltage drop actually occurs over the tunnel gap; the major decay of the potential is in a space-charge region within the sample, as described in Sect.14.3.5.

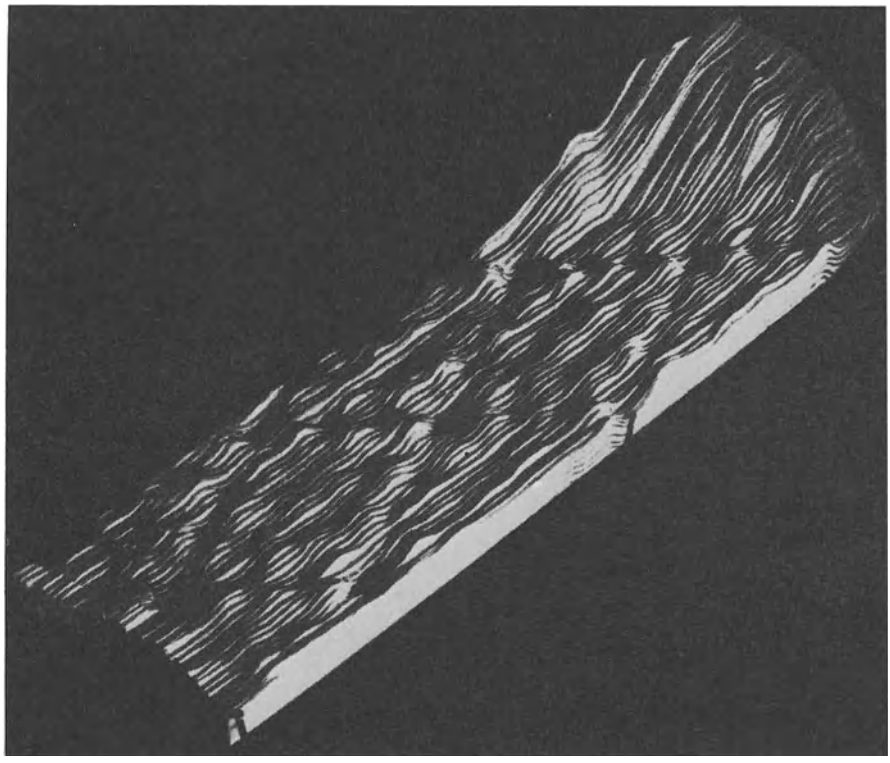

Fig.14.14. Relief of two complete (7 × 7) unit cells, each with nine minima and twelve maxima, taken at 300°C. Heights are enhanced by 55%, the hill at right grows to a maximal height of 15 Å. The [$\bar{2}$11] direction points from right to left, along the long diagonal. (After [14.78])

On the basis of the initial STM results of *Binnig* et al. [14.78], a large number of structure models formerly proposed for the Si{111}-(7 × 7) surface could be ruled out. Subsequent proposals for this structure [14.106-110], based on, for example, TEM results [14.107] or medium energy ion scattering data [14.106], reproduced the essential features of this corrugation pattern.

Especially for the structure determination of periodic surfaces, an instructive (two-dimensional) representation of the one-dimensionally measured data and, if necessary, the removal of characteristic instrumental artifacts is required. The different levels of applicable data processing range from a simple display of the surface in a gray scale or color map (where color corresponds to local height) involving corrections of apparent lattice distortions (e.g., due to thermal drift), up to more complex operations like the removal of specific noise frequencies by Fourier filtering. An overview is given in [14.111]. Examples can also be found in [14.38,79,94]. The dif-

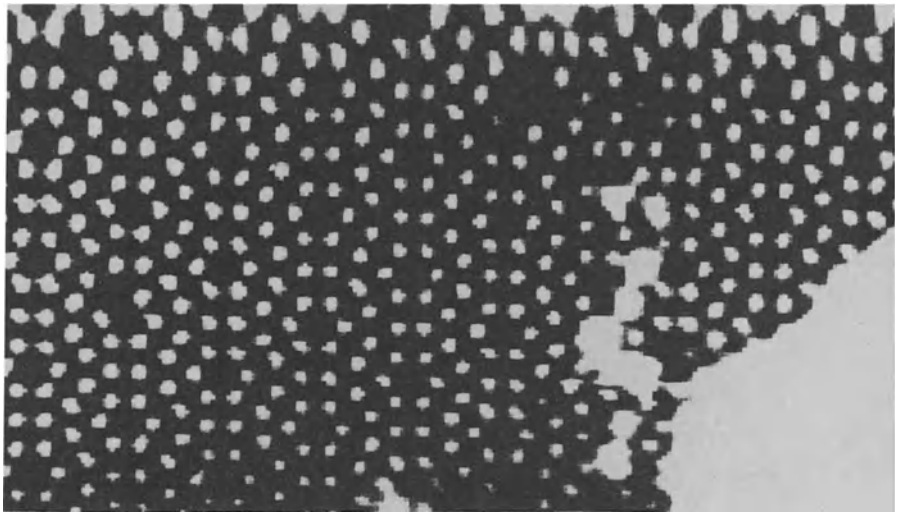

Fig.14.15. Processed tunneling image of the Si{111} - (7 × 7) surface. The full range of the gray scale corresponds to changes in the z distance of 1.5 Å. (After [14.38])

ferent representations of the Si{111}-(7 × 7) surface in Figs.14.14 and 15 illustrate the effect of simple methods of image processing.

14.4.3 Surface Defects

The high local resolving power of the STM is exploited more directly for the observation of local features, especially of nonperiodic features in periodic surroundings. This includes all sorts of lattice defects like steps, domain boundaries, and point defects. While all of these features contribute to the overall intensity distribution in diffraction techniques, it is extremely difficult to extract specific local correlations from diffraction data. In the following, we demonstrate the capability of the STM not only to identify and characterize such surface defects but also to describe their respective correlation.

The hexagonal reconstructed Pt{100} surface is known from LEED studies to form four different rotational domains. These could be identified in the STM images by their different corrugation direction [14.88]. It could be demonstrated directly that on a well-annealed, clean Pt{100} surface, boundaries between rotational domains are confined to step edges between different terraces, i.e., there exists only one rotational domain on a given terrace [14.93]. In the same study and under similar conditions, exceedingly wide terraces with step distances of 500-2000 Å were found. In a thermodynamic picture, such measurements on an equilibrated surface can thus serve

to estimate interaction energies or energy differences between certain structural elements such as, for instance, the potential (free) energy contained in domain boundaries and steps.

On semiconductor surfaces, Demuth observed the transition between translational domains on the (7 × 7) reconstructed Si{111} surface. In Fig.14.15, one can clearly resolve a shift between the (7 × 7) unit cells in the left and center parts and those in the right part of the displayed surface area [14.38]. Upon closer inspection, this figure reveals a second type of lattice defect, namely missing adatoms in the upper left and upper right hand corners. Such defects had previously been seen by *Binnig* et al. [14.79] and were initially assigned to dopant atoms (boron) at or close to the surface, implying a surface concentration of dopant atoms enhanced by four orders of magnitude over that expected from the bulk doping [14.79]. Recent EELS results gave strong evidence for a depletion of carriers and dopant atoms at the surface [14.112], therefore the nature and origin of the missing features is still unclear [14.38]. *Becker* et al. proved the existence of (2 × 2) and c(4 × 2) domains together with c(2 × 8) reconstructed areas for Ge{111} [14.98]. These structures were not detected by previous diffraction experiments because the diffraction pattern coincides with that of the c(2 × 8) related beams. Point defects like missing atoms, as described above, were also observed [14.98].

Information about the interaction between steps and the reconstruction in the adjoining surface area is of special interest for the mechanistic understanding of surface reconstructions. Contradictory results about a step-related local inhibition of the c(2 × 2) reconstruction on W{100} were reported in two recent LEED studies [14.113,114]. The corrugation pattern of the Pt{100} surface in Fig.14.13 provides clear evidence that the corrugation, and therefore also the reconstruction, extends up to the step, which rules out a long-range inhibition and favours a local rather than a long-range mechanism for the reconstruction [14.115].

In the above mentioned studies, native structural defects on an otherwise ideal single-crystalline surface in its thermodynamically stable state were primarily investigated. These defects are to be contrasted with metastable defects, which in general can be studied equally well by STM. Sputter-induced surface modifications represent one example of this type. *Feenstra* and *Oehrlein* characterized a heavily ion sputtered silicon <100> oriented wafer and found a mean roughness of 4 Å; the surface was covered with characteristic hillocks of 50 Å diameter [14.116]. The initial stages of the sputter process become more clearly visible in an experiment on an atomically flat Pt{100} surface.

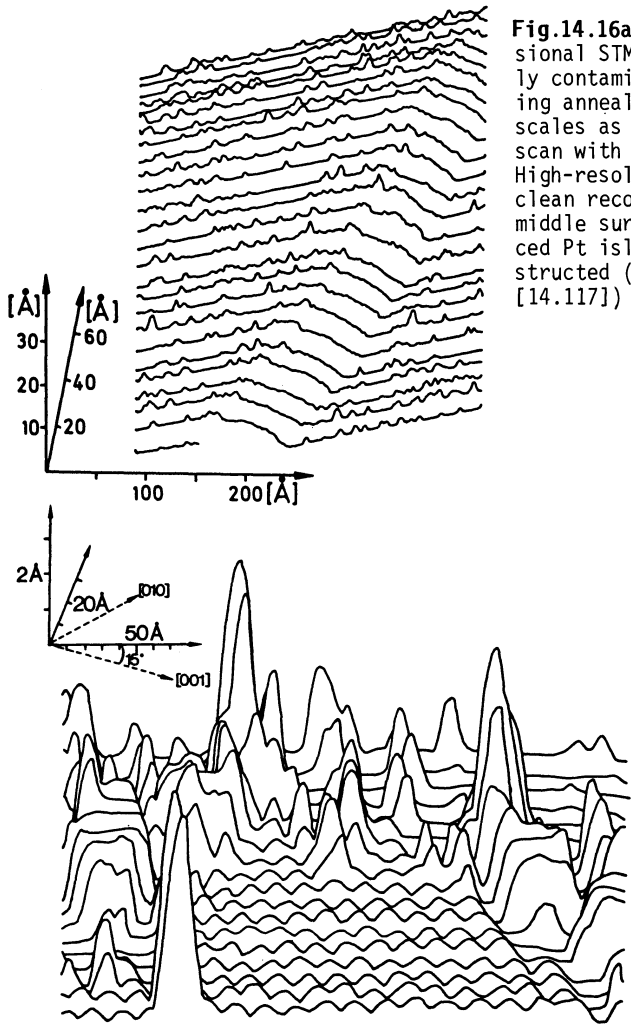

Fig.14.16a,b. Sets of two-dimensional STM scans of Pt{100} slightly contaminated with carbon following annealing to 1100 K (T_S = 550 K, scales as indicated. (**a**) Survey scan with low z-sensitivity. (**b**) High-resolution scan exhibiting clean reconstructed area in the middle surrounded by carbon-induced Pt islands and an nonreconstructed (1 × 1) area. (After [14.117])

Following a brief sputter treatment (~30 s, 1 μA/cm^2, 1 kV Ar^+ ions) at 550 K the STM image of this surface is characterized by small terraces of 30-50 Å extension, which is different from the atomically rough surface one might have expected. The formation of terraces indicates that Pt surface atoms are already sufficiently mobile at 550 K to heal out local (point) defects and condense into small islands [14.117].

Finally, chemical contaminations or additives can also be considered as lattice defects. Due to their interaction with the underlying substrate, they can in fact also lead to geometric changes. *Comsa* et al., for instance, reported the stabilization of double steps on Pt{111} in the presence of ad-

sorbed oxygen [14.118]. The Pt{100} surface likewise provides a good example of such an effect: STM measurements revealed that well-annealed surfaces (~1100 K) that contained small amounts of adsorbed carbon (<10% of a monolayer) exhibited many small islands on an otherwise flat background (Fig. 14.16a) [14.117]. They were assigned to small Pt clusters which are formed at high temperatures at enhanced Pt mobility, and are pinned together by incorporated carbon atoms, since their height always resembled multiples of the Pt{100} interlayer spacing. This is illustrated in a high-resolution image in Fig.14.16b. While the center part of the surface is still chemically clean, as indicated by the corrugation of the reconstructed surface, the corrugation is removed in the surrounding area and a variety of islands with a height identical to one, two, or three Pt layers are shown. (The spikelike shape is due to a much higher sensitivity in the z-scale of this figure.)

In view of these results, the carbon islands reported by *Binnig* et al. on the Au{100} surface might also be due to carbon-pinned gold clusters rather than to carbon clusters [14.91]. The observation of round structures on single-crystalline metal surfaces rather than of flat terraces, as noted in Sect.14.4.1, is probably also due to a stabilization of those surfaces by incorporated/adsorbed foreign atoms.

14.4.4 Reactivity and Stability of Surfaces

The STM is not only well suited for the characterization of static surface defects but is also extremely useful for monitoring dynamic effects of local surface structure elements during reactions on/of surfaces. This permits (a) direct determination of the local activity of surfaces and (b) observation of changes in the surface structure inflicted by reactions on/of these surfaces. The information described in (a) is normally obtained indirectly from comparative measurements on differently stepped surfaces, for example. Surface processes as mentioned in (b) include, for example, corrosion processes. Adsorbate-induced surface phase transitions also belong to this category.

There has long been disagreement about what mechanism can lead to the formation of smooth surfaces following a structural transition of a surface at lower temperatures, where the surface mobility of metal atoms is believed to be small. Figure 14.17 illustrates the change in surface topography during the CO-induced removal of the hexagonal reconstruction on Pt{100}. Due to the different densities of the two Pt surface phases, the hexagonal $\rightarrow (1 \times 1)$ transformation produces a surplus of Pt atoms in the topmost layer (~20% of a monolayer) [14.119]. These STM observations demonstrate that

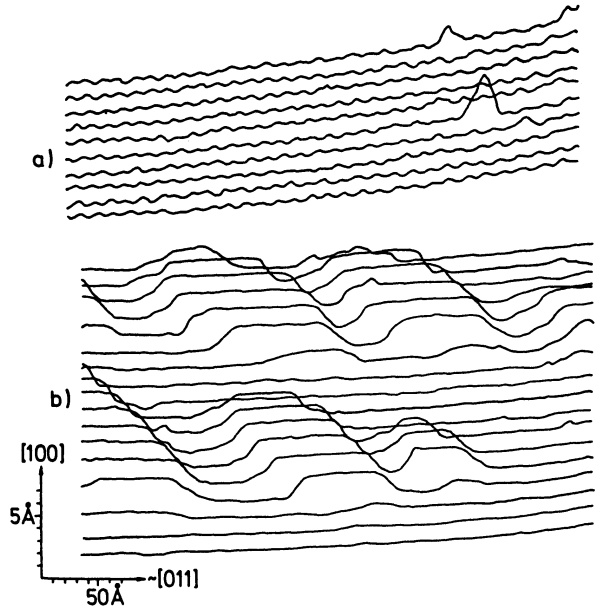

Fig.14.17a,b. Structural transition, rotated hexagonal ⟶ (1 × 1) phase, on Pt{100}, induced by CO adsorption. (**a**) Series of STM scans over the clean reconstructed surface (T_S = 460 K). (**b**) Similar scans following exposure to CO at $p_{CO} = 5 \times 10^{-6}$ mbar (T_S = 460 K). (After [14.119])

at temperatures of 300-450 K the resulting nonreconstructed (1 × 1) surface is flat only over rather short distances (30-70 Å) and that the extra atoms are accommodated in small islands on top of the otherwise flat surface. In this way the mass transport is reduced to single atom diffusion over distances of at most 30-40 Å. (This was shown to be readily achievable by Pd atoms on a W tip at 400 K using FIM [14.25]). Upon annealing to T ≈420 K for a clean surface or to the respective higher desorption temperature for an adsorbate-covered surface (e.g., 480 K for CO), the surface reconverts into the hexagonally reconstructed phase. Simultaneously, the characteristic Pt islands disappear and are almost entirely dissolved upon annealing to ~500 K [14.117]. The second example concerns the decomposition of ethylene on Pt{100} which can be considered as being representative of hydrocarbon decompositions [14.120-122]. The decomposition is known to occur more efficiently on stepped surfaces and therefore it was concluded that the fragmentation process is initiated at steps [14.121,122]. This conclusion was recently verified by direct observations with the STM [14.117]. The presence of decomposition products was detected again by the adsorbate-induced transition of the reconstructed surface layer and by the subsequent surface roughening. During

C_2H_4 exposure at 450 K, the roughening process was shown to proceed from a step edge over the flat terrace.

14.4.5 Non-Surface-Science Applications of the STM

In the preceding part we discussed mainly the use of the STM in problems of "classic" surface science exploiting particularly its atomic resolution. There are, however, a variety of potential applications for which other conceptual and instrumental features of the STM are attractive. These include the ease of direct and nondestructive imaging and its dependence of a special environment such as UHV. Consequently, no decoration techniques are necessary and—of special interest for biological studies—specimens can be investigated in their natural state.

Experiments on more practical surfaces aim mostly at resolutions in the nanometer rather than the angstrom range. In these cases, the STM images are dominated by structural effects and electronic contributions play a minor role. Aside from possible distortions due to the finite tip size [14.81], these images thus reflect the topographical structure of the sample. The requirement of a certain sample or surface layer conductivity has not proved to be a limitation as yet, not even for studies on biological matter [14.123].

The first published results of studies belonging into this category deal with the topology of metal glasses [14.35-37], of condensed or epitaxially grown thin films—e.g., Ag [14.81,82,124-126] and GaAs [14.127]—and of silicon wafers [14.116]. Also, on a silicon surface, individual crystallites were resolved and their shape and size were found to be in good agreement with results of other structure-sensitive methods [14.128]. In other studies, the influence of different preparation techniques on the surface structure under "real-life" conditions (ambient pressure, room temperature) was investigated [14.124,129] and new standards for the microroughness of technological surfaces were proposed [14.130]. Finally, work is in progress on the topological characterization of biological matter also under real-life conditions and promising first results have been published [14.123,124]. For these experiments, the respective samples were suspended on a pyrolytic graphite substrate which had been shown before [14.12,129] to fulfill the requirements of being flat, conducting, and structureless in comparison to the structural features of the specimen.

Other applications of the STM exploit its capability to serve as a very precise position control. This has been used, for example, for driving an optical microscope ("near field optical scanning microscopy") [14.131] and for monitoring the spatial decay of an electrical potential applied externally to the sample ("scanning potentiometry") [14.132]. This latter method

is expected to give valuable insight into the electrical behavior of small surface structures and is therefore of considerable technological interest. Finally, the STM can also be used for mechanical (by elastic [14.133] or inelastic effects [14.46,47]) or chemical [14.89] (e.g., by local decomposition of hydrocarbons) modifications of the surface to facilitate surface lithography on a nanometer scale.

14.4.6 Surface Diffusion and Surface Mobility

The capability of the STM to detect surface diffusion processes was demonstrated recently by *Binnig* et al. [14.134]. During measurements on an oxygen-covered Ni{110} surface, they detected many brief "spikes" in the tunnel current on an otherwise very stable and flat current signal. They assigned these features to oxygen atoms which moved intermittently into the tunneling area and thus lead to a variation in the tunnel current. The width of these pulses is related to the time the adsorbed atom spends within the tunneling area. Measurements at different temperatures indeed yielded reasonable numbers for the preexponential factor and the activation energy [14.134]. Another method for determining diffusion constants was proposed by *Gomer* and is based on an evaluation of the fluctuations in the tunnel current caused by fluctuations in the respective adsorbate layer seen by the STM [14.135].

In considering experimental artifacts which might contribute to such measurements, it should be noted that in a first approximation both models neglect any influence of the electrical field between tip and surface upon particle mobility. The resulting "normal" values for the diffusion rates of O/Ni{110} in turn indicate that the O_{ad} is not trapped in the field gradient between tip and surface but can freely diffuse over the surface. Similar effects of course would happen if particles adsorbed on the tip diffused into the tunneling area (on the tip), but there is experimental evidence that this process can be neglected in this case [14.134]. Tunneling of an adsorbed particle from the surface onto the tip was proposed recently to occur only for short tip-surface distances of 2-4 Å [14.136].

14.5 Tunneling Spectroscopy

This final chapter focuses on the use of the STM to characterize the electronic properties of a surface. In addition to the three spatial dimensions x, y, and z, also the tunnel current I_t, the tunnel voltage V_t, and the gap width s represent parameters of an STM measurement. Including them as variables allows various experiments which give information concerning the electronic properties of the surface on a local scale.

Table 14.3. Main techniques of tunneling spectroscopy arranged according to their constant and variable parameters and their observable quantities

Observable quantity	Variable parameters V (X,Y,I)	V (X,Y,s)	(Constant parameters) I (X,Y,V)	X,Y (I,V)
z	V-s	-	I-s	Topography
I	-	I-V	-	-
$\left(\frac{dI}{dV}\right)$	LTS (distorted)	LTS	-	STS
$\left(\frac{dI}{ds}\right)$	-	$\phi = f(V)$	$\phi = f(s)$	ϕ-images
$\left(\frac{d^2I}{dV^2}\right)$	-	Inelastic tunneling	-	Inelastic images

LTS: local tunneling spectroscopy; STS: scanning tunneling spectroscopy

To give an overview, the main techniques are organized in Table 14.3 according to their respective constant and variable parameters and to their observable quantities. Columns 1-3 list measurements of electronic properties at a fixed and freely selectable position on the surface. These experiments are performed by sweeping the respective variable and monitoring the corresponding observable quantity. For the measurements in the derivative mode (rows 3-5), a small modulation voltage is superimposed on V_t or on the z-piezo voltage (gap width modulation) and the AC component of the modulated signal is monitored by a lock-in amplifier while the feedback loop keeps the DC component of the tunnel current constant. The modulation frequency and the sweep velocity of the I-V curves have to be much faster than the bandwidth of the feedback loop, to avoid simultaneous compensating changes in the gap width. In all other cases, the sweep velocity must be smaller than this bandwidth in order to maintain constant tunnel current.

Column 4 refers to two-dimensional STM images. Depending on the observable quantity, these are topographical images (z), spectroscopic images (dI/dV) or "Work function" (dI/ds) images. In all of them, I_t, and thus the gap width, is kept constant, i.e., the electronic properties are probed along equicurrent lines.

For a qualitative understanding of the physical quantities probed in these experiments it is most instructive to use the Bardeen picture [14.54], in which the tunnel conductance is determined by the overlap of the wave functions of the tunnel electrodes in the gap region. Consequently, the tunnel current probes the densities of filled states in the cathode and of empty states in the anode and their respective extension into the gap region.

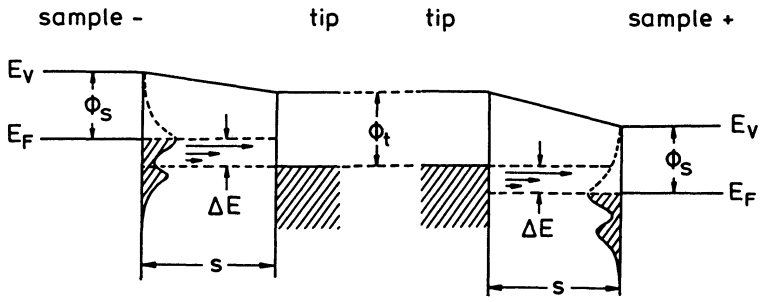

Fig.14.18. Energy diagram: The left (right) junction corresponds to a negative (positive) bias on the sample so as to permit tunneling from occupied states on the sample (tip) into empty states on the tip (sample). Only states within the energy window ΔE can contribute. The associated density of states N_S (E) of the sample is sketched (*solid line* : occupied states, *broken line* : empty states), the arrows indicate the barrier-dependent tunneling probability. ϕ_S, ϕ_t: work function of sample and tip, respectively, s: gap width

Only states within the energy gap ΔE are considered, which is illustrated in Fig.14.18. The energy gap ΔE is determined by the applied tunnel voltage V_t. For conducting materials, $\Delta E = V_t$ (Sect.14.3.5). The contribution of each of these states is weighted exponentially by their respective barrier height. The latter reflects the total charge density at the surface, among other properties. For the interpretation of the spectroscopic data, it is important to note that the tunnel conductance is dominated by those states that extend far out into the barrier region, that are at the top of the energy window (close to E_F for the cathode), and that exhibit a high density of states and of course the proper symmetry for overlap.

The density of states is tested by the voltage dependence of the tunnel current. Depending on the polarity of the applied voltage, either empty or filled states of the sample are detected (Sect.14.5.1). Resonances in the tunnel current observed at higher voltages are discussed in Sect.14.5.2. The correlation between tunnel current and distance yields information about the barrier height ("local work function"), since the decay of the contributing wave functions at the surface into vacuum is determined by the respective tunnel barrier (Sect.14.5.4). Specific applications of the STM to spectroscopic problems include the local detection of superconductivity (Sect.14.5.3) and the yet-to-be-realized resolution of vibrational modes via inelastic tunneling. The voltage-dependent spectroscopy of electronic states, tunneling studies of superconductivity, and inelastic tunneling for the detection of vibrational modes have already been widely applied in classic oxide junctions [14.21], however, without achieving local resolution.

Spectroscopic measurements of comparatively small variations in the tunnel current require a rather stable gap width. Because of the exponential dependence of I_t on s, the current signal will otherwise be dominated by those instabilities. (For typical values, I_t changes by an order of magnitude over 1 Å.) The use of modulation techniques as mentioned above, however, can considerably reduce the impact of instabilities, especially if the modulation frequencies are much higher than the eigenfrequencies of the system. The upper limits for these frequencies are given by the bandwidth of the I-V converter (V_t modulation) and of the power supplies for the z-piezo (gap width modulation).

14.5.1 Valence Band Spectroscopy

For small bias potentials, the barrier height is independent of the applied voltage, and the tunnel probability of an electron is given by dI/dV, while the (measured) tunnel conductance also includes the density of states at the anode and cathode the term. (dI/dV) is measured on one particular position of the surface as V_t is swept through the spectral range [local tunneling spectroscopy (LTS)]. In this mode, a peak in (dI/dV)-V, corresponding to a sudden change in the I-V curve, will always result if a new state enters (or leaves) the energy window at its high-energy side (Fig.14.18). Measuring at a constant tunnel resistance R_t rather than at constant tunnel current I_t, will minimize distortions of the spectra due to distance variations so that $(dI/dV)_R$-V curves directly reflect the density of states at the respective upper edge of the energy window ΔE [14.33,34].

In an investigation of the electronic structure of Pd{111} and Au{111}, distinct structures in the tunnel conductance spectra were found on characterized flat parts of these surfaces [14.33,34]. On Pd{111}, three peaks are clearly resolved at -1.4 eV, -0.4 eV, and + 1.0 eV, and a weak feature shows up at -2.1 eV (Fig.14.19). They can be correlated with, respectively, the position of the d-band edge (-1.4 eV) [14.137], the L saddle point at + 1.0 eV, and surface states at -0.4 eV and -2.1 eV, which were also seen by UPS on the clean surface [14.138].

Similar spectroscopic measurements on an oxidized Ni{100} surface revealed an extremely strong feature at ~0.6 eV above the Fermi level, which was at least one order of magnitude more intense than those observed typically on clean metal surfaces [14.139]. The authors attributed this peak to a d-electron state in the oxide layer and judged its low energy as confirmation of a band-structure model rather than a localized model (Mott insulator [14.139, 140]) as a proper description for NiO. Based on their calculations, Garcia

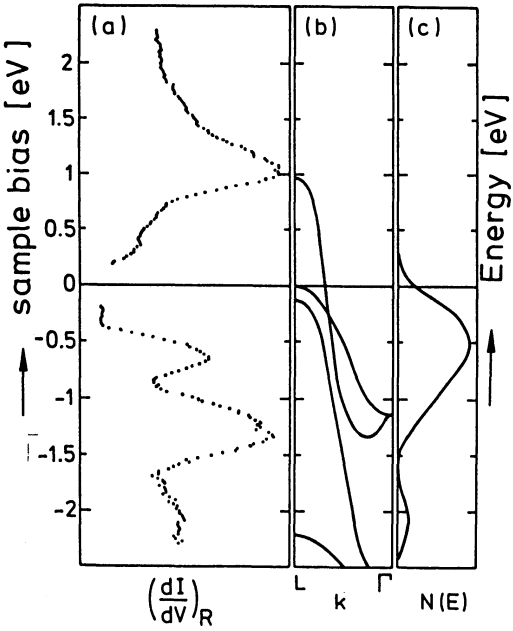

Fig.14.19. (*a*) Constant resistance conductance versus voltage spectrum for Pd{111} taken with 200-mV peak-to-peak modulation at room temperature. (*b*) Sketch of the Pd{111} band structure where the s-d bands are prominent in this energy range and there is a forbidden gap extending above the saddle point at 0.94 eV [14.136]. (*c*) Plot of the surface state peaks derived from UPS measurements. (After [14.33])

et al. demonstrated that in such measurements the number of oxide layers strongly affects the tunnel conductivity and that, therefore, the former quantity can be extracted from the detailed shape of the low-energy peak [14.141].

In comparison with photoemission (UPS) and inverse photoemission (BIS), where surface sensitivity results from the mean free path of the electrons in the sample material, the STM measurements have an inherently high surface sensitivity: The tunnel electrons can proceed only into or out of states with an appreciable amplitude at and outside the surface to achieve overlap of the wave functions of the electronic states in the two electrodes.

As mentioned above, measurements of I-V curves and of the differential conductance in order to characterize the energy gap in superconductors were reported in 1981 by *Poppe* et al. [14.17]. Similar recent measurements together with two-dimensional images of the local superconducting character of the surface by Elrod et al. are discussed in Sect.14.5.3.

In several laboratories, efforts are being made to exploit inelastic tunneling in the STM as a means to detect locally resolved vibrational excitations, but results are still awaited. This measurement suffers from two experimental problems. First of all, because of the very small changes in tunnel current ($\leqslant$0.1% [14.21]), these measurements require an extremely stable gap width, even if modulation techniques (second derivative mode) are used

for noise suppression. This becomes even more of a problem because of the second limitation, the requirement to work at very low temperatures in order to reduce thermal broadening of the Fermi edge [14.142].

14.5.2 Resonant Tunneling

A new phenomenon in addition to the structure in the (dI/dV)-V spectra described above occurs in the high bias limit. In a variety of experiments now characteristic oscillations in (dI/dV) were reported at higher voltages, e.g., on Au{110} [14.4,143], Ni{100} [14.144], Si{111} [14.145], and on Pt{100} [14.32]. Earlier, Gundlach had predicted oscillations in the tunneling probability at energies close to those of the bound states within a triangular potential defined by the top of the potential barrier in the tunneling gap in front of the cathode (e.g., the tip) and a partially reflecting boundary at the cathode (e.g., at the sample surface, see also the inset in Fig.14.20) [14.146]. Since their positions are extremely sensitive to small changes in the shape of the metal insulator boundary, it was also noted that they are not likely to be observed experimentally because of fluctuations in the height and thickness of the barrier [14.147]. Indeed, only a few measurements on solid tunnel junctions showed evidence of such behavior

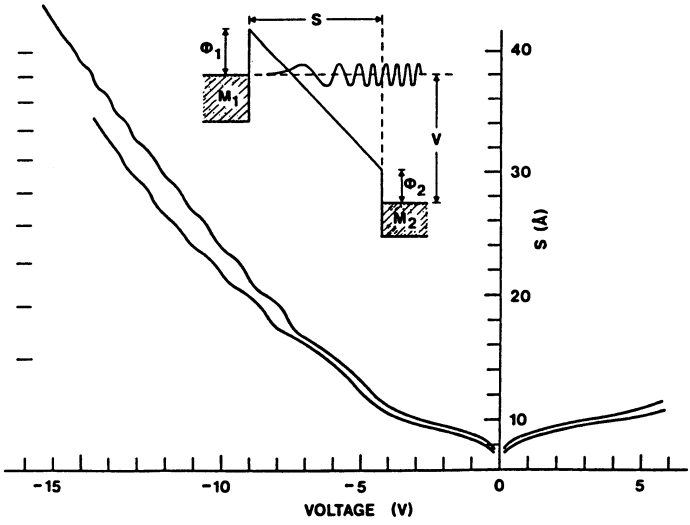

Fig.14.20. Distance-voltage tunnel characteristics exhibiting resonant tunneling. The "levels" shown on the left are obtained from the resonance condition and give the distance for constructive interference. The inset shows schematically a metal (M_1)-vacuum-metal(M_2) tunnel junction under field-emission conditions ($V>\phi_2$) and the propagating wave in the "quasi-potential well" with corresponding decay in the triangular vacuum barrier (left) and the mismatch at the vacuum-M_2 interface. (After [14.4])

[14.148,149]. The STM results thus confirmed the correctness of these predictions and underlined the local character of STM tunneling, where these fluctuations are not expected to play a role. In accord, the intensity of these oscillations depends critically on the flatness of the surface.

Near the vacuum level E_V, and between E_V and E_F, the triangular potential is distorted by the contribution of the image potential, as described in Sect.14.3.3 and Fig.14.5. Consequently, bound states or resonances are possible even at rather low bias voltages where the triangular potential is effectively replaced by the image potential. *Binnig* et al. correspondingly attributed these oscillations in the I-V characteristics for tunneling into a Ni{100} surface to image states, as observed in inverse photoemission [14.150] or two-photon-photoemission [14.151]. This surface exhibits a large band gap in the projected bulk band structure right above E_F [14.152] and the resulting high reflectivity of (low transmission into) the surface allows the formation of rather long-lived states in front of the surface. *Becker* et al. performed extensive measurements on a Au{110} sample [14.143]. In this case, the lifetime of the electrons in front of the surface is always short since there is no comparable band gap [14.153]. Emphasizing these properties, they used the term "electron interferometry", but the features are equivalent to those described as resonances by *Gundlach* [14.146] and also by *Salvan* et al. [14.145] for STM results on Si{111}, also with no comparable band gap.

The STM experiments were performed under feedback control, i.e., at constant current rather than at constant gap width s. The resulting variations in s with V are directly correlated to oscillations in $(dI/dV)_s$, which are observed in the standard mode for calculations or measurements on solid junctions. Therefore, the oscillations show up also in the gap width. For constant I_t, we can write

$$dI = \left(\frac{\partial I}{\partial V}\right)_s dV + \left(\frac{\partial I}{\partial s}\right)_V ds = 0 \quad , \tag{14.11}$$

$$\left(\frac{\partial I}{\partial V}\right)_s = - \left(\frac{\partial I}{\partial s}\right)_V \left(\frac{\partial s}{\partial V}\right)_I \quad , \tag{14.12}$$

and from (14.12) it is evident that maxima in $(dI/dV)_s$ are accompanied by maxima in $(ds/dV)_I$ or steps in the s-V curves since $(dI/dS)_V$ is a smooth and structureless function [14.141]. These steps are clearly resolved in Fig.14.20, which also represents the first reported example of I-V oscillations in the STM [14.4].

In the STM, the electric field in the tunnel junction has the effect of continuously shifting and expanding the image state spectrum (Stark shift).

For comparison with results from other techniques, this shift has to be accounted for. This was demonstrated by *Binnig* et al. who recorded (dI/dV)-V curves at different currents and thus also at different field strengths [14.144]. From these series they extrapolated the energies to zero field conditions. The resulting energies compared well with those found in inverse photoemission on this surface [14.154].

14.5.3 Scanning Tunneling Spectroscopy

In this mode the surface is scanned at constant given DC values for I_t and V_t and thus at roughly constant gap width s, while $(dI/dV)_I$ is monitored. In essence, this is equal to looking at the difference in corrugation of two topographical images taken at slightly different voltages [14.155]. In the framework of this more general definition, topographic images dominated by specific voltage-dependent features may also be included in this section.

In scanning tunneling spectroscopy (STS), mainly the corrugation of the states at the lower energy boundary of the window in Fig.14.18 is probed, in contrast to topography, which is sensitive to the electronic charge in the entire energy window (Sect.14.5.3). Therefore, STS is ideally suited to detecting the spatial distribution of localized states associated with d-bands or directed covalent bonds (dangling bonds), surface states, resonances, etc., and to their correlation to the topographical image taken simultaneously [14.64]. Spectroscopy and topography, although emphasizing different features, are not completely decoupled. This is mostly due to finite bias effects which cause I_t to slowly change from the low bias approximation into the high bias limit (Table 14.1). Here I_t loses its ohmic behavior and the exponential term for I_t becomes voltage dependent. Including the contribution of the image potential as well, this leads to a general expression for the tunnel current of

$$\ln I_t \approx -A \cdot h(\phi(V,s,)) \cdot f(V,s) \quad . \tag{14.13}$$

Only in the low bias limit, with $f(V,s) = s$ and neglecting the image potential $h(\phi(V,s)) = \phi^{\frac{1}{2}}$, will this yield a constant value for the observed derivative $(dI/dV)_I$ or $(d\ln I/dV)_I$. Therefore, only under these conditions will spatial variations in the topography not affect the spectroscopic signal while the tip follows the equicurrent line over the surface. In general, i.e., at higher voltages, the spectroscopic signal will also reflect changes in the topography since both terms in (14.13) are now energy dependent and contribute to the derivative.

In connection with their LTS measurements on an oxidized Ni{100} surface, *Binnig* et al. followed the process of surface oxidation by STS [14.139].

Utilizing the extreme intensity of the peak at -0.6 eV in the (dI/dV)-V spectra, they were able to monitor the associated nucleation and growth process by scanning the surface at this particular energy while hardly any changes were detectable in the topographical images taken simultaneously. These measurements thus provide an impressive demonstration of the potential of STS for monitoring chemical changes on a surface.

In their original studies on p- and n-doped Si{111} *Binnig* et al. noted slight differences in the apparent topography which were attributed to the different tunnel voltages [14.78,79]. Subsequent results of a detailed study of the correlation between topographic and spectroscopic images and their variation with the tunnel voltage indeed revealed a strongly state-selective corrugation on this surface [14.155]. *Feenstra* et al. performed a systematic STM investigation on the Si{111}-(2 × 1) reconstructed surface at a variety of different tunnel voltages between -2 and +2 eV [14.48,95]. From the voltage dependence of reconstruction-induced corrugation and defect-related features, they deduced the presence of (a) a band gap for the (2 × 1)-related surface states at $|V_t| \leq 0.4$ eV, and (b) defect states with energies in or near this band gap.

In the following examples as well, the corrugation observed in topographic images was clearly dominated by electronic effects: *Coleman* et al. showed STM images that, in addition to resolving single atoms, directly reflected superlattices due to the formation of charge density waves on a 1T-TaS_2 surface [14.30]. In agreement with calculations [14.156], the STM image on a 2H-$TaSe_2$ surface in contrast was dominated by the lattice modulation. On a graphite surface, *Binnig* et al. could distinguish between two electronically different carbon atoms at low voltages (50 mV) while at high voltages (1.5 V) these differences disappear because of the integration over the density of states in a much wider energy window [14.12]. The STM image seen at low voltages thus represents a corrugation of states close to E_F which is very different from that of the total charge density.

These examples underline the potential of the STM for studies of semiconductor surfaces. While perhaps impeding pure structure determination, the state selectivity of the STM measurements is extremely helpful for a more comprehensive understanding of the correlated electronic *and* geometric sturcture of these surfaces. Correspondingly, in all of these cases, the charge-density approximation proposed by *Tersoff* and *Hamann* [14.57,58] to model STM scans would be invalid (Sect.14.3.4).

Elrod et al. imaged the spatial variations in the superconducting character of a niobium-tin sample at 6.2 K [14.27-29]. Using a modified modulation

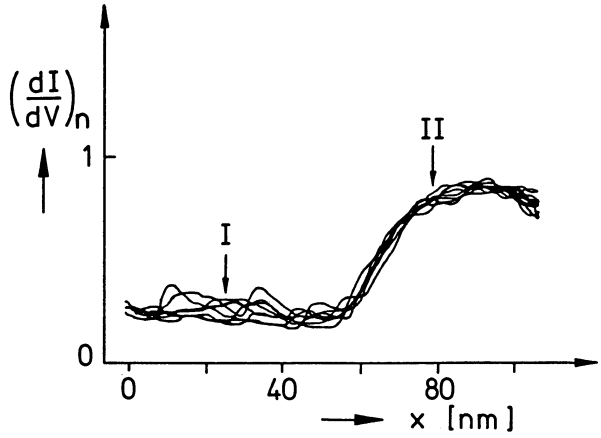

Fig.14.21. Repeated spectroscopic scans (normalized zero bias conductance line scans) over a region of a Nb_3Sn sample showing a continuous spatial transition between normal (*II*) and superconducting (*I*) behavior. The normalized value $(dI/dV_n$ at the ordinate represents $(dI/dV)_{V=0}/(dI/dV)_{V>>0}$ (After [14.28])

technique, this was quantified by essentially measuring (dI/dV) at zero bias and then normalizing this to the average value outside the superconducting gap. {For a superconduction-insulator-normal (SIN) junction within this gap, $(dI/dV)_0 \approx 0$ [14.28]}. Figure 14.21 displays repeated spectroscopic scans over an area of the sample that shows a continuous spatial transition between superconducting (I) and nearly "normal" (II) regions. Two-dimensional scans were also published reflecting the correlation between topographic roughness and super superconducting character.

Inelastic images when they become measurable will provide another mode in addition to STS to detect chemical changes or adsorbed species spatially resolved on a surface.

14.5.4 The Work Function and Work Function Images

The correlation between the slope of I-s curves, the (distance-dependent) tunnel barrier, and the macroscopic work function, as well as the barrier-lowering effects of the image potential and surface roughness ($<R_t$) in the STM were treated in Sect.14.3.3. For flat metal surfaces, barrier heights of 3-4.5 eV seem to be typical [14.2,8,9,88]. This was demonstrated for a Pt{100} surface which was previously characterized as chemically clean by the presence of the "hex" reconstruction and as topographically flat [14.88]. Rougher surfaces tend to exhibit lower tunnel barriers, but anomalously low values of a few tenths of an electronvolt must have other sources [14.157].

In addition to its distance dependence, the tunnel barrier was also predicted to be voltage dependent [14.69] in agreement with preliminary results [14.32]. Systematic experimental studies, however, have not yet been published.

The spatial variation of the tunnel barrier (work function image), monitored in a comparable mode to STS, but by modulating the gap width instead of V_t, can stem from chemical or geometric heterogeneities on the surface. In practice, work function images have received less attention than spectroscopic images, despite their principcal sensitivity to chemical surface modifications: From considerations identical to those in 14.5.3, also the work function image and topography are not strictly decoupled. In addition, work function measurements are particularly sensitive to surface roughness and more susceptible to mechanical instabilities because of the mechanical modulation of the gap width.

In a zero-order approximation, the electronic corrugation is assumed to decay with distance leading to a lower value for the tunnel barrier at topographical minima (Smoluchowski effect [14.158]). The geometric surface heterogeneity, of course, also includes different sites within a large unit cell. This local sensitivity is demonstrated in Fig.14.22 by a work function scan over the hex reconstructed Pt{100} surface in which a modulation in the measured tunnel barrier of about 100 meV with the corrugation length identical to that of the topographic corrugation is exhibited [14.88].

The use of work function images as a technique for chemical distinction was demonstrated by *Binnig* et al. for gold deposits on a silicon sample

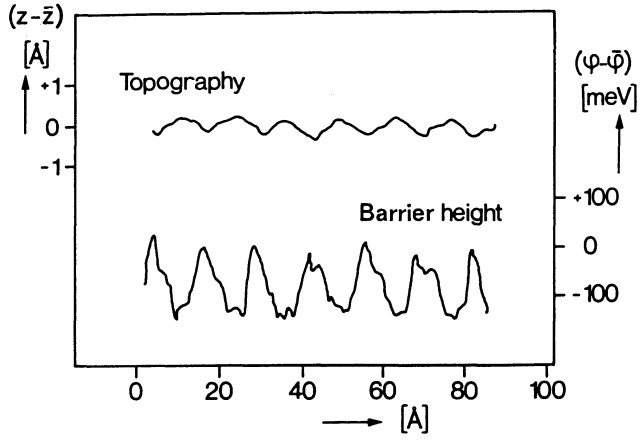

Fig.14.22. Tunnel barrier and topography in a line scan over the hex reconstructed Pt{100} (After [14.88])

where the gold clusters were clearly identified on the work function image and on the topographic image [14.6].

In the same way that STS is correlated to (inverse) photoemission measurements, the locally resolved work function images also have a corresponding integrating technique: the photoemission of adsorbed xenon (PAX), which is a titration technique yielding a histogram of the local work function values on a surface [14.159]. A quantitative comparison of results from both methods will be of particular interest with respect to the representative character of STM images.

14.6 Conclusions

Scanning tunneling microscopy has become a unique technique, mostly because of its capability to simultaneously image topographic and electronic structures with a local resolution on an atomic scale, with relatively few restraints on the experimental environment. This attractive combination accounts for the wide applicability of the STM not only in surface science but also in a variety of other fields of scientific or technological interest.

The STM benefits from and complements existing techniques for surface characterization, such as diffraction methods or direct imaging for structure determination, and photoemission or electron energy loss techniques for the investigation of electronic structures. The direct combination with almost any of these techniques really allows the full exploitation of the potential of the STM as a local probe with very high resolution for surface science.

The technological interest in the STM stems in part from its application as a writing or micropositioning tool, e.g., for the detection of local electric potentials. However, imaging in air with – for most technological and many scientific purposes – no significant loss in resolution is expected to find many future application for a variety of problems, including studies of biological specimens in their natural state.

Acknowledgements. We would like to thank all colleagues who generously provided preprints of unpublished results, permitted the use of their figures, or contributed in other ways to this work. We wish to especially mention G. Binnig and H. Rohrer, who freely shared their expert knowledge, and Ch. Gerber, who gave always helpful technical advice. The authors also want to thank G. Ertl for his continuous interest and support. Finally, financial support by the Deutsche Forschungsgemeinschaft through SFB 128 is gratefully acknowledged.

References

14.1 G. Binnig, H. Rohrer, Ch. Gerber, E. Weibel: Physica (Utrecht) **107B+C**, 1335 (1981)
14.2 G. Binnig, H. Rohrer, Ch. Gerber, E. Weibel: Appl. Phys. Lett. **40**, 178 (1982)
14.3 G. Binnig, H. Rohrer, Ch. Gerber, E. Weibel: Phys. Rev. Lett. **49**, 57 (1982)
14.4 G. Binnig, H. Rohrer: Helv. Phys. Acta **55**, 726 (1983)
14.5 G. Binnig, H. Rohrer: Phys. Bl. **39**, 16,176 (1983)
14.6 G. Binnig, H. Rohrer: Surf. Sci. **126**, 236 (1983)
14.7 G. Binnig, H. Rohrer: Surf. Sci. **152/153**, 17 (1985)
14.8 M.D. Pashley, J.B. Pethica, J. Coombs: Surf. Sci. **152/153**, 27 (1985)
14.9 R.F. Willis, M.C. Payne, J.B. Pethica, M.D. Pashley, J.H. Coombs: In *Festkörperprobleme XXV*, ed. by P. Grosse (Vieweg, Braunschweig 1985)
14.10 E. Stoll: In conference handouts of 26. Cours de Perfectionnement de l'Association Vaudoise des Chercheurs en Physiques, "Physique des Surfaces", Saas Fee, Switzerland 1984, ed. by E. Bornand, A. Chapelain, P. Millet, pp.87-156
14.11 G. Binnig, H. Rohrer: Sci. Am. **253**, 40 (1985)
14.12 G. Binnig, H. Rohrer, Chr. Gerber, H. Fuchs, E. Stoll, E. Tosatti: To be published
14.13 J.R. Oppenheimer: Phys. Rev. **31**, 66 (1928)
14.14 R.H. Fowler, L. Nordheim: Proc. R. Soc. London, Ser. A**119**, 173 (1928)
14.15 J. Frenkel: Phys. Rev. **36**, 1104 (1930)
14.16 W. Thompson, S.F. Hanrahan: Rev. Sci. Instrum. **47**, 1303 (1976)
14.17 U. Poppe: Physica **108**B, 805 (1981)
U. Poppe, H. Schröder: In Proc. 17th Int. Conf. Low Temp. Phys., Karlsruhe 1984, ed. by U. Eckern, A. Schmid, W. Weber, H. Wühl (Elsevier, Amsterdam 1984) p.835
U. Poppe: J. Magn. & Magn. Mater. **52**, 157 (1985)
14.18 R.D. Young: Rev. Sci. Instrum. **37**, 275 (1966)
R.D. Young, J. Ward, F. Scire: Phys. Rev. Lett. **27**, 922 (1971)
14.19 C. Teague: Ph.D. Thesis, North Texas State University, Denton (1978)
C. Teague: Bull. Am. Phys. Soc. **23**, 230 (1978)
14.20 R.D. Young: Private communication
14.21 E. Burstein, S. Lundquist (eds.): *Inelastic Phenomena in Solids* (Plenum, New York 1969)
T. Wolfram (ed.): *Inelastic Electron Tunneling Spectroscopy*, Springer Ser. Solid-State-Sci., Vol.4 (Springer, Berlin, Heidelberg 1978)
E.L. Wolf: Rep. Prog. Phys. **41**, 1439 (1978)
E.L. Wolf: *Principles of Electron Tunneling Spectroscopy* (Oxford U. Press, Oxford 1985)
P. Hansma (ed.): *Tunneling Spectroscopy* (Plenum, New York 1982)
14.22 J.W. Gadzuk, E.W. Plummer: Rev. Mod. Phys. **45**, 487 (1973)
14.23 C.B. Duke: In *Tunneling in Solids*, Solid State Physics, Vol.10, ed. by F. Seitz, D. Turnbull, H. Ehrenreich (Academic, New York 1969)
14.24 E.W. Müller: Phys. Z. **37**, 838 (1936); Z. Phys. **106**, 541 (1937)
E.W. Müller, T.T. Tsong: *Field Ion Microscopy* (Elsevier, New York 1969)
14.25 G. Ehrlich: In *Chemistry and Physics of Solid Surfaces V*, ed. by R. Vanselow, R. Howe, Springer Ser. Chem. Phys., Vol.35 (Springer, Berlin, Heidelberg 1984)
14.26 Chr. Gerber: IBM J. Res. Dev., in press
14.27 S. Elrod, A.L. de Lozanne, C.F. Quate: Appl. Phys. Lett. **45**, 1240 (1984)
14.28 A.L. de Lozanne, S.A. Elrod, C.F. Quate: Phys. Rev. Lett. **54**, 2433 (1985)

14.29 S.A. Elrod: IBM J. Res. Dev., in press
14.30 R.V. Coleman, B. Drake, P.K. Hansma, G. Slough: Phys. Rev. Lett. **55**, 394 (1985)
14.31 S. Chiang, R.J. Wilson: IBM J. Res. Dev., in press
14.32 W. Hösler, R.J. Behm: Unpublished results
14.33 W.J. Kaiser, R.C. Jaklevic: IBM J. Res. Dev., in press
14.34 W.J. Kaiser, R.C. Jaklevic: Bull. Am. Phys. Soc. **30**, 309 (1985)
14.35 M. Ringger, H. Hidber, R. Schlögl, P. Oelhafen, H.J. Güntherodt, K. Wandelt, G. Ertl: In Proc. 17th Int. Conf. Low Temp. Phys., Karlsruhe 1984, ed. by U. Eckern, A. Schmid, W. Weber, H. Wühl (Elsevier, Amsterdam 1984)
14.36 M. Ringger, H.R. Hidber, R. Schlögl, P. Oelhafen, H.J. Güntherodt, K. Wandelt, G. Ertl: In *The Structure of Surfaces*, ed. by M.A. Van Hove, S.Y. Tong, Springer Ser. Surf. Sci., Vol.2 (Springer, Berlin Heidelberg 1985) p.48
14.37 M. Ringger, H.J. Güntherodt, B.W. Corb, H.R. Hidber, P. Oelhafen, R. Schlögl, A. Stemmer, R. Wiesendanger: IBM J. Res. Dev., in press
14.38 J.E. Demuth, R.J. Hamers, R.M. Tromp, M.E. Welland: IBM J. Res. Dev., in press
14.39 P.K. Hansma: IBM J. Res. Dev., in press
14.40 J. Moreland, S. Alexander, M. Cox, R. Sonnenfeld, P.K. Hansma: Appl. Phys. Lett. **43**, 387 (1983)
14.41 J. Moreland, P.K. Hansma: Rev. Sci. Instrum. **55**, 399 (1984)
14.42 J. Moreland, J. Drucker, P.K. Hansma, J.P. Katthaus, A. Adams, R. Kvaas: Appl. Phys. Lett. **45**, 104 (1984)
14.43 S. Vieira: IBM J. Res. Dev., in press
14.44 U. Tietze, Ch. Schenk: *Halbleiter-Schaltungstechnik*, 7. Aufl. (Springer, Berlin, Heidelberg 1985)
14.45 D. Pohl: IBM J. Res. Dev., in press
14.46 G.F.A. van de Walle, J.W. Gerritsen, H. van Kempen, P. Wyder: Rev. Sci. Instrum. **56**, 1573 (1985)
14.47 H. van Kempen: IBM J. Res. Dev., in press
14.48 R.M. Feenstra, W.A. Thompson, A.P. Fein: Phys. Rev. Lett., in press
14.49 S. Chiang, R.J. Wilson: Private communication
14.50 H.W. Fink: IBM J. Res. Dev., in press
14.51 Y. Kuk: Private communication
14.52 H.W. Fink: Private communication
14.53 J.G. Simmons: J. Appl. Phys. **34**, 1793 (1963). The effect of the image potential was overestimated by a factor of two in this work [14.23]
14.54 J. Bardeen: Phys. Rev. Lett. **6**, 57 (1961)
14.55 G. Binnig, N. Garcia, H. Rohrer, J.M. Soler, F. Flores: Phys. Rev. B**30**, 4816 (1984)
14.56 T.E. Feuchtwang, P.H. Cutler, N.M. Miskowsky, A.A. Lucas: In *Quantum Metrology and Fundamental Physical Constants*, ed. by P.H. Cutler, A.A. Lucas, NATO ASI Series B, Vol.3 (Plenum, New York 1983) p.529
14.57 J. Tersoff, D.R. Hamann: Phys. Rev. Lett. **50**, 1998 (1983)
14.58 J. Tersoff, D.R. Hamann: Phys. Rev. B**31**, 805 (1985)
14.59 T.E. Feuchtwang, P.H. Cutler, N.H. Miskovsky: Phys. Lett. **99**A, 167 (1983)
14.60 N. Garcia, C. Ocal, F. Flores: Phys. Rev. Lett. **50**, 2002 (1983)
14.61 E. Stoll, A. Baratoff, A. Selloni, P. Carnevali: J. Phys. C**17**, 3073 (1984)
14.62 E. Stoll: Surf. Sci. **143**, L411 (1984)
14.63 N. Garcia, F. Flores: Physica **127**B, 137 (1984)
14.64 A. Baratoff: Physica **127**B, 143 (1984)
14.65 N. Garcia: J. Chem. Phys. **67**, 897 (1977)
14.66 N. Garcia, N. Cabrera: Phys. Rev. B**18**, 576 (1978)
14.67 N. Garcia, J. Barker, I.P. Batra: J. Electron. Spectrosc. Relat. Phenom. **30**, 137 (1983)

14.68 N. Esbjerg, J.K. Nørskov: Phys. Rev. Lett. **45**, 807 (1980)
14.69 M.C. Paynes, J.C. Inkson: Surf. Sci. **159**, 485 (1985)
14.70 T.E. Feuchtwang, P.H. Cutler, E. Kazer: J. Phys. (Paris) C9, 111 (1985)
14.71 A.A. Lucas, J.P. Vigneron, J. Bono, P.H. Lütler, T.E. Feuchtwang, R.H. Good, Jr., Z. Huang: J. Phys. (Paris) C9, 125 (1985)
14.72 J. Bono, R.H. Good, Jr.: Surf. Sci. **151**, 543 (1985)
14.73 M. Büttiker, R. Landauer: Phys. Rev. Lett. **49**, 1739 (1982)
M. Büttiker: Phys. Rev. B**27**, 6178 (1983)
14.74 M. Büttiker: IBM J. Res. Dev., in press
14.75 Z.A. Weinberg, A. Hartstein: Solid State Commun. **20**, 179 (1976)
14.76 N.D. Lang, W. Kohn: Phys. Rev. B3, 1215 (1971)
14.77 O.C. Wells: *Scanning Electron Microscope* (McGraw-Hill, New York 1974)
14.78 G. Binnig, H. Rohrer, Ch. Gerber, E. Weibel: Phys. Rev. Lett. **50**, 120 (1983)
14.79 G. Binnig, H. Rohrer, F. Salvan, Ch. Gerber, A. Barô: Surf. Sci. **157**, L373 (1985)
14.80 G. Binnig, H. Rohrer, Chr. Gerber, E. Weibel: Surf. Sci. **131**, L 379 (1983)
14.81 J.K. Gimzewski, A. Humbert, J.G. Bednorz, B. Reihl: Phys. Rev. Lett. **55**, 951 (1985)
14.82 A. Humbert: IBM J. Res. Dev., in press
14.83 R. Miranda: Private communication
14.84 F. Flores, N. Garcia: Phys. Rev. B**30**, 2289 (1984)
14.85 T.E. Hartmann: J. Appl. Phys. **33**, 3427 (1962)
14.86 N.D. Lang: Phys. Rev. Lett. **55**, 230 (1985)
14.87 N.D. Lang: IBM J. Res. Dev., in press
14.88 R.J. Behm, W. Hösler, E. Ritter: To be published
14.89 M. Ringger, H. Hidber, R. Schlögl, P. Oelhafen, H.J. Güntherodt: Appl. Phys. Lett. **46**, 832 (1984)
14.90 P.A.M. Benistant, G.F.A. van de Walle, H. van Kempen, P. Wyder: To be published
14.91 G.K. Binnig, H. Rohrer, Chr. Gerber, E. Stoll: Surf. Sci. **144**, 321 (1984)
14.92 R.J. Behm, W. Hösler, E. Ritter, G. Binnig: J. Vac. Sci. Technol., in press
14.93 R.J. Behm, W. Hösler, E. Ritter, G. Binnig: Phys. Rev. Lett., in press
14.94 A.M. Barô, G. Binnig, H. Rohrer, Chr. Gerber, E. Stoll, A. Baratoff, F. Salvan: Phys. Rev. Lett. **52**, 1304 (1985)
14.95 R.M. Feenstra: IBM J. Res. Dev., in press
14.96 R.M. Tromp, R.J. Hamers, J.E. Demuth: Phys. Rev. Lett. **55**, 1303 (1985)
14.97 R.M. Feenstra, A.P. Fein: Phys. Rev. B**32**, 1394 (1985)
14.98 R.S. Becker, J.A. Golovchenko, B.S. Swartzentruber: Phys. Rev. Lett. **54**, 2678 (1985)
14.99 See, e.g., P. Heilmann, K. Heinz, K. Müller: Surf. Sci. **83**, 487 (1979)
14.100 D.G. Fedak, N.A. Gjostein: Surf. Sci. **8**, 77 (1967)
14.101 W. Moritz: Habilitationsschrift, Universität München (1984)
14.102 W. Moritz, D. Wolf: Surf. Sci. **163**, L655 (1985)
14.103 H.P. Bonzel, S. Ferrer: Surf. Sci. **118**, L263 (1982)
S. Ferrer, H.P. Bonzel: Surf. Sci. **119**, 234 (1982)
14.104 I.K. Robinson: Phys. Rev. Lett. **50**, 1145 (1983)
I.K. Robinson, Y. Kuk, L.C. Feldman: Phys. Rev. B**29**, 4762 (1984)
14.105 H. Jagodzinski, W. Moritz, D. Wolf: Surf. Sci. **77**, 233 (1978)
J.C. Campuzano, M.S. Forster, G. Jennings, R.F. Willis, W. Unertl: Phys. Rev. Lett. **54**, 2684 (1985)
14.106 R.M. Tromp, E.J. van Loenen: Surf. Sci. **155**, 441 (1985)
R.M. Tromp: Surf. Sci. **155**, 432 (1985)
14.107 K. Takyanagi, Y. Tanishiro, M. Takahashi: J. Vac. Sci. Technol. A3, 1502 (1985)

14.108 D.J. Chadi: Phys. Rev. B**30**, 4470 (1984)
14.109 L.C. Snyder: Surf. Sci. **140**, 101 (1984)
14.110 E.C. McRae, P.M. Petroff: Surf. Sci. **147**, 385 (1984), and references therein
14.111 E. Stoll: IBM J. Res. Dev., in press
14.112 J.A. Stroscio, W.H. Ho: Phys. Rev. Lett. **54**, 1573 (1985)
14.113 M.K. Debe, D.A. King: Surf. Sci. **81**, 193 (1979)
14.114 J.F. Wendelken, G.C. Wang: J. Vac. Sci. Technol. A**3**, 1593 (1985)
14.115 R.F. Willis: In *Proc. Many Body Phenomena at Surfaces*, ed. by D.C. Langreth, D. Newns, H. Suhl (Academic, New York 1984)
14.116 R.M. Feenstra, G.S. Oehrlein: Appl. Phys. Lett. **47**, 1136 (1985); J. Vac. Sci. Technol. B**3**, 1136 (1985)
14.117 W. Hösler, R.J. Behm, E. Ritter: IBM J. Res. Dev., in press
14.118 G. Comsa, G. Mechtersheimer, B. Poelsema: Surf. Sci. **119**, 159 (1982)
14.119 W. Hösler, E. Ritter, R.J. Behm: Ber. Bunsenges. Phys. Chem., in press
14.120 See, e.g., S.M. Davis, G.A. Somorjai: In *The Chemical Physics of Solid Surfaces and Heterogeneous Catalysis*, ed. by D.A. King, D.P. Woodruff (Elsevier, Amsterdam 1982)
14.121 A.E. Morgan, G.A. Somorjai: J. Chem. Phys. **51**, 3309 (1969)
14.122 K. Baron, D.W. Blakely, G.A. Somorjai: Surf. Sci. **41**, 157 (1974)
14.123 A.M. Barô, R. Miranda, J. Alaman, N. Garcia, G. Binnig, H. Rohrer, Ch. Gerber, J.L. Carrascosa: Nature (London) **315**, 253 (1985)
14.124 A.M. Barô, R. Miranda: IBM J. Res. Dev., in press
14.125 A. Humbert, J.K. Gimzewski, B. Reihl: Phys. Rev. B**32**, 4252 (1985)
14.126 H. Raether: Surf. Sci. **140**, 31 (1984)
14.127 H.J. Scheel, G. Binnig, H. Rohrer: J. Cryst. Growth **60**, 199 (1982)
14.128 J.K. Gimzewski, A. Humbert, D.W. Pohl, S. Veprek: Surf. Sci., in press
14.129 R. Miranda, N. Garcia, A.M. Baro, R. Garcia, J.L. Pena, H. Rohrer: Appl. Phys. Lett. **47**, 367 (1985)
14.130 N. Garcia, A.M. Barô, R. Miranda, H. Rohrer, Ch. Gerber, R. Garcia Cantu, J.L. Pena: Metrologia **21**, 135 (1985)
14.131 U. Dürig, D.W. Pohl, F. Rohner: IBM J. Res. Dev., in press; and to be published
14.132 P. Muralt, D.W. Pohl, W. Denk: IBM J. Res. Dev., in press
P. Muralt, D.W. Pohl: To be published
14.133 H.H. Farell, D.M. Levinson: Phys. Rev. B**31**, 3593 (1985)
14.134 G. Binnig, H. Fuchs, E. Stoll: To be published
14.135 R. Gomer: IBM J. Res. Dev., in press
14.136 R. Gomer: To be published
14.137 F.J. Himpsel, D.E. Eastman: Phys. Rev. B**18**, 5236 (1978)
N.E. Christensen: Phys. Rev. B**14**, 3446 (1976)
14.138 J.E. Demuth: Surf. Sci. **65**, 369 (1977)
14.139 G. Binnig, H. Fuchs, J. Kübler, F. Salvan, A.R. Williams: To be published
14.140 N.F. Mott: *Metal Insulator Transitions* (Taylor and Francis, London 1974)
14.141 R. Garcia, J.J. Saenz, N. Garcia: To be published
14.142 R.C. Jaklevic: Phys. Rev. **165**, 821 (1965)
14.143 R.S. Becker, J.A. Golovchenko, B.S. Swartzentruber: Phys. Rev. Lett. **55**, 987 (1985)
14.144 G. Binnig, K.H. Frank, H. Fuchs, N. Garcia, B. Reihl, H. Rohrer, F. Salvan, A.R. Williams: Phys. Rev. Lett. **55**, 991 (1985)
14.145 F. Salvan, H. Fuchs, A. Baratoff, G. Binnig: Surf. Sci., in press
14.146 K.H. Gundlach: Solid-State Electron. **9**, 949 (1966)
14.147 M.E. Alferieff, C.B. Duke: J. Chem. Phys. **46**, 938 (1967)
14.148 J. Maserijan, N. Zamani: J. Appl. Phys. **53**, 559 (1982)

14.149 T.W. Hickmott, P.M. Solomon, R. Fischer, H. Morkorc: Appl. Phys. Lett. **44**, 90 (1984)
14.150 See, e.g., V. Dose, W. Altmann, A. Goldmann, U. Kolac, J. Rogozig: Phys. Rev. Lett. **52**, 1919 (1984)
N. Garcia, B. Reihl, K.H. Frank, A.R. Williams: Phys. Rev. Lett. **54**, 591 (1985)
14.151 K. Giesen, F. Hage, F.J. Himpsel, H.J. Riess, W. Steinmann: Phys. Rev. Lett. **55**, 300 (1985)
14.152 P.D. Johnson, N.V. Smith: Phys. Rev. B**27**, 2577 (1983)
14.153 H. Eckardt, L. Fritsche, J. Noffke: J. Phys. F**14**, 97 (1984)
14.154 D.F. Woodruff, N.V. Smith, P.D. Johnson, W.D. Royer: Phys. Rev. B**26**, 2943 (1982)
14.155 G. Binnig, H. Fuchs, F. Salvan: Verh. Dtsch. Phys. Ges. (VI) **20**, 898 (1985)
14.156 N.J. Doran, A.M. Woolley: J. Phys. C**14**, 4257 (1981)
14.157 J.H. Coombs, J.B. Pethica: IBM J. Res. Dev., in press
14.158 R. Smoluchowski: Phys. Rev. **60**, 661 (1941)
14.159 K. Wandelt: J. Vac. Sci. Technol. A**2**, 802 (1984)

15. High-Resolution Electron Microscopy in Surface Science

D.J. Smith

Center for Solid State Science and Dept. of Physics,
Arizona State University, Tempe, AZ 85287, USA

A wide variety of diffraction, spectroscopy, and microscopy techniques are now available for the characterisation of surfaces, but only the microscopical methods, primarily using electrons, are able to provide direct real-space information about local inhomogeneities such as surface steps, terraces, domains, and defects. As a consequence of technical improvements, high-resolution electron microscopes in particular are nowadays capable of atomic imaging, and electron microscopists are already starting to utilise this capability in their studies of surfaces. Subnanometer surface detail can be resolved in the reflection imaging mode and atomic-scale features are visible in the transmission and profile imaging modes. The results already available indicate that these high-resolution electron microscopy (HREM) techniques should be indispensable to obtaining a detailed understanding of many surfaces and their macroscopic properties.

Our objective is to provide a comprehensive review of the applications of high-resolution electron microscopy in surface science. We exclude, for example, scanning electron microscopy (SEM) and scanning Auger microscopy (SAM) which are generally capable of moderate resolution (2-10 nm), and the interested reader is referred to recent reviews [15.1,2] for details of the relevance of these techniques in surface science investigations. Critical reviews of scanning tunneling microscopy and field emission microscopy, techniques which are complementary to HREM, are found in Chaps.13,14 of this volume. We begin here by describing various HREM approaches, in particular discussing their respective advantages and shortcomings in relation to surface imaging. The body of the review concentrates on the different materials and the particular surface features which have been studied. The desirability of generally improved (ultra-high) vacuum and the usefulness of certain accessories are stressed. Finally, the future outlook for applications of the technique is briefly discussed.

15.1 Imaging Methods

A detailed description of HREM imaging theory and applications is beyond the scope of this chapter and reference should be made to reviews and monographs elsewhere for further information [15.3-5]. For the uninitiated, and for later reference, a list of common acronyms is provided in Table 15.1. Reference to this list indicates that there is a multiplicity of HREM surface imaging modes but, as will become apparent, each of these has a different sensitivity for particular surface features so that there is often little choice in practice about which is the most appropriate mode to use when imaging a given surface or material.

The geometries for the different imaging modes can be understood by referring to the line drawings in Fig.15.1, which depict the electron microscope only in the region of the objective lens. Note that for the scanning methods, STEM and SREM, the geometry is identical except that the direction of the electron beam is reversed and the objective aperture and lens actually precede the sample.

Table 15.1. Common acronyms in electron microscopy

BF	Bright-Field
DF	Dark-Field
HREM	High-Resolution Electron Microscopy
REM	Reflection Electron Microscopy
RHEED	Reflection High-Energy Electron Diffraction
SAM	Scanning Auger Microscopy
SEM	Scanning Electron Microscopy
SREM	Scanning Reflection Electron Microscopy
STEM	Scanning Transmission Electron Microscopy
TED	Transmission Electron Diffraction
TEM	Transmission Electron Microscopy
WBDF	Weak-Beam Dark-Field

15.1.1 Transmission Electron Microscopy

There are two basic modes of TEM operation, namely the bright-field mode, where the transmitted (unscattered) beam contributes to the final image (Fig.15.1a), and the dark-field mode, where this beam is excluded (Fig. 15.1b). In the BF case, the microscopist has the option of varying the objective aperture size over a considerable range. When the size is chosen so as to exclude the diffracted (scattered) beams, one has the configuration normally used by material scientists for so-called diffraction contrast. In this case, a (crystalline) specimen is tilted to excite a particular diffracted beam, or systematic row of reflections. This imaging mode is sensitive to differences in specimen thickness, particularly in the vicinity of

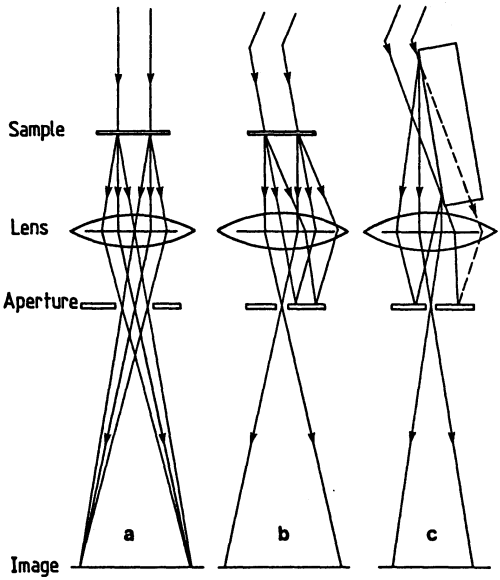

Fig.15.1a-c. Ray diagram showing the different geometries used for imaging surfaces in the electron microscope. (**a**) bright-field TEM; (**b**) axial dark-field TEM; (**c**) REM

the first extinction thickness where, due to dynamic scattering within the crystal, the transmitted beam intensity has a minimum (not usually zero). Single-atom-height steps can be seen with acceptable contrast in this manner [15.6], even under conditions where the effective (lateral) resolution of the same image, which is limited by the objective aperture size, might be only 0.5 nm or worse. A considerable contrast enhancement is sometimes possible by tilting the sample so that the incident beam direction is well away from the surface normal, whilst retaining the strongly excited systematic row of reflections [15.6,7].

An interesting, and particularly effective, variant of this method has been employed to image surface monolayers with atomic resolution in the lateral direction as well [15.8]. In face-centered cubic (fcc) metals it is well known [15.9-11] that termination, for example, of a {111} foil with a thickness of $3N \pm 1$ (N integer) atom layers corresponding to a partially filled unit cell, causes some weak scattering into normally forbidden diffracted beams. With an axial objective aperture large enough to allow passage of these beams, but still excluding the allowed diffracted beams of the bulk crystal, the BF image clearly reveals the surface lattice. A similar result, which again takes advantage of "forbidden" reflection to highlight thickness variations, also holds for the fcc <100> projection [15.8,12] and for molybdenum trioxide [15.13].

When the objective aperture size is increased to allow transmission of the bulk-diffracted beams through to the final viewing screen, the general

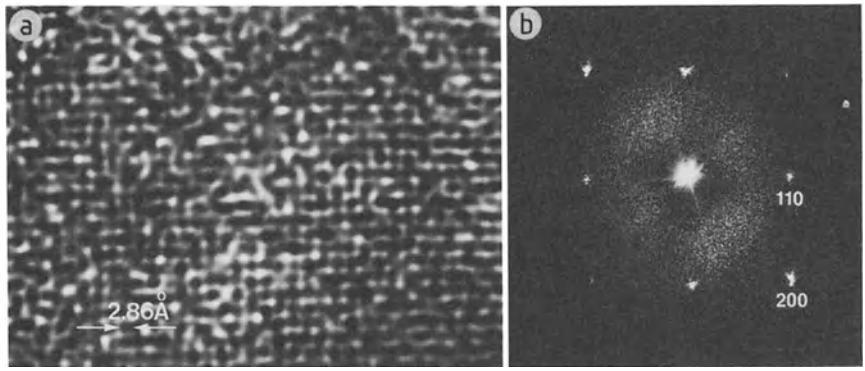

Fig.15.2. (**a**) Bright-field TEM image from a 40 Å gold foil which shows 2.86 Å periodicities due to {110}-type surface reflections. (**b**) Power spectrum (optical transform) of (**a**) showing the bulk {200} reflections as well as the surface {110} reflections. Reproduced with permission of *Krakow* [15.14]

result is a lattice image. For a sufficiently thin sample, and at the correct objective lens defocus, the lattice image may become a structure image in which the positions of the atomic columns are directly visible. Whilst structure images can be invaluable as a means of characterizing crystalline imperfections in some materials, surface detail is not usually visible except under further restricted conditions. In one particular case, the periodic 0.2 nm bulk lattice detail visible in micrographs of gold lattices was filtered out by a posteriori image processing [15.9,14] leaving the surface-sensitive information due to the forbidden reflections referred to above (Fig.15.2).

The other situation corresponds to the so-called *surface profile imaging* mode. Under circumstances where the specimen is thin enough for structure imaging to be applicable, and provided that the surface is devoid of impurities, then the image shows the crystal profile. If the microscope is capable of atomic resolution, then this profile image reveals the projected arrangement of atomic columns along the surface [15.15]. The information provided about the surface topography by the technique is direct, and often striking (see Sects.15.3.4 and 5) although, because the surface profile is projected onto the final image plane, no relative height discrimination is available.

The DF imaging mode is necessarily limited in resolution by the objective aperture size since the final image is usually formed from only one diffracted beam. (Note that it is customary to tilt the incident beam as indicated in Fig.15.1b so that the required diffracted beam passes axially through the objective lens thereby avoiding off-axis chromatic aberration effects.)

Nevertheless, as was the case for the small-aperture BF image, there are imaging conditions which are particularly sensitive to thickness variations within the sample. For example, if the sample is tilted to bring a higher-order diffracted beam to the Bragg condition, then the WBDF image formed from one of the lower-order reflections can show monolayer height differences [15.16]. For appropriate materials, such as fcc gold, an image formed with one of the forbidden reflections can also show atomic-level steps across the crystal, even though the lateral resolution might only be 1 nm [15.10]. A serious problem with this latter type of image, however, is that image intensities are generally very low, necessitating very long exposure times, and this places very stringent demands on specimen stage stability. Nowadays, alternative methods of surface imaging are generally used.

Finally, it is worth emphasizing that TEM images of surfaces, whether BF or DF, do not require changes from the normal operating procedures of the microscope and, in particular, the image magnification is unaltered. Imaging in REM is not quite so straightforward, and the image is foreshortened in one direction, but the extra effort is often justified by the detailed information and insight about many surfaces which can be provided only by this technique.

15.1.2 Reflection Electron Microscopy

The specimen configuration for the REM imaging mode is indicated schematically in Fig.15.1c. The incident electron beam is tilted through a considerable angle, typically 1.5 to 2°, strikes the steeply inclined surface of the sample at a glancing angle and gives rise to an electron diffraction pattern, usually called the Reflection High-Energy Electron Diffraction (RHEED) pattern, in the back focal plane of the objective lens. The REM image is then formed by passing one of these diffracted beams through the objective aperture, which is again usually arranged to be in the axial position in order to avoid off-axis chromatic aberration. In fact, obtaining a REM image is quite similar to obtaining a DF image. However, because of the different specimen-beam geometry, the REM image will be substantially foreshortened in the incident beam direction, typically being reduced by factors of 20 to 50, depending on such parameters as the diffracted beam used for imaging, the specific material and the operating voltage. A careful geometrical analysis is therefore necessary in practice to establish this foreshortening factor for any particular REM image: the interested reader is referred to [15.17] for a detailed and lucid explanation of this process.

The lateral resolution of the REM image, like the BF and DF TEM modes, is limited by the size of the objective aperture, and the only obvious restriction on this is that other diffracted beams must be prevented from contribu-

ting to the image (because the in-focus images occur at very different specimen heights). However, because of the usual compromise between resolution and depth of field, the best point-to-point resolutions are typically around 1 nm [15.18]. On the other hand, monolayer details such as ledges, extended terraces, and pits can be readily distinguished in REM images of extended surfaces and this capability has resulted in the technique attracting a great deal of recent attention, see Sect.15.3.3. This extraordinary sensitivity to near-surface detail arises from the use of the near-grazing incidence angle of the incident beam.

Recent work has shown that increased image contrast, and shorter exposure times, can be expected using a specific REM imaging condition which has been termed surface resonance [15.19]. This involves the use of an orientation where, as well as the Bragg reflection used for the REM image, another reflection parallel to the surface is also excited [15.19]. With any given material, it requires some extra manipulation of the incident beam and the specimen to reach this condition; a double-tilt specimen holder is essential.

15.2 Instrumentation and Accessories

A great advantage of all the techniques described above is that, in principle at least, surface images can be readily obtained from conventional TEM without instrumental modifications. In practice, the addition of certain accessories substantially increases the range of surface phenomena and types of materials which can be studied with useful and acceptable results. It is relatively straightforward, for example, to attach a TV camera and viewing screen to the base of a microscope column. Video recordings then enable dynamic events to be studied and analysed in detail [15.20]. A specimen heating cartridge makes it possible to investigate surface phase transitions [15.21], although stage drift and stability usually compromise the available resolution. Correction of image drift using on-line computer processing and higher speed electronic recording may, however, overcome this problem [15.22]. An energy-loss spectrometer can be used to investigate surface energy states [15.23,24] and to follow surface transformations induced by the electron beam [15.25].

Until recently, a major shortcoming of most tranmission electron microscopes with regard to surface imaging was the comparatively poor vacuum in the region of the specimen chamber (10^{-5} Torr or worse). It seems more than circumstantial that the recent activity and rapid increase of interest in TEM surface studies has coincided with a period when manufacturers have made

major efforts to improve the vacuum levels, and general cleanliness, of their latest TEM models. (Another factor has undoubtedly been the demands of many workers for convergent beam and microdiffraction facilities which require small probes). The transition to clean and dry pumping systems, for example with turbomolecular and ion sputtering pumps, has meant that, for many materials, it really does seem as though surface contamination arising from hydrocarbon cracking when the sample is in the electron beam is almost a relic of the past. The remaining, generally carbonaceous, overlayers can then be removed in several ways, depending on the material; by gentle heating; by etching during observation due to residual water vapour [15.26]; or by desorption processes induced by the electron beam [15.27].

In surface science terms, particularly if the interest is in metal or semiconductor surface reconstructions, these measures are still inadequate. Residual gas pressures at the specimen of 10^{-9} Torr or better are desirable, and it is also necessary to provide for specimen cleaning to remove the intrinsic surface contamination, as well as near-surface impurities. Attachments have been added to microscopes which allow these heating/cleaning cycles to be carried out with the sample in the column ready for imaging. Though clearly workable [15.21,28], the addition of such facilities to existing microscopes is not entirely satisfactory and it seems preferable to design the microscope and specimen stage as an integral unit from the outset [15.29].

15.3 Survey of Results

The results of high-resolution studies of surfaces are surveyed here, with separate subdivisions to highlight profile imaging (Sect.15.3.4) and the observation of dynamic processes (Sect.15.3.5); a further section (Sect.15.3.6) reviews the progress made with image calculations. For ease of reference, separate tables also summarise the surface imaging carried out under the various headings. In some cases, conference abstracts have been omitted where the same results appear to have been written up later in a journal publication.

15.3.1 Bright-Field Transmission Electron Microscopy

It seems remarkable, given the concurrent and widespread application of SEM to surface studies, that TEM was never seriously used to observe surfaces directly, except for a few isolated cases [e.g., 15.30,31], until within the last decade. Table 15.2 indicates that a wide spread of materials have since been observed in the BF TEM mode, more than half in the last few years. Most of the features observed have been related to local variations in the

Table 15.2. Surfaces studied by bright-field TEM

Surface	References
MgO	[15.6,30-34]
Si	[15.35-37]
Graphite	[15.38]
SiC	[15.39]
Au	[15.7,12,14,26,40-43]
Ag	[15.8,44-46]
Ag_2O/Au(111)	[15.47,48]
Diamond	[15.34]
Au, Pd, Ag/MgO	[15.49-51]

surface topography, namely surface steps in silicon [15.35,36] and several ceramics [15.30-33,38,39], surface roughness in Au [15.7,12,14,40-42] and Ag [15.8,44-46], and surface layer reconstructions in Ag_2O [15.47,48], Au{111} [15.26,43] and Si{111} [15.37] —see also Fig.15.2. Morphological changes have been followed with this imaging mode only in the case of MgO [15.30,31] and diamond [15.34] and when noble metals have been deposited on MgO [15.49-51]. In general, this is probably because the image contrast has been rather poor.

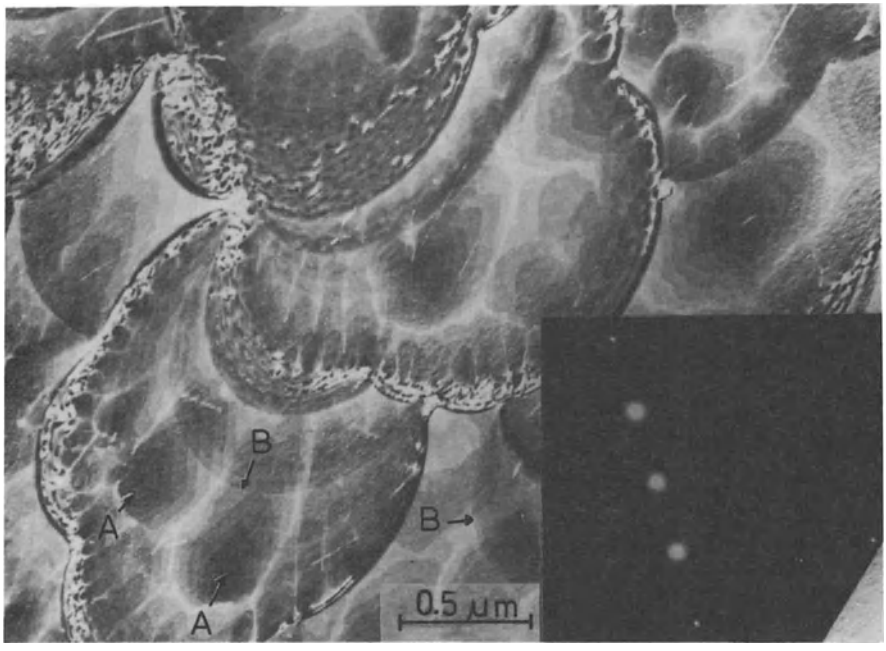

Fig.15.3. Bright-field image of a Au{111} film with a mean thickness of only 3.5 monolayers. Specimen tilted by 47° into a <105> direction of incidence, with (200) systematics excited. Growth spirals emerge at screw dislocations (*A*) and atomic-height steps (*B*) are clearly visible. Reproduced with permission of *Klaua* and *Bethge* [15.7]

Low contrast is certainly not a problem with the striking micrograph shown in Fig.15.3 which is from an Au foil estimated to have an average thickness of only 3.5 monolayers [15.7]. The high contrast of this image is due to the enhancement process referred to in Sect.15.1.1 whereby the crystal normal is tilted well away from the incident beam direction (47° in the case of Fig. 15.3) but with a systematic row of reflections still in the strongly diffracting condition. This particular result reinforces the view that it should prove worthwhile to search for similar imaging conditions with other materials.

15.3.2 Dark-Field Transmission Electron Microscopy

Image contrast is not a restriction with the DF TEM mode, particularly when advantage is taken of forbidden reflections to highlight variations in specimen thickness. However, because of the very low amplitude of the diffracted beams in this configuration [15.9,13], image intensity then becomes a serious limitation. The original images of MgO [15.16] and Au [15.10] attracted considerable attention but the typical exposure times of 60 s or more seem generally to have discouraged others from adopting the technique. Dynamic events clearly could not be followed in real time. Experimentation with the specimen-beam geometry can again lead to more favorable imaging conditions for particular materials, and an excellent example is the WBDF image of an Si foil in a <110> orientation shown in Fig.15.4 [15.52].

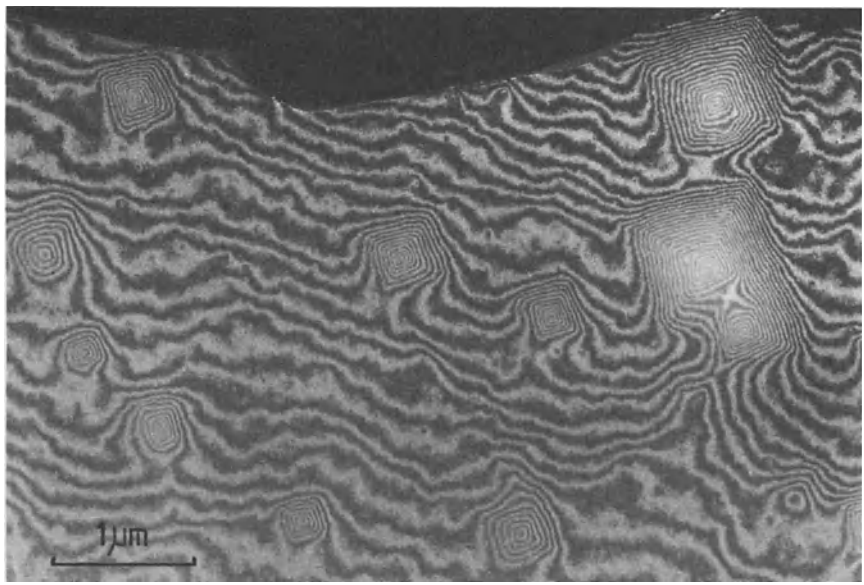

Fig.15.4. Weak-beam dark-field micrograph of a Si{100} plate recorded at 1 MeV. Note the atomic steps, particular around the etch pits. Reproduced with permission of *Lehmpfuhl* [15.52]

Table 15.3. Surfaces studied by dark-field TEM

Surface	References
MgO	[15.6,16,32,33]
Au	[15.7,10,11,53-60]
Pb/Ag/Au	[15.54,61-63]
Si	[15.52,64,65]

The list of materials studied by DF TEM is comparatively short (Table 15.3). Surface steps have been observed in MgO [15.6,16,32,33], Au{111} [15.7,10,11,53-55], and Au{100} [15.56]. A detailed comparison has been made of metal/metal epitaxy and overgrowths involving Pb, Ag, and Au [15.54, 61-63]. Surface reconstructions on Au{111} [15.57,58] and Si{111} [15.64,65] have also been investigated. Finally, a novel and interesting application to the characterization of exit-surface sputtering induced in thin gold foils by high-energy electron irradiation should be noted [15.59,60].

15.3.3 Reflection Electron Microscopy

Despite the complications introduced by the unusual geometry and by the image foreshortening, there is no doubt that REM is the most versatile HREM method for studying surfaces, particularly since bulk samples may be used essentially without modification. The advantages were appreciated thirty years ago [15.66] but the method was not really taken up seriously until the mid-seventies when it was realized that the images formed from diffracted beams under glancing incidence geometry had such exceptional sensitivity to the surface structure [15.67,68]. The technique has been extensively used during the past five years – see Table 15.4.

The characterization of surface topography has, in fact, been the most common application of REM and the materials studied include the ceramics

Table 15.4. Surfaces studied by REM

Surface	References
Graphite	[15.69]
Diamond	[15.70,71]
MgO	[15.72]
PbS (galena)	[15.71]
Fe_2O_3	[15.73]
$TiS_{1.5}$	[15.73]
Au	[15.17-19]
Pt	[15.17-19,69]
GaAs	[15.37,73,74]
GaP	[15.75]
$Ga_xAl_{1-x}As/GaAs$	[15.76-78]
Au/MgO	[15.49,79]
Si	[15.37,63,80-87]

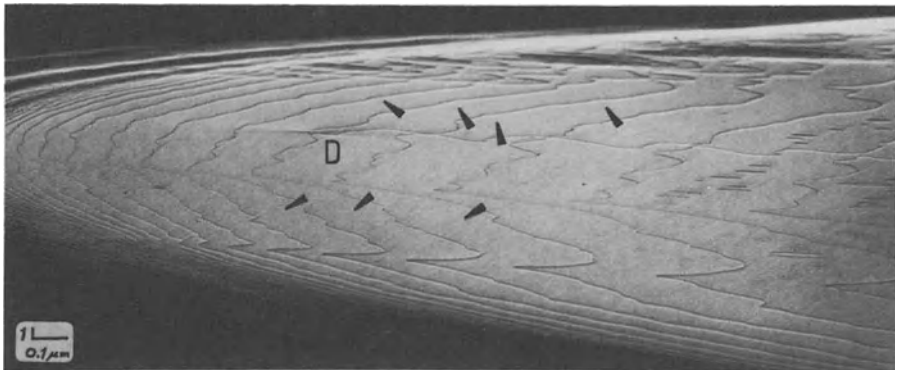

Fig.15.5. A REM image of Pt{111} surface showing atomic steps and a dislocation (*D*) emerging at the surface. Arrows indicate the "downwards" step direction. Reproduced with permission of *Hsu* [15.69]

graphite [15.69], diamond [15.70,71], and MgO [15.72], the minerals galena (PbS) [15.71] and hematite (Fe_2O_3) [15.73] as well as Au{111} [15.17-19] and Pt{111} [15.17-19,69] and the semiconductors GaAs{110} [15.37,73,74], GaP{110} [15.75] and $Ga_xAl_{1-x}As$/GaAs [15.76-78]. Gold deposited on MgO has also been observed [15.49,79]. The REM image of a Pt{111} surface shown in Fig.15.5 represents a good example of the technique. Reflection electron microscopy has been used for a comprehensive study of the Si{111} surface [15.62] and, in particular, to study the transformation from the room temperature (1 × 1) bulk lattice termination to the (7 × 7) reconstructed surface [15.80-82]. The controlling influence of surface steps and dislocations [15.83] and the effects of Au deposition [15.62,84] have also been studied. The process of oxidation of the Si{111} surface has been followed [15.85,86]. Another brief study of reconstructions on Si{111} and on GaAs{100} has also been published [15.37]. Different contrast at alternate steps in the layer compound $TiS_{1.5}$ has been observed [15.73]. Perhaps the most significant result from the REM work has been the determination of the order of the 7 × 7 to 1 × 1 Si{111} phase transition [15.83].

15.3.4 Profile Imaging

Just as REM is clearly the most versatile surface imaging mode, likewise there is no question that profile imaging at atomic resolution is the most immediate and striking. Dramatic effects are also visible using video recording (Sect.15.3.5). The work in this field is comparatively recent, having been initiated with observations of CdTe less than five years ago [15.88] but a considerable number of other materials have since been studied—see Table 15.5.

Table 15.5. Surfaces studied by profile imaging

Surface	References
CdTe[a]	[15.88]
Au[a]	[15.15,26,89-99]
Pb/Au	[15.100,101]
Al_2O_3	[15.102,103]
$ZnFeCrO_4$	[15.104,105]
ZrO_2	[15.106]
γ-Al_2O_3	[15.107]
UO_2	[15.108]
$Ti_2Nb_{10}O_{29}$	[15.27,108]
WO_3	[15.27,109]

[a]Also includes some real-time dynamic processes

Gold has attracted the most interest [15.15,26,89-99]. It is relatively inert, unlike other metals it does not develop an oxidation layer, and surface contaminants are easily desorbed by electron irradiation. Small Au particles were first studied [15.15,89] and it was found that topographical features such as steps and terraces could be readily seen. Direct evidence for a "missing-row" (2 × 1) reconstruction of the {110} surface was obtained [15.15] and careful image analysis indicated that the outermost atomic columns were relaxed outwards by about 20% [15.90,91]. Subsequent observations of extended Au foils failed to reveal a similar superstructure on {110}, although other interesting features were seen, including stacking faults on {111} [15.26], dislocations on {111} and {100} [15.26,92,93], and the development of a hill-and-valley morphology on {111} [15.26,92]. Figure 15.6 shows profile images of extended {110}, {111}, and {100} Au surfaces. Other dynamic events occurring on Au surfaces and small particles [15.94-99] are described below. The effects of evaporating Pb onto Au particles has most recently been studied [15.100-101].

Attention has also been directed toward the surface morphology of various oxide particles [15.102-109]. The characteristics of a new type of alumina particle have been investigated [15.102,103] and the structure of a complex spinel catalyst has been studied both before [15.104], and after [15.105], the material was used in a catalytic reaction. A profile image of this material indicating the presence of surface rafts, believed to be ZnO, is shown in Fig.15.7. Other oxides studied include ZrO_2 [15.106], γ-Al_2O_3

Fig.15.7. A <110> profile image of a $ZnCrFeO_4$ spinel crystallite showing surface growths, believed to be ZnO, on {111} faces as a result of prolonged use an an oxidation catalyst. Reproduced with permission of *Hutchison* [15.105]

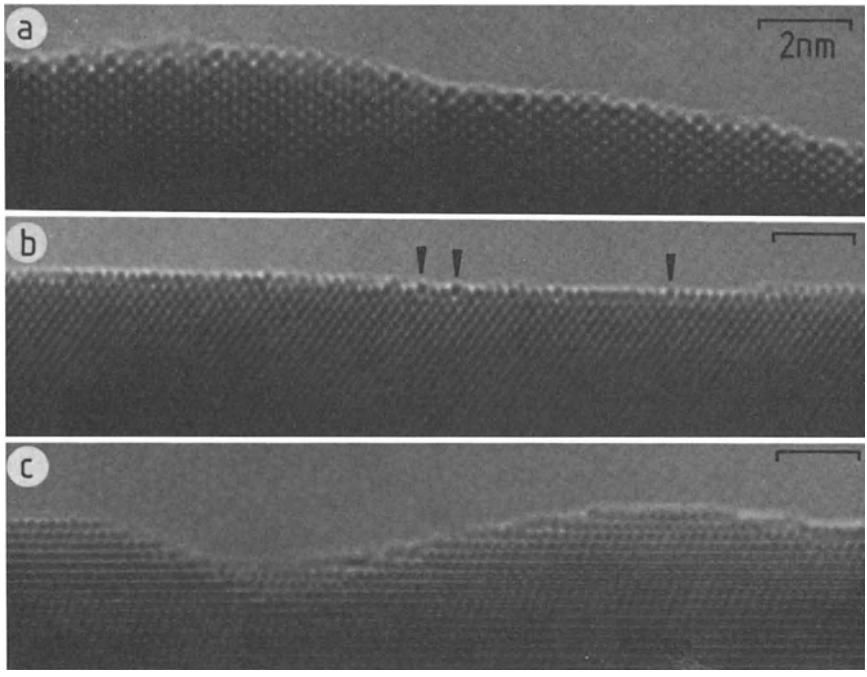

Fig.15.6a-c. Surface profile images comparing the atomic arrangements visible on extended Au surfaces. (**a**) {110}; (**b**) {100}; (**c**) {111}. Note the surface defects, believed to be dislocations, arrowed in (**b**) and the irregular hill-and-valley topography in (**c**). [15.26,92,93]

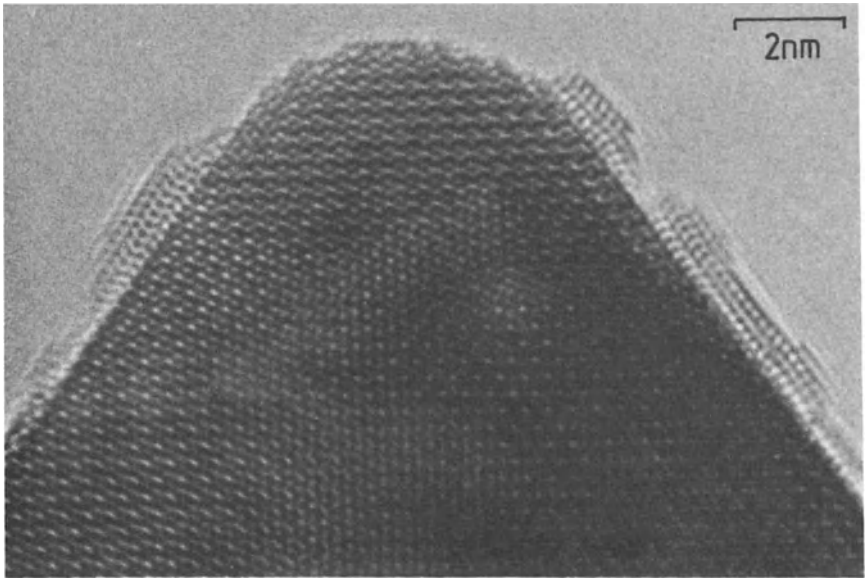

Fig.15.7. Caption see opposite page

[15.107], UO_2 [15.108], $Ti_2Nb_{10}O_{29}$ [15.27,108], and WO_3 [15.27,109]. Given the crucial role of surfaces and surface reactions in these and similar materials, many more studies can be anticipated in the near future.

15.3.5 Dynamic Processes

The earliest electron microscope observations of dynamic processes on surfaces, on the atomic scale, involved STEM in a DF imaging mode with signal manipulation being used to highlight the positions of single atoms, or clusters, on thin, low-contrast supports. The diffusion of Ag atoms [15.110,111] and U atoms [15.110-113] between successive scans was noted and estimates of jump frequencies and diffusion rates were derived. The initial TEM profile imaging of surface rearrangements on CdTe [15.88] and Au [15.94] involved sequential micrographs, but later Au studies used real-time video recordings [15.95-99] and included images photographed directly from the viewing monitor. Recursive filtering or image averaging were sometimes used but single TV frame images were often of adequate contrast and quality.

An unfortunate "shortcoming" of still micrographs, even those taken directly from the monitor, is that the impact of the dynamic events is somewhat lost. For example, Fig.15.8 shows images of a small Au particle and the hopping of Au columns between the surface sites is clearly visible. However, when viewed on the TV monitor, the effect is far more dramatic. One intriguing dynamic process recently observed in three separate laboratories, but not really understood, is the apparent presence of atom clouds just above, and interacting with, certain faces of the small Au particles [15.98,114,115]. The extent to which this process is affected by such factors as the microscope's residual gases, the specimen support, and the electron-beam voltage and current density remains to be determined.

15.3.6 Image Contrast Calculations

Electron microscopists have traditionally adopted a conservative attitude toward the interpretation of surface images. This is because, in common with photographic techniques, electron micrographs offer many possibilities for artifactual image detail. Accordingly, whenever the results of a novel approach to surface imaging have first appeared, they have, more often than not, been accompanied by calculations of diffracted beam intensities or by image simulations. In the particular case of profile images of Au surfaces, a comprehensive analysis has been carried out which even determined the accuracy (about 5%) with which the outward relaxation of the outermost {110} surface columns could be measured in experimental images [15.91]. Further

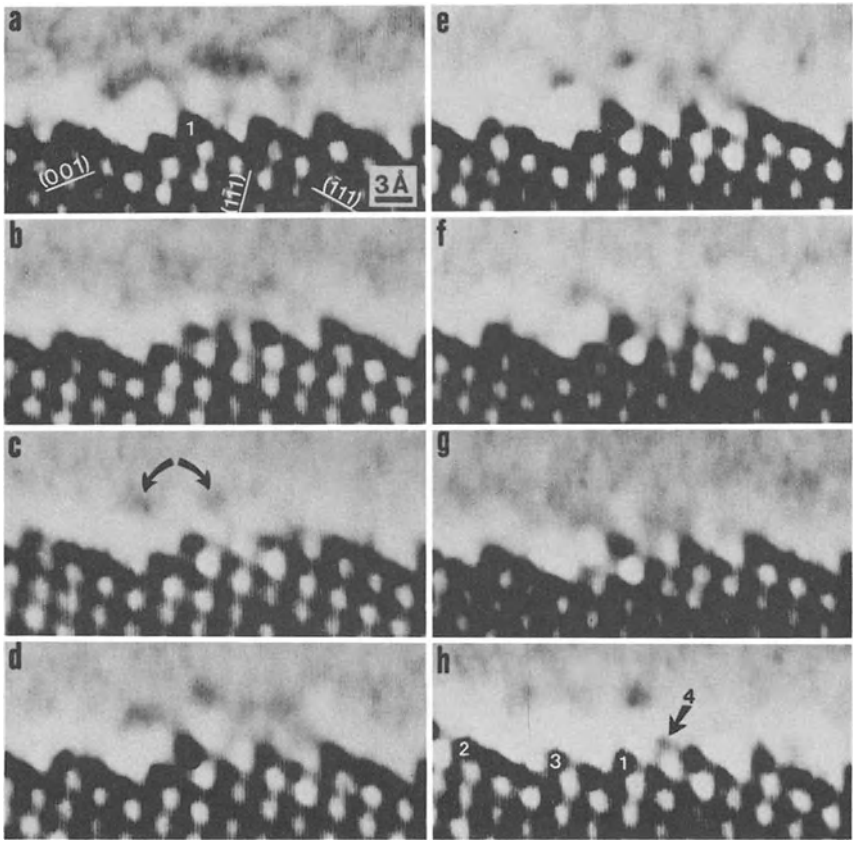

Fig.15.8a-h. Surface profile images of a small Au cluster photographed directly from the TV monitor showing rapid column "hopping" (total elapsed time <0.5s). The column marked 1 is changing position during the interaction; columns 2, 3 and 4 are new in (**h**). [15.98,99]

BF TEM image calculations for Au{100} [15.12,14,40,41] and Au{111} [15.42, 116] have confirmed that the electron micrographs really could be interpreted in terms of surface roughness, and simulations of Ag_2O reconstructions on Au{111} have also been reported [15.47]. Image simulations for a Pb monolayer on Ag{111}, and for a {100}Sn overgrowth on {100}SnTe, indicated that HREM imaging could provide information about the location of adsorbates under favorable imaging conditions [15.63]. Simulations also suggested that adatom sites on clean Si{111} surfaces could be determined with high contrast (40%) using BF imaging when the bulk crystal reflections were excluded and also indicated that the multiple scattering of surface superlattice Bragg beams interacting with bulk reflections may be a small effect [15.117]. Recent

image simulations predicted that the profile imaging method should readily be able to distinguish between different models for the Si{111} 7 × 7 surface reconstruction [15.118]. As yet, these predictions regarding Si{111} surface imaging have yet to be verified experimentally because of the difficulties involved in producing a clean surface. The appropriate absorption potential for use in profile imaging, where surface excitations are strong, remains to be determined.

Further studies have generally concentrated on calculations of diffracted beam intensities, rather than images, and several workers have shown, for example, how partially filled unit cells in Au{111} [15.9-11,53,55], in Si{111} [15.35], and in MoO_3 [15.13], result in "forbidden" reflections. Calculations confirmed that the contrast differences visible in WBDF images of MgO corresponded to monoatomic steps [15.6], and later studies investigated variations in image contrast with crystal thickness and incidence angle in order to determine the optimum BF imaging conditions for observing atomic steps in silver [15.44].

Relatively few calculations have been reported for the REM technique. Images of dislocations have been calculated [15.119] using many-beam dynamical theory, and similar computations were later compared with experimental micrographs [15.81]. The image contrast of surface steps has also been calculated and compared with some existing REM micrographs [15.120].

15.4 Perspective and Outlook

In order to judge the accomplishments of high-resolution electron microscopy with regard to surface science, it is useful and instructive to tabulate the various surface phenomena described above which have already been investigated by the different imaging methods. Table 15.6 indicates that, as well as a range of topographical features, a wide variety of surface processes and reactions have been studied. In some cases, the studies are clearly only preliminary and, indeed, the majority have been published only within the past few years. It might thus seem premature to state, categorically, that the HREM will prove to be an indispensable tool to the scientist interested in surfaces. On the other hand, a wealth of atomic-level detail is clearly available that is not accessible by other techniques. Even the scanning tunneling and the field ion and field electron emission microscopy methods, despite their impressive achievements in certain restricted geometrical configurations and highly specific materials, are not competitive with HREM in

Table 15.6. Surface features studied in HREM images

Topography	Steps Terraces Etch pits Adatoms Domains Defects (dislocations)
Surface rearrangements	Reconstructions
Dynamic processes	Atomic diffusion Phase transitions Surface reactions
Deposition	Growth kinetics Mechanics of growth Influence of reconstructions
Oxidation mechanisms Desorption processes Effect of annealing	

terms of their ability to study surface irregularities and inhomogeneities in a whole host of materials: real-time evolutionary studies are the province of HREM. These techniques also lack the ability of the HREM to search rapidly for interesting or significant events, or to change magnifications so that processes can be studied on many scales. The obvious shortcoming of much HREM work so far undertaken has been the comparatively poor control of the local specimen environment, and hence the likely presence of unknown impurities. Both these factors could have a considerable influence of the results obtained, particularly in the studies of dynamic processes. Nevertheless, the trend towards in situ treatments, coupled with true ultra-high vacuum in the specimen region, should soon settle any doubts about the validity of particular findings. It should also be appreciated that the "real" surfaces of many materials, which are so critical in many physical and chemical (particularly catalytic) processes, are usually not clean, regular, or homogeneous. It seems that HREM offers the best prospect for obtaining the vital, localized information required to explain the surface behavior and properties of such materials.

15.5 Further Reading

In this review of HREM in surface science, the objective has been to provide a general description of the methods, materials, and phenomena, including a comprehensive set of references to original studies. A number of review

papers are also available for those readers interested in pursuing particular aspects. Several describing the HREM technique and applications have already been mentioned [15.3-5]. Short overviews relating to surface imaging can be found in [15.121-124] and useful reviews of REM in [15.68,125,126]. Further papers which emphasize the value of in situ ultra-high-vacuum studies include [15.46,55,62,94,127,128]. Applications of scanning methods are summarized in [15.123,129,130]. Earlier volumes in the series "Chemistry and Physics of Solid Surfaces" have included articles reviewing the use of TEM methods to study small particles [15.131,132].

Acknowledgements. I would like to thank all those authors who have supplied me with details of their work, and I would particularly like to thank those who have so kindly provided the illustrative micrographs. I am grateful to my colleagues J.M. Cowley, R.W. Carpenter, Tung Hsu, and J.C.H. Spence for their constructive comments on an earlier draft of this chapter. Many of the results discussed here were obtained during research conducted at the High Resolution Electron Microscopy Facility in the Center for Solid State Science at Arizona State University, supported by the Division of Materials Research, National Science Foundation, grant DMR-8308501.

References

15.1 J.A. Venables: Ultramicroscopy **7**, 82 (1981)
15.2 J.A. Venables, D.R. Batchelor, M. Hanbuchen, C.J. Harland, G.W. Jones: In press
15.3 J.M. Cowley: *Diffraction Physics*, 2nd Ed. (North-Holland, Amsterdam 1981)
15.4 J.C.H. Spence: Experimental High Resolution Electron Microscopy (Clarendon, Oxford 1981)
15.5 D.J. Smith: Helv. Phys. Acta **56**, 463 (1983)
15.6 G. Lehmpfuhl, Y. Uchida: Ultramicroscopy **4**, 275 (1979)
15.7 M. Klaua, H. Bethge: Ultramicroscopy **11**, 125 (1983)
15.8 K. Takayanagi, K. Kobayashi, Y. Kodaira, Y. Yokoyama, K. Yagi: In Proc. 7th Int. Conf. HVEM, ed. by R.M. Fisher, R. Gronsky, K. Westmacott (Lawrence Berkeley Laboratory, Berkeley 1983) p.47
15.9 D.F. Lynch: Acta Crystallogr., Sect. A**27**, 299 (1971)
15.10 D. Cherns: Philos. Mag. **30**, 549 (1974)
15.11 J.C.H. Spence: "Developments in Electron Microscopy and Analysis", Inst. Phys. Conf. Ser. **32**, 257 (1975)
15.12 W. Krakow, D.G. Ast: Surf. Sci. **58**, 485 (1976)
15.13 P. Goodman, A.F. Moodie: Acta Crystallogr., Sect. A**30**, 280 (1974)
15.14 W. Krakow: Ultramicroscopy **4**, 55 (1979)
15.15 L.D. Marks, D.J. Smith: Nature (London) **303**, 316 (1983)
15.16 K. Kambe, G. Lehmpfuhl: Optik (Stuttgart) **42**, 187 (1975)
15.17 Tung Hsu, J.M. Cowley: Ultramicroscopy **11**, 239 (1983)
15.18 Tung Hsu: Ultramicroscopy **11**, 167 (1983)
15.19 Y. Uchida, G. Lehmpfuhl, J. Jager: Ultramicroscopy **15**, 119 (1984)

15.20 D.J. Smith: J. Vac. Sci. Technol. B3, 1563 (1985)
15.21 K. Takayanagi, K. Yagi, K. Kobayashi, G. Honjo: J. Phys. E**11**, 441 (1978)
15.22 P. Atkin, K.C.A. Smith: In *Electron Microscopy 1982*, Vol.1 (Deutsche Gesellschaft für Elektronenmikroskopie e.V., Frankfurt 1982) p.525
15.23 J.M. Cowley: Surf. Sci. **114**, 587 (1982)
15.24 O.L. Krivanek, Y. Tanishiro, K. Takayanagi, K. Yagi: Ultramicroscopy **11**, 215 (1983)
15.25 N.J. Long, A.K. Petford: Unpublished results
15.26 L.D. Marks, D.J. Smith: Surf. Sci. **143**, 495 (1984)
15.27 D.J. Smith, L.A. Bursill: Ultramicroscopy **17**, 387 (1985)
15.28 R.J. Wilson, P.M. Petroff: Rev. Sci. Instrum. **54**, 1534 (1983)
15.29 G. Honjo, K. Yagi, K. Takayanagi, S. Nagakura, S. Katagiri, M. Kubozoe, I. Matsui: In *Electron Microscopy 1980*, Antwerp 1980, Vol.4, ed. by P. Brederoo, J. van Landuyt (Seventh European Congress on Electron Microscopy Foundation, Leiden 1980) p.22
15.30 A.F. Moodie, C.E. Warble: Philos. Mag. **16**, 891 (1967)
15.31 A.F. Moodie, C.E. Warble: J. Cryst. Growth **10**, 26 (1971)
15.32 G. Lehmpfuhl, Y. Uchida: In Proc. 37th Annu. Meet. EMSA, San Antonio 1979, ed. by G.W. Bailey (Claitors, Baton Rouge, LA 1979) p.208
15.33 G. Lehmpfuhl, Y. Uchida: Inst. Phys. Conf. Ser. **52**, 393 (1980)
15.34 L.A. Bursill: Chem. Scr. **14**, 83 (1978-1979)
15.35 S. Iijima: Ultramicroscopy **6**, 41 (1981)
15.36 Y. Uchida, G. Lehmpfuhl, U. Klengler: In *Electron Microscopy 1982*, Vol.2 (Deutsche Gesellschaft für Elektronenmikroskopie e.V., Frankfurt 1982) p.289
15.37 P. Petroff: Mat. Res. Soc. Symp. Proc. **31**, 117 (1984)
15.38 S. Iijima: Optik (Stuttgart) **47**, 437 (1977)
15.39 S. Iijima, Tung Hsu: In Proc. 38th Annu. Meet. EMSA, Reno 1980, ed. by G.W. Bailey (Claitors, Baton Rouge, LA 1980) p.376
15.40 W. Krakow, G. Trafas: In Proc 39th Annu. Meet. EMSA, Atlanta 1981, ed. by G.W. Bailey (Claitors, Baton Rouge, LA 1981) p.20
15.41 W. Krakow: Surf. Sci. **111**, 503 (1981)
15.42 W. Krakow: Thin Solid Films **93**, 235 (1982)
15.43 G. Nihoul, K. Abdelmoula, J.J. Metois: Ultramicroscopy **12**, 353 (1984)
15.44 G. Lehmpfuhl, K. Takayanagi: Ultramicroscopy **6**, 195 (1981)
15.45 K. Takayanagi: Jpn. J. Appl. Phys. **22**, L4 (1983)
15.46 K. Takayanagi, K. Yagi: Trans. Jpn. Inst. Met. **24**, 337 (1983)
15.47 W. Krakow: Mat. Res. Soc. Symp. Proc. **31**, 189 (1984)
15.48 W. Krakow: Surf. Sci. **140**, 137 (1984)
15.49 J.M. Cowley, Z.C. Kang: Ultramicroscopy **11**, 131 (1983)
15.50 C.E. Warble, J.M. Cowley: In Proc. 41st Annu. Meet. EMSA, Phoenix 1983, ed. by G.W. Bailey (San Francisco Press, San Francisco 1983) p.319
15.51 E.A. Lodge, J.M. Cowley: Ultramicroscopy **13**, 213 (1984)
15.52 Y. Uchida, G. Lehmpfuhl, F. Fujimoto: In 4th Int. Conf. HVEM, Toulouse 1975, ed. by B. Jouffrey, P. Favard (Société Francaise de Microscopie Electronique, Paris 1976) p.113
15.53 P.J.F. Levitt, A. Howie: J. Microsc. (Oxford) **116**, 89 (1979)
15.54 K. Yagi, K. Takayanagai, K. Kobayashi, N. Osakabe, Y. Tanishiro, G. Honjo: Surf. Sci. **86**, 174 (1979)
15.55 C.J. Roussouw, S.E. Donnelly, D.F. Lynch: Ultramicroscopy **16**, 41 (1985)
15.56 K. Takayanagi: J. Microsc. (Oxford) **136**, 287 (1984)
15.57 J.C. Heyraud, J.J. Metois: Surf. Sci. **100**, 519 (1980)
15.58 Y. Tanishiro, H. Kanamori, K. Takayanagi, K. Yagi, G. Honjo: Surf. Sci. **111**, 395 (1981)
15.59 D. Cherns, F.J. Minter, R.S. Nelson: Nucl. Instrum. Methods **136**, 369 (1976)
15.60 D. Cherns: Philos. Mag. **36**, 1429 (1977)

15.61 K. Takayanagi: Surf. Sci. **104**, 527 (1981)
15.62 K. Takayanagi, H. Kanamori, Y. Tanishiro, K. Yagi: Acta Crystallogr., Sect. A**37**, C-300 (1981)
15.63 K. Takayanagi: Ultramicroscopy **8**, 145 (1982)
15.64 K. Takayanagi, Y. Tanishiro, M. Takahashi, S. Takahashi: J. Vac. Sci. Technol. A3, 1502 (1985)
15.65 P. Petroff, R.J. Wilson: Phys. Rev. Lett. **51**, 199 (1983)
15.66 J.W. Menter: J. Photogr. Sci. **1**, 12 (1953)
15.67 P.E. Hojlund-Nielsen, J.M. Cowley: Surf. Sci. **54**, 340 (1976)
15.68 J.D. Landry, G.G. Hembree, P.E. Hojlund-Neilsen, J.M. Cowley: In *Scanning Electron Microscopy/1976*, ed. by O. Johari (IITRI, Chicago 1976) p.239
15.69 T. Hsu, J.M. Cowley: In *The Structure of Surfaces*, ed. by M.A. Van Hove, S.Y. Tong, Springer Ser. Surf. Sci., Vol.2 (Springer, Berlin, Heidelberg 1985) p.55
15.70 Z.C. Kang: J. Micr. Spectr. Electron. **7**, 33 (1982)
15.71 Tung Hsu, S. Iijima: *Electron Microscopy 1982*, Vol.1 (Deutsche Gesellschaft für Elektronenmikroskopie e.V., Frankfurt 1982) p.301
15.72 Y. Uchida, J. Jager, G. Lehmpfuhl: Ultramicroscopy **13**, 325 (1984)
15.73 S. Iijima, Tung Hsu: *Electron Microscopy 1982*, Vol.1 (Deutsche Gesellschaft für Elektronenmikroskopie e.V., Frankfurt 1982) p.293
15.74 T. Hsu, S. Iijima, J.M. Cowley: Surf. Sci. **137**, 551 (1984)
15.75 N. Yamamoto, J.C.H. Spence: Thin Solid Films **104**, 43 (1983)
15.76 N. Yamamoto, S. Muto: Jpn. J. Appl. Phys. **23**, 2804 (1984)
15.77 B.C. Coonan, K.-H. Kuesters, C.B. Carter, Tung Hsu, G. Wicks: Philos. Mag. A**50**, 849 (1984)
15.78 Tung Hsu: J. Vac. Sci. Technol. B**4**, 1035 (1985)
15.79 J.M. Cowley: Ultramicroscopy **7**, 181 (1981)
15.80 N. Osakabe, Y. Tanishiro, K. Yagi, G. Honjo: Surf. Sci. **97**, 393 (1980)
15.81 N. Osakabe, Y. Tanishiro, K. Yagi, G. Honjo: Surf. Sci. **102**, 424 (1981)
15.82 Y. Tanishiro, K. Takayanagi, K. Yagi: Ultramicroscopy **11**, 95 (1983)
15.83 N. Osakabe, Y. Tanishiro, K. Yagi, G. Honjo: Surf. Sci. **109**, 353 (1981)
15.84 Y. Tanishiro, K. Takayanagi, K. Kobayashi, K. Yagi: Acta Crystallogr. Ser. A**37**, C-300 (1981)
15.85 N. Shimizu, Y. Tanishiro, K. Kobayashi, K. Takayanagi, K. Yagi: Ultramicroscopy **18**, 453 (1985)
15.86 K. Yagi, K. Kobayashi, Y. Tanishiro, K. Takayanagi: Thin Solid Films **126**, 95 (1985)
15.87 Tung Hsu: In 3rd Asian-Pacific Conf. E.M., Singapore 1984, ed. by Chung Mui Fatt (Applied Research Corporation, Singapore 1984), p.242
15.88 R. Sinclair, T. Yamashita, F.A. Ponce: Nature (London) **290**, 386 (1981)
15.89 D.J. Smith, L.D. Marks: Proc. 7th Int. Conf. HVEM, Berkeley 1983, ed. by R.M. Fisher, R. Gronsky, K. Westmacott (Lawrence Berkeley Laboratory, Berkeley 1983) p.53
15.90 L.D. Marks: Phys. Rev. Lett. **51**, 1000 (1983)
15.91 L.D. Marks: Surf. Sci. **139**, 281 (1984)
15.92 D.J. Smith, L.D. Marks: Ultramicroscopy **16**, 101 (1985)
15.93 L.D. Marks, D.J. Smith: Surf. Sci. **157**, L367 (1985)
15.94 D.J. Smith, L.D. Marks: Mat. Res. Soc. Symp. Proc. **41**, 129 (1985)
15.95 D.J. Smith, L.D. Marks: Surf. Sci., in press
15.96 L.R. Wallenberg, J.-O. Bovin, G. Schmid: Surf. Sci. **156**, 256 (1985)
15.97 S. Iijima, T. Ichihashi: Jpn. J. Appl. Phys. **24**, L125 (1985)
15.98 J.-O. Bovin, L.R. Wallenberg, D.J. Smith: Nature (London) **317**, 49 (1985)
15.99 L.R. Wallenberg, D.J. Smith, J.-O. Bovin: Naturwissenschaften **72**, 539 (1985)
15.100 K. Yagi: In 3rd Asian-Pacific Conf. E.M., Singapore 1984, ed. by Chung Mui Fatt (Applied Research Corporation, Singapore 1984) p.232

15.101 Yokoyana et al.: To be published
15.102 S. Iijima: Jpn. J. Appl. Phys. **23**, L347 (1984)
15.103 S. Iijima, S. Ichikawa: J. Catal. **94**, 313 (1985)
15.104 N.A. Briscoe, J.L. Hutchinson: Inst. Phys. Conf. Ser. **68**, 249 (1984)
15.105 J.L. Hutchison, N.A. Briscoe: Ultramicroscopy **18**, 435 (1985)
15.106 C.E. Warble: Ultramicroscopy **15**, 301 (1984)
15.107 C.E. Warble: J. Mater. Sci., in press
15.108 D.J. Smith, L.A. Bursill, L.D. Marks, Peng Ju Lin: In Proc. 43rd Annu. Meet. EMSA, Louisville 1985, ed. by G.W. Bailey (San Francisco Press, San Francisco 1985) p.256
15.109 L.D. Marks, A.K. Petford, M. O'Keeffe: In Proc. 43rd Annu. Meet. EMSA, Louisville 1985, ed. by G.W. Bailey (San Francisco Press, San Francisco 1985) p.266
15.110 J.P. Langmore, M.S. Isaacson, A.V. Crewe: In Proc. 32nd Annu. Meet. EMSA, St. Louis 1974, ed. by G.W. Bailey (Claitors, Baton Rouge, LA 1974) p.378
15.111 M.S. Isaacson, J. Langmore, N.W. Parker, D. Kopf, M. Utlaut: Ultramicroscopy **1**, 359 (1976)
15.112 M.S. Isaacson, D. Kopf, M. Utlaut, N.W. Parker, A.V. Crewe: Proc. Nat. Acad. Sci. U.S.A. **14**, 1802 (1977)
15.113 J.S. Wall, J.F. Hainfield, J.W. Bittner: Ultramicroscopy **3**, 81 (1978)
15.114 S. Iijima: Paper presented at Arizona State University Centennial Conference on HREM (Scottsdale, January 1985)
15.115 J.-O. Bovin, L.R. Wallenberg: Paper presented at Arizona State University Centennial Conference on HREM (Scottsdale, January 1985)
15.116 W. Krakow: Inst. Phys. Conf. Ser. **61**, 365 (1982)
15.117 J.C.H. Spence: Ultramicroscopy **11**, 117 (1983)
15.118 G.J. Wood, O.L. Krivanek: Proc. 43rd Annu. Meet. EMSA, Louisville, 1985, ed. by G.W. Bailey (San Francisco Press, San Francisco 1985) p.262
15.119 H. Shuman: Ultramicroscopy **2**, 361 (1977)
15.120 J.M. Cowley, Lianmao Peng: Ultramicroscopy **16**, 59 (1985)
15.121 A. Howie: Inst. Phys. Conf. Ser. **61**, 419 (1982)
15.122 A. Howie: In *Quantitative Electron Microscopy*, ed. by J.N. Chapman, A.J. Craven (Scottish Universities Summer Schools in Physics, Edinburgh 1984) pp.37-43
15.123 J.M. Cowley: Mat. Res. Soc. Symp. Proc. **31**, 177 (1984)
15.124 D.J. Smith: Contem. Physics, in press
15.125 Tung Hsu, J.M. Cowley: Mat. Res. Soc. Symp. Proc. **41**, 121 (1985)
15.126 Tung Hsu: Norelco Rep. **31**, 1 (1984)
15.127 K. Yagi: In 38th Annu. Meet. EMSA, Reno 1980, ed. by G.W. Bailey (Claitors, Baton Rouge, LA 1980) p.290
15.128 K. Yagi, K. Takayanagi, G. Honjo: Crystals, Growth, Properties and Applications **7**, 47 (1982)
15.129 J.M. Cowley: In *Scanning Electron Microscopy/1982*, ed. by O. Johari, Vol.1 (SEM Inc., Chicago 1982) p.51
15.130 J.M. Cowley: ACS Symp. Ser. **353**, 248 (1984)
15.131 M.J. Yacaman, K. Heinemann, H. Poppa: In *Chemistry and Physics of Solid Surfaces*, Vol.III, ed. by R. Vanselow, W. England (CRC, Boca Raton, FL 1982) p.109
15.132 M.J. Yacaman: In *Chemistry and Physics of Solid Surfaces*, ed. by R. Vanselow, R. Howe, Springer Ser. Chem. Phys., Vol.35 (Springer, Berlin, Heidelberg 1984) p.183

16. Surface Electronic States

F.J. Himpsel

IBM T.J. Watson Research Center, Yorktown Heights, NY 10598, USA

To characterize a surface completely, one needs to know the position and motion of atoms and electrons. In this chapter, we focus on the electronic part and assume that the atomic structure and atomic motion (e.g., surface vibrations) have been determined already by using techniques as described in several other parts of this series. To characterize an electron in a crystalline solid, it is sufficient to know its quantum numbers, i.e., energy, momentum, spin, and angular (point group) symmetry. For disordered solids, some of these quantum numbers become meaningless and it is useful to think in terms of a molecular picture where only the immediate neighborhood of an atom is considered, which exhibits short-range order. In this case, the characteristic quantities are energy levels, the coordination number, the oxidation state, etc.

In selecting the surfaces to study, one can follow two extremes. In basic physics, it is desirable to have a very simple system, e.g., a well-ordered surface with constituents of low atomic number (typical examples: hydrogen on "jellium" and the Si{111} 2×1 surface). For such systems, one can measure all quantum numbers and perform principles from first calculations which determine atomic and electronic structure with the atomic number and crystallographic orientation of the surface as the only input. As a consequence, one has a detailed understanding of the electronic structure and can learn from the calculation how the surface structure is established by minimizing the energy of electrons and ion cores. Unfortunately, very few of these ideal surfaces are realized in nature and almost none of them are relevant to technology. Therefore, it is useful to go to the other extreme of mostly disordered surfaces and interfaces with inhomogeneous stoichiometry, such as dispersed transition metal catalysts and the Si/SiO_2 interface. The knowledge obtained from a model system can be transferred to a complex case by gradually increasing the complexity of the problem. Such an example will be discussed for the etching of silicon surfaces by fluorine.

To demonstrate the power of various surface spectroscopies, we will discuss a variety of surfaces, starting with the idealized Si{111} 2×1 sur-

face and moving to the more complex practice-oriented Si-SiO_2 interface. The methods developed here are applicable to many active fields of surface science, such as chemical reactions at transitiom metal surfaces and the formation of semiconductor interfaces. Examples will be chosen from among semiconductor surfaces and interfaces which have been the author's principal research area in recent years. There has been a long-standing interest in semiconductor surfaces stimulated by the increasing engagement of the semiconductor industry. The principal motivations for studying surfaces and interfaces come from the trend to ever smaller structures and from more and more sophisticated processing methods involving surface chemical reactions. The characteristic length scale of semiconductor devices [16.1] has been decreasing exponentially over the past decades, with a reduction by a factor of 2 every 7 years. Within the next decade, a new regime will be reached, where the device dimensions become comparable with several characteristic lengths (e.g., the Debye screening length, the diffusion length, the de Broglie wavelength). As a consequence, the performance of the device is determined by surface and interface properties. For example, charge carriers can freely cross the active volume of the device and be trapped at an interface where they may get lost by recombination or stay and lead to charging. There is an increasing urge to understand chemical reactions at semiconductor surfaces because many essential processing steps have to be considered more an art than a science at the present time. Typical examples are oxidation [16.2], reactive ion etching [16.3], chemical vapor deposition, and molecular beam epitaxy. In most applications, one knows from trial and error how to chose the process parameters to achieve a desired result.

16.1 Experimental Techniques

The experimental technique used to study electronic states at a surface depends on the choice of the problem. For ideal surfaces, one gets the largest amount of information from valence states because they are involved in the chemical bonding. For complex surfaces, the information hidden in the valence electronic structure tends to be irretrievable and one has to use core levels which are simpler to analyze. They reflect the local order around an atom which remains for most systems in spite of long-range disorder. In narrowing down the choice of a surface spectroscopy it is useful to look at a scheme like Table 16.1 where various spectroscopies are classified according to the probing particles. Note that only techniques relevant to the electronic structure are shown; techniques giving the atomic structure are omitted. For gen-

Table 16.1. Spectroscopies that can be used for measuring electronic states at the surface

Incoming Particle	Outgoing Particle: Photon	Outgoing Particle: Electron, positron	Outgoing Particle: Ion, atom
Photon	Optical Sp. Luminescence Raman Sp.	Photoemission Auger Sp.	Photon Stimulated Desorption
Electron, Positron	Inverse Photoemission Appearance Pot. Sp. Positron Annhilation	Electr. En. Loss Sp. Auger Sp. Appearance Pot. Sp.	Electron Stimulated Desorption
Ion, Atom	Chemoluminescence	Ion Neutralization Sp. Penning Ionization Sp.	Secondary Ion Sp.

eral purposes one would prefer a spectroscopy that involves electronic transitions only and not atomic motion, i.e., the Franck-Condon principle should be valid. With atoms or ions in the incoming or outgoing channel, this is difficult to achieve. Therefore, we will focus on techniques involving photons and electrons, although atoms and ions do have advantages, such as sensitivity to the outermost atomic layer only. Photoemission and its time-reversed counterpart, inverse photoemission, are special because of two features:

(i) They are able to probe both energy and momentum of electrons.

(ii) They measure absolute electron energies. Most other spectroscopies measure differences between energy levels and not their absolute position. Photoemission and inverse photoemission are complementary to each other since they probe occupied and unoccupied states, respectively (lower states in Fig.16.1). There is some overlap for states above the vacuum level (upper states in Fig.16.1) where the final state in photoemission corresponds to the time-reversed initial state in inverse photoemission.

In core level spectroscopy one wants to optimize two parameters: the surface sensitivity and the energy resolution. Using photoelectron spectroscopy, the surface sensitivity is determined by the mean free path of the photoelectrons, which has a minimum (about 4 Å) for kinetic energies of about 50 eV [16.4]. For higher kinetic energies an electron becomes more penetrating due to its speed and for lower kinetic energies it cannot lose energy to the solid because excitations of the solid (e.g., plasmons) have a threshold. In order to achieve a certain kinetic energy for the photoelectron, we have to tune the photon energy to the binding energy of the core level. The optimum tunable light source is synchrotron radiation [16.5]. It was used for the core level studies given in this article. In order to estimate the spectral range that is required for core level spectroscopy, one can pick the sharpest

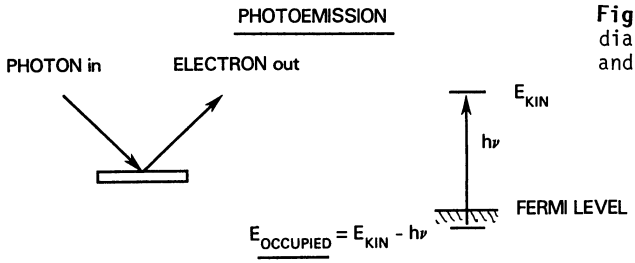

Fig.16.1. Schematic energy diagrams for photoemission and inverse photoemission

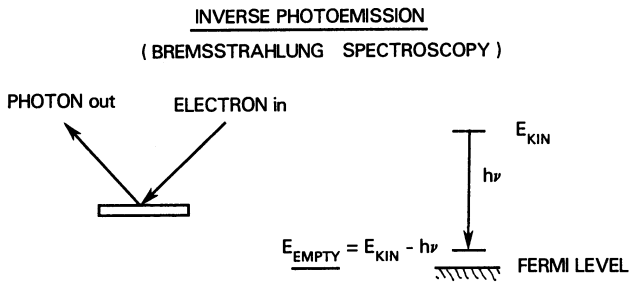

H 1s 14																	He 1s 25
Li 1s 55	Be 1s 112											B 1s 189	C 1s 284	N 1s 410	O 1s 543	F 1s 698	Ne 1s 870 2p 22
Na 2p 31	Mg 2p 49											Al 2p 73	Si 2p 100	P 2p 135	S 2p 163	Cl 2p 200	Ar 2p 248 3p 16
K 2p 295 3p 18	Ca 2p 346 3p 25	Sc 2p 399	Ti 2p 454	V 2p 512	Cr 2p 574	Mn 2p 639	Fe 2p 707	Co 2p 778	Ni 2p 853	Cu 2p 933	Zn 3d 10	Ga 3d 19	Ge 3d 29	As 3d 42	Se 3d 55	Br 3d 69	Kr 3d 94 4p 14
Rb 3d 112 4p 15	Sr 3d 134 4p 20	Y 3d 156	Zr 3d 179	Nb 3d 202	Mo 3d 228	Tc 3d 253	Ru 3d 280	Rh 3d 307	Pd 3d 335	Ag 3d 368	Cd 4d 11	In 4d 16	Sn 4d 24	Sb 4d 32	Te 4d 40	I 4d 50	Xe 4d 68 5p 12
Cs 4d 78 5p 12	Ba 4d 90 5p 15	La 4d 103	Hf 4f 14	Ta 4f 22	W 4f 31	Re 4f 41	Os 4f 51	Ir 4f 61	Pt 4f 71	Au 4f 84	Hg 5d 8	Tl 5d 13	Pb 5d 18	Bi 5d 24	Po 5d 31	At 5d 40	Rn 5d 48 6p 11
Fr 5d 58 6p 15	Ra 5d 68 6p 19	Ac 5d 80															

Ce 4d 109 4f 1	Pr 4f 3	Nd 4f 5	Pm 4f 5	Sm 4f 5	Eu 4f 2	Gd 4f 8	Tb 4f 2	Dy 4f 4	Ho 4f 5	Er 4f 5	Tm 4f 5	Yb 4f 1	Lu 4f 7
Th 5d 85	Pa 5d 94	U 5f 1	Np 5f	Pu 5f 2	Am 5f	Cm 5f	Bk 5f	Cf 5f	Es 5f	Fm 5f	Md 5f	No 5f	Lw 5f

Fig.16.2. The sharpest core levels for each element taking into account Auger lifetime broadening [16.6] and band dispersion [16.7], with their binding energies [eV]

core level for each element, as done in Fig.16.2. The intrinsic lifetime broadening is determined by Auger decay (see the calculation in [16.6]). For shallow core levels this width is increased by band dispersion [16.7]. Many other mechanisms exist (e.g., phonon broadening) which tend to broaden all core levels of a given element by a similar amount. It turns out that the best choice is to use the $1s_{1/2}$, $2p_{3/2}$, $3d_{5/2}$, $4d_{5/2}$, $4f_{7/2}$, $5d_{5/2}$, $5f_{7/2}$ levels after they move down from the valence shell to become core levels. To reach

the sharpest core level of each element with optimum surface sensitivity, it is sufficient to have photon energies from 50 eV to 1000 eV. This range can be spanned by state-of-the-art monochromators [16.8]. The energy range above 200 eV is more difficult because a high relative energy resolution is needed. A new generation of dedicated synchrotron radiation sources will make work in this energy range more of a routine operation in the years to come.

16.2 Valence Electronic States: Ideal Surfaces

One of the simplest semiconductor surfaces is the metastable Si{111} 2×1 surface, which can be obtained by cleaving in vacuo. This surface will be used to demonstrate how two-dimensional energy bands of surface states are mapped by angle-resolved photoemission and how calculations from first principles are able to predict both the atomic and the electronic structure of a surface with the atomic number of silicon and the surface orientation as the only input.

The band structure, or energy versus momentum E(k) dispersion relation, for electrons in crystalline solids is one of the fundamental concepts in solid state physics. It combines the two principal quantum numbers of an electron in a solid. Conceptually, all properties relating to electrons in a solid (electrical conductivity), magnetism, optical properties, etc.) can be derived from the band structure. Band dispersions have been calculated theoretically for decades but could not be measured directly until the advent of angle-resolved photoemission (for a review see [16.9,10]). The way in which E(k) is determined experimentally is almost trivial for two-dimensional energy bands at surfaces. One has conservation of energy E and of momentum parallel to the surface k", up to a reciprocal surface lattice vector. With photoemission in the ultraviolet, the photon momentum can be taken as negligible. Measurement of the photoelectron kinetic energy E_K and its escape angle θ with respect to the surface normal immediately yields an experimental value for k" via

$$k'' = (2m/\hbar^2)^{\frac{1}{2}} E_K^{\frac{1}{2}} \sin\theta$$

$$= 0.51 E_K^{\frac{1}{2}} \sin\theta \quad , \tag{16.1}$$

where k" is in $\text{Å}\text{ngstroms}^{-1}$ and E_K is in electron volts.

Figure 16.3 shows the angular distribution of photoelectrons emitted from a broken-bond-like surface state on silicon (after [16.11]). The photoelectrons do indeed exhibit characteristic momenta. The momentum distribution

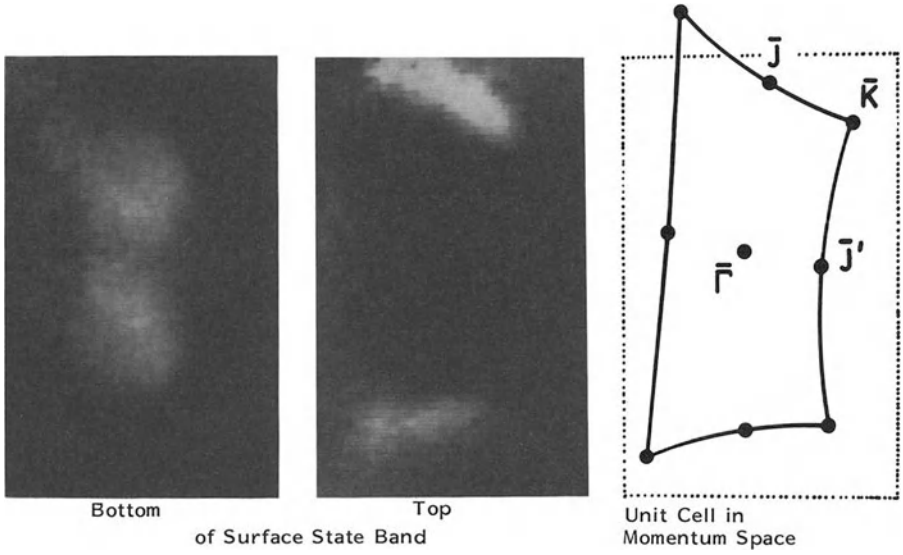

Fig.16.3. Momentum distribution [16.11] of photoelectrons emitted from the surface states on Si{111}2×1. The rectangular unit cell in momentum space is distorted by the electron optics of the spectrometer

depends on the kinetic energy of the emitted photoelectrons. At the top of the surface state energy band, the momentum distribution is centered around the short edge of the unit cell in k" space (i.e., the surface Brillouin zone). In order to measure energy bands, it is useful to plot energy distributions versus momentum (Fig.16.4). The binding energy of electrons in surface states is obtained by subtracting the photon energy from the kinetic energy of the emitted photoelectrons. By simply plotting binding energy versus momentum one obtains the two dimensional band dispersion [16.9,11-13] of the surface states (Fig.16.4). For the Si{111} 2×1 surface one is in the fortunate position of having first-principles band calculations [16.14,15] for comparison. In these calculations, the atomic and electronic structure of the surface is determined by total energy minimization. Actually, the structural model for this surface was found by theory and not by experiment. The energy bands of the optimum structure agree qualitatively with the data, which is quite gratifying since there are no free parameters in the theory. In concert with the band calculation, one can draw several conclusions regarding the bonding at the surface. This band dispersion is almost one dimensional, i.e., along the $\bar{\Gamma}\bar{J}$ azimuthal direction there is strong variation of E with k", whereas in the perpendicular direction there is hardly any observable dispersion. This reflects the chainlike structure of the surface with strong overlap between orbitals of adjacent atoms within the chain but

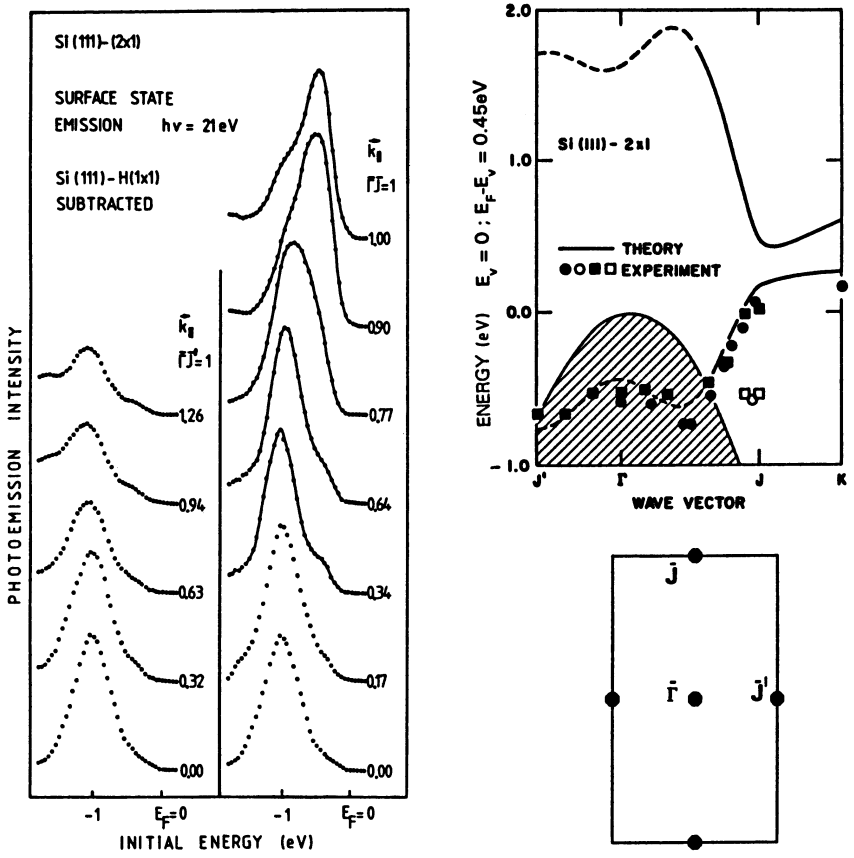

Fig.16.4. Experimental determination [16.9,11-13] of two-dimensional energy bands for surface states on Si{111}2×1. Peaks in the energy distribution curves are plotted versus momentum and compared with a band calculation from first principles [16.14]

weak overlap between separate chains. Qualitative information about the energetics of the rebonding at the surface can be derived from the binding energy of the surface states. For a truncated bulk structure, one has isolated broken bonds and expects half-filled orbitals located around the Fermi level. For the real surface the surface atoms rearrange in polyacetylene-like chains, such that π-bonding between adjacent chain atoms becomes possible. Thereby, the borken bond orbitals split into bonding/antibonding π/π^* pairs, one below the Fermi level, the other above. The energy lowering of the occupied state due to π-bonding is about 1 eV (Fig.16.4) and makes up for the broken bond (0.9 eV for half of a broken bond in Si). Of course, this is not the complete energy balance. Electrons in back-bonding orbitals are adversely affected by the strain that accompanies the rearrangement of surface atoms.

The (calculated) net energy gain due to the formation of π-bonded chains is only 0.4 eV per surface atom [16.14,15].

To reach a complete picture of the electronic structure, it is necessary to map out unoccupied states, e.g., the antibonding π^* band predicted for Si{111} 2×1. With photoemission one can reach only states below the Fermi level and above the vacuum level. The time-reversed process, i.e., inverse photoemission (see Fig.16.1, Chap.18 and [16.16-19]) creates access to the forbidden energy region. Inverse photoemission is an extremely inefficient process, producing about 1 photon per 10^8 electrons integrated over the complete emission solid angle and a typical energy spectrum, therefore, the technique has not been developed until recently and only a few results exist for semiconductor surfaces. In Fig.16.5, it is shown that there exist unoccupied counterparts to the occupied surface states on various silicon surfaces. The position of the surface states is sensitive to the surface structure.

So far we have considered clean semiconductor surfaces only. The same techniques apply equally well to surfaces with adsorbates and to metal surfaces. Angle-resolved photoemission work on such systems has been reviewed relatively recent [16.9,10]. Inverse photoemissions is progressing too fast to

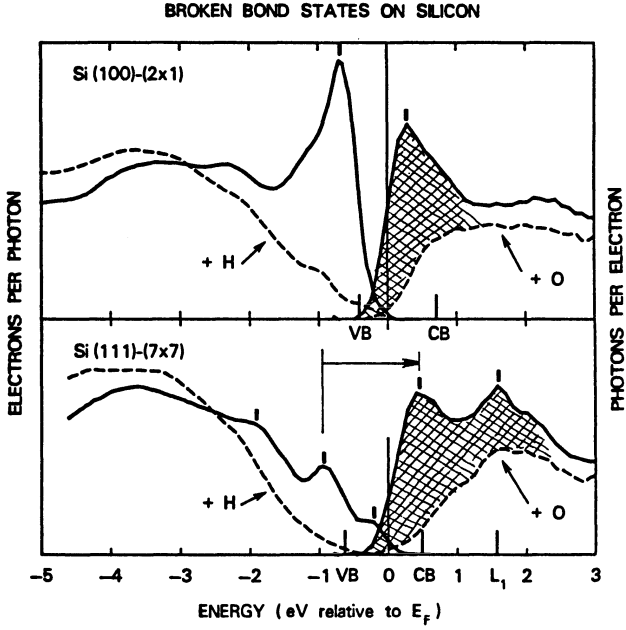

Fig.16.5. Comparison between photoemission and inverse photoemission for surface states (short, thick, vertical lines) on different Si surfaces [16.19]. Photoemission measures occupied states whereas inverse photoemission measures unoccupied states

have an up-to-date review, but good status reports exist (Chap.18 and [16.16-19]). The spectroscopy of electronic surface excitations is reviewed in [16.20].

16.3 Valence States: New Developments

A natural development of valence state spectroscopy is towards higher energy and momentum resolution. With an order-of-magnitude improvement in momentum resolution, one would be able to tackle many of the more typical semiconductor surfaces with long-range surface reconstruction, e.g., the thermally stable Si{111} 7×7 and III-V surfaces grown by molecular beam epitaxy. Their unit cells in k" space are too small to be probed with the momentum resolution that is currently used in photoemission. Electron energy-loss spectroscopy (EELS) already achieves such high energy and momentum resolution routinely and shows promising results (Fig.16.6). In the work of *Layet* et al. [16.21], it is shown that there exists significant band dispersion of surface states within the tiny surface Brillouin zone of Si{111} 7×7. The energy loss at $\Delta E \simeq 1.5$ eV has been assigned to a transition from one of the occupied surface states to an unoccupied surface state (the long arrow in Fig.16.5). The fact that the energy transfer ΔE depends on the momentum transfer Δk" shows

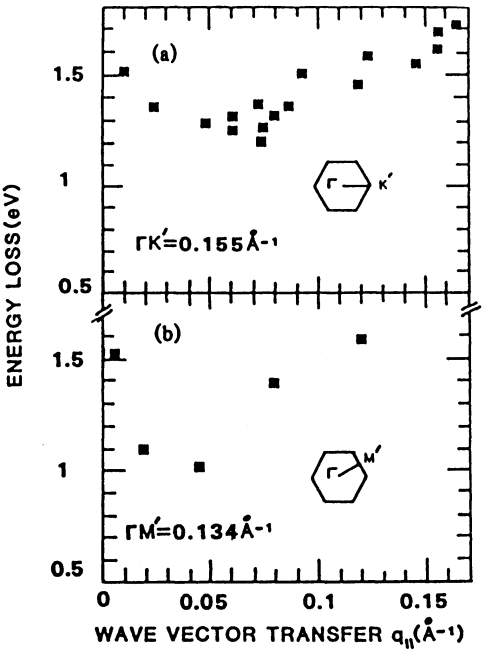

Fig.16.6. Band dispersion within the small surface Brillouin zone of Si{111}7×7. After [16.21]

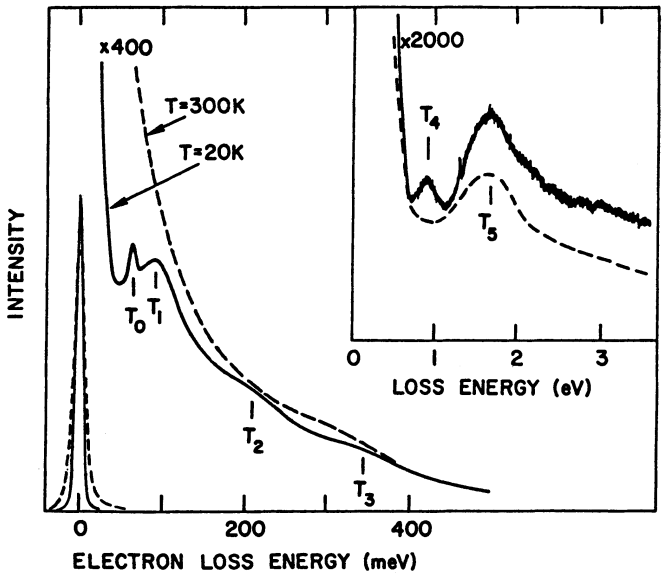

Fig.16.7. High-resolution electron energy-loss spectra of Si{111}7×7 demonstrating the existence of sharp surface states near the Fermi level. After [16.22]

that either the occupied or the empty state exhibits band dispersion, i.e., E versus k" dependence. In order to establish which one disperses (or possibly both), it would be necessary to perform angle-resolved (inverse) photoemission experiments with comparable momentum resolution.

Improved energy resolution also promises new insights. In this case one has to focus on states near the Fermi level, which exhibit small lifetime broadening. With an order of magnitude better energy resolution, one will be able to resolve energy differences that are comparable with thermal energies. Such energies are involved in common transport phenomena like electrical conductivity, magnetism, diffusion and in phase transitions. Again, EELS is showing the way. The result of *Demuth* and co-workers [16.22] in Fig.16.7 for Si{111} 7 × 7 shows that at low temperatures a new fine structure appears in the loss spectrum at low ΔE. This must be due to transitions between previously unresolved surface states very close to the Fermi level, except for the loss at 63 meV which is due to a surface phonon. Their absolute position has yet to be established, e.g., by photoemission and inverse photoemission. Such states could be associated with a single odd electron in the 7 × 7 unit cell. Being so close to the Fermi level these electrons will also easily react with adsorbates to increase their binding energy.

Angle-resolved photoemission experiments are underway with an energy and momentum resolution close to the EELS standard. *Kevan* and *Stoffel* [16.23]

found a surface state near the Fermi level on the Ge{100} 2×1 surface which is very localized in k space. It is correlated with a surface phase transition from ordered $c(4 \times 2)$ to disordered 2×1. Such experiments help to make the promise come true that energy levels can be measured with the accuracy of thermal energies and that the energetics of phase transitions can be determined experimentally.

Another new development is the spectroscopy of surfaces in an excited state. Powerful sources of laser radiation make it possible to lift enough electrons into higher levels to create an excited solid with an electronic structure that is completely different from the ground state. Well-known examples are the formation of exciton droplets in semiconductors and the formation of an excited phase of silicon with metallic reflectivity during laser annealing. Recently, *Haight* and co-workers [16.24] have observed the formation of an excited electron gas at the surface of a semiconductor using two-photon photoemission (Fig.16.8). A combination of two lasers is used to first pump electrons into a normally unoccupied surface state with 2.3 eV photons and to probe the surface with 10.5 eV laser photons. In the photoelectron spectrum, one can see photoelectrons at high kinetic energy that originate from the excited electron gas in the surface state. At lower kinetic energy, the normal photoemission spectrum from electrons in the ground state can be seen (both surface and bulk). A substantial density of electrons in the excited state is achieved ($2 \times 10^{19} cm^{-3}$ in the bulk). This can be conjectured already from the intensity ratio of excited-state versus ground-state photoemission and is confirmed by measuring the width of the filled portion of the excited surface state band.

It is more difficult to build up a significant excited-state population for metals than for semiconductors because the lifetimes of the higher-lying states are very short. There is always the possibility of creating an elec-

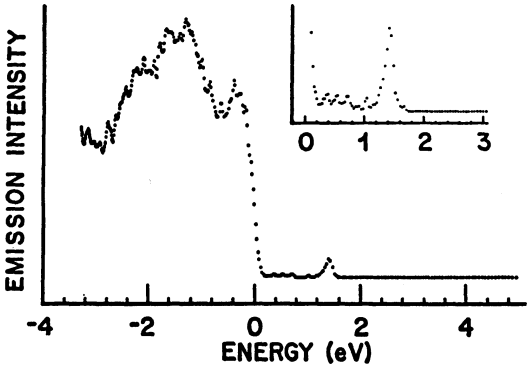

Fig.16.8. Photoemission spectrum from a laser-excited InP{110} surface (after [16.24]). Photoemission from excited electrons in a surface state is seen at 1.5 eV above the valance band maximum

tron-hole pair in a metal, whereas in a semiconductor this process does not occur for electrons less than two band gap energies above the conduction band minimum. Nevertheless, there exists a class of surface states on metals, namely the image potential states [16.25-28], that have lifetimes one or two orders of magnitude longer [16.29] than bulk states at the same energy. The reason for this long lifetime is the small overlap of the image potential state wave function with the solid. Essentially, the electron is bound outside the surface. These states are formed in the attractive Coulomb potential of the image charge and exhibit a hydrogenic series of energy levels converging towards the vacuum level. The equivalent Rydberg constant, i.e., the binding energy of the n = 1 image state, is 16 times smaller than for the hydrogen atom since the image potential has an extra factor of 1/4 compared with the hydrogen potential. These states have been observed with inverse photoemission (Fig.16.9 and [16.26-28]). A recent experiment [16.30] shows that one can optically pump a large number of electrons into image potential states and create a two-dimensional electron gas just outside the surface. A second photon is used to probe the excited electrons in a two-photon photoemission experiment (Figs.16.9,10). For Ag{111} there exists a sharp occupied surface state just below the Fermi level, which is used as the starting level. If the optical excitation energy $h\nu$ is tuned properly, one reaches an image potential state as intermediate level and ionizes from there with a second photon. The intensity of the resulting two-photon photoemission is given in Fig.16.10 versus photon energy. A strong resonance is observed at $h\nu = 3.84$ eV when the photon energy matches the difference between the occupied surface state and the n = 1 image state. A 40-times weaker resonance occurs for the

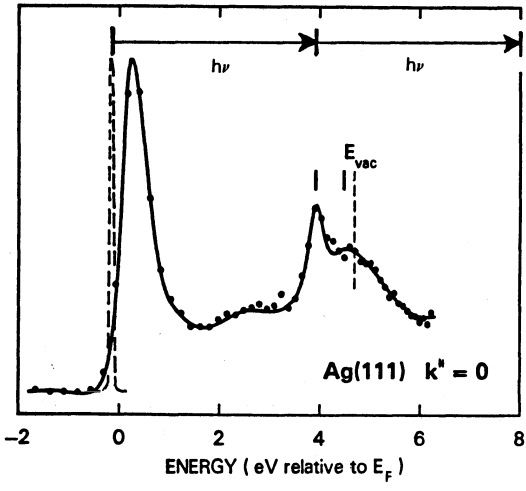

Fig.16.9. Surface states on Ag{111} at k" = 0 determined with inverse photoemission [16.28] and photoemission [16.30]. The short vertical lines just below the vacuum level denote image potential states

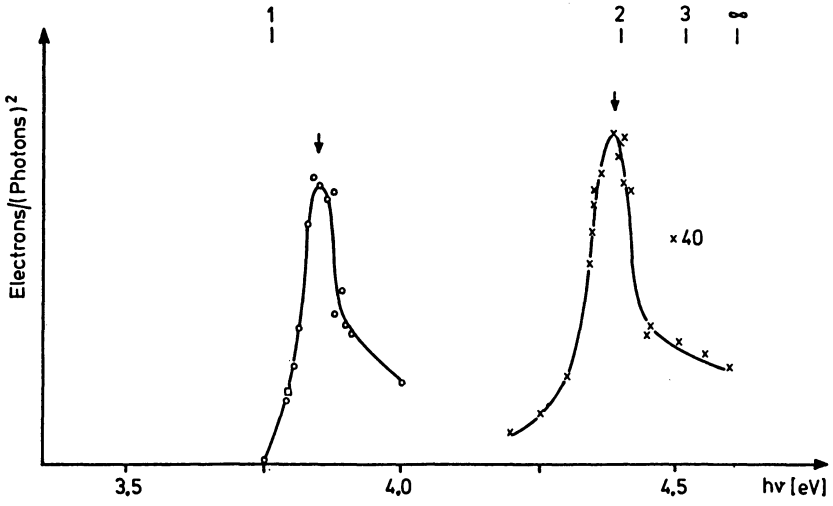

Fig.16.10. Resonance curves for two-photon photoemission from Ag{111} via image potential states as intermediates. See Fig.16.9. After [16.30]

n = 2 image state because the overlap of the wave functions is poorer. The high energy resolution achievable with a tunable dye laser as a light source makes it possible to resolve the n = 2 image state for the first time. Actually, the resolution of this experiment (80 meV FWHM for the resonance curves) is neither limited by the laser nor by the intrinsic width of the states but by inhomogeneous broadening due to work function inhomogenities. The starting level is tied to the Fermi level but the intermediate level is tied to the vacuum level, i.e., the difference varies across the sample surface. To obtain the optimum lifetime-limited resolution, it will be necessary to observe transitions between image states. Such experiments promise exciting two-dimensional electron-gas physics in a very simple holding potential. Previous work on electrons held above the surface of liquid helium by their dielectric image has already revealed an interesting phase transition from a fluid to a two-dimensional hexagonal solid [16.25]. The image states on metals are bound three orders of magnitude more strongly than on helium. This strong holding potential should allow one to reach much higher densities than on liquid helium ($2 \times 10^9 cm^{-2}$ maximum) and get into the regime of the quantum Wigner lattice [16.31].

16.4 Core Levels: Surfaces and Interfaces in Technology

The structure and composition of surfaces (interfaces) encountered in technology is much more complex than we would like to have it for perfomring basic studies and obtaining an understanding from first principles. Therefore, one has to resort to simpler probing techniques and must concentrate on determining the short-range order and the local properties (e.g., coordination, valence, oxidation state) that are left when the long-range order is lost. Core levels are well-suited for this purpose. They are not affected by the loss of long-range order because of their localiezd nature. The core level binding energy has a simple relation with chemical properties, e.g., charge transfer and oxidation state. It is shown in Fig.16.11 that for some model compounds of C and Si the levels shift proportional to the number of fluorine ligands [16.32]. This is caused by charge transfer towards the F atoms. A positively-charged C or Si atom pulls all electronic levels down in energy. In the model compounds there is hydrogen to saturate all remaining bonds without significantly affecting the core level energies because the electronegativity of hydrogen is close to that of carbon and silicon. These concepts have been developed extensively for molecules and bulk compounds by *Siegbahn* and co-workers [16.34] in their Nobel prize winning work. It is our aim, to apply this method to surfaces. Thereby, we use the advantage of synchrotron radiation as a tunable and very bright light source. The tunability allows one to excite the core electrons at about 50 eV above their ionization threshold where their mean free path has a minimum (about 4 Å or 3 atomic

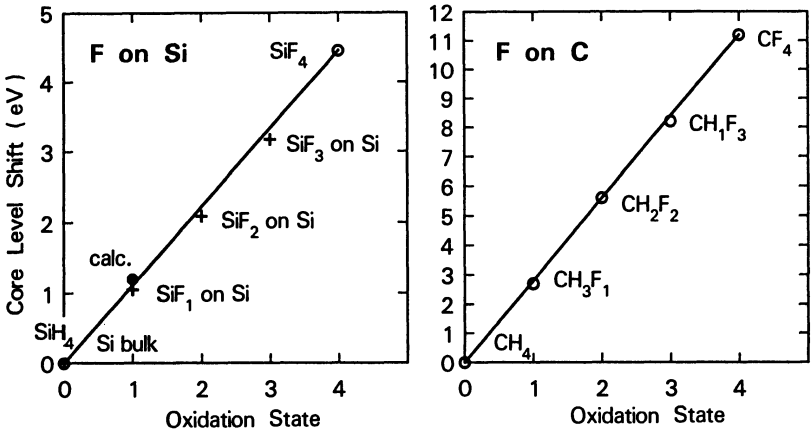

Fig.16.11. Linear relation between core level shift [16.32] and oxidation state for fluorinated silicon and carbon. Fluorine on Si surfaces (crosses [16.33]; see Fig.16.12) exhibits similar core level shifts, as expected from an interpolation between SiH_4 and SiF_4. The calculated shift (*dot*) is for a fluorine-terminated Si{111}1×1 surface

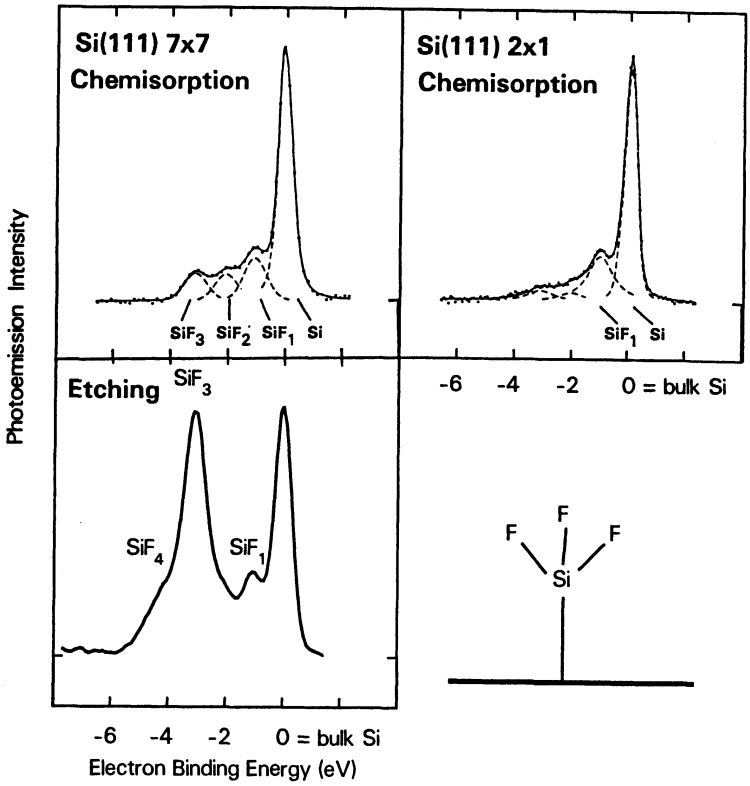

Fig.16.12. Silicon $2p_{3/2}$ core level spectra for fluorine-exposed Si surfaces [16.33]. The Si $2p_{1/2}$ contribution has been subtracted. At low exposure, about a monolayer of fluorine is chemisorbed and exhibits a distribution of oxidation states that varies with the surface structure. At high exposure, where the surface is etched, one finds predominantly SiF_3 indicating that the removal of SiF_3 from the surface is a bottleneck of the etching reaction

layers [16.4]). The brightness of synchrotron radiation [16.5] makes it easier to obtain highly monochromatic photons and, thus, to resolve smaller core level energy shifts. Figure 16.12 shows spectra from the Si $2p_{3/2}$ core level for about a monolayer of fluorine atoms adsorbed onto different Si{111} surfaces [16.34]. The fluorosilyl species SiF_1 to SiF_3 can be clearly resolved by their different chemical shifts from the bulk silicon line. Each F atom pulls off a certain amount of charge from a Si surface atom, thereby lowering the Si $2p_{3/2}$ core level by about 1 eV. The relationship between chemical shift and number of F atoms binding to the silicon appears to be linear all the way to SiF_4 (compare Fig.16.11). Such a clear-cut distinction between coexisting $SiF_{x;x=1,2,3}$ species is difficult, it not impossible, with other techniques.

Studies such as these are motivated by the desire to understand important processing steps in the semiconductor industry on a microscopic scale. In order to produce fast integrated circuits, it is necessary to etch micrometer-scale anisotropic features into silicon. Plasma processing is currently the method of choice. Silicon wafers are exposed to a fluorocarbon plasma which produces fluorine atoms which bring about etching via the removal of volatile silicon fluorides. The fundamental chemical mechanisms underlying this technology are not fully understood. As a first step toward their elucidation, it is useful to study the chemisorption of fluorine atoms on some model silicon surfaces. On the Si{111} 2×1 surface (Fig.16.12), one sees a single chemically shifted Si 2p core level, indicative of a surface monofluoride. On the Si{111} 7×7 surface, several peaks characteristic of mono-, di-, and trifluoride species are detected. The monofluoride is characteristic of a truncated bulk structure where F atoms terminate the single broken bond on each surface atom. The core level shift is in good agreement with calculations from first principles [16.35] for this geometry (the dot in Fig.16.11). Higher fluorides can be formed only by breaking back bonds and this is consistent with a more open structure for Si{111} 7×7, where F atoms can penetrate through the surface and attack back bonds. At higher fluorine exposures one gets into the more realistic etching regime; SiF_3 species predominate at the surface, independent of crystallographic orientation and other paramters. It appears that the removal of SiF_3 is a bottleneck of the etching reaction. Thus, one can go from an idealized well-ordered surface all the way to a complex etched surface using core level spectroscopy.

Core level spectroscopy is also applicable to interfaces, as long as they are not buried too deeply to let the photoelectrons penetrate out into the vacuum. The classic interface in semiconductor applications is the Si/SiO_2 interface. Many studies have been performed [16.2] and it has been found that this interface is (almost) atomically abrupt and that it contains an extraordinary low density of electrically active defects (typically one defect per 10^5 interface atoms). Of course, these properties allow the silicon MOSFET technology to play a dominating role in today's computer industry. Despite an abundance of electrical and other measurements, the microscopic structure of the interface atoms is not known. Only recently has it been possible to get some insight into these questions by using core level spectroscopy [16.36]. In Fig.16.13 photoelectron spectra are shown for two very thin oxide layers (5 Å and 11 Å). The kinetic energy distribution of the photoelectrons reflects the distribution of binding energies for the Si $2p_{3/2}$ core level. The spectra

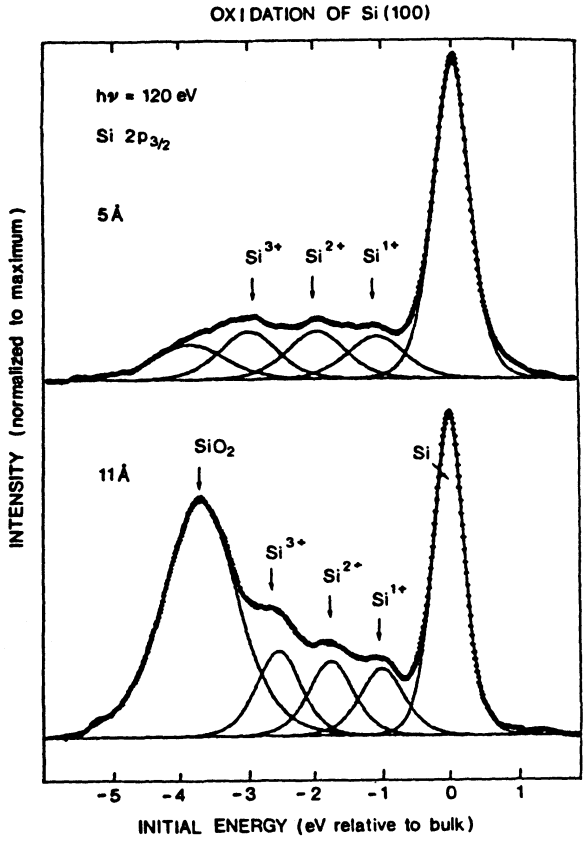

Fig.16.13. Distribution of oxidation states at the Si/SiO_2 interface as measured with core level photoemission from the $Si2p_{3/2}$ core level [16.36]. The $Si2p_{1/2}$ contribution has been subtracted. The interface is not quite atomically sharp with about two layers of silicon atoms in oxidation states intermediate between Si and SiO_2

display five components. It is easy to identify the components related to the silicon substrate and to the top SiO_2 layer (with 3.5 eV shift). The three intermediary components with shifts of 1.0, 1.8, and 2.7 eV are assigned to silicon atoms bonded to 1, 2 and 3 oxygen atoms (Si^{1+}, Si^{2+}, Si^{3+}). It is possible to evaluate the thickness of the intermediary layer from the relative intensities of the various components using the electron escape depth of 5 Å. For oxidation in dry oxygen, the same thickness (5 ± 1 Å, i.e., about two layers of Si atoms in SiO_2) is found for intermediary layers on Si{111} and Si{100} surfaces. The distribution of intermediary oxidation states is almost independent of the thickness of the SiO_2 overlayer. Thus, it makes sense to make a model for a universal Si/SiO_2 interface structure which does not depend strongly on preparation conditions. Several such models have been pro-

posed but none of them reproduces the equal proportions of the Si^{1+}, Si^{2+}, and Si^{3+} oxidation states correctly. The main failure of existing models lies in the fact that they assume an atomically abrupt interface. This would give rise to Si^{2+} only for Si{100} and to Si^{1+} and Si^{3+} for Si{111} because Si{100} has two broken bonds per surface atom and Si{111} has alternatingly 1 and 3 broken bonds. The core level data indicate that the interface is not quite atomically abrupt but has a finite width of about two silicon layers. In this transition layer the distribution of oxidation states is randomized. After determining the bonding at the Si/SiO_2 interface, one can explore the variations that occur under different preparation conditions and try to optimize the growth parameters for obtaining a sharp interface. Recent data [16.37] indicate that wet chemical oxidation produces a sharper interface than dry oxidation in pure oxygen, possibly because some of the interface bonds are saturated by hydrogen. Eventually, it would be very useful to correlate electrical properties with the interface structure.

References

16.1 S.M. Sze: *Physics of Semconductor Devices* (Wiley, New York 1981) p.432
16.2 Su Y.C. Cheng: Prog. Surf. Sci. **8**, 181 (1977)
S.T. Pantelides (ed.): *The Physics of SiO_2 and its Interfaces* (Pergamon, New York 1978)
16.3 R.G. Poulsen: J. Vac. Sci. Technol. **14**, 266 (1977)
J.W. Coburn, H.F. Winters: J. Vac. Sci. Technol. **16**, 391 (1979)
16.4 B. Feuerbacher, B. Fitton, R.F. Willis: In *Photoemission and the Electronic Properties of Surfaces*, ed. by B. Feuerbacher, B. Fitton, R.F. Willis (Wiley, New York 1978) p.12
16.5 E.E. Koch (ed.): *Handbook on Synchrotron Radiation* (North-Holland, Amsterdam 1983)
16.6 O. Keski-Rahkonen, M.O. Krause: At. Data Nucl. Data Tables **14**, 139 (1974)
16.7 F.J. Himpsel, D.E. Eastman, E.E. Koch, A.R. Williams: Phys. Rev. B**22**, 4604 (1980)
16.8 F.J. Himpsel, Y.J. Jugnet, D.E. Eastman, J.J. Donelon, D. Grimm, G. Landgren, A. Marx, J.F. Morar, C. Oden, R.A. Pollak, J. Schneir, C.A. Crider: Nucl. Instrum. Methods **222**, 107 (1984)
16.9 F.J. Himpsel: Adv. Phys. **32**, 1 (1983)
16.10 E.W. Plummer, W. Eberhardt: Adv. Chem. Phys. **49**, 533 (1982)
16.11 F.J. Himpsel, P. Heimann, D.E. Eastman: Phys. Rev. B**24**, 2003 (1981)
16.12 R.I.G. Uhrberg, G.V. Hansson, J.M. Nicholls, S.A. Flodstrom: Phys. Rev. Lett. **48**, 1032 (1982)
16.13 F. Houzay, G. Guichar, R. Pinchaux, G. Jezequel, F. Solal, A. Barsky, P. Steiner, Y. Petroff: Surf. Sci. **132**, 40 (1983)
16.14 K.C. Pandey: Phys. Rev. Lett. **47**, 1913 (1981); **49**, 223 (1982)
16.15 J.E. Northrup, M.L. Cohen: Phys. Rev. Lett. **49**, 1349 (1982)
16.16 V. Dose: Prog. Surf. Sci. **13**, 225 (1983)
16.17 N.V. Smith: Vacuum **33**, 803 (1983)
16.18 F.J. Himpsel: Comments Solid State Phys., in press
16.19 F.J. Himpsel, T. Fauster: J. Vac. Sci. Technol. A**2**, 815 (1984)
16.20 Ph. Avouris, N.J. Di Nardo, J.E. Demuth: J. Chem. Phys. **80**, 491 (1984)
Ph. Avouris, J.E. Demuth: Surf. Sci. **158**, 21 (1985)

16.21 J.M. Layet, J.Y. Hoarau, H. Lüth, J. Derrien: Phys. Rev. B**30**, 7355 (1984)
16.22 J.E. Demuth, B.N.J. Persson, A.J. Schell-Sorokin: Phys. Rev. Lett. **51**, 2214 (1983)
16.23 S.D. Kevan, N.G. Stoffel: Phys. Rev. Lett. **53**, 702 (1984)
16.24 R. Haight, J. Bokor, J. Stark, H. Storz, R.R. Freeman, P.H. Bucksbaum: Phys. Rev. Lett. **54**, 1302 (1985)
16.25 T. Ando, A.B. Fowler, F. Stern: Rev. Mod. Phys. **54**, 437 (1982)
C.C. Grimes, G. Adams: Phys. Rev. Lett. **42**, 795 (1979)
16.26 P.D. Johnson, N.V. Smith: Phys. Rev. B**27**, 2527 (1983)
16.27 V. Dose, W. Altmann, A. Goldmann, U. Kolac, J. Rogozik: Phys. Rev. Lett. **52**, 1919 (1984)
16.28 D. Straub, F.J. Himpsel: Phys. Rev. Lett. **52**, 1922 (1984); Phys. Rev. B**33**, 2256 (1986)
16.29 P.M. Echenique, F. Flores, F. Sols: Phys. Rev. Lett. **55**, 2348 (1985)
16.30 K. Giesen, F. Hage, F.J. Himpsel, H.J. Riess, W. Steinmann: Phys. Rev. Lett. **55**, 300 (1985)
16.31 E. Wigner: Phys. Rev. **46**, 1002 (1934)
16.32 For a compilation of core level binding energies see: A.A. Bakke, H.-W. Chen, W.L. Jolly: J. Electron Spectrosc. Relat. Phenom. **20**, 333 (1980)
16.33 F.R. McFeely, J.F. Morar, G. Landgren, F.J. Himpsel, N.D. Shinn: Phys. Rev. B**30**, 764 (1984)
F.R. McFeely, J.F. Morar, F.J. Himpsel: Surf. Sci. **165**, 277 (1986)
16.34 K. Siegbahn: Rev. Mod. Phys. **54**, 709 (1982)
16.35 M. Seel, P.S. Bagus: Phys. Rev. B**28**, 778 (1983)
16.36 G. Hollinger, F.J. Himpsel: Appl. Phys. Lett. **44**, 93 (1983)
16.37 M.H. Hecht, P.J. Grunthaner, F.J. Grunthaner: Proc. 17th Int. Conf. Phys. Semiconductors, San Francisco 1984, ed. by J.D. Chadi, W.A. Harrison (Springer, New York 1985) p.217
J.F. Morar, G. Hollinger, F.J. Himpsel, G.J. Hughes, J.L. Jordan: To be published

17. The Use of Spin-Polarized Electrons in Surface Analysis

J. Kirschner

Institut für Grenzflächenforschung und Vakuumphysik, KFA Jülich, Postfach 1913, D-5170 Jülich, F. R. G.

Electron spectroscopies have been playing a vital role in the development of surface science over the past two decades. Information on the sample has mostly been obtained from the energy and angular distribution of emitted or scattered electrons, while the "spin" property has been exploited to a much lesser extent. This chapter is intended to show what kind of new information can be gained if the electron spin is explicitly taken into account, in addition to the electron momentum.

17.1 Introduction to Spin-Polarized Electrons

Let us first consider the definition of electron spin polarization. Figure 17.1 shows a "snapshot" of a beam of electrons whose spins are oriented parallel or antiparallel to the vertical axis. This picture applies either to electrons moving slowly in the laboratory frame or to fast electrons in the rest frame. (Relativistic electrons have their spin parallel or antiparallel to the momentum when seen in the laboratory frame, due to spin-orbit coupling.) In all practical circumstances, however, the first case applies to a good approximation, since electron spectroscopies deal with nonrelativistic electrons. The degree of polarization of the electron ensemble is defined by the relative difference of the number of electrons with

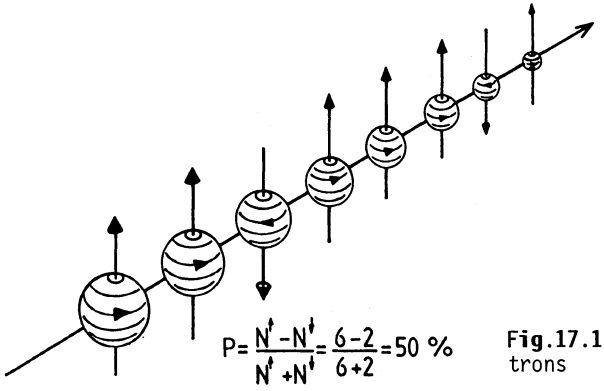

Fig.17.1. Beam of polarized electrons

up-spin ($N^{\uparrow}$) and down-spin ($N^{\downarrow}$):

$$P = \frac{N^{\uparrow} - N^{\downarrow}}{N^{\uparrow} + N^{\downarrow}} \quad . \tag{17.1}$$

Thus P is a normalized quantity $-1 \leqslant P \leqslant +1$, independent of the intensity of the beam. In the case of Fig.17.1 the polarization is +50%, since two electrons out of eight have the "wrong" spin orientation. More precisely, we mean the z-component of the total spin precessing on a cone around the z-axis. The alignment axis of the spins may be oriented arbitrarily in space (in the nonrelativistic limit), thus the electron spin polarization, **P**, in general is a *vector* quantity and a complete characterization of emitted or scattered electrons comprises an analysis of the vectors of momentum and spin polarization.

Considering the interaction of electrons with surfaces, there are two main mechanisms giving rise to spin-dependent effects: the spin-orbit interaction and exchange interaction. Other interactions, e.g., the dipole-dipole interaction, typically are orders of magnitude weaker. The origin of the spin-orbit interaction may be understood in the simplest case when scattering an electron from a central potential, such as an atomic nucleus. The orbital momentum $\boldsymbol{\ell}$ of the electron during scattering interacts with its spin momentum **s**, giving rise to an additional scattering potential $U_{SO} \sim \mathbf{s} \cdot \boldsymbol{\ell}$. Because of the scalar product, the sign and magnitude of this additional potential depend on the orientation of the spin relative to the normal to the scattering plane. Thus, when we scatter a beam such as in Fig.17.1 from an atom, the electrons with up-spin will experience a scattering potential which is somewhat different from that for down-spin electrons. Consequently, the differential scattering cross section becomes spin-dependent, and we may find, for example, that up-spin electrons are scattered preferentially to the left ($-\theta$), while down-spin electrons are scattered preferentially to the right ($+\theta$) for a particular choice of the scattering angle $\pm\theta$ relative to the primary beam direction. Scattering of a polarized beam thus may give rise to a characteristic left-right intensity asymmetry, and a measurement of spin polarization is reduced to two intensity measurements. This is the operating principle of all detectors for spin-polarized electrons used to date. We note that the spin-orbit interaction is strong also for slow electrons since they become "relativistic" by acceleration in the strong electric field of the nucleus. The strength of the interaction depends on the gradient of the potential, so it is stronger in high-Z materials than in light materials.

The other important spin-dependent interaction of electrons with surfaces is that of exchange interaction. While in the case of the spin-orbit inter-

action the conduction electrons of the solid are not essential, here they are decisive. The exchange interaction is due to the Pauli principle requiring the total wave function of a Fermion system to be antisymmetric with respect to the interchange of each two particles. The interaction resulting from this principle is essentially of a Coulombic nature. (The fact that the spin is associated with a magnetic moment is not essential in this context.) Let us consider again the simplest possible case: the scattering of two free electrons with parallel or antiparallel spins. In the singlet state (antiparallel spins) the spin part of the total wave function is antisymmetric, hence, the spatial part must be symmetric, and the scattering amplitude is written as a sum of two terms of which the second one is derived from the first one by replacing the spatial coordinates by their negative. In the triplet case the spatial part must be antisymmetric and the scattering amplitude is the difference of these two terms. The terms are the same since explicitly spin-dependent forces are negligible relative to the Coulomb force. Since the differential cross section corresponds to the square of the scattering amplitude, we see that the scattering cross section of two electrons depends on their relative spin orientation. Although the interaction is of Coulombic nature, the symmetry requirements upon exchange of the particles make the triplet scattering cross section smaller or equal to the singlet cross section. Formally, this difference in scattering cross sections can be traced back to the action of a spin-dependent "exchange potential", which adds to or subtracts from the direct scattering potential. Thus, if we scatter polarized electrons from a ferromagnetic surface, the exchange interaction with the aligned electrons in the sample may enhance or reduce the scattered intensity, depending on the sign and magnitude of the surface magnetization. An intensity asymmetry is measured upon reversal of magnetization or primary polarization, which may serve to investigate the magnetization in the near-surface region.

In dealing with real samples, we should keep in mind that both types of interactions are always present simultaneously, and may interfere with each other. However, in the following we shall seek cases where one or the other plays the dominant role. Therefore, we distinguish between experiments on nonmagnetic materials, preferably heavy ones, and magnetic materials, which mostly have low atomic numbers. The emphasis is on elastic and inelastic scattering and on photoemission, while other techniques are mentioned briefly. For further reading the review articles or books [17.1-7] are recommended.

17.2 Nonmagnetic Materials

The first attempt to observe the polarization of "electron waves" was made by *Davisson* and *Germer* in 1929 [17.8]. They used a double reflection experiment with two Ni single crystals, in analogy to a polarization experiment with light reflected from two mirrors. This experiment had a negative result and it took almost 50 years until spin polarization effects were observed in elastic diffraction from W{001} [17.9]. The dynamical theory of spin-polarized low-energy electron diffraction (LEED) started with the work of *Jennings* [17.10] and *Feder* [17.11] and has been refined considerably since then [17.2]. Subsequently, a variety of materials has been studied, mostly high-Z elements like Pt, W, and Au on low-index crystal surfaces, but also Ni, where the spin-orbit-induced effects are substantially smaller, as expected from its low atomic number. The influence of light and heavy adsorbates in submonolayer quantities was also studied and evidence was found that to some extent the spin polarization is a probe for the heavy component in a light/heavy adsorbate/substrate system. For a detailed discussion of this work and further references see [17.2,4,6,7].

17.2.1 Electron Diffraction

At the beginning of spin-polarized LEED it was not clear to what extent a kinematic (i.e., single-scattering) approximation was adequate to describe spin-polarization effects. This same question arose in the early days of LEED, since it was found that I-V spectra sometimes looked very "kinematical", while in other cases a satisfactory description could be obtained only by a dynamical calculation (i.e., multiple scattering included). In the kinematic theory the diffracted intensity is determined by a lattice sum, where the structure of the crystal enters. Let us assume the simple case of one atom per unit cell. We recall from (17.1) that the expression for the spin polarization is a normalized difference of particular intensities. Thus, the lattice sum enters numerator and denominator simultaneously and cancels! There remains exactly the spin polarization of the single atom at the particular energy and scattering angle chosen. Thus, if the kinematic approximation was valid, no structural information could be drawn from the spin-polarization analysis. An experimental decision on whether this is true can most directly be obtained from "rotation diagrams", i.e., the polarization of the specularly reflected beam as a function of the azimuthal rotation angle ϕ of the crystal at a fixed polar angle θ. Since the kinematic scattering parameters are not changed by rotating the crystal, the polarization should be constant, independent of ϕ. The experiment on W{001} [17.12] clearly de-

monstrated the importance of multiple scattering since the polarization was found not to be constant, but showed the fourfold symmetry of this crystal face. Thus, the spin polarization is structure sensitive, and it owes its sensitivity to multiple scattering.

This being demonstrated, structural parameters like surface contraction or lattice constant can be determined. As an example, the question of the temperature-dependent lattice expansion at the surface is addressed here. Because of the broken symmetry at the surface, the anharmonicity of the vibration potential normal to the surface should be stronger than in the plane and the top-layer distance might increase more rapidly with temperature than in the bulk. This type of problem was studied before by means of LEED where it was found that the surface Debye temperature was lower than in the bulk (indicating larger vibration amplitudes), but that the effective thermal surface expansion coefficient was close to that of the bulk [17.13]. The measurements were usually made on Bragg peaks which shifted towards lower energy with increasing temperature, i.e., with increasing lattice constant. At a Bragg condition, the amplitudes from the top 5 to 10 atomic layers add constructively to give a high intensity. When the lattice expands, the maximum occurs at a slightly longer wavelength, but the total amplitude is not much affected by the amplitude from the top layer which may be out of phase because of a different rate of expansion. Thus, the effective expansion coefficient will be close to the bulk value, with a rather large uncertainty though, since the peak shape may change due to temperature-dependent multiple scattering.

When the electron spin is used, this unfavorable situation can be avoided by making use of the observation that strong polarization structures are often found near relative minima of the diffracted intensity. In this case, the amplitudes from most of the near-surface layers add destructively and one might expect to see a much larger effect from the top layer when it moves with an expansion rate different from that of the bulk. An experimental result for the specular beam from W{100} at $\theta = 13^{\circ}$ is shown in Fig.17.2. With increasing temperature, we observe a shift of the polarization feature towards lower energies and a slight change of its shape [17.14]. From a comparison to theoretical calculations, employing a relativistic dynamical theory, it was found that the shape changes are mainly due to temperature-dependent multiple scattering, while the shift on the energy scale is related to structural parameters. By varying the top-layer and bulk expansions in the calculations it was found that roughly two-thirds of the shift is due to the bulk lattice expansion, while one-third is due to the top layer expan-

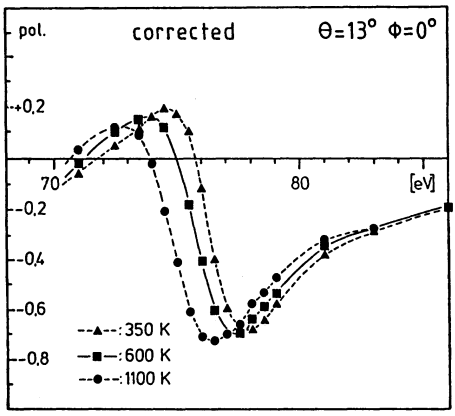

Fig.17.2. Spin polarization of the (0 0) beam from W{100} as a function of energy for three different temperatures. The polarization has been corrected for the temperature-dependent diffuse background. The shift of the polarization feature towards lower energies is caused by the lattice expansion and by the top-layer expansion

sion. Thus, the top-layer movement does indeed have a relatively strong influence, as expected from the above arguments. A quantitative evaluation showed that the thermal expansion coefficient for the top layer is about two to three times larger than the bulk expansion coefficient. This is a rather strong effect which is, however, consistent with model calculations by *Kenner* and *Allen* [17.15]. This example shows that spin polarization analysis may provide structural information which is hardly accessible by conventional means of electron diffraction.

17.2.2 Application of Spin-Polarized LEED: Spin-Polarization Detectors

The detection of spin-polarized electrons has traditionally been considered a rather complicated matter, since the conventional high-energy Mott detector is usually a rather bulky and expensive piece of apparatus [17.1,3,4]. Spin-polarized LEED offers a welcome alternative since only low energies are involved and good sensitivity may be obtained. Unlike a Mott detector, a device based on spin-polarized LEED can be made very small so that it may be used as an adjunct to a conventional electron spectrometer. Such an apparatus, which has been developed for momentum- and spin-resolved photoemission, is shown schematically in Fig.17.3.

The electrons from the sample are accepted by a zoom lens, accelerated or decelerated to the chosen pass energy, and focused into the energy analyzer. The spectrometer of the CMA-type operates with a virtual entrance slit which allows the exciting radiation to pass through the whole system onto the sample. After energy analysis, the electrons are brought to a fixed energy and fed into the spin-polarization detector, which is essentially a miniaturized LEED system. At normal incidence onto the W{001} crystal, equivalent beams like the (2,0) and ($\bar{2}$,0) beams have equal intensity. If the electrons have a

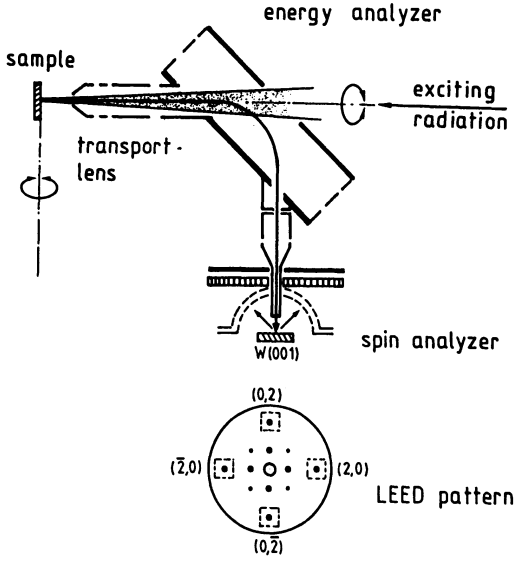

Fig.17.3. Momentum- and spin-resolving electron spectrometer system with the LEED spin-polarization detector. The spin analyzer is attached to the electrostatic energy analyzer and is rotated with it about two perpendicular axes. The LEED pattern is obtained with single electron counting and is observed on an oscilloscope

transverse spin-polarization component, e.g., normal to the plane of the paper, the degeneracy of equivalent beams is removed due to the spin-orbit-induced additional scattering potential. For example, the (2,0) beam may have a higher intensity than the $(\bar{2},0)$ beam. When the polarization sensitivity of the scattering process is known by calibration [17.12], the measurement of the relative intensity difference of the two beams yields the spin polarization of the corresponding component of the polarization vector of the electron beam leaving the energy analyzer. The elastically diffracted electrons are amplified by a two-stage channelplate which is placed behind the retarding grids. The collector is of the resistive anode type which provides an electronic readout of single electron diffraction events. Electronic windows are set around the diffraction spots and the beam intensities are measured in a quasi-parallel way. In the geometry shown, the $(0,2)/(0,\bar{2})$ beam pair detects the longitudinal polarization component along the optical axis of the transport lens. Of the remaining beams, the {1,1} beams measure independently the projections at 45°. The {1,0} beams, which have small polarization sensitivity at the fixed scattering energy, serve to control the apparatus asymmetry. The whole spectrometer system is rotatable about a vertical axis lying in the sample surface. The second transverse polarization component, lying in the plane of the paper, can also be measured by rotating the spectrometer plus spin analyzer out of the plane of the paper. In this way, all three components of the polarization vector can be determined. This system has been used in spin-polarized photoemission [17.16], secondary electron analysis [17.17], and inelastic electron scattering [17.18].

The LEED spin-polarization detector uses a clean surface of the detector crystal. Thus it is bound to ultra-high-vacuum (UHV) surroundings. In surface physics experiments, this is a necessity anyhow; in other applications differential pumping would perhaps be necessary.

17.2.3 Photoemission

Spin-orbit coupling occurs not only in scattering of electrons from a crystal surface, but is also important for the energy eigenvalues of the electrons in the crystal and their wave functions. By spin-orbit coupling, the spatial parts and the spin parts of the electronic wave functions are mixed and single-group symmetries are replaced by double-group symmetries. In general, symmetries are lowered, and energetic degeneracies are removed. The concept of parity of a wave function with respect to a mirror plane breaks down and the nonrelativistic selection rules for dipole transitions in photoemission are no longer applicable. On the other hand, for circularly polarized light the dipole selection rules for the "magnetic" quantum number m play a dominant role and the excitation of photoelectrons becomes spin selective. This means that in direct transitions induced by circularly polarized light, the upper bands are preferentially populated by electrons with a particular spin orientation, although the lower bands are not split energetically and are populated by electrons of both spins. The sign, magnitude, and orientation of the polarization vector of photoemitted electrons thus depends on the symmetry of the bands involved and also on their hybridization. For a more extensive discussion of this subject see [17.4,5]. The analysis of the electron spin provides a direct means of characterizing the symmetry properties of the wave functions of occupied and empty electronic bands of solids. A direct analysis of wave function symmetries complements and exceeds that of energy eigenvalues by photoemission.

In the following, the potential and feasibility of this technique will be demonstrated with photoemission from Pt{111}. The experiments were done at the BESSY storage ring, where a UV monochromator for circularly polarized light has been installed [17.19]. The spin- and momentum-resolved photoelectron analysis was carried out with the spectrometer system shown in Fig. 17.3. The sample was irradiated normally by photons in the energy range of from 7 to 30 eV with about 90% circular polarization. The electron takeoff was along the surface normal and a typical result for intensity and polarization distributions is shown in Fig.17.4a,b.

Comparing these data, one sees a correlation between intensity peaks and local extrema of the spin polarization. This is even more clearly visible

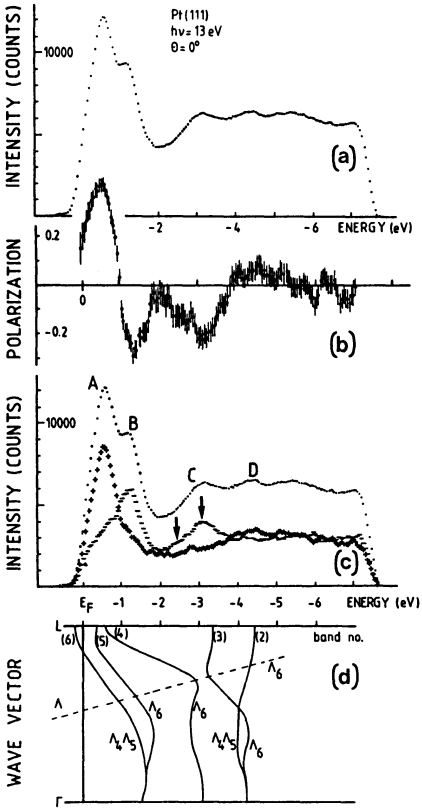

Fig.17.4. (**a**) Total intensity I in the (0 2)-(0 $\bar{2}$) beam pair as a function of binding energy at $h\nu = 13$ eV for normal takeoff. (**b**) Spin polarization as a function of binding energy. The error bars correspond to the variance of the Poisson distribution. (**c**) Total intensity I and partial intensities I^+ (+) and I^- (-). Features A-D are discussed in the text. (**d**) Theoretical band structure of Pt along Λ, with symmetry labels as determined from the spin-polarization analysis. The bands are numbered at the L point with increasing energy [band (1) is off scale]. The dashed line corresponds to the final-state band, shifted by 13 eV

in Fig.17.4c, where partial intensities (+ and -) have been derived such that their sum gives the total intensity of **a** and their normalized difference gives the spin polarization of **b**. This is not new information, but this kind of data representation may considerably aid the interpretation of spectra. Peaks A and D correspond to peaks in the positive partial intensity, while the features B and C correspond to peaks in the negative partial intensity. In particular the feature C is seen to consist of two neighboring peaks, indicated by arrows, of the same sign of the spin polarization. Most of the structure in the spectra can be understood in terms of direct transitions, as has also recently been verified by relativistic one-step photoemission calculations [17.20,21]. Figure 17.4d shows a section of the band structure of Pt along the Λ direction, with the final-state band shifted downwards by the photon energy. The crossings with the occupied bands correspond quite well to the peak positions in the partial intensity curves, although the splitting of the two topmost bands is somewhat larger in the experiment. The symmetry labels are determined from the spin polarization analysis. Since peaks A and

D corresponds to peaks in the positive partial intensities, the bands (6) and (2) must both be of $\Lambda_4\Lambda_5$ symmetry. Likewise, since features B and C correspond to peaks in the negative partial intensity, bands (5), (4), and (3) must be of Λ_6 symmetry. In particular, the doublet structure of C is seen to stem from the hybridization point of bands (4) and (3) around 3 eV binding energy. This resolves definitively a discrepancy between two previous theoretical band structure calculations, one of which predicted a band crossing while the other predicted an anti-crossing. The polarization analysis shows that the two bands are of the same symmetry, hence a band crossing is not allowed. It is emphasized that the experimental decision is not based on the measurement of energy eigenvalues but rather on the determination of the symmetry character of the wave functions.

In the present case of polarization analysis along the surface normal, the polarization vector is normal to the surface, as was expected from group theory considerations [17.22]. The investigations are currently being extended to off-normal analysis, where it is found that the polarization vector may have any orientation in space. For emission in a mirror plane, the orientation of the vector is related to the parity- and spin-mixing of the relativistic electronic wave functions, which may be determined in this way [17.23]. Thus, polarization analysis is expected to add a new dimension to the study of the electronic structure of solids by photoemission.

17.2.4 Application of Spin-Polarized Photoemission: Polarized Electron Sources

In principle, the output of the electron analyzer in the above experiment represents a beam of polarized electrons. However, since momentum- and energy-selection is applied, the intensities are too weak. Taking the total yield of electrons near the emission threshold does produce a beam of polarized electrons, but the polarization is low since many transitions in momentum space between different bands may occur simultaneously [17.24]. An elegant way to circumvent this problem is to excite a direct semiconductor across the band gap with radiation tuned to the band gap energy and sufficiently monochromatic to prevent transitions from spin-orbit-split neighboring bands. If the surface barrier is sufficiently low to allow electrons in the conduction band to escape into vacuum, an efficient source of polarized electrons may be obtained.

This principle was shown to work by *Pierce* and *Meier* [17.25] for GaAs, which has a direct band gap near the Γ point of about 1.5 eV. Therefore, light in the near infrared has to be used. The surface barrier can be lowered by heavy

p-doping and a coverage of Cs until negative electron affinity (NEA) is reached. When the light is circularly polarized, the emitted electrons are spin polarized according to the same principle as discussed in Sect.17.2.3 for Pt, i.e., the dipole selection rules for the "m" quantum numbers in direct transitions. The polarization is not complete, however, since the topmost valence band at the Γ point is twofold degenerate, which causes electrons of the "wrong" sign also to be excited, although with less probability. The theoretical limit for the spin polarization is 50%, which, however, is not reached in typical source applications because of several depolarization mechanisms. A detailed study on GaAs has been made recently by *Drouhin* et al. [17.26] and the design and operation of a source has been described by *Pierce* et al. [17.27]. From an instrumental point of view, GaAs is not ideal, since the handling and polarization of the invisible infrared light is somewhat inconvenient. Thus, instead of tuning the photon energy to the band gap, one may tune the band gap energy to a convenient light source, such as the red HeNe laser. This may be done by replacing As by P or Al, which increases the band gap while the material remains a direct band gap semiconductor up to about $x = 0.4$ in $GaAs_{1-x}P_x$. The combination of a HeNe laser with GaAsP [17.28] or GaAlAs [17.29] results in a convenient and intense source of polarized electrons.

As observed by *Kirschner* et al. [17.30] the energy distribution of the emitted electrons may be made quite narrow by adjusting the vacuum level of the activated cathode closely to the conduction band edge. This is achieved by a controlled coverage with cesium and oxygen. Energy distribution curves as narrow as 30 meV have been observed [17.26] and an emission current of 1 μA at 31 meV FWHM has been obtained [17.31]. This performance makes photoemission from GaAs and its derivatives an interesting alternative to thermal electron sources with an electrostatic monochromator [17.31].

At present, there are several dozens of polarized electron sources in use. Their applications range from high energy physics over solid state and surface physics to atomic physics (for a review see [17.32]). An example of a particularly simple and efficient source [17.33] is shown in Fig.17.5. The $GaAs_{0.62}P_{0.38}$ wafer is activated by heating from the rear and covering with Cs from a Cs-dispenser and with oxygen from a gas inlet. A part of the subsequent electrode structure may be transformed electrically into a simple ion gun which serves to clean the surface in cases of heavy contamination. Photoelectrons are excited by a HeNe laser beam (in reality above the plane of the paper) which passes by the sample and through the electrode structure. The electron beam is polarized longitudinally, with a component paral-

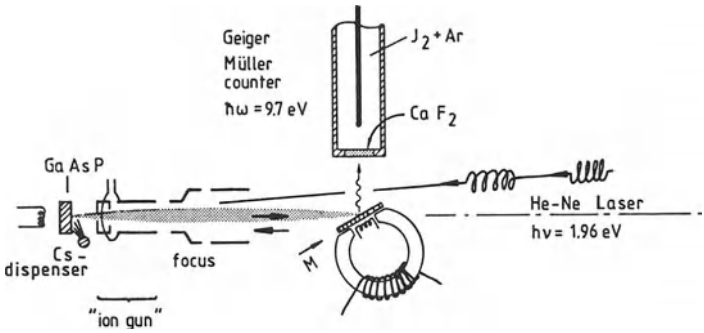

Fig.17.5. Simple high-intensity polarized electron source based on spin-polarized photoemission from GaAsP. The electron beam is longitudinally polarized. The distance from cathode to target is about 15 cm. The source is used here in spin-polarized inverse photoemission from iron by means of an energy-selective Geiger-Müller counter

lel to the magnetization of the iron sample. In the present case, the source is used for spin-polarized inverse photoemission [17.34]. The bremsstrahlung photons are detected and analyzed by an energy-selective Geiger-Müller counter. With a 15-mW laser, emission currents in excess of 100 μA are routinely obtained. Of this, about 20 μA is obtained at the target at 10 eV kinetic energy, due to space charge limitations. This source has also been used in appearance potential spectroscopy [17.35], LEED [17.33], and inelastic electron scattering [17.36].

17.3 Magnetic Materials

Exchange effects are most clearly observable with ferromagnetic materials since there is a net surplus of electrons with one spin orientation. Using polarized electrons as a probe, either in scattering or in emission, the magnetization, the underlying electronic structure, or elementary excitations may be studied. There are several experimental techniques available which are briefly characterized in the following and some of their results are discussed.

17.3.1 Elastic Electron Scattering

As noted in Sect.17.1, the elastic spin-dependent interaction of an electron with the aligned electrons of a ferromagnetic solid may be described by an exchange contribution to the scattering potential [17.2]. Thus, an unpolarized primary beam may become polarized by elastic diffraction, since the effective scattering potential is different for electrons of opposite spin orientations, which the primary beam may be thought to be composed of.

Likewise, for a polarized primary beam, the diffracted intensity may change when the polarization is reversed and everything else remains constant. The intensity asymmetry A_{ex}, therefore, carries information on the magnetization in the near-surface region. This was shown experimentally by *Celotta* et al. with Ni [17.37]. Unfortunately, multiple scattering complicates the matter considerably, so that the exchange asymmetry is not directly proportional to the magnetization [17.38]. As in a structure determination by means of LEED, one has to assume a certain top-layer value of the magnetization and a profile (mostly based on the mean field approximation), do the calculation, and compare the result with the measured exchange asymmetry. It is noteworthy that an enhanced magnetization may lead to a reduced exchange asymmetry over certain portions of an asymmetry versus energy curve. This approach is viable, however, and it was shown that clean surfaces of Fe and Ni have the top-layer magnetization enhanced (at $T = 0$ K) relative to the bulk magnetization. The enhancement ranges from 5% for Ni{100} [17.39] to about 30% for Fe{110} [17.40], in general agreement with first-principles ground-state calculations [17.41,42]. Very recently, *Weller* et al. [17.43] found by the same technique that on Gd{0001} there exists a surface-enhanced magnetic order with a critical temperature which is about 20 K higher than the bulk Curie temperature (see also [17.44]).

On raising the temperature of the sample, the magnetization decreases and one would naively expect to see the exchange asymmetry decrease correspondingly. As demonstrated by *Kirschner* [17.45], however, the asymmetry may vary non-monotonically and even change sign. Among several temperature-dependent effects [17.45], it is the multiple scattering and the magnetization profile which vary simultaneously and each have an effect on the asymmetry. Extracting the temperature-dependent magnetization profile seems possible but will require a very detailed study of each factor. There is a limiting case where the exchange asymmetry may be expected to be proportional to the surface magnetization: at the Curie temperature and in a narrow range around it. The magnetization profile may be assumed constant in the limit $T \rightarrow T_c$ and other effects may be assumed to change slowly over a small temperature interval. Under these assumptions, the decay of the surface magnetization on approaching T_c may be studied by measuring the exchange asymmetry. The critical exponent in the power law was found to be $\beta_s = 0.81 \pm 0.02$ for Ni{100} and $\beta_s = 0.79 \pm 0.02$ for Ni{110} [17.46], which is higher than in the bulk ($\beta_b \sim 0.35$). A higher value is unanimously predicted by several different models of surface magnetism, and a definite decision in favor of one of them cannot yet be made [17.46].

The complications due to multiple scattering can to some extent be suppressed by working with amorphous or microcrystalline samples. Although multiple scattering is by no means absent, one may hope that it averages out in the absence of long-range order. As in scattering from liquids, a kinematical approximation may then be sufficient to describe the gross features of intensity and exchange asymmetry [17.47]. Experimentally, this question has been studied in elastic scattering from iron-based metallic glasses [17.48,49]. As expected, the asymmetry to first order depends only on the scattering angle, although there are substantial deviations in detail. Nevertheless, these results have successfully been used to check the applicability of a spin-dependent pseudopotential [17.47] to describe the scattering from Fe atoms. Averaging out the multiple scattering is also useful if one wishes to study the surface magnetization as a function of temperature. One is no longer able to determine a magnetization profile, since the structure sensitivity is lost when multiple scattering is suppressed, but one may determine a mean value of the magnetization, averaged over the depth of information of the electrons. In the low-temperature regime, it is known that the bulk magnetization is predominantly reduced by thermally excited spin waves. Sufficiently far below T_c, the bulk magnetization curve follows Bloch's $T^{3/2}$-law. *Pierce* et al. [17.48] were able to show that the near-surface magnetization follows the same law, in agreement with early predictions [17.50], although with a different prefactor. Thus, one may conclude that at low temperatures, surface spin waves play the same role for the surface magnetic properties as spin waves do for the bulk.

So far we have discussed clean surfaces only. Now we ask what happens to the surface magnetization in the presence of an adsorbate. The magnetization may change by two effects. First, one may expect that the number of majority spins may be reduced by covalent chemical bonds with the adsorbate atoms. As predicted recently by electronic structure calculations for hydrogen on Ni{100} [17.51], the surface magnetic moment may be reduced drastically (from $\sim$0.7 μB to 0.2 μB at 0 K). The drastic changes of the surface spin density may be an explanation for the order-of-magnitude decrease of the spin polarization observed in electron capture on Ni{110} [17.44]. Also, a structural rearrangement of the surface atoms upon chemisorption may occur (this seems to be the rule rather than the exception). Since the magnetic exchange constant depends sensitively on the overlap of the d wave functions, the magnetic moment may change drastically even for slight changes of the bond lengths. A few percent change in lattice constant might change the exchange constant by a factor of two [17.44]. Con-

sidering elastic electron diffraction, we have to be aware that the measured exchange asymmetry may also be influenced by effects of nonmagnetic origin. Besides the effects of a structural rearrangement, there is also a contribution from the adsorbate layer to the diffracted intensity, and there is multiple scattering between the adsorbate layer and the substrate [17.52]. The interpretation of experimental results is, therefore, not straightforward. In theoretical calculations, *Tamura* and *Feder* [17.52] found conditions where the exchange asymmetry responds only very slightly to the top layer magnetization. However, with a probing depth of about two atomic layers, one would expect a sizeable reduction if the sample became "magnetically dead" at the surface upon adsorption. From the absence of drastic effects, it was concluded [17.33] that a coverage of about 1/4 monolayer of O or S on Fe{110} does not produce a "dead layer". Recent photoemission experiments with Ni{110} and on Fe-based metallic glass showed little or no changes of the electronic structure for 1 L CO and O on amorphous Fe and for CO on Ni [17.53]. For O on Ni{110} a merging of the exchange-split peaks was observed. For CO on Ni{110} at coverages up to 4 L, a vanishing surface magnetic moment was inferred by *Onellion* et al. [17.54] from the results of spin-polarized metastable-atom deexcitation spectroscopy. Seen as a whole, the topic of adsorbate-induced magnetic effects is rather incompletely understood at the present time and much more experimental and theoretical work is necessary.

17.3.2 Secondary Electron Emission and Magnetic Structure Analysis

It was first observed by *Chrobok* and *Hofmann* [17.55] in 1976 that secondary electrons from ferromagnets are spin-polarized and that the polarization vector is antiparallel to the magnetization of the sample. With EuO they found up to 32% polarization. The energy and polarization distributions of the secondary electron spectrum have subsequently been studied with Fe-based ferromagnetic glasses [17.56,57], and single crystals of Fe, Co [17.58], and Ni [17.59]. Generally, it was found that the electrons of lowest energy have the highest spin polarization. As an example, Fig.17.6 shows measurements by *Mauri* et al. [17.57] for the ferromagnetic glass $Fe_{83}B_{17}$. The spin polarization of the secondaries is shown as a function of their kinetic energy E_s for various primary energies E_p from 50 eV to 2000 eV. The maximum of the polarization at high primary energy reaches almost P = 20%, while it decreases signficantly towards higher kinetic energy E_s. A similar behavior was observed for clean single-crystal surfaces of Fe, Co, and Ni; the maxima attained P = 45%, 35%, and 17%, respectively, while the asymptotic values towards high energies approached the values expected from the average spin

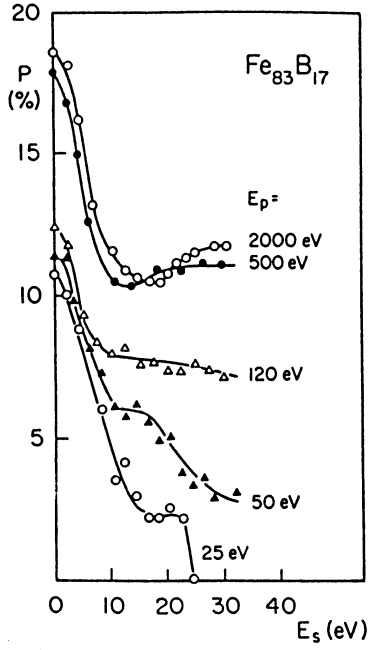

Fig.17.6. Secondary electron spin polarization as a function of kinetic energy E_S, for various primary energies E_p. Note the increase of polarization towards small energies

polarization of the valence band (27%, 19%, and 5.5%, respectively). These are the values to be expected if the secondary electrons were simply removed from the valence band, without further interaction with other electrons. However, the low-energy secondaries stem from late generations of the collision cascade initiated by a primary electron, and they may have lost energy during their way to the surface in inelastic particle-hole excitations. At low energies, exchange collisions leading to an apparent spin-flip gain in weight relative to nonflip excitations because of the energy dependence of the exchange cross section. Since in ferromagnets the empty density of states is predominantly of minority type near the Fermi level, an incident minority electron may transfer its energy in an exchange process to a majority electron below the Fermi level and find a place below the vacuum level while the majority electron is well above. Thus, a certain fraction of minority-type electrons seem to have flipped their spin while loosing energy. Since these inelastic processes may have occurred many times with electrons of very low escape energy, the low-energy end of the energy spectrum should show enhanced majority-type spin polarization as is observed in the experiments.

At present there is no realistic theory to predict quantitatively the amount of spin polarization enhancement, but model calculations by *Penn* et al. [17.60] are consistent with the above simplified picture. The mechanism sketched here is also important for the observation of Stoner excitations

to be discussed in Sect.17.3.3. The second feature we note in Fig.17.6 is that the polarization distribution curves are lower for low primary energies than at high energies, though the shape remains similar. This is explained by the presence of an ill-defined thin surface layer of reduced magnetization. At low primary energies, the penetration of the primary electrons is small and the secondaries stem mainly from the top layers. At high kinetic energies, the range of the primaries is large relative to that of the low-energy secondaries (of the order of 50 Å) and further increase of the primary energy does not affect the secondary electron energy and spin-polarization distributions. Thus, within certain limits, the in-depth distribution of the magnetization may be probed by varying the primary energy. One may expect to measure essentially bulk properties for primary energies above 1 keV (in Fe and similar materials) and for secondary electron energies above about 30 eV.

The polarization properties of secondary electrons are expected to find an important application in a new method of magnetic structure analysis [17.61,62]. With a sufficiently narrow primary beam, the magnetization of a sample may be imaged as in a scanning electron microscope when the sign and magnitude of the spin polarization is used to modulate the brightness (and/or colour) of the oscilloscope screen. For this purpose, the secondary electrons have to be collected and to be analyzed by a spin-polarization detector. The feasibility of this idea has already been demonstrated by *Koike* and *Hayakawa* [17.63,64] who used a Mott detector for polarization analysis. This is a rather bulky device which is much bigger than a scanning electron microscope. Recently it was demonstrated [17.17] that the LEED detector is also suitable for this purpose. Since it is much smaller, there is the promise that it can be used as an add-on to existing electron microscopes. The main features of this new type of magnetic structure analysis are summarized in the following:

(1) The signal is directly proportional to the magnetization, not to the magnetic induction like in most other techniques.

(2) Since the signal is a normalized quantity, the magnetic information is largely decoupled from the sample topography. Both types of information can be obtained simultaneously but separately.

(3) The technique is surface sensitive, given by the escape depth of the secondary electrons or by the penetration of the primary electrons. In the former case it is around 5 nm.

(4) The ultimate lateral resolution is given by the radius of the spot from which most of the secondary electrons are emitted. This is of the order of 5 nm. A practical limit is given by the useful beam size which may be of

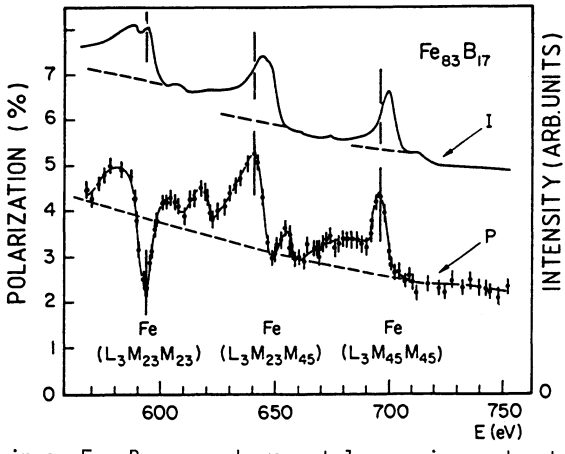

Fig.17.7. Intensity I and spin polarization P of Auger electrons from Fe in an $Fe_{83}B_{17}$ amorphous metal superimposed onto a smooth background of secondary electrons. The latter are assumed to contribute a polarization corresponding to the dashed line

the order of 10 nm [17.62,64]. This is one to two orders of magnitude better than can be obtained by conventional methods. Thus, the outer 5 nm or so of domains and the internal structure of domain walls may be viewed with unprecedented resolution.

Auger electrons too are secondary electrons, since their energy is bound to the Fermi level, independent of the energy of the ionizing primary radiation. They ride on a large background due to the cascade of secondaries, but recently Landolt and co-workers [17.65,66] were able to analyze the polarization properties of Auger electrons from ferromagnetic materials. An example of their results is shown in Fig.17.7, showing intensity and polarization distributions of the Fe LMM Auger lines from $Fe_{83}B_{17}$. The $L_3M_{23}M_{23}$ line near 600 eV involves only transitions between core levels. The final state is characterized by two holes in the $M_{23}(3p)$ level, which may be in a singlet or a triplet state. According to the Hund rules, the Auger electrons associated with the singlet state should have lower kinetic energy. The low-energy peak of the two-peak structure is, therefore, due to a singlet final state, while the high-energy peak corresponds to a triplet state (which may be further split due to exchange coupling with the 3d electrons [17.67]). The initial 2p hole may couple to the net spin of the 3d electrons in a ferromagnet. The positive polarization of the singlet state is due to the coupling of the 3d electrons to the 2p hole, while the negative polarization of the triplet peak mainly results from the coupling of the 3d electrons to the 3p holes [17.68]. The $L_3M_{45}M_{45}$ Auger line around 700 eV has a final state with two holes in the valence band. Since the Coulomb interaction energy is re-

latively small compared to the band width [17.66], the two holes are nearly independent of each other. The line shape and polarization are, therefore, to first order, determined by convolutions of the occupied one-particle densities of states for the two spin systems. A positive polarization is obtained simply because there are more majority spins in the occupied bands. The $L_3M_{23}M_{45}$ line around 650 eV is characterized by a final state with one hole in the 3p shell and one in the valence band. This case is intermediate between the two discussed above and the polarization shows a more complicated behavior. For more details (also on the MMM lines) see [17.66-69].

A point of interest for magnetic structure analysis is the observation [17.57] that the KLL Boron peak from the FeB sample is not spin polarized. This is due to the zero magnetization at the boron site. The spin polarization of Auger electrons apparently is intimately related to the local magnetic structure and may serve to analyze magnetic properties on an atomic level. We briefly remark that the magnetic properties of the unoccupied states may be probed by spin-polarized appearance-potential spectroscopy [17.35] and ionization loss spectroscopy [17.70].

17.3.3 Electronic Structure and Stoner Excitations

The microscopic understanding of the "itinerant" ferromagnets (e.g., Fe, Co, Ni) has been particularly difficult and is not yet complete (for a review, see [17.71]. The difficulty stems from the fact that in these materials the electrons forming the conduction band simultaneously carry the magnetic moment. The existence and strength of ferromagnetism is controlled by a delicate balance between the gain in Coulomb energy by allowing (some) spins to be parallel and the increase of kinetic energy brought about by the splitting of the bands and the resulting shift of the minority electron levels towards the Fermi edge. Thus, a microscopic understanding of itinerant ferromagnetism requires a detailed knowledge of the band structure (of its occupied part as well as of its empty part). The techniques at hand to study energy eigenvalues in momentum space are photoemission [17.72] and isochromat spectroscopy [17.73], also called inverse photoemission.

While band splittings and band dispersions can be determined in the conventional way, the determination of the spin character of the bands requires an explicit consideration of the spin quantum number. Either the emitted photoelectrons have to be spin analyzed or the primary electrons in inverse photoemission have to be spin polarized. Momentum resolution in spin-polarized photoemission [17.74,75] and inverse photoemission [17.76] is achieved by

working under conditions of zero external magnetic field, since otherwise the electron trajectories are disturbed too much to obtain adequate angular definition [17.1,5,7]. The magnetic stray fields can be eliminated either by using very thin samples [17.77] or by an external magnetic short circuit [17.76]. With the spin-polarized techniques, several studies have been made, mainly on Ni and Fe at room temperature, i.e., well below the Curie temperature (see [17.4,78] and references therein). In general, the peak positions of experimental spectra compare well with ground-state energy eigenvalues calculated self-consistently at T = 0 K. For the occupied bands of Ni, however, the measured exchange splitting ($\sim$ 0.3 eV) is generally smaller by a factor of 2 than in most theoretical band structure calculations. This has generally been attributed to many-body effects in the relaxation of the hole generated by the photoemission event, and the use of so-called correlated band structures for photoemission calculations has been suggested [17.79]. On the other hand, this discrepancy may also be due to neglecting electron correlations in the ground-state band structure calculations [17.80]. This question remains as yet undecided.

The utility of the spin-polarization analysis has been demonstrated quite clearly on Ni{100}, where the existence of a majority-type surface state was inferred from intensity data. The spin analysis revealed that the feature in question is of minority-type and, moreover, that it stems from a bulk band [17.78]. As far as the empty states are concerned, spin-polarized isochromat spectroscopy revealed empty minority states on Ni{110}, in agreement with theory [17.76]. First results for the dispersion of spin-split empty bands in iron are due to *Scheidt* et al. [17.34]. Reasonable agreement with theory was found, with an exception at the H-point, where in the experiment the minority band lies somewhat closer to the Fermi level than in theory. Recently, the chemisorption of oxygen on Ni{110} was studied by *Seiler* et al. [17.81]. While no evidence for a reduction of the exchange splitting was found (in contrast to the photoemission results quoted above [17.53]), they observed a reduction in the number of minority-spin d-holes.

So far, the interpretation has mostly relied on bulk bands. Several spin-polarized one-step photoemission calculations have been carried out in recent years, for photoemission [17.82] as well as for inverse photoemission [17.83], which showed that experimental spectra can be reproduced in a quite satisfactory way. While the major peaks could be associated with direct transitions in the bulk, typical surface contributions were also to be found in the spectra, such as from spin-split surface density of states and surface resonances.

At elevated temperatures, especially around the Curie temperature, the electronic structure of ferromagnets is much less well known. In particular, the changes of the electronic structure which accompany the decrease of the macroscopic magnetization have been the subject of intense interest for about half a century. In the simplest approach, based on the Stoner model, one might postulate that the magnetic moment, and with it the band splittings, vanish at the Curie temperature. If this was true, one would expect to see the spin-split bands "collapse" on approaching T_C. The difficulty with this model is that $k_B T_C$ should be of the order of the average exchange splitting $\langle\Delta\rangle$, and the Curie temperature for Ni, Co, and Fe would come out far too high. More recent theories, like the local band theory [17.84,85] and the disordered local moment model [17.86] agree on the existence of magnetic moments above T_C, but there is disagreement on the wavelength distribution of the spin-density fluctuations. In one of the limiting cases, the short-range magnetic order is assumed to be very large, while in the other there is none at all.

Experimental results of spin-polarized photoemission from Ni [17.87] showed a merging of the exchange-split peaks when the Curie temperature was approached, although the distribution above T_C was much too broad to stem from a single collapsed band. This behavior was qualitatively explained in the framework of the local band theory [17.88], under the assumption of a temperature-independent exchange splitting. In iron, the occupied bands were indeed found not to collapse [17.89], as far as the photoemission results are concerned. A cluster calculation for bcc iron was made very recently by *Haines* et al. [17.90]. Assuming a constant exchange splitting of 2.5 eV for the d-bands, the comparison of calculated and experimental photoemission spectra yielded a lower limit of about 4 Å for the short-range magnetic order. This means that the spin fluctuations spread coherently over roughly two lattice constants. Somewhat different experimental results were obtained for the empty states in iron by spin-polarized inverse photoemission [17.91]. It was found that an apparently collapsing behavior at one point in the Brillouin zone may coexist with a noncollapsing behavior at another point, in qualitative agreement with a prediction of the disordered local moment model [17.86]. We conclude from these observation that the temperature behavior of peak features in photoemission or inverse photoemission spectra may depend strongly on the point in momentum space, its surroundings and perhaps on the symmetry of the bands. It cannot be excluded, however, that the exchange splitting, although it remains finite on average, may show a

variable temperature behavior over the Brillouin zone when the Curie temperature is approached.

As in nonmagnetic crystals, there exist collective and single-particle excitations in ferromagnets, with the peculiarity that in the latter case a spin-flip is involved. Collective excitations carry the name spin waves, while electron-hole pairs with opposite spin are called Stoner excitations. Their relation is to some extent similar to that of plasmons and inter- or intra-band transitions in "ordinary" crysals: both types of elementary excitations have dispersion relations and regions of existence in ω-q space, and may hybridize. Spin waves are well known and have been studied extensively by neutron scattering, and spin-wave theory is known to work well at low temperatures. By contrast, Stoner excitations are largely "terra incognita" because they occupy regions in ω-q space which are hardly accessible to neutron scattering. It is only very recently that Stoner excitations have been directly observed by means of inelastic spin-polarized electron scattering [17.92,93].

Consider the following experiment (inset in Fig.17.8a). A monochromatized electron beam with spin parallel or antiparallel to the magnetization of the Ni{110} sample is scattered specularly, and the intensity of elastically and inelastically scattered electrons is measured. A typical result is shown in Fig.17.8a, which demonstrates that the loss intensity depends on the primary spin orientation. Obviously, incident minority-type ("down") electrons have a higher probability of losing energy than majority-type ("up") electrons. The difference is seen to depend on energy and appears to vanish at high energy loss. The magnetic origin of this effect is demonstrated in Fig.8b where the intensity asymmetry, i.e. the normalized difference, is plotted as a function of energy loss for reversed sample magnetization. The less-than-perfect symmetry (in particular the line crossing slightly below the zero line) is due to a small contribution from spin-orbit coupling which is neglected in the following. Similar results have been obtained for other primary energies. Since they agreed, within the statistical error, the average over all data points has been taken, which is displayed in Fig.8c.

The meaning of this asymmetry curve is the following [17.92]. The actual scattering process is a two-electron process: the one injected and another one excited from occupied states into empty states above the Fermi level. Since exchange processes are possible [17.94], the one detected after scattering may not be the same as the one sent in. For example, an incident minority-type electron of energy E_0 may drop into an empty minority state close to E_F, while its energy is transferred to an electron from an oc-

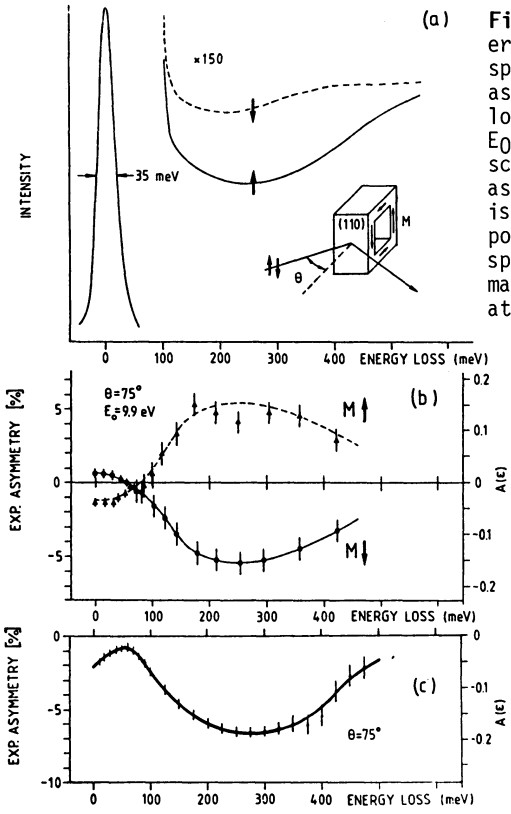

Fig.17.8. (**a**) Typical electron energy-loss spectra for spin-up and spin-down electrons. (**b**) Intensity asymmetries as a function of energy loss for reversed magnetizations at $E_0 = 9.9$ eV and $\Theta = 75°$. The left-hand scale is the experimentally measured asymmetry; the right-hand scale $A(\varepsilon)$ is the asymmetry for a completely polarized primary beam. (**c**) Asymmetry spectrum averaged over different primary energies E_0. The asymmetry peaks at $\varepsilon = 0.28$ eV with a FWHM of 0.32 eV

cupied majority-type band. The latter electron emerges with a kinetic energy given by the primary energy E_0 minus the energetic difference ε between the spin-split states below and above E_F.

There are several other channels to be considered, also those without exchange, but, as discussed in [17.92], the one just described is mainly responsible for the structure of the asymmetry. The final state is characterized by a hole in the majority spin band and an electron in the minority spin band above E_F. This is precisely the configuration of a Stoner excitation and this is why Stoner excitations can be probed via exchange processes in inelastic scattering. The measured asymmetry function reflects the spectrum of Stoner excitations in Ni with a specific momentum q. In the present case the momentum transfer is zero, since we observe in the specular direction. Because we observe two-electron processes, the transitions may occur in the whole Brillouin zone, provided they are "vertical" in the photoemission sense and that they have the proper spin characteristics. Therefore, the measured distribution function reflects the abundance distribution

of all vertical splittings across the Fermi energy, integrated over the Fermi surface. It has a maximum at about 0.3 eV which represents the most abundant exchange splitting, and a width of about 0.3 eV. This shows directly that the exchange splitting is not a single constant but varies considerably over the Brillouin zone. Our distribution function accommodates all experimental exchange splittings obtained by photoemission, which cluster around 0.3 eV. It appears remarkable that the two experimental techniques, although quite different as far as the physical processes are concerned, give essentially the same answer for the average exchange splitting in Ni. The technique is currently being extended to momentum transfers other than zero and to other materials [17.95].

The experiment above may also be conducted in a complementary form: unpolarized primary electrons and spin polarization analysis after scattering. Since minority electrons tend to be captured below the vacuum level and majority electrons emerge instead, the scattered beam will become enriched in majority electrons. This was demonstrated by *Hopster* et al. [17.93] with an iron-based ferromagnetic glass. Although the experiment was basically momentum resolving, arbitrary momentum transfers are included in this case. Therefore, a rather broad polarization structure was found, of the order of 5 eV wide, which is in rough agreement with relatively simple model calculations by *Glazer* and *Tosatti* [17.96]. The relative importance of exchange versus direct scattering processes depends on the energy of the primary electrons. At high energies, electrons behave like distinguishable particles and the exchange cross sections goes to zero. Thus, as *Modesti* et al. [17.97] pointed out, a rough account of the exchange contribution may be obtained from a comparison of nonpolarized energy-loss spectra at high and low primary energy, provided the nonexchange contribution is independent of energy.

However, in iron, the simplifications made for Ni are perhaps not valid since it is a nonsaturated (or weak) ferromagnet with a nonnegligible empty majority density of states. A more detailed study of the scattering process, including polarized primaries and spin analysis of the scattered electrons, will probably be necessary to study the spectrum of Stoner excitations. Work along these lines is in progress [17.95].

17.4 Conclusion

The use of spin-polarized electrons for surface analysis has been shown to yield fairly detailed insights into the electronic and atomic structure of ferromagnetic and nonmagnetic materials. Convenient sources and detectors

have become available and their use is increasing. The future will see a search for completely polarized sources and for more efficient detectors, perhaps based on entirely new principles. The spin-polarized scanning electron microscope for magnetic structure analysis is expected to have a strong technological impact. Perhaps even polarized-electron-beam techniques will play a role in data storage. A basic understanding of the finite temperature properties of ferromagnets is beginning to emerge and spin-polarized electrons will be a major experimental tool in this development. The study of single-particle excitations is a whole new field of research and spin-polarized electrons may become for Stoner excitations what neutrons have been for spin waves.

References

17.1 S.F. Alvarado, W. Eib, F. Meier, H.C. Siegmann, P. Zürcher: In *Photoemission and the Electronic Properties of Surfaces*, ed. by B. Feuerbacher, B. Fitton, R. Willis (Wiley, New York 1978)
17.2 R. Feder: J. Phys. C**14**, 2049 (1981)
17.3 J. Kessler: *Polarized Electrons*, Texts and Monographs in Physics (Springer, Berlin, Heidelberg 1976)
17.4 J. Kirschner: *Polarized Electrons at Surfaces*, Springer Tracts Mod. Phys., Vol.106 (Springer, Heidelberg 1985)
17.5 F. Meier, B. Zakharchenya (eds.): *Optical Orientation* (North-Holland, Amsterdam 1984)
17.6 D.T. Pierce, R.J. Celotta: Adv. Electron. Electron. Phys. **56**, 000 (1982)
17.7 H.C. Siegmann, F. Meier, M. Erbudak, M. Landolt: Adv. Electron. Electron. Phys. **62**, 000 (1984)
17.8 C.J. Davisson, L.H. Germer: Phys. Rev. **33**, 760 (1929)
17.9 M.R. O'Neill, M. Kalisvaart, F.B. Dunning, G.K. Walters: Phys. Rev. Lett. **34**, 1167 (1975)
17.10 P.J. Jennings: Surf. Sci. **20**, 18 (1970)
17.11 R. Feder: Phys. Status Solidi (b) **46**, K31 (1971)
17.12 J. Kirschner, R. Feder: Phys. Rev. Lett. **42**, 1008 (1979)
17.13 M.G. Lagally: "Surface Vibrations", in *Surface Physics of Materials*, ed. by J.M. Blakely (Academic, New York 1975)
17.14 J. Kirschner, R. Feder: Surf. Sci. **104**, 448 (1981)
17.15 V.E. Kenner, R.E. Allen: Phys. Rev. B**8**, 2916 (1973)
17.16 H.P. Oepen, K. Hünlich, J. Kirschner, A. Eyers, F. Schäfers, G. Schönhense, U. Heinzmann: Phys. Rev. B**31**, 6846 (1985)
17.17 J. Kirschner: Appl. Phys. A**36**, 121 (1985)
17.18 J. Kirschner: Phys. Rev. Lett. **55**, 973 (1985)
17.19 A. Eyers, Ch. Heckenkamp, F. Schäfers, G. Schönhense, U. Heinzmann: Nucl. Instrum. Meth. **208**, 303 (1983)
17.20 B. Ackermann, R. Feder: Solid State Commun. **54**, 1077 (1985)
17.21 B. Ginatempo, P.J. Durham, B.L. Gyorffy, W.M. Temmerman: Phys. Rev. Lett. **54**, 1581 (1985)
17.22 M. Wöhlecke, G. Borstel: In [17.5]
17.23 H.P. Oepen, K. Hünlich, J. Kirschner: To be published
17.24 D. Pescia, F. Meier: J. Appl. Phys. **53**, 2035 (1982)
17.25 D.T. Pierce, F. Meier: Phys. Rev. B**13**, 5484 (1976)
17.26 H.-J. Drouhin, C. Hermann, G. Lampel: Phys. Rev. B**31**, 3859,3872 (1985)

17.27 D.T. Pierce, R.J. Celotta, G.-C. Wang, W.N. Unertl, A. Galejs, C.E. Kuyatt, S.R. Mielczarek: Rev. Sci. Instrum. **51**, 478 (1980)
17.28 C. Conrath, T. Heindorff, A. Hermanni, E. Ludwig, E. Reichert: Appl. Phys. **20**, 155 (1979)
17.29 S.F. Alvarado, F. Ciccacci, S. Valeri, M. Campagna, R. Feder, H. Pleyer: Z. Phys. B**44**, 259 (1981)
17.30 J. Kirschner, H.P. Oepen, H. Ibach: Appl. Phys. A**30**, 177 (1983)
17.31 C.S. Feigerle, D.T. Pierce, A. Seiler, R.J. Celotta: Appl. Phys. Lett. **44**, 866 (1984)
17.32 D.T. Pierce, R.J. Celotta: In [17.5]
17.33 J. Kirschner: Surf. Sci. **138**, 191 (1984)
17.34 H. Scheidt, M. Glöbl, V. Dose, J. Kirschner: Phys. Rev. Lett. **51**, 1688 (1983)
17.35 J. Kirschner: Solid State Commun. **49**, 39 (1984)
17.36 J. Kirschner: Surf. Sci. **162**, 83 (1985)
17.37 R.J. Celotta, D.T. Pierce, G.-C. Wang, S.D. Bader, G.P. Felcher: Phys. Rev. Lett. **43**, 728 (1979)
17.38 R. Feder, H. Pleyer: Surf. Sci. **117**, 285 (1982)
17.39 R. Feder, S.F. Alvarado, E. Tamura, E. Kisker: Surf. Sci. **127**, 83 (1983)
17.40 U. Gradmann, G. Waller, R. Feder, E. Tamura: J. Magn. Magn. Mat. **31-34**, 883 (1983)
17.41 O. Jepsen, J. Madsen, O.K. Andersen: Phys. Rev. B**26**, 2790 (1982)
17.42 A.J. Freeman: J. Magn. & Magn. Mater. **35**, 31 (1983)
17.43 D. Weller, S.F. Alvarado, W. Gudat, K. Schröder, M. Campagna: Phys. Rev. Lett. **54**, 1555 (1985)
17.44 C. Rau: J. Magn. & Magn. Mater. **30**, 141 (1982)
17.45 J. Kirschner: Phys. Rev. B**30**, 415 (1984)
17.46 S.F. Alvarado, M. Campagna, F. Ciccacci, H. Hopster: J. Appl. Phys. **53**, 7920 (1982); Phys. Rev. Lett. **48**, 51,1768 (1982)
17.47 J.S. Helman, W. Baltensperger: Phys. Rev. B**30**, 2715 (1984)
17.48 D.T. Pierce, R.J. Celotta, J. Unguris, H.C. Siegmann: Phys. Rev. B**26**, 2566 (1982)
17.49 J. Unguris, D.T. Pierce, R.J. Celotta: Phys. Rev. B**29**, 1381 (1984)
17.50 D.L. Mills: In *Surface Excitations*, ed. by V.M. Agranovich, R. Loudon (North-Holland, Amsterdam 1984)
17.51 M. Weinert, J.W. Davenport: Phys. Rev. Lett. **54**, 1547 (1985)
17.52 E. Tamura, R. Feder: Surf. Sci. **139**, L191 (1984)
17.53 W. Schmitt, H. Hopster, G. Güntherodt: Phys. Rev. B**31**, 4035 (1985)
17.54 M. Onellion, M.W. Hart, F.B. Dunning, G.K. Walters: Phys. Rev. Lett. **52**, 380 (1984)
17.55 G. Chrobok, M. Hofmann: Phys. Lett. A**57**, 257 (1976)
17.56 J. Unguris, D.T. Pierce, A. Galejs, R.J. Celotta: Phys. Rev. Lett. **49**, 72 (1982)
17.57 D. Mauri, R. Allenspach, M. Landolt: J. Appl. Phys. **58**, 902 (1985)
17.58 E. Kisker, W. Gudat, K. Schröder: Solid State Commun. **44**, 591 (1982)
17.59 H. Hopster, R. Raue, E. Kisker, G. Güntherodt, M. Campagna: Phys. Rev. Lett. **50**, 70 (1983)
17.60 D.R. Penn, S.P. Apell, S.M. Girvin: Phys. Rev. Lett. **55**, 518 (1985)
17.61 R.J. Celotta, D.T. Pierce: In *Microbeam Analysis*, ed. by K.F.J. Heinrich (San Francisco, San Francisco 1982)
17.62 J. Kirschner: Scanning Electron Microsc. **1984/III**, 1179 (1984)
17.63 K. Koike, K. Hayakawa: Jpn. J. Appl. Phys. **23**, L85 (1984)
17.64 K. Koike, K. Hayakawa: J. Appl. Phys. **57**, 4244 (1985)
17.65 M. Landolt, D. Mauri: Phys. Rev. Lett. **49**, 1783 (1982)
17.66 M. Landolt, R. Allenspach, D. Mauri: J. Appl. Phys. **57**, 3626 (1985)
17.67 K.H. Bennemann: Phys. Rev. B**28**, 5304 (1983)
17.68 A. Kotani, H. Mizuta: Solid State Commun. **51**, 727 (1984)

17.69 A. Kotani: J. Appl. Phys. **57**, 3632 (1985)
17.70 D. Mauri, R. Allenspach, M. Landolt: Phys. Rev. Lett. **52**, 152 (1984)
17.71 T. Moriya (ed.): *Electron Correlation and Magnetism in Narrow-Band Systems*, Springer Ser. Solid-State Sci., Vol.29 (Springer, Berlin, Heidelberg 1981)
17.72 F.J. Himpsel: Adv. Phys. **32**, 1 (1983)
17.73 V. Dose: Prog. Surf. Sci. **13**, 225 (1983)
17.74 J. Kirschner, R. Feder, J.F. Wendelken: Phys. Rev. Lett. **47**, 614 (1981)
17.75 E. Kisker, R. Clauberg, W. Gudat: Rev. Sci. Instrum. **53**, 1137 (1982)
17.76 J. Unguris, A. Seiler, R.J. Celotta, D.T. Pierce, P.D. Johnson, N.W. Smith: Phys. Rev. Lett. **49**, 1047 (1982)
17.77 G. Waller, U. Gradmann: Phys. Rev. B**26**, 6330 (1982)
17.78 M. Campagna: Physica **127**B, 117 (1984) and references therein
17.79 R. Clauberg: Phys. Rev. B**28**, 2561 (1983) and references therein
17.80 A.M. Oles, G. Stollhoff: Phys. Rev. B**29**, 314 (1984)
17.81 A. Seiler, C.S. Feigerle, J.L. Pena, R.J. Celotta, D.T. Pierce: J. Appl. Phys. **57**, 3638 (1985)
17.82 R. Feder, W. Gudat, E. Kisker, A. Rodriguez, K. Schröder: Solid State Commun. **46**, 619 (1983)
R. Feder, A. Rodriguez, U. Baier, E. Kisker: Solid State Commun. **52**, 57 (1984)
17.83 R. Feder, A. Rodriquez: Solid State Commun. **50**, 1033 (1984)
17.84 H. Capellmann: Z. Phys. B**34**, 29 (1979)
17.85 V. Korenman, T.L. Murray, R.E. Prange: Phys. Rev. B**16**, 4032,4048,4058 (1977)
17.86 B.L. Gyorffy, J. Kollar, A.J. Pindor, G.M. Stocks, J. Staunton, H. Winter: In *The Electronic Structure of Complex Materials*, ed. by P. Phariseau, W. Temmerman, NATO Advanced Study Institute Series B (Plenum, New York 1984)
17.87 H. Hopster, R. Raue, G. Güntherodt, E. Kisker, R. Clauberg, M. Campagna: Phys. Rev. Lett. **51**, 829 (1983)
17.88 V. Korenman, R.E. Prange: Phys. Rev. Lett. **53**, 186 (1984)
17.89 E. Kisker, K. Schröder, M. Campagna, W. Gudat: Phys. Rev. Lett. **52**, 2285 (1984)
17.90 E.M. Haines, R. Clauberg, R. Feder: Phys. Rev. Lett. **54**, 932 (1985)
17.91 J. Kirschner, M. Glöbl, V. Dose, H. Scheidt: Phys. Rev. Lett. **53**, 612 (1984)
17.92 J. Kirschner, D. Rebenstorff, H. Ibach: Phys. Rev. Lett. **53**, 698 (1984)
17.93 H. Hopster, R. Raue, R. Clauberg: Phys. Rev. Lett. **53**, 695 (1984)
17.94 H.C. Siegmann: Physica **127**B, 131 (1984)
17.95 J. Kirschner: To be published
17.96 J. Glazer, E. Tosatti: Solid State Commun. **52**, 905 (1984)
17.97 S. Modesti, F. Della Valle, R. Rosei, E. Tosatti, J. Glazer: Phys. Rev. B**31**, 5471 (1985)

Additional References with Titles

Allenspach, R., Taborelli, M., Landolt, M., Siegmann, H.C.: "Surface Precursor to Magnetic-Domain Nucleation Observed by Secondary-Electron Spin Polarization", Phys. Rev. Lett. **56**, 953 (1986)

Feder, R. (ed.): *Polarized Electrons in Surface Physics* (World Scientific, Singapore 1985)

Kirschner, J.: "Single Particle Excitations and Electronic Structure of Ferromagnets in the Near-Surface Region", Surface Sci. **162**, 83 (1985) [Ref.17.95]

Kirschner, J.: "Direct and Exchange Contributions in Inelastic Scattering of Spin-Polarized Electrons from Iron", Phys. Rev. Lett. **55**, 973 (1985)
Oepen, H.P., Hünlich, K., Kirschner, J.: "Spin-Dependent Photoemission Intensities from Solids", Phys. Rev. Lett. **56**, 496 (1986) [Ref.17.23]
Unguris, J., Hembree, G.G., Celotta, R.J., Pierce, D.T.: "High Resolution Magnetic Microstructure Imaging Using Secondary Electron Spin Polarization Analysis in a Scanning Electron Microscope", J. Microscopy **139**, RP1 (1985)

18. Inverse Photoemission Spectroscopy

Th. Fauster and V. Dose

Physikalisches Institut der Universität Würzburg, Am Hubland,
D-8700 Würzburg, F.R.G.

Inverse photoemission spectroscopy is the modern appellation of experiments which analyze the photons produced by electrons hitting a solid sample. Techniques for experiments of this kind are still developing, so in this chapter, after a historical survey in Sect.18.1, we try to give a "snapshot" of their present state. In Sect.18.2, we present the current state of the experimental instrumentation. Section 18.3 gives a short review of the work on densities of unoccupied states, making the connection to the older work in the kilo electron volt photon energy regime. Since there is a comprehensive review of this work available [18.1], we will limit ourselves in the following sections to the photon energy range below 100 eV. Band structure determinations including surface states are the topic of Sect.18.4. For results obtained with spin-polarized electrons and on semiconductors, we direct the reader's attention to Chaps.17 and 16, this volume, respectively. In Sect.18.5, we discuss the work on unoccupied adsorbate states, which are spatially more extended than occupied states, and, therefore, more sensitive to changes in bonding etc. After a summary, we try to look forward to future developments in the exciting field of inverse photoemission, in Sect.18.6.

18.1 Historical Overview

The first experiment dealing with photons produced by electrons hitting a solid sample was done by Röntgen in 1895. He observed a new kind of radiation – named X-rays – when an anode was hit by cathode rays [18.2]. The phenomenon was then called bremsstrahlung, which means radiation emitted by decelerated electrons. In 1915, *Duane* and *Hunt* [18.3] derived a simple relation between the maximum frequency ν_{max} of the emitted radiation and the voltage U, applied between cathode and anode of an X-ray tube:

$$h\nu_{max} = e\,U + \phi_C \quad . \tag{18.1}$$

Going beyond the original work, we have added the work function ϕ_C of the cathode on the right-hand side of (18.1) to take into account the kinetic

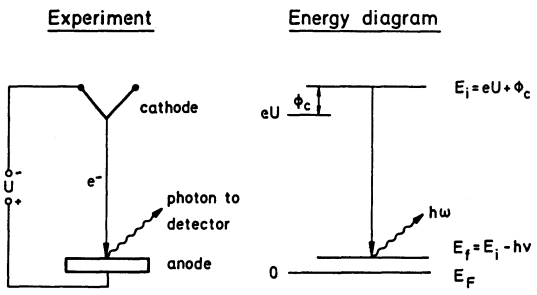

Fig.18.1. Schematic of a inverse photoemission experiment (*left*) and corresponding energy diagram (*right*)

energy of the electrons overcoming the surface barrier of the cathode. We then arrive at an expression for the Duane-Hunt limit analogous to *Einstein*'s relation for the photoelectric effect [18.4]. We recognize the complementary nature of light emission and absorption, which has led to a unified description of the interaction of radiation and matter in modern quantum mechanics.

A more careful study of bremsstrahlung spectra by *Ohlin* in 1942 [18.5] revealed structures and maxima at the high-energy end which were characteristic for the anode material. Four years later, *Nijboer* [18.6] explained these observations in terms of the density of unoccupied states above the Fermi level of the anode. This is illustrated in Fig.18.1, which shows, on the left, a schematic drawing of the experimental setup and, on the right, the corresponding energy diagram. We can immediately confirm (18.1), since the incident electrons cannot populate states below the Fermi level E_F which are already occupied. The maximum energy available for creation of a photon is then $E_i = e\,U + \phi_c$. The energy of the emitted photon $h\nu$ in a transition to a state of energy E_f is determined by energy conservation, so

$$h\nu = E_i - E_f \quad . \tag{18.2}$$

The number of transitions into states above the Fermi level, in the most simple picture, will be proportional to the number of available states, i.e., the spectrum will give an image of the density of unoccupied states. This is in good agreement with experiments, especially for photon energies above 100 eV [18.7].

In the simple density-of-states model, we have completely neglected the matrix element for the electronic transition from the initial state $|\psi_i\rangle$ of energy E_i to the final state $|\psi_f\rangle$ with energy E_f. The operator coupling the two states is given by $\mathbf{p}\cdot\mathbf{A}$, where $\mathbf{p}$ is the momentum operator and $\mathbf{A}$ is the vector potential. The matrix element M_{if} is then

$$M_{if} = \langle\psi_f|\mathbf{p}\cdot\mathbf{A}|\psi_i\rangle \quad . \tag{18.3}$$

For a photon of energy $h\nu = \hbar\omega$ and wave vector $\mathbf{q}$, the vector potential can be written as

$$\mathbf{A} = \mathbf{A}_0 \exp[i(\omega t - \mathbf{q}\cdot\mathbf{r})] \quad . \tag{18.4}$$

Here $\mathbf{A}_0$ is independent of time t and space coordinates $\mathbf{r}$. The time dependence of the matrix element can be eliminated by energy conservation (18.2). We shall further neglect the spatial variation of $\mathbf{A}$. This is the well-known dipole approximation, which is applicable whenever the wavelength of the radiation is large compared to the dimensions of emitter or absorber. The incident electron moves outside the sample as a free particle, and we can describe the wave function by a plane wave $\exp(i\mathbf{K}\cdot\mathbf{r})$ with the wave vector

$$|K| = \frac{1}{\hbar}(2mE_{kin})^{\frac{1}{2}} \quad . \tag{18.5}$$

Here, E_{kin} is the kinetic energy of the electron at the sample with a work function ϕ_s,

$$E_{kin} = E_i - \phi_s \quad . \tag{18.6}$$

If the energy E_i is sufficiently high, the wave function of the incident electron in the sample is not affected by the spatial variation of the crystal potential and feels only the constant part V_0 which contains the average interaction with the ions and electrons of the solid. The wave function of the electron before the radiative transition inside the sample is, therefore,

$$|\psi_i\rangle = \exp(i\mathbf{k}_i\cdot\mathbf{r}) \quad , \quad \text{with} \tag{18.7}$$

$$|\mathbf{k}_i| = \frac{1}{\hbar}[2m(E_i + V_0)]^{\frac{1}{2}} \quad , \quad V_0 > 0 \quad . \tag{18.8}$$

We are now going to discuss the limiting case of a localized final state $|\psi_f\rangle$ described by an atomic-like wave function $f(r)Y_L^M(\vartheta,\varphi)$, where Y_L^M is the usual spherical harmonic. The plane-wave initial state can also be expressed in spherical harmonics

$$e^{i\mathbf{k}\cdot\mathbf{r}} = 4\pi \sum_{l=0}^{\infty} \sum_{m=-l}^{l} i^l j_l(kr) Y_l^{m*}(\vartheta_k,\vartheta_k) Y_l^m(\vartheta,\varphi) \quad , \tag{18.9}$$

where j_l is the spherical Bessel function of order l and ϑ_k, φ_k define the direction of $\mathbf{k}$. Inserting (18.9) into (18.3), we obtain

$$M_{if} \sim \mathbf{A}\cdot\mathbf{k}\, Y_L^M(\vartheta_k,\varphi_k) \cdot \int_0^{\infty} j_L(kr) f(r) r^2 \, dr \quad . \tag{18.10}$$

The first factor $\mathbf{A}\cdot\mathbf{k}$ in (18.10) is independent of the symmetry of the final state $|\psi_f\rangle$. It suppresses light emission with polarization normal to the

incident electron beam. The spherical harmonic Y_L^M contains the information about the symmetry of the final state. The radial integral depends parametrically on the electron wave vector $|\mathbf{k}_i|$ and the final-state angular momentum L. Since the wave vector k is related to the initial-state energy E_i (18.8), the matrix element will show a characteristic energy dependence for different angular momenta L. The detailed behavior will depend on the radial part of the final-state wave function. This energy dependence of the cross section will be illustrated in Sect.18.3.

The case opposite to a localized atomic-like final state is the periodic Bloch wave function in a solid crystal. In a plane-wave representation, the final state is then described by

$$|\psi_f\rangle = \sum_{\mathbf{G}} c_{\mathbf{G}} \exp[i(\mathbf{k}_f + \mathbf{G})\cdot\mathbf{r}] \quad . \tag{18.11}$$

The sum runs over all reciprocal lattice vectors $\mathbf{G}$ and the $c_{\mathbf{G}}$ are the expansion coefficients. Evaluation of (18.3) for this case shows that M_{if} vanishes unless

$$\mathbf{k}_f + \mathbf{G} = \mathbf{k}_i \quad . \tag{18.12}$$

This equation describes the momentum conservation and means that optical transitions occur vertically in a reduced-zone scheme. There are again polarization dependencies, since the direction of the vector potential enters the dipole operator. We have additional selection rules for states along high-symmetry directions of the crystal lattice from group theoretical considerations, which reflect the dipole selection rules due to rotational symmetry. Energy conservation (18.2) and momentum conservation (18.12) allow in principle a complete determination of the band structure of a crystalline solid by suitably designed inverse photoemission experiments. This is one of the great prospects of this technique. There is, however, the problem that we do not know the wave vector $\mathbf{k}_i$ of the electron in the sample. The experiment defines the energy E_i and the wave vector $\mathbf{K}$ in vacuo. The potential step at the surface changes the normal component of the electron momentum $k_i^{\perp}$ and destroys the information on the carefully prepared electron beam. For a periodic surface, the electron momentum parallel to the surface $\mathbf{K}^{\parallel}$ can change only in discrete steps given by the reciprocal lattice vectors $\mathbf{G}_s$ of the surface. This leads to the conservation law

$$\mathbf{k}_i^{\parallel} = \mathbf{K}^{\parallel} + \mathbf{G}_s \quad . \tag{18.13}$$

The normal component $k_i^{\perp}$ of the wave vector $\mathbf{k}_i$ is generally not conserved. This poses no problem for two-dimensional systems such as layered structures,

and we will discuss the example of graphite in Sect.18.4. Another class of two-dimensional systems are adsorbate-induced states and surface states. These are frequently observed in inverse photoemission experiments due to the short penetration length of the low-energy electron beam and the resulting surface sensitivity.

For a three-dimensional band structure, the normal component $k_i^{\perp}$ in the sample can be obtained by the triangulation or energy coincidence method, where we look for the same transition on two different crystal surfaces. The knowledge of the parallel components relative to two different surface planes permits a complete determination of the wave vector $\mathbf{k}_i$ via two independent measurements. For the evaluation of a single measurement, additional information is needed. One sometimes resorts to calculated band structures in order to fix the momentum associated with the initial state energy E_i. This is in a way like moving in a circle, since our goal is the determination of the band structure just by experiment. Another solution to the determination of $k_i^{\perp}$ is the assumption that the initial state should be free-electron-like in a constant average inner potential V_0. This has been surprisingly successful in the evaluation of photoemission experiments.

The determination of band structure requires experiments with an electron beam of well-defined momentum and energy. The absolute value of the wave vector component parallel to the surface is given by the angle of incidence θ relative to the surface normal

$$|\mathbf{k}_i^{\parallel}| = \frac{1}{\hbar}(2mE_{kin})^{1/2}\sin\theta \quad . \tag{18.14}$$

We note that the spread of the kinetic energy of electrons from a thermal emitter results in a corresponding uncertainty in the momentum. For high energies, the momentum spread is then larger than the diameter of the Brillouin zone, which is the density of states possibly weighted by cross-section variations. This brings us back to the starting point of *Nijboer* [18.6], who interpreted the high-energy end of the bremsstrahlung spectra in terms of density-of-states effects.

Band structure determinations require, therefore, low photon energies, which were introduced into bremsstrahlung spectroscopy in 1977 [18.8]. In 1980, the relation to ordinary photoemission was pointed out and the physics involved in bremsstrahlung production was explained as an "inverse photoelectric effect". The appellation "inverse photoemission", coined by *Pendry* [18.9] in 1980, has since become the most popular and points out the complementary nature of photoemission experiments. We have indicated this correspondence by comparing the Duane-Hunt limit, from (18.1) and [18.3], to Einstein's equation [18.4]. Photoemission detects the electrons excited

into states above the vacuum level by incident photons and can be regarded as related to bremsstrahlung spectroscopy by time reversal. The main difference is that photoemission measures only occupied states, while inverse photoemission complements the picture by accessing the unoccupied states above the Fermi level. The theoretical considerations presented in the foregoing paragraphs apply to photoemission accordingly. The mutual relation between the electron current per incident photon in photoemission and the photon current per incident electron in inverse photoemission has long been known as the Milne relation [18.10]. It predicts a cross section for inverse photoemission which is about four orders of magnitude smaller than for photoemission in the UV. Pendry estimated a total current of 10^{-8} photons per incident electron in a 1-eV wide spectrum emitted into the whole half-space, which is in agreement with experiments [18.11]. This makes an inverse photoemission experiment quite difficult, and therefore, it was not until 1982 that the first angle-resolved data were published [18.12,13]. Since then, the development of this technique has continued to progress.

18.2 Instrumentation

A spectrometer for inverse photoemission consists of three basic parts: an electron source, an energy analyzer for the photons, and the detector. Since the cross section for photon production is very low [18.9,10], we need a high-intensity electron gun and a photon detection system with a large acceptance. The first requirement is difficult to satisfy in the low-energy regime, where space-charge effects set a limit for the currents which can be achieved. The first experiments [18.8,14,15] used, therefore, a tungsten filament close to the sample, but they lacked angular resolution [18.12]. The space-charge problem can be overcome with electron guns accelerating the electrons over a very short distance [18.16,17] or by decelerating an electron beam of high energy towards the sample [18.18-20]. These designs can deliver currents of several microamperes at an energy of 10 eV. For higher currents, space-charge-limited electron guns of a Pierce-type design are used, which allow sample currents of 100 μA at 20-eV energy [18.11,21]. Besides the intensity of the electron source, the energy spread is important. This requires electron emitters operating at low temperatures, such as BaO [18.11,19] or LaB_6 cathodes [18.22]. These have an energy spread of ~0.25 eV, whereas tungsten filaments have a corresponding value of ~0.6 eV [18.14].

Narrow electron energy distributions (~0.15 eV) can be obtained also with negative electron affinity GaAs cathodes which can also produce spin-polar-

ized electrons [18.23,24]. They have been employed in spin-polarized inverse photoemission experiments [18.25,26]. Field emission tips [18.27] or monochromatized electron beams would give even better energy resolution but at the expense of intensity and have not yet been used for inverse photoemission spectroscopy. The angular resolution of most experiments is estimated as 2°-5°[18.11,16,20], which is sufficient for band structure determinations.

Two different types of photon detection systems are presently used for bremsstrahlung spectroscopy. The first detects only one fixed photon energy, whereas the other can measure a spectrum of wavelengths. Correspondingly, we have two different modes of operation. For fixed photon energy, the electron energy E_i is varied over the spectrum to scan the final states E_f (18.2). This is called bremsstrahlung isochromat spectroscopy, since emission of the same color is detected. This mode is complementary to photoemission using a light source of fixed photon energy, such as a resonance lamp. The disadvantage of isochromat spectroscopy is that both the initial and final states vary over the spectrum, which makes data analysis more difficult. In the second mode, the electron energy E_i is kept constant, and the photon spectrum translates into the energy distribution of the final states (18.2). This bremsstrahlung mode corresponds to constant final state spectroscopy in photoemission, where it requires access to a synchrotron light source. The disadvantage is that this mode requires knowledge of the light detection efficiency as a function of photon energy. There are, however, experiments, such as band structure measurements, which cannot be done without tunable photon energies.

Detection systems for fixed photon energy usually integrate energy analysis and photon detection into one piece. The most popular design uses a Geiger-Müller counter with iodine as the active gas and a CaF_2 single crystal as the entrance window [18.8,12]. As seen in Fig.18.2, the photoionization threshold of I_2 (dotted line) gives a low-energy cutoff, whereas the absorption of the CaF_2 (dashed line) cuts off at the high energy end. The solid line gives the calculated detection efficiency of the combined system with a mean detection energy of 9.7 eV and a total energy resolution of 0.8 eV. Using a SrF_2 window improves the energy resolution by a factor of 2, as indicated by the shaded area in Fig.18.2 [18.28,29]. Detectors using windows and the low-energy onset of the yield of photocathodes [18.30] or channel electron multipliers [18.20] seem to be easier to operate than a Geiger-Müller counter, but show inferior energy resolution or detection efficiency. The acceptance angle of fixed-photon-energy instruments can be quite large. This can be achieved by short distances between sample and de-

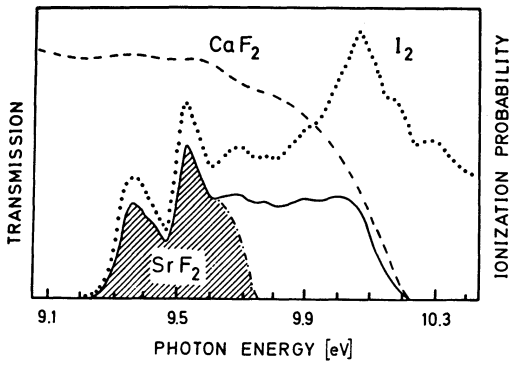

Fig.18.2. Energy dependence of the photoionization efficiency of I_2 (•••) and of the optical transmission of CaF_2 (---). The combined effect provides a bandpass (——) centered at 9.7 eV. For SrF_2 the resulting bandpass (*shaded area*) has an improved energy resolution and is centered at 9.5 eV

tector or by the use of mirrors with high reflectivity in the UV [18.16,17]. Bremsstrahlung isochromat spectra have been reported at a photon energy of 73 eV [18.31,32] using the Al $L_{II,III}$ absorption edge as a low-pass filter in a modified soft X-ray appearance-potential spectrometer [18.33]. It is not clear whether angle-resolved experiments are possible with this detection system.

Instruments for the detection of the bremsstrahlung spectrum generally use gratings as dispersive elements to tune the photon energy [18.11,15,21]. For high acceptance, designs in normal incidence are favorable, but then the energy range is limited due to the decreasing reflectivity of the gratings above 25 eV. Off-normal or grazing-incidence mounts offer higher reflectivity at high energies, but the aberrations of the optical systems set a limit for the grating size.

Figure 18.3 shows a normal incidence spectrograph developed in our laboratory. It has two gratings covering two different energy ranges. On the

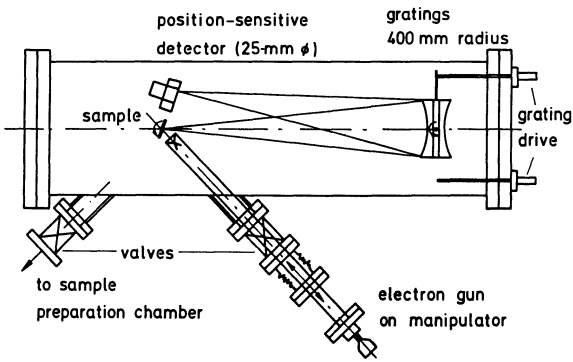

Fig.18.3. Top view of a grating spectrograph for inverse photoemission showing retractable electron source and sample. The light from the sample is dispersed by one of the two gratings and focused on a position-sensitive detector. Sample preparation is performed in a separate vacuum chamber

Rowland circle, the complete spectrum is focused simultaneously, and a position-sensitive detector registers a whole range of wavelengths in parallel. The wavelength window can be selected by rotation of the grating around an axis perpendicular to the plane of Fig.18.3 using the grating drive. The same axis is used to switch to the other grating. Parallel registration of the spectrum is achieved with a position-sensitive device placed tangential to the Rowland circle. It consists of a chevron of microchannel plates serving as photocathode and electron multipliers. The photoyield of the channel plates is enhanced by in situ evaporation of CsI onto the front face of the detector. At the output of the channel plates is a resistive anode. From the signal picked up at the corners of the anode, the location of the primary event can be calculated by electronic circuits. The resolution is 100 lines over the whole detector, which allows the collection of a spectrum in one-hundredth of the time necessary with a single channel detector. The resolution of grating spectrographs is determined by the entrance and exit slits. Values of 0.16 eV have been measured at 10.2 eV [18.21]. To overcome the decreasing resolution at higher energies, different entrance slits can be selected by rotation of the electron gun in our new design (Fig.18.3). The electron gun can be serviced without breaking the vacuum in the main chamber. This is necessary since the CsI coating on the microchannel plates is hygroscopic, and the gratings are not bakeable, which makes venting of the system undesirable. For the same reason, sample preparation is done in a separate chamber, and samples are transferred to the main chamber through an interlock.

Grating spectrographs are powerful instruments for band structure measurements, but the detection efficiency is lower than for a Geiger-Müller counter combined with a mirror [18.16,17]. A different design for an inverse photoemission spectrometer, with tunable photon energies in the range of 8 to 11.7 eV, exploits the anomalous dispersion of LiF lenses [18.34,35]. Good energy resolution and a large acceptance angle make this kind of instrument seem very interesting.

18.3 Density of States

The density of unoccupied states can be measured in inverse photoemission experiments at high energies or from polycrystalline samples, where the randomly oriented crystallites lead to an average over the whole Brillouin zone [18.36]. Bremsstrahlung isochromat spectra from graphite for three different photon energies are shown in Fig.18.4 [18.37]. The count rate at the

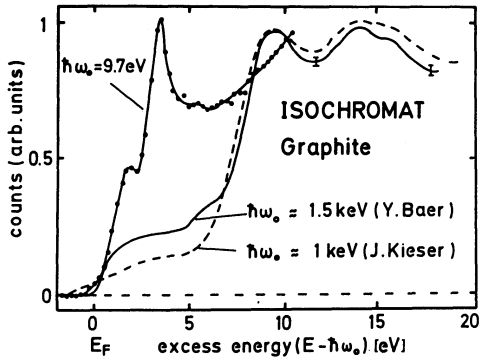

Fig.18.4. Bremsstrahlung isochromat spectra from graphite for photon energies in the UV and X-ray regime [18.37-39]

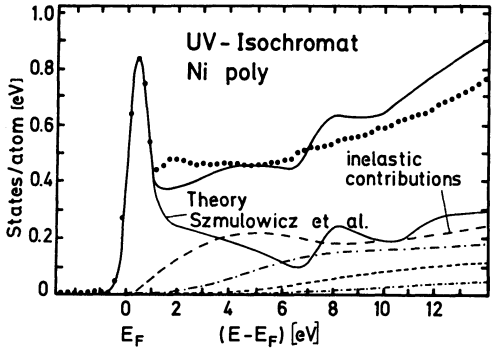

Fig.18.5. Bremsstrahlung isochromat spectrum at 9.7-eV photon energy from a polycrystalline Ni sample (•••). The solid line is the density of unoccupied states (*lower curve*) corrected for contributions resulting from inelastic processes (*dashed and dash-dotted lines*) prior to the radiative process. The corrected upper curve agrees reasonably well with the experimental data [18.41,42]

fixed photon energy $\hbar\omega_0$ is measured as a function of the electron energy and plotted versus the final state energy E_f relative to the Fermi level E_F. The data for 1 keV [18.38] and 1.5 keV [18.39] photon energy agree quite well apart from a small intensity difference below 6 eV. The spectrum for $\hbar\omega_0$ = 9.7 eV shows a sharp peak at 3.4 eV, which is probably the interlayer or surface state [18.40] discussed in Sect.18.4. We note that the spectra change with photon energy, although some of the differences might be attributed to the sample preparation for the 9.7 eV spectrum [18.37].

A bremsstrahlung isochromat spectrum for $\hbar\omega_0$ = 9.7 eV from a polycrystalline Ni sample is shown in Fig.18.5 (dots) [18.41]. The unoccupied d-states appear as a peak right at the Fermi level. The slowly increasing background at higher energies comes from transitions with 9.7 eV photon energy after the incident electron has lost some energy in inelastic processes such as electron-hole pair production [18.43]. The inelastic contributions were calculated using the theoretical density of states by *Szmulowicz* and *Pease* [18.42]. They are indicated by the dashed and dash-dotted curves. The total spectrum is the sum of these inelastic contributions and the density of states. It is shown by the solid line and agrees quite well with the experi-

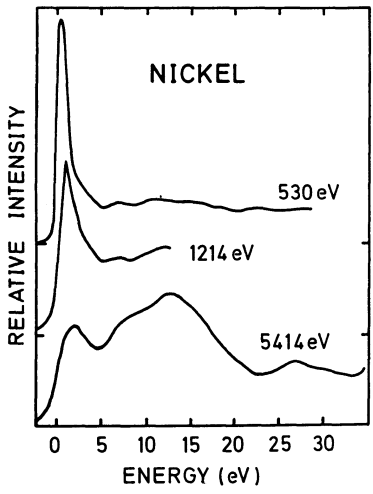

Fig.18.6. Bremsstrahlung isochromat spectra from Ni in the X-ray regime. Strong cross-section variations for the 3d and 4s, p-states are observed. After [18.44]

mental data. Even better agreement can be obtained by inclusion of matrix elements for momentum-conserving transitions [18.36].

Cross-section variations can be seen in Fig.18.6, which shows spectra taken from a Ni sample at three different photon energies in the x-ray region [18.44-46]. The data are corrected for contributions from energy-loss processes and should therefore represent directly the density of states. The intensity of the empty 3d-states decreases with photon energy and at 5.4 keV, transitions into 4s,p-states become dominant. A sum of partial densities of states [18.42] weighted with cross sections for atomic systems is in qualitative agreement with the observed behavior [18.44]. Such a procedure is strictly valid only in the limit of localized states, such as the 4f-states in rare earth metals. Very strong cross-section variations have in fact been observed for Gd [18.47]. An improved understanding of the Ni data would have to start from the itinerant character of the states involved in the transition.

18.4 Band Structure and Surface States

Angle-resolved inverse photoemission spectroscopy is a particularly powerful tool for the measurement of two-dimensional band structures. Its application avoids the problem of determining the perpendicular component of the wave vector $k_i^{\perp}$. On the other hand, we can use a grating spectrograph with variable photon energies to prove the two-dimensional character of the observed states by showing that the energy of the observed final states is independent of initial-state energy E_i.

Fig.18.7.

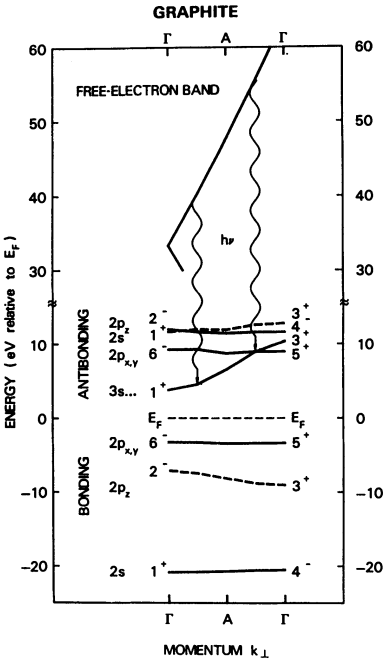

Fig.18.8.

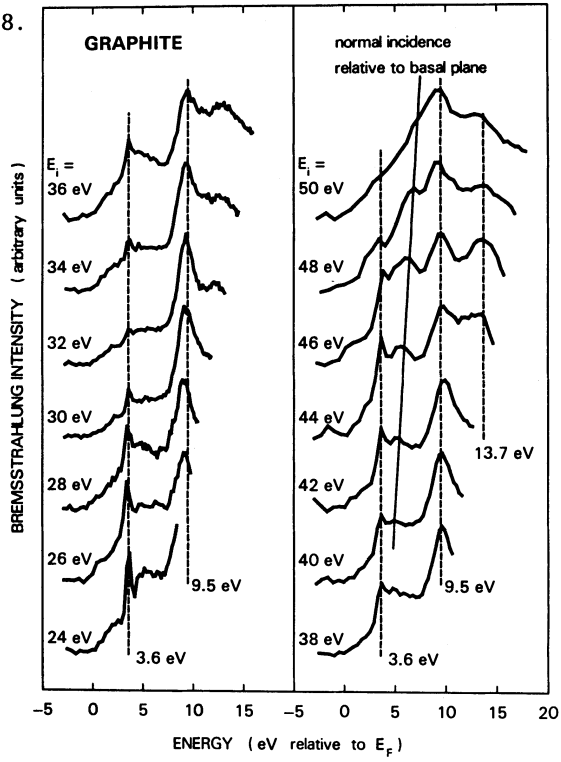

Fig.18.7. Band dispersion of graphite along the ΓA-direction (after [18.48]). The wavy lines show transitions from a free-electron-like band to the dispersing interlayer band

Fig.18.8. Inverse photoemission spectra from a graphite sample in normal incidence for initial-state energies between 24 and 50 eV

Figure 18.7 shows the energy bands of graphite along the ΓA-direction [18.40,48]. We see that the bonding and antibonding 2s- and 2p-like states have almost no dispersion in the direction normal to the hexagonal carbon layers, indicating very little interaction between the layers. The 3s-like band has considerable dispersion and a charge-density concentrated between the layers [18.48,49]. The wavy lines illustrate transitions from two different initial states leading to two different final-state energies for the interlayer band, whereas the 2s- and 2p-like states would show up at a fixed energy. For the initial band used, the free-electron approximation was employed (18.8) with V_0 at the bottom of the valence band. Spectra for initial-state energies between 24 and 50 eV, taken in normal incidence ($k_i^{\perp} = 0$), are plotted in Fig.18.8. We identify the peak at 9.5 eV with transitions into the $2p_{x,y}$-like states in good agreement with theoretical calculations [18.48]. The solid line in Fig.18.8 connects emission features from transi-

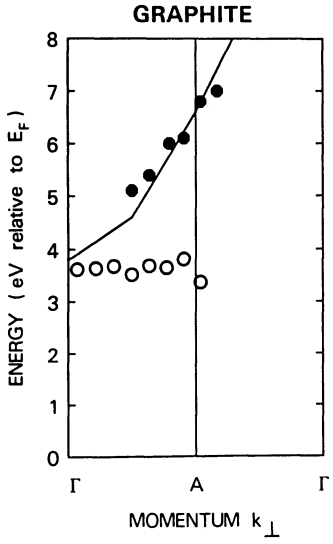

Fig.18.9. The band dispersion determined by the experiment (•••) is in excellent agreement with theoretical calculations (——) [18.48]. The circles correspond to a surface state at 3.6 eV

tions into the interlayer band, and we clearly observe dispersion in the direction normal to the layers. Using (18.8), $\mathbf{k}_i^{\parallel} = 0$ for normal incidence, and the assumption $G_s = 0$ (18.13), we can determine the momentum $\hbar k_f$ and mark the energy of the peaks in a band-structure plot (dots in Fig.18.9). The agreement with theory (solid line) is excellent. The circles in Fig. 18.9 correspond to the peaks at 3.6 eV seen most pronouncedly for low energies E_i in Fig.18.8. We have here another example of cross-section effects. The energy diagram (Fig.18.7) predicts no two-dimensional state in this energy range, and we arrive at the hypothesis of a surface state split off from the bottom of the interlayer band. More recent calculations confirmed this interpretation [18.50].

The dispersion of the two-dimensional states can be mapped out for off-normal incidence of the electron beam ($\mathbf{k}_i^{\parallel} = 0$), and good agreement with band-structure calculations is found also in this case [18.40]. Other examples of two-dimensional layer structures are the transition metal dichalcogenides. For $TiSe_2$, the band dispersion and interlayer interaction has been studied by inverse photoemission [18.51,52].

The determination of the band structure of a three-dimensional solid by inverse photoemission is more complicated due to the nonconservation of $k_i^{\perp}$. We have illustrated the procedure with the free-electron approximation in the previous paragraph on interlayer states in graphite. A semiempirical band dispersion for the initial state has been used for Co [18.53]. Band-structure determinations which do not rely on any assumptions or approxima-

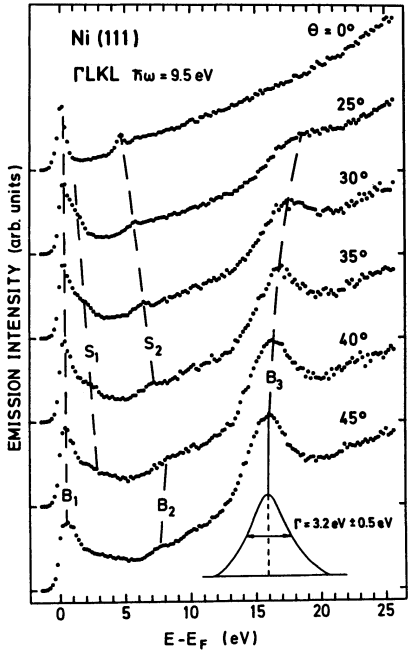

Fig.18.10. Inverse photoemission spectra at 9.5 eV photon energy from a Ni{111} surface for various angles of incidence Θ in the ΓLKL mirror plane

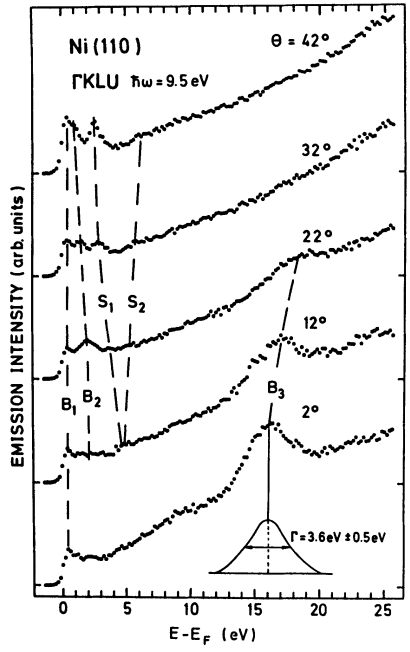

Fig.18.11. Inverse photoemission spectra at 9.5 eV photon energy from a Ni{110} surface for various angles of incidence Θ in the ΓKLU mirror plane

tions are possible with the triangulation or energy-coincidence method [18.54]. This method can be applied if we observe the same transition on two different surfaces of the same sample. An example is the peak labeled B_3 in Figs.18.10 and 11, which show inverse photoemission spectra at 9.5-eV photon energy from Ni{111} and Ni{110}, respectively [18.28]. Arguments for it being indeed the same transition that we observe are the comparable peak widths of about 3.5 eV and the absence of any other structures in the energy range between 10 and 20 eV. Additional support comes from the top panel of Fig.18.12, where the positions of the measured peaks B_3 are plotted as dots and circles in the ΓKLUX-plane of the Brillouin zone using the free-electron approximation for the initial state. An absolute determination of the transition in **k**-space is now possible, since we know $\mathbf{k}_i^{\parallel}$ relative to two different surface planes. Using the two values for peaks coinciding in energy, we can use triangulation to determine $\mathbf{k}_i$ completely. The bottom panel of Fig.18.12 shows the measured final-state energies as a function of $k_i^{\perp}$ relative to the {110}-direction (dots) and {111}-direction (squares). The rhomboids in the top panel mark the positions of the observed transi-

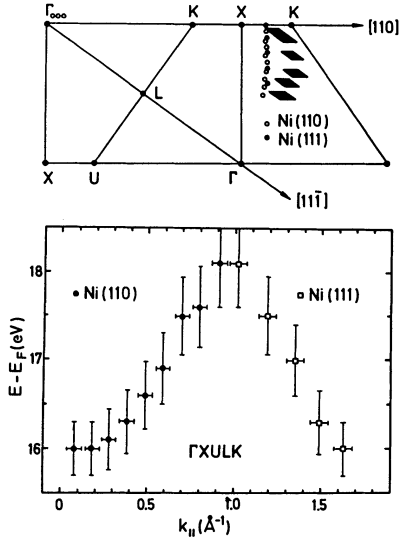

Fig.18.12. Positions of the observed transitions B_3 from Figs.18.10 and 11 in the ΓKLUX-plane of the Brillouin zone by the free-electron approximation (*dots* and *circles*) and by the triangulation method (*rhomboids*). The bottom panel shows the dispersion of the peak B_3 as a function of $k_i^{||}$ relative to the corresponding direction for the data of Figs.18.10 and 11 to illustrate the energy coincidence method

tions in **k**-space obtained by the triangulation method. Taking into account the large error bars, we note a considerable deviation from a free-electron-like dispersion even for energy bands 17 eV above the Fermi level.

We now turn to the other peaks observed in the experimental data. We concentrate here on the Ni{111} surface (Fig.18.10), since the discussion for the Ni{110} surface would not introduce any new ideas or concepts. The interpretation of the data starts at a plot of the observed final-state energies E_f as a function of $k_i^{||}$ similar to the bottom panel of Fig.18.12. For the lower-lying transitions B_1, B_2, S_1, and S_2, the corresponding dispersions are marked with dots in Fig.18.13. The spectra for the ΓLUX-azimuth are similar to the ΓLKL-azimuth (Fig.18.10), and we refer the reader to the original paper [18.28]. The shaded areas in Fig.18.13 mark the edges of the regions where energy bands in the three-dimensional band structure of Ni exist (projected bulk band structure). Dashed lines labeled a' through e' stand for direct transitions energetically allowed by the detection energy. This information was obtained from a band-structure calculation [18.55] by a combined interpolation scheme [18.56].

We see that the observed transitions B_1 and B_2 correspond to the calculated transitions c' and d', respectively. Good agreement between theory and experiment has been found previously for Ni by other authors [18.57-59]. Several other energetically allowed transitions in Fig.18.13 are not observed in the experiment due to additional selection rules and coupling conditions for the incident electron wave function [18.28]. The structures la-

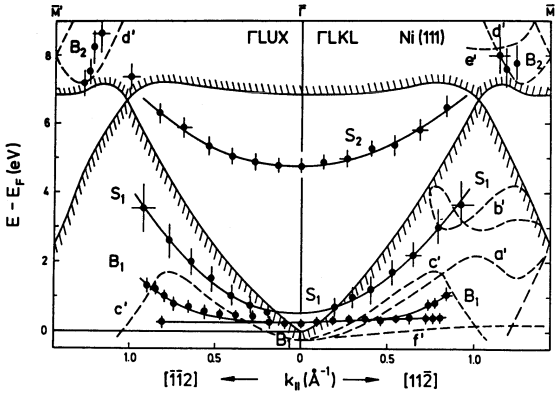

Fig.18.13. Final-state energy E_f as a function of the parallel component of the wave vector $k_i^{\parallel}$ in the ΓKLUX mirror plane for a Ni{111} surface (•••). The shaded area indicates the projected bulk band structure and the dashed lines are calculated transitions energetically allowed by the detection energy

beled S_1 and S_2 in Figs.18.10 and 13 are surface resonances and surface states, respectively. The structure S_1 is a surface resonance similar to occupied surface states observed in photoemission split off from a bulk band due to the breakup of the translational periodicity at the surface of the crystal [18.60]. Analogous states have been observed on Cu{111} [18.60] and Pd{111} [18.61], on Ni{110} (S_1 in Fig.18.11 and [18.28]), Cu{110} [18.19] and Ag{110} [18.62]. The surface state in graphite (Figs.18.8,9) belongs to this class as well as surface resonances observed on Cu{100} surfaces [18.35,63,64].

A different class of surface states observed in inverse photoemission experiments arises from the attractive interaction of the incident electron with its image charge in the sample. The image potential follows a 1/z dependence at large distances from the surface [18.65]. The energies of bound states in this one-dimensional Coulomb potential are usually less than 1 eV with respect to the vacuum level. Note that all other electronic states of either bulk or surface origin are given relative to the Fermi level. Image potential states exist only in gaps of the projected bulk band structure as seen for S_2 on Ni{111} in Fig.18.13. They have been observed on a wide variety of surfaces in inverse photoemission experiments [18.60,61,66,67]. In the absence of lateral forces, an effective mass $m^* = 1$ would be expected for the off-normal dispersion, i.e., the electron should behave like a free particle in its motion parallel to the surface. The experimental data reveal effective masses up to $m^* = 1.7$ [18.28]. The nature of the lateral forces leading to such high values is currently not understood. An explanation in terms of surface corrugation [18.68] is unlikely to be correct.

18.5 Adsorbate States

We begin this section with a short discourse on the oxidation of Ni observed by inverse photoemission. We then proceed to the chemisorption of oxygen on Ni and of CO on various substrates. Bremsstrahlung isochromat spectra at 9.7 eV photon energy are shown in Fig.18.14 for different stages of oxidation of Ni [18.41]. The data represent the density of unoccupied states since they were obtained on a polycrystalline sample. We recognize the spectra for clean Ni from Fig.18.5 again with the peak near the Fermi level arising from transition into the empty d-band. With increasing oxidation, this peak disappears until it has vanished completely for NiO after an O_2-exposure of 20 000 L = 1000 s $\times 2 \times 10^{-5}$ Torr. The peak seen at 4 eV is attributed to Ni_2O_3 in the surface region, and the density of states for NiO is indicated by the solid line in Fig.18.14. NiO is an insulator, and we can clearly see the evolution of the band gap upon oxidation. In combination with photoemission experiments, the gap width is determined to be 4.1 eV [18.69]. The small peak at 1 eV indicated by the dashed line in the 20 000L spectrum of Fig.18.14 is interpreted as arising from transitions into localized states of the configuration d^9. Since photoemission observes a d^7 configuration, an estimate of the Coulomb correlation energy as the difference to the d^8 configuration in the ground state gives U = 2.5 eV [18.41].

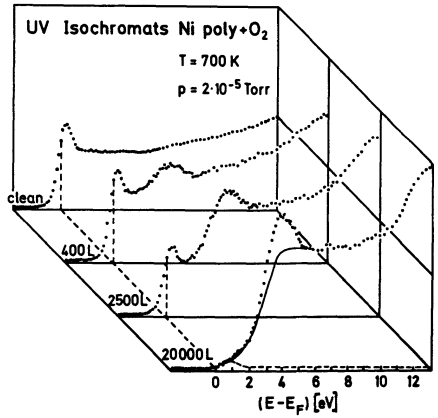

Fig.18.14. Bremsstrahlung isochromat spectra at 9.7 eV photon energy from a polycrystalline Ni surface for various states of oxidation

The initial stage of the chemisorption of oxygen has been studied on various Cu [18.19,35] and Ni [18.70-74] single-crystal surfaces by inverse photoemission. We are going to discuss here the results of *Altmann* et al. on Ni{111} [18.73]. Bremsstrahlung isochromat spectra taken at 9.5-eV photon energy for increasing oxygen exposure are shown in the left-hand panel of Fig.18.15. We note a decrease in the d-band intensity at the Fermi level and

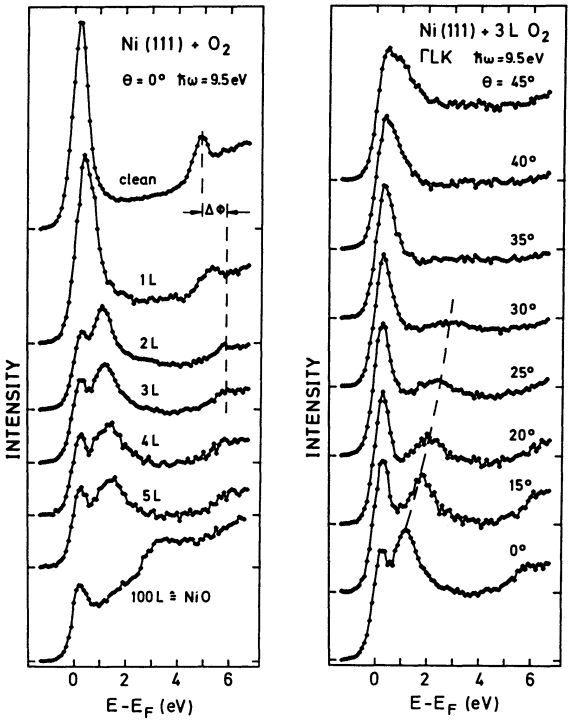

Fig.18.15. Angle-resolved bremsstrahlung isochromat spectra at 9.5 eV photon energy from a Ni{111} surface for various oxygen exposures (*left panel*). The right panel shows the spectra for an ordered p(2 × 2) structure as a function of incidence angle Θ

the emergence of an oxygen-induced peak around 1.5 eV. Its energetic position appears to be slightly coverage dependent. After 100 L oxygen exposure, the spectrum is dominated by NiO emission. For the clean surface, the image potential state is observed at 5 eV. It broadens and shifts to higher energy upon oxygen adsorption. The shift is consistent with the change in the work function and demonstrates the pinning of these states to the vacuum level. A well-ordered p(2 × 2) structure is developed around 3 L exposure. The right-hand panel of Fig.18.15 shows spectra obtained at this coverage for various angles of incidence in the ΓLK-azimuth of the mirror plane. The oxygen-induced peak is seen to disperse to higher energy with increasing angle.

The dispersion obtained with the help of (18.14) is plotted in Fig.18.16 in the extended Brillouin zone of the adsorbate structure (dots and solid line). The shading indicates the projected bulk band structure of the Ni{111} substrate, and we note that near $\bar{\Gamma}$ the experimental band lies in a bulk band gap. This is, however, not sufficient to identify the observed peak as an oxygen-derived state, because the reduced unit cell permits surface umklapp processes by introducing a new reciprocal lattice vector G_s (18.13). The data could then be interpreted as the transitions a' and b' of Fig.18.13 folded

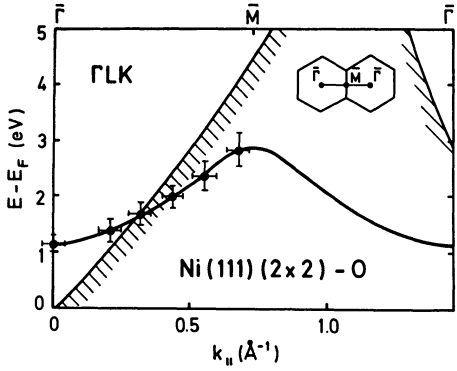

Fig.18.16. Energy dispersion of the oxygen-induced state on a Ni{111} p(2 × 2) surface in the adsorbate Brillouin zone. The shading indicates the edges of the projected bulk band structure

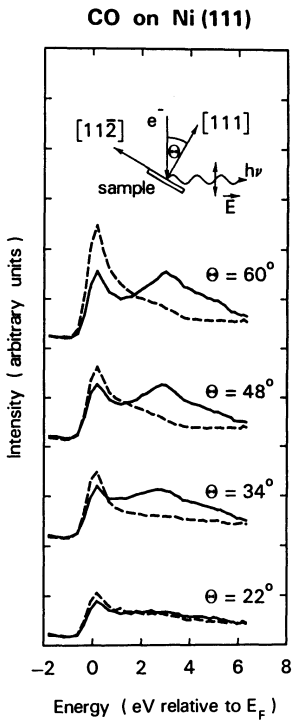

Fig.18.17. Inverse photoemission spectra at 20 eV initial-state energy E_i from a clean (---) and CO-covered (——) Ni{111} surface for various angles of incidence. The experimental geometry is sketched in the upper part of the figure

back to $\bar{\Gamma}$. The energy shift with coverage and a comparison with data on other Ni surfaces [18.74], however, supports the identification of the observed peak as an oxygen $2p_z$-like state.

Unoccupied states induced by chemisorbed molecules are easier to identify. They are more localized on the molecule and retain much of their gas-phase character. The lowest-lying unoccupied orbital of a simple molecule like CO is the 2π-orbital, and there have been several inverse photoemission studies of the chemisorption of CO on various substrates [18.22,70,75-79]. As a first example, we consider the adsorption of CO on Ni{111} [18.75]. We see in Fig.18.17 inverse photoemission spectra taken at an initial-state energy of 20 eV for various angles of incidence for a clean (dashed line) and CO-covered (solid line) Ni{111} surface. For the saturation coverage at room temperature, it is known that the CO molecule is bound normal to the surface via the carbon atom [18.80]. We note in Fig.18.17 a reduction of the d-band emission and the emergence of a broad peak at 3 eV upon CO adsorption. We assign this extra emission to the 2π-derived orbital of the adsorbed CO molecule, which has mainly $2p_{x,y}$ character. Confirmation of this assignment comes from the observation that we have negligible emission intensity for

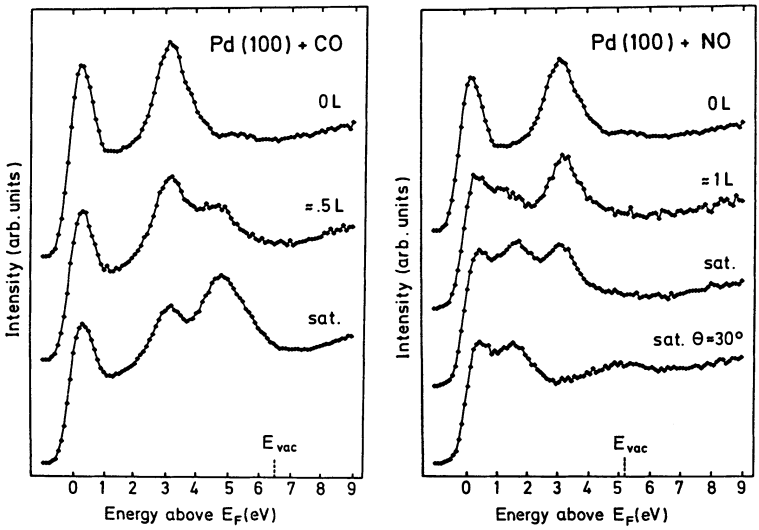

Fig.18.18. Bremsstrahlung isochromat spectra at 9.7 eV photon energy from a clean Pd{100} surface and after CO (*left panel*) and NO (*right panel*) adsorption

near-normal incidence ($\theta = 22^{\circ}$) increasing with angle. For the experimental conditions sketched in the upper part of Fig.18.17, the dipole selection rules allow only emission from p_z-like orbitals at normal electron incidence. In a more sophisticated model including the effect of the surface on the initial state, the selection rules might be relaxed permitting observation of the 2π-orbital even in normal incidence [18.75,78].

Having shown that we can detect the lowest unoccupied orbital of CO by inverse photoemission spectroscopy, it is straightforward to extend these studies to other molecules. This has been done for CO and NO on Pd{100} [18.77]. Figure 18.18 shows bremsstrahlung isochromat spectra at 9.7 eV photon energy in normal incidence for clean Pd{100} and after CO and NO exposure in the left- and right-hand panels, respectively. The clean surface spectrum exhibits emission features from transitions into empty d-states near the Fermi level and from a direct transition around 3 eV. These features are attenuated upon gas adsorption. For CO, the 2π-level appears at about 4.5 eV, whereas the NO-induced emission is observed around 1.5 eV. For an angle of incidence $\theta = 30^{\circ}$, the direct transition disperses, and the NO peak can be seen more clearly (right-hand panel of Fig.18.18). The NO molecule has an extra electron compared to CO, and therefore the 2π-orbital is singly occupied. This explains the position at lower energy, and an examination of the right-hand panel of Fig.18.18 suggests an extension of the NO peak below the Fermi level.

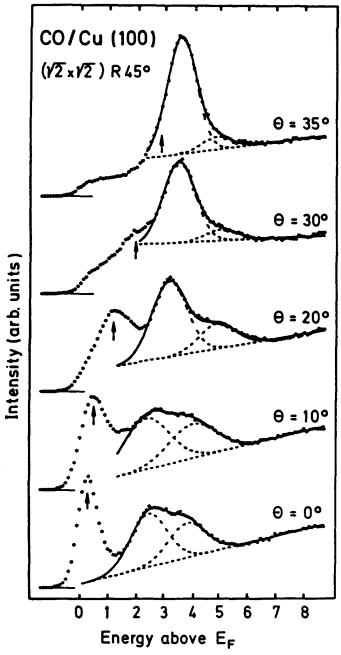

Fig.18.19. Bremsstrahlung isochromat spectra at 9.7 eV photon energy of the adsorption system CO on Cu{100} for various incidence angles. The dashed lines show the decomposition of the CO-induced structure into two peaks and the arrows mark the positions of direct transitions seen also on the clean surface

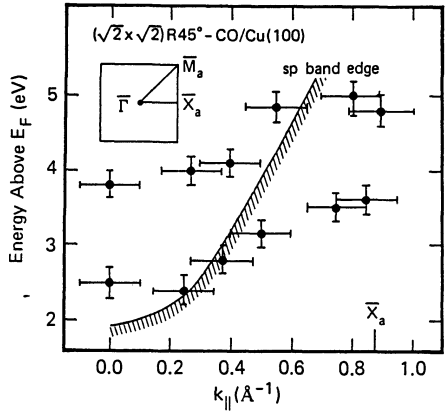

Fig.18.20. Dispersion of the two peaks from Fig.18.19

We now turn to the question of the dispersion of the 2π-orbital of CO chemisorbed on a single-crystal surface. Dispersion is observed for oxygen on Ni{111} (Figs.18.15,16), but for CO on Ni{111}, the peak position remains stationary (Fig.18.17). For CO adsorbed on Cu{100}, the peak width is much smaller, and we note the appearance of two dispersing peaks in Fig.18.19 [18.79]. The spectra were taken at 9.7-eV photon energy for various incidence angles in the bremsstrahlung isochromat mode. The $(\sqrt{2}\times\sqrt{2})R45^\circ$ structure was prepared at a sample temperature of 110 K and corresponds to one-half of a monolayer of CO on the Cu substrate. The decomposition of the CO peak into two peaks of equal width is indicated by the dashed lines in Fig. 18.19. The arrows mark the energetic positions where bulk direct transitions show up for the clean Cu{100} crystal. Such contributions do not interfere with the CO-induced structures. In Fig.18.20, the positions of the experimental peaks from Fig.18.19 are plotted in a band-structure diagram. The line with the shading indicates the edge of the projected bulk band structure. One possible explanation for the occurrence of two different peaks begins with a CO 2π-state of fixed energy (~3.8 eV) and a Cu 4p-band dispersing between 2.5 and 5 eV. The crossing of these levels at $k^{\parallel} \sim 0.4$ Å^{-1} causes a level splitting with a corresponding change of character from CO-2π to Cu4p for the upper band and vice versa for the lower band. This inter-

pretation is confirmed by cluster calculations [18.79] and gives valuable insight into the bonding of CO to metal surfaces.

Inspection of the inverse photoemission spectra for CO on different metal surfaces shows considerable variation of the energetic position of the 2π-level (Figs.18.17-19). An attempt to understand these differences falls back on the chemisorption model of *Blyholder* [18.81]. Within this model, the bonding between the CO molecule and the metal results from a donation of charge from the occupied 5σ-orbital of the CO to the metal and a backdonation into the 2π-orbital. This would mean a lowering of the 2π-level with respect to the vacuum level with a concomitant increase of the strength of the chemisorption bond. A measure of the binding energy of the molecule to the metals is the desorption temperature, which is easily accessible experimentally. We have, therefore, plotted in Fig.18.21 the energy of the 2π-level of CO relative to the vacuum level versus the desorption temperature for all the systems studied by inverse photoemission so far [18.22,70,75-79,82]. We see a good correlation between these two quantities, in spite of quite a bit of scatter. Differences in the Fermi level calibration in data from different groups, as well as shortcomings of the very simple model, may be responsible. Since the discussion of CO adsorption on Cu{100} has shown that the bonding mechanisms may be rather complicated, a correlation as in Fig.18.21 cannot be expected to provide more than a general trend.

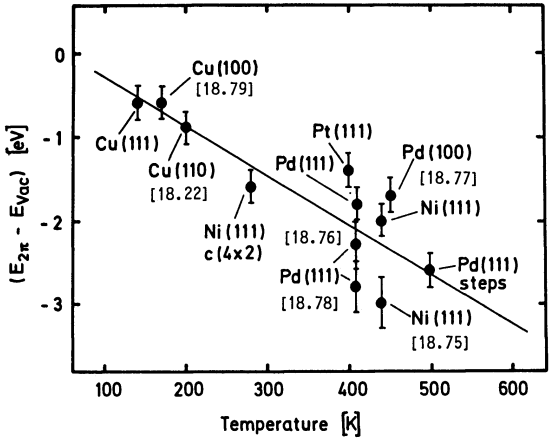

Fig.18.21. Energy position of the CO 2π-level relative to the vacuum level as a function of the desorption temperature for various metal surfaces. The solid line serves as a guide to see the general trend. The numbers in square brackets give the references. Data points without labels are from [18.82]

18.6 Summary and Outlook

We have tried to illustrate in this chapter the wealth of information on unoccupied electronic states that can be obtained by inverse photoemission spectroscopy. The density of unoccupied states can be measured in angle-integrated experiments. In angle-resolved measurements, we can follow the dispersion of unoccupied bands in the Brillouin zone. For adsorbate systems, the unoccupied states near the Fermi level are at least as important as the occupied states observed with photoemission. A complete understanding of bonding at surfaces requires the knowledge of both, and it turns out that the empty, spatially more extended orbitals are often more sensitive probes of the chemisorption bond. We believe that this will be an area of great importance in the future. This will imply the development of more efficient instruments for the study of more fragile molecules. The energy resolution available today is adequate for most systems, considering the line widths of the observed peaks. An extension of the range of photon energies would be interesting for the study of cross-section and matrix-element effects.

Optical absorption and electron energy-loss spectroscopy can also yield information on unoccupied states. They always involve transitions between two states of the sample, making interpretation difficult. Angular resolution cannot be obtained. Angle-resolved electron spectroscopies can sample the unoccupied energy bands above the vacuum level, but they have no access to the important energy range directly above the Fermi level. Photoemission of excited states seems to have the potential of becoming a competitor to inverse photoemission spectroscopy, but it has been applied only to unoccupied surface states so far [18.83,84].

Most of the work reviewed here has been published within the last five years, and we are confident that inverse photoemission spectroscopy is still a growing field which will provide many exciting results in the next five years and beyond.

References

18.1 H. Scheidt: Fortschr. Phys. **31**, 357 (1983)
18.2 W.C. Röntgen: Sitzungsber. Med.-Phys. Ges. Würzburg, **1895**, 137 (1895)
18.3 W. Duane, F.L. Hunt: Phys. Rev. **6**, 166 (1915)
18.4 A. Einstein: Ann. Phys. (Leipzig) **17**, 132 (1905)
18.5 P. Ohlin: Ark. Mat. Astron. Fys. **29A**, 1 (1942)
18.6 B.R.A. Nijboer: Physica **12**, 461 (1946)
18.7 G. Böhm, K. Ulmer: Z. Phys. **228**, 473 (1969)
18.8 V. Dose: Appl. Phys. **14**, 117 (1977)
18.9 J.B. Pendry: Phys. Rev. Lett. **45**, 1356 (1980); J. Phys. C**14**, 1381 (1981)
18.10 E.A. Milne: Philos. Mag. **47**, 209 (1924)

18.11 Th. Fauster, F.J. Himpsel, J.J. Donelon, A. Marx: Rev. Sci. Instrum. **54**, 68 (1983)
18.12 G. Denninger, V. Dose, H.P. Bonzel: Phys. Rev. Lett. **48**, 279 (1982)
18.13 D.P. Woodruff, N.V. Smith: Phys. Rev. Lett. **48**, 283 (1982)
18.14 G. Denninger, V. Dose, H. Scheidt: Appl. Phys. **18**, 375 (1979)
18.15 G. Chauvet, R. Baptist: J. Electron Spectrosc. Relat. Phenom. **24**, 255 (1981)
18.16 K. Desinger, V. Dose, M. Glöbl, H. Scheidt: Solid State Commun. **49**, 479 (1984)
18.17 V. Dose, M. Glöbl, H. Scheidt: Phys. Rev. B**30**, 1045 (1984)
18.18 D.P. Woodruff, N.V. Smith, P.D. Johnson, W.A. Royer: Phys. Rev. B**26**, 2943 (1982)
18.19 R.A. Bartynski, T. Gustafsson, P. Soven: Phys. Rev. B**31**, 4745 (1985)
18.20 N. Babbe, W. Drube, I. Schäfer, M. Skibowski: J. Phys. E**18**, 158 (1985)
18.21 Th. Fauster, D. Straub, J.J. Donelon, D. Grimm, A. Marx, F.J. Himpsel: Rev. Sci. Instrum. **56**, 1212 (1985)
18.22 J. Rogozik, H. Scheidt, V. Dose, K.C. Prince, A.M. Bradshaw: Surf. Sci. **145**, L481 (1984)
18.23 D.T. Pierce, R.J. Celotta, G.-C. Wang, W.N. Unertl, A. Galejs, C.E. Kuyatt, S.R. Mielczarek: Rev. Sci. Instrum. **51**, 478 (1980)
18.24 J. Kirschner, H.P. Oepen, H. Ibach: Appl. Phys. A**30**, 177 (1983)
18.25 J. Unguris, A. Seiler, R.J. Celotta, D.T. Pierce, P.D. Johnson, N.V. Smith: Phys. Rev. Lett. **49**, 1047 (1982)
18.26 H. Scheidt: M. Glöbl, V. Dose, J. Kirschner: Phys. Rev. Lett. **51**, 1688 (1983)
18.27 J.W. Gadzuk, E.W. Plummer: Rev. Mod. Phys. **45**, 487 (1973)
18.28 A. Goldmann, M. Donath, W. Altmann, V. Dose: Phys. Rev. B**32**, 837 (1985)
18.29 J.A.R. Samson: *Techniques of Vacuum Ultraviolet Spectroscopy* (Wiley, New York 1967)
18.30 A. Kovacs, P.O. Nilsson, J. Kanski: Phys. Scr. **25**, 791 (1982)
18.31 D. Straub, V. Dose, W. Altmann: Surf. Sci. **133**, 9 (1983)
18.32 S. Hüfner, P. Steiner, V. Dose, D. Straub, A. Härtl: Solid State Commun. **48**, 257 (1983)
18.33 M. Conrad, V. Dose, Th. Fauster, H. Scheidt: Appl. Phys. **20**, 37 (1979)
18.34 T.T. Childs, W.A. Royer, N.V. Smith: Rev. Sci. Instrum. **55**, 1613 (1984)
18.35 D.P. Woodruff, S.L. Hulbert, P.D. Johnson, N.V. Smith: Phys. Rev. B**31**, 4046 (1985)
18.36 V. Dose, Th. Fauster: Solid State Commun. **50**, 67 (1984)
18.37 V. Dose, G. Reusing, H. Scheidt: Phys. Rev. B**26**, 984 (1982)
18.38 J. Kieser: In *Band Structure Spectroscopy of Metals and Alloys*, ed. by P.J. Fabian, L.M. Watson (Academic, New York 1973) p.557
18.39 Y. Baer: J. Electron Spectrosc. Relat. Phenom. **24**, 95 (1981)
18.40 Th. Fauster, F.J. Himpsel, E.W. Plummer, J.E. Fischer: Phys. Rev. Lett. **51**, 430 (1983)
18.41 H. Scheidt, M. Glöbl, V. Dose: Surf. Sci. **112**, 97 (1981)
18.42 F. Szmulowicz, D.M. Pease: Phys. Rev. B**17**, 3341 (1978)
18.43 V. Dose, G. Reusing: Appl. Phys. **23**, 131 (1980)
18.44 C.C. Chu, P.E. Best: Phys. Rev. B**19**, 3414 (1979)
18.45 R.R. Turtle, R.J. Liefeld: Phys. Rev. B**7**, 3411 (1973)
18.46 R. Kleber: Z. Phys. **264**, 309 (1973)
18.47 Th. Fauster, F.J. Himpsel: Phys. Rev. B**30**, 1874 (1984)
18.48 N.A.W. Holzwarth, S.G. Louie, S. Rabii: Phys. Rev. B**26**, 5382 (1982)
18.49 M. Posternak, A. Baldereschi, A.J. Freeman, E. Wimmer, M. Weinert: Phys. Rev. Lett. **50**, 761 (1983)
18.50 M. Posternak, A. Baldereschi, A.J. Freeman, E. Wimmer: Phys. Rev. Lett. **52**, 863 (1984)

18.51 W. Drube, I. Schäfer, G. Karschnick, M. Skibowski: Phys. Rev. B**30**, 6248 (1984)
18.52 D. Straub, M.J. Skibowski, F.J. Himpsel, W. Drube: Phys. Rev. B**31**, 8254 (1985)
18.53 F.J. Himpsel, Th. Fauster: Phys. Rev. B**26**, 2679 (1982)
18.54 U. Kolac, Th. Fauster, V. Dose, W. Altmann: Solid State Commun. **54**, 791 (1985)
18.55 B. Schiekel, H. Bross: Private communication
18.56 N.V. Smith, L.F. Mattheiss: Phys. Rev. B**9**, 1341 (1974)
18.57 N.V. Smith, D.P. Woodruff: Phys. Rev. B**25**, 3400 (1982)
18.58 D.W. Jepsen, Th. Fauster, F.J. Himpsel: Phys. Rev. B**29**, 1078 (1984)
18.59 G. Thörner, G. Borstel: Solid State Commun. **49**, 997 (1984)
18.60 S.L. Hulbert, P.D. Johnson, N.G. Stoffel, W.A. Royer, N.V. Smith: Phys. Rev. B**31**, 6815 (1985)
18.61 D.A. Wesner, P.D. Johnson, N.V. Smith: Phys. Rev. B**30**, 503 (1984)
18.62 B. Reihl, R.R. Schlittler, H. Neff: Phys. Rev. Lett. **52**, 1826 (1984)
18.63 V. Dose, U. Kolac, G. Borstel, G. Thörner: Phys. Rev. B**29**, 7030 (1984)
18.64 G. Thörner, G. Borstel, V. Dose, J. Rogozik: Surf. Sci. **157**, L379 (1985)
18.65 P.M. Echenique, J.B. Pendry: J. Phys. C**11**, 2065 (1978)
18.66 D. Straub, F.J. Himpsel: Phys. Rev. Lett. **52**, 1922 (1984)
18.67 V. Dose, W. Altmann, A. Goldmann, U. Kolac, J. Rogozik: Phys. Rev. Lett. **52**, 1919 (1984)
18.68 N. Garcia, B. Reihl, K.H. Frank, A.R. Williams: Phys. Rev. Lett. **54**, 591 (1985)
18.69 D.E. Eastman, J.L. Freeouf: Phys. Rev. Lett. **34**, 395 (1975)
18.70 F.J. Himpsel, Th. Fauster: Phys. Rev. Lett. **49**, 1583 (1982)
18.71 H. Scheidt, M. Glöbl, V. Dose: Surf. Sci. **123**, L728 (1982)
18.72 V. Dose, M. Glöbl, H. Scheidt: J. Vac. Sci. Technol. A**1**, 1115 (1983)
18.73 W. Altmann, K. Desinger, M. Donath, V. Dose, A. Goldmann, H. Scheidt: Surf. Sci. **151**, L185 (1985)
18.74 K. Desinger, V. Dose, A. Goldmann, W. Jacob, H. Scheidt: Surf. Sci. **154**, 695 (1985)
18.75 Th. Fauster, F.J. Himpsel: Phys. Rev. B**27**, 1390 (1983)
18.76 P.D. Johnson, H.H. Farrell, N.V. Smith: Vacuum **33**, 775 (1983)
18.77 J. Rogozik, J. Küppers, V. Dose: Surf. Sci. **148**, L653 (1984)
18.78 P.D. Johnson, D.A. Wesner, J.W. Davenport, N.V. Smith: Phys. Rev. B**30**, 4860 (1984)
18.79 J. Rogozik, V. Dose, K.C. Prince, A.M. Bradshaw, P. Bagus, K. Hermann, Ph. Avouris: Phys. Rev. B**32**, 4296 (1985)
18.80 G. Apai, P.S. Wehner, R.S. Williams, J. Stöhr, D.A. Shirley: Phys. Rev. Lett. **37**, 1497 (1976)
18.81 G. Blyholder: J. Phys. Chem. **68**, 2772 (1964)
18.82 J. Rogozik: Private communication
18.83 R. Haight, J. Bokor, J. Stark, R.H. Storz, R.R. Freeman, P.H. Bucksbaum: Phys. Rev. Lett. **54**, 1302 (1985)
18.84 K. Giesen, F. Hage, F.J. Himpsel, H.J. Riess, W. Steinmann: Phys. Rev. Lett. **55**, 300 (1985)

19. The Structure of Surfaces

S.Y. Tong, M.W. Puga, H.C. Poon, and M.L. Xu

Department of Physics and
Laboratory for Surface Studies, University of Wisconsin-Milwaukee,
Milwaukee, WI 53201, USA

The structure of a surface influences many of its important properties. For example, the chemical, electronic, and vibrational properties of surfaces are affected by small changes (i.e., 0.01 to 0.05 Å) in the surface bond lengths. The surfaces of most semiconductors and of some noble metals are reconstructed, producing new and important properties of the surface region. Indeed, modern surface science is anchored on the ability of novel microscopic and spectroscopic techniques to yield quantitative information about surface structure.

In the past decade, a host of surface analytical tools, using photons, electrons, ions, atoms and molecules as probes, were developed to unravel the geometric arrangement of atoms in the surface region. This diversity of techniques is important because not only do the different techniques produce useful cross-checks, they often produce a new level of information that individual techniques alone cannot provide. In this chapter, we will review the use of a number of electron and photon probes and discuss some of the structural results that they have determined. The examples given are primarily based on research work performed in our group in recent years.

19.1 Structure of the GaAs{111}-(2×2) Surface

19.1.1 Reconstruction Mechanisms on the GaAs{111} Surface

Because of the many technological applications and the scientific importance of semiconductor surfaces, their geometric structure has been diligently studied for over three decades. A feature commonly found on semiconductor surfaces is that the surface atoms rearrange to occupy equilibrium sites other than bulk-terminated sites—we call this surface reconstruction. Monopolar and heteropolar semiconductor surfaces offer a wide variety of reconstructed structures. On Si surfaces, for example, there are the (2 × 1) structures of {100} and {111} faces, and (7 × 7) structure of the {111} face. For III-V compound semiconductors, there are the (1 × 1) structure of the

{110} face, (2 × 2) structures of (111) and ($\bar{1}\bar{1}\bar{1}$) faces, and a series of structures [e.g., c(4 × 4), c(2 × 8), c(8 × 2), p(1 × 6), p(4 × 6)]on the {100} face.

It has long been recognized [19.1-3] that dangling bonds of the sp^3 type are unstable on the surfaces of III-V compound semiconductors. In order to lower surface electronic energy, the orbitals of surface atoms rehybridize to form three planar sp^2-type bonds plus an empty dangling hybrid on the group III species. The group V species will have a doubly occupied dangling hybrid and three p-type bonds separated by approximately 90°. In both cases, the rehybridized orbitals resemble more closely the atomic configurations than the sp^3 configuration found for bulk atoms. The orbital rehybridization, and the lowering of energy that follows, are consequences of the chemical properties of III-V atoms. Chemically, the rehybridization lowers the energy of the As dangling states, which are doubly occupied. It also raises the energy of the Ga dangling states, but these are empty. Thus, the buckling process is energetically favorable. Generally, the amount of charge transfer is less for the surface atoms than for bulk atoms.

The orbital rehybridization is most favorable if there are equal numbers of dangling bonds on the nearest Ga and As neighbors. On the {110} surface, the bulk-terminated surface already satisfies this condition, so complete relaxation can take place without altering the (1 × 1) periodicity. The reconstructed structure has Ga surface atoms receding towards the bulk, while As surface atoms rotate outwards. On a bulk-terminated GaAs{111} surface, the situation is quite different. The surface is polar and metallic, with one Ga-derived dangling bond per surface atom. This configuration is unstable and the surface atoms will relax to reduce the Coulomb forces between them. In the next section, we describe a model proposed by *Tong* et al. [19.4] that involves Ga vacancies on the {111} surface.

19.1.2 Vacancy-Buckling Model of GaAs{111}-(2×2)

Consider that a Ga vacancy is formed on the {111} surface. Then, three As dangling bonds are created. To achieve equal numbers of Ga and As dangling bonds on nearest neighbors, the new unit cell must contain three surface Ga atoms. A (2 × 2) periodicity satisfies this condition—each unit cell has three surface Ga atoms, each of which is bonded to an As atom in the layer below. The fourth Ga atom is missing, while the fourth As atom has no dangling bonds, being tetrahedrally bonded to three Ga atoms on the surface and one Ga atom in the layer below.

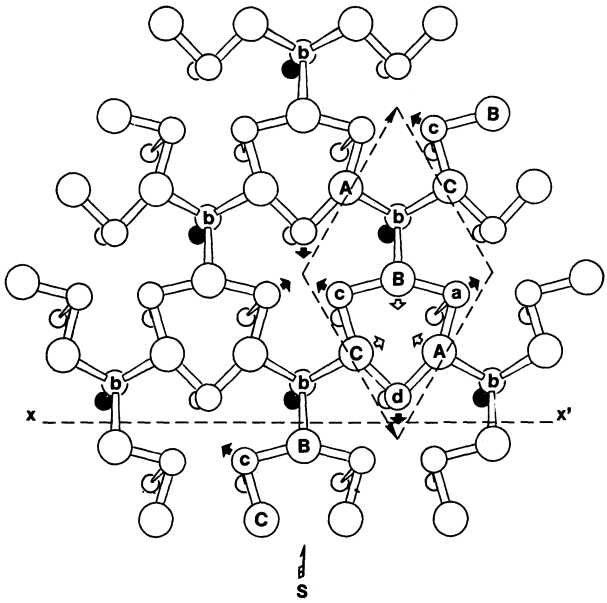

Fig.19.1. Top view of (2×2) vacancy-buckling model. The broken arrows bound a unit cell. (*A, B, C*): surface Ga atoms. (*a, b, c, d*): As atoms

A top view of the vacancy-buckling model [19.4] is shown in Fig.19.1. In this model, each unit cell, bounded by the broken arrows of Fig.19.1, has a Ga atom missing. The remaining three surface Ga atoms, denoted by A, B, and C, recede towards the bulk. By symmetry, they stay on a single plane parallel to the surface. These Ga atoms are bonded to three As atoms in the layer below; the latter (As atoms labeled a, c, and d) also form a single plane, by symmetry. Each of these Ga and As atoms has a dangling bond.

The fourth As atom (labeled b) is tetrahedrally bonded to Ga atoms above and below. This As atom is displaced deeper towards the bulk, relative to the other three As atoms in the unit cell. The Ga atoms in the third layer are also displaced to form two planes; three Ga atoms (smallest empty circles in Fig.19.1) are raised towards the surface while the fourth Ga atom (solid circles) is depressed towards the bulk. Deeper layers have the (1×1) bulk structure. Thus, there are five atomic planes having the (2×2) periodicity in the reconstructed structure. The coordinates of surface atoms of this model are listed in Table 19.1.

The atomic positions of the GaAs{111} surface were determined by analysis of low-energy electron-diffraction (LEED) intensity-energy (I-V) spectra using the multiple scattering slab method [19.5]. The data used contain 5 integral order and 5 half-order beams [19.6]. Because LEED analysis depends

Table 19.1. Atomic positions, with origin at the (bulk) missing atom, for the unreconstructed and reconstructed structures of GaAs(111). The x,y,z axes are along $[1\bar{1}0]$, $[11\bar{2}]$, $[111]$ directions respectively, with the crystal on the +z side

			Unreconstructed surface			Reconstructed surface		
			z	x	y	z	x	y
	Ga	1	0.000	0.000	0.000		missing	
		2	0.000	1.999	-3.462	0.706	1.912	-3.512
		3	0.000	3.997	0.000	0.706	3.997	0.100
		4	0.000	1.999	3.462	0.706	2.086	3.412
First bilayer								
	As	5	0.816	1.999	1.155	0.776	1.757	1.015
		6	0.816	3.997	-2.308	0.896	3.997	-2.308
		7	0.816	5.996	1.155	0.776	6.238	1.015
		8	0.816	3.997	4.616	0.776	3.997	4.896
	Ga	1'	3.264	3.997	-2.308	3.344	3.997	-2.308
		2'	3.264	5.997	-5.770	3.254	5.997	-5.770
		3'	3.264	7.995	-2.308	3.254	7.995	-2.308
		4'	3.264	5.997	1.155	3.254	5.997	1.155
Second bilayer								
	As	5'	4.081	5.997	-1.155	4.081	5.997	-1.155
		6'	4.081	7.995	-4.616	4.081	7.995	-4.616
		7'	4.081	9.994	-1.155	4.081	9.994	-1.155
		8'	4.081	7.995	2.308	4.081	7.995	2.308

on comparing calculated and measured I-V profiles of a large number of structural models, some of which are only very slightly different, it is extremely important that the calculation is accurate [19.5]. There have been examples where wrong structures were selected due to nonconvergent calculations. In the analysis of GaAs{111}, we used the Combined Space Method [19.7], in which multiple scattering within each atomic plane and between different planes are evaluated and summed until numerical convergence is achieved. Up to 229 beams, reduced to 47 symmetrized beams at normal incidence, are used. At typical energies, seven to ten bilayers are included in the calculation.

To help in picking the best structure, we used a reliability factor (R-factor) which is a normalized average of 10 algorithms [19.8,9]. The 10 algorithms compare key features in calculated and measured I-V spectra such as the position, width, and area of peaks, number of peaks, energy of turning points [19.10]. A smaller R-factor indicates better agreement, and a perfect match has a R-factor of zero.

The structure was found by starting with a bulk-terminated (1×1) GaAs{111} surface and displacing the surface Ga plane vertically towards the bulk, keeping the atomic coordinates of all other atoms at those of the bulk.

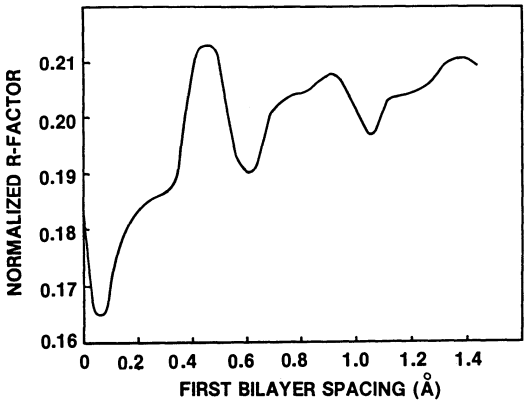

Fig.19.2. Plot of Van Hove-Tong R-factor versus bilayer spacing

The R-factor value is plotted as a function of the first bilayer spacing in Fig.19.2. We found a deep minimum in the range 0.05-0.09 Å. This very small bilayer spacing, being about only 10% of the bulk value, strongly suggests the rehybridization of surface Ga orbitals into the sp^2 type.

Symmetry among beams was used to guide us in the next step of the structural search. If the surface Ga plane, having one vacancy per (2 × 2) unit cell, is displaced vertically towards the bulk, and if the As plane below it retains the (1 × 1) bulk periodicity, then the I-V spectra for the (0,1/2) and (1/2,0) beams should be very similar. The measured spectra for these two beams are, however, very different, as can be seen from Fig.19.3. From the lack of symmetry of these two beams, one can deduce that the correct structure must have lateral displacements of the surface Ga atoms, or rearrangement of the As plane into two or more subplanes having the new (2 × 2) periodicity, or both.

Further information can be obtained from the widths of the measured peaks. If only the surface Ga plane has the (2 × 2) periodicity and all deeper layers retain the bulk periodicity, then the widths of peaks in the half-order beams should be substantially wider than those in the integral-order beams. The data in Figs.19.3 and 4 show that all peaks have about the same widths. This suggests that three or more atomic planes have the (2 × 2) periodicity.

Following these hints, we laterally displaced the surface Ga atoms, A, B and C of Fig.19.1, as well as the As atoms a, c and d. A smaller R-factor was obtained. We then argued that since the fourth As atom, marked b in Fig.19.1, is tetrahedrally bonded, its vertical distance from the surface may be different from that of the other three As atoms. Therefore, we divided the As plane into two subplanes and varied the distance between them. We obtained a smaller R-factor when the subplane containing atom b was below that containing a, c, and d.

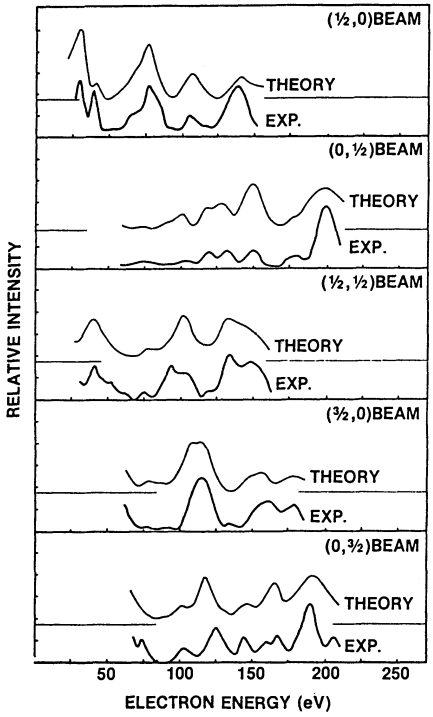

Fig.19.3. Comparison between calculated I-V curves and experiment, for half-order beams, for GaAs{111}

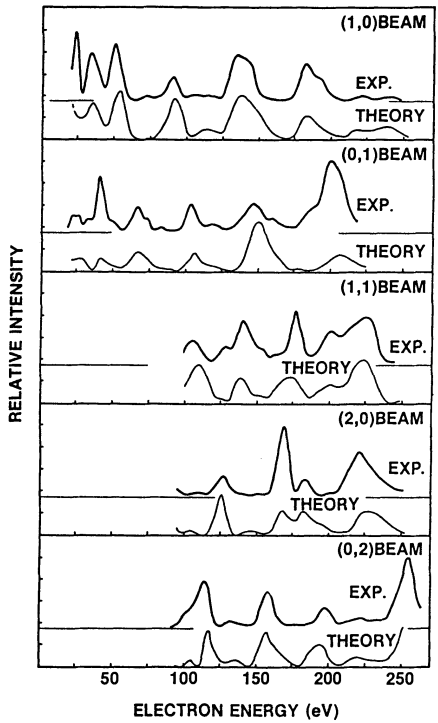

Fig.19.4. Comparison between calculated I-V curves and experiment, for integral-order beams for GaAs{111}

A final improvement in the R-factor was obtained when we divided the Ga plane in the second bilayer into two subplanes. The Ga atom directly below b is despressed into the bulk while the Ga atoms below a, c, and d are raised towards the surface. No lateral displacements are considered for these atoms as they are probably too small to be conclusively determined (<0.03 Å). As each set of new displacements was introduced, we simultaneously varied the spacing within the first bilayer and the spacing between the first two bilayers.

Thus the model has the following features:

(i) One-fourth of a layer of surface Ga atoms are missing.

(ii) Three-quarters of a layer of surface Ga atoms (A,B,C) are pushed 0.706 Å towards the bulk and 0.1 Å laterally along the arrows of Fig.19.1.

(iii) Three-fourths of a layer of As atoms (a,c,d) are raised 0.04 Å towards the surface and displaced 0.28 Å laterally along the arrows of Fig.19.1. The resulting first bilayer has a separation of 0.07 Å.

(iv) One-fourth of a layer of As atoms (b), tetrahedrally bonded, are

pushed 0.08 Å towards the bulk. A distance of 0.12 Å separates the two As subplanes.
(v) The three-fourths of a layer of Ga atoms directly below atoms a,c,d are raised 0.01 Å towards the surface.
(vi) The one-fourth of a layer of Ga atoms directly below atoms b are displaced 0.08 Å towards the bulk. A distance of 0.09 Å separates the two Ga subplanes.
(vii) All atoms in deeper layers occupy bulk sites.

The comparisons between theory and data for the structure listed in Table 19.1 are shown in Figs.19.3 and 4. A side view of the reconstructed (2 × 2) GaAs{111} surface, showing the almost flat surface bilayer, is shown in Fig.19.5.

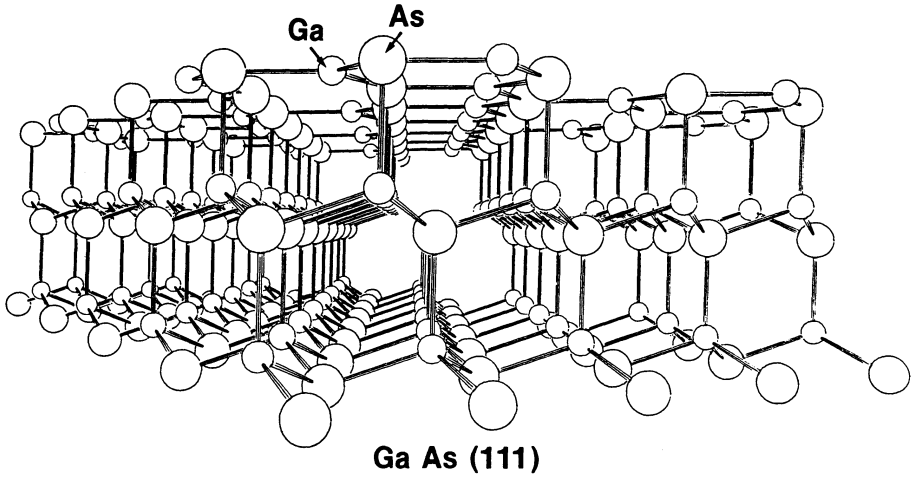

Fig.19.5. Side view of (2×2)GaAs{111}, showing an almost flat surface layer, with ¼ layer Ga atoms absent

Chadi has used energy-minimization calculations on GaAs{111} and found that the vacancy-relaxed model lowers the total energy by 2.3 eV per (2 × 2) unit cell [19.11]. He has also found that the relaxed structure has five sublattices with the (2 × 2) periodicity, in agreement with our result. His determination of the directions of atomic displacements of each subplane are in complete agreement with our results. The only quantitative disagreement of significance between the two works is in the surface bilayer distance: 0.175 Å in Chadi's work compared to 0.07 Å in ours. All other displacements agree to better than 0.03 Å.

Alonso et al. have used quantitative Auger analysis and found a composition of 0.75 Ga versus 1.0 As in the first bilayer of GaAs{111}. This result

is in agreement with our scheme [19.12]. A recent structural determination by surface X-ray diffraction has bound that the InSb{111}(2×2) surface is also vacancy relaxed [19.13].

A key ingredient in the vacancy-relaxed model is that bonds are broken on a surface to allow for electronic relaxation. This is contrary to the heretofore prevailing idea that one must minimize the number of surface dangling bonds and hence, should not break bonds. If surface bonds are not broken, then one can decrease the number of surface bonds by adsorption of As (or Ga) atoms at a threefold site. Each adsorbed atom decreases the number of surface bonds by two. However, the remaining surface bonds cannot rehybridize because they are on distant atoms. Thus, the surface remains electronically unrelaxed with half-filled dangling bonds remaining on the surface. It is believed that such an adsorption model is not energetically favored on the {111} surface.

19.2 Structure of the GaAs{110}-(1×1) Surface

19.2.1 Surface Relaxation on the {110} Surface

In 1964, *MacRae* and *Gobeli* [19.3] concluded that the GaAs{110} face must have a different geometric structure from that of a bulk-terminated face, even though the LEED pattern showed a (1×1) periodicity. They based their conclusion on a lack of symmetry and lack of cancellation in the intensity of certain LEED spots. Subsequent investigators, for example, *Miller* and *Haneman* [19.14], *Rowe* et al. [19.15], and *Harrison* [19.16], came to the conclusion that the reconstruction consisted of surface Ga atoms receding towards the bulk while the As atoms rotated outwards. Arguments analogous to the Jahn-Teller effect were used.

None of the above analyses had the quantitative precision to determine atomic positions. The atomic geometry of the surface was determined by LEED I-V spectral analysis. Results of dynamical LEED calculations show that the Ga-As projected tilt angle on the surface is $27^{\circ} \leqslant \omega \leqslant 31^{\circ}$ [19.6,17, 18]. For the second layer, there are small strain-relieving distortions of the order of 0.01-0.03 Å. Surface state calculations [19.19,20] using these atomic displacements showed the removal of both filled and empty surface states from the band gap, in agreement with previous photoemission results [19.21-23] which found no Fermi-level pinning in GaAs. Energy minimization calculations [19.24,25] found a reduction of 0.3-0.5 eV/surface atom for this reconstruction model.

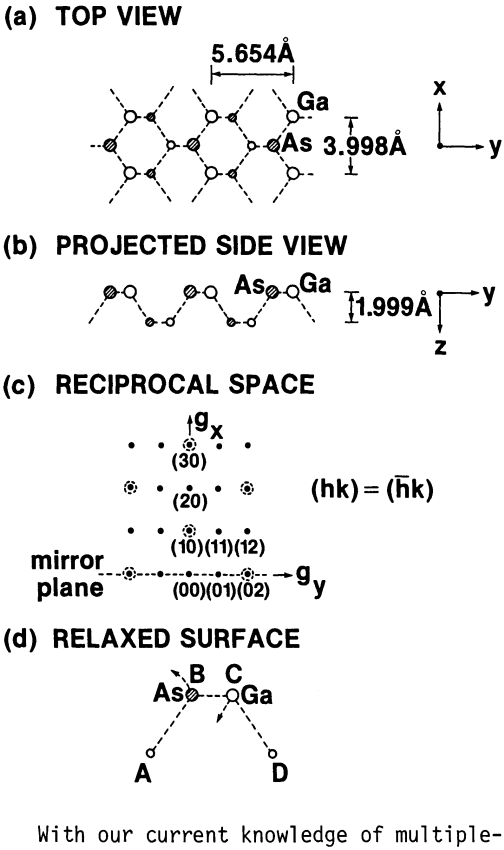

Fig.19.6a-d. Schematic diagrams of ideal (**a**, **b**), and relaxed (**d**) structures of GaAs{110}. Large circles denote surface atoms, small circles denote atoms in second atomic plane. The reciprocal-lattice beams circled in (**c**) are predicted to be weak for the ideal surface structure but are not weak in a relaxed structure. The beam convention follows that of [19.3]

With our current knowledge of multiple-scattering theory of LEED [19.5], it is interesting to review the two observations which led *MacRae* and *Gobeli* [19.3] to the (correct) conclusion that the GaAs{110} surface is geometrically relaxed. The authors based their conclusion on the observations that (i) the (hk) and (hk̄) beams lacked symmetry and (ii) the (10) spectra had strong intensities (i.e., comparable to those of other beams). In Fig.19.6, we show the real and reciprocal spaces of GaAs{110}, using the same beam convention as MacRae and Gobeli.[1]

MacRae and *Gobeli* [19.3] suggested that if the surface is unrelaxed, and if the scattering factors of Ga and As are equal, then beams (hk) = (hk̄). This statement is, in fact, not correct. We now know that an incident electron is rapidly damped as it enters a solid. This means that a deeper layer reflects far fewer electrons than a surface layer. In other words, inelastic damping breaks the symmetry in the direction normal to the surface. Since

1 In our previous work, i.e., [19.17], the beam convention has a sign difference from that of MacRae and Gobeli, i.e., (hk) (*Tong* et al. [19.4]) = (hk̄) (*MacRae* and *Gobeli* [19.3]). In this work, we have switched to the beam convention of MacRae and Gobeli.

an individual layer, see Fig.19.6a, does not have a mirror plane in the xz-plane, beams (hk) and ($h\bar{k}$) are unequal even for a bulk-terminated surface.

The second observation of *MacRae* and *Gobeli* [19.3] was that the (10) beam should be zero if the surface is unrelaxed and the scattering factors of Ga and As are equal. We can expand on this observation. Under the conditions imposed by MacRae and Gobeli, then, at normal incidence, the (10) beam, and the family of (30), (50),... beams, are all zero due to a glide plane symmetry. However, there are other beams, (02), ($0\bar{2}$), (22), ($2\bar{2}$), etc., which should have very weak intensities. This is because these beams have zero intensity in the single scattering (i.e., kinematical) limit. Multiple scattering does scatter electrons into these beams, but the intensities due to multiple scattering are generally smaller (about a factor of 10 smaller, at E = 100 eV and normal incidence). Since the symmetry (hk) = ($\bar{h}$k) holds even after reconstruction, we know that the atomic displacements are confined in the yz-plane. If these are lateral displacements only, and if the Ga and As atoms move by different amounts, then the (02), ($0\bar{2}$), (22), ($2\bar{2}$), etc., beams should become strong, but the (10), (30), (50), etc., beams should remain weak, because in the single-scattering limit, their intensities are still zero. The fact that *all* beams are strong and comparable [19.3], suggests vertical and unequal displacements for Ga and As atoms.

Thus, by analyzing beam symmetry and noting beam intensities as MacRae and Gobeli did, we can now draw the following conclusions: (i) The geometric relaxation consists of atomic displacements confined in the yz-plane (of Fig.19.6a). (ii) If the atomic displacements are lateral only, the (20) beam (and family) should be strong but the (10) beam (and family) should remain weak. (iii) Since the (10) and (20) beams are both observed to be strong, there must be large, unequal vertical displacements of the Ga and As atoms in the unit cell. It is interesting to note that observation (iii), that of large, *unequal vertical* displacements for Ga and As atoms, suggests the Jahn-Teller distortion.

19.2.2 Value of the ω Tilt Angle on the {110} Surface

The geometric structure of GaAs(110) determined by low-energy electron-diffraction (LEED) intensity-voltage (I-V) spectra analysis generally agreed on the following points: In the surface diatomic layer, the Ga atoms recede towards the bulk and As atoms rotate outwards with an angle ω projected on a plane normal to the surface of between 27° and 31° [19.17,18]. In the second diatomic layer, there are strain-relieving distortions of the order of 0.03-0.09 Å. The atomic displacements cause surface bonds to re-

hybridize, and surface bond lengths vary somewhat from that of the bulk. Lateral displacements have been found to be relatively large for both Ga and As atoms in the surface layer.

These results were challenged, however, by recent studies. First a high energy ion scattering work [19.26] found that a surface model with large lateral displacements was incompatible with the measured surface peak intensity. This analysis predicted an upper bound of less than 0.1 Å in lateral displacements for either the surface Ga or As atom. Adding to the confusion was a recent LEED study [19.27] which found that for a bond-length-conserving top-layer rotation model, a small angle of tilt, $\omega = 7.3^{\circ}$, gave a slightly better X-ray R-factor (R_X) than larger angles of tilt, $\omega \simeq 27^{\circ} - 31^{\circ}$. However, after using a different R-factor, the so-called integrated beam R_I, the present authors [19.18] preferred a large tilt angle of $\omega = 31.1^{\circ}$.

These two works raised important questions concerning the surface geometry of GaAs{110}. In particular the following questions needed to be answered: (i) Are lateral displacements of less than 0.1 Å compatible with analysis by accurate dynamical LEED theory? (ii) If one uses an accurate dynamical LEED theory, does one still find an ambiguity of R_X between $\omega = 7.3^{\circ}$ and $\omega = 27^{\circ} - 31^{\circ}$?

To answer the above questions, *Puga* et al. [19.18] have carried out a fully convergent multiple-scattering calculation for GaAs{110}. Three R-factors were used in the analysis: the Van Hove-Tong R-factor (R_{VHT}) [19.8,28,29], the Zanazzi-Jona R-factor (R_{ZJ}) [19.30], and the X-ray R-factor (R_X) [19.27]. The bond-length-conserving top-layer rotation model was tested and the three R-factors versus ω are plotted in Fig.19.7.

From the figure, it is clear that there is no ambiguity between $\omega = 7^{\circ}$ and $\omega = 30^{\circ}$. All three R-factors, R_X, R_{ZJ}, and R_{VHT}, strongly prefer the larger ω values. There is a local minimum at 10° but its R_X value is 78% larger than that at $\omega = 30^{\circ}$. Local minima, besides the global minimum, in an R-factor curve are very common. This is so because LEED I-V spectra have many peaks. As surface geometric parameters (e.g., the value of ω) are changed, the calculated peak positions shift in energy. This leads to an oscillatory behavior in the comparison between calculated and measured I-V curves. As long as the global minimum is well below each local minimum, as it is the case in Fig.19.7, there is no ambiguity in selecting the correct structure.

Once the optimal value of ω had been found via a bond-length-conserving model, *Puga* et al. [19.18] relaxed the structure to optimize the rest of the parameters. This search was performed by keeping the relative positions

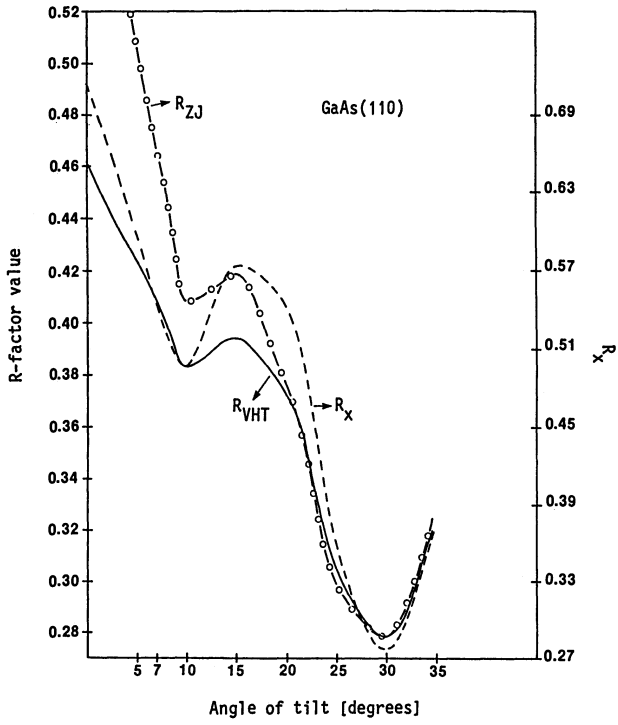

Fig.19.7. Plots of R-factor values versus tilt angle ω for the bond-length-conserving top-layer rotation model. Solid line: R_{VHT}; broken line: R_X; and chained line: R_{ZJ}

between the Ga and As atoms of the first layer constant (i.e., at $\omega = 30^{\circ}$) and optimizing their positions with respect to the second layer. A second layer tilt in the range 0.03-0.09 Å was implemented to relieve strain. The results are shown in Table 19.2. The best structure corresponds to a situation in which the Ga atom in the second layer moves vertically up by 0.03 Å and the As atom moves down by the same amount, yielding a combined tilt of 0.06 Å with an R-factor (R_{VHT}) of 0.256. This result, however, does not discriminate against other possible tilts. In fact we observe from Table 19.2 that tilts of 0.03 Å and 0.09 Å yield structures with values of R_{VHT} higher by only 5.8% and 1.8%, respectively. Such variations are within the error bars of the method and we therefore conclude that a second layer tilt in the range 0.03-0.09 Å is compatible with the experimental data.

Puga et al. [19.18] then kept the second layer tilt at 0.06 Å and optimized the positions of the first layer atoms relative to the bulk. The results as shown in Table 19.3, where for each ω, the best structure obtained out of the 15 structures is listed with the corresponding R-factors. For

Table 19.2. Values of R_{VHT} as a function of the second layer tilt Δ_2. The Ga atoms in the second layer are displaced vertically downward by $\Delta_2/2$ while the As atoms are displaced vertically upwards by an equal amount

Δ_2 [Å]	R_{VHT}	Change from minimum [%]
0.00	0.278	7.1
0.03	0.271	5.8
0.06	0.256	0
0.09	0.258	1.8

Table 19.3. Displacements of the first layer atoms which produce the smallest R_{VHT} values for each value of ω

	ω [°]	$(As)_{\perp}\uparrow$	$(As)_{\parallel}$	$(Ga)_{\perp}\downarrow$	$(Ga)_{\parallel}$	R_{VHT}	Change from minimum [%]
(a)	27	0.155	0.163	0.487	0.317	0.261	1.9
(b)	28	0.157	0.165	0.507	0.331	0.258	0.8
(c)	29	0.161	0.167	0.525	0.345	0.258	0.8
(d)	30	0.193	0.169	0.515	0.359	0.256	0
(e)	31	0.195	0.170	0.535	0.373	0.260	1.6

each structure we show vertical and lateral displacements of both surface atoms.

The numbers in Table 19.3 show a fairly consistent trend in which the optimal structures select very similar values of the four displacements of the surface atoms regardless of the numerical value of the tilt angle ω. This means that the parameters most sensitive to the I-V curve are the physical displacements of the atoms from their bulk positions. The tilt angle ω can be varied by changes in the vertical as well as horizontal distances between surface Ga and As atoms. Its value varies from 27° to 31°, while the R-factor changes by less than 2%. These findings indicate that ω *is not* a sensitive indicator of the structure and that the physical quantities that affect the I-V curves are the displacements of the atoms themselves. The effect is particularly pronounced for the parallel displacement of the As atom. The optimal structures listed in Table 19.3 (one for each different value of ω) have variations in this parameter of ≤ 0.007 Å although ω varies from 27° to 31°.

Since the R-factor values for the structures listed in Table 19.3, are so similar, all these structures are acceptable. Of these, structure (d) has the smallest R-factor. It corresponds to parallel shifts of 0.17 Å and 0.36 Å for the As and Ga top-layer atoms, respectively. These shifts fall outside the 0.1 Å upper bound suggested by the ion scattering results [19.26]. To address this question and to study the effects of reducing

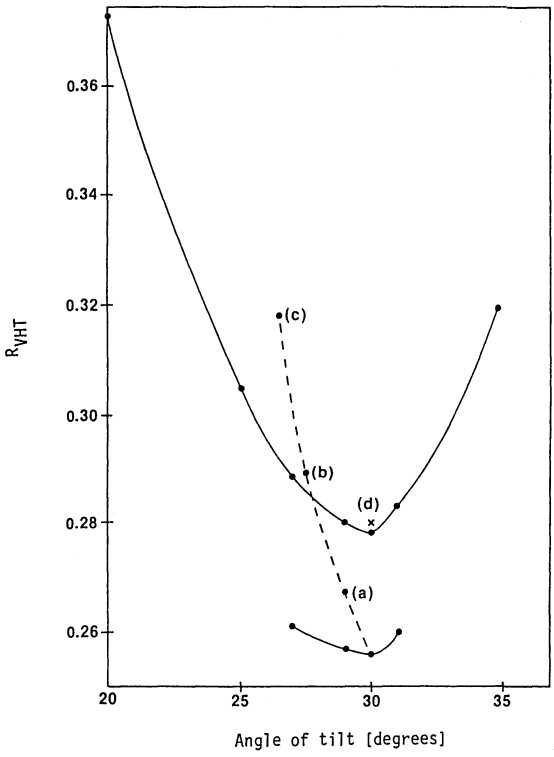

Fig.19.8. Plot of R_{VHT} versus tilt angle ω. Upper and lower curves correspond to one- and two-layer reconstruction models, respectively. Points (a)-(d) correspond to reducing the surface Ga and As lateral shifts

lateral shifts, Puga et al. started with the best structure [Table 19.3, structure (d)] and systematically reduced the lateral shifts. The results are shown in Fig.19.8, where we have redrawn part of the R_{VHT} curve already shown in Fig.19.7 and added the points listed in Table 19.3 which included a second layer tilt of 0.06 Å. The figure shows that as the lateral shifts are reduced, the R_{VHT} values increase rapidly. Points a, b, c of the broken line in Fig.19.8 represent the R_{VHT} values corresponding to reducing the lateral shifts of Ga and As by 1/3, 2/3, and 3/3, respectively. We note that as we do this, the two atoms are shifted by different amounts, hence the tilt angle ω changes value. Reducing the shifts by 2/3 [i.e., (b): $\Delta As_{||} = 0.056$ Å, $\Delta Ga_{||} = 0.120$ Å] has the Ga atom lying outside the ion-scattering upper bound of 0.1 Å [19.27]. The corresponding R_{VHT} value at (b) is 13% worse, which is well above the error bar of the LEED analysis. It is concluded, therefore, that the LEED result would rule out a structure whose surface atom lateral displacements are $\leqslant 0.1$ Å.

There is an additional point shown in Fig.19.8. This point (d) corresponds to reducing the lateral shifts by subtracting 0.169 Å from both the toplayer

Table 19.4. Values of R_{VHT} corresponding to reducing the surface Ga and As lateral shifts

Shift	$\Delta As_{\parallel}$ [Å]	$\Delta Ga_{\parallel}$ [Å]	R_{VHT}	Change [%]
$\Delta_{\parallel}$	0.169	0.359	0.256	0
$2\Delta_{\parallel}/3$	0.113	0.240	0.267	4
$\Delta_{\parallel}/3$	0.056	0.120	0.289	13
0	0.000	0.00	0.318	24
Equal shifts of $\Delta_{\parallel} = 0.169$ Å	0.00	0.190	0.280	9

$\Delta Ga_{\parallel}$ and $\Delta As_{\parallel}$. In this structure the surface As atom has zero lateral shift and the Ga atom has a lateral shift of 0.19 Å. This point (d) yields R-factor which is worse by 9%. Further reduction of the surface Ga lateral shift (e.g., to ≤ 0.1 Å) again pushes the R_{VHT} values above the error limit of the method. The R_{VHT} values corresponding to points (a)-(d) are listed in Table 19.4 for easy reference.

It is concluded that for GaAs{110}, results of a fully dynamical theory of LEED unambiguously select an angle of tilt $27^{\circ} \leq \omega \leq 31^{\circ}$. The smaller tilt angle $7^{\circ} \leq \omega \leq 10^{\circ}$ gives a result which is outside the error bar of the method. Moreover, lateral shifts >0.1Å for the surface atoms are necessary to obtain acceptable agreement with the experimental data. The reconstructed GaAs{110} surface, under these conditions, is almost totally electronically relaxed [19.31].

19.3 Structure of the GaP{111}-(2×2) Surface

Structural determination of the {111} surface of another III-V compound semiconductor, GaP, was reported recently [19.32]. The results again indicate a vacancy-stabilized structure, with one-fourth of surface Ga atoms missing. The orbitals on the remaining surface Ga atoms rehybridize into sp^2 orbitals while those in the nearest-neighbor P atoms rehybridize into s^2p^3 orbitals. This result is consistent with the reconstruction model found on GaAs{111}, and together with results of a recent X-ray scattering analysis [19.13] on the InSb{111} surface, strongly suggests that the {111} surface of many III-V compound semiconductors undergoes the same (2 × 2) vacancy-stabilized reconstruction.

The LEED study was done by analyzing ten beams; five integral beams (1,0; 0,1; 1,1; 2,0; and 0,2) and five half-order beams (1/2,0; 0,1/2; 1,1/2; 3/2,0; and 0,3/2). The I-V data were taken on a GaP(111) surface which was polished and chemically etched to differentiate the (111)-Ga rich face from the $(\bar{1}\bar{1}\bar{1})$-P rich face. Using an etching solution of HCl: HNO_3: H_2O =3:1:4 and an etching time of about 2 minutes, the (111) face showed dislocation pits with hexagonal shapes. The $(\bar{1}\bar{1}\bar{1})$ face did not show this feature due to the high etching speed.

The sample was then placed in an ultra-high-vacuum chamber (3×10^{-10} Torr) with the (111) face towards the electron gun. A bombard-annealing cycle was used to clean the sample using Ar ions at 500 eV and temperatures of 550°C. After several cycles, the surface showed no detectable oxygen signal and a very minute trace of carbon (<1 in 10^2 atoms) using Auger electron spectroscopy.

A sharp and stable (2×2) pattern was observed and it was easily reproduced. Scanning over the sample, it was found that every place in the surface showed a (2×2) pattern with a 3-fold symmetry. This indicated that the surface structure has a true (2×2) periodicity and the LEED pattern was not made up of domain averages of patches with lower symmetry [e.g., three domains of (2×1) structures].

For the theoretical analysis, a fully convergent multiple-scattering program of LEED [19.7] was used. All the dynamical inputs were left the same as those used for the GaAs{111} surface [19.31], with the obvious exception that different phase shifts were used for the Ga and P potentials. Thus, only structural parameters were allowed to vary in optimizing the agreement between calculated and measured I-V curves. The Van Hove-Tong [19.8,28,29] and Zannazi-Jona [19.30] R-factors were used in the intensity spectra analysis. The calculation used 6 partial waves and 229 beams, and a temperature correction with surface and bulk root-mean-square vibration amplitudes of 0.13 Å. The C_{3V} symmetry among beams was used to reduce the 229 unsymmetrized beams to 47 symmetrized beams.

An important parameter in the structural search is d_1, the spacing between the first (Ga) and second (P) atomic planes. This spacing was first varied, while keeping a (1×1) structure and all other structural parameters at bulk values. Figure 19.9 shows the dependence of R_{VHT} on d_1, using comparison between theory and experiment for the five integral beams (no half-order beams were used at this stage, since we were testing a 1×1 structure). From Fig. 19.9, it is clear that we can rule out the bulk spacing (0.79 Å). There are two regions where R_{VHT} has minima (d_1 =0.59 Å and 0.06 Å). Further search

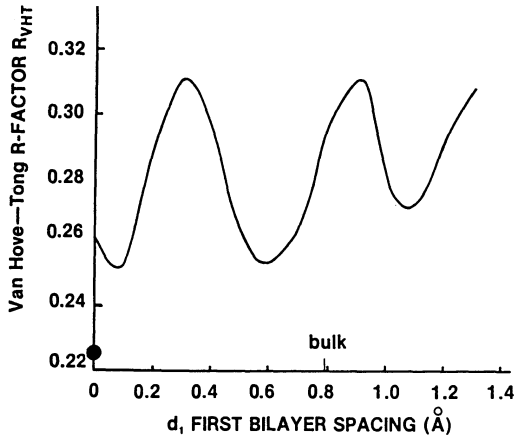

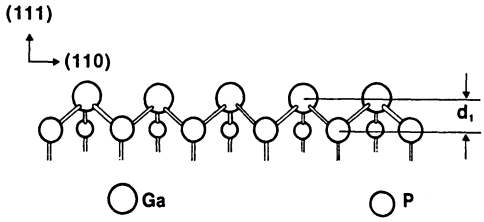

Fig.19.9. Plot of R-factor versus the surface bilayer spacing for GaP(111). Three minima occur at $d_1 = 0.06$, 0.59, and 0.79 Å. The solid circle on the y-axis indicates the R-factor value of the optimal structure listed in Table 19.5. Lower figure indicates the first bilayer atoms in an ideal bulk structure

near the $d_1 = 0.59$ Å minimum produced very poor (i.e., large) R_{VHT} values ($R_{VHT} \sim 0.3$ to 0.4). The optimal structure was found by searching in the vicinity of the minimum near $d_1 = 0.06$ Å. By introducing lateral and vertical displacements on surface and subsurface atoms, and by removing one-fourth of the Ga atoms from the surface, the final R_{VHT}-factor was 16% below the minimum of the curve in Fig.19.9 (see solid circle at $d_1 = 0$).

The final structural parameters are listed in Table 19.5. Figures 19.10 and 11 show the agreement obtained between calculated and measured I-V curves. Such good agrement, corresponding to our optimal structure, has an R-factor of $R_{VHT} = 0.19$ for the integral beams and $R_{VHT} = 0.25$ for the half-order beams. The combined R-factor for all beams is $R_{VHT} = 0.21$ (different beams are weighted differently because of the different energy range of the measured data). As noted earlier, this final value of the R-factor is indicated as an extra point in Fig.19.9, the solid circle on the y-axis of the figure. The very small d_1 value in the final structure is significant. It indicates that the Ga surface atoms are almost entirely rehybridized into planar sp^2 bonds. This coplanarity is indicative of vacancy formation, since in each (2 × 2) unit cell 3 Ga atoms rehybridize into sp^2 bonds. This can be achieved by having the fourth Ga missing, creating 3 P atoms with dangling bonds to accept the (3) additional electrons. If it were a buckled model, and the fourth Ga atom were simply raised on the surface, it would have to receive the (almost) 3

Table 19.5. Atomic positions, with origin at the (bulk) missing atom, for the unreconstructed and reconstructed structures of GaP(111). The x,y,z axes are along the [1$\bar{1}$0], [11$\bar{2}$], [$\bar{1}\bar{1}\bar{1}$] directions, respectively, with the crystal on the +z side

			Unreconstructed surface			Reconstructed surface		
			z	x	y	z	x	y
		1	0.000	0.000	0.000		missing	
	Ga	2	0.000	1.927	-3.338	0.746	1.809	-3.406
		3	0.000	3.854	0.000	0.746	3.854	0.136
		4	0.000	1.927	3.338	0.746	2.045	3.270
First bilayer								
		5	0.787	1.927	1.113	0.746	1.728	0.998
	P	6	0.787	3.854	-2.225	0.836	3.854	-2.225
		7	0.787	5.781	1.113	0.746	5.980	0.998
		8	0.787	3.854	4.450	0.746	3.854	4.680
		1'	3.147	3.854	-2.225	3.237	3.854	-2.225
	Ga	2'	3.147	5.781	-5.563	3.127	5.781	-5.563
		3'	3.147	7.708	-2.225	3.127	7.708	-2.225
		4'	3.147	5.781	1.113	3.127	5.781	1.113
Second bilayer								
		5'	3.934	5.781	-1.113	3.934	5.781	-1.133
	P	6'	3.934	7.708	-4.450	3.934	7.708	-4.450
		7'	3.934	9.635	-1.113	3.934	9.635	-1.113
		8'	3.934	7.708	2.225	3.934	7.708	2.225

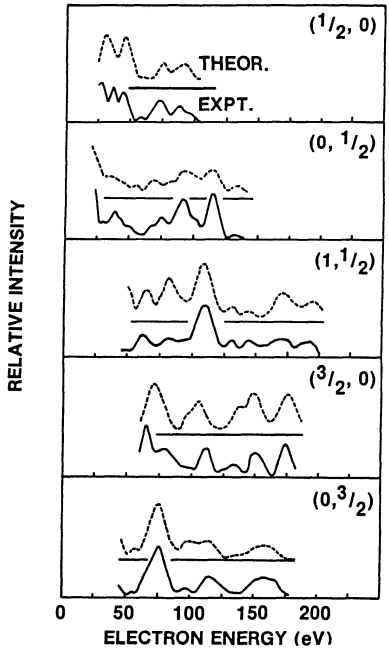

Fig.19.10. Comparison between calculated I-V curves and experiment, for half-order beams, for GaP(111)

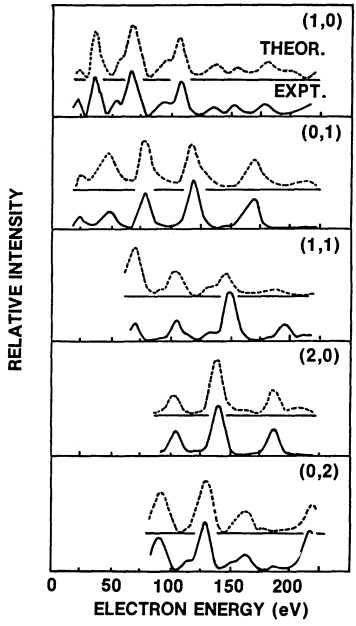

Fig.19.11. Comparison between calculated I-V curves and experiment, for integral-order beams, for GaP(111)

electrons transferred from the planar Ga atoms. This would result in a much less complete rehybridization and the structure would have less coplanarity than the one that was determined.

19.4 General Trend on Reconstructed {110} and {111} Faces of III-V Compounds

From the discussions presented in Sects.19.1-3, we have shown that orbital rehybridizations, of the $sp^3 \rightarrow sp^2$ type for group III atoms, and $sp^3 \rightarrow s,p_{x,y,z}$ type for group V atoms, are responsible for the reconstructed structures found on the {110} and {111} surfaces of GaAs, and the {111} faces of GaP and InSb. On each reconstructed surface, an equal number of dangling hybrids of each type exist, with the group V-derived hybrids filled and the group III-derived hybrids empty. To achieve this, the {111} surface must have one vacancy per (2×2) unit cell. It is reasonable to expect that similar process could occur on the {110} and {111} faces of other III-V compound semiconductors.

19.5 Forward-Focusing Effects in X-Ray Photoemission Spectroscopy

We now turn our discussion to another surface analytical tool for structure determination. This technique is a specific use of angular-dependent photoelectron diffraction and is called forward-focusing X-ray photoelectron spectroscopy (XPS). For a general discussion of angular- and energy-dependen photoelectron diffraction for structural analysis, the reader is referred to the review article "Diffraction Effects in Angle-Resolved Photoemission Spectroscopy [19.33].

In forward-focusing XPS, photoelectrons at fixed photon energies are measured as a function of polar exit angles for particular azimuthal directions. Particular attention is paid to photoelectrons that are scattered in the forward direction. In recent measurements by *Egelhoff* [19.34], large variations in the intensities of angle-resolved XPS and Auger electron spectroscopy (AES) were found as a function of the emission angle. Some peaks coincide with the directions of internuclear axes of the emission site and its neighbors (Fig.19.12). Other peaks, however, are not related to such directions. As the energy is varied, the internuclear peaks stay at almost the same angles, while other peaks undergo changes in their angular positions. We shall discuss the physical origins of these peaks as well as their energy and temperature dependence. We shall also show that multiple scattering effects play an important role in determining the intensity of the internuclear

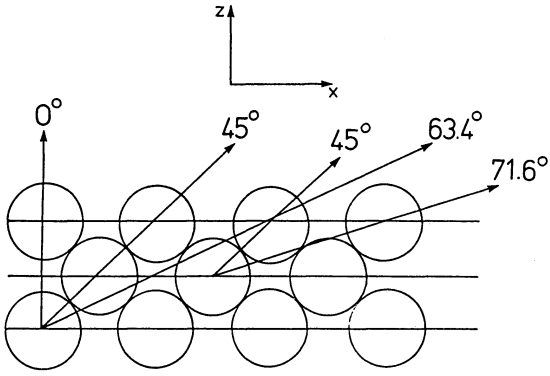

Fig.19.12. Internuclear directions for 3 layers of atoms for Cu{100}; the x-axis is along <100>.

peaks when there are more than two atoms lying on the same axis. The small-atom approximation, also known as the plane-wave approximation, which is commonly used in back-scattering electron spectroscopies such as extended x-ray absorption fine structure (EXAFS) or angle-resolved ultraviolet photoelectron spectroscopy (ARUPS), is found to be inadequate in the case of forward scattering.

19.5.1 Physical Origin of Peaks in Egelhoff's Experiment

Let us consider a classical model with electrons emitted isotropically from a source atom. These electrons are scattered by a neighboring atom which has an attractive cut-off Coulomb potential (Fig.19.13). For scattering angles close to zero ($\theta \sim 0^\circ$), the electrons diverging from the source are "focused" into a much smaller area, causing an intensity enhancement in the forward direction.

An exact quantum mechanical treatment also gives rise to such a focusing effect. The focusing peak in the forward direction is due to constructive interference of scattered waves from different parts of the atom. For directions away from the internuclear axis, the scattered wave and the primary

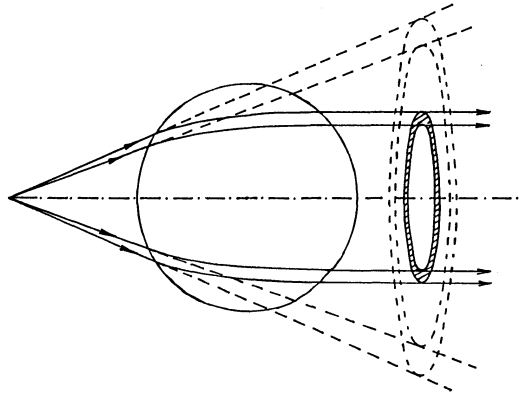

Fig.19.13. Schematic diagram showing forward-focusing of electrons by an attractive potential

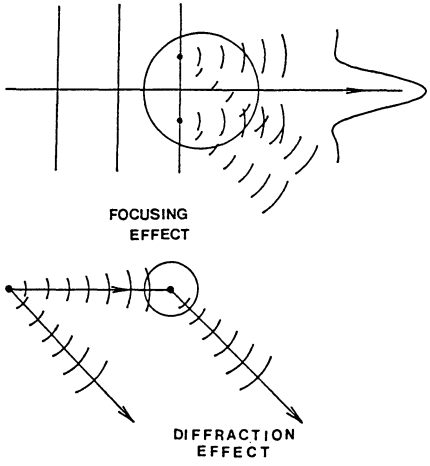

Fig.19.14. Above a threshold energy, constructive interference produces the focusing peak. Positions of diffraction peaks depend on electron energy

wave interfere with each other, giving rise to interference peaks which depend on both the electron energy and internuclear distance [19.35] (Fig.19.14).

As will be discussed in the next section, the small-atom approximation overestimates the height of the forward peak, but the qualitative features of its prediction remain the same as those of the exact curved wave expression. In Fig.19.15, we show the enhancement in the small-atom approximation for an emitting Cu atom and a neighboring atom of Cu placed 2.56 Å from it. We note that the enhancement along the forward direction increases as E_k increases from 20 eV to 800 eV, while its half-width decreases.

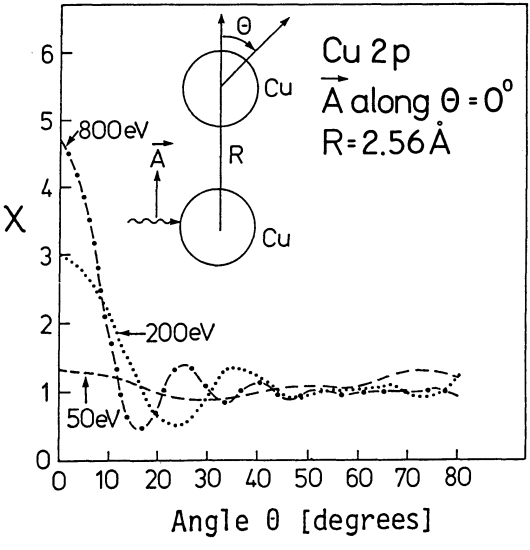

Fig.19.15. The enhancement κ as a function of electron exit angle for electron energies 50, 200, and 800 eV

From Fig.19.15, we see that the secondary peak moves closer to zero as E_k increases. To understand this effect, we have plotted the real and imaginary parts of the scattering factor $f(\theta)$, and the real and imaginary parts of the structure factor $\exp[ik_R(1-\cos\theta)]$ for energies of 800 and 1600 eV in Figs. 19.16 and 17, respectively. We note that the secondary peaks are mainly caused by the structure factor which is an oscillating function of θ. The first minimum of the structure factor moves closer to the zero angle as E_k is increased. High-order peaks at large angles are extremely small since $f(\theta)$ approaches zero as θ increases.

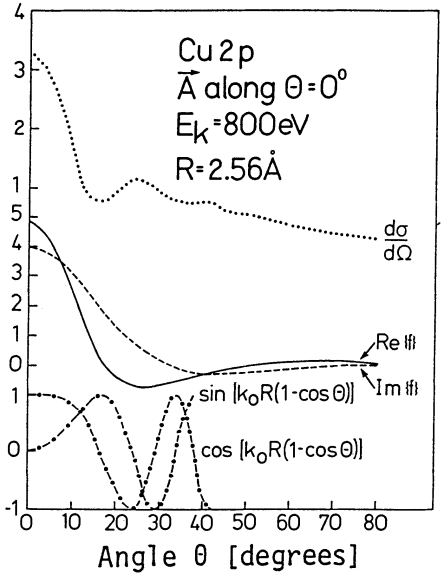

Fig.19.16. Real and imaginary parts of scattering factor of Cu, real and imaginary parts of $\exp[ikR(1-\cos\Theta)]$, and $d\sigma/d\Omega$ (system) as a function of electron exit angle at $E_k = 800$ eV

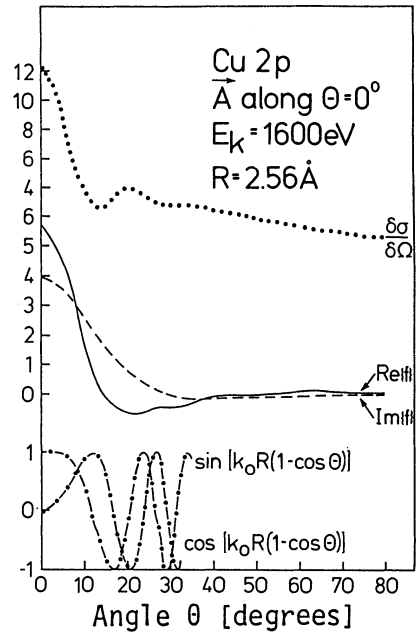

Fig.19.17. Real and imaginary parts of scattering factor of Cu, real and imaginary parts of $\exp[ikR(1-\cos\Theta)]$, and $d\sigma/d\Omega$ (system) as a function of electron exit angle at $E_k = 1600$ eV

19.5.2 The Small-Atom (Plane-wave) Approximation

In the usual theoretical analysis of extended X-ray absorption fine structure (EXAFS) [19.36-38] and angle-resolved photoemission extended fine structure (ARPEFS) [19.39], the "small-atom approximation" is used to treat the single back-scattering process of the photoelectron from neighboring atoms. The simple expression thus obtained can be Fourier-transformed to give the bonding distances of neighboring atoms directly. Recently, *Müller* and *Schaich*

[19.40] have shown that this is equivalent to expanding the spherical hankel function

$$i^{\ell+1} h_\ell^{(1)}(\rho) = \frac{e^{i\rho}}{\rho}\left[1 + i\,\frac{\ell(\ell+1)}{2\rho} + \ldots\right]$$

and retaining the first term by assuming $\rho \gg \ell^2$.

The same approximation has also been applied to forward-scattering cases like C(1s) photoemission of CO on Ni{001} [19.41] and Cu(2p) photoemission of Cu on Ni{001} [19.35,42,43]. Though the small atom approximation gives the same peak positions in the polar plot as the exact single scattering spherical wave calculation, the small-atom approximation tends to overestimate the peak heights.

The propagation of an electronic wave from a source atom to a neighboring atom is described by a Green's function, $G^+_{L_1L_2}(\mathbf{R})$, which contains a sum over L, each of which has a factor $h_\ell^{(1)}(k_0R)$. The small-atom approximation is equivalent to taking the asymptotic form of $h_\ell^{(1)}(k_0R)$. Therefore the small atom approximation corresponds to neglecting a term $\ell(\ell+1)/k_0R$ compared to 1 in a sum over angular momenta involved in scattering. Since one might expect all ℓ's up to k_0a to be involved in the sum, it is by no means obvious that the small-atom approximation is valid where "a", the radius of the potential, is ~R/2.

We can divide the discussion into low- and high- ($k_0 \gg Z$ in atomic units) energy regimes. In the low-energy regime, the quasi-classical approximation is valid [19.44]. It can be shown [19.45] that those with ℓ approximately equal to the classical angular momentum contribute most significantly to the above sum, for fixed energy and scattering angle. Therefore, the condition for the small-atom approximation can be written as $k_0R \gg \ell^2_{\text{classical}}$. Large-angle scattering requires a trajectory of low angular momentum, so this condition is always satisfied in these large-angle scattering directions. Conversely, we expect the small-atom approximation to be bad for the forward direction scattering.

If we define a XPS enhancement factor as [19.46-48]

$$\chi = \frac{d\sigma/d\Omega\ (\text{system})}{d\sigma/d\Omega\ (\text{atom})} \quad ,$$

we show in Figs.19.18a-j the enhancement factor χ as a function of energy for different scattering angles, using quantum mechanical calculations with and without the small-atom approximation. The system is the case of two nearest-neighbor copper atoms, using the scattering potential of *Burdick* [19.49].

From Figs.19.18a-j, it is clear that the small-atom approximation is not valid for scattering angles $\theta \leq 20^\circ$ ($E < 1600$ eV). As θ increases, it becomes

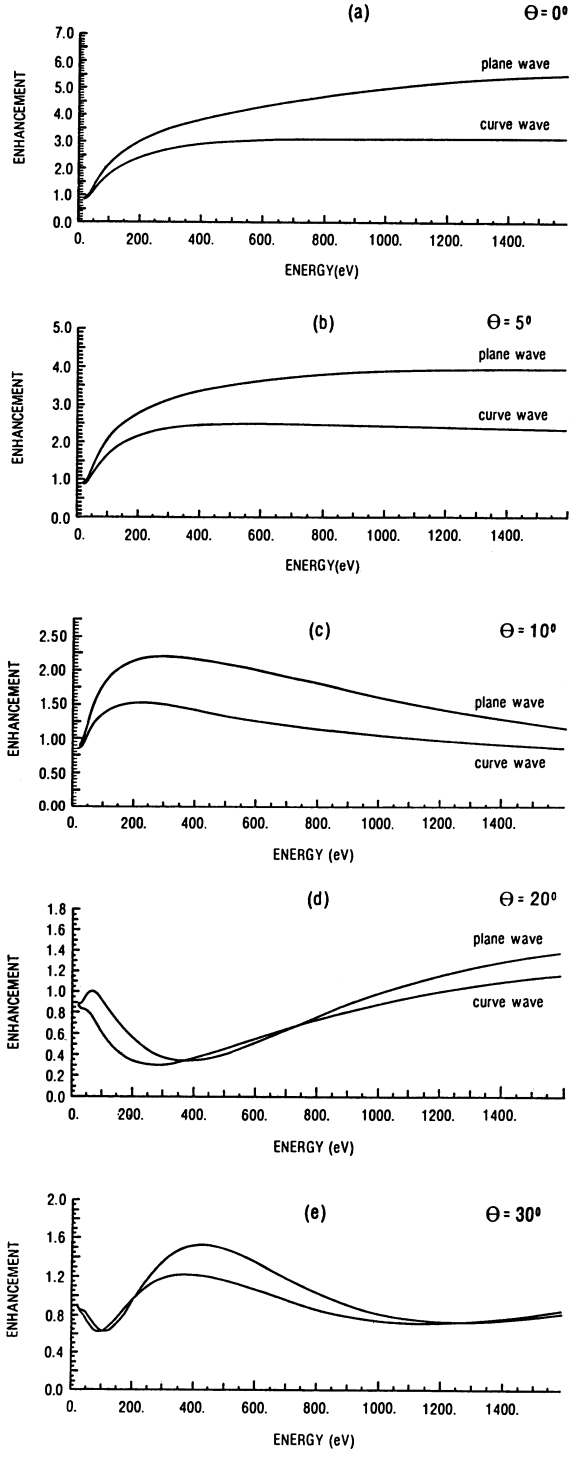

Fig.19.18a-j. Comparison of enhancement factors with and without the small-atom (plane-wave) approximation for two Cu atoms 2.56 Å apart. (**a - j**) correspond to different scattering angles Θ

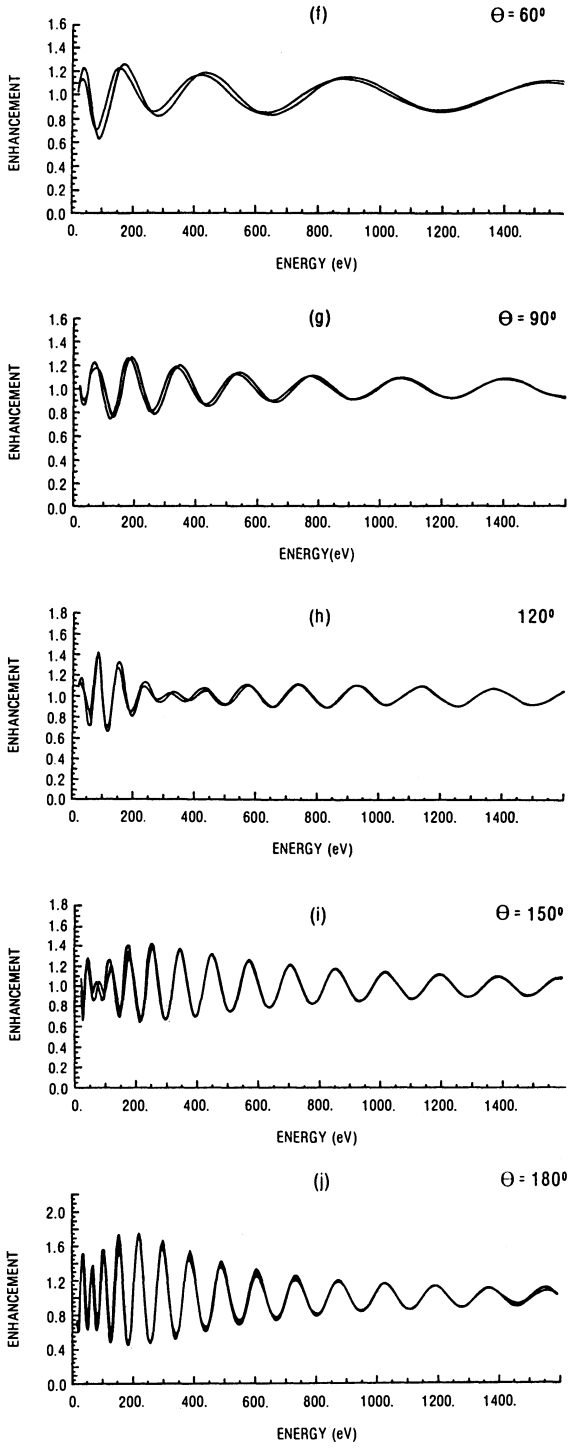
(f)
Θ = 60°
ENHANCEMENT
ENERGY (eV)
(g)
Θ = 90°
ENHANCEMENT
ENERGY(eV)
(h)
120°
ENHANCEMENT
ENERGY (eV)
(i)
Θ = 150°
ENHANCEMENT
ENERGY (eV)
(j)
Θ = 180°
ENHANCEMENT
ENERGY (eV)

Fig.19.18f-j

valid over a larger energy range. At $\theta = 180^{\circ}$, i.e., direct back-scattering, the small-atom approximation becomes valid at all energies. This explains why the small-atom approximation can be used in EXAFS.

For higher electron energy ($k_0 > Z$), the Born approximation can be used. Due to interference, the main contribution to the Born integral is from a region near the atomic center. Therefore, it is generally possible to regard the atom as small. However, because of the curved wave front, a correction factor has to be included which becomes important in the forward direction. We show in Fig.19.19 the enhancement factor χ as a function of polar angle for energies of 1000 and 5000 eV with and without the small-atom approximation. A cut-off Coulomb potential with $Z = 1$ is used. We note that $\chi(\theta)$ calculated using the small-atom approximation becomes worse near the forward direction, as the energy is increased. However, the angular range near 0° within which this happens gets smaller.

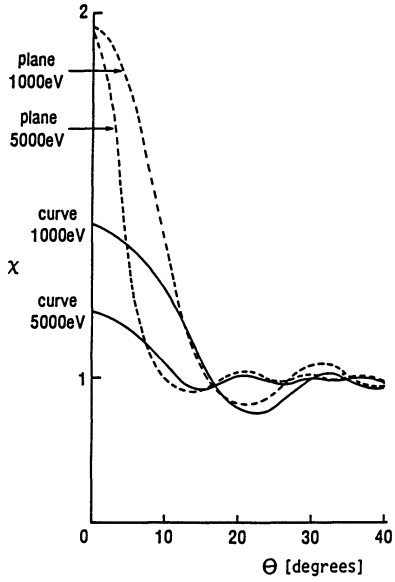

Fig.19.19. Enhancement factor in the Born approximation for a cut-off Coulomb potential ($Z = 1$) at high energy

19.5.3 Temperature Effect

In the case of Cu on Ni{100}, an experiment by *Armstrong* and *Egelhoff* [19.43] shows strong temperature dependence of the internuclear focusing peak at 45°, contrary to what is expected according to the small-atom approximation. We show the results of a full calculation (using the curved wave front) of the temperature dependence of the 2p emission of Cu on Ni{100} at 317 eV in Fig. 19.20. The curved wave calculation shows the temperature dependence observed in the experiments.

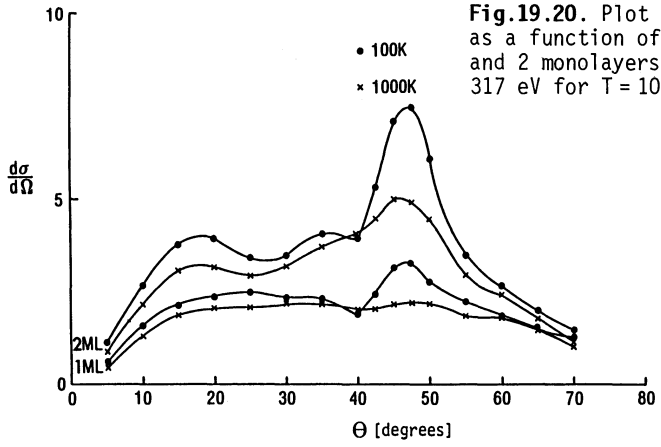

Fig.19.20. Plot of XPS cross section as a function of polar angle Θ for 1 and 2 monolayers of Cu on Ni{100} at 317 eV for T = 100, 1000 K

19.5.4 Effect of Multiple Scattering

In Fig.19.21, we show the XPS cross section for Cu{100} at 317 eV, for emission from the 2p state, for 1,2, and 3 monolayers (ML). The multiple-scattering formulas [19.46] are used. From Fig.19.21, we see that the internuclear peak around 45° is enhanced by a factor of 2.4 going from 1 ML to 2 ML. The heights of the internuclear peak for 2 and 3 ML, normalized by that of 1 ML, are tabulated in Table 19.6, for results using multiple-scattering theory, single-scattering theory (with spherical-wave and plane-wave formulas, i.e.,

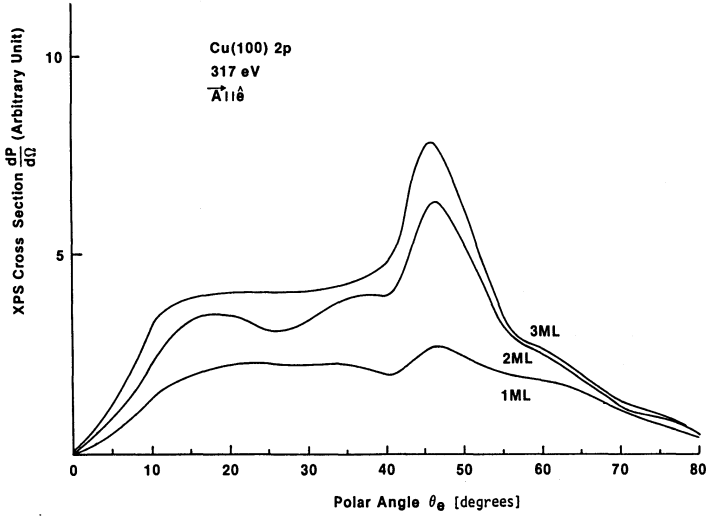

Fig.19.21. Angle-resolved XPS cross section, calculated by multiple-scattering theory, for 2p Cu{001} at 317 eV as a function of emission polar angle. The photon A vector is along the emission direction and Θ = 0° is the direction of the surface normal. The emission plane is {100}

Table 19.6. Values of XPS cross sections (normalized to unity for the 1 monolayer case) at $\theta = 45^{\circ}$ for combined emissions from 1,2, and 3 monolayers of Cu{001} at 317 eV, from the 2p core level

No. of layers [ML]	Experiment (a)	Multiple scattering (b)	Single scattering (spherical wave) (c)	(d)	Single scattering (plane wave) (e)
1	1	1	1	1	1
2	2.3	2.35	2.46	2.50	3.40
3	2.7	2.97	4.0	4.15	6.16
No. of partial waves	8	8	8	20	20

the small-atom approximation), and the data of *Egelhoff* [19.34]. Compared with the experimental data, spherical-wave single-scattering theory works for 2 ML, plane-wave single-scattering theory fails even there, and only the multiple-scattering result adequately reproduces the emission intensity for the 3 ML case. The single-scattering spherical-wave result overestimates the 3 ML cases by 48%, while the plane-wave result overestimates it by 128%. In Table 19.6, we also compare results of spherical-wave single-scattering theory using 20 partial waves (column d) with those of 8 partial waves (column c). The comparison shows that at 317 eV, results of 8 partial waves have converged to an accuracy of 4%. The multiple-scattering calculations (column b) were done with 8 partial waves.

Relative contributions to the internuclear peak from individual layers, at a range of energies between 250 and 400 eV, are tabulated in Table 19.7. The tabulated numbers are ratios of second and third monolayer emission contributions to that of the first monolayer, using multiple-scattering and single-scattering theories. The numbers show that with multiple scattering, the third-layer contribution is rather small, being about 30% to 50% of that of the second layer. Single-scattering theory, on the other hand, overestimates the third-layer contribution, with values of third-layer contribution ranging from about equal to bigger than that of the second layer. These numbers illustrate an important physical effect which is correctly described by multiple-scattering theory, but not by single-scattering theory: An electron emitted from a third-layer atom, after being focused into the forward direction by a second-layer atom, is further deflected to directions other than forward by an atom in the first layer. In multiple-scattering theory, such electrons are discarded from the forward-direction peak. In single-scattering theory, however, the defocusing effect is neglected because it is a second-order scattering event. As a consequence, single-scattering theory overestimates the forward-direction peak in cases of 3 or more monolayers.

Table 19.7. Normalized XPS cross sections for emission from an atom located in the (a) surface layer, (b) second layer, and (c) third layer, respectively. The intensity of emission from an atom in the surface layer is normalized to unity

Energy [eV]		Multiple scattering (8 partial waves)	Spherical-wave single scattering (8 partial waves)
250	(a)	1.00	1.00
	(b)	1.6	1.37
	(c)	0.66	1.21
300	(a)	1.00	1.00
	(b)	1.52	1.42
	(c)	0.66	1.43
317	(a)	1.00	1.00
	(b)	1.35	1.46
	(c)	0.62	1.54
350	(a)	1.00	1.00
	(b)	1.91	1.50
	(c)	1.01	1.59
400	(a)	1.00	1.00
	(b)	1.22	1.30
	(c)	0.60	1.44

Because of the strong focusing peak in the forward direction, any attempt to treat the forward scattering as a weak perturbation (as in a kinematical theory) is bound to fail. Even in EXAFS, if a third atom lies in the shadow of a scatterer (i.e., source, scatterer, and a third atom lying almost in a straight line), multiple scattering effects have to be included [19.36].

The focusing technique can be used in the determination of surface structure. For Cu, the forward enhancement may reach 300% while the back-scattering modulation is only about 30% of the unscattered emission at high enough energies (e.g., $E_k \sim 1000$ eV). This indicates that forward focusing peaks are the dominant features in polar plots of photoemission intensity. As a consequence, the focusing effect provides direct information about the orientation of surface bonds [19.35].

19.6 Structure Analysis by High-Resolution Electron Energy-Loss Spectroscopy

Finally, we present results of another surface analytical tool: high-resolution electron energy-loss spectroscopy (HREELS). In this technique, electrons at incident energy and angles (E_i, θ_i, ϕ_i) are reflected by a sample and measured at final energy and angles (E_f, θ_f, ϕ_f). The relation $E_f = E_i - \hbar\omega_{ph}$

holds, where $\hbar\omega_{ph}$ is the energy of a surface phonon. Since $\hbar\omega_{ph}$ is usually ~10-100 meV, and the incident electron energy is ~10-400 eV, a machine of high energy resolution is needed. By varying θ_i, θ_f. E_i, and E_f, dispersion curves of surface phonons and adsorbate-induced phonons can be measured.

If the measurement is made near the specular angle, the inelastic cross section is dominated by electrons scattering off an induced dipole moment normal to the surface. Electrons scattering off the short-range part of the atomic potential form an inelastic cross-section which is spread over both specular and off-specular directions. It is this short-range scattering at different off-specular directions that is used to map out the phonon ω versus $\mathbf{q}$ dispersion curves.

Because of its high surface sensitivity and wide spectral range, HREELS has rapidly emerged as a major tool for studying vibrational properties of clean and adsorbate-covered surfaces. An experimental innovation was introduced recently by *Lehwald* et al. [19.50] who collected off-specular HREELS data at high incident energies, E_i = 180 eV and 322 eV. The combination of a short electron mean free path and large surface-localized displacements make HREELS cross sections of surface phonons and resonances much larger than that of bulk modes. For a fcc{001} surface, lattice dynamics yielded three surface modes: S_1, S_4, and S_6. The S_1 mode is a shear horizontal wave with odd polarization with respect to the {110} plane. If the scattering plane is also along the <110> direction, then a selection rule requires that this mode has a zero cross section [19.51]. The other two surface modes, S_4 and S_6, however, should have nonzero cross sections. Near a zone boundary, e.g., $\bar{X}$, the frequencies of the S_4 and S_6 modes occur in gaps of bulk modes. As we shall show below, measurement of the S_6 frequency provides an important check of the lattice dynamical model [19.52], while measurement of the S_6 phonon cross section provides a very sensitive structural indicator.

A theory of phonon intensities has been developed [19.51,52] which incorporates the muffin-tin approximation for the scattering potential and the additional assumption that the ions move rigidly when the nuclei are displaced through the excitation of a phonon [19.53]. At energies of the order of 100 eV, electrons scatter mainly from the near-core region of the atoms. Hence, we expect cross sections calculated from this rigid-ion multiple-scattering (RIMS) slab method to be rather accurate.

In Fig.19.22, we show the displacement directions of the S_4 and S_6 surface phonons at $\bar{X}$. Also shown is the scattering geometry. Note that the surface unit cell convention is used and q_x is along the <110> direction. The phonon eigenvectors of the first five atomic layers of the two surface

Table 19.8. Eigenvectors of S_4 and S_6 surface modes at $\bar{X}$ for Ni{001}. Model (a) is for a 20% increase in the force constant which couples atoms in the first and second layers and no contraction in the surface interlayer spacing. Model (b) is for the same force-constant model as in model (a) and a 3% contraction in the surface interlayer spacing

	Model	1st layer			2nd layer			3rd layer			4th layer			5th layer		
		e_x	e_y	e_z	e_x	e_y	e_z	e_x	e_y	e_z	e_x	e_y	e_z	e_x	e_y	e_z
S_4	(a)	0	0	-0.83i	-0.41	0	0	0	0	0.32i	0.13	0	0	0	0	-0.10i
	(b)	0	0	-0.85i	-0.40	0	0	0	0	0.30i	0.12	0	0	0	0	-0.09i
S_6	(a)	0.64	0	0	0	0	0.22i	0.54	0	0	0	0	0.15i	0.35	0	0
	(b)	0.63	0	0	0	0	0.22i	0.54	0	0	0	0	0.14i	0.36	0	0

Fig.19.22. Direction of atomic displacements of S_4 and S_6 modes at $\bar{X}$: plus, up; minus, down. In the top view, the smaller circles denote second-layer atoms. The lower right-hand figure shows the scattering plane

modes at $\bar{X}$ are listed in Table 19.8. These eigenvectors are based on the nearest-neighbor central-force model [19.54], with the force constant in the bulk adjusted to fit the maximum bulk Ni phonon frequency, and the surface force constant which couples atoms in the first layer to those in the second increased by 20% [19.50,54]. This lattice dynamical model was found to provide the best agreement with the measured phonon dispersion curves [19.50,55].

With the eigenvectors of the S_4 and S_6 modes, the inelastic cross sections were evaluated in the 40-250 eV energy range using the RIMS method. The method allows the electron to scatter elastically or inelastically at each atomic layer, and is exact in terms of the number of multiple-scattering events or atomic layers included [19.51,52]. In Fig.19.23, we show the energy dependence of the calculated phonon-loss differential probability (i.e., number of phonon-loss electrons per solid angle and per incident electron) for S_4 and S_6, evaluated at $\bar{X}$ and $\theta_f = 65^\circ$. We see substantial modulations in the differential probability, and at three energy intervals, E_i from 110

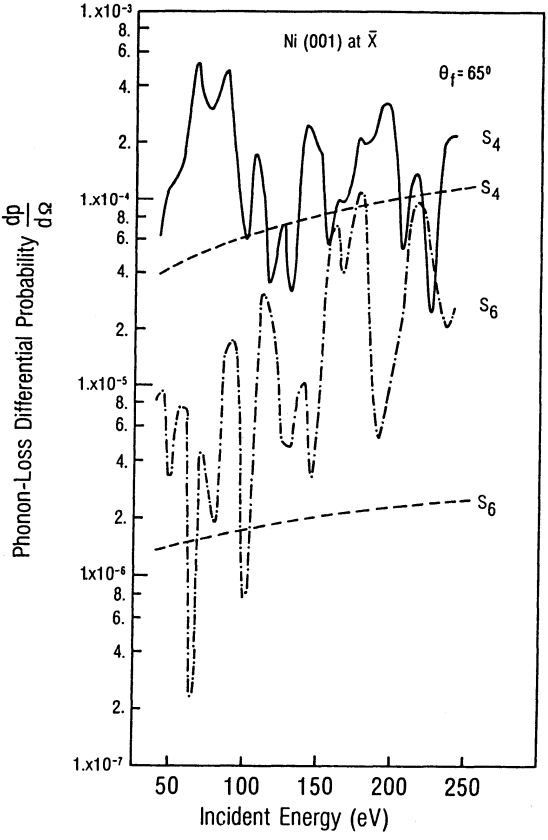

Fig.19.23. Calculated phonon-loss differential probability for S_4 and S_6 surface phonons versus incident energy. The Born approximation results are shown by the dashed lines

to 115 eV, from 155 to 180 eV, and from 210 to 230 eV, the two modes have comparable probabilities. Also shown (dashed lines) are estimates of the probability based on the Born approximation (BA) arbitrarily normalized to 1.0×10^{-4} at $E_i = 200$ eV for the S_4 mode. In the BA model, the probabilities are smooth functions of energy and the probability of S_6 is too small to be detected by experiment. From Fig.19.23, we see that the S_6 probability is very much enhanced by multiple scattering to such a magnitude that it can easily be measured under current experimental conditions. In the multiple-scattering picture, an electron is scattered into a direction essentially parallel to the surface. Through subsequent umklapp scattering, it can couple strongly to parallel displacements of the S_6 mode. The experimental detection of the S_6 mode confirms the correctness of this picture.

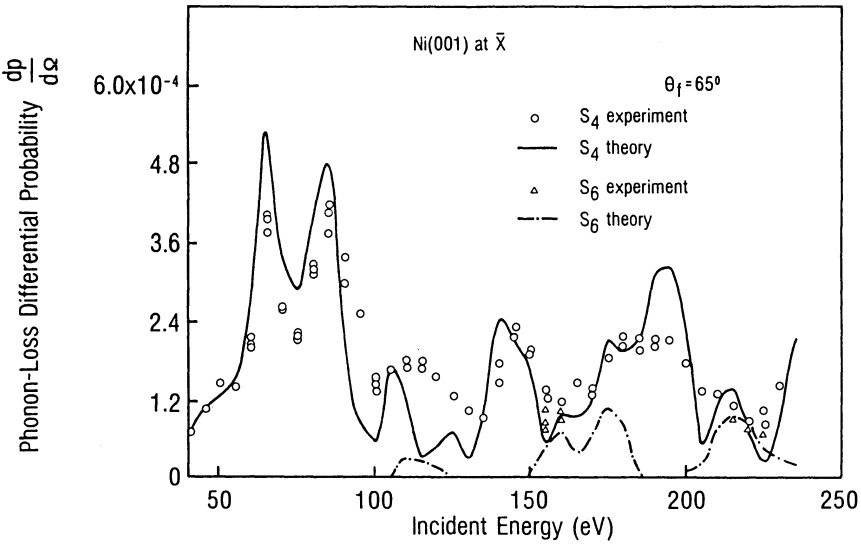

Fig.19.24. Comparison between experimental and theoretical phonon-loss I-V profiles of S_4 and S_6 surface modes, at $\bar{X}$ and $\Theta_f = 65°$

The measured phonon-loss I-V profiles are shown in Fig.19.24 for the S_4 mode (circles) and, when measurable, the S_6 mode (triangles), together with the calculated results (solid and dot-dashed lines, respectively), at $\bar{X}$ and $\theta_f = 65^o$. The reproducibility of the data can be seen from the relatively small scatter of the data points. There is close tracking between theory and experiment in the energy dependence of the intensities. The remaining differences may be at least partly due to the experimental difficulties mentioned above. In order to extract structural information from the data, one should therefore focus on the ratio of intensities of the S_4 and S_6 modes in the spectra

Table 19.9. Phonon-loss intensity ratio S_4/S_6 versus surface interlayer spacing at 155 eV and $\theta_f = 65^\circ$

Contraction [%]	Interlayer spacing d_{12} [Å]	S_4/S_6
Experiment		1.15
0	1.765	0.57
1	1.747	0.70
2	1.730	0.87
3	1.712	1.16
4	1.694	1.65
5	1.677	2.60

where both appear, since this ratio is independent of the particular focusing conditions of the lens elements. At energies and angles where the ratio is sensitive to structural parameters, it is possible to use it to discriminate between different surface models. For example, the measured intensity ratio of S_4/S_6 at 155 eV is 1.15. This ratio has been determined by subtraction of a multiphonon background as indicated in Fig.19.25. In Table 19.9, we show the calculated S_4/S_6 intensity ratio for different percentage contractions of the interlayer spacing between the surface and the layer immediately below it (i.e., d_{12}). This ratio is very sensitive to d_{12} and varies, on the average, by 40% for every 1% change in d_{12}. For example, if we eliminate the 20% increase in the first-to-second layer force constant in the lattice dynamics calculation, the eigenamplitudes vary by approximately 22%. The cal-

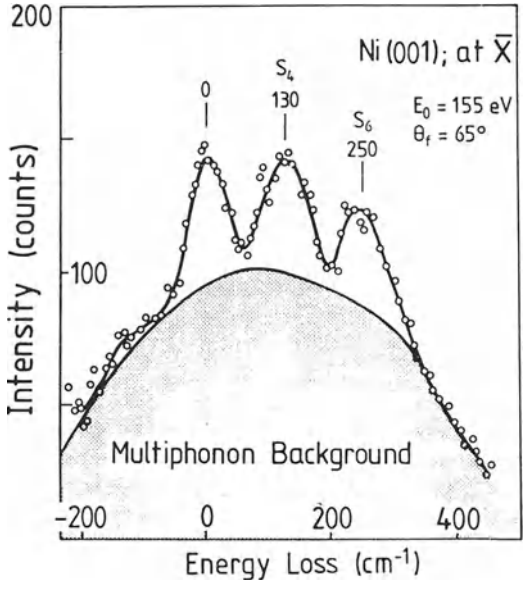

Fig.19.25. Experimental loss spectrum at $\bar{X}$ ($q_\parallel = 1.26$ Å^{-1}) and $E_i = 155$ eV, $\theta_f = 65^\circ$, showing both S_4 and S_6 modes. The multiphonon background is calculated in the minima between the peaks by fitting Gaussian functions to the peaks with a half-width taken from the resolution. The full curve is generated by the assumption that the multiphonon background is a smooth function of energy. Above 295 cm^{-1}, the entire intensity is due to multiprocesses

Table 19.10. Experimental phonon-loss intensity ratio, with errors, at different energies and scattering angles

E_0	θ_f	S_4/S_g	Remark
160	60	$0.5^{+0.5}_{-0.25}$	Contribution of bulk resonance to "S_4" peak
220	65	1.4 ±0.2	
155	65	1.15±0.15	
160	65	1.2 ±0.5	Contribution of bulk resonances to both peaks

culated S_4/S_6 intensity ratio decreases by over 30%, but this produces only a 1% change in the surface spacing contraction. Of course, the elimination of the 20% increase in the surface force constant is unreasonable because it would bring the S_4 frequency from 131 cm^{-1} (compared to an experimental value of 130 cm^{-1}) to 125 cm^{-1}, and the S_6 frequency from 252 cm^{-1} (experimental value of 250 cm^{-1}) to 247 cm^{-1}. Thus, while the eigenfrequencies are sensitive to surface force constants, the S_4 and S_6 phonon intensities are mostly sensitive to surface structure.

Data which include other energies and θ_f, where the S_6 mode is observed simultaneously with S_4, are listed in Table 19.10, together with experimental errors. Using these data and errors, we evaluate a reliability factor defined as

$$R = \frac{\Sigma_i |S_i(\text{expt.}) - S_i(\text{theory})|^2}{\Sigma_i |S_i(\text{expt.})|^2} , \tag{19.1}$$

where S_i(expt.) or S_i(theory) are the i^{th} measured or calculated intensity ratios, respectively. A plot of R versus interlayer spacing using the upper bounds of the measured data yields a surface spacing contraction of $\leqslant$3.3%. A similar plot using the lower bounds of the measured data yields a surface spacing contraction of $\geqslant$1.7%. Thus, we conclude that the surface interlayer spacing determined from this study to be a contraction of 1.7%-3.3%, in excellent agreement with a recent ion-surface-scattering result [19.56].

19.7 Conclusion

In summary, we have shown how surface analytical techniques using the scattering of elastic and inelastic electrons are used to extract the structure of surfaces. A few structural results on metal and semiconductor surfaces have been discussed. Under favorable conditions, these methods determine surface bond lengths to a precision of better than 0.05 Å. Such spectro-

scopic techniques complemented by surface imaging tools such as the scanning tunneling microscope (STM) and transmission electron microscope (TEM), will provide detailed and quantitative information on the arrangements of atoms in the surface region of solids.

Acknowledgement. We acknowledge our collaborators for the works discussed, particularly Dr. G. Xu, Dr. D.R. Snider, and Dr. W.Y. Hu. This work is supported in part by the National Science Foundation through Grant No. DMR-8405049, the U.S. Department of Energy under Grant No. DE-FG0284ER45076 and the Petroleum Research Fund under Grant No. 1154-Ac5,6.

References

19.1 H.C. Gatos, M.C. Lavine: J. Electrochem. Soc. **107**, 427 (1960)
19.2 D. Haneman: Phys. Rev. **121**, 1093 (1961)
19.3 A.U. MacRae, G.W. Gobeli: J. Appl. Phys. **35**, 1629 (1964); in *Physics of III-V Compounds*, Vol.2, ed. by R.K. Willerdson, A.C. Beer (Academic, New York 1966) p.115
19.4 S.Y. Tong, G. Xu, W.N. Mei: Phys. Rev. Lett. **52**, 1693 (1984)
19.5 S.Y. Tong: In *Progress in Surface Science*, Vol.7, ed. by S.G. Davisson (Pergamon, New York 1975) p.1
19.6 S.Y. Tong, W.N. Mei, G. Xu: J. Vac. Sci. Technol. B**2**, 393 (1984)
19.7 S.Y. Tong, M.A. Van Hove: Phys. Rev. B**16**, 1459 (1977)
19.8 M.A. Van Hove, S.Y. Tong, M.H. Elconin: Surf. Sci. **64**, 85 (1977)
19.9 S.Y. Tong, W.M. Kang, D.H. Rosenblatt, J.G. Tobin, D.A. Shirley: Phys. Rev. B**27**, 4632 (1983)
19.10 S.Y. Tong, K.H. Lau: Phys. Rev. B**25**, 7382 (1982)
19.11 D.J. Chadi: Phys. Rev. Lett. **52**, 1911 (1984)
19.12 M. Alonso, F. Soria, J.L. Sacedon: J. Vac. Sci. Technol. A**3**, 1598 (1985)
19.13 J. Bohr, R. Feidenhans'l, M. Nielsen, M. Toney, R.L. Johnson, I.K. Robinson: Phys. Rev. Lett. **54**, 1275 (1985)
19.14 D.J. Miller, D. Haneman: Phys. Rev. B**3**, 2918 (1971)
19.15 J.E. Rowe, S.B. Christman, G. Margaritondo: Phys. Rev. Lett. **35**, 1471 (1975)
19.16 W. Harrison: Surf. Sci. **55**, 1 (1976)
19.17 S.Y. Tong, A.R. Lubinsky, B.J. Mrstik, M.A. Van Hove: Phys. Rev. B**17**, 3303 (1978)
19.18 M.W. Puga, G. Xu, S.Y. Tong: Surf. Sci. Lett., in press
19.19 D.J. Chadi: Phys. Rev. B**18**, 1800 (1978)
19.20 R. Chelikowsky, M.L. Cohen: Phys. Rev. B**20**, 4150 (1979)
19.21 J. Van Laer, J.J. Scheer: Surf. Sci. **8**, 342 (1967)
19.22 W.E. Spicer, I. Lindau, D.E. Gregory, C.M. Garner, P. Pianetta, F.W. Chye: J. Vac. Sci. Technol. **13**, 780 (1976)
19.23 W. Gudat, D.E. Eastman, J.L. Freeouf: J. Vac. Sci. Technol. **13**, 25 (1976)
19.24 D.J. Chadi: Phys. Rev. Lett. **41**, 1062 (1978)
19.25 K.C. Pandey: Phys. Rev. Lett. **49**, 223 (1982)
19.26 W.M. Gibson, H.J. Gossman: J. Vac. Sci. Technol. B**2**, 343 (1984)
19.27 C.B. Duke, S.L. Richerdson, A. Paton, A. Kahn: Surf. Sci. **127**, L135 (1983)
19.28 M.L. Xu, S.Y. Tong: Phys. Rev. B**31**, 6332 (1985)

19.29 M.A. Van Hove, S.Y. Tong: *Surface Crystallography by LEED*, Springer Ser. Chem. Phys., Vol.2 (Springer, Berlin, Heidelberg 1979)
19.30 E. Zanazzi, F. Jona: Surf. Sci. **62**, 61 (1977)
19.31 S.Y. Tong, G. Xu, W.Y. Hu, M.W. Puga: J. Vac. Sci. Technol. B**3**, 1076 (1985)
19.32 G. Xu, W.Y. Hu, M.W. Puga, S.Y. Tong, J.L. Yeh, S.R. Wang, B.W. Lee: Phys. Rev., in press
19.33 S.Y. Tong, C.H. Li: In *Chemistry and Physics of Solid Surfaces III*, ed. by R. Vanselow, W. England (CRC Press, Boca Raton, FL 1982)
19.34 W.F. Egelhoff, Jr.: Phys. Rev. B**30**, 1052 (1984)
19.35 H.C. Poon, S.Y. Tong: Phys. Rev. B**30**, 6211 (1984)
19.36 P.A. Lee, J.B. Pendry: Phys. Rev. B**11**, 2795 (1975)
19.37 D.E. Sayers, E.A. Stern, F.W. Lytle: Phys. Rev. Lett. **27**, 1204 (1971)
19.38 P.A. Lee: Phys. Rev. B**13**, 5261 (1976)
19.39 J.J. Barton, C.C. Bahr, Z. Hussain, S.W. Roley, J.G. Tobin, L.E. Klebanoff, D.A. Shirley: Phys. Rev. Lett. **51**, 272 (1983)
19.40 J.E. Müller, W.L. Schaich: Phys. Rev. B**27**, 6489 (1983)
19.41 L.G. Petersson, S. Kono, N.F.T. Hall, C.S. Fadley, J.B. Pendry: Phys. Rev. Lett. **42**, 1545 (1979)
19.42 E.L. Bullock, C.S. Fadley: Phys. Rev. B**31**, 1212 (1985)
19.43 R.A. Armstrong, W.F. Egelhoff, Jr.: Surf. Sci. **154**, 225 (1985)
19.44 L.D. Landau, E.M. Lifshitz: *Quantum Mechanics (Non-Relativistic Theory)* (Pergamon, New York 1977)
N.F. Mott, H.S.W. Massey: *The Theory of Atomic Collisions* (Oxford U. Press, Oxford 1963)
19.45 H.C. Poon, D. Snider, S.Y. Tong: Phys. Rev. B, in press
19.46 C.H. Li, A.R. Lubinsky, S.Y. Tong: Phys. Rev. B**17**, 3128 (1978)
19.47 S.Y. Tong, C.H. Li, A.R. Lubinsky: Phys. Rev. Lett. **39**, 498 (1977)
19.48 C.H. Li, S.Y. Tong: Phys. Rev. Lett. **43**, 526 (1979)
19.49 G.A. Burdick: Phys. Rev. **129**, 138 (1963)
19.50 S. Lehwald, J.M. Szeftel, H. Ibach, T.S. Rahman, D.L. Mills: Phys. Rev. Lett. **50**, 518 (1983)
19.51 S.Y. Tong, C.H. Li, D.L. Mills: Phys. Rev. Lett. **44**, 407 (1980)
19.52 S.Y. Tong, M.L. Xu, B.M. Hall: J. Vac. Sci. Technol. A3, 1452 (1985)
19.53 See, for example, J.M. Ziman: *Electrons and Phonons* (Oxford U. Press, Oxford 1960) p.183
19.54 J.E. Black, D.A. Campbell, R.F. Wallis: Surf. Sci. **105**, 629 (1981)
19.55 M. Rocca, S. Lehwald, H. Ibach, T.S. Rahman: Surf. Sci. **138**, L123 (1984)
19.56 J.W.M. Frenken, J.F. van der Veen, G. Allan: Phys. Rev. Lett. **51**, 1876 (1983)

20. Surface Structure Analysis by Low-Energy Alkali Ion Scattering

E. Bauer and T. von dem Hagen

Physikalisches Institut, Technische Universität Clausthal,
D-3392 Clausthal-Zellerfeld, F. R. G.

Surface structure analysis is now 25 years old but we still know little about the structure of surfaces, at least when we use the first 25 years of structure analysis of the bulk for comparison. The reason for the slow progress is obvious when we compare the techniques with which the two fields started; X-ray diffraction and low-energy electron diffraction (LEED). In the first case the interaction with the sample is weak which makes a simple analysis possible, e.g., in terms of the first Born approximation (kinematic theory, single scattering), in the second case the interaction is strong so that the weak interaction approximations break down.

Initially [20.1] it was hoped that the interaction was so strong that only the topmost atomic layer had to be taken into account in LEED and that the geometry of the pattern could be uniquely analyzed, but these hopes soon vanished [20.2-4]. By the mid-sixties it was widely accepted that there was no easy way out and that multiple scattering and atoms in deeper layers had to be taken into account (dynamical theory). This made LEED more interesting from the theoretical point of view but also drove away those LEED users who just wanted to understand the structure of surfaces.

The consequence was a vigorous search for and development of other surface analysis techniques in the following years (for a brief review see [20.5]). Two philosophies emerged in this search: (1) Use "weak" interactions under conditions which suppress the volume contribution or enhance the surface contribution. Rutherford backscattering under channeling conditions and total reflection X-ray diffraction are examples of this approach. (ii) Use such "strong" interactions that really only the topmost layer interacts with the probe or that multiple scattering is at least reduced to the immediate environment of an atom, if possible to double scattering. Examples are atomic beam diffraction and low-energy ion scattering spectroscopy (LEISS).

In the early seventies we chose LEISS, after a half-hearted attempt at atomic beam diffraction in the late sixties had had to be aborted because of low signal/background ratio. This technique became a viable surface ana-

lysis technique only after the introduction of intense nozzle-skimmer sources and powerful pumping systems. However, LEISS had already been introduced successfully into surface science by *Smith* [20.6], although only for chemical analysis, and some first indications of its usefulness for structure analysis were already available [20.7]. Our initial effort, as far as LEISS is concerned, was modest. It was a one-man project [20.8] and aimed at a comparison of electron- and ion-beam techniques: LEED and LEISS for structure analysis, Auger electron spectroscopy (AES) and secondary-ion mass spectrometry (SIMS) for chemical analysis. He^+ and Ne^+ ion beams with 200-1000 eV energy were used and the energy distribution of the scattered ions was measured with the cylindrical mirror analyzer used for AES [20.9].

Most of this work was of an exploratory nature but even so it produced some important information on the structure of chemisorbed layers. An example is oxygen at high coverages on W{110}. Previously believed to be a two-dimensional oxide, it was shown by LEISS to be a pure oxygen layer [20.10]. Attempts to determine atomic positions in chemisorbed layers using shadowing —the shadow cone concept was at that time still foreign to LEISS —did not give information beyond that obtainable by LEED [20.11,12]. It was evident that the LEISS spectrum was dominated by single scattering due to the high neutralization rate of the noble gases and that it would be possible to see double scattering between neighboring atoms only if the neutralization probability could be reduced considerably.

Thus in 1974 we embarked on a program to set up alkali LEISS. At that time *Hulpke* had already studied the scattering of 2-20 eV Li^+ ions from W{110} [20.13] with the goal of determining the interaction potential between particle and surface. The encouragement for structure analysis came not from this study but from earlier Russian work with higher-energy Na^+, K^+, and Cs^+ ions, which showed clear evidence of double scattering, although done under rather poor vacuum conditions [20.14]. A paper by *Veksler* and *Evstifeev* [20.15] on 500-eV Cs^+ ion scattering from W{100} was particularly convincing. Our project was delayed by personnel changes [20.16]. In addition several other groups also started using alkali LEISS for surface structure analysis. Their work is included in this review but most of this chapter is based on [20.16] of which only a small fraction has been published [20.17,18].

20.1 Theoretical Background

In LEED the wavelength λ of the probing particle is of the order of the interatomic distances d, e.g., about 1.2 Å for 100-eV electrons, so that diffraction from the periodic structure occurs, which makes LEED a reciprocal-lattice method. In LEISS $\lambda \ll d$, e.g., about 0.002 Å for 500-eV K^+ ions, so that diffraction from the periodic structure may be neglected and the particle-specimen interaction may be described by a sequence of individual scattering processes. Thus LEISS is a real-space method and free from the ambiguities connected with the transition from reciprocal to real space, which are particularly serious in the presence of dynamical effects.

20.1.1 Single Scattering and Differential Scattering Cross Section

Consider first the individual elastic scattering process. It can be described by the energy transfer in the collision, resulting in elastic scattering at the angle θ, and by the probability that this collision—which is connected with a momentum change $\Delta p = 2p \sin\theta/2$—occurs. The energy of the particle after collision is determined by energy and momentum conservation, which leads to

$$\frac{E_f}{E_0} = \frac{1}{(1+A)^2} \left[\cos\theta \pm (A^2 - \sin^2\theta)^{1/2}\right]^2 \quad , \tag{20.1}$$

with $A = M_2/M_1$ (see Fig.20.1a; binary collision model). For $A > 1$, only the plus sign is valid, while for $1 \leq A \leq \sin\theta$, both signs are valid. The probability of the collision, i.e., the differential scattering cross section $d\sigma/d\Omega = |f(\theta)|^2$ is determined by the scattering amplitude $f(\theta)$ which can, in principle, be obtained by solving the Schrödinger equation for the interaction potential V(r) between the projectile and target. In the case of alkali-ion scattering, both are many-electrón systems and the Thomas-Fermi model as treated by Firsov appears to be the most reasonable approximation to the complicated many-body interaction potential. In this case,

$$V(r) = \frac{Z_1 Z_2}{4\pi\varepsilon_0} \frac{1}{r} \varphi\left(\frac{r}{a_F}\right) \quad , \tag{20.2}$$

where $\varphi(r/a_F)$ is the Thomas-Fermi screening function and

$$a_F = \frac{0.4685}{(Z_1^{1/2} + Z_2^{1/2})^{2/3}} \text{ [Å]} \tag{20.3}$$

is the Firsov screening length. The function $\varphi(r/a_F)$ cannot be given in analytic form and decreases too slowly with r due to the neglect of exchange.

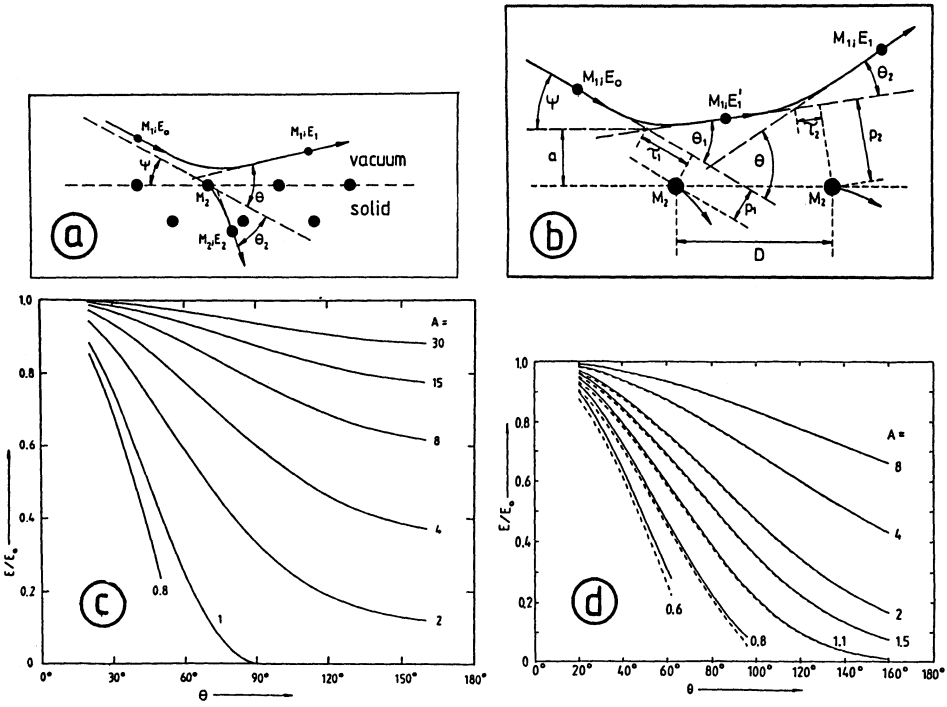

Fig.20.1. Single (**a**) and planar double (b) scattering processes. Energy of the scattered ion (divided by E_0) as a function of scattering angle Θ for various mass ratios A, for single (**c**) and planar double (**d**) scattering. The dashed curves are for small deviations ($\Theta_1 - \Theta_2 = 10°$) from symmetric ($\Theta_1 = \Theta_2$) scattering

A better and at the same time analytic expression for the screening function is the Molière approximation $\varphi(r/a_F) = \varphi(x)$, with

$$\varphi(x) = 0.35\, e^{-0.3x} + 0.55\, e^{-1.2x} + 0.10\, e^{-6x} \quad . \tag{20.4}$$

For this potential the Schrödinger equation can be solved analytically in the first Born approximation but this approximation—useful as it may be in MeV H^+ and He^+ scattering—breaks down at the low energies used in LEISS. Therefore, the scattering process is usually described in terms of classical mechanics. The differential scattering cross section $d\sigma/d\Omega = |f(\theta)|^2$ can then be given only numerically and is tabulated in [20.19]. It must be kept in mind, however, that this approximation is a very crude one and that, for example, it can not describe diffraction effects in ion-atom scattering such as observed in Li^+-noble gas atom collisions [20.20]. Their explanation requires a quantum mechanical treatment with the partial wave expansion method. Comparison with experimental results shows that restriction to the

first term in (20.4) —which makes a Yukawa potential out of (20.2) —gives already good agreement [20.20].

At present, it is difficult to assess the quality of the Thomas-Fermi-Firsov-Molière (TFFM) potential by absolute scattering cross-section measurements because of the numerous instrumental parameters which have to be taken into account. It can be tested, however, by comparing experimental single and double scattering (Sect.20.1.2) intensities (S, D) with computer simulations. Such comparisons have been made by *Algra* [20.21] for 1-10-keV K^+ scattering from Cu{410} ("stepped {100}") with the result that the TFFM potential gives good agreement with experiment, even with the simple two-atom model, provided that zigzag collisions (Sect.20.1.2) are included in the calculations. Because of the importance of zigzag scattering, even the best two-dimensional computer simulations of the D/S ratio disagree with experiment by a factor of two or more in, e.g., 600-eV K^+ scattering from Ag and Au{111} [20.22]. A full three-dimensional simulation eliminates this discrepancy [20.22]. Thus, it appears that even at low energies, classical scattering in the TFFM potential describes experiments well and that for the calculation of relative intensities the simple double scattering model is already a good approximation.

The situation in LEISS is, therefore, quite different from that in LEED. There, a full dynamical intensity calculation is necessary to extract atomic positions from the experimental intensity versus voltage curves, here, simple calculations promise to give the same information. As will be seen in Sect.20.3, even just the positions of the intensity maxima in the E spectra allow the determination of the short-range order, while the **k** positions of the intensity maxima (diffraction spots) in LEED give only the size and shape of the unit mesh, i.e., the long-range order.

20.1.2 Double Scattering

The simplest process of this type is that illustrated in Fig.20.1b [planar double scattering (PDS)]. For the special case of the symmetric PDS the energy E_1^D of the doubly scattered ion can be calculated easily using (20.1) twice. Figure 20.1d shows E_1^D as a function of θ and various $A = M_2/M_1$ ratios for comparison with the energy E_1^S of the single scattering process (Fig. 20.1c). It is evident that the energies differ significantly and that lighter atoms M_2 become accessible by double scattering.

In addition to the two-dimensional PDS, there are also three-dimensional double scattering processes which lead to scattering in the plane of incidence [zigzag scattering (ZZS), shown in a projection on the surface in

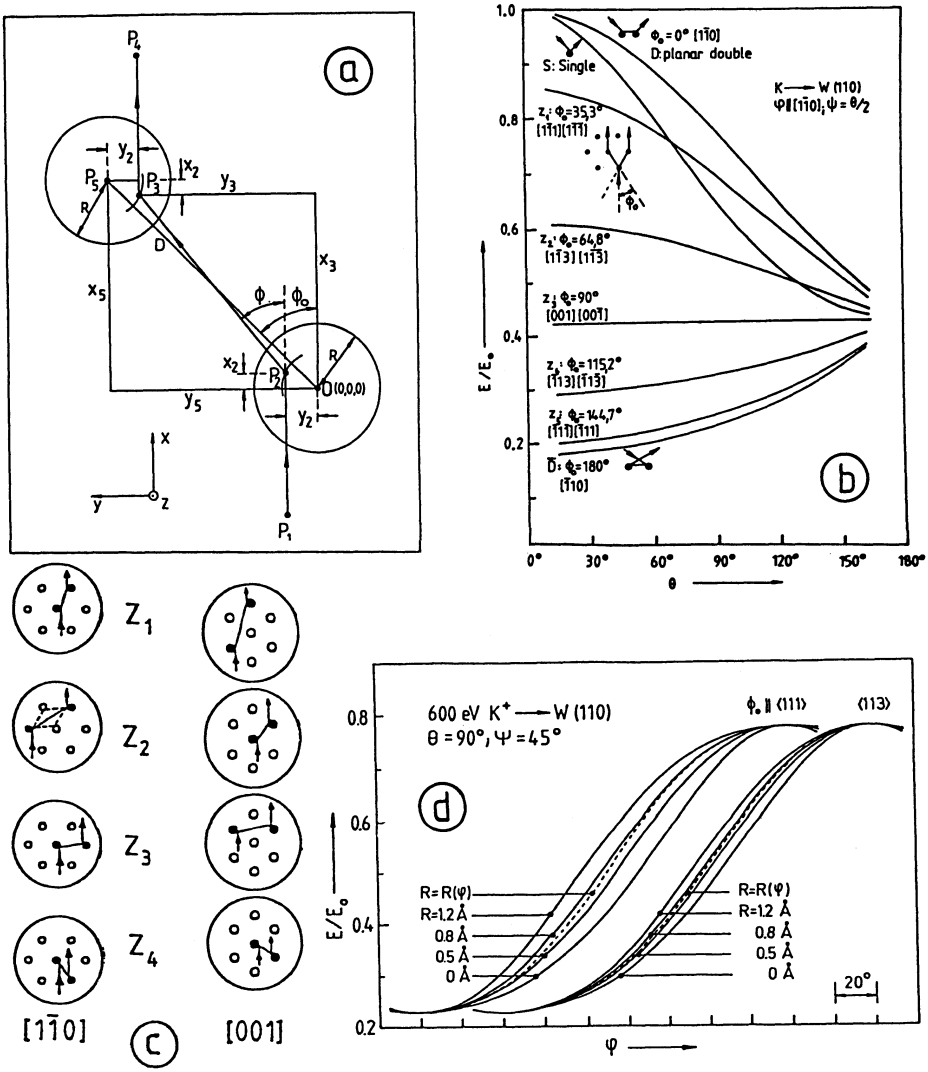

Fig.20.2a-d. Symmetric zigzag scattering in the hard sphere model. (**a**) Model configuration; the trajectory is $P_1P_2P_3P_4$; P_2P_3 are the impact points on the hard spheres. (**b**) Relative energy E/E_0 for single (S), planar double (D,$\bar{D}$), and the various zigzag processes shown in (**c**) (R = 0). (**d**) The ratio E/E_0 for two zigzag processes as a function of azimuthal angle φ for various (φ-independent) hard sphere radii R and the φ-dependent theoretical R(φ) [20.16]

Fig.20.2a (trajectory $P_1P_2P_3P_4$)]. *Von dem Hagen* [20.16] has calculated the ion energies after various ZZS processes for the symmetric case ($\theta_1 = \theta_2 = \theta/2$), representing the interaction potential by a hard sphere potential. Figure 20.2c shows some of these ZZS processes on a bcc{110} surface in the <110> and the <001> azimuth and Fig.20.2b shows the corresponding $E_1^Z(\theta)$ for the

mass ratio K^+/W and the simplest case, a hard sphere radius R = 0. The radius R is, of course, strictly speaking θ dependent because different θs correspond to different penetration depths. The R dependence is, however, not strong as seen in Fig.20.2d for the two ZZS processes $Z_1(\phi_0 \| <111>)$ and $Z_2(\phi_0 \| <113>)$ as a function of azimuthal angle φ. The R values needed to fit the K^+/W scattering data are between 0.6 Å and 0.8 Å. The E/E_0 values obtained with these fixed φ-independent R values differ little from those obtained with the φ-dependent R from *Robinson*'s tables [20.19]. The maxima in Fig.20.2d correspond to the planar double scattering ($\varphi = \phi_0$, D in Fig. 20.2b), the minima to the backward PDS ($\varphi = \phi_0 + 180^\circ$, $\bar{D}$ in Fig.20.2b).

These examples show that double scattering between neighboring atoms produces scattered ions with several energies characteristic of the atomic structure of the surface. Thus, short-range order determination should be possible via energy analysis just by comparison with double scattering model calculations. These calculations still have to be extended to asymmetric

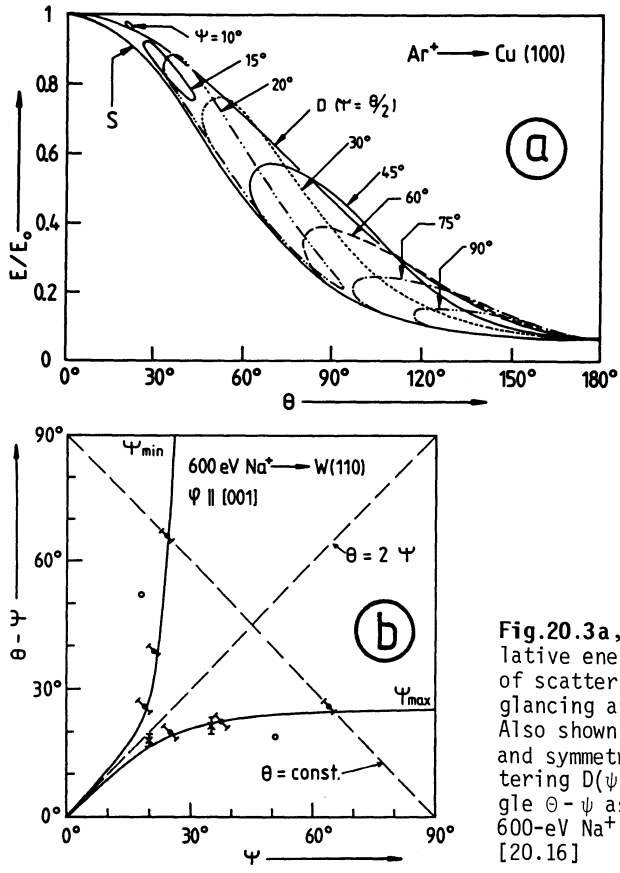

Fig.20.3a,b. Chain model. (**a**) Relative energy E/E_0 as a function of scattering angle Θ for various glancing angles of incidence ψ. Also shown are E/E_0 for single (S) and symmetric planar double scattering $D(\psi = \Theta/2)$. (**b**) Limiting angle $\Theta - \psi$ as a function of ψ for 600-eV Na^+ scattered from W{110} [20.16]

scattering ($\theta_1 \neq \theta_2$) and unequal masses. It should be noted, however, that the strong decrease of $d\sigma/d\Omega$ favors nearly symmetric collisions, as confirmed by the data in Sect.20.3.

Neither single scattering nor double scattering appear usually in pure form. The atoms are surrounded by other atoms which also contribute to the scattering. In general, each large-angle scattering process is accompanied by a series of small-angle scattering events (chain model) which causes a deviation from the E value calculated for the pure double scattering process. This is illustrated in Fig.20.3a for Ar^+/Cu{100} [20.23]. The continuous curves from $\theta = 0^\circ$ to $\theta = 180^\circ$ are for the pure single (S) and symmetric double (D) scattering processes. The loops for the various ψ are obtained from the chain model. The lower half of the loop with $E \approx E_1^S$ is the quasi-single collision (QS), the upper half, which deviates in general ($\psi \neq \theta/2$) from E_1^D, the quasi-double collision (QD). Another consequence of the multiple collisions in the chain model is the limitation of the scattering to a ψ-dependent θ region (left and right loop ends in Fig.20.3a) and to a θ-dependent ψ region as illustrated in Fig.20.3b by experimental results for 600-eV Na^+ ions incident in the <001> azimuth on W{110} [20.16]. Thus, the chain model indicates a considerable limitation of the energy analysis in terms of pure single and double scattering, which will be examined in Sect.20.3.

20.1.3 Shadowing, Blocking, and Focusing; Thermal Vibrations; Inelastic Scattering

Even if the scattered intensity I(E) is not evaluated in detail by comparison with simulations, it has to be understood at least qualitatively in order to allow identification of the peaks (E_i) in the spectrum with the proper double scattering process. Three processes are of importance in this connection: shadowing, blocking, and focusing. The scattering process produces a shadow cone behind the atom and an angular region with high intensity (Fig.20.4a). This has several consequences. Atoms within the shadow cone do not contribute to the overall scattering and atoms in the intensity-enhanced region make a disproportionately large contribution, an effect which allows the measurement of the shadow cone and which can also be used very effectively for structure analysis. If an atom is at small ψ in the shadow cone, then the backscattering into large angles will suddenly increase with increasing ψ when the atom moves into the high-intensity region at a critical angle ψ_c [impact-collision ion-scattering spectroscopy" (ICISS)] [20.24]. *Oen* [20.25] has proposed an empirical expression for the radius s of the shadow cone at a distance l behind the target atom which agrees well with experiment [20.24].

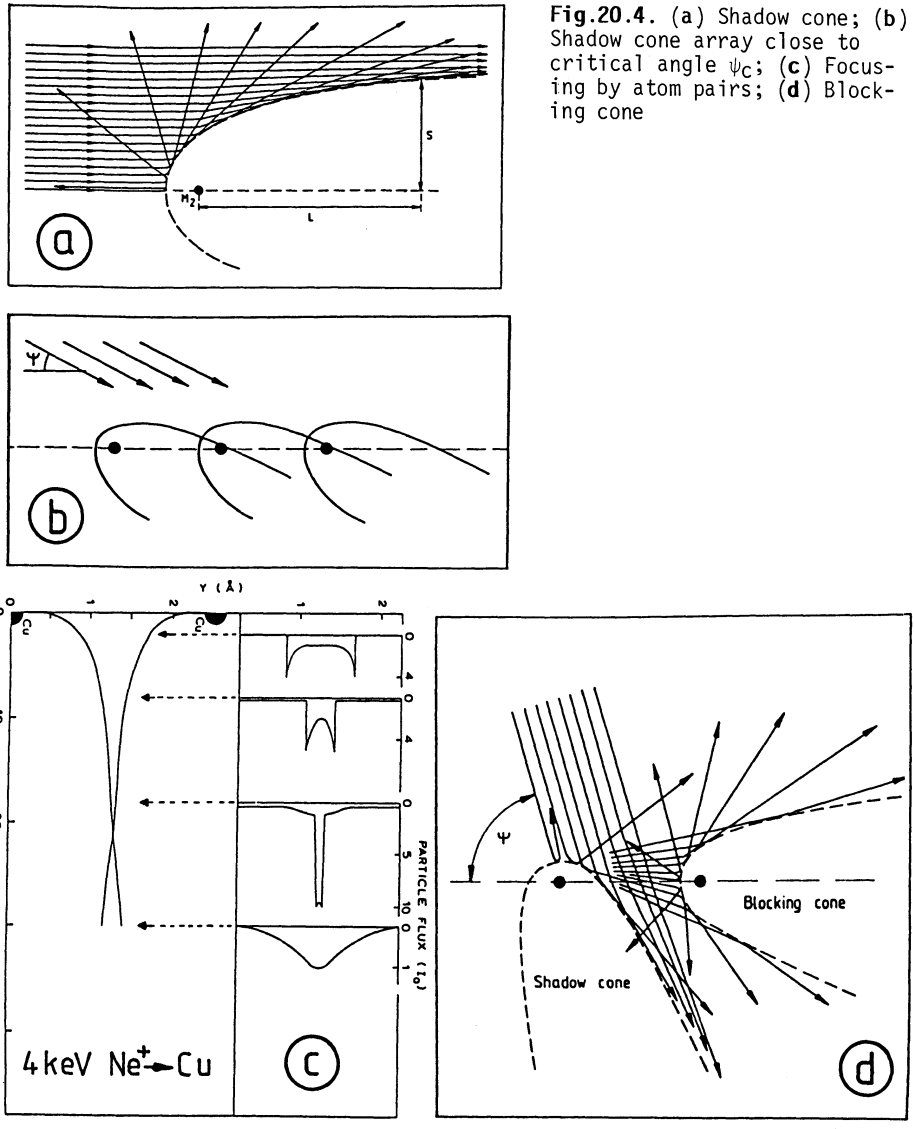

Fig.20.4. (a) Shadow cone; (b) Shadow cone array close to critical angle ψ_c; (c) Focusing by atom pairs; (d) Blocking cone

When the shadow cones of two atoms overlap, strong focusing can occur (Fig.20.4c). This is particularly important when neutralization is weak, as in K^+/W scattering, see Sect.20.3). Finally, blocking of scattered ions by other atoms, as indicated in Fig.20.4d, also has to be taken into account. While the processes just discussed complicate the spectra, they are at the same time very useful for structure analysis, such as in ICISS.

Thermal vibrations reduce the sharpness of the shadow cone due to the continuously changing position of the atom producing it. As a consequence, strong intensity changes occur in the spectrum, which in the case of the single scattering peak can be described by the simple two-atom model [20.26]. Double scattering peaks are more sensitive to thermal vibrations because of the correlation of the atomic positions necessary for their appearance. Depending upon these correlations—about which little is known—the intensity decrease with temperature may be more or less severe.

Also very little is known as yet about inelastic scattering (electronic excitations) in alkali LEISS. For structure analysis the only important aspect of it is some peak broadening.

20.1.4 Neutralization

The main motivation for alkali LEISS is the low neutralization probability of alkali ions and the (expected) trajectory independence of the ionization probability. Of the various charge exchange processes discussed in the literature, resonance neutralization is probably the most important if not the only one for alkali ions. In these ions, the ionization levels are near the Fermi level of the metal so that neutralization occurs via tunneling from the conduction band. Independently of the specific model used to describe this process [20.27-32], the fate of the ion is decided in a narrow zone several Ångstroms above the surface. The neutralization is determined to a large extent by the normal component of the velocity, $v_\perp$, with which the particle passes this zone, and not by the details of its trajectory. A typical expression for the ionization probability [20.28] is

$$\alpha^+(E) = \frac{2}{\pi} \exp\left(- \pi c_1 \frac{I - \phi + c_2}{\hbar \gamma v_\perp}\right) , \qquad (20.5)$$

where $I = \varepsilon_a(\infty)$ is the alkali ionization energy, ϕ the metal work function, γ the decay constant of the level width $\Delta(z) = \Delta_0 \exp(-\gamma z)$, and c_1, c_2 are constants describing the variation of the level position $\varepsilon_a(z)$ with distance. The essential dependences are those on $I - \phi$ and on $v_\perp$, c_1, and c_2. In general, they are not known so that the theory has little predictive power. With simplifying assumptions it is, nevertheless, possible to describe, for example, the temperature dependence of $\alpha^+(E)$ for 30 to 400-eV Na atoms ($I = 5.14$ eV) on W{110} ($\phi = 5.3$ eV) [20.29,33]. Both theory and experiment show that for 100- to 500-eV Na^+ ions, $\alpha^+(E) = 0.94$-0.96, and for K^+ with its lower ionization energy ($I = 4.34$ eV), $\alpha^+(E) \approx 1$. On other high work function surfaces such as Au ($\phi = 5.4$ eV) and Pt ($\phi = 5.6$ eV) there is also no

significant neutralization. *Algra* et al. [20.34] have made a detailed study of $\alpha^+(E)$ for 2- to 10-keV Li^+ (I = 5.39 eV), Na^+, and K^+ scattered from Cu{100} (ϕ = 4.6 eV) and found that α^+ is almost *independent* of the type of trajectory about 60%, 75%, and 99%, respectively, confirming the expectations mentioned initially.

However, when ϕ is reduced by adsorption, $\alpha^+(E)$ decreases significantly. Thus, a ϕ reduction of W{110} by 1.5 eV due to Na adsorption causes an α^+ decrease from 0.94 to 0.1 for 100-eV Na atoms [20.35], a reduction by 0.75 eV due to Cu adsorption causes an α^+ decrease from 1.0 to 0.6 for 600-eV Na^+ ions [20.16] (Sect.20.2). In the case of strongly electropositive adsorbates, such as Ce, strong local neutralization and/or strong focusing onto the substrate atom occurs [20.36]. A comparison of the still sparse $\alpha^+(E)$ data shows that though $I - \phi$ is the quantity dominating $\alpha^+(E)$, the other parameters in (20.5) have also significant influence.

20.2 Experimental Techniques

Surface structure analysis by alkali LEISS needs, in principle, only an ultra-high-vacuum (UHV) system with an alkali ion gun, an angle-resolving

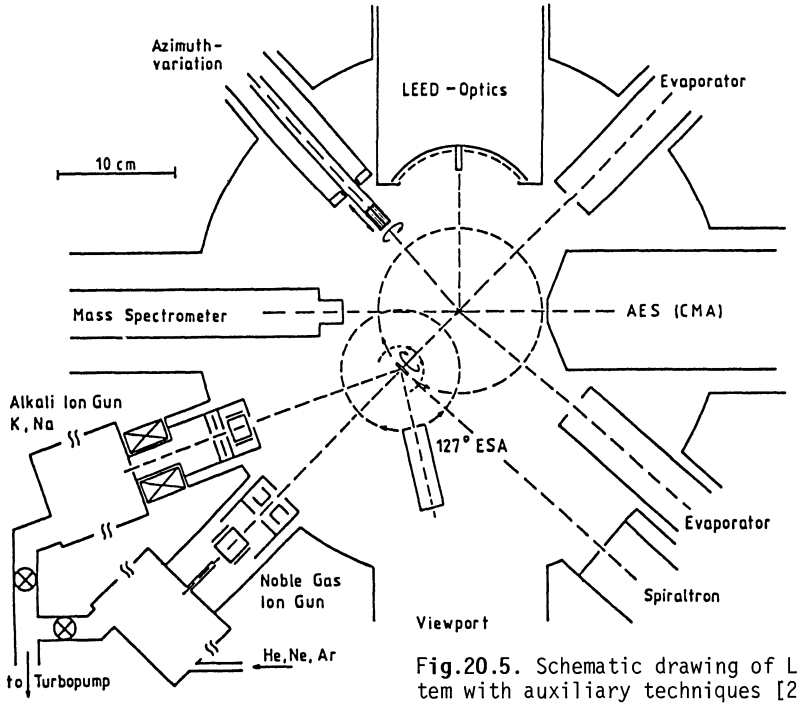

Fig.20.5. Schematic drawing of LEISS system with auxiliary techniques [20.16]

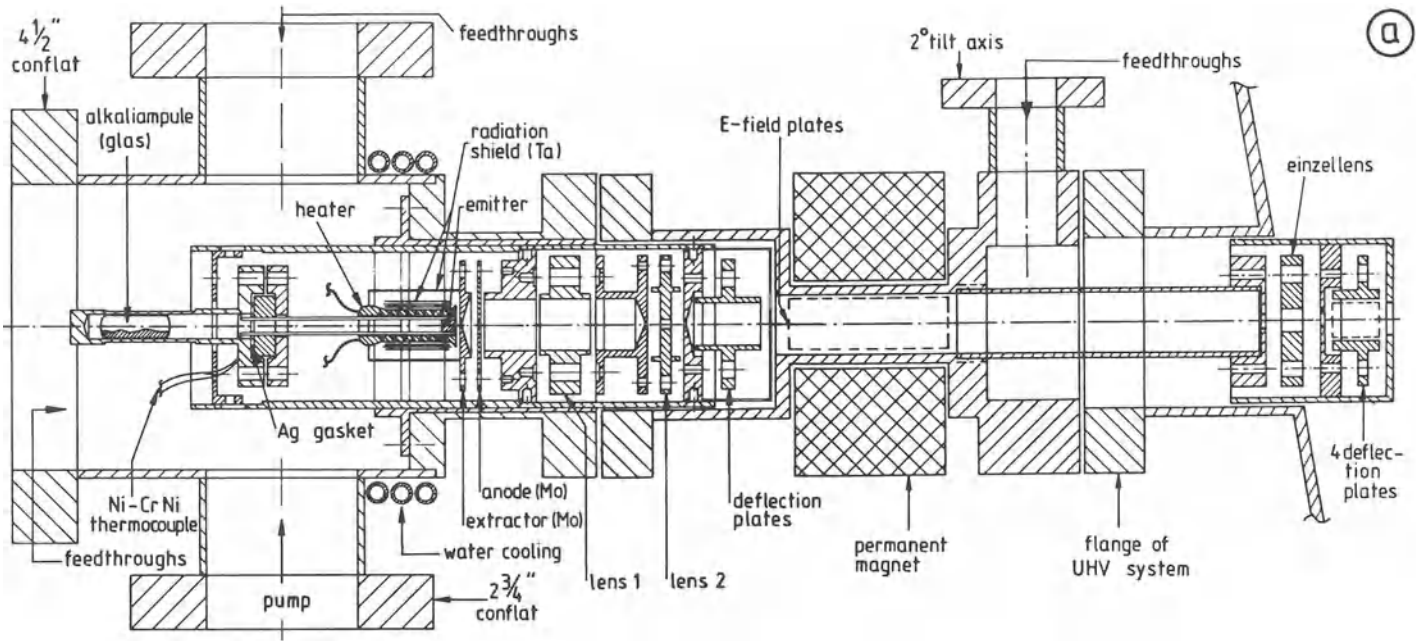

Fig.20.6a. Caption see opposite page

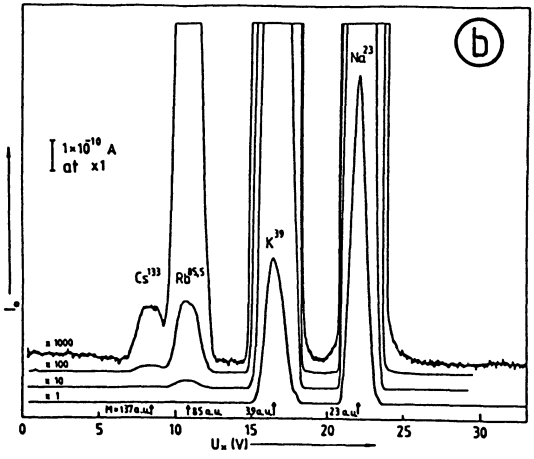

Fig.20.6. (a) Alkali ion gun with Wien filter; (b) Typical mass spectrum obtained with Wien filter [20.16]

energy analyzer with an appropriate data acquisition system, and a specimen manipulator with sufficient precision and several degrees of freedom. In practice, auxiliary techniques are necessary for surface characterization: LEED for the determination of the long-range order and AES for the determination of the surface composition. Figure 20.5 shows a typical system [20.16] which, in addition, is equipped with a mass spectrometer for residual gas analysis and thermal desorption spectroscopy, a noble gas ion gun for comparative studies, a fixed-energy integrating detector for calibration purposes, and several evaporators for adsorbate and thin film studies. The coaxial gun of the cylindrical mirror analyzer (CMA) is used not only for AES but also for work function change ($\Delta\phi$) measurements. The system has a base pressure in the low 10^{-11} Torr range which is necessary for studies of surfaces with high sticking coefficients for residual gases.

The ion gun in this system is not typical. Several other gun designs have been used [20.13,37-40], some of which have integrated the alkali ion source into the noble gas ion gun by using small commercial alkali-ion emitters [20.38-40]. In the ion gun shown in Fig.20.6a [20.16] the emitter is a heated porous W plug ($T \approx 1000$-1150 K) through which the alkali from a broken glass ampule diffuses and is surface-ionized on the W surface. The ion optical system produces a monochromatic ion beam of 10^{-8}-10^{-10} Å and about 1-mm half-width consisting of all alkali ions. These are then mass-separated by a Wien filter (Fig.20.6b) which allows rapid switching between different ions. The specimen can be rotated about axes in and normal to the surface (accuracy $\approx 1^{\circ}$) and in addition translated in the x, y, and z directions and be brought into any of the experimental positions indicated in Fig.20.5. Although time-of-

flight energy analysis has been used too [20.13], most energy analyzers are of the electrostatic type (ESA), either hemispherical or 127° analyzers, with energy resolutions ranging from 0.5% [20.40] to 3.5% [20.39] and angular resolutions ranging from ±0.5°[20.16] to ±2.2° [20.39]. The analyzer is rotatable so that the scattering angle θ can be changed; it is usually determined to within ±0.5° [20.16,40] to ±1° [20.39]. Thus the angular accuracy

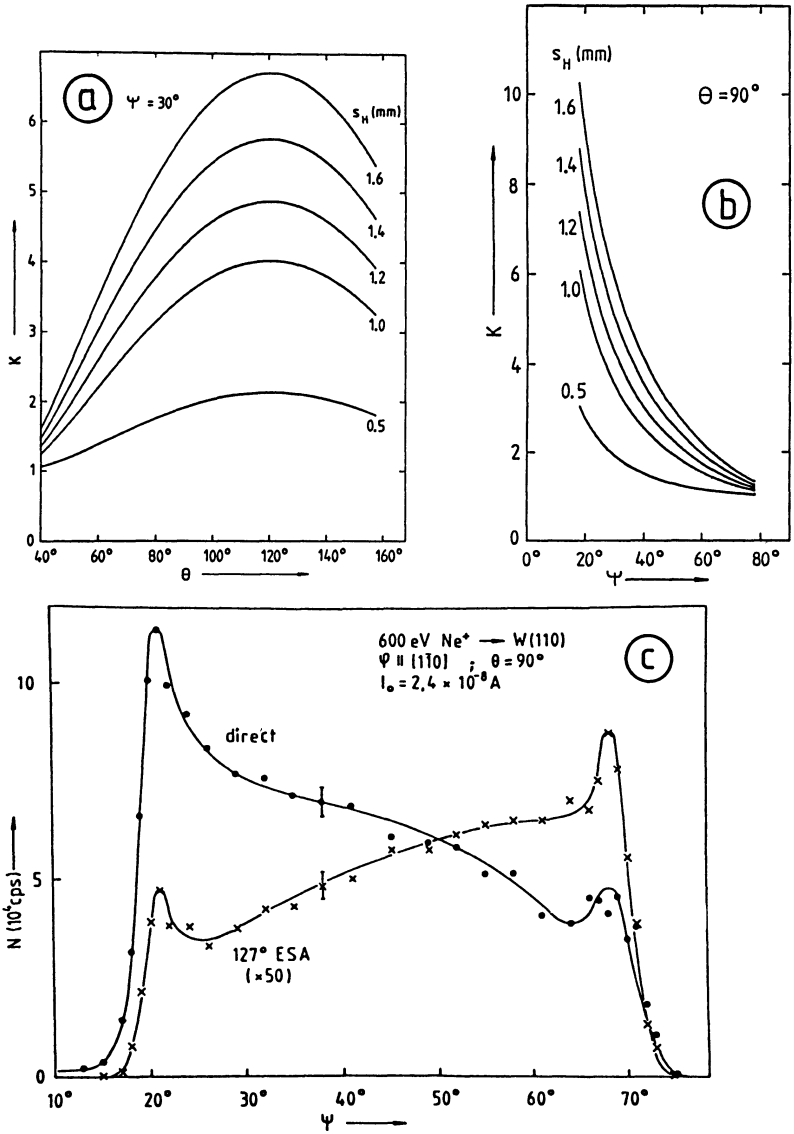

Fig.20.7. (**a**, **b**) Accepted area correction factor; for explanation see text; (**c**) Influence of accepted area on detected current as a function of ψ [20.16]

is much less severe than in a LEED diffractometer. Important factors are the geometric adjustments and corrections which are necessary for correct angle and intensity measurements. Figure 20.7a,b gives an idea of the magnitude of the intensity corrections for the system shown in Fig.20.5, in which the incident beam is assumed to have a Gaussian profile with half-width S_H and the 127° analyzer to have transmission functions of Gaussian shape with half-width 0.54 mm in the scattering plane and 3.2 mm normal to it. This correction is necessary because the specimen area accepted by the analyzer is different from the bombarded area. If it is neglected, serious errors arise as illustrated in Fig.20.7c, which compares directly measured—with the large acceptance area spiraltron in Fig.20.5—intensities with those measured with the 127°ESA [20.16]. Agreement between the two measurements is obtained with $K(S_H = 1.2)$ in Fig.20.5b.

Another factor which has to be taken into account is the modification of the specimen by the probing beam within the measurement time, due to sputtering and implantation. The work function ϕ is a sensitive indicator of these changes. Figure 20.8 [20.16] shows the change $\Delta\phi$ as a function of ion dose for several species and energies, and compares it with the change caused by adsorption of an equal amount of W and Na on the W{110} surface. The doses necessary for a complete spectrum are indicated by arrows. The corresponding $\Delta\phi$ for 600-eV ions is the same for Ne^+ and Na^+ so that the problem is equally serious in noble-gas and alkali-ion scattering.

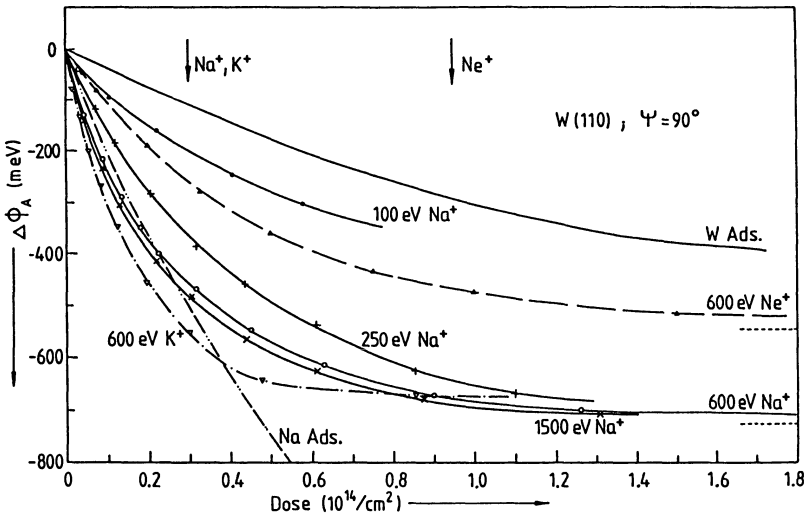

Fig.20.8. Influence of ion bombardment and adsorption on the work function of the W{110} surface [20.16]

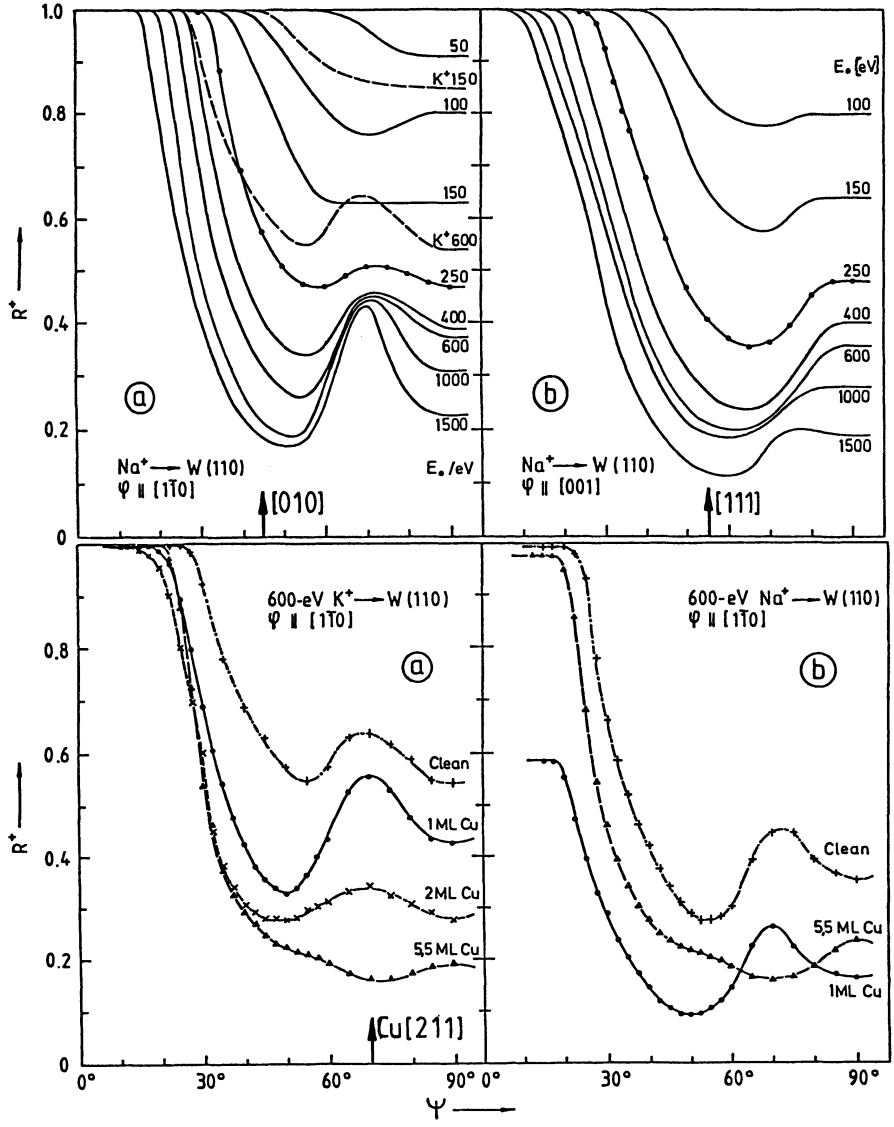

Fig.20.9. Ion reflection coefficient R^+ for K^+ and Na^+ as a function of glancing angle of incidence. *Top*: for various energies in two azimuths. *Bottom*: for various Cu coverages [20.16]

Some information on the type of surface modification may be deduced from measurements of $\alpha^+(E)$ as a function of glancing angle of incidence ψ and azimuthal angle φ. Results of such measurements for Na^+ and K^+ are shown in Fig.20.9 {[20.16], $\alpha^+(E) = R^+$}. Below a critical ψ, ψ_c, the ions cannot pene-

trate into the crystal due to the overlap of the shadow cones of the surface atoms, see Fig.20.4b, and are totally reflected: $R^+ = 1$, provided that $\phi > I$. With increasing ψ, R^+ decreases, particularly strongly near densely packed directions which are at the same time open channels in the crystal, whether it is W or Cu [5.5 monolayer (ML) curve; 1 ML Cu is pseudomorphous with W]. It is apparent that under typical LEISS conditions ($\psi > \psi_c$) as much as 80-90% of the incident ions are lost even at energies as low as 600 eV. Most of these ions will certainly not be implanted but diffuse to the surface and are adsorbed there. The difference between Ne^+ and Na^+ in Fig.20.8 is probably mainly due to this adsorption layer which is absent in the case of Ne. It should be noted (i) that with increasing $\Delta\phi$, unthermalized Na may also be reemitted in the form of fast atoms, (ii) that with increasing coverage it may be sputtered off, and (iii) that even if all Na or K were to remain at the surface, the coverage at the end of one spectrum would be only 0.02 ML.

20.3 Basic Studies of the Scattering Mechanisms

Before alkali LEISS can be used with confidence for structure analysis, the basic scattering mechanisms must be understood. Studies with this goal have been made by several groups [20.14-18,21,40-44]. We will illustrate the results with data from [20.16] which were all obtained from a W{110} surface. Figure 20.10 shows typical K^+, Na^+, and Ne^+ spectra from a clean W{110} surface. Due to the absence of neutralization, the K^+ and Na^+ spectra are much more complicated than that of Ne (dotted line) in which only the quasi-single scattering (QS) peak is seen. In addition to the QS peak S and the QD peak D, several other peaks are seen. The location and intensity of all peaks depend more or less on azimuth, which clearly demonstrates the strong structure sensitivity. Unfortunately, the structure is strongly temperature dependent as seen in Fig.20.11 for K^+ on W{110}. At low energies all peaks, including the S peak, decrease strongly with T, at higher energies mainly the multiple scattering peaks decrease. As a consequence, a D/S intensity analysis has to be done with considerable caution, even for surfaces with high Debye temperatures such as W{110}.

The dependence of the energy positions (E/E_0) and intensities (I) of the peaks in Fig.20.11 upon the energy E_0 of the incident ions is shown for K^+ and Na^+ and $\theta = 2\psi = 90^\circ$ at 300 K in Fig.20.12. It is seen that more peaks can be identified for Na^+, that some peaks (e.g., F) appear only at very low E_0, others (I) in the intermediate E_0 range. The intensities of the various peaks differ by orders of magnitude (B for K^+, C and K for Na^+)

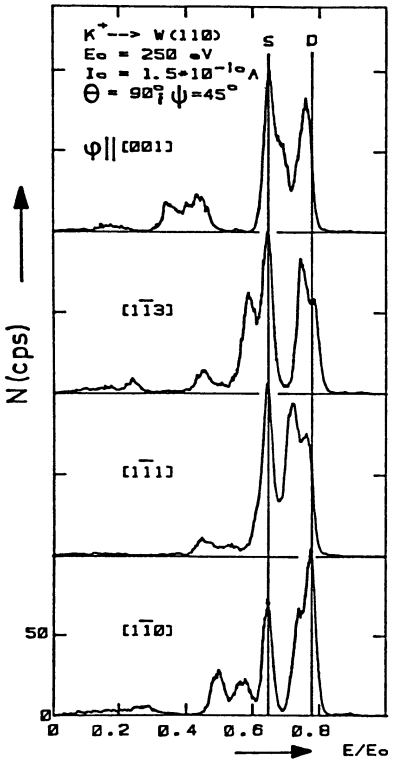

Fig.20.10.

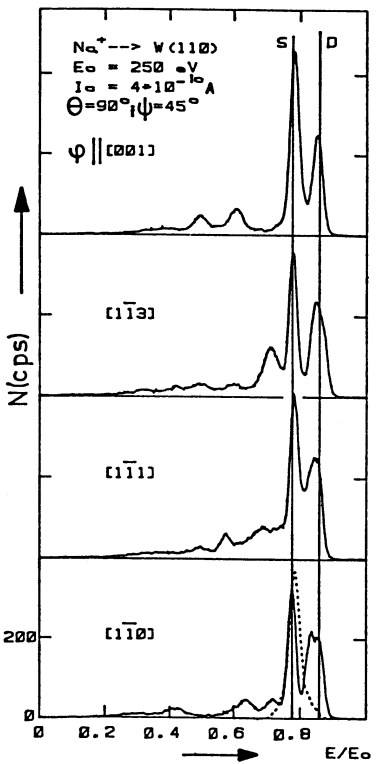

Fig.20.11.

Figure captions see opposite page

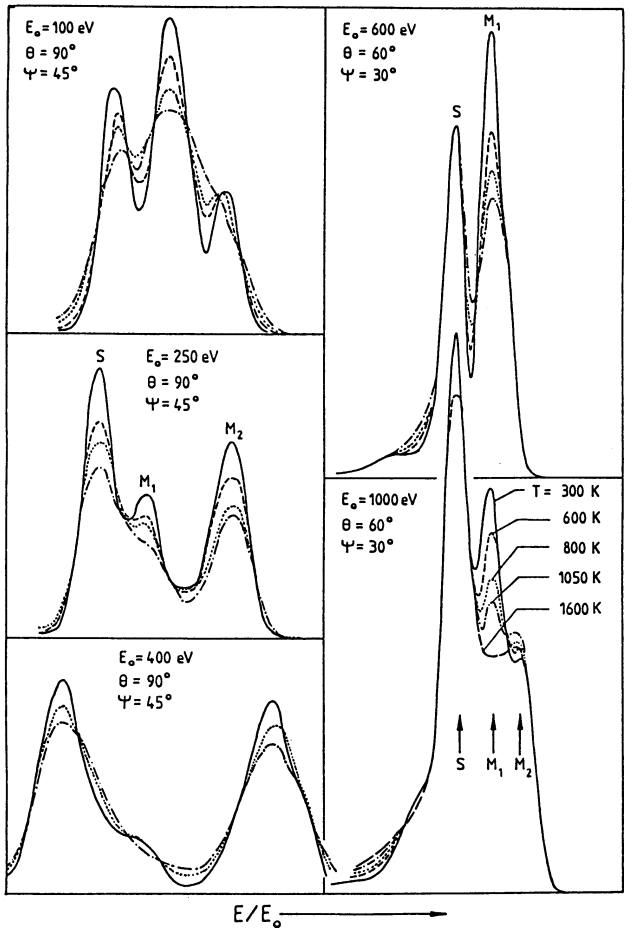

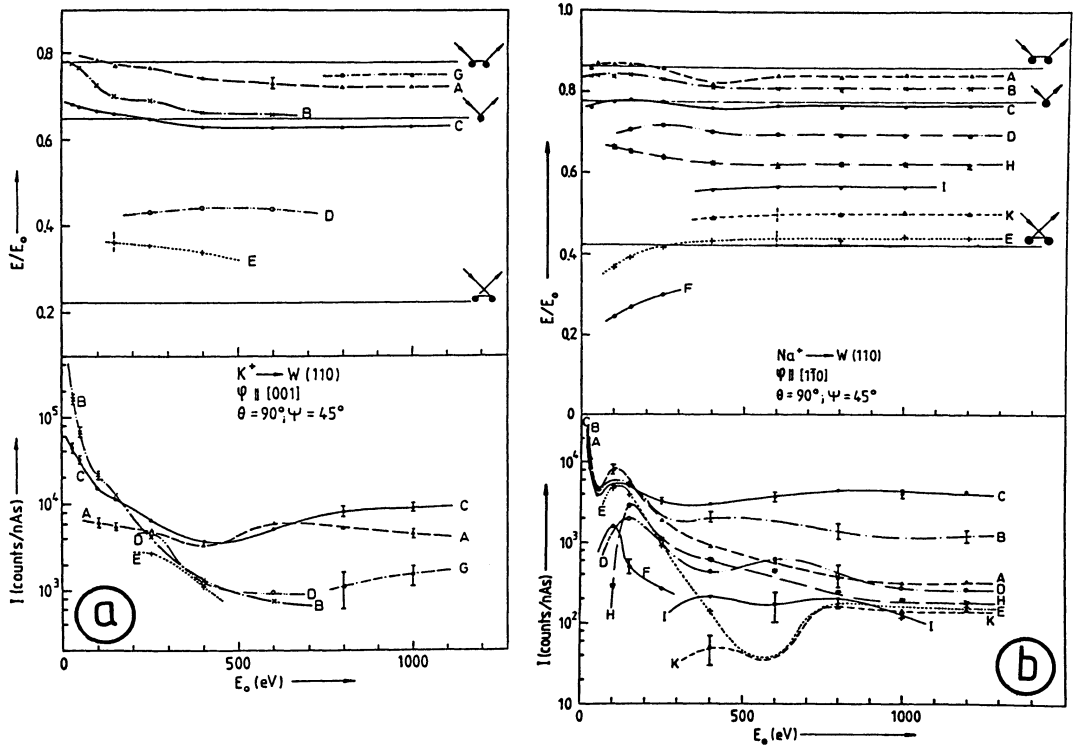

Fig.20.10. Typical LEISS spectra of 250-eV K^+ and Na^+ ions scattered from W{110} in various azimuths [20.16]. The dotted line represents a Ne^+ spectrum for comparison

Fig.20.11. Temperature dependence of K^+ LEISS spectra for various primary energies E_0, on W{110}, <001> azimuth [20.16]

Fig.20.12. Primary energy E_0 dependence of energies (*top*) and intensities (*bottom*) of (**a**) K^+ and (**b**) Na^+ scattered symmetrically at $\Theta = 90°$ from W{110} [20.16]

but those of the major peaks of Na^+ (C, B, A, D) change little above several hundred electron volts as their energies do too. This makes Na^+ appear more suitable for structure analysis than K^+. Another comparison between K^+ and Na^+ is provided by Figs.20.13 and 14 in which the θ dependence of peak energies (E/E_0) and intensities (S) is shown for $E_0 = 250$ eV and $\theta = 2\psi$. The choice of $\theta = 2\psi$ allows a comparison between the simple two hard spheres model (Sect. 20.1.2) and the observed E/E_0 values and thus an identification of the scattering processes (without computer simulation) of all peaks except E and F. The peaks S^* and D^* will be discussed later in this section. It should be noted that double backward scattering, either planar (D) or zigzag (Z_4) is quite pronounced above $\theta \approx 60^\circ$. All peaks except C, D, S, and Z_1 show typical shadow cone features, that is, the sudden onset of the peak at a critical angle $\psi_c = \theta_c/2$. The C peak which appears only at $\theta \lessapprox 60^\circ$ splits into the clearly identifiable D and Z_1 peaks and is without doubt the multiple small angle scattering peak of the chain model (Sect.20.1.2).

How much less structural information is contained in a noble-gas ion spectrum can be seen also in Fig.20.14. Only the S peak and an M peak attributed

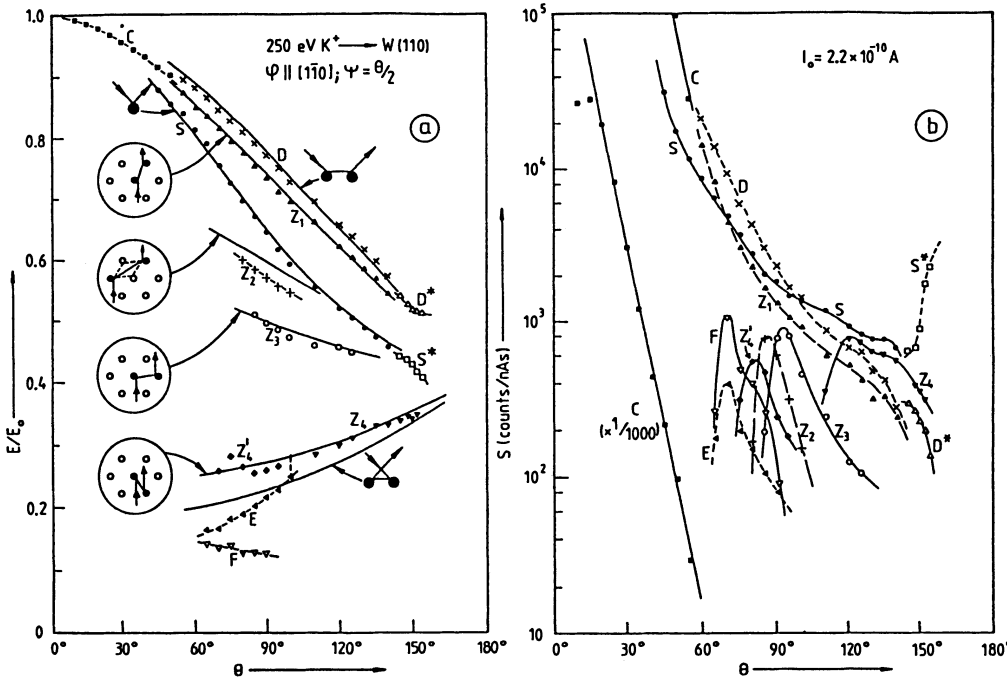

Fig.20.13. Scattering angle (Θ) dependence of (**a**) energies and (**b**) intensities of symmetric ($\Theta = 2\psi$) 250-eV K^+ scattering from W{110} in the <110> azimuth [20.16]

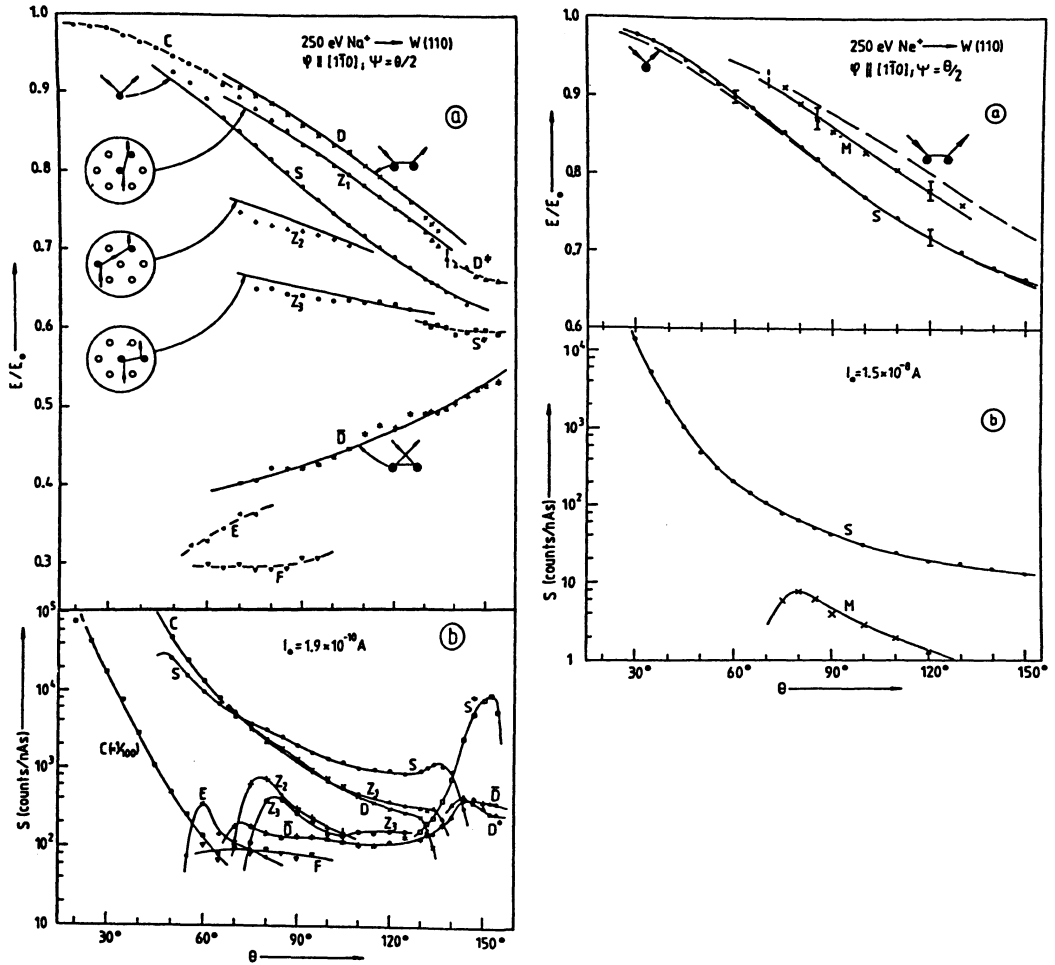

Fig.20.14. Scattering angle dependence of (**a**) energies and (**b**) intensities of symmetric ($\Theta = 2\psi$) 250-eV Na^+ (*bottom*) and Ne^+ (*top*) scattering from W{110} in the <110> azimuth [20.16]

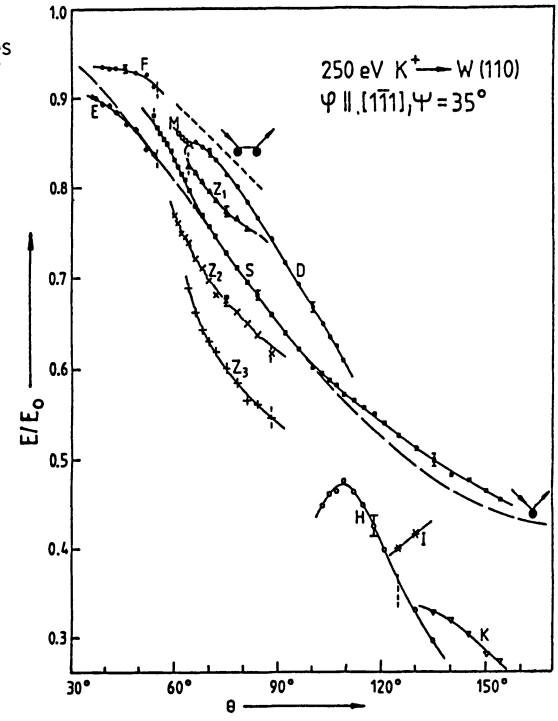

Fig.20.15. Scattering angle (Θ) dependence of (**a**) energies and (**b**) intensities of 250-eV K^+ scattering from W{110} in the <111> azimuth at fixed glancing angle of incidence $\psi = 35°$ [20.16]

to multiple scattering because of its large deviation from the D curve are observed. In addition, the intensities are two orders of magnitude lower.

In Figs.20.13 and 14, ψ was changed simultaneously with θ in the interest of simple analysis. A clearer picture of the θ dependence is obtained when ψ is constant as in Fig.20.15. By comparison with $\psi = \theta/2$ measurements, most peaks can be identified easily. The E and F peaks (different from those in Figs.20.13 and 14) are obviously due to atoms on top of the flat surface because they appear before the onset of the S peak. In Fig.20.16, θ is held constant so that the pure ψ dependence can be seen. The peak identification is again made by comparison with $\psi = \theta/2$ data. The cutoff due to shadowing and blocking can be seen particularly clearly in this mode of operation and the inferiority of Ne^+ to Na^+ with respect to structural sensitivity and intensity is again obvious.

The last variable dependence to be discussed is that on azimuth φ. In view of the marked changes with φ (Fig.20.10) and the easy identification of most peaks in the $\theta = 2\psi$ mode, the structure should be particularly accessible via φ variation. Figure 20.17 supports this expectation. Here the measured peak locations E/E_0 are plotted for a large number of φ values and the positions calculated with the two hard spheres model (Sect.20.1.2) and a fixed R value

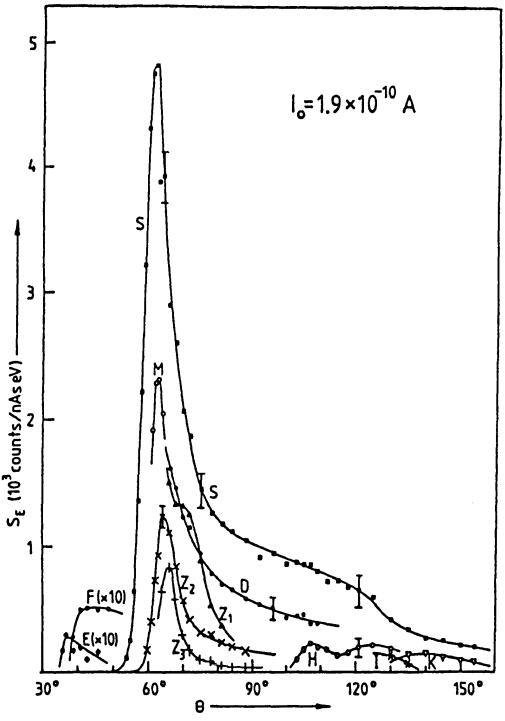

Fig.20.15b.
Caption see opposite page

for the most important zigzag collisions (Fig.20.2) are shown as lines. In general, the agreement between model and experiment is good. It appears that measurement in several high symmetry directions ($\varphi \| <001>$, <113>, <111>, and <110>) should suffice to determine the structure.

The discussion up to now has been concerned with the lateral positions of the atoms. What can alkali LEISS tell us about the positions normal to the surface? Let us first look at the depth sensitivity by depositing Cu, which grows two-dimensionally on W{110} (Fig.20.18). In the case of Na^+ and K^+ scattering, the W signals decrease linearly with coverage up to 0.7-0.9 ML, and disappear completely at about 1.2 ML, which indicates sensitivity to only the topmost layer, in contrast to Ne^+ where a weak signal is still seen at 2 ML. (A discussion of the other features of Fig.20.18 can be found in [20.16].) This is true for 250 eV. At 600 eV and $\theta_{Cu} \approx 1$ the W peaks are clearly visible and occur at practically the same energy as in the topmost layer (Fig.20.19). Thus, by varying E_0, deeper layers can be probed also, provided they are visible to beam and detector. The detectability of second-layer atoms is considerably enhanced by shadow cone focusing (Fig.20.4c) by the atoms in the topmost layer [20.17,18]. The effectiveness of this process

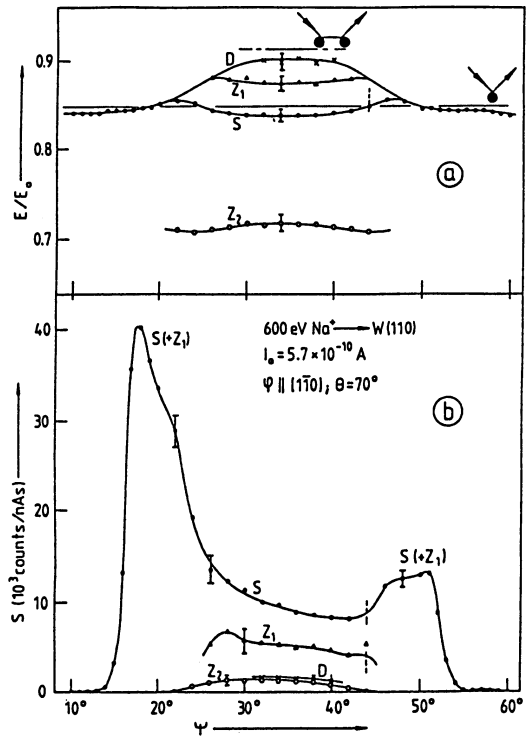

Fig.20.16. Glancing angle of incidence ψ dependence of (**a**) energies and (**b**) intensities of 600-eV Na^+ (*top*) and Ne^+ (*bottom*) scattering from W{110} in the <110> azimuth ($\Theta = 70°$) [20.16]

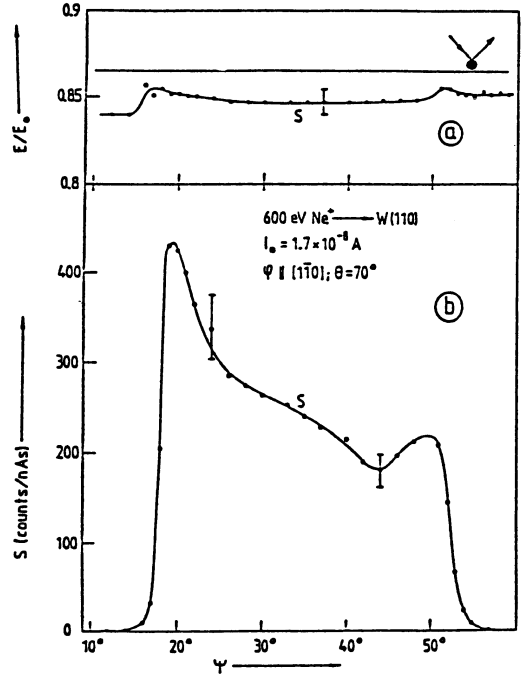

Fig.20.17. Relative peak energies E/E_0 as a function of azimuth φ for symmetric scattering ($\Theta = 2\psi = 120°$) of 600-eV K^+ ions from W{110}. (•••) measured points; (ooo) points obtained from symmetry arguments; (——): calculated with hard sphere model and φ- independent R = 0.6 Å. The zigzag processes connected with each line are indicated at sides and explained for two of them in the inset [20.16]

Fig.20.18a-c. Intensities of the major peaks in the LEISS spectra from Cu-covered W{110} as a function of Cu coverage for symmetric ($\Theta = 2\psi = 70°$) scattering of 250-eV (**a**) K^+, (**b**) Na^+, and (**c**) Ne^+ ions (<110> azimuth) [20.16]

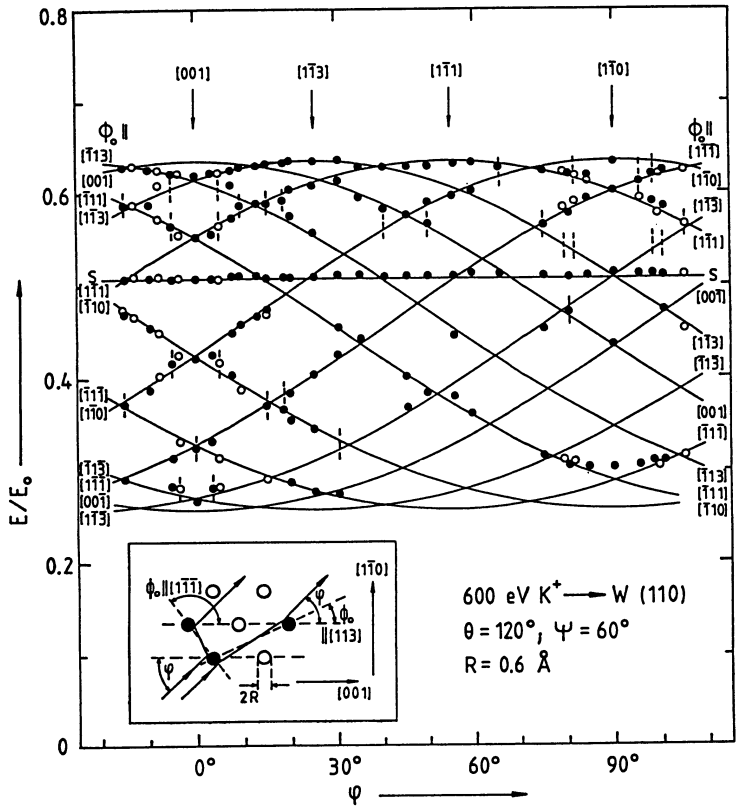

Fig.20.17

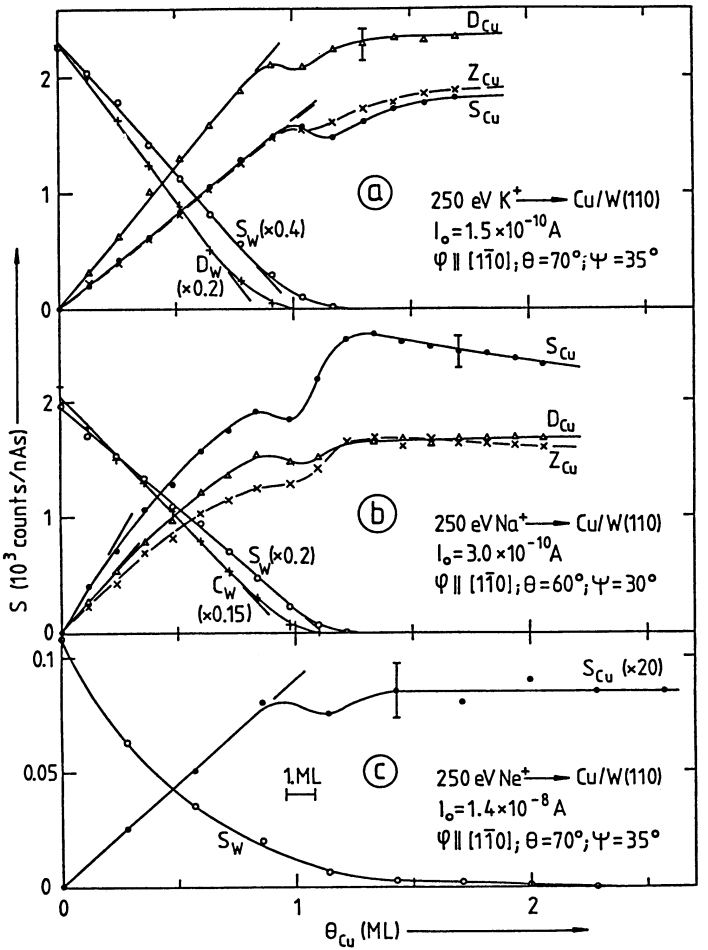

Fig.20.18

Figure captions see opposite page

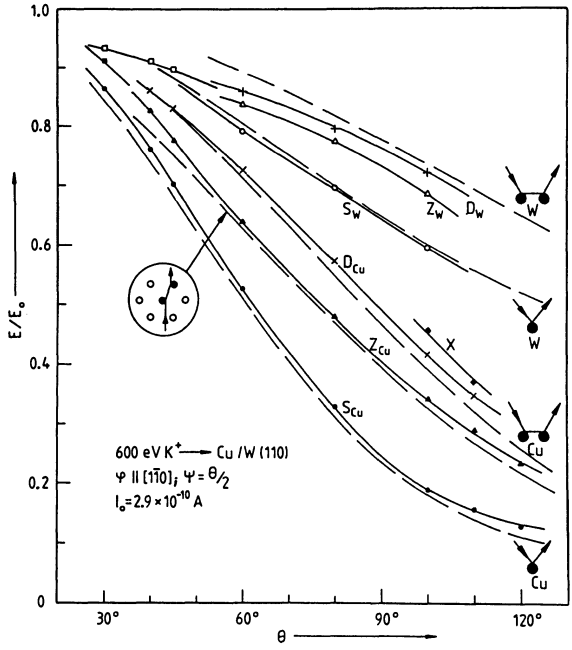

Fig.20.19. Relative peak energies E/E_0 as a function of Θ for symmetric ($\Theta = 2\psi$) scattering of 600-eV K^+ ions from W{110} covered with 0.9 - 1.0 ML Cu. Dashed lines are calculated with the hard sphere model with R = 0.8 Å [20.16]

is illustrated by the high intensity of the D^* and S^* peaks at large scattering angles (Figs.20.13,14). This angular region is shown in more detail in Fig.20.20 for 600-eV K^+ scattering in the <110> azimuth of W{110} in the $\theta = 2\psi$ mode. About 1 ML Cu reduces the D, S, and Z_1 peaks characteristic of top-layer atoms dramatically but leaves the S^* and D^* peaks nearly unchanged and adds another peak, T^*. Computer simulations for the clean surface identify these peaks with the processes shown in the lower half of Fig.20.20, in which filled circles are atoms in the plane of incidence, and open circles atoms in the adjacent parallel planes. The peak locations are very sensitive to atomic positions so that shadow cone focusing appears to be a powerful method of probing positions of second-layer and perhaps even third-layer atoms. It is unlikely that this can be done with noble gas LEISS because of the strong neutralization.

What do these studies tell us about the best way to do structure analysis? Certainly, E_0 should not be too low because the shadow cone becomes too wide and the peaks too broad. Also, if zigzag scattering is undesirable such as on surfaces consisting of atoms differing in mass (superposition of spectra!) higher energies are preferable. Although an increasing fraction of the ions

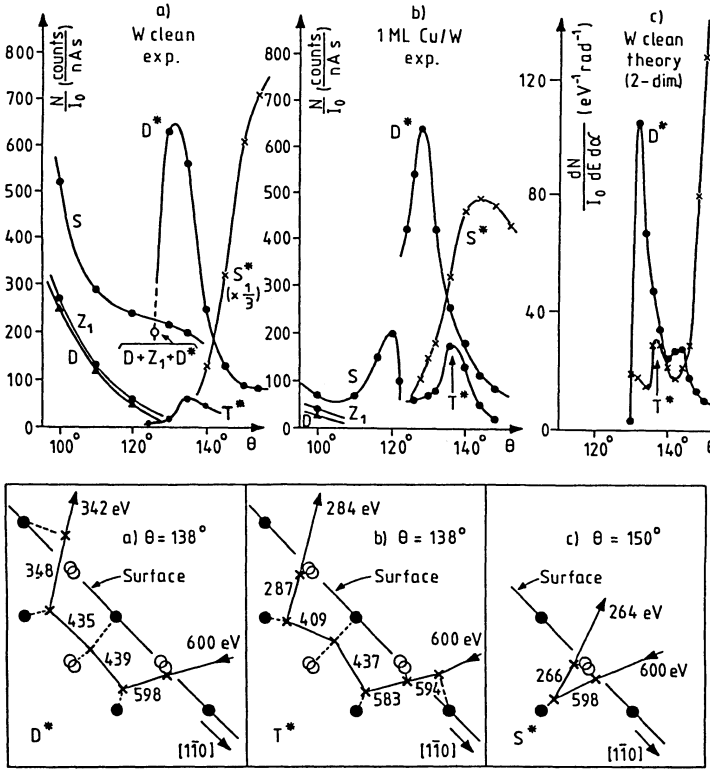

Fig.20.20. *Top*: Peak heights as a function of scattering angle Θ for symmetric ($\Theta = 2\psi$) large angle scattering of 600-eV K^+ ions from W{110} in <110> azimuth. (**a**, **c**) Clean surface; (**b**) with 1 ML of Cu. *Bottom*: Explanation of the three peaks (**a**) D*, (**b**) T*, and (**c**) S* as derived from computer simulations [20.18]

are lost in the crystal with increasing energy (Fig.20.9) the peak intensities still do not indicate any decrease up to 1500 keV. Thus, there is no critical criterion for E_0 and, in fact, energies from 500 eV to 2 keV have been used for structure analysis. The $\theta = 2\psi$ mode is convenient for peak identification within the two hard spheres model, but two angles are changed simultaneously. After peak identification in the $\theta = 2\psi$ mode, structure analysis by ψ variation at constant θ seems most appropriate. Finally, several φ values are desirable, in particular if zigzag collisions are used in the structure analysis, which has not been done systematically up to now.

20.4 Structure Analysis

Structure analysis with alkali LEISS is still in its infancy. Only a few studies have been done so far, most of them in the impact collision mode. They may be divided into three groups: (i) qualitative determinations of

the relative positions of different surface atoms, (ii) distinctions between various surface structure models, and (iii) structure analyses involving quantitative determination of atomic positions. Group (i) is illustrated by studies on the structure of oxygen [20.45-48], carbon [20.45,47,48], nitrogen [20.48] and sulphur [20.49] overlayers on Mo{100} with 500- to 1000 eV K^+ and Li^+ scattering, and a cursory study of oxygen adsorption on Ni{110} by 600-eV Li^+ scattering [20.50]. The analysis of the oxygen-induced reconstruction of the Cu{110} surface [20.51] and of the (1×2) reconstruction of the clean Pt{110} surface [20.52] by Na^+ ICISS belongs to the second group of studies. The ICISS method, in which nearly head-on collisions are measured ($\theta > 135^{\circ}$), was introduced originally by *Aono* et al. [20.24] into noble gas LEISS and was very successfully applied in alkali LEISS by *Niehus* and *Comsa* [20.53,54], as will be illustrated below. Only two studies in group (iii) have been reported to date: that of the structure of the oxygen-induced Ni{110} (2×1) phase [20.55] and a detailed computer simulation analysis of the LEISS data of *Overbury* et al. [20.39] on the (1×2) reconstruction of the clean Au{110} surface [20.56]. Only the last two studies will be discussed here briefly as an illustration of the present state of the art.

There are numerous structure proposals for the Au{110}-(1×2) surface which are derived from LEED, X-ray diffraction, high-energy ISS (HEISS) and transmission electron microscopy. Most of them attribute the superstructure to a missing row and differ only in the atomic relaxations. These and another model, the saw tooth model [20.57] are compared in Fig.20.21 with the 600-eV K^+ LEISS data [20.39]. The simulations for the various models were made with a version of the MARLOWE program. The scattering in the plane parallel to the densely packed <110> direction, i.e., in the direction of the missing rows, is nearly equally well described by all models considered, as illustrated for the Robinson model which is based on X-ray diffraction [20.58] (top left in Fig.20.21). Large differences between the various models are seen, however, when the scattering plane crosses the <110> rows. Then LEISS is very sensitive to the displacements of the rows relative to each other. In this manner, not only the saw tooth model [20.57] but also various missing-row models with different relaxations can be excluded: the Robinson model [20.58], the Kuk model derived from HEISS studies [20.59] and the unrelaxed missing-row model. Only the Moritz and Wolf model based on LEED [20.60] in which the distance Δz_1 between the top two planes is contracted is compatible with the LEISS data [20.39]. The best agreement is obtained for $0.21\ \text{Å} < \Delta z_1 < 0.27\ \text{Å}$ (15-23% contraction).

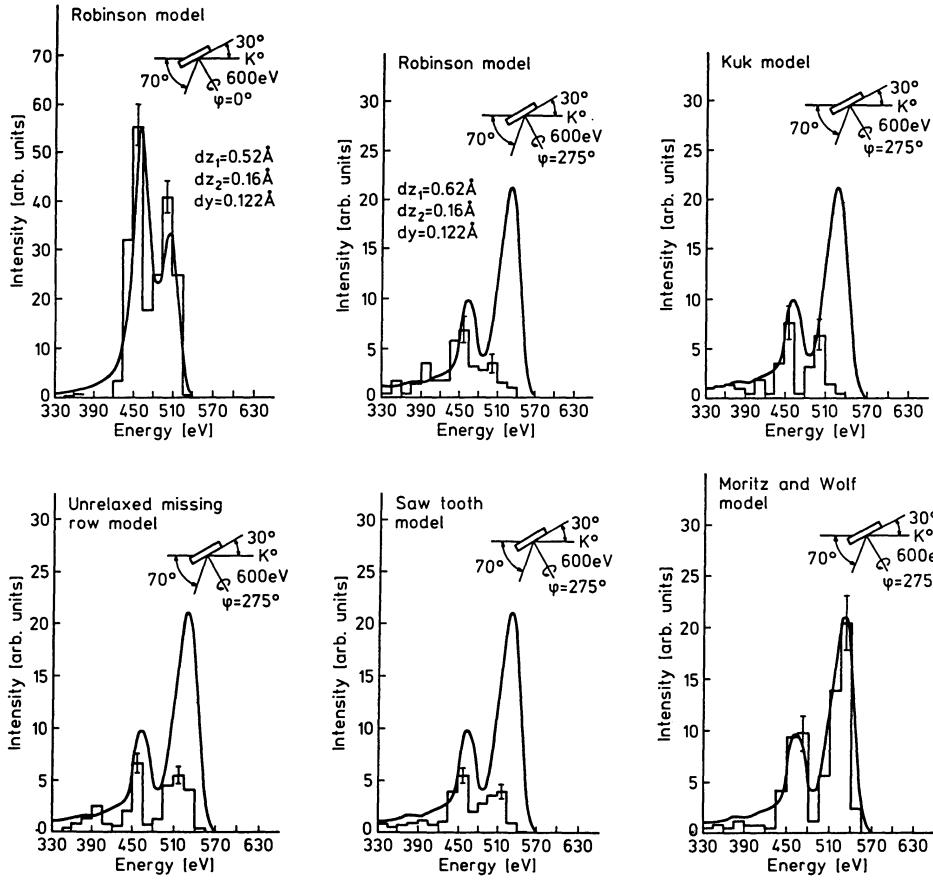

Fig.20.21. Comparison between computer simulations and experiment (continuous curves) for 600-eV K^+ scattering from Au{110} - (1 × 2). *Top left*: <110> azimuth; all others rotated by $\varphi = 27.5°$. For explanation see text [20.56]

A similar clear decision in favor of one of several competing models could be made by alkali ICISS [20.55] in the case of the oxygen-induced Ni{110}-(2 × 1) phase. Again, only the most favored models (saw tooth and missing-row with oxygen in the <001> bridge position, see Fig.20.22) are considered. The single scattering of 2-keV Na^+ ions from Ni atoms into $\theta = 145^\circ$ in the <112> azimuth (left side of Fig.20.22) ($E/E_0 = 0.216$) was measured as a function of the glancing angle of incidence ψ_{in} for the clean surface (1 × 1) (top right) and for the O - (2 × 1) structure (bottom right). The sharp increases of the signal are due to the emergence of atoms (shaded in Fig.20.22) from the shadow cone of the neighboring atom. On the clean surface, the shadow cone radius can be determined. This can then be used to distinguish be-

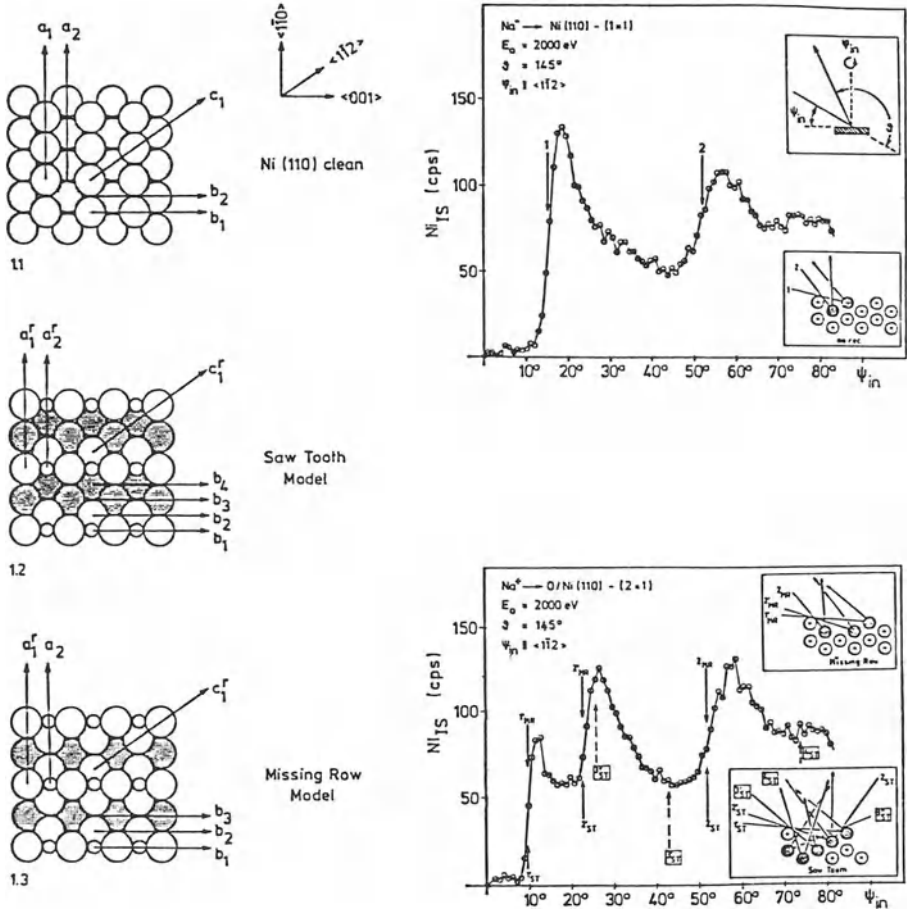

Fig.20.22. Oxygen-induced Ni{110}-(2 × 1) reconstruction. *Left*: structure models; *right*: 2-keV Na^+ ICISS intensity at $E/E_0 = 0.216$ for $\Theta = 145°$ as a function of ψ for clean surface (*top*) and O - (2 × 1) structure (*bottom*). The scattering processes are indicated in the insets [20.55]

tween the two structure models for the reconstructed surface whose spectra differ in a characteristic manner, as can be seen easily in the inserts. The absence of features due to the two deepest atoms in the saw tooth model clearly speaks for the missing-row model which is confirmed by measurements in other azimuths. The position of the O atoms can also be determined because their height h above the Ni atoms has a strong influence on blocking and focusing. A comparison with computer simulations gives the best agreement with experiment for h = 0.25 Å.

20.5 Conclusions and Summary

Structure analysis with alkali LEISS is still a very young field in which only a few researchers are working. Nevertheless, it is already starting to compete with old, established techniques such as LEED and HEISS, as the last two examples show. It can be expected that with increasing effort in this field, alkali LEISS may become the complementary tool to LEED, which was our hope when we started the project: alkali LEISS for the determination of the atomic positions within the unit mesh, LEED for the determination of the size and shape of the unit mesh. There is still a long way to go and many factors still have to be determined, such as the accuracy of the position determination, the quality of simple analysis procedures based on shadow cone constructions, and the usefulness of double scattering versus impact collision scattering experiments.

Alkali LEISS has a great advantage over conventional noble gas LEISS: the low neutralization probability and its trajectory independence. This advantage is large when the work function ϕ of the surface is high, but it may turn into a disadvantage when ϕ decreases below the ionization energy I of the ion. Then the neutralization of alkali ions becomes much more sensitive to ϕ changes than does that of noble gas ions, because of the differences in the neutralization mechanism. A second limitation, which is in principle inherent to both alkali and noble gas ion scattering, is the sample modification by sputtering and implantation. The acquisition of data with sufficient signal/noise ratio usually requires such a large dosage that the sample has to be regenerated several times. This is usually easy on clean surfaces, more tedious with adsorbates, and very cumbersome with systems which can alloy. Although the doses required with alkali ions are smaller than with noble gas ions, alkali atoms implanted near the surface will accumulate at the surface while noble gas atoms desorb.

To sum up, alkali LEISS has great potential as a simple method for surface structure analysis but it may well be quite limited in its range of application.

References

20.1 L.H. Germer, C.D. Hartman: J. Appl. Phys. **31**, 2085 (1960)
20.2 E. Bauer: Phys. Rev. **123**, 1206 (1961); Surf. Sci. **5**, 152 (1966); **7**, 351 (1967)
20.3 J.J. Lander: J. Appl. Phys. **34**, 3517 (1963)
20.4 C.W. Tucker, Jr.: Appl. Phys. Lett. **3**, 98 (1963); J. Appl. Phys. **35**, 1897 (1964)
20.5 E. Bauer: In *Interfacial Aspects of Phase Transformations*, ed. by B. Mutaftschiev (Reidel, Dordrecht 1982) p.1

20.6 D.P. Smith: J. Appl. Phys. **38**, 340 (1967); Surf. Sci. **25**, 171 (1971)
20.7 S.H. Begemann, A.L. Boers: Surf. Sci. **30**, 134 (1971)
20.8 H. Niehus: Ph.D. Thesis, Technische Universität Clausthal (1975)
20.9 H. Niehus, E. Bauer: Rev. Sci. Instrum. **46**, 1275 (1975)
20.10 H. Niehus, E. Bauer: Surf. Sci. **47**, 222 (1975)
20.11 S. Prigge, H. Niehus, E. Bauer: Surf. Sci. **65**, 141 (1977)
20.12 W. Heiland, E. Taglauer: Surf. Sci. **68**, 96 (1977)
20.13 E. Hulpke: Rept. 125, Max-Planck-Inst. Strömungsforschung, Göttingen, June 1973; see also Surf. Sci. **52**, 615 (1975)
20.14 U.A. Arifov: *Interaction of Atomic Particles with the Surface of a Metal*, AEC-tr-6089 (1963); *Interaction of Atomic Particles with a Solid Surface* (Consultants Bureau, New York 1969)
20.15 V.I. Veksler, V.V. Evstifeev: Sov. Phys. Tech. Phys. (Engl. Transl.) **17**, 1178 (1973)
20.16 T. von dem Hagen: Ph.D. Thesis, Technische Universität Clausthal (1982)
20.17 T. von dem Hagen, E. Bauer: Phys. Rev. Lett. **47**, 579 (1981)
20.18 T. von dem Hagen, Y. Hou, E. Bauer: Surf. Sci. **117**, 134 (1982)
20.19 M.T. Robinson: *Tables of Classical Scattering Integral*, ORNL-4556 (Oak Ridge National Laboratory, Oak Ridge 1970)
20.20 H.-J. Beyer: Z. Phys. **267**, 49, 55 (1974)
20.21 A.J. Algra: Ph.D. Thesis, Groningen (1981)
20.22 P. Mahavadi, M. Hou: Private communication
20.23 A.L. Boers: Surf. Sci. **63**, 475 (1977)
20.24 M. Aono, C. Oshima, S. Zaima, S. Otani, Y. Ishizawa: Jpn. J. Appl. Phys. **20**, 829 (1981)
20.25 O.S. Oen: Surf. Sci. **131**, L407 (1983)
20.26 G. Engelmann, E. Taglauer, D.P. Jackson: Surf. Sci. **162**, 921 (1985)
20.27 A. Blandin, A. Nourtier, D.W. Hone: J. Phys. (Paris) **37**, 369 (1976)
20.28 J.K. Nørskov, B.I. Lundquist: Phys. Rev. B**19**, 5661 (1979)
20.29 R. Brako, D.M. Newns: Surf. Sci. **108**, 253 (1981)
20.30 N.D. Lang: Phys. Rev. B**27**, 2019 (1983)
20.31 B.J. Garrison, A.C. Diebold, J..-H. Lin, Z. Sroubek: Surf. Sci. **124**, 461 (1983)
20.32 See also several articles in *Dynamical Processes and Ordering on Solid Surfaces*, ed. by A. Yoshimori, M. Tsukada, Springer Ser. Solid-State Sci., Vol.59 (Springer, Berlin, Heidelberg 1985)
20.33 E.G. Overbosch, B. Rasser, A.D. Tenner, J. Los: Surf. Sci. **92**, 310 (1980)
20.34 A.J. Algra, E. v. Loeven, E.P.Th.M. Suurmeijer, A.L. Boers: Radiat. Eff. **60**, 173 (1982)
20.35 E.G. Overbosch, J. Los: Surf. Sci. **108**, 99 (1981)
20.36 P. Mahavadi: Private communication
20.37 I. Terzić, B. Gončić, D. Ciric, J. Vulkanić: J. Phys. E**10**, 420 (1977)
20.38 E. Taglauer, W. Englert, W. Heiland, D.P. Jackson: Phys. Rev. Lett. **45**, 740 (1980)
20.39 S.H. Overbury, W. Heiland, D.M. Zehner, S. Datz, R.S. Thoe: Surf. Sci. **109**, 239 (1981)
20.40 S.H. Overbury: Surf. Sci. **112**, 23 (1981)
20.41 H. Niehus, E. Preuss: Surf. Sci. **119**, 349 (1982)
20.42 I. Terzić, D. Ciric, B. Perović: Surf. Sci. **85**, 149 (1979)
20.43 S.H. Overbury, P.C. Stair, P.A. Agron: Surf. Sci. **125**, 377 (1983)
20.44 E. Hulpke, K. Mann: Surf. Sci. **133**, 171 (1983)
20.45 S.H. Overbury, P.C. Stair: J. Vac. Sci. Technol. A**1**, 1055 (1983)
20.46 S.H. Overbury, B.M. DeKoven, P.C. Stair: Nucl. Instrum. Methods Phys. Rev. B**2**, 384 (1984)
20.47 S.H. Overbury: Nucl. Instrum. Methods Phys. Res. B**2**, 448 (1984)
20.48 B.M. DeKoven, S.H. Overbury, P.C. Stair: Phys. Rev. Lett. **53**, 481 (1984)

20.49 B.M. DeKoven, S.H. Overbury, P.C. Stair: J. Vac. Sci. Technol. A**3**, 1640 (1985)
20.50 W. Englert, E. Taglauer, W. Heiland: Nucl. Instrum. Methods **194**, 663 (1982)
20.51 H. Niehus, G. Comsa: Surf. Sci. **140**, 18 (1984)
20.52 H. Niehus: Surf. Sci. **145**, 407 (1984)
20.53 H. Niehus: Nucl. Instrum. Methods Phys. Res. **218**, 230 (1983)
20.54 H. Niehus, G. Comsa: Surf. Sci. **152/153**, 93 (1985)
20.55 H. Niehus, G. Comsa: Surf. Sci. **151**, L171 (1985)
20.56 H. Hemme, W. Heiland: Nucl. Instrum. Methods Phys. Res. B**9**, 41 (1985)
20.57 H.P. Bonzel, S. Ferrer: Surf. Sci. **118**, L263 (1982)
20.58 I.K. Robinson: Phys. Lett. **50**, 1000 (1983)
20.59 Y. Kuk, L.C. Feldman, I.K. Robinson: Surf. Sci. **138**, L168 (1984)
20.60 W. Moritz, D. Wolf: Surf. Sci. **77**, L29 (1979)

21. Multilayer Adsorption and Wetting Phenomena

C. Ebner

Department of Physics, Ohio State University, Columbus, OH 43210, USA

In this chapter, phenomena arising in multilayer physisorbed films are described; these include complete and incomplete wetting behavior, first-order and critical wetting transitions in liquid and solid films, prewetting, layering, and triple-point wetting. We review continuum and lattice models of multilayer adsorption in Sect.21.2, with emphasis on the latter, and present several applications of the Ising and Potts lattice-gas models to fluid and solid adsorption in Sect.21.3. The particular case of wetting in the presence of long-range Van der Waals forces is discussed at some length. Finally (in Sect.21.4) we consider current trends in research on multilayer adsorbed films.

21.1 Introduction to Wetting and Layering Behaviors

If an attempt is made to coat a substrate γ with a given material α, under an atmosphere β with which α coexists, then from a macroscopic point of view one of two things can happen. Either the α phase will form droplets or islands on the substrate as in Fig.21.1a, or it will spread uniformly along the substrate, forming a macroscopically thick film as in Fig.21.1b. In the former case one says that α does not wet or incompletely wets the substrate, and in the latter, that it wets or completely wets it. Such phenomena are

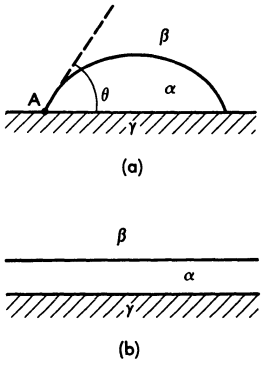

Fig.21.1. Incomplete (**a**) and complete (**b**) wetting configurations. In (**a**) the droplet of phase α meets the substrate γ at point A with a finite contact angle Θ

well known in binary or multicomponent mixtures with α and β being two immiscible fluid phases and γ, a container wall or even the vapor phase of the mixture. However, they are by no means limited to these systems. For example, α and β could be liquid and gas phases of a one-component system and γ, a solid substrate; or β and γ could be crystallites of a given material with two distinct orientations meeting at a grain boundary, while α is the coexisting liquid phase of the same material.

Figure 21.1a is representative of the first of these two possibilities in the case of nonwetting behavior. Notice that there is a finite contact angle θ $(0 < \theta < \pi)$, at A where the three phases meet. This angle is determined by the condition of mechanical equilibrium of A and depends on the various interfacial surface tensions or excess grand free energies per unit area of interface. If $\sigma_{\mu\nu}$ denotes the surface tension between phases μ and ν, the equilibrium condition gives immediately

$$\sigma_{\beta\gamma} = \sigma_{\alpha\gamma} + \sigma_{\alpha\beta}\cos\theta \quad , \tag{21.1}$$

which is known as Young's condition [21.1]. For it to make sense, the surface tensions must satisfy the inequality $-1 \leqslant D \leqslant 1$, where $D \equiv (\sigma_{\beta\gamma}-\sigma_{\alpha\gamma})/\sigma_{\alpha\beta}$. Should $|D|$ exceed unity, the configuration portrayed in Fig.21.1a is not possible; complete wetting must occur. Consider first that $D > 1$ or $\sigma_{\beta\gamma} > \sigma_{\alpha\beta} + \sigma_{\alpha\gamma}$. Then it is thermodynamically favorable to have a macroscopic layer of α interposed between β and γ, as in Fig.21.1b, so that a given length of β-γ interface is replaced by two equal lengths of α-β and α-γ interfaces. For $D < -1$ the same picture is applicable but with a layer of β between α and γ which is just the wetting of γ by β beneath an "atmosphere" of α.

Although complete and incomplete wetting behaviors have been recognized for a long time, it was realized [21.2,3] only in 1977 that there can be a phase transition, called a wetting transition [21.4-7], from one to the other as some appropriate thermodynamic parameter, usually the temperature or the concentration of a chemical component of the system, is varied. In terms of the surface tensions, the transition will take place when D crosses the value +1 or the value -1. The latter has been termed [21.8] a "drying transition", as the phase α loses contact with the substrate at this point. However, as explained above, it is not distinct from a wetting transition with the roles of α and β interchanged. The terminology presumably stems from the fact that the simplest wetting system is visualized as having a liquid film (α) on the substrate beneath a bulk vapor (β) of the same material; the phenomenon of drying for this system is to have a layer of vapor come between the substrate and the liquid.

Cahn [21.3] invented a version of the following argument[1] [21.8] to demonstrate the existence of wetting transitions. Suppose that α and β are coexisting liquid and vapor phases of a simple material with a liquid-vapor critical temperature T_c and that γ is an appropriately chosen substrate giving nonwetting behavior, i.e., $|D| < 1$, at some temperature $T < T_c$. From this starting point we want to consider the behavior of $|D|$ as T approaches T_c. Both $\sigma_{\alpha\beta}$ and $|\sigma_{\alpha\gamma} - \sigma_{\beta\gamma}|$ vanish at T_c. For $T \to T_c$, $\sigma_{\alpha\beta} \sim |T_c - T|^b$ and, assuming an inert substrate, one expects $|\sigma_{\beta\gamma} - \sigma_{\alpha\gamma}| \sim |n_\beta - n_\alpha| \sim |T_c - T|^\beta$, where n_β and n_α are the densities of the bulk β and α phases and the critical exponents b and β are roughly 1.3 and 0.3. (More correctly, n_α and n_β should be the densities of the α and β phases close to the substrate and the exponent should be the surface order parameter $\beta_1 \simeq 0.8$ [21.8].) Thus, $|D| \sim |T_c - T|^{\beta - b}$, which diverges as $T \to T_c$, showing that $|D| > 1$ for T sufficiently close to T_c, i.e., a wetting transition must take place. This has been referred to as critical-point wetting and should not be confused with critical wetting which refers to a continuous or critical wetting transition, as opposed to a first-order transition.

Let us examine these phenomena from a somewhat different point of view. Once again we imagine a planar, inert substrate γ beneath a bulk phase β of the adsorbate material which, for simplicity, we take to be the gas phase of a single chemical species. The system is "open" in that we control T and the chemical potential μ (or, equivalently, the pressure p) of the adsorbate. The question to ask is whether in thermodynamic equilibrium a film will form on the substrate and become a macroscopic liquid or solid bulk phase α if T and μ change in such a way as to approach the α-β coexistence line starting from a region of stable β. The conditions we have in mind are easily visualized using Fig.21.2 which is a T-μ phase diagram displaying regions of

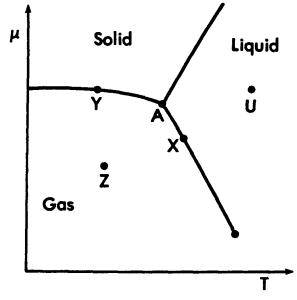

Fig.21.2. Phase diagram of a simple material in T - μ space

1 This argument can be made much more elaborate. See, for example, [21.6] and references therein.

stable gas, liquid, and solid; coexistence lines for pairs of these; a triple point A; and a liquid-gas critical point C. Starting from a point such as Z in the domain of stable gas, we may imagine changing T and μ so as to move to point Y on the gas-solid line or to X on the liquid-gas line. If a thick solid or liquid film forms beneath the gas at Y or X, respectively, then we have complete wetting, otherwise we have incomplete wetting. Notice that the latter does not produce the type of behavior depicted in Fig.21.1a as that is not a thermodynamically stable configuration in an open system. Rather, one finds at most a few adsorbed molecular layers of material resembling a liquid or solid.

If there is not wetting (i.e., no complete wetting) at X, then as one moves from X toward C along the liquid-gas line, Cahn's argument [21.3] predicts that a wetting transition will take place—unless, of course, D passes through -1 and goes off to $-\infty$. In this case, if we start with bulk liquid above the substrate at point U, say, and go first to X and then along the line toward C, a drying transition should occur when D crosses -1.

The behavior that takes place along the gas-solid line can be quite different. If there is incomplete wetting at Y, i.e., no thick solid film forms, then such a film could still appear somewhere between Y and A. If it does not, another sort of wetting may take place [21.9]. Specifically, the thickness of the adsorbed film can grow as A is approached and become a macroscopically thick liquid film at A. This phenomenon has become known as triple-point wetting. Even if the solid does wet the substrate at some $T < T_3$, the triple-point temperature, it may melt below T_3 and so allow triple-point wetting to occur.

If there is a wetting transition at some temperature T_w, then one may ask whether it is continuous or critical, with the coverage Γ diverging continuously as T_w is approached, or whether it is first order with Γ jumping from a finite to an infinite value at T_w. By coverage, we mean the excess surface density,

$$\Gamma \equiv \int dz[n(z) - n_\beta] \quad , \tag{21.2}$$

where n(z) is the adsorbate number density as a function of the distance z from the substrate and n_β is the density of the bulk β phase. In the case of densities which vary in directions lateral to the substrate surface, n(z) is an average of $n(\mathbf{r})$ over the lateral directions.

The original predictions [21.2,3] were of first-order wetting transitions; continuous transitions were first predicted by *Sullivan* [21.10]. Figure 21.3a shows schematically the adsorption phase diagram for a continuous wetting transition at W, while Fig.21.3b shows the diagram for a first-order transi-

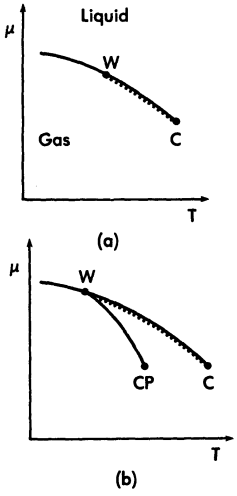

Fig.21.3. Wetting phase diagrams for (**a**) a continuous and (**b**) a first-order wetting transition. The wetting transitions are at *W* on the bulk liquid-gas (or α-β) coexistence line. In case (**b**), *W-CP* is a line of prewetting transitions. In both cases there is wetting (...) along the bulk coexistence line from *W* to the critical point *C*

tion. In the latter, there is a line of first-order "prewetting" transitions [21.2,3] in the domain of stable gas. One end of this line is at W, while the other is a critical point. The prewetting transition is marked by a finite discontinuity in Γ which vanishes as the prewetting critical point CP is approached and which diverges continuously as W is approached [21.2,3]. The prewetting line meets the bulk line tangentially [21.11].

The prewetting transition should not be confused with layering transitions which are found in solid adsorbed films and possibly in the first few layers of liquid films. In Fig.21.4, we show schematically several possible adsorption phase diagrams for a solid film. Given complete wetting at all

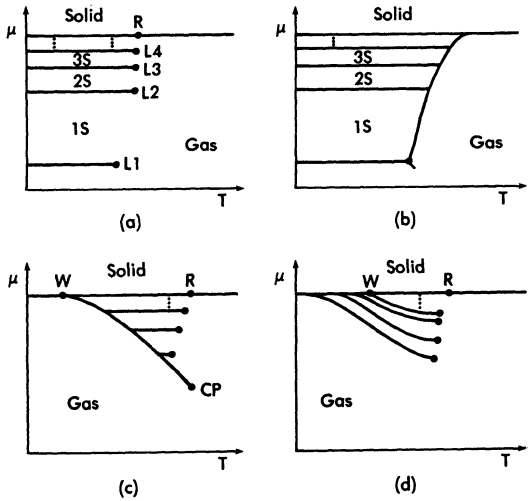

Fig.21.4. Solid adsorption showing (**a** and **b**) complete wetting at all temperatures, (**c**) a first-order wetting transition, and (**d**) a continuous wetting transition. In all cases there may be infinite sequences of layering transitions Ln (n = 1, 2, 3, ...), separating solid films of n - 1 and n layers, nS (n = 1, 2, 3, ...)

temperatures, there may be a set of first-order layering transitions as shown in Fig.21.4a terminating at critical points Ln (n = 1,2,3,...). Each such transition is accompanied by the addition of approximately one molecular layer to the film. If there is complete wetting, there can be an infinite sequence of layering transitions as gas-solid coexistence is approached. This sequence was first studied by *de Oliveira* and *Griffiths* [21.12] using an Ising lattice-gas model and a mean-field approximation. In this approximation, the critical temperatures T_{cn} of the transitions increase with n, apparently approaching the bulk critical temperature as $n \to \infty$. De Oliveira and Griffiths conjectured, however, that T_{cn} should approach the roughening temperature T_R of the facet of the crystal normal to that to which the layers are being added. Subsequent Monte Carlo studies of the Ising lattice gas [21.13,14] verified this assertion, as have variational [21.15] and renormalization group [21.16,17] studies of the solid-on-solid model.

More generally, other mechanisms can be responsible for terminating the lines of layering transitions. For example, the film may undergo first-order melting before it roughens, as in Fig.21.4b, so that the lines end at triple points [21.9,18]. Figure 21.4c shows the layering transitions if there is first-order wetting at $T_w < T_R$ with a prewetting line W-CP. In this situation, the layering lines terminate on the prewetting line, which in general prevents them from extending to T = 0. If there is instead continuous wetting at T_w, the layering lines will appear as in Fig.21.4d, accumulating at $T_w^{(-)}$ on the gas-solid line.

The layering transitions may show a variety of configurations [21.8,18], more complicated than those in Fig.21.4. For example, they may branch, with one line (corresponding to the addition of two or more layers) splitting into two or more lines. In the case of lattice models, one may perform an exact T = 0 analysis and so determine in this limit the manner in which the configuration of lines depends on the various interactions in the systems.

Generally speaking, the qualitative features of the adsorption phase diagram are determined by the relative properties of the interaction between adsorbate and substrate particles and the interaction between adsorbate particles. The most important properties are the relative strength and the relative range of the attractive parts of the interactions with the short-range parts of the interactions playing a secondary role. In the following discussion we shall once again focus on the simplest case, an adsorbate composed of a single chemical species. Let v_{aa} be the pair potential of two adatoms or molecules while v_{as} is the interaction between an adatom and a building block of the substrate. Then the basic rules governing wetting by

the liquid phase are as follows: If v_{as} is sufficiently attractive in comparison with v_{aa}, the "strong" substrate regime, there is wetting of the substrate by the liquid phase of the adsorbate at all T. For somewhat weaker v_{as}, there is an "intermediate" substrate regime in which incomplete wetting takes place below some T_w while there is complete wetting above T_w, i.e., there is a wetting transition. Finally, for sufficiently weakly attractive v_{as} in comparison with v_{aa}, there is incomplete wetting by the liquid at any T. This is the "weak" substrate regime; in this case, drying or a drying transition is expected.

The conditions for wetting by the solid phase are somewhat different. Starting from the weak substrate regime and gradually increasing the strength of v_{as}, there are again incomplete and complete wetting regimes, but at still stronger v_{as} there is a return to incomplete wetting. A systematic description of this overall behavior has been given by *Pandit* and co-workers [21.8], except for the reentrant nonwetting behavior exhibited by solid films on strong substrates. This feature was pointed out by *Seguin* et al. [21.19] and explained [21.19-24] in terms of distortions of the solid film near the substrate, the resulting strain energy being sufficient to prevent wetting.

The order of the wetting transition is determined primarily by the relative range of v_{as} and v_{aa}. Roughly, if the range of v_{as} is greater than that of v_{aa}, the transition is first-order and if the opposite is true, it is continuous. If both potentials fall off about equally rapidly at large distances, then a wetting transition may be first-order or continuous depending on other parameters in the system [21.25]. A particular example, which has been studied in some detail [21.10,11,26-28], is the exponential potential $v \sim \exp(-r/r_0)$, where the ranges r_0 of v_{as} and v_{aa} can differ.

A special case of considerable recent interest [21.5,11,17,26,27,29-39], and some controversy, is the physically important one of potentials which vary at large distances as an inverse power of r, $v \sim r^{-n}$, n = 6 being the Van der Waals potential (at not-too-large distances). The picture that appears to have emerged is that if v_{aa} and v_{as} both vary as r^{-6} at large r, then there can be a wetting transition, and it may be either first-order or continuous depending on other features of the potentials, especially their behavior at small distances. Further, if potential parameters are varied in such a way as to cause the transition to change from first-order to continuous, at the crossover it may be either tricritical or tetracritical [21.38,39]. The behavior is similar to, but distinct from, what is found for short-range interactions [21.40]. This topic will be covered in more detail in Sect.21.3.

Regarding experiments, the benchmark observation of a wetting transition was made by *Moldover* and *Cahn* [21.41] in a liquid mixture of methanol and cyclohexane below the consolute point, the two liquid phases playing the roles of phases α and β. The substrate was the vapor phase above the liquid, and the transition was produced by varying the concentration of a third component, water. There have since been observations of wetting transitions in several other liquid mixtures [21.42-44]. Although all of these transitions appear to be first-order, no prewetting transitions in fluids were seen. Very recently one was reported [21.45] in a mixture of 2,6-lutidine and H_2O against Pyrex glass. As for a wetting transition involving an adsorbed solid, *Carmi* et al. [21.46] have recently reported first-order wetting by ^{4}He on gold-plated beryllium-copper when the hexagonal crystal grows with the $\langle 10\bar{1}0\rangle$ direction normal to the substrate, and continuous wetting when the normal is in the <0001> direction. First-order wetting has also been reported [21.47,48] for CF_4 on graphite. Triple-point wetting has been seen in a number of simple systems [21.49] such as ethylene on graphite [21.50-52]. Layering transitions in adsorbed, multilayer solid films are also well documented [21.53-61]. The work reported in [21.61] is particularly significant in that enough layering transitions (seven) were observed to be reasonably certain that the corresponding critical temperatures were approaching the roughening temperature in qualitatively the manner expected theoretically [21.13,16,17]. The experimental system was a solid ^{4}He film on graphite beneath bulk liquid.

21.2 Theoretical Approaches

A variety of theoretical models and techniques have been employed to expose the essential features of multilayer adsorption and wetting. On the one hand are lattice models such as the Ising lattice gas, the Potts lattice gas, and the solid-on-solid (SOS) models. These have been most often treated in a simple mean-field approximation but have also been studied using Monte Carlo simulations and renormalization group methods. On the other hand are continuum models. The starting point in this case is, generally, an expression for the grand free energy Ω of the system as a functional of the adsorbate particle number density $n(\mathbf{r})$ (or some appropriate generalization in the case of systems with more than one chemical constituent or systems with orientational molecular degrees of freedom) and then the determination of the particular density which minimizes $\Omega[n(\mathbf{r})]$.

The continuum models are most obviously applicable to fluid adsorption where the density does not vary with position as dramatically as in a solid and where there are presumably no layering transitions, except possibly close to the substrate. The lattice models complement the continuum ones as they possess roughening and layering transitions and are most obviously applicable to solid adsorption. However, the Ising and Potts lattice gases both possess a critical point terminating a line of first-order transitions reminiscent of a liquid-gas coexistence line. The Potts lattice-gas model is without doubt the most realistic for a simple system such as a classical rare gas; it can be designed [21.9] to have a bulk phase diagram with three phases, a triple point, and "liquid-gas" critical point, as in Fig.21.2.

Continuum and lattice models are by no means unrelated. By taking the continuum limit of a simple lattice model, such as the Ising lattice gas with short-range interactions, one may generate [21.6,25,40] what amounts to a Landau theory for adsorption phenomena, applicable in the case of slowly varying adsorbate density. A somewhat different Landau theory may be produced in like manner in the case of longer-range interactions [21.36-39].

There are a variety of other continuum models which are similar in spirit to the Landau theory but which can be considerably more complex and more broadly applicable, i.e., valid for a greater range of phenomena. The first explicit calculations [21.2,3] of wetting transitions were based on such theories. In one case [21.2], an approximate version of an exact density functional formalism [21.62] was employed. This particular version may be generated by expanding Ω for a nonuniform system in powers of the deviation of the density from that in a uniform system and truncating at the second-order term. As the second variational derivative $\delta^2\Omega/\delta n(\mathbf{r})\delta n(\mathbf{r}')$ is essentially the direct correlation function $c(\mathbf{r},\mathbf{r}';n)$, the eventual expression for Ω is couched in terms of this function; specifically,

$$\Omega[n] = \int d^3r[f(n(\mathbf{r})) + V(\mathbf{r}) - \mu]n(\mathbf{r}) + \frac{1}{4} k_B T \int d^3r d^3r' \times c(\mathbf{r},\mathbf{r}';\bar{n})[n(\mathbf{r}) - n(\mathbf{r}')]^2 \quad , \tag{21.3}$$

where $V(\mathbf{r})$ is the substrate potential, $f(n)$ the Helmholtz free energy of a uniform system (which was obtained from c), and k_B the Boltzmann constant. In this approximate functional, c is the correlation function at uniform density $\bar{n}$ in the vicinity of $\mathbf{r}$ and $\mathbf{r}'$. The accuracy of this method turns upon two points [21.63], one being the replacement of the exact functional by (21.3) and the other being the choice of c (solutions of the Percus-Yevick equation).

Cahn's original paper on wetting transitions [21.3] also made use of an expression for the grand free energy as a functional of the density in the spirit of Landau theory. Probably the most widely used continuum model for wetting is a modern version of Van der Waal's theory. Developed by a number of workers (see [21.64] and, for example, the discussion in [21.6] for applications to multilayer adsorption), the basic idea is to decompose v_{aa} somewhat arbitrarily into a short-range repulsive piece $v_{aa}^{(s)}$, nominally taken as a hard-sphere interaction, and a longer-ranged attractive piece $v_{aa}^{(a)}$, and then to write the free energy functional as

$$\Omega[n] = \int d^3r\{f^{(s)}(n(\mathbf{r})) + [V(\mathbf{r}) - \mu]n(\mathbf{r})\}$$
$$+ \frac{1}{2}\int d^3r d^3r' n(\mathbf{r}) v_{aa}^{(a)}(\mathbf{r} - \mathbf{r}')n(\mathbf{r}') \quad , \tag{21.4}$$

where $f^{(s)}(n)$ is the Helmholtz free energy of a uniform reference system in which particles interact only via $v_{aa}^{(s)}$.

De Oliveira and *Griffiths* [21.12] introduced an Ising lattice-gas model with nearest-neighbor interactions v_{aa} in a mean-field study of layering transitions. The substrate interaction v_{as} was taken to be of the Van der Waals form, $v_{as} \sim r^{-6}$, at large distances. Subsequently, the model was used to produce a wetting transition [21.65]. Various versions of the model have since been employed to investigate multilayer adsorption [21,6,8,13,14,20, 24,25,37-39].

The Potts lattice-gas model of adsorption, introduced by *Berker* et al. [21.66] to study monolayer adsorption, was first applied to multilayer adsorption to study solid films, layering, melting, and triple-point wetting with nearest-neighbor interactions v_{aa} using both mean-field and Monte Carlo analyses [21.9]. Recently, a more systematic mean-field study of these phenomena in the presence of Van der Weals forces has been carried out [21.67]. The SOS model has been employed in studies [21.15-17, 31,68] of layering transitions as well as of the wetting transition itself. A bewildering collection of variations on the lattice and continuum model themes outlined above have been introduced to study different aspects of multilayer adsorption. The reader is encouraged to consult [21.5-7] as well as the review articles by *Binder* [21.69], *Jasnow* [21.70], and *Wortis* [21.71].

We present next a quantitative introduction to the simple lattice-gas models. Let the substrate occupy the space $z \leqslant 0$ and let there be a regular lattice of points at sites $\mathbf{r}_{ki}$ with $z > 0$. The subscript $k = 1,2,\ldots$ identifies a layer of points at a distance $z_k = ka$ from the substrate and i identifies a site within a given layer. For simplicity we shall suppose that the lat-

tice is simple cubic[2] and that a given site is either occupied by a single particle or empty. Further, a particle may occupy any of q states at each site. For the Ising and SOS models, $q = 1$, for the Potts models, $q > 1$. There is an energy of interaction $w_{pp'}(ki;k'i')$ between particles in states p and p' at sites ki and k'i'. For the Potts model, $w_{pp'}$ is of the form $A + B\delta_{pp'}$. i.e., the interaction is enhanced if $p = p'$ and is otherwise independent of p and p'. For the Ising and SOS models, $p = p' = 1$ always, and so may be ignored. The SOS model is the extreme anisotropic version of the Ising model in which $w(k,i;k+1,i) \to -\infty$ so that "overhangs" and vacancies will not occur. In general, $w_{pp'}$ is chosen to represent some particular v_{aa}.

There is also an interaction $V_p(ki)$ between an adatom in state p at site ki and the substrate. This is generally taken to be independent of i and of p, although an interaction depending on p is of interest in the case of a substrate with lateral variation that happens to be commensurate with the adsorbate crystal structure [21.67]. The interaction $V_p(ki)$ represents v_{as} summed over the entire substrate. It is useful to introduce

$$w_{pp'}(k - k') \equiv \sum_{i'} w_{pp'}(ki;k'i') \quad , \tag{21.5}$$

which is the interaction between an adsorbate atom in state p with a layer of adsorbate atoms in state p' and $|k - k'|$ layers away. The term $i' = i$ is omitted if $k = k'$. Further, define

$$W_{pp'}(k) = \sum_{k'=0}^{\infty} w_{pp'}(|k| + k') \quad ; \tag{21.6}$$

$W_{pp'}(k)$ is the interaction energy of a particle in state p with a "substrate" $|k|$ layers away of adatoms in state p', and it is the natural analogue of $V_p(k)$. The relative properties of these functions determine the nature of the multilayer adsorption phenomena.

We now make a mean-field approximation (MFA) in which the average occupation of state p at site ki is taken to be $n_p(k)$, independent of i. (This procedure will miss any lateral ordering that may otherwise take place, such as epitaxial ordering. See [21.20] for a treatment of epitaxial ordering in the Ising lattice gas.) Then, using standard procedures [21.39], one arrives at the mean-field free energy per unit area of substrate,

---

2 Both simple cubic and fcc lattices have been used extensively in actual calculations.

$$\Omega[n] = \frac{1}{2} \sum_{\substack{p,p' \\ k,k'}} w_{pp'}(k - k')n_p(k)n_{p'}(k') \tag{21.7}$$

$$+ \sum_{p,k} [V_p(k) - \mu]n_p(k)$$

$$+ k_B T \sum_k \left\{ \sum_p n_p(k) \ln n_p(k) + \left[1 - \sum_p n_p(k)\right] \ln \left[1 - \sum_p n_p(k)\right] \right\} .$$

The mean-field equations are obtained from the extremum conditions $\partial\Omega/\partial n_p(k) = 0$ and are

$$\sum_{k'p'} w_{pp'}(k - k')n_{p'}(k') + V_p(k) - \mu + k_B T \ln \left(\frac{n_p(k)}{1 - \sum_{p'} n_{p'}(k)} \right) . \tag{21.8}$$

These may be put into another form, more convenient for numerical solution,

$$n_p(k) = \exp[-\beta A_p(k)] / \left\{ 1 + \sum_{p'} \exp[-\beta A_{p'}(k)] \right\} \quad \text{where} \tag{21.9}$$

$$A_p(k) = \sum_{k'p'} w_{pp'}(k - k')n_{p'}(k') + V_p(k) - \mu \quad . \tag{21.10}$$

A simple method of solution is to start from some reasonable set of densities $n_p(k)$, use (21.10) to formulate $A_p(k)$, then use (21.9) to get a new set of densities, and repeat these steps until convergence is obtained. In some cases this procedure works quite well but in others convergence is slow, at best. Then, more sophisticated methods are preferable; a particularly good one was introduced by *Ng* [21.72] in solving the hypernetted chain equation.

Often, for given potentials, μ, and T, there is more than one solution to the mean-field equations, corresponding to different relative minima[3] of Ω. The particular one found is determined by the initial densities $n_p(k)$ and by the method of solution. To determine which solution corresponds to the stable state, one must evaluate $\Omega[n]$.

The bulk mean-field equations may be obtained by setting $V_p(k) = 0$ and letting k and k' range from $-\infty$ to ∞. Assuming $n_p(k)$ is independent of k, one finds

$$n_p = \exp(-\beta A_p) / \left[1 + \sum_{p'} \exp(-\beta A_{p'}) \right] \tag{21.11}$$

$$A_p = \sum_{p'} [w_{pp'}(0) + 2W_{pp'}(1)]n_{p'} - \mu \quad . \tag{21.12}$$

---

3 Occasionally, one finds a solution which is a relative maximum of Ω.

In the particular case of the Ising lattice gas, the bulk phase diagram consists of a line of first-order transitions at $\mu = \mu_0 = W(1) + w_0/2$ extending from $T = 0$ to $T_c = -\mu_0/2k_B$, assuming predominantly attractive interactions so that $\mu_0 < 0$. The stable bulk density n_b is the solution of

$$n_b = \{\exp[\beta(2\mu_0 n_b - \mu)] + 1\}^{-1} \tag{21.13}$$

that minimizes the free energy per site

$$\Omega_b = n_b^2\mu_0 - n_b\mu + k_BT[n_b \ln n_b + (1 - n_b)\ln(1 - n_b)] \quad . \tag{21.14}$$

For $T < T_c$, the stable phase at $\mu < \mu_0$ has $n_b < 1/2$ and is generally interpreted as a gas phase; at $\mu > \mu_0$, the stable phase has $n_b > 1/2$ and is variously interpreted as liquid or solid, depending on the application.

For the Potts lattice gas, the couplings $w_{pp'}(k)$ between particles in the same state, $p = p'$, are taken to be more attractive than those between particles in different states. The "liquid" and "gas" phases are such that all n_p are equal, $n_p = n'$ and the total density is $n_b = qn'$, where q is the number of Potts states at a site. The "solid" phase is such that all n_p are equal except for one, say n_1, which is larger than the others. In the particular case of the bulk fluid states, the mean-field equation is

$$n_b = \{\exp[\beta(2\mu_0' n_b - \mu')] + 1\}^{-1} \tag{21.15}$$

where

$$\mu_0' = \frac{1}{q}\sum_{p'}\left[\frac{1}{2}w_{pp'}(0) + W_{pp'}(1)\right] \quad \text{and} \tag{21.16}$$

$$\mu' = \mu + k_BT \ln q \quad . \tag{21.17}$$

Similarly, the grand free energy per site for a bulk fluid state is

$$\Omega_b = n_b^2\mu_0' - \mu' n_b + k_BT[n_b \ln n_b + (1 - n_b)\ln(1 - n_b)] \quad . \tag{21.18}$$

Comparison of these equations with the analogous ones for the Ising lattice gas demonstrates that, in the MFA, the Potts model produces a liquid-gas coexistence curve given by

$$\mu = \mu_0' - k_BT \ln q \quad , \tag{21.19}$$

with a critical point at $T_c = -\mu_0'/2k_B$, and

$$\mu_c = \mu_0'\left(1 - \frac{1}{2}\ln q\right) \quad .$$

Thus we find that insofar as fluid phases are concerned, the Potts model

predicts the same bulk phenomena in the MFA as the Ising model. Similarly, if the substrate potential $V_p(k)$ is independent of p, both models will produce identical adsorption phenomena for fluids. The Potts model is, therefore, an improvement upon the Ising lattice gas in the MFA only if solid phases of the adsorbate—either in the bulk or in the film—play a role, or if one wishes to use a substrate potential which can distinguish between different Potts states at a site, for example, in an attempt to model lateral variation of the substrate.

21.3 Applications

21.3.1 Importance of Relative Potential Strengths and Ranges

We shall look first at the connection between potential strengths and wetting. It is sufficient and simplest to employ the Ising model, beginning at T = 0, where an exact solution may be obtained from the mean-field equations. Dropping all subscripts and sums over p and p', we have, from (21.7),

$$\Omega_0(\ell) = \frac{1}{2} \sum_{k,k'=1}^{\ell} w(k - k') + \sum_{k=1}^{\ell} [V(k) - \mu] \quad , \tag{21.20}$$

given an ℓ-layer film (i.e., $n(k) = 1$, $k = 1,2,\ldots\ell$ and $n(k) = 0$, $k > \ell$) at T = 0. Equation (21.20) may also be written as

$$\Omega_0(\ell) = \sum_{k=1}^{\ell} [V(k) - W(k) - \Delta\mu] \quad , \tag{21.21}$$

with $\Delta\mu = \mu - \mu_0$. The thickness ℓ_0 of the stable film is that value of ℓ for which Ω_0 is minimized. Note that $\Omega(0) = 0$, so a stable film of nonzero thickness must have $\Omega(\ell_0) < 0$, at the very least. The question of wetting deals with the case of $\Delta\mu = 0$, i.e., bulk coexistence. Clearly, if $V(k) < W(k)$ for all k, then the minimum of $\Omega(\ell)$ is for $\ell_0 \to \infty$, i.e., complete wetting. This is the strong substrate regime. [Remember that V(k) and W(k) are negative, at least for $k \geq 1$, and so the strong substrate regime has $|V(k)| > |W(k)|$.] However, if $V(k) > W(k)$ for all except some finite number of k's, then ℓ_0 will be strictly finite and we have incomplete wetting at T = 0. If W(k) is not far below V(k), there may still be complete wetting at higher temperatures (Sect.21.3.1) and, therefore, a wetting transition somewhere between; this is the intermediate substrate regime. For W(k) well below V(k), incomplete wetting is expected at all temperatures. For the specific case of Van der Waals forces, $W(k) \sim V(k) \sim 1/k^3$ at large k. Hence, if we write

$$W(k) = -\frac{J}{k^3}\left(1 + \frac{\gamma_{w4}}{k} + \frac{\gamma_{w5}}{k^2} + \ldots\right) \quad , \tag{21.22}$$

$$V(k) = -\frac{RJ}{k^3}\left(1 + \frac{\gamma_{v4}}{k} + \frac{\gamma_{v5}}{k^2} + \ldots\right) \quad , \tag{21.23}$$

where γ_{wm} and γ_{vm} are constants, as are R and J, then complete wetting at T = 0 requires

$$\sum_{k=\ell}^{\infty}\left(\frac{(R-1)}{k^3} + \frac{R\gamma_{v4} - \gamma_{w4}}{k^4} + \frac{R\gamma_{v5} - \gamma_{w5}}{k^5} + \ldots\right) > 0 \quad , \tag{21.24}$$

for all $\ell > 0$. If the γ's are small or balance well, in the sense that $|R\gamma_{vm} - \gamma_{wm}|$ is small, then for some $R > 1$ the inequalities are likely to be satisfied. This is then the strong substrate regime, while smaller R's are the regime of intermediate or weak substrates.

Equation (21.21) also provides insight into the behavior of the layering transitions at T = 0. Let us suppose that $V(k) < W(k)$ for all k (strong substrate regime) and that $W(k) - V(k)$ is a monotonically decreasing function of k. Then the extremum condition on $\Omega(\ell)$ for a stable film tells us that layers are added one at a time as $\Delta\mu$ rises toward zero, the k^{th} layer being added at

$$\Delta\mu_k = V(k) - W(k) \quad . \tag{21.25}$$

Other sequences of layering transitions can occur if $W(k) - V(k)$ is not monotonic.

The behavior at finite T may be inferred from a variety of approximate treatments without solving the full MFA. One standard procedure [21.36-39, 73] (which is often called the "slab" approximation, see [21.73], for example) is to assume that n(k) is adequately represented by a step function.

$$n_s(k) = \begin{cases} n_\alpha \ , & k \leq \ell \\ n_\beta \ , & k > \ell \end{cases} \tag{21.26}$$

where n_α and n_β are suitably chosen to represent the bulk liquid and gas, respectively. For example, they could be the bulk mean-field densities found by solving (21.13). For such a density profile, the free energy is

$$\Delta\Omega_s(\ell) = (n_\alpha - n_\beta)\sum_{k=1}^{\ell}\left[V(k) - n_\alpha W(k) - \Delta\mu\right] \quad , \tag{21.27}$$

where $\Delta\Omega_s(\ell) = \Omega_s(\ell) - \Omega_s(0)$ is the free energy relative to having bulk gas everywhere. The important feature of this result is that it is now the relative behavior of V(k) and $n_\alpha W(k)$ that determines whether the layers are

filled. Suppose, for example, that $V(k) = RW(k)$. As T rises from 0 to T_c at $\Delta\mu = 0$, n_α decreases from 1 to 1/2 and so if $1/2 < R < 1$, (21.27) predicts a wetting transition at T_w such that $n_\alpha(T_w) = R$. Furthermore, for the Van de Waals potentials (21.22,23) with $\gamma_{vm} = \gamma_{wm}$, it is a continuous transition of infinite order, as may be shown by carrying out the sums in (21.27) and casting the result at $\Delta\mu = 0$ into the form of an expansion in inverse powers of ℓ,

$$\Delta\Omega_s(\ell) = \Delta\Omega(\infty) + \frac{a_2}{2\ell^2} + \frac{a_3}{3\ell^3} + \ldots \quad . \tag{21.28}$$

Explicit evaluation of the constants a_m, $m = 2,3,\ldots$, is a straightforward if tedious matter. In particular, one finds $a_2 = J(n_\alpha - n_\beta)(n_\alpha - R)$, which shows that there is a minimum of $\Omega(\ell)$ at $\ell \to \infty$ if $n_\alpha < R$ and a maximum for $n_\alpha > R$. Thus, T_w is a possible wetting temperature. Whether the minimum is a relative or absolute one depends on the behavior of other coefficients a_m, $m > 2$. Again for $V(k) = RW(k)$, all of the a_m's vanish at $n_\alpha = R$ (in the slab approximation), producing the infinite-order critical transition. On the other hand, if $V(k) = RW(k)(1 + \gamma/k)$, where γ is a constant, then $a_3 \neq 0$ when $T = T_w$, i.e., when $a_2 = 0$. If $\gamma > 0$, then $a_3 > 0$ and an ordinary critical transition results at T_w; if $\gamma < 0$, then $a_3 < 0$ and there may be first-order wetting at some $T > T_w$. Further, if $V(k) = RW(k)(1 + \gamma/k^2)$, then $a_3 = 0$ at T_w but $a_4 \neq 0$, leading to tricritical wetting when $\gamma > 0$, etc.

To a certain extent, the preceding results are an artifact of the slab approximation (21.26). One may examine the consequences of the thermal smoothing of the film's density profile by taking $n(k) = n_s(k) + \delta n(k)$ and then minimizing the mean-field free energy after linearizing the adsorbate-adsorbate interaction energy in $\delta n(k)$. (An alternative procedure [21.38,39, 74] leading to the same result is to evaluate the partition function and free energy in a low-temperature expansion, keeping only single-particle and single-hole excited states.) The essential new feature produced in this calculation is an ℓ-dependent term in $\Delta\Omega(\ell)$ of the form

$$\Delta\Omega'(\ell) \propto T \sum_{k=\ell+1}^{\infty} [W(k)]^2 \quad . \tag{21.29}$$

If $W(k) \sim 1/k^3$ at large k, then $\Delta\Omega' \sim 1/\ell^5$ and is always positive. Thus, it controls the free energy in the case $V(k) = RW(k)$ so as to give $a_5 > 0$ at T_w where $a_2 = a_3 = a_4 = 0$. The result is fourth-order critical wetting.

More generally, solution [21.38,39] of the full mean-field approximation gives rise to a free energy of the form shown in (21.28) with $a_2 \sim J(n_\alpha - n_\beta)(n_\alpha - R)$. The higher-order coefficients a_m, however, depend in a complex manner on the parameters of the potentials V(k) and W(k). From detailed

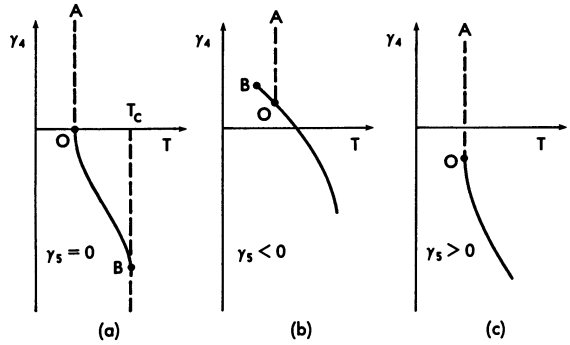

Fig.21.5. Adsorption phase diagrams in T - γ_4 space for (**a**) $\gamma_5 = 0$, (**b**) $\gamma_5 < 0$, and (**c**) $\gamma_5 > 0$. In (**a**), O is a fourth-order critical point; in (**b**), a critical end point; and in (**c**), a tricritical point. The lines AO are critical wetting lines while the solid lines are of first-order wetting transitions except for BO in (**b**) which is a line of partial wetting transitions. At $\gamma_4 < 0$, the line of first-order transitions ends at T_c (shown explicitly in (**a**) at B); below this is a line of critical drying transitions at T_c

numerical studies [21.74], one concludes that only the relative values $\gamma_m \equiv \gamma_{vm} - \gamma_{wm}$ are of qualitative importance, and so the following discussion, based on numerical study [21.38,39,74] of the MFA, will be limited to the special case $\gamma_{wm} = 0$ for all m and $\gamma_{vm} \equiv \gamma_m$. Further, only the intermediate substrate regime is considered.

As expected, if all $\gamma_m = 0$, there is fourth-order critical wetting at $T = T_w$. If all γ_m except γ_4 are zero, there is ordinary critical wetting at T_w when $\gamma_4 > 0$ and first-order wetting at $T_1 > T_w$ for $\gamma_4 < 0$. As γ_4 decreases, T_1 increases and reaches T_c, the bulk critical temperature, at some γ_{40}. For $\gamma_4 < \gamma_{40}$, there is no longer a wetting transition; rather, it appears that in this regime there is a critical drying transition at T_c. Figure 21.5a presents a sketch of the T - γ_4 adsorption phase diagram in the case $\gamma_m = 0$, $m > 4$. If, instead of γ_4, it is some other $\gamma_m (m > 4)$ which is non-zero, while all others are zero, the resulting phase diagram in T - γ_m space is qualitatively the same. Thus, one may infer that, given V and W with the same long-range behavior and with relative strength in the appropriate range, then if V has relatively more short-range attraction than W, a critical wetting transition should result, whereas, if it has relatively less, a first-order wetting transition or incomplete wetting should result. However, if there are competing short-range terms involving both repulsion and attraction, for example, $\gamma_4 > 0$ and $\gamma_5 < 0$, other behavior is possible. Figure 21.5b shows a T - γ_4 phase diagram for $\gamma_5 < 0$. At $\gamma_4 < 0$, there is again a first-order transition or incomplete wetting as expected on the basis of the preceding results. However, the line of first-order wetting transitions becomes, at the

critical endpoint O, a line of first-order partial-wetting transitions in which the film thickness changes by some *finite* amount. The line OA is again one of critical wetting transitions. Figure 21.5c shows the case of $\gamma_5 > 0$. Now there is a tricritical wetting transition at a point O with $\gamma_4 < 0$.

The various qualitative properties of the wetting transitions, for example, the critical exponents, may be determined by analyzing the mean-field equations. Of course, it is usually true that critical exponents in a three-dimensional system are given incorrectly by the MFA. The present case, however, is an interesting exception [21.33]. The upper critical dimension for all of the wetting phenomena except those at the bulk critical temperature is less than three, provided the interactions are algebraic at large distances, i.e., provided V(k) and W(k) are proportional to some positive power of 1/k. Hence the mean-field critical exponents are in fact correct. This is not the case for short-range v_{aa}, such as an exponential. Further, the analysis is much simpler [21.75], and the results the same, if the Landau theory embodied in (21.28) is used[4]. The basic procedure is to find from (21.28) the appropriate scaling form (see, for example [21.69,76]) for $\Delta\Omega$ for each type of critical transition. These are as follows: Fourth-order critical wetting may occur when a_2, a_3, and a_4 vanish simultaneously with $a_5 > 0$. The scaling form is

$$\Delta\Omega = \tilde{t}^{2-\alpha_s} F_4\left(\frac{a_3}{\tilde{t}^{\Delta 3}}, \frac{a_4}{\tilde{t}^{\Delta 4}}, \frac{\Delta\tilde{\mu}}{\tilde{t}^{\Delta}}\right) , \tag{21.30}$$

where $\tilde{t} = a_2$ and $\Delta\tilde{\mu} = (n_\alpha - n_\beta)\Delta\mu$. The exponents α_s, Δ_3, Δ_4, and Δ are listed in Table 21.1, along with the correlation length exponent ν_s ($\xi^{-1} \sim \tilde{t}^{\nu_s}$, where ξ is the correlation length), the exponent β_s governing the equilibrium film

Table 21.1. Critical exponents and upper critical dimension for the critical wetting transitions [21.39]

Exponents	Critical wetting	Tricritical wetting	Tetracritical wetting
α_s	- 1	0	1/3
Δ_1		1/2	2/3
Δ_2			1/3
Δ	4	5/2	2
β_s	1	1/2	1/3
ν_s	5/2	3/2	7/6
d_u^s	11/5	7/3	17/7

4 One must include a term $\ell(n_\beta - n_\alpha)\Delta\mu$ to account for the possibility that $\mu \neq \mu_0$.

thickness ℓ_0 at the transition ($\ell_0^{-1} \sim \tilde{t}^{\beta_s}$), and the upper critical dimension d_u. The latter is found from the hyperscaling relation [21.77,78] $2 - \alpha_s = \nu_s(d_u - 1)$, while β_s and ν_s are found from the scaling function. Tricritical wetting requires a_2 and a_3 to vanish with $a_4 > 0$. In this instance the scaling form of $\Delta\Omega$ is

$$\Delta\Omega = \tilde{t}^{2-\alpha_s} F_3\left(\frac{a_3}{\tilde{t}^{\Delta_3}}, \frac{\Delta\tilde{\mu}}{\tilde{t}^{\Delta}}\right) \tag{21.31}$$

The various exponents and d_u for tricritical wetting are included in Table 21.1. Finally, critical wetting may result when a_2 vanishes with $a_3 > 0$. Then

$$\Delta\Omega = t^{2-\alpha_s} F_2\left(\frac{\Delta\tilde{\mu}}{\tilde{t}^{\Delta}}\right) \quad ; \tag{21.32}$$

the exponents and d_u are listed in Table 21.1.

A critical endpoint can appear when, for $a_2 = 0$, there are equal minima in $\Delta\Omega$ at some finite ℓ_0 and at $\ell \to \infty$. If such a point is approached along a path such that ℓ diverges continuously, it has the same exponents as the critical wetting line that it terminates.

On the basis of the theory outlined here, it would seem that all wetting transitions in fluids found to date must involve systems in which V has relatively more short-range repulsion than does U, thus leading to first-order wetting. Such a pair of potentials will produce a configuration in which the first layer of adsorbed film will be held away from the substrate in comparison with the distance between layers of the film. This has been called the excluded volume effect and provides an alternative way of analyzing the question of whether the wetting transition is continuous or first-order [21.36].

In order to produce a continuous wetting transition, according to the theory, it is desirable to make V relatively more attractive at short distances and so reduce or eliminate the excluded volume effect. One way to achieve this goal would be to coat a substrate with a very thin layer of material which is relatively more attractive to the adsorbate than is the uncoated substrate, and the atoms of which, if possible, have smaller hard core diameters than those of the substrate. This point is discussed at some length in [21.39].

21.3.2 Solid Films: Wetting and Melting

The adsorption of a solid film introduces added complications having to do with both the compatibility of the crystal structures of film and substrate and the compatibility of the structure of the film close to the substrate

with that of the film far away. We treat the second point first. Using phenomenological arguments for the free energy of an adsorbed film, including elastic strain energy, *Huse* [21.23] showed that the strain would introduce a term of the form $-A/\ell$, with $A > 0$, for a film of thickness ℓ. When included in a free energy expansion such as (21.28), this term leads inexorably to the conclusion that Ω is minimized at some finite value of ℓ. Hence, there cannot be wetting except when A, which is proportional to some combination of stresses squared, vanishes. Strictly speaking, the stress will not vanish in a solid film and so there is no wetting by solid films in the sense of forming an infinitely thick stable film.

This point was also addressed by *Gittes* and *Schick* [21.24] who, in addition to giving a rather more detailed analysis of the elastic strain energy, studied a lattice-gas model (at $T = 0$) in which the spacings between successive layers of the adsorbate were treated as variational parameters in minimizing the free energy. The conclusions of this study are in agreement with those from the strain analysis. As the substrate potential V increases in strength relative to W, there is a sequence of incomplete/complete/incomplete wetting behaviors with the "complete" wetting regime being characterized by a macroscopically thick but not infinitely thick film. Further, using appropriate adatom-adatom and substrate-adatom potentials [21.79,80], Gittes and Schick found, in agreement with experiment [21.19,21] that Ar, Kr,and Xe all wet a graphite substrate. They found further that Ne is a borderline case in that small changes of the potentials are sufficient to change the behavior from complete to incomplete wetting, the latter being the consequence of too strong a substrate potential. Experimentally, Ne does not wet graphite. Finally, in [21.23,24] it is argued that the continuous relaxation of strain envisaged in these calculations is energetically favored over relaxation by the introduction of dislocations, at least in the body of a thick film.

Given that a solid film—whether a few or many molecular layers thick—does form close to gas-solid coexistence, then one expects to see layering transitions below the roughening temperature. Also, the film must eventually melt as the temperature is raised. Precisely along the gas-solid coexistence line, the bulk solid will melt at the triple point. However, the temperature at which the adsorbed film melts is governed not by bulk properties but by the relative free energies of a fluid film and a solid one which means that the properties of the substrate will be of some importance. For example, if the substrate potential possesses lateral variations commensurate with the structure of an adsorbed solid film, that would favor the formation of the solid film over a liquid film and so lead to a relatively high melting tem-

perature in comparison with what would be found in the absence of the lateral variation or in the presence of lateral variation of the potential incommensurate with the structure of solid adsorbate.

The Potts lattice-gas model may be used to gain some qualitative insight into the melting of a solid adsorbed film. If one employs a potential W that produces a qualitatively reasonable bulk phase diagram[5] and if V is independent of p and strong enough to produce wetting at T = 0, then one finds that the solid film melts at a temperature $T_m(\mu)$ which is lower than the triple-point temperature, as indicated in Fig.21.6a. Further, the melting transition is first order. If, on the other hand, V(1) becomes $V_p(1)$ with, e.g., $V_1(1)$ more attractive than $V_p(1)$, $P \neq 1$, then the substrate potential encourages the formation of a solid film, that is, a film in which one Potts state is preferentially occupied. Hence, this model represents a system in which the substrate favors the formation of a solid film in its immediate vicinity. Calculations [21.67] using this model produce phase diagrams such as those

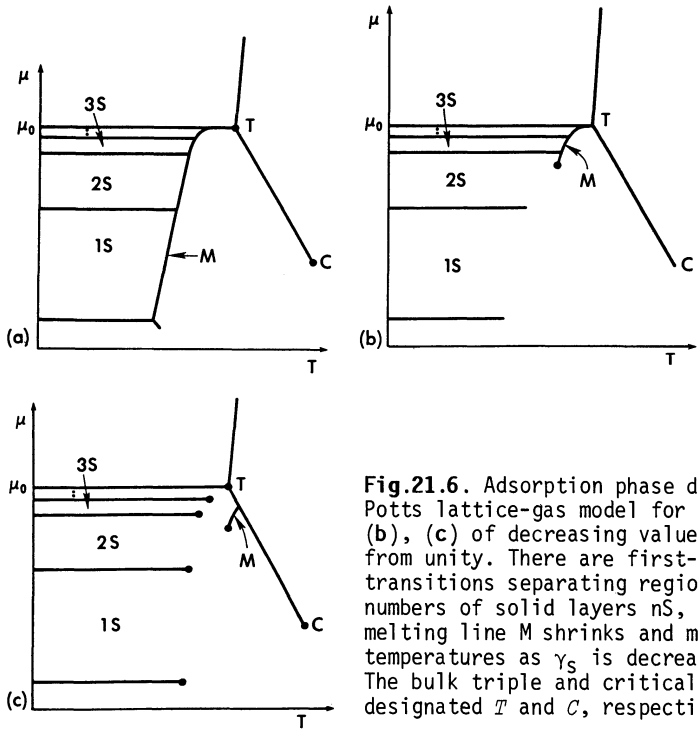

Fig.21.6. Adsorption phase diagrams from the Potts lattice-gas model for a sequence (a), (b), (c) of decreasing values of γ_s, starting from unity. There are first-order layering transitions separating regions of different numbers of solid layers nS, n = 1, 2, 3. The melting line M shrinks and moves to higher temperatures as γ_s is decreased from unity. The bulk triple and critical points are designated T and C, respectively

5 This can be achieved, e.g., for q = 6 and $W_{pp'} \simeq W_{pp}/2$, where $p \neq p'$. Then the latent heats at the triple point are in about the correct ratio as compared with simple materials such as Ar [21.9,67].

shown in Figs.21.6b,c as $\gamma_s \equiv V_p(1)/V_1(1)$ $(P \neq 1)$ decreases. The first-order melting line now ends at a critical point (T_{cm},μ_{cm}) and the film melts continuously at $\mu < \mu_{cm}$. Further, in Fig.21.6c, the melting film along the liquid-gas coexistence line is solid in character in the layers close to the substrate. It is liquidlike in the body of the film, and the "melting" transition is nothing more than a discontinuous change in the extent of solidlike character, measured by $n_1(k) - n_2(k)$, in the first few layers. For γ_s sufficiently small this discontinuity disappears altogether and there is no longer any "melting" phase transition. Rather, as one moves along the gas-solid coexistence line to the triple point and then along the gas-liquid line, the character of the film changes continuously from solid to liquid, first in layers far from the substrate and then in closer layers. At a point on the gas-liquid line, the film is typically predominantly liquid with one or two solid layers next to the substrate. The latter behavior is not uncommon in nature, although the physical reason for it may be the compression of the first few layers of adsorbate in the case of a strong substrate.

21.3.3 Triple-Point Wetting

In those cases in which the solid film melts to a thin fluid film at gas-solid coexistence at $T_m < T_3$ (the triple-point temperature), the Potts lattice-gas model gives triple-point wetting as described in Sect.21.1. In some sense, this is the same phenomenon as the growth of a liquid film when gas-liquid coexistence is approached from the region of stable gas in the absence of a solid phase. The thickness ℓ of the film varies according to

$$\frac{1}{\ell^{\delta_s}} \sim |\mu - \mu_{gl}| \quad ,$$

where μ_{gl} is the chemical potential at coexistence and δ_s is the exponent in the leading term of the substrate potential (assuming W is not longer ranged than V and assuming power-law potentials). Thus

$$\ell \sim |\mu - \mu_{gl}|^{-1/\delta_s} \quad .$$

If the path to gas-liquid coexistence is such that $|T - T_{gl}| \sim |\mu - \mu_{gl}|$, then

$$\ell \sim |T - T_{gl}|^{-1/\delta_s} \quad ,$$

and if T_{gl} is really T_3, then

$$\ell \sim |T - T_3|^{-1/\delta_s} \quad .$$

For Van der Waals potentials, $\delta_s = 3$. In this scenario, the role of the solid

phase is simply to provide a path in μ-T space leading to the gas-liquid curve at the triple point.

Recent experimental measurements of ℓ along the gas-solid coexistence line for a variety of simple materials on graphite and gold substrates have revealed wetting transitions at or very close to the triple point [21.49-52, 81-84]. The work of *Krim* et al. [21.49] in particular shows the expected $\ell \sim |T - T_3|^{-1/3}$, but that of *Bartosch* and *Gregory* [21.84] reveals an exponent larger than 0.5 for O_2 on graphite.

Additional, qualitatively different adsorption phase diagrams may be obtained [21.67] from the Potts lattice-gas model of adsorption by choosing the potentials in other ways. More generally, *Pandit* and *Fisher* [21.18] have made a phenomenological investigation of the possible adsorption phase diagrams in the vicinity of a bulk adsorbate triple point.

21.3.4 Epitaxy

The formation of a multilayer film can involve phase transitions in which the essential ordering takes place in the direction normal to the substrate as, for example, in layering transitions and the wetting transition. There is also the possibility of ordering in directions lateral to the substrate. In this category there are two basic phenomena.

First, the adsorbate may demonstrate periodic lateral variation which is either commensurate or incommensurate with the variation of the substrate. In the adsorbate liquid phase, the variation should be commensurate as the liquid has no intrinsic periodic long-range structure of its own. However, when the solid forms, it is usually incommensurate with the substrate, so the melting transition is also a commensurate-incommensurate transition. Alternatively, there can be a commensurate-incommensurate transition between two solid adsorbed phases.

The second type of lateral ordering transition is the epitaxial transition. This can take place when the substrate has a definite periodic structure and a specific group of symmetry translations (translations under which the substrate is invariant) parallel to the surface. A transition in which the corresponding symmetry group of the adsorbate changes from that of the substrate to a subgroup of it is called an epitaxial transition [21.85]. If the new symmetry group is not a subgroup of the substrate's symmetry group, then we have a commensurate-incommensurate transition [21.85]. The following is an example of an epitaxial transition. Suppose that the substrate surface presents a square array of adsorption sites, i.e., a potential $V(\mathbf{r})$ which has the lateral symmetry of a square lattice with spacing a. If, in addition,

the adatoms have diameters d significantly larger than a, say $d \simeq \sqrt{2}a$, then they will not be able to occupy nearest-neighbor sites. Rather, a dense layer may instead form on a square lattice of next-nearest-neighbor sites with spacing $\sqrt{2}a$. However, if the first layer is a dilute gas, then the adsorbate density is likely to be the same at all sites. Between these two configurations there is an epitaxial phase transition which is either first order or continuous.

Transitions involving lateral ordering have been extensively studied in the submonolayer to monolayer adsorption regime [21.86], but relatively little has been done for multilayer adsorption. Our discussion is drawn largely from [21.20], which treats a simple cubic Ising lattice-gas model in which there are repulsive nearest-neighbor interactions u_1 and attractive next-nearest-neighbor interactions $-u_2$ between adatoms. Then u_1, which represents hard core repulsion, drives an epitaxial transition such that one of two fcc sublattices becomes preferentially occupied.

The principal aim of [21.20] is to determine the effects of lateral ordering on layering and wetting phenomena. Broadly speaking, the effects are minimal in that layering and wetting transitions continue to be present under conditions such that epitaxy also occurs. There are, however, some changes in the various critical phenomena. For example, in the case of an intermediate strength substrate producing first-order wetting and a prewetting line, the prewetting transition is typically accompanied by epitaxial ordering. This line of first-order transitions terminates at a tricritical point[6] beyond which there is a line of continuous epitaxial transitions as shown in

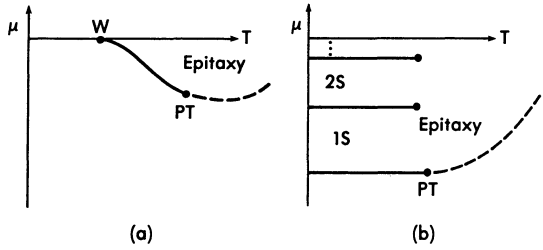

Fig.21.7. Adsorption phase diagrams showing regions of epitaxial ordering for intermediate (**a**) and strong (**b**) substrate potentials; *PT* is a tricritical point and the regions nS, n = 1, 2,..., are domains of n-layer solid films; *W* - *PT* is a line of first-order prewetting transitions, and there are continuous epitaxial transitions along the dashed lines. For still stronger substrate potentials, wetting may be absent altogether

6 Critical endpoint behavior may also be possible. See [21.20] for a more detailed discussion.

Fig.21.7a. For stronger substrates producing wetting at all temperatures, layering transitions appear, with the first one playing the same role as the prewetting transitions in the intermediate substrate regime in that it is also an epitaxial transition ending at a tricritical point[6] beyond which there is a continuous epitaxial transition, as in Fig.21.7b. For sufficiently strong substrates, the epitaxy will be quenched in the first layer by the filling of both fcc substrates, and this effect can prevent wetting altogether. As the potential parameters are changed, many variants of these simple pictures can be developed. For example, there may be not one but several regions of epitaxy in μ-T space. The reader is referred to the original paper [21.20] for details.

21.4 Summary and Future Directions

In this chapter we have reviewed recent developments in theoretical research on multilayer physisorbed films including continuous and first-order wetting transitions, prewetting transitions, wetting by solid films, layering, and triple-point wetting. Many of the theoretical predictions have been qualitatively verified by experiments, although much remains to be done to establish detailed agreement. The prewetting and continuous wetting transitions have proven to be particularly elusive experimentally; both are being actively sought.

We have not discussed the extensive work done on the importance (or lack thereof, in some cases) of fluctuations in the various phenomena. This topic is reviewed extensively in [21.6] and more briefly in [21.5]. Neither have we dealt with any dynamical properties of physisorbed films, a topic still in its infancy and on which much work has yet to be done. Some interesting problems of this kind are reviewed in [21.7]. Another area which is likely to receive more attention in the future is adsorption and wetting by films of nonspherical molecules such as liquid crystals.

Finally, it would appear that the basic concepts encountered in wetting phenomena should be of utility in studies of numerous fascinating and complex systems, such as microemulsions, for which there is currently no microscopic statistical mechanical theory.

Acknowledgement. This work was supported in part by National Science Foundation Grant No. DMR 84-04961.

References

21.1 T. Young: Philos. Trans. **95**, 65 (1805)
21.2 C. Ebner, W.F. Saam: Phys. Rev. Lett. **38**, 1486 (1977)
21.3 J.W. Cahn: J. Chem. Phys. **66**, 3667 (1977)
21.4 References [21.5-7] are recent review articles concerned with wetting phenomena. Reference [21.5], concise and highly readable, is an excellent overview of the topic. Reference [21.6] is much more complete and contains extensive references. Reference [21.7] treats a number of special topics not found in the other articles, especially nonequilibrium phenomena
21.5 E.H. Hauge: In *Fundamental Problems in Statistical Mechanics VI*, ed. by E.G.D. Cohen (North-Holland, New York 1985)
21.6 D.E. Sullivan, M.M. Telo da Gamma: In *Fluid Interfacial Phenomena*, ed. by C.A. Croxton (Wiley, New York 1985)
21.7 P.G. de Gennes: Rev. Mod. Phys. **57**, 827 (1985)
21.8 R. Pandit, M. Schick, M. Wortis: Phys. Rev. B**26**, 5112 (1982)
21.9 C. Ebner: Phys. Rev. B**28**, 2890 (1983)
21.10 D.E. Sullivan: Phys. Rev. B**20**, 3991 (1979)
21.11 E.H. Hauge, M. Schick: Phys. Rev. B**27**, 4288 (1983)
21.12 M.J. de Oliveira, R.B. Griffiths: Surf. Sci. **71**, 687 (1978)
21.13 C. Ebner: Phys. Rev. A**23**, 1925 (1981)
21.14 I.M. Kim, D.P. Landau: Surf. Sci. **110**, 415 (1981)
21.15 J.D. Weeks: Phys. Rev. B**26**, 3998 (1982)
21.16 D.A. Huse: Phys. Rev. B**30**, 1371 (1984)
21.17 M.P. Nightingale, W.F. Saam, M. Schick: Phys. Rev. B**30**, 3830 (1984)
21.18 R. Pandit, M.E. Fisher: Phys. Rev. Lett. **51**, 1772 (1983)
21.19 J.L. Seguin, J. Suzanne, M. Bienfait, J.G. Dash, J.A. Venables: Phys. Rev. Lett. **51**, 122 (1983)
21.20 C. Ebner, C. Rottman, M. Wortis: Phys. Rev. B**28**, 4186 (1983)
21.21 M. Bienfait, J.L. Seguin, J. Suzanne, E. Lerner, J. Krim, J.G. Dash: Phys. Rev. B**29**, 983 (1984)
21.22 R.J. Muirhead, J.G. Dash, J. Krim: Phys. Rev. B**29**, 5074 (1984)
21.23 D.A. Huse: Phys. Rev. B**29**, 6985 (1984)
21.24 F.T. Gittes, M. Schick: Phys. Rev. B**30**, 209 (1984)
21.25 R. Pandit, M. Wortis: Phys. Rev. B**25**, 3226 (1982)
21.26 P. Tarazona, R. Evans: Mol. Phys. **48**, 799 (1983)
21.27 G.F. Teletzke, L.E. Scriven, H.T. Davis: J. Chem. Phys. **78**, 1431 (1983)
21.28 T. Aukrust, E.H. Hauge: Phys. Rev. Lett. **54**, 1814 (1985)
21.29 W.F. Saam: Surf. Sci. **125**, 253 (1983)
21.30 P.G. de Gennes: C.R. Acad. Sci., Ser. II **297**, 9 (1983)
21.31 M.P. Nightingale, W.F. Saam, M. Schick: Phys. Rev. Lett. **51**, 1275 (1983)
21.32 R. Evans, P. Tarazona: J. Chem. Phys. **80**, 587 (1984)
21.33 R. Lipowsky: Phys. Rev. Lett. **52**, 1429 (1984)
21.34 R. Lipowsky, D.M. Kroll: Phys. Rev. Lett. **52**, 2303 (1984)
21.35 V. Privman: J. Chem. Phys. **81**, 2463 (1984)
21.36 D.M. Kroll, T.F. Meister: Phys. Rev. B**31**, 392 (1985)
21.37 S. Dietrich, M. Schick: Phys. Rev. B**31**, 4718 (1985)
21.38 C. Ebner, W.F. Saam, A.K. Sen: Phys. Rev. B**31**, 6134 (1985)
21.39 C. Ebner, W.F. Saam, A.K. Sen: Phys. Rev. B**32**, 1558 (1985)
21.40 H. Nakanishi, M.E. Fisher: Phys. Rev. Lett. **49**, 1565 (1982)
21.41 M.R. Moldover, J.W. Cahn: Science **207**, 1073 (1980)
21.42 D.W. Pohl, W.I. Goldberg: Phys. Rev. Lett. **48**, 1111 (1982)
21.43 J.W. Schmidt, M.R. Moldover: J. Chem. Phys. **79**, 379 (1983)
21.44 D. Beaglehole: J. Phys. Chem. **87**, 4749 (1983)
21.45 D. Beysens, D. Estève: Phys. Rev. Lett. **54**, 2123 (1985)

21.46 Y. Carmi, S.G. Lipson, E. Polturak: Phys. Rev. Lett. **54**, 2042 (1985)
21.47 J. Suzanne, J.L. Seguin, M. Bienfait, E. Lerner: Phys. Rev. Lett. **52**, 637 (1984)
21.48 J.M. Gay, M. Bienfait, J. Suzanne: J. Phys. (Paris) **45**, 1497 (1984)
21.49 J. Krim, J.G. Dash, J. Suzanne: Phys. Rev. Lett. **52**, 640 (1984)
21.50 J. Menaucourt, A. Thomy, X. Duval: J. Phys. (Paris) **38**, Colloq. C**4**, 195 (1977)
21.51 M. Sutton, S.G.J. Mochrie, R.J. Bergeneau: Phys. Rev. Lett. **51**, 407 (1983)
21.52 S.G.J. Mochrie, M. Sutton, R.J. Birgeneau, D.E. Moncton, P.M. Horn: Phys. Rev. B**30**, 263 (1984)
21.53 A. Thomy, X. Duval: J. Chim. Phys. **66**, 1969 (1969)
21.54 A. Thomy, X. Duval: J. Chim. Phys. **67**, 286 (1970)
21.55 A. Thomy, X. Duval: J. Chim. Phys. **67**, 1101 (1970)
21.56 A. Thomy, X. Duval, J. Regnier: Surf. Sci. Rep. **1**, 1 (1981)
21.57 S. Ramesh, J.D. Maynard: Phys. Rev. Lett. **49**, 47 (1982)
21.58 J.J. Hamilton, D.L. Goodstein: Phys. Rev. B**28**, 3838 (1983)
21.59 R. Miranda, E.V. Albano, S. Daisler, G. Ertl, K. Wandelt: Phys. Rev. Lett. **51**, 782 (1983)
21.60 R. Miranda, E.V. Albano, S. Daisler, K. Wandelt, G. Ertl: J. Chem. Phys. **80**, 2931 (1984)
21.61 S. Ramesh, Q. Zhang, G. Torzo, J.D. Maynard: Phys. Rev. Lett. **52**, 2375 (1984)
21.62 W.F. Saam, C. Ebner: Phys. Rev. A**15**, 2566 (1977)
21.63 R. Evans, P. Tarazona: Phys. Rev. A**28**, 1864 (1983)
21.64 P.C. Hemmer, J.L. Lebowitz: In *Phase Transitions and Critical Phenomena*, Vol.5B, ed. by C. Domb, M.S. Green (Academic, New York 1976)
21.65 C. Ebner: Phys. Rev. A**22**, 2776 (1980)
21.66 A.N. Berker, S. Ostlund, F.A. Putnam: Phys. Rev. B**17**, 3650 (1978)
21.67 L. Conner, C. Ebner: Unpublished
21.68 D.B. Abraham: Phys. Rev. Lett. **44**, 1165 (1980)
21.69 K. Binder: In *Phase Transitions and Critical Phenomena*, Vol.8, ed. by C. Domb, J.L. Lebowitz (Academic, London 1983)
21.70 D. Jasnow: Rep. Prog. Phys. **47**, 1059 (1984)
21.71 M. Wortis: In *Fundamental Problems in Statistical Mechanics VI*, ed. by E.G.D. Cohen (North-Holland, New York 1985)
21.72 K.-C. Ng: J. Chem. Phys. **61**, 2680 (1974)
21.73 W.A. Steel: *The Interaction of Gases with Solid Surfaces* (Pergamon, Oxford 1974)
21.74 A.K. Sen: Ph.D. Dissertation, Ohio State University (1985)
21.75 S. Krinsky, D. Mukamel: Phys. Rev. B**11**, 399 (1975)
21.76 M.E. Fisher: J. Vac. Sci. Technol. **10**, 665 (1973)
21.77 B. Widom: In *Phase Transition and Critical Phenomena*, Vol.2, ed. by C. Domb, M.S. Green (Academic, London 1972)
21.78 B. Widom: J. Chem. Phys. **43**, 3892 (1965)
21.79 M.W. Cole, J.R. Klein: Surf. Sci. **124**, 547 (1983)
21.80 R.A. Aziz: Mol. Phys. **38**, 177 (1979)
21.81 G. Bomchil, N. Harris, M. Leslie, J. Tabony, J.W. White, P.H. Gamlen, R.K. Thomas, T.D. Trewern: J. Chem. Soc., Faraday Trans. 1, **75**, 1535 (1979)
21.82 P.H. Gamlen, R.K. Thomas, T.D. Trewern, G. Bomchil, N. Harris, M. Leslie, J. Tabony, J.W. White: J. Chem. Soc., Faraday Trans 1, **75**, 1542, 1553 (1979)
21.83 W.L. Lee, L.J. Slutsky: J. Phys. Chem. **86**, 842 (1982)
21.84 C.E. Bartosch, S. Gregory: Phys. Rev. Lett. **54**, 2513 (1985)
21.85 M.P.M. den Nijs: Unpublished
21.86 See, for example, S.K. Sinha (ed.): *Ordering in Two Dimensions* (North-Holland, New York 1980)

22. Diffraction Studies of Layering and Wetting Transitions

L. Passell[1], *S.K. Satija*[2], *M. Sutton*[3], *and J. Suzanne*[4]

[1]Brookhaven National Laboratory, Upton, NY 11973, USA
[2]Department of Physics, University of Delaware, Newark, DE 19711, USA
[3]Department of Physics, McGill University, Montreal, H3A 2T8, Canada
[4]Departement de Physique, Faculté des Sciences de Luminy, Case 901, F-13288 Marseille Cedex 9, France

22.1 Introduction

Thermodynamic arguments [22.1] show that when liquid and vapor phases co-exist in the presence of a surface several different types of behavior are possible: depending on the interfacial tensions between the three components, either the liquid can form droplets which contact the surface at a finite angle or it can spread out over the surface forming a uniform, macroscopically thick film interposed between the surface and the vapor phase. In the former case the liquid is said to partially wet the surface, in the latter it is said to wet it completely. A third possibility is that it will not wet the surface at all or, viewed another way, that the vapor phase will be interposed between the liquid and the surface. Co-existing solid and liquid or solid and vapor phases on a surface are also expected to show the same basic pattern of behavior

Only recently has it been recognized that the temperature and/or concentration dependence of the relevant interfacial tensions can be quite different and that changes in these quantities can shift the system from one wetting state to another. A change from a partial to a non-wetting state is described as a "drying transition"; when the change is from a partial to a complete wetting state, it is referred to as a "wetting transition".

It has been suggested, for example, by *Sullivan* [22.2] that these alternative growth modes might result from competition between the microscopic forces of adhesion and cohesion. It was proposed that complete wetting takes place when adhesive (adsorbate - substrate) interactions are dominant, that the non-wetting condition develops at the other extreme when cohesive (adsorbate - adsorbate) interactions prevail, and that partial wetting results when adhesive and cohesive interactions are comparable in magnitude.

Later, *Pandit* et al. [22.3] took up this basic idea and used it to develop a lattice gas model of adsorption. Analyzing their model in mean field approximation, they showed that many subtle gradations of wetting behavior were possible depending on the relative strengths of the adhesive and cohesive interactions involved. Because their results provide a basic theoretical frame-

work within which to view experimental wetting and layering studies we will review them briefly here.

In the strong substrate regime where adhesive interactions are completely dominant, this model indicates that an infinite number of layering transitions should occur, each layering transition extending over a finite temperature range and ending at a critical point. When the temperature of the system is below the highest critical layering temperature, increasing the chemical potential by adding adsorbate is predicted to cause the film to thicken layer by layer, the excess surface density diverging as the chemical potential approaches its bulk value. As the number of layers increases, the critical temperatures of the individual layering transitions are expected to approach a limiting value, T_R, called the roughening temperature. Above T_R the model predicts the sharp layering transitions to broaden rapidly and the film growth to become progressively smoother and smoother as the temperature rises. But even though layering no longer occurs, the excess surface density is still expected to diverge as the chemical potential approaches its bulk value. This divergence of the excess density is the identifying feature of complete wetting behavior. It is predicted to persist until the temperature reaches T_C, the critical temperature of the co-existing bulk phases. Above T_C, although smooth growth is thought to continue, the film thickness is not expected to diverge as the chemical potential approaches its bulk value. Thus, even a strong substrate system is only believed to exhibit complete wetting behavior below T_C.

As cohesive interactions increase in strength relative to adhesive interactions we enter the intermediate substrate regime. Here the picture changes and a new type of phase transition, the wetting transition, characterized by a wetting temperature, T_W, is expected to appear. Three subregions have now to be distinguished. When the relative interaction strengths are such that $T_W < T_R$, we are in what Pandit et al. define as the layering subregion of the intermediate substrate regime. Above T_W in this subregion, the system is predicted to behave like its strong substrate counterpart. But below T_W, although layering transitions are expected to continue to occur, their number is predicted to decrease with decreasing temperature and the film is expected to remain of finite thickness indicating a partial wetting process. Thus in the layering subregion complete wetting is expected between T_C and T_W and partial wetting below T_W.

Further increasing the relative strength of cohesive to adhesive interactions causes the wetting temperature to rise until, finally, T_W exceeds T_R and we enter a new part of the intermediate substrate regime called by Pandit et al. the prewetting subregion. Here the individual layering transitions are predic-

ted to coalesce into a single thin-film to thick-film transition spanning a finite temperature range and terminating at a temperature called the prewetting temperature. At temperatures above T_W but below the prewetting temperature, the film is expected to grow smoothly but remain thin as the chemical potential is increased until suddenly, at the thin-film to thick-film phase boundary, it is expected to make a first-order transition to a thick film and then continue to grow smoothly with the excess density diverging as the chemical potential approaches its bulk value. Above the prewetting temperature the system is predicted to behave like a strong substrate system. Thus in the prewetting subregion complete wetting should occur at temperatures between T_C and T_W and partial wetting below T_W as in the layering subregion. What distinguishes one from the other is the dramatic change in the layering process.

As the relative strength of cohesive to adhesive interactions is increased yet further, T_W will continue to increase and the model predicts that the thin-film to thick-film phase boundary will shrink until the prewetting and wetting temperatures coalesce into a single point, T_{CW}, called the critical wetting temperature. Here we enter the third subregion of the intermediate substrate regime which Pandit et al. have named the critical wetting subregion. In this subregion growth below T_C but above T_{CW} is expected to be smooth and to lead to divergence of the excess density. Below T_{CW}, although growth is also predicted to be smooth, it is expected to lead only to films of finite thickness. Wetting is complete between T_C and T_{CW} and partial below T_{CW}.

Finally, in the weak substrate regime where cohesive interactions are completely dominant, the non-wetting condition is predicted to prevail. In this situation no overlayer film should form and only the bulk phase of the adsorbate is expected to appear.

Although this lattice gas model represents a notable advance over previous wetting theories, Pandit et al. recognized that it had two important shortcomings. First, it assumed only one dense phase whereas in real systems both liquid and solid phase will appear. Second, there is a built-in assumption that the structures of the film and bulk phases are the same. It cannot, therefore, take into account effects arising from differences between film and bulk structures such as often occur in solid overlayers.

Pandit and *Fisher* [22.4] later adressed the first of these points, noting that different bulk phases might have different interactions with the substrate and that a bulk triple point could bring about a discontinuous change in the relative strengths of adhesive and cohesive interactions and thus alter wetting behavior. Alternatively, a change of state of the film, such as melting or a structural transition, might well be imagined to have a similar effect.

Adsorption isotherm measurements have confirmed the existence of the basic growth modes outlined above and have also provided clear evidence of layering transitions. However, they offer little insight into the underlying microscopic behavior of the system. Thus, interest has developed in probing these processes on an atomic scale. In this article we will review current efforts to apply spectroscopic methods to the study of both wetting and layering transitions, focusing our attention on physisorbed overlayers on graphite basal plane surfaces. All of the systems studied appear to be classifiable as either strong or intermediate substrate systems. Experiments of two types will be described: (i) electron diffraction studies of a number of gas films on single crystal graphite surfaces and (ii) X-ray and neutron diffraction studies of layering transitions in ethylene and xenon-ethylene films co-adsorbed on exfoliated, crystalline graphite powders.

As will soon be evident, each of these spectroscopic methods has its particular areas of application. Electrons, being strongly interacting charged particles, are primarily scattered by the topmost layers of atoms and thus can be used not only to identify overlayer structures on single crystal surfaces but also to determine how they are oriented on such surfaces. But this sensitivity brings with it certain inherent limitations. In thick films electrons probe only the outermost layers of atoms. Often multiple scattering makes interpretation of the scattered intensities difficult and electrons therefore tend to be of limited value for definitive structural determinations. Also, local ionization and heating effects sometimes disturb the structures being probed. Finally, there is the problem that vapor present in the system can obscure the surface scattering. To date this has restricted the use of electrons to systems where the vapor pressures can be kept below roughly 10^{-4} Torr, although this limit may be raised in the future to perhaps 10^{-3} Torr by the introduction of differential pumping. As applied to physisorbed systems, the need to maintain low vapor pressures currently limits electron diffraction to the low-coverage and/or low-temperature regimes.

X-rays and neutrons, in contrast, are not strongly interacting probes and, therefore, do not disturb even the most weakly bound films. Unfortunately, they lack the specific surface sensitivity of electrons and the employment of either X-rays or neutrons as surface probes has, until recently, only been practical when high-surface-area powder substrates are available to enhance the surface contribution to the scattering. And even when such powders are used the surface scattering is sometimes difficult to identify in the presence of a substantial background of substrate scattering. There are other drawbacks to X-rays and neutrons as well. The need for large specific surface

areas limits application to those few special substrates which can be prepared not only as fine powders but with single facet surfaces of high quality. It also introduces the possibility of capillary condensation which could easily alter the characteristics of wetting and layering transitions. But the weakly interacting probes offer certain compensating advantages. Once separated from the substrate part of the scattering, the surface contribution is free of multiple scattering effects. It is also insensitive to the presence of vapor. Furthermore, recent work with high-intensity rotating anode and synchrotron X-ray sources shows that X-rays can be successfully used on single crystal as well as powder substrates. Thus there is every reason to believe that X-rays, although not neutrons, will soon be routinely employed as probes of overlayer films on single crystal surfaces.

22.2 Electron Diffraction Studies of Wetting Behavior

Both low-energy electron diffraction (LEED) and reflection high-energy electron diffraction (RHEED) have proven to be very effective in examining the growth modes of films on single crystal surfaces [22.5 - 7]. LEED probes the structure and epitaxial orientation of the first few monolayers while RHEED is more sensitive to the rearrangement of the films into 3d crystallites. This is evident in studies of Xe, Ar, Kr, Ne, N_2, O_2, CF_4, and CH_4 films adsorbed on graphite basal plane surfaces [22.8 - 12], where LEED and RHEED techniques were used in conjunction to examine the behavior of the films. Investigations of layer formation in physisorbed systems have also been made using LEED alone [22.13,14] but these have tended to be less informative.

In the following sections we will first briefly describe the experimental methods employed in electron diffraction studies of overlayer films and then summarize the results of the combined LEED-RHEED experiments mentioned above. Finally, we will describe a recent investigation of the wetting behavior of CF_4 on graphite. This system will be discussed in considerable detail because it is the only one known in which a transition from partial to complete wetting takes place at a temperature below the triple point of the bulk adsorbate [22.11]. Occurring below the bulk melting temperature, the transition involves only solid phases.

22.2.1 Experimental Methods

The apparatus used for the LEED-RHEED experiments is shown schematically in Fig.22.1. The LEED diffractometer, designed specifically for measurements with electron beam currents as low as 10^{-9} Å, contains conventional, four-grid

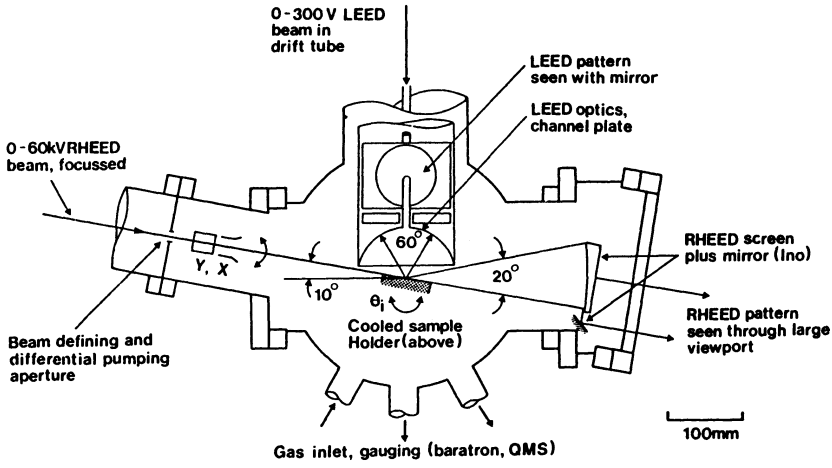

Fig.22.1. Schematic of electron diffraction apparatus

optics followed by a channel plate intensifier and fluorescent screen. Accuracy of parameter determination with this instrument is about one percent [22.15]. A commercial Riber model 510 RHEED gun with magnetic focusing and x,y deflection plates is also incorporated into the system. Its screen (modeled after one developed by *Ino* [22.16]) is a plano-concave half sector of a sphere of radius 240 nm centered on the sample and can be viewed either directly (to give a conventional RHEED pattern) or via an angled plane mirror which gives a projection similar to a LEED pattern. In normal operation the beam is incident at a grazing angle of 2-3 degrees and the electron energy is set within the range 0 - 50 keV. A RHEED pattern is typically obtained using a current of about 10^{-8} Å with an electron energy in the neighborhood of 30 keV.

For purposes of structural analysis both the LEED and RHEED patterns are photographed with a 35-mm Nikon camera. Ideally, azimuthal angle control is required for accurate structural determinations but that was not possible when the experiments described below were carried out. Instead, the azimuthal angle was simply determined to be 17 ± 2 degrees relative to the (01) axis of the reciprocal lattice of the graphite surface [22.10]. After this series of experiments was completed, however, azimuthal angle control was added to the apparatus.

The cryogenic sample holder has been described previously [22.15]. It allows samples to be maintained at any temperature between 8 and 200 K with a stability of 0.1 K or less. The absolute value of the temperature is estimated to be accurate to within ± 2 K.

Gas pressures in the ultrahigh vacuum chamber are measured with a Bayard-Alpert ionization gauge calibrated against a Baratron capacitance manometer. A quadrupole mass spectrometer is used to monitor gas purity.

Before starting an experiment the system is first baked at 160°C for 24 hours which reduces the residual gas pressure to 10^{-10} Torr or less. Then, after baking, a monolayer of the adsorbate is condensed on the single crystal graphite substrate surface and its structure determined. If the measured lattice parameter agrees well with the established value, the surface is assumed to be uniform and free of contamination. Film thickness is estimated from the impinging flux of adsorbate atoms. To do this, the deposition rate is calibrated by measuring the attenuation of the graphite (01) LEED beam and assuming the sticking coefficient to be constant over the entire thickness range.

22.2.2 RHEED Studies of Wetting

a) Two- and Three-Dimensional Diffraction Patterns—Streaks vs. Spots

RHEED patterns depend sensitively on the type of overlayer that forms. If complete wetting occurs and the film condenses layer by layer, the diffraction pattern is composed of parallel streaks. Alternatively, if small 3D crystallites form, sharp spots appear on the screen. In partial wetting cases both streaks and spots are observed simultaneously as long as the 3D crystallites (which sit on top of the uniform layers of the film) are small enough for appreciable beam transmission.

Since detailed discussions of how RHEED diffraction patterns are formed can be found in [22.5-7] we will only give a brief summary of the basic ideas here. The reciprocal lattice of a 2D solid monolayer is a set of rods perpendicular to the monolayer plane as shown in Fig.22.2a. Electrons of energies in the range 10 - 50 keV have wavelengths less than 0.1 Å. Their Ewald sphere is, therefore, of large radius and its surface very nearly planar. The intersections of the sphere with the rods—which determine the directions of the diffracted beams—are lines which appear as streaks on the observing screen concentric with the sphere.

The penetration depth of electrons is only about 10 Å when they are incident at grazing angles on the order of 2 - 3 degrees. Thus, in a complete wetting situation in which the film is many layers thick, electrons will only be diffracted from the top 3 or 4 layers of the film and the reciprocal lattice becomes effectively a set of rods (slightly modulated by interference effects between the individual layers of the film) whose intersections with the Ewald sphere produce a series of modulated streaks on the screen.

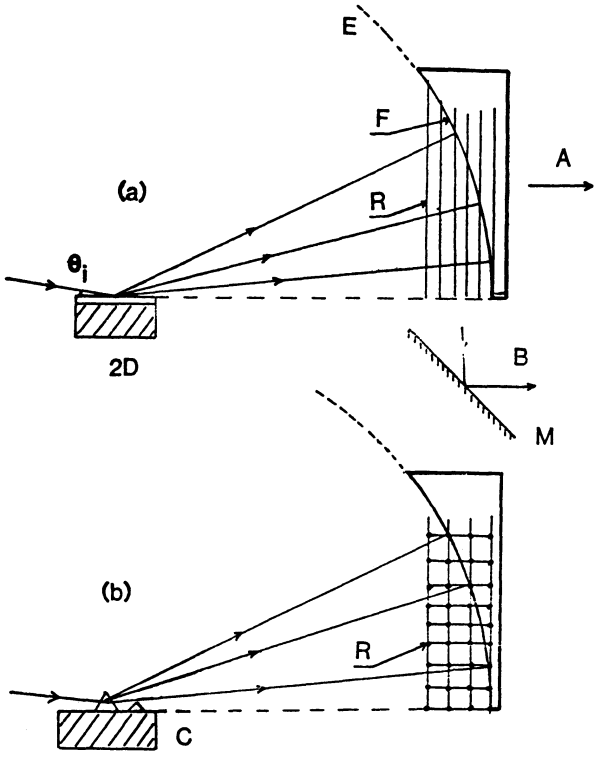

Fig.22.2a,b. Formation of RHEED streak and spot patterns. (**a**) A uniform ordered monolayer on a flat substrate will diffract electrons like a two-dimensional (2D) crystal. The reciprocal lattice (*R*) of such a crystal is composed of rods perpendicular to the crystal plane. For certain values of the electron azimuth and energy, one (or more) of these rods will be tangent to the Ewald sphere (*E*) and thus to the fluorescent screen (*F*) which is concentric with it. The electron beam is incident at an angle of 2-3 degrees. From view (*A*) streaks are visible; from view (*B*) (through the mirror *M*) the intersections of the reciprocal lattice rods with (*E*) (or *F*) give spots analogous to a LEED pattern [22.16]. (**b**) Three-dimensional (3D) crystallites (*C*) have reciprocal lattices of points rather than rods. The equivalent Ewald construction gives a spot pattern on the screen whether it is viewed from (*A*) or (*B*)

When small 3D solid crystallites are present, however, the reciprocal lattice is composed of points rather than rods as shown in Fig.22.2b. In this case it is evident that the RHEED pattern will consist of a series of spots corresponding to intersections of the Ewald sphere with particular points of the reciprocal lattice.

b) Experimental Results

A number of investigations of the wetting of metal films on clean, uniform metal [22.5 - 7] and semiconductor [22.7,17] surfaces have already been des-

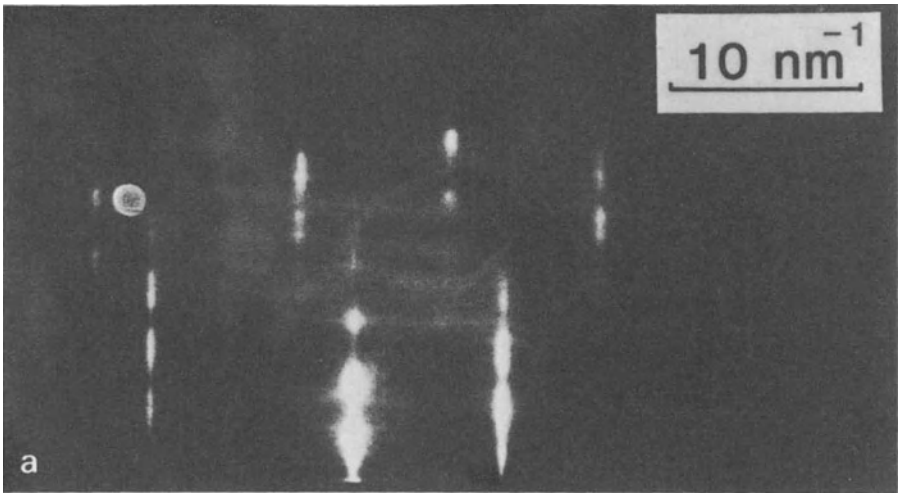

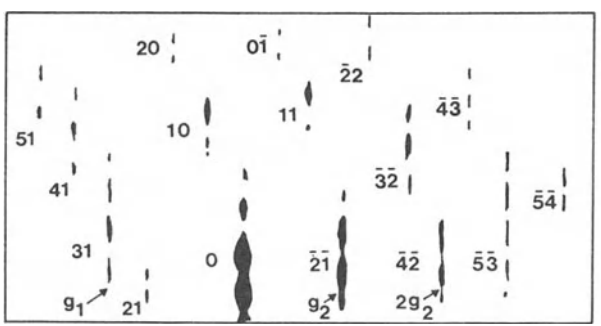

b

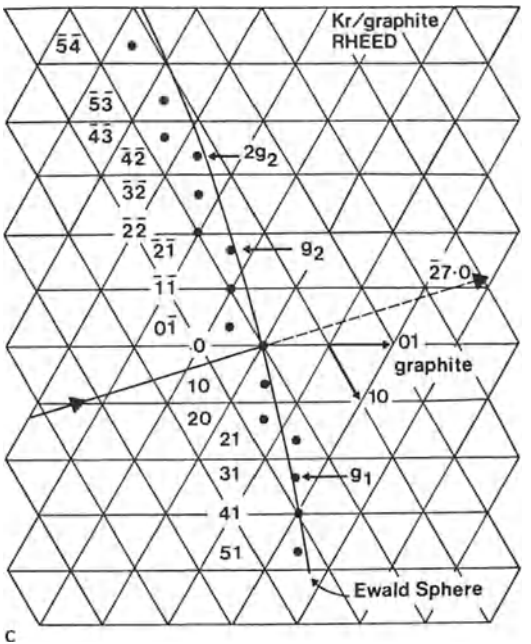

c

Fig.22.3a-c. RHEED pattern of Kr/graphite. (**a**) 10 monolayers of Kr/graphite at 10 K. (**b**) Schematic representation of (**a**) showing indexing of modulated streaks. (**c**) Ewald construction for interpretation of (**a**) and (**b**). For a more detailed explanation see [22.9]

cribed in the literature. These systems, of course, form strongly bound, chemisorbed phases and it is doubtful that their wetting transitions take place under equilibrium conditions. To avoid this difficulty, we will restrict our review to studies of the more mobile and volatile physisorbed overlayers where equilibrium conditions are more easily achieved. The specific systems that will be discussed are Xe, Ar, Ne, N_2 [22.8,10], Kr, O_2 [22.9,10], CF_4 [22.11] and CH_4 [22.12] on graphite basal plane surfaces.

Xe, Ar, and Kr were observed to exhibit complete wetting behavior down to 8 K, the lowest accessible temperature. CH_4, Ne, N_2, and O_2, on the other hand, were found to be partial wetting systems at low temperatures.

Figure 22.3a shows a typical RHEED pattern for a complete wetting system, Kr/Graphite, observed at 16 K with 30 keV electrons. The film was about 10 monolayers thick. (Unit coverage is here defined as the amount of gas necessary to form a commensurate, $\sqrt{3} \times \sqrt{3}$ solid monolayer on the graphite basal plane surface.) As noted above, the modulation of the streaks—evident in the figure—increases as the films thicken until the number of layers ultimately reaches a limit determined by the grazing angle. In this particular apparatus the grazing angle is 2 - 3 degrees and the modulation amplitude ceases to change after about five monolayers are deposited. The indexing of the pattern is shown in Fig.22.3b and the Ewald sphere construction in Fig.22.3c.

As an example of a partial wetting system, Fig.22.4a shows the RHEED pattern obtained at 10 K from two solid Ne monolayers condensed on graphite. The streaks indicate that the bilayer forms two domains rotated + and - 17 degrees with respect to the commensurate $\sqrt{3} \times \sqrt{3}$ orientation. The result agrees well with an earlier LEED study of a Ne monolayer on the same substrate [22.15]. Figure 22.4b shows the RHEED pattern of a 13-monolayer Ne film. Sharp spots are now visible along with the streaks indicating that 3D crystallites have formed on top of the bilayer film. A similar pattern of behavior is observed with N_2 [22.8,10] with O_2 [22.9,10], and CF_4 [22.10,11], the latter two at temperatures below 32 K and 37 K respectively.

The results for both complete and partial wetting systems can be summarized as follows:

i) When complete wetting is observed (Xe, Kr, and Ar), the structure of the monolayer or bilayer film is nearly identical to that of the densest plane of the corresponding 3D phase. Differences in the lattice constant are typically less than one percent.

ii) In partial wetting systems (Ne, N_2, O_2, and CF_4) the 3D crystallite islands that appear at higher coverages have the same orientation as the bilayer domains on which they are (presumably) formed.

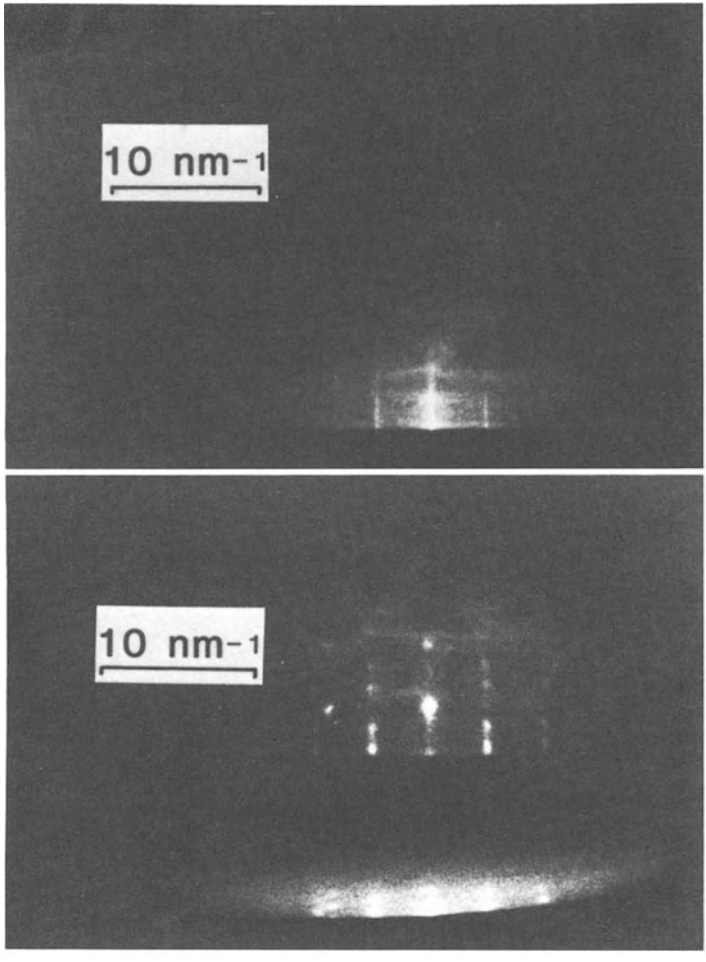

Fig.22.4 a,b. RHEED pattern of Ne on graphite. (**a**) Two monolayers at 14 K showing streak pattern. (**b**) 13 monolayers at 8 K showing spot patterns in both the normal (*A*) and mirror (*B*) views (see Fig.22.2). This pattern is typical of partial wetting behavior

iii) In the case of Ne, the nearest-neighbor spacing in the 3D crystallites is two percent greater than in the 2D layers that form on the surface.

iv) In molecular systems, a considerable reorganization of the film structure occurs at the time the third or fourth layer is deposited.

22.2.3 Combined RHEED and LEED Studies of the CF_4-on-Graphite Wetting Transition

a) RHEED Measurements

When one or two nominal layers of CF_4 are deposited on graphite, the RHEED pattern below 37 K consists of streaks, indicating a 2D phase. At 35 K, adding a third layer causes the pattern to disappear with a proportionate increase in the background. Only when two more layers are added, bringing the total to five, is the RHEED pattern restored. It is then composed of streaks with

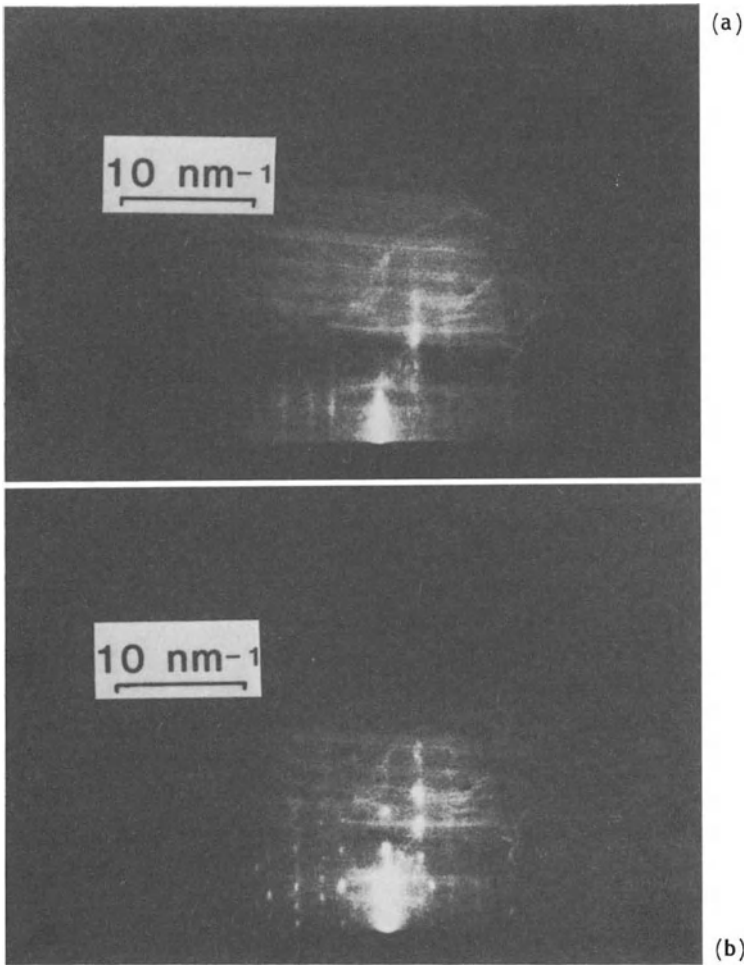

Fig.22.5a,b. Comparison of RHEED patterns of CF_4 on graphite above and below the wetting transition at 37 K. (**a**) 50 monolayers at 40 K. The modulated streaks indicate complete wetting. (**b**) 50 monolayers at 25 K. Only a spot pattern is visible indicating partial wetting

sharp spots close to the streaks indicating that a partial wetting system has formed with islands of 3D crystallites sitting on top of two to four uniform layers of film.

This sequence is interpreted in the following way: the sudden disappearance of the pattern when the third layer is added clearly shows that the 2D bilayer is undergoing a dramatic restructuring. In the two-to-four layer regime, pronounced local strains develop as evidenced by the RHEED patterns which show some of the spots diffracted by 3D crystalites lying outside the streaks from the 2D portions of the film. The displacement of the spots indicates a 2 to 3% misfit between the 2D layers and 3D crystallites oriented parallel to the graphite surface. These strains, probably arising from a structural mismatch between the bilayer and either the thick 2D film or bulk 3D crystallites (or both), then cause clusters to form.

As more CF_4 is added the streak pattern gradually disappears and sharp spots emerge (Fig.22.5b). Presumably, at these high coverages (20 - 100 monolayers) the surface is completely covered by 3D crystallites. But when the temperature is raised above 37K the pattern changes abruptly: the sharp spot disappear and a modulated streak pattern emerges (Fig.22.5a) indicating that a wetting transition has taken place and that the 3D crystallites have been replaced by a uniform, multilayer film. Alternately heating and cooling the system through the transition produces a slight hysteresis indicative of a first-order process [22.11]. It should also be noted that the transition occurs well below 89.5 K, the triple point of bulk CF_4.

An analysis of the RHEED pattern shows that the plane spacing perpendicular to the surface is 7 ± 0.3 Å, which matches the {001} plane spacing (7.29 Å) of the alpha phase of bulk CF_4 [22.18]. But a single azimuth is not enough to determine the epitaxial orientation of the 3D crystallite islands and more work (using the new azimuth control system) will be needed before this point can be clarified.

b) LEED Measurements

Earlier it was mentioned that LEED is used to probe the structure and initial orientation (on the substrate) of the first few layers of adsorbed film. But it has other applications as well. LEED can also be employed to make equilibrium adsorption isotherm measurements. This is done by observing the attenuation of the (01) substrate spot intensity as adsorbate is added to the system at a fixed temperature. When complete wetting occurs the appearance of each new layer will cause a sharp drop in intensity, equivalent to a step in an adsorption isotherm. As many as three or four distinct steps have been seen in

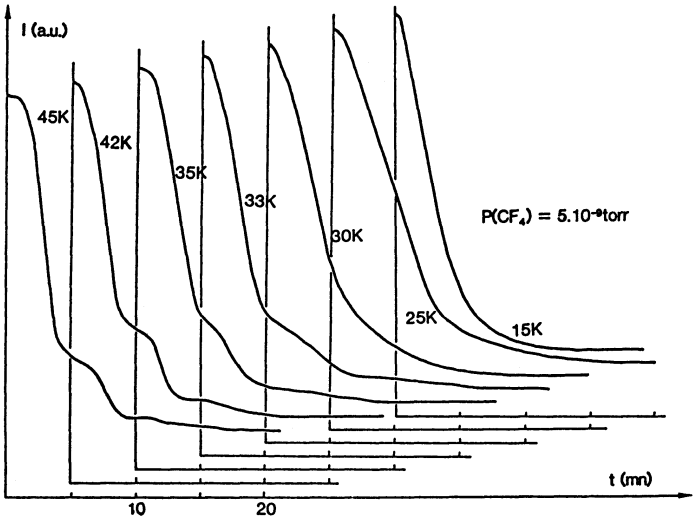

Fig.22.6. Adsorption kinetic measurements of CF_4 on graphite. Plotted is the time dependence of the graphite (01) spot intensity under a constant flux of CF_4 vapor as observed at different temperatures. The discontinuities indicate successive monolayer condensation. For reasons of clarity the curves have been spaced five minutes apart

this way [22.11,13,14]. Moreover, by plotting the logarithm of the pressure at which each step occurs against 1/T, the heats of condensation can be easily determined [22.13,14,19,20]. These are a measure of the binding energies of the individual layers, quantities thought to be important in mediating wetting and layering transitions [22.3,21-23].

All of the LEED isotherm measurements made between 51 and 58 K are consistent with the view that the CF_4 film completely wets the graphite surface in this temperature range. Unfortunately, it was not possible to extend the measurements down to temperatures near the wetting transition temperature (37 K) because the vapor pressure of bulk CF_4 is well below 10^{-10} Torr in this temperature range. It was, however, possible to obtain a set of what might be called "kinetic" isotherms by rapidly producing a given pressure within the ultrahigh vacuum chamber and then monitoring the decrease with time of the graphite (01) spot intensity [22.11] while holding the system at a fixed temperature. The resulting curves, plotted in Fig.22.6, exhibit discontinuities at higher temperatures due to layered growth. Although the technique is limited by the depth penetration of LEED to films no more than two to three layers thick, these discontinuities should provide evidence of any decrease in the thickness of the uniform part of the film with decreasing temperature. And indeed, the 30-K curve in Fig.22.6 shows no sign of the discontinuities that are evident at higher temperatures. Thus it appears that at this temperature the film

consists of 3D crystallites formed on top of one uniform layer. Assuming that this change in the character of the kinetic curves genuinely arises from a change in the structure of the overlayer and is not simply a manifestation of the reduced surface mobility of the molecules, it is reasonable to interpret the data of Fig.22.6 as indicating a wetting transition taking place somewhere in the interval between 33 and 42 K, consistent with the RHEED evidence of a transition at 37 K.

LEED studies of the CF_4/graphite system have also been made in the monolayer and multilayer regimes with results in good agreement with those obtained earlier [22.24]. The monolayer LEED pattern consists of six double spots indicating a two-domain structure. It is close to being a commensurate 2×2 hexagonal 2D solid but slightly rotated with respect to the 2×2 direction of the graphite surface. The same pattern is observed for a bilayer film. When the coverage is further increased, however, the LEED pattern disappears altogether with a corresponding increase in the background. It reappears when a fourth layer is deposited but the six doublet spots of the bilayer are then replaced by six broad spots close to the 2×2 directions. When a fifth and sixth layer are added the intensity of these spots increases further.

This evidence of a restructuring of the film above two monolayers agrees well with the RHEED experiments. We note, however, that the abrupt disappearance of long-range order occurs both above and below 37 K and is, therefore, unlikely to be related to the wetting transition. Also, one should remark that for coverages below 10 monolayers there is no way to decide from the LEED pattern alone whether the system is exhibiting complete or partial wetting behavior. Above 10 monolayers, however, the LEED patterns above and below 37 K are distinctly different. In the complete wetting regime above 37 K six broad spots are observed; below 37 K the six spots are replaced by six doublets corresponding to two hexagonal domains. Like those observed in the monolayer and bilayer systems, they are slightly rotated with respect to the 2×2 direction. The corresponding lattice parameter is 4.5 ± 0.2 Å which is close to the nearest-neighbor distance in the close-packed {001} plane of the alpha phase of solid CF_4 [22.18]. Earlier we mentioned that the LEED penetration depth is no greater than three or four layers. Since the whole surface is covered with 3D crystallites below 37 K at coverages above 10 monolayers, we have to assume that the 3D crystallites are oriented with a well-developed face parallel to the graphite surface to explain the LEED pattern. Above the wetting transition the LEED pattern of broad spots implies a uniform, layered solid film with only short-range structural order. This probably results from defects such as dislocations, stacking faults, grain boundaries, etc., in other

words, the usual mechanisms for strain accommodation in epitaxially grown overlayer films [22.25-27].

22.2.4 Summary of RHEED and LEED Investigations

Complete wetting has been shown to occur in Xe, Kr, and Ar films on graphite down to 10 K. Films of CH_4, Ne, N_2, O_2, and CF_4 on graphite exhibit partial wetting behavior, while CF_4 is found to undergo a wetting transition at 37 K. Above this temperature a multilayer 2D solid phase is formed.

The results suggest the following general conclusions:

i) In films that completely wet the surface the structural mismatch between the first two or three layers and the thick film is negligibly small, typically less than one percent.

ii) If the mismatch is greater than about two percent, considerable restructuring of the film takes place when it reaches a thickness of about two or three layers.

iii) In partial wetting systems, the 3D crystallite islands that form are epitaxially oriented on the film surface.

22.3 X-Ray and Neutron Studies of Layering Transitions

X-rays and neutrons have also been used, although not as extensively as electrons, to explore wetting behavior. All applications to date have been to layering transitions in partial wetting physisorbed systems. In this section our attention will focus primarily on one of these systems, ethylene (C_2H_4)/graphite since it has been investigated in greater detail than any of the others and is regarded as a prototype system for the study of solid-on-solid layering transitions.

The first evidence that ethylene does not completely wet graphite surfaces came from the adsorption isotherm measurements of *Menaucourt* et al. [22.28]. In 1977, when the measurements were made, the observed behavior pattern seemed bizarre and inexplicable. Now, viewed from the perspective of *Pandit, Schick*, and *Wortis's* theory of wetting [22.3], it can be recognized as typical of layering transitions in an intermediate substrate system. What *Menaucourt* et al. observed was that the isotherm below 80 K had only a single sharp step (indicating formation of a single monolayer) and then the vapor pressure rose rapidly to its bulk value. Between 80 and 98 K, however, two steps appeared and above 98 K the number increased to three. Heating the system above its triple point temperature, 103.8 K, caused the sharp steps to broaden and ultimately

disappear indicating that the film thickness had then begun to increase smoothly. From analysis of their measurements *Menaucourt* et al. deduced the critical points T_{nC} of the three layering transitions to be $T_{1C} = 114.2$ K, $T_{2C} = 119$ K, and T_{3C} about 116 K.

Later *Larese* and *Rollefson* [22.29] using the minimum of the nuclear magnetic resonance (NMR) spin-lattice relaxation time as the indication of melting, traced out the solid-liquid boundary of the C_2H_4 / graphite monolayer and bilayer phases. At coverages below 0.81 monolayers the film was found to melt at a fixed temperature of 69 K. Above 0.81 monolayers the melting temperature was seen to increase rapidly; then, at coverages above 1.1 monolayers, it restabilized at 89 K. Large spin-lattice relaxation times, indicating an orientationally disordered solid, were observed in the solid phase down to 55 K. At all coverages below 1.3 monolayers, the film signal strength increased with coverage. Above 1.3 monolayers, however, it no longer changed. And at very high coverages (10 monolayers) the signal was seen to exhibit both the short decay time and the temperature dependence of the signal from bulk ethylene. It was inferred from this that at low temperatures, after approximately 1.3 monolayers of film were deposited on the surface, a bulk solid phase started to form.

22.3.1 Experimental Methods

a) X-ray Spectrometers

Two different X-ray spectrometers were employed for the investigation of ethylene films on graphite. At the Massachusetts Institute of Technology, a relatively low-resolution, 12-KW, rotating anode spectrometer like the one shown schematically in Fig.22.7a was used [22.30]. In this spectrometer slits define the beam divergence before the graphite crystal monochromator and between the monochromator and sample, while Soller slits determine the angular acceptance between the sample and the NaI detector. Typically, the spectrometer is operated with X-rays of wavelength 1.54 Å and provided a longitudinal resolution of 0.012 $Å^{-1}$ (hwhm).

The high-resolution measurements were made at Beamline VII-2 at the Stanford Synchrotron Radiation Laboratory using a configuration like that shown in Fig.22.7b [22.31]. In this arrangement X-rays are emitted from an eight-pole wiggler, then focused by a platinum coated, glancing angle mirror and monochromated by an asymmetrically cut, Ge{111} double crystal monochromator. After scattering from the sample and reflection by a Ge{111} crystal analyzer, the X-rays are detected by a NaI scintillation counter. Slits limit the in-

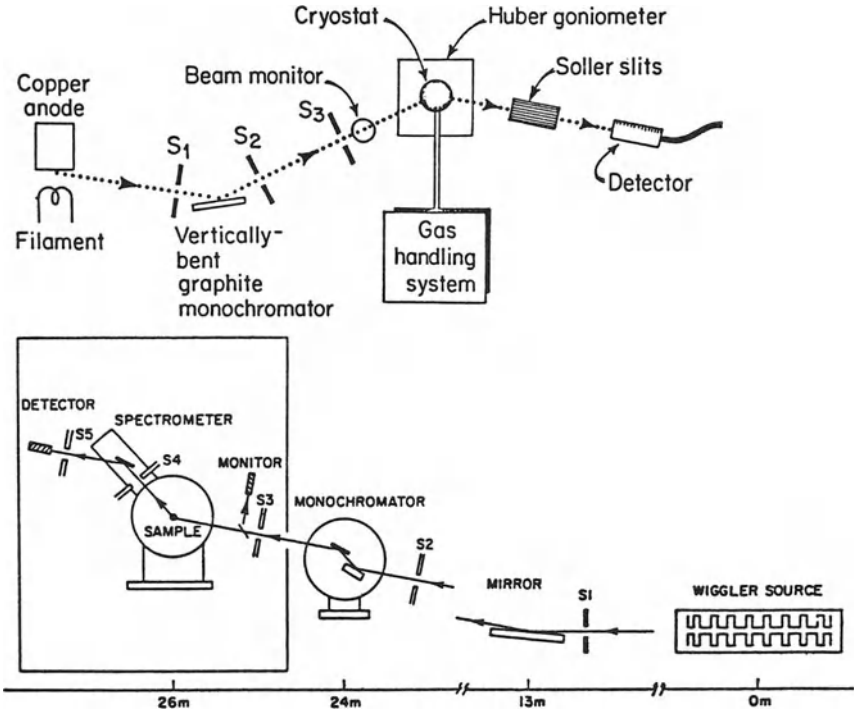

Fig.22.7a,b. Schematic representations of X-ray spectrometers used for film studies. (**a**) Rotating anode spectrometer. (**b**) Synchrotron source spectrometer

cident and scattered beam divergences. All synchrotron source measurements were made with X-rays of 1.742 Å wavelength and with a longitudinal resolution of 5×10^{-4} Å^{-1} (hwhm).

b) Neutron Spectrometers

Most of the neutron scattering work to date on layering transitions has been done with triple-axis spectrometers of the type shown in Fig.22.8. In these instruments Soller collimators define the beam divergence in front of the monochromating crystal, between monochromating crystal and sample, between sample and analyzing crystal, and between analyzing crystal and BF_3 or ^{3}He detector. Most often, pyrolytic graphite crystals are employed as monochromators and analyzers. Since the scattering of interest in layering experiments is elastic in nature, the spectrometers are generally operated in the elastic configuration, i.e., with the analyzing section set to accept only elastically scattered neutrons, although sometimes measurements are made in the two-axis mode with the analyzer crystal removed and the analyzer section aligned with the detector.

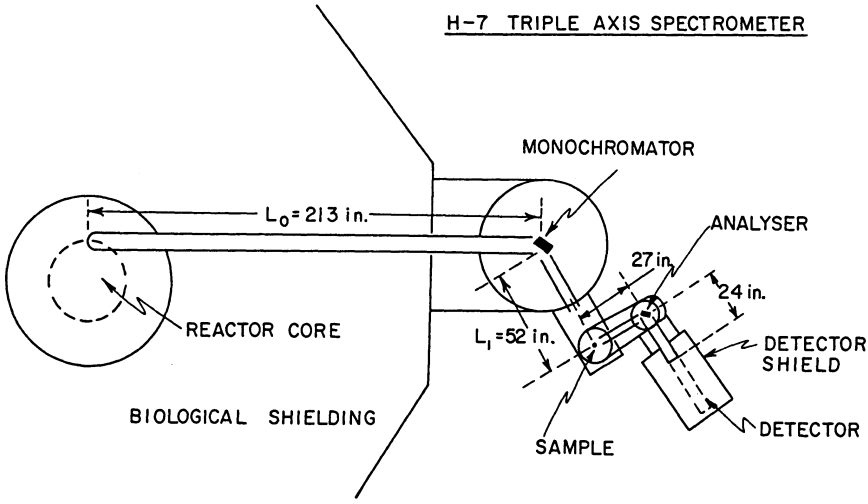

Fig.22.8. Schematic representation of a neutron triple-axis spectrometer

Most measurements are made with 2.4 Å neutrons using a pyrolytic graphite filter to remove higher order (shorter wavelength) contamination from the beam. Scattering vector resolution is typically in the range from 0.012 to 0.018 $Å^{-1}$.

c) Samples

In the X-ray studies, loosely packed vermicular graphite is the substrate of choice because it has a large specific area, no significant preferred orientation, and a surface coherence length in the neighborhood of 500 Å [22.30]. For neutron studies a slightly more compressed vermicular graphite is preferred because a larger surface area per unit volume is needed to obtain satisfactory scattered intensities. (As a general rule, overlayer atoms have to constitute about 0.1% or more of the total number in the system if the substrate is to be satisfactory for neutron measurements.) In the X-ray experiments, surface areas are usually determined from krypton isotherm measurements. Nitrogen isotherms are more often used for the neutron measurements. In either case, unit coverage is defined as the amount of gas necessary to cover the basal plane surface with a $\sqrt{3} \times \sqrt{3}$ commensurate monolayer.

All X-ray studies of adsorbed ethylene were made with non deuterated C_2H_4, as were the quasi-elastic neutron scattering measurements. However, deuterated ethylene (C_2D_4) was used for the neutron diffraction measurements since it is a more effective coherent scatterer.

d) Diffraction from 2D Powders

Detailed discussions of the diffraction profiles arising from scattering by 2D crystals can be found in the literature [22.32,33]. Here we will give only a

brief outline of the factors underlying coherent (Bragg) reflection in 2D crystalline powder samples.

As was noted above, the reciprocal lattice of an ordered 2D array consists of a set of rods perpendicular to the crystal plane. Defining the scattering vector $\mathbf{Q} = \mathbf{k}_i - \mathbf{k}_f$, where $\mathbf{k}_i$ and $\mathbf{k}_f$ represent, respectively, the wave vectors of the incident and scattered photons (or neutrons), the condition for Bragg reflection by a 2D crystal reduces to the simple statement that $\mathbf{Q}$ must terminate on a reciprocal lattice rod. In a powder composed of 2D crystallites there will be a minimum value of $\mathbf{Q}$ that will satisfy this condition. This will occur in crystallites with planes oriented parallel to $\mathbf{Q}$; for other crystallites titled at progressively larger angles with respect to $\mathbf{Q}$, the Bragg condition will only be satisfied for increasingly larger values of the scattering vector. This leads to a characteristic "sawtooth" lineshape—the identifying feature of Bragg reflection from 2D powders— with the peak position determined by the spacing between the lines of diffracting atoms, the leading edge width by the range of spatial correlation in the crystallites, and the shape of the trailing edge by the orientational distribution of crystallites within the powder. Figure 22.9 shows a typical 2D diffraction profile: the (10) X-ray reflection from a commensurate $\sqrt{3} \times \sqrt{3}$ Kr monolayer on graphite. The solid line is a powder averaged, finite-size-limited (500 Å), Gaussian lineshape [22.34] folded with the instrument resolution. In this particular example, the resolution is smaller than the separation between experimental points.

When the 2D crystallites are composed of a pair of commensurate layers of atoms rather than a single layer, interference effects can significantly alter the diffraction profile. If the overlayer is a close-packed bilayer, as is

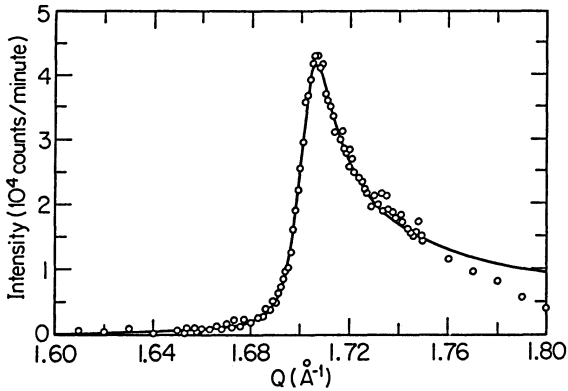

Fig.22.9. X-ray diffraction profile of a commensurate Kr monolayer measured at the Stanford Synchrotron Laboratory. A graphite background of ~9000 cts/min has been subtracted. In the interest of clarity not every data point is shown in this and subsequent X-ray profiles. The solid line is a Gaussian profile fitted to the data as described in the text

often the case, the width of the leading edge will remain the same but scattered intensity will be shifted out from the peak to larger values of Q, making the profile appear flattened compared to its single layer equivalent. Examples of experimentally observed monolayer and bilayer powder diffraction profiles can be found in [22.31].

In both X-ray and neutron measurements the diffraction profiles of the overlayer films are obtained by taking the difference between scattered intensities observed with and without the adsorbate in the sample cell. Corrections for absorption have also to be made to the X-ray (but not the neutron) data.

e) Samples and Thermometry

Since neither X-rays nor neutrons are strongly attenuated in passing through small amounts of vapor, and since both probes are normally used with samples of such large specific area that surface contamination is not a major problem, it is seldom necessary to maintain ultrahigh vacuum conditions in the region traversed by the beam. Typically, thin-walled cylindrical beryllium cells are used for the X-ray experiments while for neutron measurements cylindrical aluminum cells with walls about 0.5 mm thick are employed. Normal procedure is to bake the graphite (or other) substrate material in vacuum at high temperature to remove surface contaminants and then load it into the cells under an inert gas atmosphere. Access for the adsorbate—usually introduced at a temperature near the upper end of the (bulk) liquid range—is provided by thin-walled capillaries attached to the cells.

In all cases discussed here, the cells were clamped to the refrigeration blocks of Displex, closed-cycle helium refrigerators. This allowed the samples to be held at any fixed temperature between 12 and 300 K. Except for the high-resolution X-ray measurements made at the Stanford Synchrotron Laboratory (where Si diodes were employed), calibrated Pt and Ge resistance thermometers fastened to the cells were used for all temperature measurements. With thermometers of this type reproducibility is typically of the order of ± 0.01 K although absolute values of the temperature are probably not determined to an accuracy of better than ± 0.1 K.

22.3.2 X-Ray and Neutron Studies of Layering Transitions in Ethylene Adsorbed on Graphite Basel Plane Surfaces

In Figure 22.10 we show a representative set of neutron diffraction scans taken with ethylene coverages between 0.75 and 1.5 monolayers [22.35]. The low coverage scan is typical of all low-temperature ethylene/graphite scans below 0.83 monolayers. It shows a pair of typical asymmetric 2D peaks at 1.56 and

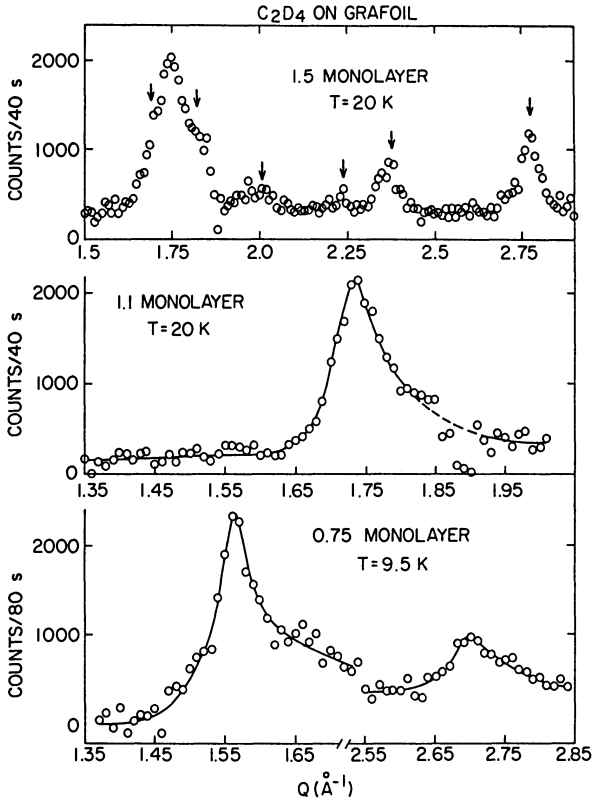

Fig.22.10. Low-temperature neutron diffraction patterns from ethylene on graphite at various coverages. The solid lines are Gaussian lineshape fits to the data. The arrows indicate the positions of the diffraction peaks of bulk, monoclinic-solid ethylene

2.70 Å^{-1} which can be indexed as the (10) and (11) reflections from an incommensurate, close-packed, triangular-lattice solid with a nearest-neighbor distance of 4.65 Å. Both the neutron and NMR data indicate that this phase, which has come to be known as the LD solid, melts at a constant temperature of 68 K. Behavior of this type is typical of a 2D solid-liquid-vapor triple point such as is found in the Xe/graphite system [22.36,37]. Recent evidence obtained by *Chan* and his collaborators from heat capacity measurements [22.38] shows that there is also a coexisting 2D liquid-vapor phase boundary in the ethylene/graphite system in this coverage regime extending from 68 K, the triple point temperature, up to 110 K. The latter value is in reasonable agreement with the estimate by *Menaucourt* et al. [22.28] that $T_{1C} = 114$ K. Thus, below a coverage of 0.83 monolayers the adsorbed film forms a coexisting 2D solid and vapor phase up to 68 K; then it melts into a co-existing 2D liquid and vapor phase with a critical point temperature of 110 K.

Above 0.83 monolayers the peaks at 1.56 and 2.70 Å^{-1} are still in evidence but a new reflection appears at 1.72 Å^{-1} showing that the higher coverage film consists of LD solid coexisting with a second, higher density solid phase.

Assuming the new phase—which has come to be known as the HD solid—also has a close-packed structure, the observed peak can be indexed as the (10) reflection from an incommensurate, triangular-lattice solid with a nearest-higher distance of 4.22 Å. At coverages above 1.05 monolayers only the 1.72 $Å^{-1}$ peak remains (see Fig.22.10) indicating complete transformation to a film with a density matching that of the assumed HD triangular-lattice structure.

Configuration energy calculations and steric considerations suggest that the C=C bond (which defines the long axis of the ethylene molecule) is parallel to the surface in the LD phase and that the LD-to-HD transition involves reorientation of the C=C bond from the parallel to the perpendicular direction. Similar transition have been observed in both O_2 [22.39] and N_2 [22.40] overlayers on graphite.

At coverages above 1.05 monolayers, new, symmetric, 3D diffraction peaks begin to appear but the intensity of the 1.72 $Å^{-1}$ peak remains the same. The new peaks index as reflections of the monoclinic phase of bulk-solid ethylene [22.41] indicating coexistence of the HD solid monolayer with bulk ethylene. The neutron data thus directly confirm the isotherm and NMR studies from which it had earlier been inferred that bulk-solid ethylene forms at low temperatures in preference to a second layer. It should be noted that the appearance of bulk solid is also seen in the X-ray studies of ethylene on graphite [22.42].

When the LD solid is heated, the neutron data show that it expands slightly and then melts at 67 K as indicated by the NMR measurements. There is evidence of a slight thermal expansion of the HD solid on heating as well. At 72 K, however, an abrupt change is seen in the higher coverage diffraction pattern: along with the HD peak at 1.72 $Å^{-1}$, a new Bragg peak appears at 1.64 $Å^{-1}$ indicating formation of a lower density, incommensurate solid phase. This phase is believed to be the LD solid phase, compressed—at the higher coverage—to a higher density. Earlier referred to in the literature as the ID solid phase, it has more recently been given the name "compressed LD solid phase" since it is thought to evolve continuously at higher coverages and temperatures by compression of the LD solid. With further heating, the compressed LD solid is seen to expand slightly and then melt in the temperature range 85-90 K as observed in the NMR experiments. The HD-solid to compressed-LD-solid phase transition shows a hysteresis of about 5K. There is also evidence that the HD and compressed LD solids coexist. Thus, the phase change appears to be a first-order, two-dimensional, incommensurate-solid to incommensurate-solid transition.

Quasi-elastic neutron scattering measurements [22.43] show that molecules in the LD phase begin to rotate freely at about 30 K. Below this temperature,

some type of orientational ordering process sets in but no evidence of an orientationally ordered phase is seen in diffraction data. This has led to the suspicion that the low-temperature state is one of "frozen-in" orientational disorder as suggested by recent molecular dynamics simulations [22.44]. These simulations also suggest that the HD phase forms an orientationally ordered herringbone structure between 12 and 48 K. No evidence of such ordering has ever been found in neutron diffraction measurements. However, it is known from quasi-elastic scattering measurements that molecular rotation in the HD phase becomes too slow to be observed at low temperatures.

From what has been said thus far, it can be deduced that the single step in the isotherm at 77 K—measured by *Menaucourt* et al. [22.28] represents at first the formation of a coexisting 2D liquid and vapor film. As the coverage is increased further, it also includes a sequence of successive transitions to a pure 2D liquid, to a coexisting 2D liquid and compressed LD solid, and, finally, to a pure compressed-LD-solid monolayer. In the temperature range between 80 and 98 K, where two-step isotherms were observed, the same transition sequence must have been followed for the first step. The X-ray scans of Fig.22.11 show what happens on further increasing the coverage. At 0.92 monolayers, only the (10) peak from the compressed LD solid is evident. But when the coverage is increased to 1.55 monolayers the diffraction pattern changes to the more flattened form characteristic of a bilayer. Additional structure also appears, which is identifiable, in the higher coverage scans, as coming from bulk, monoclinic-solid ethylene. Thus the X-ray scans show clearly the sequence of transitions from monolayer to bilayer to 3D solid. It should be noted that the solid lines fitted to the three higher coverage scans in Fig.22.11 were obtained assuming a primary 2D scattering vector $Q_{10} = 1.58$ Å^{-1} and a close-packed, triangular-lattice bilayer film plus bulk ethylene. Although, the quality of fit is good and clearly identifies the film part of the scattering as arising from a bilayer solid, it should not be viewed as providing a definitive determination of the bilayer structure.

Another interesting and informative way to study layering behavior is to place sufficient ethylene in the cell to assure a 3D as well as 2D contribution to the scattering and then monitor the temperature dependence of the 3D Bragg reflections. Figure 22.12 shows a sequence of such scans, made with X-rays, in which the individual layering transitions are clearly evident as sharp drops in intensity as ethylene is shifted from the bulk to the film phase. The drop at 75 K is the monolayer to bilayer transition. Although not as well resolved, the transition from bilayer to trilayer at 98 K is also evident. Layering transitions like those seen here should represent triple points

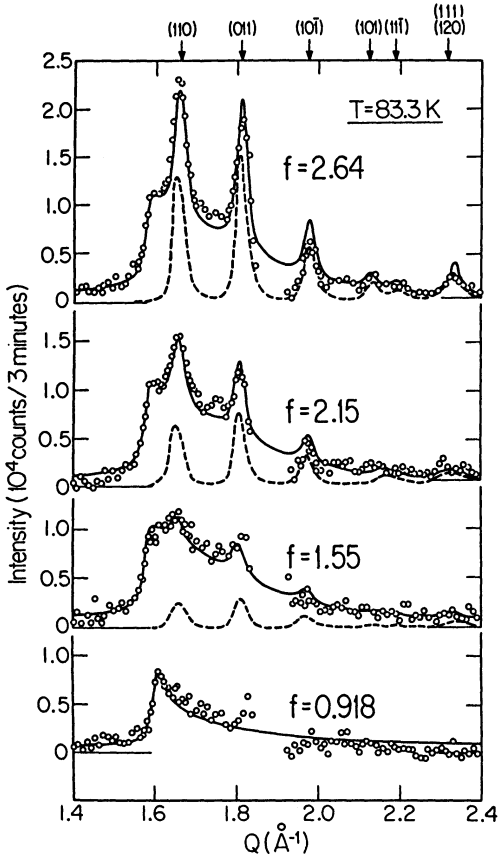

Fig.22.11. X-ray diffraction profiles of ethylene on graphite at a temperature of 83.3 K obtained with the rotating anode X-ray spectrometer. The solid lines were fitted assuming contributions from both 2D and 3D solid as explained in the text. Data in the region from 1.85 to 1.95 Å^{-1} are not plotted because of distortions introduced by the intense scattering from the graphite substrate (002) reflection

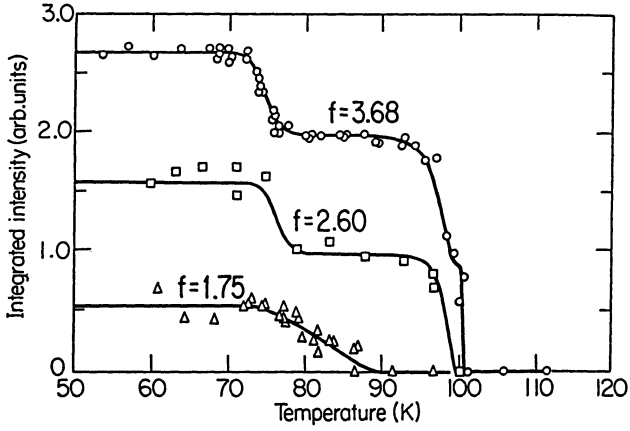

Fig.22.12. Integrated intensity of X-ray peaks from bulk, monoclinic-solid ethylene at three different coverages and various temperatures. The solid lines are guides to the eye. The ordinate scale was normalized by assigning a value of 2.7 to the intensity of the coverage 3.68 observed below 70 K

with two film phases and a bulk phase coexisting. Thus, each such transition would be expected to occur at a fixed pressure and temperature. This is not, in fact, what is observed. The layering transition temperatures decrease slightly as more material is added and each transition is spread out over a finite temperature interval. Furthermore, scattering from 3D crystallites appears at pressures below the saturated vapor pressure. These extraneous effects are thought to arise primarily from capillary condensation although both surface inhomogeneities and the broad distribution of particle sizes in the substrate could also be contributing factors.

Determining what happens after the third layering transition takes place, i.e., at temperatures above 98 K, is less straightforward. Adsorption isotherms measured at temperatures of 103 K and 105.8 K, i.e., just below and just above the bulk-solid triple point temperature of $T_t = 103.75$ K, appear nearly identical: they show three steps and then, after the third step, the definitive indication of complete wetting behavior—a smooth, asymptotic increase in pressure towards the bulk coexistence value. No sign of a fourth layering transition could be found even though a warming scan (like that of Fig.22.12), made with the equivalent of six monolayers of ethylene in the cell, showed bulk-solid ethylene to be present right up to T_t. There was, however, clear evidence of hysteretic behavior, i.e., X-ray profiles obtained as part of an adsorption isotherm at 103 K showed no indication of the coexisting bulk-solid phase seen in the above-mentioned warming scan. Even with the equivalent of eight monolayers of ethylene in the cell, only a liquid-like structure factor appeared. But, from the perspective of *Pandit* et al. [22.3] what is really of interest is not the hysteresis, which is an expected feature of first-order phase changes, but rather the fact that a transition from partial wetting behavior below T_t to complete wetting behavior above T_t could take place without the system ever exhibiting more than three layering transitions. We can only conjecture that a shift to some type of prewetting behavior in the temperature interval between 98 and 103 K preempted further layering transitions. A similar effect was observed in the CCl_4/graphite system [22.45] and may, in fact, be characteristic of triple point wetting.

One final question remains to be addressed: at what temperature exactly does the transition to complete wetting occur? Hysteresis makes it difficult to give a precise answer but if the disappearance of the coexisting bulk phase is used as a criterion of complete wetting, then in the ethylene/graphite system complete wetting begins either at, or very close to, 103.75 K, the bulk triple point temperature.

22.3.3 X-Ray and Neutron Studies of Layering Transitions in Co-Adsorbed Xenon and Ethylene Films on Graphite

In attempting to come to grips with the details of the wetting process, our attention has thus far been centered on how different adsorbates behave on graphite basal planes. But there is another potentially interesting way to approach the problem: it is also possible to focus one's attention on a given adsorbate and see how the presence of a second adsorbate influence its wetting and layering behavior. In this section we will review briefly what has recently been learned about the influence of xenon on the layering transitions of ethylene [22.46].

Xenon is known to form a stable, triangular-lattice solid monolayer on graphite surfaces [22.36,47]. Like other incommensurate solid monolayers, the xenon solid is reasonably compressible: depending on coverage and temperature the nearest-neighbor distance (a_{nn}) can expand to as much as 4.56 Å (Q_{10} = 1.59 $Å^{-1}$) or be reduced to as little as 4.32 Å (Q_{10} = 1.68 $Å^{-1}$). But even at the highest coverages the solid cannot quite be forced into $\sqrt{3} \times \sqrt{3}$ registry, i.e., a_{nn} cannot be reduced to 4.26 Å (Q_{10} = 1.70 $Å^{-1}$). Solid xenon monolayers melt at about 100 K at all coverages between 0.1 and 0.73 monolayers; above 0.73 monolayers the melting temperature rises, reaching 140 K at unit coverage and continuing to higher temperatures as the coverage is increased further. The xenon/graphite system has the distinction of being one of the few known solid-on-solid systems that exhibits complete wetting. Since it shows every evidence of being extremely stable, the adsorbed xenon solid has long been assumed to act as an inert substrate for other, less tightly bound overlayers. All that was thought to be necessary to maintain a xenon underlayer film was that the system temperature be kept well below the xenon monolayer melting temperature. Indeed, xenon "preplating" has often been used for surface modification. But as will soon be evident, the xenon layer can, and—in some circumstances—clearly does, play a far more active role than had originally been imagined.

Exploring fully the properties of two-component overlayers requires that the behavior of each component be investigated separately. This can be done for the xenon-ethylene system by combining the results of X-ray and neutron diffraction measurements. X-rays are strongly scattered by xenon but not by ethylene; for neutrons, exactly the opposite situation prevails. Thus, xenon diffraction peaks will be relatively prominent on X-ray scans and ethylene peaks much less evident, while on neutron scans (deuterated) ethylene peaks will be prominent and xenon peaks almost unobservable.

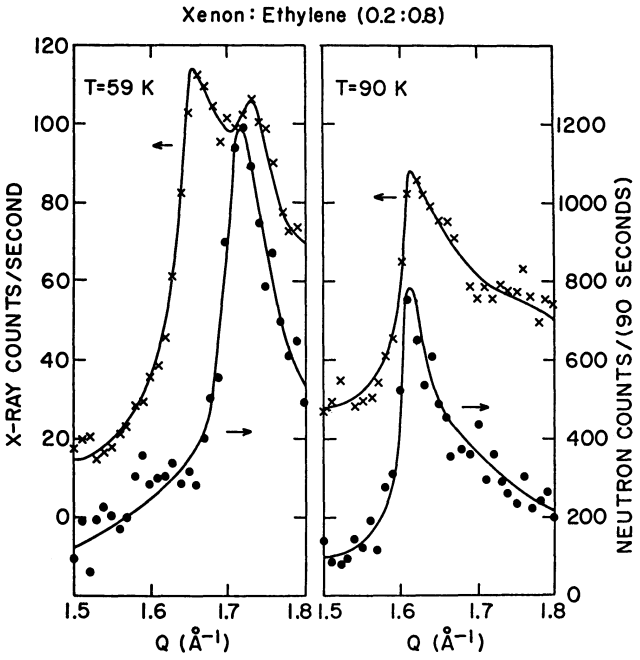

Fig.22.13. X-ray (×××) and neutron (•••) diffraction peaks from a xenon:ethylene = 0.2:0.8 monolayer. The solid lines are guides to the eye

Figure 22.13 shows X-ray and neutron diffraction data obtained from a xenon: ethylene = 0.2 : 0.8 monolayer film on graphite. Profiles like those on the left-hand side of the figure were observed at all temperature below 65 K. The X-rays show the strong, asymmetric (10) peak at 1.65 $\AA^{-1}$ typical of a solid xenon monolayer. There is also a weaker, but recognizable, ethylene peak at 1.73 $\AA^{-1}$. The neutrons, on the other hand, show only a well-defined, asymmetric 2D peak at 1.72 $\AA^{-1}$. This, as we earlier saw, is the (10) peak of the ethylene HD solid phase. [The peak at 1.73 $\AA^{-1}$ in the X-ray scan is the (10) HD ethylene peak. It appears at a slightly larger value of Q because the film is slightly more compressed.] The right-hand side of Fig. 22.13 shows X-ray and neutron scans typical of those observed above 69 K. Here, nearly identical X-ray and neutron peaks appear at 1.62 $\AA^{-1}$. Evidently, the ethylene film has undergone the same HD-solid-to-compressed-LD-solid transition observed in the pure ethylene overlayer. This, in itself, is not unexpected. What is surprising, however, is that at the higher temperature the xenon and ethylene films appear to have identical structures. Moreover, investigation shows that the HD-solid-to-compressed-LD-solid phase transition shifts monotonically to lower temperatures with increasing xenon

concentration. And, in addition, it is found that the high-temperature solid phase melts at a temperature some 6-10 K higher than the equivalent pure compressed-LD-solid ethylene phase. Thus, at low temperatures it appears that there is a separation of the monolayer into either pure xenon and pure ethylene solid phase or (more likely) into xenon-rich and ethylene-rich solid phases. And at higher temperatures the evidence suggests that the system undergoes a mixing transition, possibly coinciding with the HD-solid-to-compressed-LD-solid phase transition, which converts the monolayer into a mixed xenon-ethylene solid phase with the same—or nearly the same—structure as the equivalent pure xenon and ethylene phases. Indeed, it is quite possible that the essentially identical structures of the pure xenon and compressed-LD-solid ethylene phases are the reason for the formation of a mixed solid phase.

Figure 22.14 shows diffraction data obtained from a higher-coverage xenon: ethylene = 1 : 1 overlayer on graphite. On the left the 40-K X-ray profile shows a compressed xenon (10) monolayer peak at 1.70 $\mathring{A}^{-1}$. The structure on its leading edge is identifiable in the neutron scan as the (110) peak from bulk

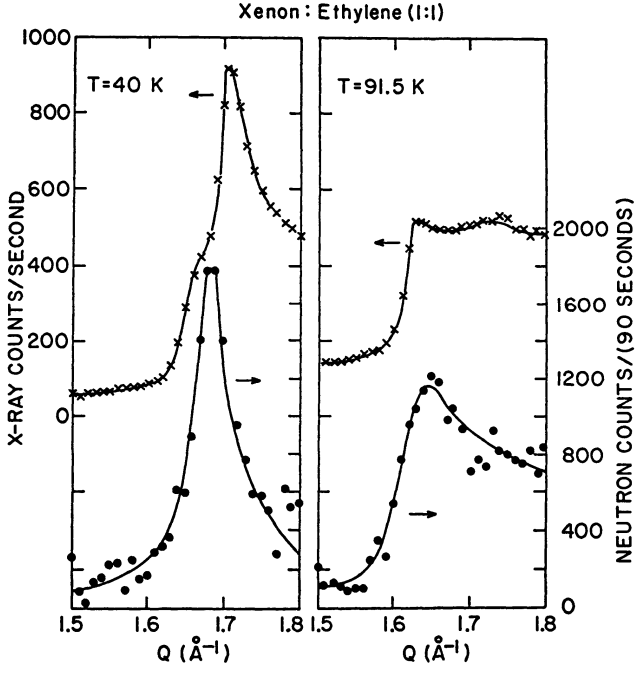

Fig.22.14. X-ray (×××) and neutron (•••) diffraction peaks from a xenon: ethylene = 1:1 bilayer. The more flattened profiles on the right (like those in Fig.22.11) identify the peaks as originating from 2D solid bilayers. The more symmetric neutron peak on the left originates from 3D bulk monoclinic-solid ethylene. The solid lines are guides to the eye

monoclinic ethylene. At this higher coverage and relatively low temperature 3D bulk ethylene evidently coexists with a commensurate or nearly commensurate monolayer film that is either a highly compressed pure xenon or (more likely) a xenon-rich 2D solid. Ethylene seems not to wet the xenon covered graphite surface, at least under these conditions. As before, striking changes take place in the film at higher temperatures. The scans at 91.5 K plotted on the right show markedly asymmetric peaks at 1.64 $\AA^{-1}$. Noticeably flatter than the monolayer peaks of Fig.22.13, the profiles strongly suggest (see also the profiles of Fig.22.11) the formation of a structurally ordered bilayer. The flattened peaks first appear at 82 K and persist to about 95 K. Since the X-ray and neutron scans show peaks of nearly identical shape, it is clear that both xenon and ethylene are present in each layer. Thus a layering and, possibly at the same time, a mixing transition appears to have taken place somewhere below 82 K, converting the system from coexisting 3D solid ethylene and 2D xenon (or xenon-rich) phases into what seems to be a mixed bilayer. This bilayer phase is found to melt at about 95 K, i.e., some 6K higher than the pure ethylene bilayer but nearly 60 K lower then its pure xenon equivalent. As would be expected, the leading edge of the bilayer peak begins to broaden at the onset of melting. But when the coverage is increased, something quite surprising occurs: a peak appears at 1.73 $\AA^{-1}$. This structure, evident in both X-ray and neutron scans, is as yet unexplained. It is probably the origin of the slight bump at 1.73 $\AA^{-1}$ in the high-temperature X-ray profile of Fig.22.14.

Investigation of subsequent layering transitions is most conveniently done, as before, by monitoring the intensities of the bulk-ethylene diffraction peaks. The data in Fig.22.15 compare the temperature dependence of the intensity of the {200} neutron diffraction peak of bulk monoclinic-solid ethylene in a xenon : ethylene = 1 : 6 system on graphite with that observed in a 0 : 6 system, i.e., in an equivalent system containing ethylene alone. In the 1 : 6 system there is an abrupt change in slope at about 68 K when the transition from a pure xenon monolayer to a mixed bilayer takes place. A similar change in slope occurs at about 73 K in the 0 : 6 system indicating, in this case, formation of a pure ethylene bilayer. The data are not of sufficient quality to identify third layer formation, which certainly occurs in the 0 : 6 system (see Fig.22.14), and probably takes place in the 1 : 6 system as well. In both systems the bulk phase melts at 104 K and complete wetting begins. Curiously, the monolayer to bilayer transition, aside from a slight shift in temperature, seems little affected by the fact that, in the first case, it starts from a layer of pure (or nearly pure) xenon and, in the second case, from pure ethy-

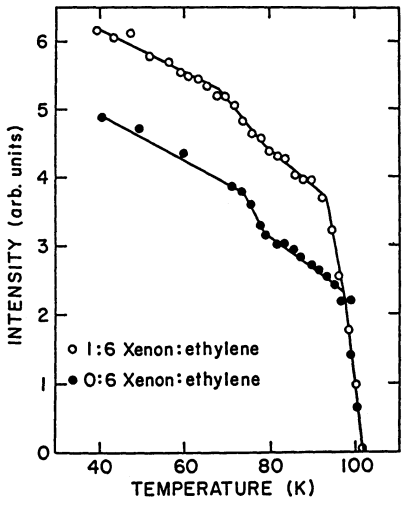

Fig.22.15. Temperature dependence of the diffracted neutron intensity from the (200) peak of bulk monoclinic ethylene in xenon:ethylene = 1:6 and 0:6 overlayers on graphite. The sharp breaks occur at layering transitions. The solid lines are guides to the eye

lene and that the bilayer, when it appears, seems to be made up, in the first instance, of a mixture of xenon atoms and ethylene molecules and, in the second instance, of ethylene molecules alone. Moreover, the transition to complete wetting behavior seems completely unaffected. In view of the large differences in the cohesive and adhesive interaction energies of the xenon and ethylene components of the film, such behavior is, to say the least, quite unexpected.

22.3.4 Summary of X-Ray and Neutron Investigations

Ethylene/graphite has long been thought to be the prototype partial wetting system and, indeed, it shows many of the characteristics predicted for such systems by *Pandit* et al. [22.3]; in particular, it shows a sequence of layering transitions occurring with increasing temperature. The layering transitions are themselves complex processes and sometimes involve several overlayer phases. Only three layers are observed to form. Further layering, therefore, appears to be prevented by some change in the properties of the system as it approaches the bulk triple point temperature. Above the triple point temperature, complete wetting occurs.

Introducing a monolayer of xenon into the ethylene-on-graphite system dramatically alters the properties of individual layers that form on the surface but has surprisingly little effect on the layering transitions themselves or on the ultimate wetting behavior of the system. In spite of the fact that the first layer in the two-component system is pure xenon, not ethylene, and the bilayer appears to be a xenon-ethylene composite, not separate xenon and ethy-

lene layers, the layering transitions occur very much as in the pure system. And, as in the pure system, the transition to complete wetting behavior takes place at the bulk-ethylene triple point temperature. Even though the cohesive and adhesive interaction energies of the two components are different enough to produce phase separation at low temperatures, layering and wetting appear little affected.

References

22.1 J.G. Dash: Phys. Rev. **B15**, 3136 (1977); C. Ebner, W.F. Saam: Phys. Rev. Lett. **38**, 1486 (1977); J.W. Cahn: J. Chem. Phys. **66**, 3667 (1977). A complete discussion of layering and wetting phenomena is given by C. Ebner: this volume
22.2 D.E. Sullivan: Phys. Rev. **B20**, 3991 (1979)
22.3 R. Pandit, M. Schick, M. Wortis: Phys. Rev. **B26**, 5112 (1982)
22.4 R. Pandit, M.E. Fisher: Phys. Rev. Lett. **51**, 1772 (1983)
22.5 E. Bauer: in *Techniques of Metal Research*, ed. by R.F. Bunshah, Vol.2, Pt.2 (Interscience, New York 1969) p.201
22.6 D.P. Woodruff: in *Chemical Physics of Solid Surfaces and Heterogeneous Catalysis*, ed. by D.A. King, D.P. Woodruff, Vol.1 (Elsevier, Amsterdam 1981) p.81
22.7 R. Kern, G. Lelay, J.J. Metois: in *Current Topics in Material Science*, ed.by Kaldis, Vol.3 (North Holland, Amsterdam 1979) p.174
22.8 J.L. Seguin, J. Suzanne, M. Bienfait, J.G. Dash, J.A. Venables: Phys. Rev. Lett. **51**, 122 (1983)
22.9 M. Bienfait, J.L. Seguin, J. Suzanne, E. Lerner, J. Krim, J.G. Dash: Phys. Rev. **B29**, 983 (1984)
22.10 J.A. Venables, J.L. Seguin, J. Suzanne, M. Bienfait: Surf. Sci. **145**, 345 (1984)
22.11 J. Suzanne, J.L. Seguin, M. Bienfait, E. Lerner: Phys. Rev. Lett. **52**, 637 (1984); J.M. Gay, M. Bienfait, J. Suzanne: J. Phys. (Paris) **45**, 1497 (1984)
22.12 J. Krim, J.M. Gay, J. Suzanne: to be published
22.13 J. Unguris, L.W. Bruch, E.A. Moog, M.B. Webb: Surf. Sci. **87**, 415 (1979); **109**, 522 (1981)
22.14 R.D. Diehl, S.C. Fain, Jr.: J. Chem. Phys. **77**, 5065 (1982)
22.15 S. Calisti, J. Suzanne, J.A. Venables: Surf. Sci. **115**, 455 (1982)
22.16 S. Ino: J. Appl. Phys. (Japan) **16**, 891 (1977)
22.17 J.A. Venables, J. Derrien, A.P. Janssen: Surf. Sci. **95**, 411 (1980)
22.18 D.N. Bol'Shutkin, V.M. Gasan, A.I. Prokhvatilov, A.I. Erenburg: Acta Crystallogr. **B28**, 3542 (1972)
22.19 Y. Larher: J. Chem. Soc. Faraday Trans. **170**, 320 (1974)
22.20 J. Suzanne, M. Bienfait: J. Phys. (Paris), Colloq. **C4**, 38, 93 (1977)
22.21 F.T. Gittes, M. Schick: Phys. Rev. **B30**, 209 (1984)
22.22 R.J. Muirhead, J.G. Dash, J. Krim: Phys. Rev. **B29**, 5074 (1984)
22.23 S. Dietrich, M. Schick: Phys. Rev. **B31**, 4718 (1985)
22.24 S. Calisti: Thesis, Marseille (1981); J. Suzanne, S. Calisti: to be published
22.25 H.M. Kramer: J. Cryst. Growth **33**, 65 (1976)
22.26 J.A. Venables, J.T. Spiller: in *Surface Mobilities on Solid Materials*, ed. by Vu Thien Binh, NATO ASI series (Plenum, New York 1982)
22.27 R. Kern: in *Interfacial Aspects of Phase Transformations*, ed. by B. Mutafchiev, NATO ASI series (Reidel, Dordrecht 1982)
22.28 J. Menaucourt: Thesis, University of Nancy (1977); J. Menaucourt, A. Thomy, X. Duval: J. Phys. (Paris) **C4**, 195 (1977)

22.29 J.Z. Larese, R.J. Rollefson: Surf. Sci. **127**, L172 (1983)
22.30 R.J. Birgeneau, P.A. Heiney, J.P. Pelz: Physica (utrecht) **109**, **110B**, 1785 (1982)
22.31 D.E. Moncton, G.S. Brown: Nucl. Instrum. Methods **208**, 579 (1983)
22.32 J.K. Kjems, L. Passell, H. Taub, J.G. Dash, A.D. Novaco: Phys. Rev. **B13**, 1446 (1976)
22.33 P.W. Stephens, P.A. Heiney, R.J. Birgeneau, P.M. Horn, D.E. Moncton, G.S. Brown: Phys. Rev. **B29**, 3512 (1984)
22.34 B.E. Warren: Phys. Rev. **59**, 693 (1941)
22.35 S.K. Satija, L. Passell, J. Eckert, W. Ellenson, H. Patterson: Phys. Rev. Lett. **51**, 411 (1983)
22.36 A. Thomy, X. Duval: J. Chim. Phys. **66**, 1966 (1969); **67**, 286 (1970); **67**, 1101 (1970)
22.37 P.A. Heiney, P.W. Stephens, R.J. Birgeneau, P.M. Horn, D.E. Moncton: Phys. Rev. **B28**, 6416 (1983)
22.38 M. Chan: Private communication
22.39 P.A. Heiney, P.W. Stephens, S.G. H. Mochrie, J. Akimitsu, R.J. Birgeneau, P.M. Horn: Surf. Sci. **125**, 539 (1983)
22.40 R.D. Diehl, S.C. Fain: Surf. Sci. **125**, 116 (1983)
22.41 W. Press, J. Eckert: J. Chem. Phys. **65**, 4362 (1976)
22.42 S.G.J. Mochrie, M. Sutton, R.J. Birgeneau, D.E. Moncton, P.M. Horn: Phys. Rev. **B30**, 263 (1984)
22.43 B.H. Grier, L. Passell, J. Eckert, H. Patterson, D. Richter, R.J. Rollefson: Phys. Rev. Lett. **53**, 814 (1984)
22.44 S. Nose, M.L. Klein: Preprint (1984)
22.45 P.W. Stephens, M.F. Huth: Phys. Rev. **B32**, 1661 (1985)
22.46 S.K. Satija, M. Sutton, R.J. Birgeneau, H. Hong, L. Passell, J.P. Wicksted: unpublished data
22.47 P.A. Heiney, P.W. Stephens, R.J. Birgeneau, P.M. Horn, D.E. Moncton: Phys. Rev. **B28**, 6416 (1983)

Subject Index

Contents of **Chemistry and Physics of Solid Surfaces IV**

(Springer Series in Chemical Physics, Vol. 20)

Contents of **Chemistry and Physics of Solid Surfaces V**

(Springer Series in Chemical Physics, Vol. 35)

Springer Series in Chemical Physics

Editors: **V. I. Goldanskii, R. Gomer, F. P. Schäfer, J. P. Toennies**

A Selection:

Volume 20

Chemistry and Physics of Solid Surfaces IV

Editors: **R. Vanselow, R. Howe**
1982. 247 figures. XIII, 496 pages
ISBN 3-540-11397-5

Chemistry and Physics of Solid Surfaces IV presents selected review articles predominantly from the area of solid/gas interfaces. These articles are written by internationally recognized experts, the invited speakers of the International Summer Institute in Surface Science (ISISS). Volume IV covers the following topics photoemission, Auger spectroscopy, SIMS ellipsometry, Doppler shift laser spectroscopy, analytical electron microscopy, He ion diffraction as a surface probe, low energy electron diffraction, Monte Carlo simulations of chemisorbed overlayers, critical phenomena of overlayers, surface defects, theoretical aspects of surfaces, EELS of surface vebrations, electronic aspects of adsorption rates, thermal desorption, field desorption, surface and internal segregation.

Volume 25

Ion Formation from Organic Solids

Proceedings of the Second International Conference, Münster, Federal Republic of Germany, Septemeber 7-9, 1982
Editor: **A. Benninghoven**
1983. 170 figures. IX, 269 pages
ISBN 3-540-12244-3

The proceedings deals with the ion formation from involatile, thermally labile organic compounds. Fundamental aspects of the ion formation process as well as present applications and future trends in the analytical application are treated. In addition, instrumental as well as technological developments as time of flight instruments or liquid matrices, are described. This book will provide the reader with an authoritative guide for analytical work in the life sciences that will retain its validity for many years to come.

Volume 35

Chemistry and Physics of Solid Surfaces V

Editors: **R. Vanselow, R. Howe**
1984. 303 figures. XXI, 554 pages
ISBN 3-540-13315-1

Contents: The Molecular Surface Science of Heterogeneous Catalysis: History and Perspective. - Fourier-Transform Infrared Spectroscopy in Heterogeneous Catalysis. - Magnetic Resonance in Surface Science. - Mössbauer Spectroscopy: Applications to Surface and Catalytic Phenomena. - Heterogeneous Photocatalysis with Semiconductor Particulate Systems. - Laser Studies of Surface Chemical Reactions. - Surface Compositional Changes by Particle Bombardment. - Structure Determination of Small Metal Particles by Electron Microscopy. - Reconstruction of Metal Surfaces. - Surface Crystallography by Means of SEXAFS and NEXAFS. - Determination of Surface Structure Using Atomic Diffraction. - An Atomic View of Crystal Growth. - Ising Model Simulations of Crystal Growth. - Phase Transitions on Surfaces. - Finite Size Effects, Surface Steps, and Phase Transitions. - Recent Developments in the Theory of Epitaxy. - Angle-Resolved Secondary Ion Mass Spectrometry. - Determination by Ion Scattering of Atomic Positions at Surfaces and Interfaces. - Surface Phonon Dispersion. - Intrinsic and Extrinsic Surface Electronic States of Semiconductors. - Work Function and Band Bending at Semiconductor Surfaces. - Subject Index.

Volume 21

Dynamics of Gas-Surface Interaction

Proceedings of the International School on Material Science and Technology, Erice, Italy, July 1-15, 1981
Editors: **G. Benedek, U. Valbusa**
1982. 132 figures. XI, 282 pages
ISBN 3-540-11693-1

Contents: Scattering of Atoms from Solid Surfaces. - Characterization of Adsorbed Phases. - Spectroscopy of Surface Optical Excitations. - Surface Phonon Spectroscopy by Atom Scattering. - Index of Contributors.

Springer-Verlag
Berlin Heidelberg New York Tokyo

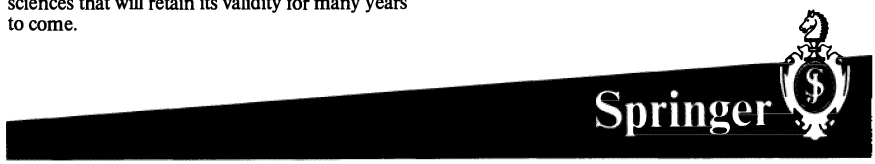

Springer Series in Chemical Physics

Editors: **V. I. Goldanskii, R. Gomer, F. P. Schäfer, J. P. Toennies**

A Selection:

Volume 9

Secondary Ion Mass Spectrometry SIMS-II

Proceedings of the Second International Conference on Secondary Ion Mass Spectrometry (SIMS II)
Stanford University, Stanford, California, USA, August 27–31, 1979
Editors: **A. Benninghoven, C. A. Evans, Jr., R. A. Powell, R. Shimizu, H. A. Storms**
1979. 234 figures, 21 tables. XIII, 298 pages
ISBN 3-540-09843-7

Contents: Fundamentals. – Quantitation. – Semiconductors. – Static SIMS. – Metallurgy. – Instrumentation. – Geology. – Panel Discussion. – Biology. – Combined Techniques. – Postdeadline Papers.

Volume 19

Secondary Ion Mass Spectrometry SIMS III

Proceedings of the Third International Conference, Technical University, Budapest, Hungary, August 30–September 5, 1981
Editors: **A. Benninghoven, J. Giber, J. László, M. Riedel, H. W. Werner**
1982. 289 figures. XI, 444 pages
ISBN 3-540-11372-X

Contents: Instrumentation. – Fundamentals I. Ion Formation. – Fundamentals II. Depth Profiling. – Quantification. – Application I. Depth Profiling. – Application II. Surface Studies, Ion Microscopy. – Index of Contributors.

Volume 36

Secondary Ion Mass Spectrometry SIMS IV

Proceedings of the Fourth International Conference, Osaka, Japan, November 13–19, 1983
Editors: **A. Benninghoven, J. Okano, R. Shimizu, H. W. Werner**
1984. 415 figures. XV, 503 pages
ISBN 3-540-13316-X

Contents: Fundamentals. – Quantification. – Instrumentation. – Combined and Stataic SIMS. – Application to Semiconductor and Depth Profiling. – Organic SIMS. – Application: Metallic and Inorganic Materials. Geology. Biology. – Index of Contributors.

Volume 44

Secondary Ion Mass Spectrometry SIMS V

Proceedings of the Fifth International Conference, Washington, DC, September 30–October 4, 1985
Editors: **A. Benninghoven, R. J. Colton, D. S. Simons, H. W. Werner**
1986. 388 figures. XXI, 561 pages
ISBN 3-540-16263-1

Contents: Retrospective. – Fundamentals. – Symposium: Detection of Sputtered Neutrals. – Detection Limits and Quantification. – Instrumentation. – Techniques Closely Related to SIMS. – Combined Techniques and Surface Studies. – Ion Microscopy and Image Analysis. – Depth Profiling and Semiconductor Applications. – Metallurgical Applications. – Biological Applications. – Geological Applications. – Symposium: Particle-Induced Emission from Organics. – Organic Applications and Fast Atom Bombardment Mass Spectrometry. – Index of Contributors.

Springer-Verlag
Berlin Heidelberg New York Tokyo